AJNR

AMERICAN JOURNAL OF NEURORADIOLOGY

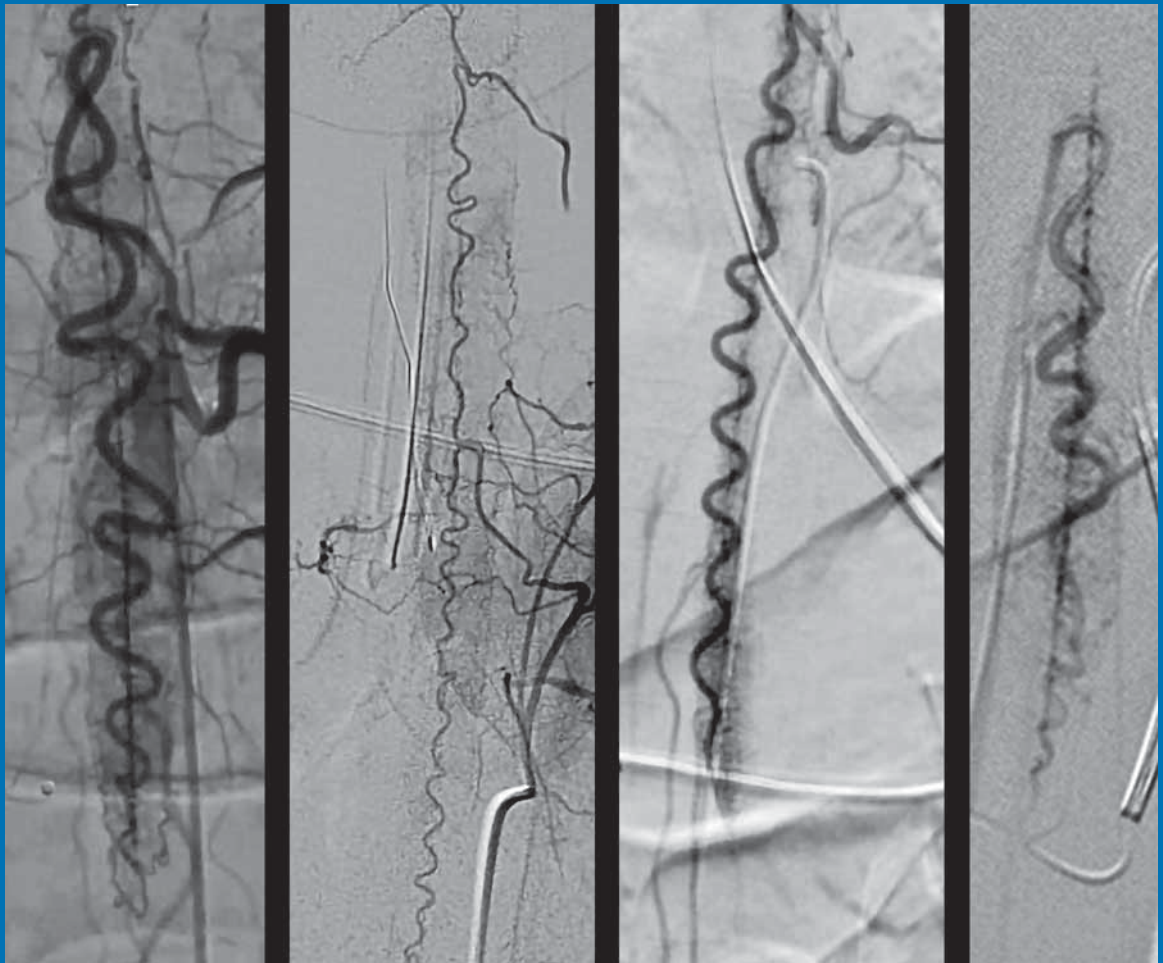THE JOURNAL OF DIAGNOSTIC AND
INTERVENTIONAL NEURORADIOLOGY

Arterioectatic spinal angiopathy of childhood

Surgical ligation of spinal CSF-venous fistulas after embolization

Heating on titanium cerebral aneurysm clips during 7T MRI

Primary intracranial pure yolk sac tumors in children

Official Journal ASNR • ASFNR • ASHNR • ASPNR • ASSR

multihance®
(gadobenate dimeglumine)
injection, 529 mg/mL

TRUST EARNED

What does seeing better with MultiHance® mean?[1-4]*

MultiHance® demonstrated significantly improved visualization and contrast enhancement of CNS lesions when compared with Gadavist® at 0.1 mmol/kg.[1†]

- The 0.1 mmol/kg dose of MultiHance demonstrated consistently better lesion visualization for all readers compared to all tested MR contrast agents.[1-4]

- 3 blinded independent readers reported superiority for MultiHance in significantly ($P = .0001$) more patients for all evaluated end points. The opinions of the 3 readers were identical for 61.9%–73.5% of the patients, resulting in values of 0.414–0.629 for inter-reader agreement.

The individuals who appear are for illustrative purposes. All persons depicted are models and not real patients.
Please see Brief Summary of Prescribing Information including Boxed Warning on adjacent page.
*MRI imaging of the CNS in adult and pediatric patients to visualize lesions with abnormal BBB or abnormal vascularity of the brain, spine and associated tissues or to evaluate adults with known or suspected renal or aorto-ilio-femoral occlusive vascular disease.

MultiHance® (gadobenate dimeglumine) injection, 529 mg/mL and
MultiHance® Multipack™ (gadobenate dimeglumine) injection, 529 mg/mL

Indications and Usage:
MultiHance® (gadobenate dimeglumine) injection, 529 mg/mL is a gadolinium-based contrast agent indicated for intravenous use in:
- Magnetic resonance imaging (MRI) of the central nervous system (CNS) in adults and pediatric patients (including term neonates) to visualize lesions with abnormal blood-brain barrier or abnormal vascularity of the brain, spine, and associated tissues and
- Magnetic resonance angiography (MRA) to evaluate adults with known or suspected renal or aorto-ilio-femoral occlusive vascular disease

IMPORTANT SAFETY INFORMATION:

WARNING: NEPHROGENIC SYSTEMIC FIBROSIS

Gadolinium-based contrast agents (GBCAs) increase the risk for NSF among patients with impaired elimination of the drugs. Avoid use of GBCAs in these patients unless the diagnostic information is essential and not available with non-contrasted MRI or other modalities. NSF may result in fatal or debilitating systemic fibrosis affecting the skin, muscle and internal organs.
- **The risk for NSF appears highest among patients with:**
  - **chronic, severe kidney disease (GFR < 30 mL/min/1.73m²), or**
  - **acute kidney injury.**
- **Screen patients for acute kidney injury and other conditions that may reduce renal function. For patients at risk for chronically reduced renal function (e.g. age > 60 years, hypertension or diabetes), estimate the glomerular filtration rate (GFR) through laboratory testing.**
- **For patients at highest risk for NSF, do not exceed the recommended MultiHance dose and allow a sufficient period of time for elimination of the drug from the body prior to re-administration.**

CONTRAINDICATIONS
MultiHance is contraindicated in patients with known allergic or hypersensitivity reactions to gadolinium-based contrast agents.

WARNINGS AND PRECAUTIONS
Nephrogenic Systemic Fibrosis: NSF has occurred in patients with impaired elimination of GBCAs. Higher than recommended dosing or repeated dosing appears to increase risk.
Hypersensitivity Reactions: Anaphylactic and anaphylactoid reactions have been reported, involving cardiovascular, respiratory, and/or cutaneous manifestations. Some patients experienced circulatory collapse and died. In most cases, initial symptoms occurred within minutes of MultiHance administration and resolved with prompt emergency treatment. Consider the risk for hypersensitivity reactions, especially in patients with a history of hypersensitivity reactions or a history of asthma or other allergic disorders.
Gadolinium Retention: Gadolinium is retained for months or years in several organs. The highest concentrations have been identified in the bone, followed by brain, skin, kidney, liver, and spleen. At equivalent doses, retention varies among the linear agents. Retention is lowest and similar among the macrocyclic GBCAs. Consequences of gadolinium retention in the brain have not been established, but they have been established in the skin and other organs in patients with impaired renal function. Minimize repetitive GBCA imaging studies, particularly closely spaced studies when possible.
Acute Renal Failure: In patients with renal insufficiency, acute renal failure requiring dialysis or worsening renal function have occurred with the use of GBCAs. The risk of renal failure may increase with increasing dose of the contrast agent. Screen all patients for renal dysfunction by obtaining a history and/or laboratory tests.
Extravasation and Injection Site Reactions: Extravasation of MultiHance may lead to injection site reactions, characterized by local pain or burning sensation, swelling, blistering, and necrosis. Exercise caution to avoid local extravasation during intravenous administration of MultiHance.
Cardiac Arrhythmias: Cardiac arrhythmias have been observed in patients receiving MultiHance in clinical trials. Assess patients for underlying conditions

MR Suite

or medications that predispose to arrhythmias. The effects on QTc by MultiHance dose, other drugs, and medical conditions were not systematically studied.

Interference with Visualization of Certain Lesions: Certain lesions seen on non-contrast images may not be seen on contrast images. Exercise caution when interpreting contrast MR images in the absence of companion non-contrast MR images.

ADVERSE REACTIONS

The most commonly reported adverse reactions are nausea (1.3%) and headache (1.2%).

USE IN SPECIFIC POPULATIONS

Pregnancy: GBCAs cross the human placenta and result in fetal exposure and gadolinium retention. Use only if imaging is essential during pregnancy and cannot be delayed.

Lactation: There is no information on the effects of the drug on the breastfed infant or the effects of the drug on milk production. However, limited literature reports that breastfeeding after MultiHance administration to the mother would result in the infant receiving an oral dose of 0.001%-0.04% of the maternal dose.

Pediatric Use: MultiHance is approved for intravenous use for MRI of the CNS to visualize lesions with abnormal blood brain barrier or abnormal vascularity of the brain, spine, and associated tissues in pediatric patients from birth, including term neonates, to less than 17 years of age. Adverse reactions in pediatric patients were similar to those reported in adults. No dose adjustment according to age is necessary in pediatric patients two years of age and older. For pediatric patients, less than 2 years of age, the recommended dosage range is 0.1 to 0.2 mL/kg. The safety of MultiHance has not been established in preterm neonates.

Please see full Prescribing Information and Patient Medication Guide for additional important safety information for/regarding MultiHance (gadobenate dimeglumine) injection, 529 mg/mL at https://www.braccoimaging.com/us-en/products/magnetic-resonance-imaging/multihance

You are encouraged to report negative side effects of prescription drugs to the FDA. Visit www.fda.gov/medwatch or call 1-800-FDA-1088.

MultiHance is manufactured for Bracco Diagnostics Inc. by BIPSO GmbH – 78224 Singen (Germany) and by Patheon Italia S.p.A., Ferentino, Italy.
MultiHance is a registered trademark of Bracco International B.V.
MultiHance Multipack is a trademark of Bracco International B.V.
All other trademarks and registered trademarks are the property of their respective owners.

References: 1. Seidl Z, Vymazal J, Mechi M, et al. Does higher gadolinium concentration play a role in the morphologic assessment of brain tumors? Results of a multicenter intraindividual crossover comparison of gadobutrol versus gadobenate dimeglumine (the MERIT Study). *AJNR Am J Neuroradiol.* 2012;33(6):1050-1058. **2.** Maravilla KR, Maldjian JA, Schmalfuss IM, et al. Contrast enhancement of central nervous system lesions: multicenter intraindividual crossover comparative study of two MR contrast agents. *Radiology.* 2006;240(2):389-400. **3.** Rowley HA, Scialfa G, Gao PY, et al. Contrast-enhanced MR imaging of brain lesions: a large-scale intraindividual crossover comparison of gadobenate dimeglumine versus gadodiamide. *AJNR Am J Neuroradiol.* 2008;29(9):1684-1691. **4.** Vaneckova M, Herman M, Smith MP, et al. The benefits of high relaxivity for brain tumor imaging: results of a multicenter intraindividual crossover comparison of gadobenate dimeglumine with gadoterate meglumine (The BENEFIT Study). *AJNR Am J Neuroradiol.* 2015 Sep;36(9):1589–1598.

Bracco Diagnostics Inc.
259 Prospect Plains Road, Building H
Monroe Township, NJ 08831 USA
Phone: 609-514-2200
Toll Free: 1-877-272-2269 (U.S. only)
Fax: 609-514-2446
© 2022 Bracco Diagnostics Inc. All Rights Reserved. US-MH-2100019 02/22

multihance®
(gadobenate dimeglumine)
injection, 529 mg/mL

Rx ONLY
Please see full prescribing information.
A brief summary follows.

WARNING: NEPHROGENIC SYSTEMIC FIBROSIS

Gadolinium-based contrast agents (GBCAs) increase the risk for NSF among patients with impaired elimination of the drugs.

Avoid use of GBCAs in these patients unless the diagnostic information is essential and not available with non-contrasted MRI or other modalities. NSF may result in fatal or debilitating systemic fibrosis affecting the skin, muscle and internal organs.

- The risk for NSF appears highest among patients with:
  - chronic, severe kidney disease (GFR <30 mL/min/1.73m2), or
  - acute kidney injury.
- Screen patients for acute kidney injury and other conditions that may reduce renal function. For patients at risk for chronically reduced renal function (e.g. age > 60 years, hypertension or diabetes), estimate the glomerular filtration rate (GFR) through laboratory testing.
- For patients at highest risk for NSF, do not exceed the recommended MultiHance dose and allow a sufficient period of time for elimination of the drug from the body prior to re-administration. [see *Warnings and Precautions (5.1)*]

---

1 INDICATIONS AND USAGE

1.1 MRI of the Central Nervous System (CNS)

MultiHance is indicated for intravenous use in magnetic resonance imaging (MRI) of the central nervous system (CNS) in adults and pediatric patients (including term neonates), to visualize lesions with abnormal blood-brain barrier or abnormal vascularity of the brain, spine, and associated tissues.

1.2 MRA of Renal and Aorto-ilio-femoral Vessels

MultiHance is indicated for use in magnetic resonance angiography (MRA) to evaluate adults with known or suspected renal or aorto-ilio-femoral occlusive vascular disease.

4 CONTRAINDICATIONS MultiHance is contraindicated in patients with known allergic or hypersensitivity reactions to gadolinium-based contrast agents [see *Warnings and Precautions (5.2)*].

5 WARNINGS AND PRECAUTIONS

5.1 Nephrogenic Systemic Fibrosis (NSF) Gadolinium-based contrast agents (GBCAs) increase the risk for nephrogenic systemic fibrosis (NSF) among patients with impaired elimination of the drugs. Avoid use of GBCAs among these patients unless the diagnostic information is essential and not available with non-contrast enhanced MRI or other modalities. The GBCA-associated NSF risk appears highest for patients with chronic, severe kidney disease (GFR <30 mL/min/1.73m²) as well as patients with acute kidney injury. The risk appears lower for patients with chronic, moderate kidney disease (GFR 30-59 mL/min/1.73m²) and little, if any, for patients with chronic, mild kidney disease (GFR 60-89 mL/min/1.73m²). NSF may result in fatal or debilitating fibrosis affecting the skin, muscle and internal organs. Report any diagnosis of NSF following MultiHance administration to Bracco Diagnostics (1-800-257-5181) or FDA (1-800-FDA-1088 or www.fda.gov/medwatch).

Screen patients for acute kidney injury and other conditions that may reduce renal function.

Features of acute kidney injury consist of rapid (over hours to days) and usually reversible decrease in kidney function, commonly in the setting of surgery, severe infection, injury or drug-induced kidney toxicity. Serum creatinine levels and estimated GFR may not reliably assess renal function in the setting of acute kidney injury. For patients at risk for chronically reduced renal function (e.g., age > 60 years, diabetes mellitus or chronic hypertension), estimate the GFR through laboratory testing.

Among the factors that may increase the risk for NSF are repeated or higher than recommended doses of a GBCA and the degree of renal impairment at the time of exposure. Record the specific GBCA and the dose administered to a patient. For patients at highest risk for NSF, do not exceed the recommended MultiHance dose and allow a sufficient period of time for elimination of the drug prior to re-administration. For patients receiving hemodialysis, physicians may consider the prompt initiation of hemodialysis following the administration of a GBCA in order to enhance the contrast agent's elimination. The usefulness of hemodialysis in the prevention of NSF is unknown [see *Dosage and Administration (2) and Clinical Pharmacology (12)*].

5.2 Hypersensitivity Reactions Anaphylactic and anaphylactoid reactions have been reported, involving cardiovascular, respiratory, and/or cutaneous manifestations. Some patients experienced circulatory collapse and died. In most cases, initial symptoms occurred within minutes of MultiHance administration and resolved with prompt emergency treatment. Prior to MultiHance administration, ensure the availability of personnel trained and medications to treat hypersensitivity reactions. If such a reaction occurs stop MultiHance and immediately begin appropriate therapy. Additionally, consider the risk for hypersensitivity reactions, especially in patients with a history of hypersensitivity reactions or a history of asthma or other allergic disorders. Observe patients for signs and symptoms of a hypersensitivity reaction during and for up to 2 hours after MultiHance administration.

5.3 Gadolinium Retention Gadolinium is retained for months or years in several organs. The highest concentrations (nanomoles per gram of tissue) have been identified in the bone, followed by other organs (e.g. brain, skin, kidney, liver, and spleen. The duration of retention also varies by tissue and is longest in bone. Linear GBCAs cause more retention than macrocyclic GBCAs. At equivalent doses, gadolinium retention varies among the linear agents with Omniscan (gadodiamide) and Optimark (gadoversetamide) causing greater retention than other linear agents [Eovist (gadoxetate disodium), Magnevist (gadopentetate dimeglumine), MultiHance (gadobenate dimeglumine)]. Retention is lowest and similar among the macrocyclic GBCAs [Dotarem (gadoterate meglumine), Gadavist (gadobutrol), ProHance (gadoteridol)].

Consequences of gadolinium retention in the brain have not been established. Pathologic and clinical consequences of GBCA administration and retention in skin and other organs have been established in patients with impaired renal function [see *Warnings and Precautions (5.1)*]. There are rare reports of pathologic skin changes in patients with normal renal function. Adverse events involving multiple organ systems have been reported in patients with normal renal function without an established causal link to gadolinium retention [see *Adverse Reactions (6.2)*]. While clinical consequences of gadolinium retention have not been established in patients with normal renal function, certain patients might be at higher risk. These include patients requiring multiple lifetime doses, pregnant and pediatric patients, and patients with inflammatory conditions. Consider the retention characteristics of the agent when choosing a GBCA for these patients. Minimize repetitive GBCA imaging studies, particularly closely spaced studies when possible.

5.4 Acute Renal Failure In patients with renal insufficiency, acute renal failure requiring dialysis or worsening renal function have occurred with the use of gadolinium-based contrast agents. The risk of renal failure may increase with increasing dose of the contrast agent. Screen all patients for renal dysfunction by obtaining a history and/or laboratory tests. Consider follow-up renal function assessments for patients with a history of renal dysfunction.

5.5 Extravasation and Injection Site Reactions Extravasation of MultiHance may lead to injection site reactions, characterized by local pain or burning sensation, swelling, blistering, and necrosis. In animal experiments, local reactions including eschar and necrosis were noted even on Day 8 post perivenous injection of MultiHance. Exercise caution to avoid local extravasation during intravenous administration of MultiHance. If extravasation occurs, evaluate and treat as necessary if local reactions develop.

5.6 Cardiac Arrhythmias Cardiac arrhythmias have been observed in patients receiving MultiHance in clinical trials [see *Adverse Reactions (6.1)*]. Assess patients for underlying conditions or medications that predispose to arrhythmias.

A double-blind, placebo-controlled, 24-hour post dose continuous monitoring, crossover study in 47 subjects evaluated the effect of 0.2 mmol/kg MultiHance on ECG intervals, including QTc. The average changes in QTc values compared with placebo were minimal (<5 msec). QTc prolongation between 30 and 60 msec were noted in 20 subjects who received MultiHance vs. 11 subjects who received placebo. Prolongations ≥61 msec were noted in 6 subjects who received MultiHance and in 3 subjects who received placebo. None of these subjects had associated malignant arrhythmias. The effects on QTc by MultiHance dose, other drugs, and medical conditions were not systematically studied.

5.7 Interference with Visualization of Certain Lesions Certain lesions seen on non-contrast images may not be seen on contrast-images. Exercise caution when interpreting contrast MR images in the absence of companion non-contrast MR images.

6 ADVERSE REACTIONS

The following adverse reactions are discussed in greater detail in other sections of the label:
- Nephrogenic systemic fibrosis [see *Warnings and Precautions (5.1)*]

- Hypersensitivity reactions [see *Warnings and Precautions (5.2)*]

6.1 Clinical Trials Experience

Because clinical trials are conducted under widely varying conditions, adverse reaction rates observed in the clinical trials of a drug cannot be directly compared to rates in the clinical trials of another drug and may not reflect the rates observed in practice.

Adult In clinical trials with MultiHance, a total of 4967 adult subjects (137 healthy volunteers and 4830 patients) received MultiHance at doses ranging from 0.005 to 0.4 mmol/kg. There were 2838 (57%) men and 2129 (43%) women with a mean age of 56.5 years (range 18 to 93 years). A total of 4403 (89%) subjects were Caucasian, 134 (3%) Black, 275 (6%) Asian, 40 (1%) Hispanic, 70 (1%) in other racial groups, and for 45 (1%) subjects, race was not reported.

The most commonly reported adverse reactions in adult subjects who received MultiHance were nausea (1.3%) and headache (1.2%). Most adverse reactions were mild to moderate in intensity. One subject experienced a serious anaphylactoid reaction with laryngeal spasm and dyspnea [see *Warnings and Precautions (5.2)*]. Serious adverse reactions consisting of convulsions, pulmonary edema, acute necrotizing pancreatitis, and anaphylactoid reactions were reported in 0.1% of subjects in clinical trials.

Adverse reactions that occurred in at least 0.5% of 4967 adult subjects who received MultiHance are listed below (Table 2), in decreasing order of occurrence within each system.

TABLE 2: ADVERSE REACTIONS REPORTED IN ≥ 0.5% OF ADULT SUBJECTS WHO RECEIVED MULTIHANCE IN CLINICAL TRIALS

Number of subjects dosed	4967
Number of subjects with any adverse reaction	517 (10.4%)
Gastrointestinal Disorders	
Nausea	67 (1.3%)
General Disorders and Administration Site Disorders	
Injection Site Reaction	54 (1.1%)
Feeling Hot	49 (1.0%)
Nervous System Disorders	
Headache	60 (1.2%)
Dysgeusia	33 (0.7%)
Paresthesia	24 (0.5%)
Dizziness	24 (0.5%)

The following adverse reactions occurred in less than 0.5% of the 4967 adult subjects who received MultiHance. Serious adverse reactions described above are not repeated below.

Blood and Lymphatic System Disorders: Basophilia; **Cardiac Disorders:** Atrioventricular block first degree; **Eye Disorders:** Eye pruritus, eye swelling, ocular hyperemia, visual disturbance; **Gastrointestinal Disorders:** Abdominal pain or discomfort, diarrhea, dry mouth, lip swelling, paraesthesia oral, tongue edema, vomiting; **General Disorders and Administration Site Conditions:** Chest pain or discomfort, chills, malaise; **Immune System Disorders:** Hypersensitivity; **Investigations:** Nonspecific changes in laboratory tests (including hematology, blood chemistry, liver enzymes and urinalysis), blood pressure and electrocardiogram parameters (including PR, QRS and QT intervals and ST-T segment changes). **Musculoskeletal and Connective Tissue Disorders:** Myalgia; **Nervous System Disorders:** Parosmia, tremor; **Respiratory, Thoracic and Mediastinal Disorders:** Dyspnea, laryngospasm, nasal congestion, sneezing, wheezing; **Skin and Subcutaneous Tissue Disorders:** Hyperhidrosis, pruritus, rash, swelling face, urticaria.

Pediatric In clinical trials of MultiHance in MRI of the CNS, 217 pediatric subjects received MultiHance at a dose of 0.1 mmol/kg. A total of 112 (52%) subjects were male and the overall mean age was 8.3 years (range 4 days to 17 years). A total of 168 (77%) were Caucasian, 12 (6%) Black, 12 (6%) Asian, 24 (11%), Hispanic, and 1 (<1%) in other racial groups. Adverse reactions were reported for 14 (6.5%) of the subjects. The frequency and the nature of the adverse reactions were similar to those seen in the adult patients. The most commonly reported adverse reactions were vomiting (1.4%), pyrexia (0.9%), and hyperhidrosis (0.9%). No subject died during study participation. A serious adverse reaction of worsening of vomiting was reported for one (0.5%) patient with a brain tumor (glioma) for which a causal relationship to MultiHance could not be excluded.

Pediatric Patients In clinical trials of MultiHance in MRI of the CNS, 307 pediatric subjects received MultiHance at a dose of 0.1 mmol/kg. A total of 160 (52%) subjects were male and the overall mean age was 6.0 years (range, 2 days to 17 years). A total of 211 (69%) were Caucasian, 24 (8%) Black, 15 (5%) Asian, 39 (13%), Hispanic, 2 (<1%) in other racial groups, and for 16 (5%), race was not reported. Adverse reactions were reported for 14 (4.6%) of the subjects. The frequency and the nature of the adverse reactions were similar to those seen in the adult patients. The most commonly reported adverse reactions were vomiting (1.0%), pyrexia (0.7%), and hyperhidrosis (0.7%). No subject died during study participation.

6.2 Post-marketing Experience

The following adverse reactions have been identified during post approval use of MultiHance. Because these reactions are reported voluntarily from a population of uncertain size, it is not always possible to reliably estimate their frequency or establish a causal relationship to drug exposure.

Immune System Disorders: Anaphylactic, anaphylactoid and hypersensitivity reactions manifested with various degrees of severity up to anaphylactic shock, loss of consciousness and death. The reactions generally involved signs or symptoms of respiratory, cardiovascular, and/or mucocutaneous abnormalities.

General Disorders and Administration Site Conditions: Extravasation of MultiHance may lead to injection site reactions, characterized by local pain or burning sensation, swelling, blistering, and necrosis [see *Warnings and Precautions (5.4)*]. Adverse events with variable onset and duration have been reported after GBCA administration [see *Warnings and Precautions (5.3)*]. These include fatigue, asthenia, pain syndromes, and heterogeneous clusters of symptoms in the neurological, cutaneous, and musculoskeletal systems. **Skin:** Gadolinium associated plaques.

7 DRUG INTERACTIONS

7.1 Transporter-Based Drug-Drug Interactions MultiHance and other drugs may compete for the canalicular multispecific organic anion transporter (MOAT also referred to as MRP2 or ABCC2). Therefore MultiHance may prolong the systemic exposure of drugs such as cisplatin, anthracyclines (e.g. doxorubicin, daunorubicin), vinca alkaloids (e.g. vincristine), methotrexate, etoposide, tamoxifen, and paclitaxel. In particular, consider the potential for prolonged drug exposure in patients with decreased MOAT activity (e.g. Dubin Johnson syndrome).

8 USE IN SPECIFIC POPULATIONS

8.1 Pregnancy *Risk Summary* GBCAs cross the placenta and result in fetal exposure and gadolinium retention. The human data on the association between GBCAs and adverse fetal outcomes are limited and inconclusive (see Data). In animal reproduction studies, gadobenate dimeglumine has been shown to be teratogenic in rabbits following repeated intravenous administration during organogenesis at doses up to 6 times the recommended human dose. There were no adverse developmental effects observed in rats with intravenous administration of gadobenate dimeglumine during organogenesis at doses up to three times the recommended human dose (see Data). Because of the potential risks of gadolinium to the fetus, use MultiHance only if imaging is essential during pregnancy and cannot be delayed. The estimated background risk of major birth defects and miscarriage for the indicated population is unknown. All pregnancies have a background risk of birth defect, loss, or other adverse outcomes. In the U.S. general population, the estimated background risk of major birth defects and miscarriage in clinically recognized pregnancies is 2 to 4% and is 15 to 20%, respectively.

Data Human Data Contrast enhancement is visualized in the human placenta and fetal tissues after maternal GBCA administration. Cohort studies and case reports on exposure to GBCAs during pregnancy have not reported a clear association between GBCAs and adverse effects in the exposed neonates. However, a retrospective cohort study, comparing pregnant women who had a GBCA MRI to pregnant women who did not have an MRI, reported a higher occurrence of stillbirths and neonatal deaths in the group receiving GBCA MRI. Limitations of this study include a lack of comparison with non-contrast MRI and lack of information about the maternal indication for MRI. Overall, these data preclude a reliable evaluation of the potential risk of adverse fetal outcomes with the use of GBCAs in pregnancy. *Animal Data Gadolinium Retention* GBCAs administered to pregnant non-human primates (0.1 mmol/kg on gestational days 85 and 135) result in measurable gadolinium concentration in the offspring in bone, brain, skin, liver, kidney, and spleen for at least 7 months. GBCAs administered to pregnant mice (2 mmol/kg daily on gestational days 16 through 19) result in measurable gadolinium concentrations in the pups in bone, brain, kidney, liver, blood, muscle, and spleen at one month postnatal age.

Reproductive Toxicology Gadobenate dimeglumine has been shown to be teratogenic in rabbits when administered intravenously at 2 mmol/kg/day (6 times the recommended human dose based on body surface area) during organogenesis (day 6 to 18) inducing microphthalmia/small eye and/or focal retinal fold in 3 fetuses from 3 separate litters. In addition, MultiHance intravenously administered at 3 mmol/kg/day (10 times the recommended human dose based on body surface area) has been shown to increase intrauterine deaths in rabbits. There was no evidence that MultiHance induced teratogenic effects in rats at doses up to 2 mmol/kg/day (3 times the recommended human dose based on body surface area), however, rat dams exhibited no systemic toxicity at this dose. There were no adverse effects on the birth, survival, growth, development and fertility of the F1 generation at doses up to 2 mmol/kg in a rat peri- and post-natal (Segment III) study.

10 OVERDOSAGE

Clinical consequences of overdosage with MultiHance have not been reported. Treatment of an overdosage should be directed toward support of vital functions and prompt institution of symptomatic therapy. In a Phase 1 clinical study, doses up to 0.4 mmol/kg were administered to patients. MultiHance has been shown to be dialyzable [see *Clinical Pharmacology (12.3)*].

12 CLINICAL PHARMACOLOGY

12.1 Mechanism of Action Gadobenate dimeglumine is a paramagnetic agent and, as such, develops a magnetic moment when placed in a magnetic field. The large magnetic moment produced by the paramagnetic agent results in a large local magnetic field, which can enhance the relaxation rates of water protons in its vicinity leading to an increase of signal intensity (brightness) of tissue.

In magnetic resonance imaging (MRI), visualization of normal and pathological tissue depends in part on variations in the radiofrequency signal intensity that occur with 1) differences in proton density; 2) differences of the spin-lattice or longitudinal relaxation times (T1); and 3) differences in the spin-spin or transverse relaxation time (T2). When placed in a magnetic field, gadobenate dimeglumine decreases the T1 and T2 relaxation time in target tissues. At recommended doses, the effect is observed with greatest sensitivity in the T1-weighted sequences.

12.2 Pharmacodynamics Unlike other tested paramagnetic contrast agents (See Table 3), MultiHance demonstrates weak and transient interactions with serum proteins that causes slowing in the molecular tumbling dynamics, resulting in strong increases in relaxivity in solutions containing serum proteins. The improved relaxation effect can contribute to increased contrast-to-noise ratio and lesion-to-brain ratio, which may improve visualization.

TABLE 3: RELAXIVITY (mM⁻¹s⁻¹) OF GADOLINIUM CHELATES

	Human plasma	
	r_1	r_2
Gadobenate	9.7[1]	12.5[1]
Gadopentetate	4.9[1]	6.3[1]
Gadodiamide	5.4[2]	---
Gadoteridol	5.4[3]	---

r, and r, relaxivities indicate the efficiency in shortening T1 and T2 relaxation times, respectively.
[1] In heparinized human plasma, at 39°C.
[2] In citrated human plasma, at 37°C.
--- Not available

Disruption of the blood-brain barrier or abnormal vascularity allows enhancement by MultiHance of lesions such as neoplasms, abscesses, and infarcts. Uptake of MultiHance into hepatocytes has been demonstrated.

12.3 Pharmacokinetics Three single-dose intravenous studies were conducted in 32 healthy male subjects to assess the pharmacokinetics of gadobenate dimeglumine. The doses administered in these studies ranged from 0.005 to 0.4 mmol/kg. Upon injection, the meglumine salt is completely dissociated from the gadobenate dimeglumine complex. Thus, the pharmacokinetics is based on the assay of gadobenate ion, the MRI contrast effective ion in gadobenate dimeglumine. Data for plasma concentration and area under the curve demonstrated linear dependence on the administered dose. The pharmacokinetics of gadobenate ion following intravenous administration can be best described using a two-compartment model.

Distribution Gadobenate ion has a rapid distribution half-life (reported as mean ± SD) of 0.084 ± 0.012 to 0.605 ± 0.072 hours. Volume of distribution of the central compartment ranged from 0.074 ± 0.017 to 0.158 ± 0.038 L/kg, and estimates of volume of distribution by area ranged from 0.170 ± 0.016 to 0.282 ± 0.079 L/kg. These latter estimates are approximately equivalent to the average volume of extracellular body water in man. In vitro studies showed no appreciable binding of gadobenate ion to human serum proteins.

Elimination Gadobenate ion is eliminated predominately via the kidneys, with 78% to 96% of an administered dose recovered in the urine. Total plasma clearance and renal clearance estimates of gadobenate ion were similar, ranging from 0.093 ± 0.010 to 0.133 ± 0.270 L/hr/kg and 0.082 ± 0.007 to 0.104 ± 0.039 L/hr/kg, respectively. The clearance is similar to that of substances that are subject to glomerular filtration. The mean elimination half-life ranged from 1.17 ± 0.26 to 2.02 ± 0.60 hours. A small percentage of the administered dose (0.6% to 4%) is eliminated via the biliary route and recovered in feces.

Metabolism There was no detectable biotransformation of gadobenate ion. Dissociation of gadobenate ion *in vivo* has been shown to be minimal, with less than 1% of the free chelating agent being recovered alone in feces.

Pharmacokinetics in Special Populations

Renal Impairment: A single intravenous dose of 0.2 mmol/kg of MultiHance was administered to 20 subjects with impaired renal function (6 men and 3 women with moderate renal impairment [urine creatinine clearance >30 to <60 mL/min] and 5 men and 6 women with severe renal impairment [urine creatinine clearance >10 to <30 mL/min]). Mean estimates of the elimination half-life were 6.1 ± 3.0 and 9.5 ± 3.1 hours for the moderate and severe renal impairment groups, respectively, as compared with 1.0 to 2.0 hours in healthy volunteers.

Hemodialysis: A single intravenous dose of 0.2 mmol/kg of MultiHance was administered to 11 subjects (5 males and 6 females) with end-stage renal disease requiring hemodialysis to determine the pharmacokinetics and dialyzability of gadobenate. Approximately 72% of the dose was recovered by hemodialysis over a 4-hour period. The mean elimination half-life on dialysis was 1.21 ± 0.29 hours as compared with 42.4 ± 24.4 hours when off dialysis.

Hepatic Impairment: A single intravenous dose of 0.1 mmol/kg of MultiHance was administered to 11 subjects (8 males and 3 females) with impaired liver function (Class B or C modified Child-Pugh Classification). Hepatic impairment had little effect on the pharmacokinetics of MultiHance with the parameters being similar to those calculated for healthy subjects.

Gender, Age, Race: A multiple regression analysis performed using pooled data from several pharmacokinetic studies found no significant effect of sex upon the pharmacokinetics of gadobenate. Clearance appeared to decrease slightly with increasing age. Since variations due to age appeared marginal, dosage adjustment for geriatric population is not recommended. Pharmacokinetic differences due to race have not been systematically studied.

Pediatric: A population pharmacokinetic analysis incorporated data from 25 healthy subjects (14 males and 11 females) and 15 subjects undergoing MR imaging of the central nervous system (7 males and 8 females) between ages of 2 and 16 years. The subjects received a single intravenous dose of 0.1 mmol/kg of MultiHance. The geometric mean Cmax was 62.3 µg/mL (n=16) in children 2 to 5 years of age, and 64.2 µg/mL (n=24) in children older than 5 years. The geometric mean AUC 0–∞ was 77.9 µg-h/mL in children 2-5 years of age (n=16) and 82.6 µg-h/mL in children older than 5 years (n=24). The geometric mean half-life was 1.2 hours in children 2 to 5 years of age and 0.93 hours in children older than 5 years. There was no significant gender-related difference in the pharmacokinetic parameters in the pediatric patients. Over 80% of the dose was recovered in urine after 24 hours. Pharmacokinetic simulations indicate similar AUC and Cmax values for MultiHance in pediatric subjects less than 2 years when compared to those reported for adults; no age-based dose adjustment is necessary for this pediatric population.

17 PATIENT COUNSELING INFORMATION

17.1 Nephrogenic Systemic Fibrosis Instruct patients to inform their physician if they:
- have a history of kidney and/or liver disease, or • have recently received a GBCA.

GBCAs increase the risk for NSF among patients with impaired elimination of the drugs. To counsel patients at risk for NSF: • Describe the clinical manifestations of NSF • Describe procedures to screen for the detection of renal impairment.

Instruct the patients to contact their physician if they develop signs or symptoms of NSF following MultiHance administration, such as burning, itching, swelling, scaling, hardening and tightening of the skin; red or dark patches on the skin; stiffness in joints with trouble moving, bending or straightening the arms, hands, legs or feet; pain in the hip bones or ribs; or muscle weakness.

17.2 Common Adverse Reactions

Inform patients that they may experience:
- reactions along the venous injection site, such as mild and transient burning or pain or feeling of warmth or coldness at the injection site • side effects of feeling hot, nausea, and headache.

17.3 General Precautions

Instruct patients scheduled to receive MultiHance to inform their physician if they:
- are pregnant or breast feeding • have a history of renal disease, heart disease, seizure, asthma or allergic respiratory diseases • are taking any medications • have any allergies to any of the ingredients of MultiHance.

[†]Multicenter double-blind randomized intraindividual crossover study design of 123 patients with known or suspected brain tumors. Each patient received 0.1-mmol/kg doses of MultiHance and Gadavist in 2 identical MR imaging examinations. Contrast agents were administered by IV using manual bolus injection (n=118) or a power injector (n=4). Both agents were administered at 0.1 mmol/kg of body weight, corresponding to 0.2 mL/kg for MultiHance and 0.1 mL/kg for Gadavist. The interval between the 2 MR imaging examinations was >48 hours to avoid carryover effects but <14 days to minimize the chance of measurable disease progression or lesion evolution. All images were evaluated by 3 blinded, independent experienced radiologists who were unaffiliated with the study centers. Each reader evaluated the patient images separately and independently. Images were evaluated qualitatively for diagnostic information and scored for: 1) lesion border delineation, 2) disease extent, 3) visualization of lesion internal morphology, and 4) lesion contrast enhancement compared with surrounding normal tissue. All assessments used a 3-point scales from 1 (examination 1 superior) through 0 (examinations equal) to 1 (examination 2 superior).

Gadavist® (gadobutrol) is a registered trademark of Bayer Healthcare. **Reference:** Seidl Z, Vymazal J, Mechl M, et al. Does higher gadolinium concentration play a role in the morphologic assessment of brain tumors? Results of a multicenter intraindividual crossover comparison of gadobutrol versus gadobenate dimeglumine (the MERIT Study). *AJNR Am J Neuroradiol.* 2012 Jun-Jul;33(6):1050–1058.

AJNR
AMERICAN JOURNAL OF NEURORADIOLOGY

CALL FOR AJNR EDITOR-IN-CHIEF CANDIDATES

Over the last 41 years, the editorial team of the *American Journal of Neuroradiology (AJNR)* has played a pivotal role in shaping our specialty of neuroradiology. In June 2023, Jeffrey S. Ross, MD, will complete an 8-year term as the sixth Editor-in-Chief (EIC) of the *AJNR*. He was preceded by a number of distinguished editors including our first *AJNR* EIC, Juan M. Taveras, MD (1980-1989), followed by Michael S. Huckman, MD (1990-1997), Robert M. Quencer, MD (1997-2005), Robert I. Grossman, MD (2006-2007), and Mauricio Castillo, MD (2007-2015).

We especially wish to thank Dr. Jeffrey Ross for his extraordinary dedication and exceptional contributions to the *AJNR*. Under his strong leadership, the *AJNR* remains the premier clinical neuroimaging journal with high-quality, peer-reviewed articles that serve as a beacon for achieving excellence in patient care, research, and teaching. There are an impressive 6867 subscribers across the globe: 1389 are in print and 5472 are digital.

Dr. Ross has assembled a talented international editorial board during his tenure. The *AJNR* issues 12 journals each year (± 200 pages per issue)—all with peer-reviewed articles from highly respected researchers in the field. With 1700+ papers, the number of submissions to the journal was record-breaking in 2020. Over 80 COVID-19 papers have received expedited publication to date, and more than 1300 original submissions are projected for 2021. The *AJNR* website had an incredible 11.7 million visits in 2021. There is also a strong presence on social media and subscribers may now avail themselves of an enhanced website platform. There are 3 monthly podcasts including "*Issue Highlights,*" "*Fellows' Journal Club,*" and "*Annotated Bibliography,*" which offers continuing medical education. In addition, during Dr. Ross' tenure, the Impact Factor and h-index for the journal have steadily increased and contribute to the *AJNR's* international recognition as the leading journal for all aspects of neuroimaging research, education, and best practice.

A search for a new Editor-in-Chief will begin in early 2022.

The new Editor-in-Chief will be announced in December 2022 and will transition into the position beginning in January 2023. The actual term will begin July 1, 2023. The EIC will provide leadership and strategic vision for the journal as well as report on all editorial matters to the ASNR Board of Directors (BOD). Other responsibilities include maintaining the journal's standard of excellence building on its reputation nationally and internationally. The EIC will be responsible for conducting, directing, and/or supervising the solicitation, evaluation, revision, and selection of all scientific and other materials to be published in the *American Journal of Neuroradiology*. The incumbent will work efficiently with the journal's online manuscript processing system to conduct initial screening of manuscripts; make timely decisions about reviewed and revised submissions; provide constructive comments for authors as appropriate; write editorials; and meet with *AJNR* staff.

In addition, the EIC shall decide upon and approve of the content and design of tables of contents, letters to the editor, book reviews, advertisements, and other pages published in the *AJNR* as well as oversight of social media related to the journal. The EIC will also work collaboratively with the journal's editorial board to determine the organizational structure, titles, functions, appointments, and terms of all editorial positions including reviewers, editorial advisory boards, and senior editors. The EIC may appoint senior editors who must be senior members of the ASNR. The number of senior editors shall be budgeted and approved by the ASNR BOD. Senior editors will serve at the pleasure of the EIC who shall establish the terms of service, including supervising and evaluating performance, and will exercise the right to retain or replace any senior editor as the workflow or operational demands require. The appointments of senior editors will be for a term of 1 year initially and may be extended at the discretion of the EIC.

The EIC in performing duties will observe the general *Policies and Procedures* established by the ASNR BOD, and will operate within the budget approved by the Board of Directors. The EIC will be consulted about, and will participate in *AJNR* operations including advertising, publication channels, expense management, and new or renewed contracts. The EIC will report regularly to the ASNR BOD and will attend Board of Director Meetings and other meetings as requested by the Executive Director. Each year the Editor will develop a budget along with the Managing Editor for approval by the ASNR Financial Management Committee and Board of Directors. This will be done in a manner consistent with the fiscal policies established by the Society.

QUALIFICATIONS OF THE SUCCESSFUL CANDIDATE INCLUDE:

- MD degree; Senior Member of ASNR in North America, neuroradiology subspecialty certification
- Familiarity with *AJNR* and its mission
- Familiarity with ASNR and its mission
- Presently or recently engaged in a leadership role in neuroradiology with broad neuroradiology knowledge
- Excellent leadership and supervisory skills to motivate and inspire professional staff as well as interpersonal skills—impartiality, diplomacy, high ethical standards and integrity including a clear understanding of the ethical guidelines established for scholarly publishing
- Leadership needed to develop and articulate a vision and the ability to inspire people with that vision
- Demonstrated track record of academic excellence including extensive experience in both publishing in and reviewing for peer-reviewed journals
- Excellent communication and writing skills and experience in critically appraising scientific articles
- Creativity and passion about finding new ways to expand the journal content
- The ability to formulate a budget and assist leadership in oversite of journal business decisions such as selecting major vendors (e.g., printing, composition, redaction, copyediting, and other technical aspects affecting journal operations), as well as expense and revenue related decisions
- Ability to appoint a strong, diverse, and representative team of editors
- High level of organizational skills
- Editorial board or prior editorial experience preferred

The term is for 5 years renewable for an additional 3 years for a total of 8 years and subject to annual review by the ASNR Board of Directors. It is expected the EIC will devote 16-20 hours per week to these duties and a stipend will be provided.

A diverse, experienced, and knowledgeable search committee has been tasked with identifying leading candidates. The search committee consists of Tina Young Poussaint, MD, FACR, Chair, Mauricio Castillo, MD, FACR, Pina Sanelli, MD, MPH, FACR, Carolyn Meltzer, MD, FACR, Erin Simon Schwartz, MD, FACR, Joshua Nickerson, MD, Courtney Tomblinson, MD, and senior editors including Harry Cloft, MD, PhD, Christopher Filippi, MD, Thierry Huisman, MD, Peter D. Chang, MD, Lubdha Shah, MD, Gregory Zaharchuk MD, PhD, C. Douglas Phillips, MD, Yvonne Lui, MD, and Bryan Comstock. The search process will include recruiting and nominating candidates, interviewing candidates, and reviewing vision statements submitted by finalists. The appointment of the new *AJNR* Editor-in-Chief will be announced in December 2022.

All interested physicians are invited to provide their curriculum vitae and a vision statement to Dr. Tina Young Poussaint, tina.poussaint@childrens.harvard.edu and Karen Halm, khalm@asnr.org. To ensure a broad and diverse pool of candidates, the committee welcomes nominations from the ASNR membership. *The deadline for receipt of submissions is August 1, 2022.*

Tina Young Poussaint, MD, FACR
Chair, Editor-in-Chief Search Committee
President, American Society of Neuroradiology

In Planning for Brain Metastases Treatment, Imaging may be the Missing Link in Cost Containment[1]

When faced with a patient presenting with metastatic brain cancer, determining whether to use up-front stereotactic radiosurgery (SRS) vs. first treating with whole brain radiotherapy (WBRT) is a significant clinical decision.

WBRT: The whole story on cognitive impairment

While whole brain radiotherapy (WBRT) has been the main treatment option for many years, experts agree that it often results in cognitive deterioration and a negative impact on quality of life. This mental decline has a devastating impact on patients and their families and adds ongoing costs for the healthcare systems managing these symptoms.

Using WBRT instead of SRS in some patients is estimated to decrease the total costs of brain metastasis management, though with increased toxicity.

SRS: Fewer side effects but greater risk of missed tumors

The cost of upfront SRS is the greatest contributor to cost of brain metastasis management.[1] SRS is often more expensive than WBRT. What's more, multiple applications of SRS can increase the cost of treatment greatly.

Stereotactic radiosurgery (SRS) has far fewer side effects, but upfront use of SRS is expensive and can carry the risk of missed tumors, requiring repeat procedures such as salvage SRS.[1]

Number of lesions and lesion size are key factors to be considered when determining the treatment plan for these patients. It follows that increased diagnostic information and accuracy could be beneficial in directing the proper therapy and improving overall long-term patient outcomes and containing costs. Getting the diagnosis right the first time is crucial to ensure proper treatment begins quickly, and high cost/high stakes procedures such as SRS need precise surgical planning.

Getting the diagnosis right the first time is crucial to ensure proper treatment begins quickly.

What does optimal visualization mean for outcomes and cost?

For surgical planning with SRS, radiologists need the best visualization achievable to accurately count the number and size of the lesions. These metrics are the key predictors of the need for SRS,[1] WBRT, or a combination of both.

By selecting the ideal contrast agent and equipment protocols, neuroradiologists can identify the proximate numbers of metastases for upfront treatment and reduced salvage treatment occurrences.

The role of radiology

As medical care for oncology patients continues to evolve, it will be increasingly important to assess the cost of various interventions given the often-limited life expectancy of cancer patients, the rising costs of cancer therapy, and the increasing prevalence of cancer in an aging population.

Through seeing all the tumors and tumor borders as clearly as technology allows, radiology can play a part in ensuring that proper treatment can begin quickly, while containing costs through optimized patient care. Efforts to carefully manage treatment approaches require improvements in protocol design, contrast administration in imaging, and utilizing multimodal imaging approaches.

In this era of precision medicine, radiology departments' contribution to this improved standard of care will have significant short and long-term implications by reducing cost of care, providing a more proximate diagnosis, and ensuring optimal patient outcomes. ∎

Reference: 1. Shenker, R. F., McTyre, E. R., Taksler, D et al. Analysis of the drivers of cost of management when patients with brain metastases are treated with upfront radiosurgery. *Clin Neurol Neurosurg.* 2019 Jan;176:10-14.

BALLAST®

LONG SHEATH

6F 088

Ø 0.88"

50cm - 70cm - 100 cm

GET THERE 〉〉

STAY THERE 〉〉

**Image courtesy of
Ameer E. Hassan D.O., FAHA, FSVIN**

Visit our products page at www.baltgroup.com to learn more.

balt

inspiring innovation

AJNR

AMERICAN JOURNAL OF NEURORADIOLOGY

Publication Preview at www.ajnr.org features articles released in advance of print. Visit www.ajnrblog.org to comment on AJNR content and chat with colleagues and AJNR's News Digest at http://ajnrdigest.org to read the stories behind the latest research in neuroimaging.

BOOK REVIEWS *R.M. Quencer, Section Editor*

Please visit www.ajnrblog.org to read and comment on Book Reviews.

Catheter-directed angiography findings in Arterioectatic Spinal Angiopathy of Childhood from Abruzzo T, et al, in this issue.
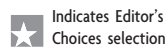
★ Indicates Editor's Choices selection

⚓ Indicates Fellows' Journal Club selection

⚷ Indicates open access to non-subscribers at www.ajnr.org

☰ Indicates article with supplemental online data

▶ Indicates article with supplemental online video

EBM 1 Evidence-Based Medicine Level 1

EBM 2 Evidence-Based Medicine Level 2

Title: Room with A Sutton Place View. "Sutton Place" is a short north-south thoroughfare, and surrounding neighborhood, on the East Side of Manhattan with numerous real and fictional associations of note including famed actors, rock stars, songs, novels, plays, and movies. The grand Ed Koch Queensboro Bridge (renamed in honor of the former Mayor) is in the foreground, with Long Island City, Queens, immediately across the bridge, and Brooklyn following to the right, each with their own fascinating stories.

Manfred Hauben, MD, MPH, Pfizer Inc and NYU Langone Health, New York City

The 2021 World Health Organization Classification of Tumors of the Central Nervous System: What Neuroradiologists Need to Know

A.G. Osborn, D.N. Louis, T.Y. Poussaint, L.L. Linscott, and K.L. Salzman

ABSTRACT

SUMMARY: Neuroradiologists play a key role in brain tumor diagnosis and management. Staying current with the latest classification systems and diagnostic markers is important to provide optimal patient care. Publication of the 2016 World Health Organization Classification of Tumors of the Central Nervous System introduced a paradigm shift in the diagnosis of CNS neoplasms. For the first time, both histologic features and genetic alterations were incorporated into the diagnostic framework, classifying and grading brain tumors. The newly published 2021 World Health Organization Classification of Tumors of the Central Nervous System, May 2021, 5th edition, has added even more molecular features and updated pathologic diagnoses. We present, summarize, and illustrate the most salient aspects of the new 5th edition. We have selected the key "must know" topics for practicing neuroradiologists.

ABBREVIATIONS: DGONC = diffuse glioneuronal tumor with oligodendroglioma-like features and nuclear clusters; EPN = ependymoma; ETMR = embryonal tumor with multilayered rosettes; FISH = fluorescence in situ hybridization; NEC = not elsewhere classified; NOS = not otherwise specified; MB = medulloblastoma; MGNT = myxoid glioneuronal tumor; MVNT = multinodular and vacuolating neuronal tumor; PF = posterior fossa; SC = spinal cord; ST = supratentorial; WHO = World Health Organization; IDH = isocitrate dehydrogenase

Publication of the 2016 World Health Organization (WHO) Classification of Tumors of the Central Nervous System introduced a paradigm shift in the diagnosis of CNS neoplasms. For the first time, both histologic features and genetic alterations were incorporated into the diagnostic framework, classifying and grading brain tumors.

The rapidly evolving molecular landscape demanded interim updates between WHO editions (typically every 7 years). In late 2016, the Consortium to Inform Molecular and Practical Approaches to CNS Tumor Taxonomy (cIMPACT-NOW) was created under the sponsorship of the International Society of Neuropathology to provide such updates.[1,2] To date, 7 updates[3-10] have been published to bridge the gap between the 4th edition and the newly published (May, 2021) 5th edition of the famed "blue book."[11]

We present, summarize, and illustrate the most salient aspects of the new 5th edition. We have selected the key "must know" topics for practicing neuroradiologists. The 2021 WHO Classification of Tumors of the Central Nervous System can be ordered in either print or digital form from the WHO website and should be part of every neuroradiologist's library.

General Features and Recommendations

Tumor Taxonomy and Nomenclature. Prior editions used the terms "entities" and "variants." The current edition uses the terms "types" and "subtypes" and keeps tumor names as simple as possible. Newly recognized or redefined types and subtypes are summarized in the Online Supplemental Data.

Tumor Grading. The 5th edition uses Arabic numerals instead of Roman numerals to conform to other WHO grading systems and decrease the likelihood of typographic errors when grading within types. Tumor grades are now designated specifically as CNS WHO grades 1–4 ("CNS" is always added to distinguish the grading system from those of systemic neoplasms because CNS grading differs conceptually, eg, grading of diffuse astrocytomas from 2 to 4, without a 1).

Not Otherwise Specified and Not Elsewhere Classified. Not otherwise specified (NOS) is used when molecular information is not available/not performed/not successful. Not elsewhere classified (NEC) is used when necessary diagnostic testing was

Layered neuropathology diagnosis[a]

Brain (right frontal)
Integrated diagnosis: glioblastoma, IDH-wildtype[b]
Histologic diagnosis: diffuse astrocytic tumor with mitotic figures
WHO CNS grade: 4
Molecular information:
IDH: wildtype (DNA sequencing)
ATRX: retained nuclear expression, consistent with wild-type (immunohistochemistry)
p53: rare positive cells, consistent with wild-type (immunohistochemistry)
EGFR: amplified (FISH)

[a] Illustrative example of a layered neuropathology report beginning with site and identifier and with integrated diagnosis as the top line.
[b] Although this tumor lacks microvascular proliferation and necrosis, the presence of *EGFR* amplification necessitates a diagnosis of glioblastoma in an IDH-wildtype diffuse astrocytic glioma.

successfully performed but the results do not readily permit a WHO diagnosis (eg, entities that are not yet recognized as part of the WHO Classification).[3] NOS and NEC can be used for any tumor type.

"Layered" Reports and Integrated Diagnosis. A matrix approach to an integrated pathologic diagnosis is used throughout the 5th edition (Table). Features such as location (eg, cerebrum or cerebellum), histopathology, and molecular information (when available) are combined into the top layer (in reality the "bottom line") to create an integrated diagnosis. Tumor grade reflects a combination of histologic features and genetically defined mutation status. If molecular information is unavailable, tumor entities are generally designated by NOS.

General Taxonomy

The WHO 5th edition organizes CNS neoplasms into several major groups: gliomas, glioneuronal, and neuronal tumors; choroid plexus tumors; embryonal tumors; pineal tumors; cranial and paraspinal nerve tumors; meningioma; mesenchymal, nonmeningothelial tumors; melanocytic tumors; hematolymphoid tumors; germ cell tumors; tumors of the sellar region; and metastases to the CNS. In this overview, we will focus on the tumor groups with specific changes such as newly recognized tumor entities, revised nomenclature, and restructured tumor groupings.

Gliomas, Glioneuronal, and Neuronal Tumors

Gliomas, glioneuronal, and neuronal tumors, along with the embryonal tumors, have undergone the most important changes since the 2016 4th edition. There are now 14 newly recognized ("new") gliomas and glioneuronal tumors in the 5th edition of the blue book. In addition, for the first time, the WHO classification divides diffuse gliomas into adult-type and pediatric-type neoplasms.

Gliomas

Neuropathologic Essentials. Glioma characterization requires more than simply determining whether a tumor exhibits 1p/19q codeletion on fluorescence in situ hybridization (FISH) and is isocitrate dehydrogenase (IDH) mutant or IDH-wildtype on immunohistochemistry, to implement the 2021 WHO classification fully. For example, IDH-wildtype diffuse astrocytic gliomas in patients 55 years of age and younger should also be investigated for noncanonical (ie, non-R132H) *IDH1* mutations and *IDH2* mutations. In other molecular markers such as loss of ATRX expression or *TERT* promoter mutations, the presence of *TP53* or histone H3 mutations, *EGFR* amplification, or *CDKN2A/B* alterations, and so forth need to be evaluated in specific diagnostic pathways.

Some genetic changes have convenient immunohistochemistry surrogate assays (eg, *IDH1* R132H, ATRX, p53, *BRAF* V600E, H3K27M, H3 G34R/V), while others can be detected with FISH (eg, *CDKN2A/B* homozygous deletion, *EGFR* amplification, 1p/19q codeletion). Next-generation sequencing assays will detect many of these and other events such as mutations and fusions. Methylome profiling has also emerged as a powerful tool that can be used itself for classification and can also either directly or indirectly identify many of the above molecular alterations.

Four general groups of diffuse gliomas are recognized in the 2021 WHO classification: 1) adult-type diffuse gliomas, 2) pediatric-type diffuse low-grade gliomas, 3) pediatric-type diffuse high-grade gliomas, and 4) circumscribed astrocytic gliomas.

Adult-type diffuse gliomas are astrocytoma, IDH-mutant; oligodendroglioma, IDH-mutant and 1p/19q-codeleted; and glioblastoma, IDH-wildtype. IDH-mutant diffuse astrocytomas are now graded 2–4 within type; the terms IDH-mutant "anaplastic astrocytoma" and "glioblastoma" have been dropped. In addition, if an IDH-mutant diffuse astrocytoma exhibits *CDKN2A/B* homozygous deletion, it is designated as a CNS WHO grade 4 neoplasm, even if histologic features of malignancy such as necrosis and microvascular proliferation are absent.

Imaging features suggestive of an IDH-mutant diffuse astrocytoma grade 2 include a homogeneous T2-hyperintense circumscribed supratentorial mass typically in the frontal or temporal lobes without calcification or enhancement. The T2-FLAIR mismatch sign, characterized by T2 homogeneity of the mass with relatively hypointense signal throughout most of the lesion on FLAIR compared with T2 sequences except for a peripheral rim of hyperintense signal, is highly predictive of IDH-mutant diffuse astrocytoma. The T2-FLAIR mismatch sign has high specificity but low sensitivity for IDH-mutant diffuse astrocytomas.[12,13] Imaging features of IDH-mutant diffuse astrocytoma grade 3 may be indistinguishable from grade 2 IDH-mutant diffuse astrocytomas. However, grade 3 astrocytomas may have T2 heterogeneity and enhancement as well as elevated maximum relative CBV. The mean maximum relative CBV is significantly higher in WHO grade 3 astrocytomas than in WHO grade 2 astrocytomas.[14] Imaging features typical of oligodendroglioma, IDH-mutant and 1p/19q-codeleted, tumors include frontal lobe location, heterogeneity, and calcification with variable enhancement (Fig 1).[12]

The presence of any one of the following 5 criteria is sufficient to designate an IDH-wildtype diffuse astrocytic glioma as a glioblastoma. IDH-wildtype is characterized by the following: microvascular proliferation or necrosis or *TERT* promotor mutation or *EGFR* gene amplification or +7/−10 chromosome copy number changes. Such tumors are no longer called "diffuse astrocytic glioma, IDH-wildtype with molecular features of glioblastoma multiforme." If an IDH-wildtype tumor exhibits none of these histologic or molecular features (eg, appears as a lower grade than a glioblastoma, CNS WHO grade 4), it would be classified as diffuse astrocytoma, NEC (Fig 1).
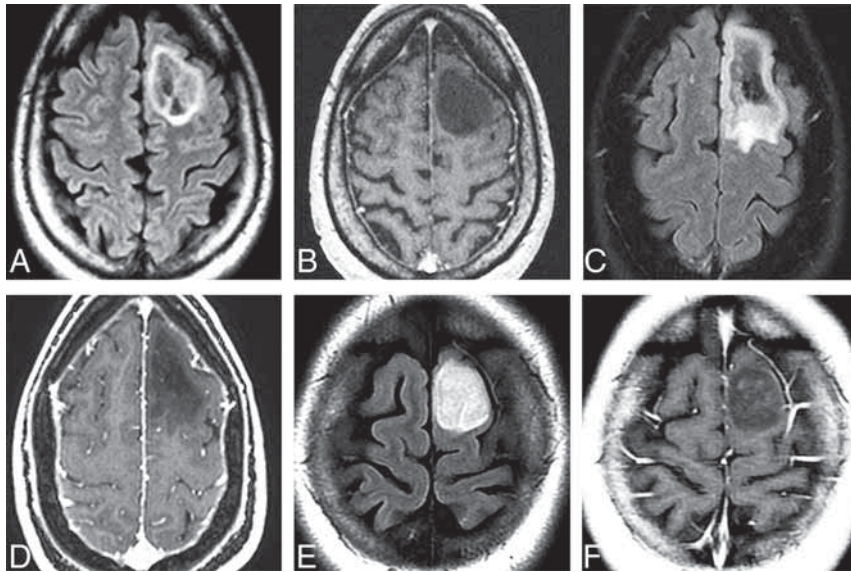
FIG 1. Adult-type diffuse gliomas. Series of 3 cases illustrates the importance of complete IDH mutation status determination and the investigation of other molecular markers in evaluation of adult-type diffuse astrocytomas. Axial FLAIR (*A*) and postcontrast T1WI (*B*) in a 54-year-old man with a first-time seizure shows a well-delineated left frontal lobe mass with a hyperintense rim surrounding a mixed signal mass. No enhancement is present. Pathology disclosed diffuse astrocytoma without necrosis or microvascular proliferation. Immunohistochemistry demonstrated that the tumor was *IDH*-mutant. Next generation sequencing disclosed *CDKN2A/B* homozygous loss, so the tumor was upgraded to WHO CNS grade 4. Axial FLAIR (*C*) and postcontrast T1WI (*D*) in a 44-year-old woman with a first-time seizure demonstrate a left frontal mass that was completely resected. Pathology findings were consistent with WHO CNS grade 3. Initial immunohistochemistry was negative for *IDH1* mutation, but further investigation disclosed the presence of an *IDH2* mutation. Final pathologic diagnosis is diffuse astrocytoma, *IDH*-mutant, grade 3. The patient is alive without evidence of disease 4 years after the initial diagnosis. Axial FLAIR (*E*) and postcontrast T1WI (*F*) in a 24-year-old woman with a first-time seizure show a well-delineated nonenhancing left frontal lobe mass that was surgically resected. Histologically, the tumor was WHO CNS grade 2 but IDH-wildtype on immunohistochemistry. No further investigation was conducted. One year later, the tumor recurred and re-resection demonstrated *EGFR* amplification and was, therefore, upgraded to glioblastoma (WHO CNS grade 4). The patient died of disseminated disease 18 months after the initial diagnosis.

Pediatric-type diffuse low-grade gliomas are diffuse astrocytomas, *MYB* or *MYBL1*-altered; angiocentric gliomas (Fig 2); polymorphous low-grade neuroepithelial tumor of the young (a newly recognized entity exhibiting oligodendroglioma-like histology with variable morphology and MAPK-pathway alterations);[15] and diffuse low-grade gliomas, MAPK pathway–altered. Angiocentric gliomas are T2-hyperintense masses typically in the temporal or frontal lobe cortex in young patients with seizures (Fig 2). Polymorphous low-grade neuroepithelial tumors of the young are typically well-circumscribed T2-hyperintense lesions on MR imaging with central calcification and peripheral cystic components (Fig 3). They are commonly supratentorial, most often within the temporal lobe.[15,16] Diffuse low-grade glioma, MAPK pathway–altered, is a group of neoplasms that are IDH- and H3-wildtype and include most tectal gliomas. Up-regulation of the *RAS/MAPK* pathway is almost universal in these lesions, with a spectrum of *FGFR1* and *BRAF* mutations. Histologic features of malignancy and molecular alterations such as *CDKN2A/B* mutations are absent.[17,18] The classic tectal gliomas are not considered a

distinct WHO entity. Most fit histologically and genetically into either pilocytic astrocytoma with *BRAF* alterations and *NRAS* mutations or diffuse low-grade glioma, *MAPK* pathway–altered.

Pediatric-type diffuse high-grade gliomas are defined primarily by molecular features and include diffuse midline glioma, H3K27-altered (note that the term "mutant" has been changed) (Fig 4); diffuse hemispheric glioma, *H3 G34*-mutant (an *H3F3A*-mutant, IDH-wildtype tumor that exhibits glioblastoma-like histology, often with primitive embryonal regions) (Fig 5); diffuse pediatric-type high-grade glioma, H3-wildtype and IDH-wildtype (a group of tumors with different possible genotypes); and infant-type hemispheric glioma (Fig 6).[19,20] The classic diffuse intrinsic pontine gliomas seen on MR imaging as expansile T2-hyperintense lesions are most commonly diffuse midline gliomas, H3K27-altered pathologically, similar to the 2016 WHO description. However, other gliomas may affect the pons.[21] In addition to the more common pediatric brainstem glioma presentation, H3K27-altered high-grade gliomas occur in adults and have the same lethality as in their pediatric counterparts.[18] Unilateral thalamic or bithalamic lesions are common in H3K27-altered high-grade gliomas as is aggressive local spread and early metastatic dissemination.

Infant-type hemispheric gliomas are tumors of early childhood that exhibit high-grade astrocytic (often glioblastoma-like) histologic features with alterations in *ALK/ROS1/NTRK/MET*. A large, bulky nearly holohemispheric, heterogeneous-appearing tumor with intratumoral hemorrhage is typical.

Circumscribed astrocytic gliomas include long-recognized neoplasms (such as pilocytic and subependymal giant cell astrocytomas) and 2 new entities, high-grade astrocytomas with piloid features and astroblastoma, *MN1*-altered. While not designated as separate entities, the molecular characterization of low-grade gliomas has had a profound effect on their treatment. For instance, the identification of BRAF V600E mutations allows targeted disruption by using BRAF inhibitors, with favorable clinical results.[22]

The diagnosis of high-grade astrocytoma with piloid features recognizes unusual cases in which a relatively circumscribed tumor with distinct piloid cytology occurs in the setting of a more malignant astrocytoma (WHO grades 3 or 4).[23] These tumors usually occur in adults, exhibit *CDKN2A/B* deletions, and have a distinct DNA methylation profile that differs from the typical childhood pilocytic astrocytomas. Most of these tumors occur in
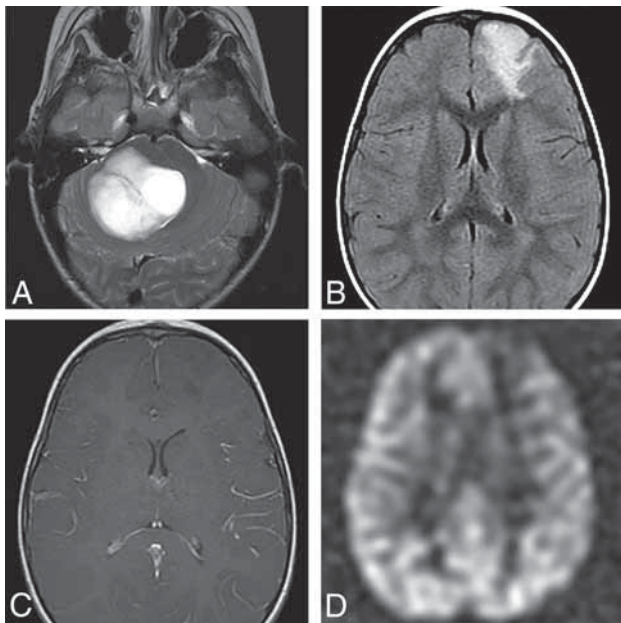
FIG 2. Pediatric-type diffuse low-grade glioma. Axial T2 (*A*) MR image in a 7-year-old boy with a diffuse astrocytoma, *MYB*-altered, shows a hyperintense mass in the pons with no significant surrounding edema. There was no enhancement and no diffusion restriction of the mass (not shown). Axial FLAIR (*B*), postcontrast T1 (*C*), and arterial spin-labeling (ASL) (*D*) in a 1-year-old child with an angiocentric glioma show a FLAIR hyperintense mass involving the cortex and subcortical white matter of the left frontal lobe. There is no enhancement (*C*) and decreased perfusion (*D*) on ASL imaging.

the posterior fossa (PF), are T2-hyperintense, and show heterogeneous enhancement.[23] The relationship with so-called "anaplastic pilocytic astrocytomas" and pre-existing pilocytic astrocytomas is currently undetermined.

Astroblastoma, *MN1*-altered, is newly classified as a circumscribed astrocytic glioma (in 2016 it was categorized with "other gliomas"). *MN-1* alterations are present in 70%.[24] If *MN-1* alteration is absent or not determined, the tumor is designated NEC or NOS, respectively. Most astroblastomas are located superficially in a cerebral hemisphere and are relatively well-circumscribed tumors that can be multicystic or "bubbly" in appearance. Edema is minimal or absent (Fig 7).[8,25,26] No formal grade for astroblastoma is assigned in the 5th edition.

Miscellaneous 5th Edition Glioma Items. In 2021, pilomyxoid astrocytoma continues to be considered a variant of pilocytic astrocytoma, not a distinct entity. The location modifier (third ventricle) has been dropped from choroid glioma. Like medulloblastoma, it only occurs in 1 location; therefore, a location modifier is not necessary.

Glioneuronal and Neuronal Tumors

Ganglioglioma, desmoplastic infantile ganglioglioma/astrocytoma, dysembryoplastic neuroepithelial tumor, and other mixed glioneuronal tumors such as rosette-forming glioneuronal tumor are unchanged. Newly clarified and added tumor entities include diffuse glioneuronal tumor with oligodendroglioma-like features and nuclear clusters (DGONC), myxoid glioneuronal tumor

(MGNT), and multinodular and vacuolating neuronal tumor (MVNT).

DGONC is included in the 5th edition as a provisional entity, defined primarily by a DNA methylation profile. As the name implies, histology is oligodendroglioma-like with large cells that have clusters of nuclei. DGONCs are primarily pediatric tumors but can occur at all ages.[27]

MGNT is a CNS WHO grade 1 neoplasm that is stereotypically located in the septum pellucidum, though it can also occur in the corpus callosum and periventricular white matter. Oligodendrocyte-like tumor cells are embedded in a prominent myxoid stroma. Specific mutations in *PDGFRA* are definitional.[28,29] In addition to location, suggestive imaging findings include T2 hyperintensity, peripheral FLAIR hyperintensity, and lack of enhancement (Fig 8). MGNTs are considered CNS WHO grade 1 neoplasms, but many cases exhibit ventricular dissemination or local recurrence/progression.[8,29]

MVNT was considered a pattern of ganglion cell tumors in the 2016 WHO. Whether MVNT represented a neoplastic or malformative process was then unknown. Now MVNTs are recognized as clonal neoplasms of the MAPK pathway with mutations in *MAPK2K1* and *BRAF* (excluding V600E) as well as *FGFR2* fusions. MVNTs are nonprogressive CNS WHO grade 1 lesions. MR imaging features are virtually pathognomonic with clusters of T2-FLAIR hyperintense nodules (little bubbles) along the undersurface of the cerebral cortex and subcortical white matter.[30,31] MVNT-like lesions have also been reported in the posterior fossa.[32]

Ependymal Tumors

Ependymomas (EPNs) are the last of the glioma/glioneuronal/neuronal tumor groupings. The 2016 WHO divided ependymal tumors into 4 subgroups: subependymoma (CNS WHO grade I), myxopapillary ependymoma (CNS WHO grade I), ependymoma (CNS WHO grade II), and anaplastic ependymoma (CNS WHO grade III).

In a major departure since the 2016 WHO, ependymomas are now uniquely grouped by location.[8,9] The WHO recognized 3 distinct anatomic sites: supratentorial (ST), PF, and spinal cord (SC) EPNs. Within each specific anatomic site, molecularly defined subgroups are defined by gene and DNA methylation profiling. Each differs in location, age, prognosis, and clinicopathologic characteristics.[9]

ST-EPN. *ZFTA* fusion–positive ependymomas (formerly *RELA*-fusion ependymoma) are extraventricular hemispheric tumors that exhibit rearrangement of partners with the *ZFTA* (formerly *C11orf95*) genes (Fig 9). These tumors are the largest group of currently defined ST-EPNs. They occur in both children and adults and are designated CNS WHO grade 2 or 3 neoplasms. They appear as relatively well-defined mixed cystic-solid masses on imaging studies. *YAP1*-fusion ST-EPNs are found mostly in children younger than 3 years of age and have a better prognosis than *ZFTA* ependymomas.[33] Tumors that do not have the *ZFTA*-or *YAP1*-fusion events are termed ST-EPN are described by their histologic features.
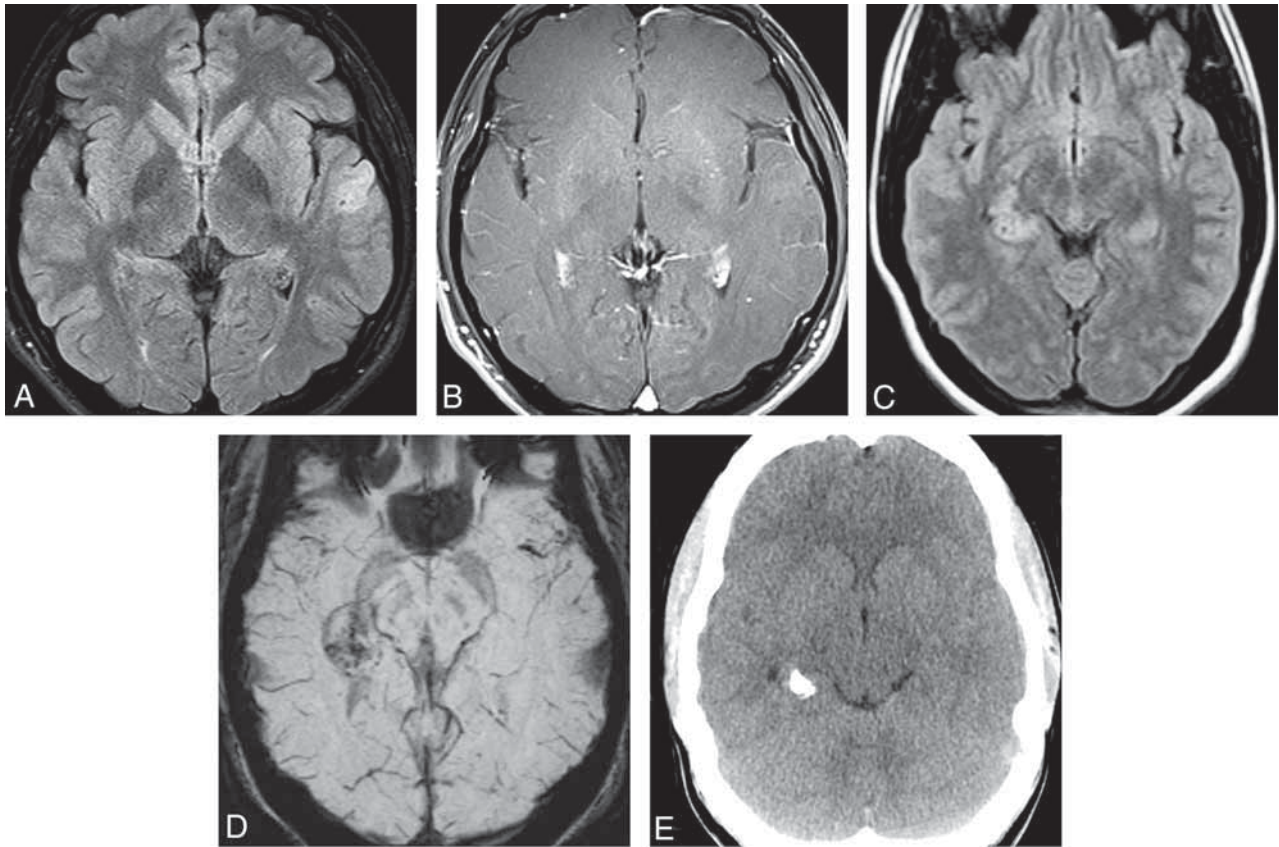
FIG 3. Two patients with the WHO 2021 new-entity polymorphous low-grade neuroepithelial tumor of the young (PLNTY). Axial FLAIR (*A*) and postcontrast T1-weighted (*B*) MR images in a 19-year-old man with refractory epilepsy show a hyperintense, nonenhancing mass in the cortex and subcortical white matter of the left temporal lobe. Axial FLAIR (*C*) and susceptibility-weighted (*D*) MR images and a noncontrast CT image (*E*) in a 19-year-old woman with progressive seizure show a FLAIR-hyperintense, SWI-hypointense mass with characteristic calcification seen on CT in the right medial temporal lobe (Case courtesy of M. Castillo, MD).

PF-EPNs can now be divided molecularly into 2 subgroups: PF-EPN A and PF-EPN-B.[34] PF-A ependymomas occur mainly in infants, exhibit loss of H3K27me3 expression on immunohistochemistry, exhibit EZHIP overexpression, and have significantly worse outcome than PF-EPN-B tumors. PF-EPN-B tumors are more common in older children and adults. Posterior fossa ependymomas are characterized on MR imaging as a lobulated, heterogeneous mass in the body or inferior fourth ventricle, which often extends through the foramen of Magendie into the cisterna magna or through the foramina of Luschka into the cerebellopontine angle cisterns. Calcification and cystic changes are often seen. Both the histology and imaging features of the 2 posterior fossa ependymoma subgroups are similar, but PF-EPN-A tumors are more likely to have a lateral location within the posterior fossa and show cerebellar invasion.[9,35] Tumors that cannot be evaluated further are termed posterior fossa ependymomas and are described by their histologic features.

Spinal Ependymomas. The 2021 WHO recognizes a new type of spinal cord ependymoma with *MYCN*–amplification. *MYCN*-amplified ependymoma is mostly found in adults and exhibits anaplastic histology. These tumors are typically located in the cervical or thoracic spinal cord and extend over many spinal segments. These spinal cord tumors are heterogeneously T2-hyperintense and enhancing and are typically extramedullary or have an exophytic portion if intramedullary and are characterized by leptomeningeal disease. Early dissemination and poor prognosis are typical.[9,36] Of note, myxopapillary ependymomas are now designated CNS WHO grade 2 neoplasms because their biologic behavior is more consistent with this designation.[9]

Choroid Plexus Tumors
The classification of choroid plexus tumors remains unchanged in 2021, though these are now listed separately from the glial and glioneuronal neoplasms.

Embryonal Tumors
The 2021 WHO classifies CNS embryonal tumors into 2 groups: medulloblastoma and other CNS embryonal tumors (the term "primitive neuroectodermal tumor" has been abandoned since 2016).

Medulloblastoma
As in 2016, medulloblastomas (MBs) can be either molecularly or histologically defined. The molecularly-defined MB subgroups are defined by DNA methylation or transcriptome profiling and remain unchanged: medulloblastoma, *WNT*-activated; medulloblastoma, *SHH*-activated and *TP53* wild-type; medulloblastoma,
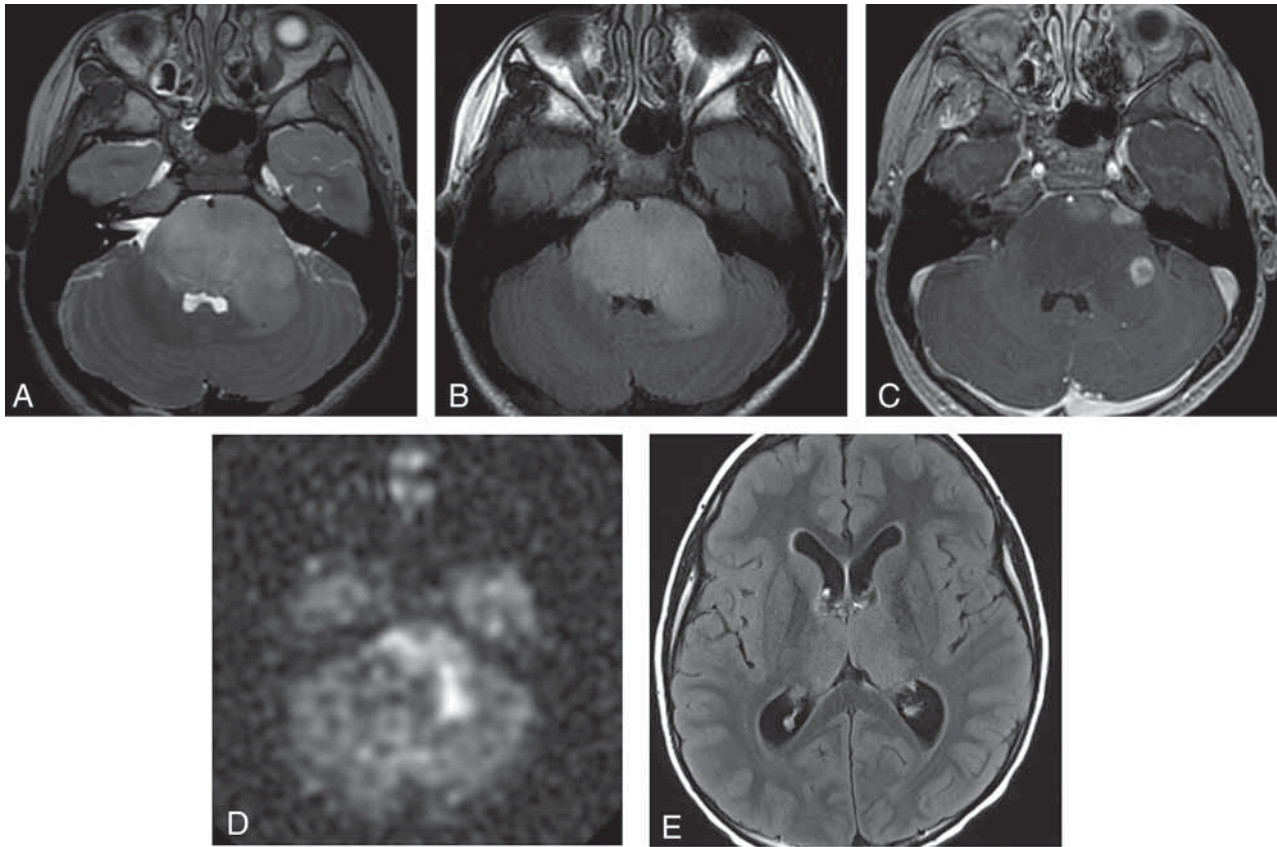
FIG 4. Pediatric-type diffuse high-grade gliomas. Diffuse midline glioma, H3K27-altered in an 8-year-old girl with cranial neuropathies. Axial T2 (*A*) and FLAIR (*B*) MR images show an expansile, hyperintense pontine mass. Axial postcontrast T1 MR image (*C*) shows heterogeneous enhancement within the mass. Arterial spin-labeling (ASL) perfusion (*D*) shows increased perfusion. *E*, Axial FLAIR MR image shows a bithalamic hyperintense mass. Postcontrast T1WI showed no significant enhancement, and ASL perfusion showed increased perfusion within the bilateral thalami (not shown). These WHO grade 4 tumors have a poor prognosis.
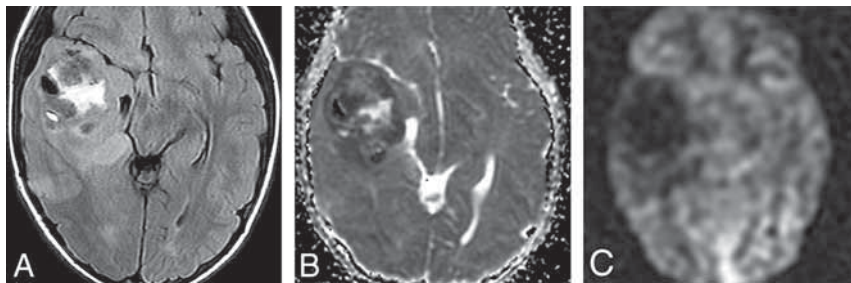
FIG 5. Diffuse hemispheric glioma, H3 G34-mutant and IDH-wildtype tumor in an 8-year-old boy. *A*, Axial FLAIR shows a large, very heterogeneous right temporal lobe mass with minimal surrounding edema. *B*, An ADC map in the same case shows restricted diffusion consistent with a high-cellularity tumor. *C*, Arterial spin-labeling perfusion shows decreased perfusion in the tumor. In pediatric tumors, perfusion is often less helpful compared with diffusion-weighted imaging in discriminating tumor grade. Histology demonstrated necrosis, hemorrhage, and neovascularity in a glioblastoma-like pattern, consistent with grade 4 tumor.

SHH-activated and *TP53*-mutant; and medulloblastoma, non-*WNT*/non-*SHH*.[11,37-39]

Medulloblastoma, *WNT*-activated, represents approximately 10% of MBs. There are 2 age-determined subtypes: children and adults. *WNT* MBs can be found in all posterior fossa locations and are thought to arise from the lower rhombic lip. Imaging studies suggest that the cerebellar peduncle and cerebellopontine angle are the most characteristic but not the only location. *WNT*-activated MBs have the best prognosis of all 4 groups. Metastases are rare at diagnosis, and the 5-year survival rate is 95%.[11,37,38]

Medulloblastoma, *SHH*-activated/*TP53* wild-type, represents approximately 30% of MBs overall but accounts for nearly two-thirds of MBs occurring between 3–16 years of age. This MB subgroup has the most striking biologic, pathologic, and clinical heterogeneity of all 4 subgroups. *SHH*-activated MBs arise from granule neuron progenitor cells in the upper rhombic lip, so a cerebellar hemispheric location is typical. These MBs have 4 provisional molecular subtypes as defined by DNA methylation or transcriptome profiling: *SHH-1* and *SHH-2* are the most common subgroups to exhibit desmoplastic or medulloblastoma with extensive nodularity histology. Desmoplastic MBs are more common in adults and have a predilection for the lateral cerebellar hemisphere.[37] *SHH-3* and *SHH-4* most commonly
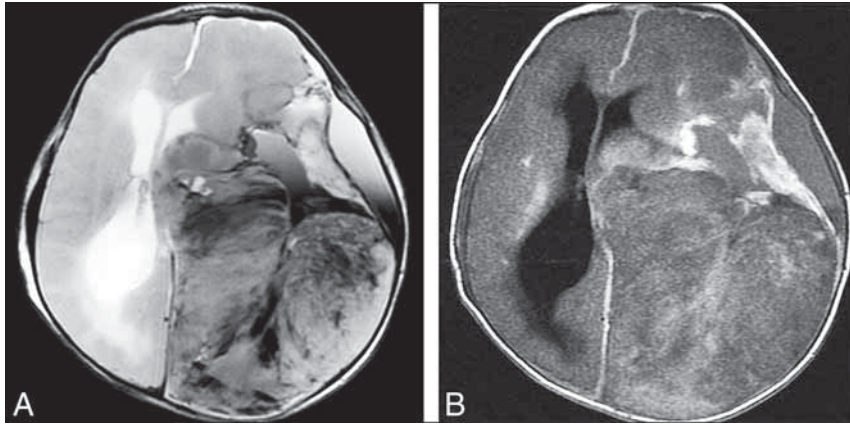
FIG 6. Infant-type hemispheric glioma, NOS. A male neonate child with macrocephaly and bulging fontanelles had a large, heterogeneous-appearing mass on an emergent CT scan (not shown). Axial T2-weighted (*A*) and postcontrast T1-weighted (*B*) MR images show a very heterogeneous mass with enhancement involving almost the entirety of the left cerebral hemisphere.
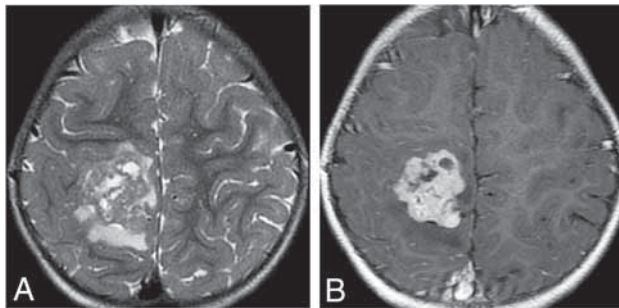
FIG 7. Axial T2WI in a 19-month-old child with astroblastoma, MN1-altered. *A,* Axial T2WI shows a bubbly-appearing mixed-signal hemispheric mass with little surrounding edema. *B,* Postcontrast T1WI shows that the mass enhances strongly but heterogeneously.

exhibit classic or large-cell anaplastic histology and can be found in all locations.[39,40]

Medulloblastoma, *SHH*-activated/*TP53*-mutant, is the rarest of the MB subtypes and has the worst overall prognosis.[11,40]

Medulloblastoma, non-*WNT*/non-*SHH*, is the most common MB subtype, representing 50%–60% of all MBs. This subtype encompasses the former group 3 (20%) and group 4 (40%–50%) MBs. This subtype has 8 molecular subgroups (Gp3/4–1 to Gp3/4–8) as determined by methylation profiling. Non-*SHH*, non-*WNT* MBs can be found in all locations and often exhibit minimal or no enhancement.[11]

Other CNS Embryonal Tumors

This group of "other" embryonal tumors includes atypical teratoid/rhabdoid tumor and the addition of several "new" tumor types: a provisional type called cribriform neuroepithelial tumor and CNS tumor with *BCOR* internal tandem duplication. One embryonal tumor with a newly identified genotype is CNS neuroblastoma, *FOXR2*-activated. This group also includes embryonal tumor with multilayered rosettes (ETMR).

Cribriform Neuroepithelial Tumor. Cribriform neuroepithelial tumor (provisional diagnosis) is a nonrhabdoid neuroectodermal tumor characterized molecularly by loss of nuclear *SMARCB1/INI1* expression and histologically by cribriform strands/ribbons. Cribriform neuroepithelial tumors occur near the ventricles in young children and have a better prognosis than atypical teratoid/rhabdoid tumors.[40]

CNS Tumor with *BCOR* Internal Tandem Duplication. CNS tumors with *BCOR* internal tandem duplication are mostly hemispheric malignant tumors of children and adolescents that are characterized by internal tandem duplication in the *BCOR* gene, similar to other systemic tumors.[41]

ETMR was included in 2016 specifically as chromosome 19 microRNA cluster–altered. An additional subtype, *DICER1*-mutated ETMR, has been recently described. ETMRs subsume many prior entities such as embryonal tumor with abundant neuropil and true rosettes, medulloepithelioma, ependymoblastoma, and many tumors formerly known as CNS primitive neuroectodermal tumors. ETMRs are tumors of infants and children younger than 4 years of age. They are seen on imaging studies as large, cellular, relatively well-demarcated-but-heterogeneous-appearing masses.[42] While they do occur in the posterior fossa, most are supratentorial hemispheric lesions (70% of cases). Necrosis and intratumoral hemorrhage are common. Solid components of the tumors typically exhibit restricted diffusion. Enhancement varies from patchy, sparse to mostly absent (Fig 10).[42]

CNS Neuroblastoma, *FOXR2*-Activated. CNS neuroblastoma is a newly recognized embryonal tumor that has a characteristic histology and *FOXR2* gene alterations.[43] These primary CNS neuroblastomas have a peak at 5 years of age and are characterized by neuronal differentiation, high vascularity, necrosis, and endothelial proliferation. Imaging shows a large, heterogeneous supratentorial mass with prominent cysts, necrosis, little surrounding edema, and variable enhancement.

Keep in mind that the imaging differential diagnosis of a large, bulky, heterogeneous hemispheric mass in an infant or young child includes ETMR, infant-type hemispheric glioma, *ZFTA* ependymoma, CNS neuroblastoma, *FOXR2*-activated and CNS embryonal tumor, NOS or NEC. The term primitive neuroectodermal tumor has been abandoned since 2016.

Pineal Tumors

With 1 exception, pineal tumors remain unchanged since 2016. A newly codified tumor, desmoplastic myxoid tumor of the pineal region, *SMARCB1*-mutant, is now recognized. This rare tumor of the pineal region (not specifically the pineal gland) has both desmoplastic and myxoid changes but no histopathologic signs of malignancy.[44] Only a limited number of cases have been reported with an age range of 15–61 years (median, 40 years).[11]
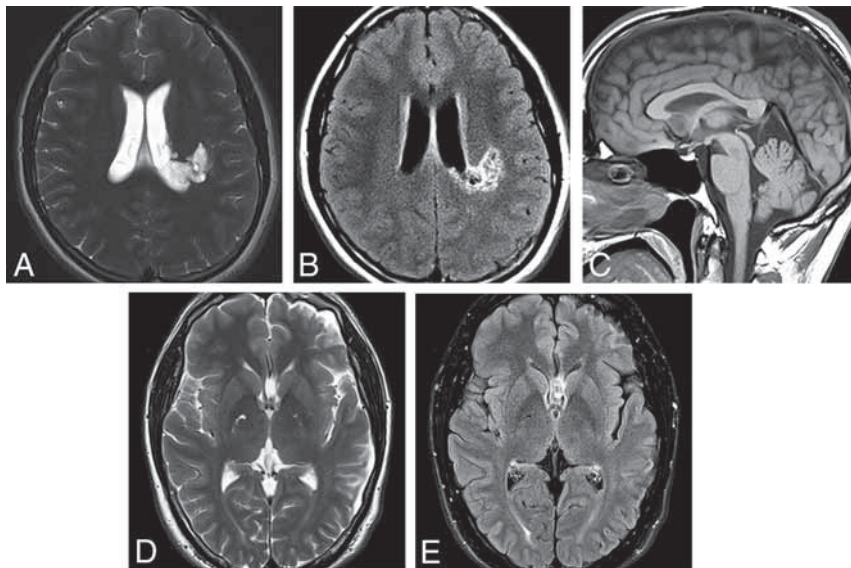
FIG 8. Two cases of MGNT are illustrated. *A*, Axial T2WI in a 14-year-old boy shows an extremely hyperintense, slightly bubbly mass in the left juxtaventricular white matter. *B*, Axial FLAIR shows a hyperintense rim surrounding a largely isointense center of the mass. Smaller-but-similar-appearing lesions are adjacent to the mass. The mass did not enhance following contrast administration. *C*, Sagittal T1WI in a 39-year-old man shows a well-demarcated mass in the corpus callosum rostrum/septum pellucidum. *D*, The mass is extremely hyperintense on T2WI. *E*, FLAIR shows that the mass has a hyperintense rim with an isointense center. The mass is thought to represent an MGNT because of its classic location and signal characteristics but is not biopsy-proven.
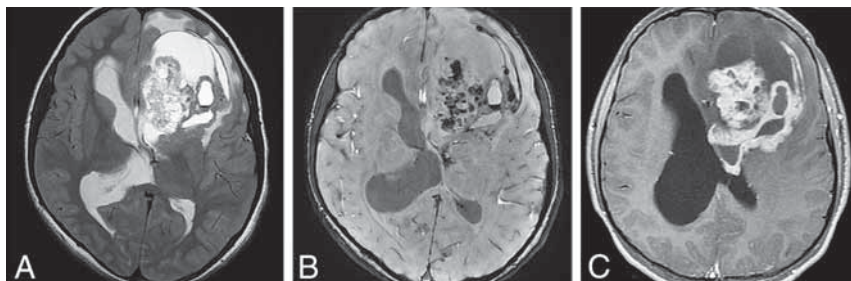
FIG 9. *ZFTA* fusion–positive ependymoma in an 11-year-old girl. *A*, Axial T2WI shows a large, bulky, heterogeneous left frontal mass. *B*, Susceptibility-weighted scan shows intratumoral hemorrhage. *C*, Strong-but-very heterogeneous enhancement is seen on postcontrast T1WI.

Cranial and Paraspinal Nerve Tumors

The term malignant melanotic nerve sheath tumor, previously called melanotic schwannoma, has been changed, in part, because it behaves more aggressively than nonmelanotic schwannomas and also to conform with soft-tissue nomenclature.

Meningiomas

In terms of the overall classification, the meningioma tumor group remains unchanged. However, there are a number of molecular alterations that are now recognized as diagnostically and prognostically useful.

Mesenchymal, Nonmeningothelial Tumors

Mesenchymal, nonmeningothelial tumors are divided into 2 groups: soft-tissue tumors and chondro-osseous tumors. The only major changes in 2021 are with soft-tissue tumors.

Soft-Tissue Tumors

Soft-tissue tumors are subcategorized into fibroblastic and myofibroblastic tumors, vascular tumors, skeletal muscle tumors, and tumors of uncertain differentiation. The term hemangiopericytoma is now considered obsolete, and the preferred term "solitary fibrous tumor" is used to correspond to extracranial solitary, fibrous tumors. Solitary, fibrous tumors are the most common nonmeningothelial mesenchymal neoplasm and share the common molecular feature of *NAB2-STAT6* gene fusions. Tumor grades vary from WHO 1–3 (WHO grade III solitary fibrous tumors were previously referred to as "anaplastic hemangiopericytomas"). Imaging features often resemble those of meningiomas.

There are 3 newly recognized intracranial soft-tissue tumors: intracranial mesenchymal tumor, *FET-creB* fusion-positive; *CIC*-rearranged sarcoma; and primary intracranial sarcoma, *DICER1*-mutant.[11,45]

Intracranial mesenchymal tumor, *FET-creB* fusion-positive, often features specific *EWSR1-creB1* fusions. These tumors can be extra-axial or intraventricular. The cerebral convexities are the most common location. They are typically T2-FLAIR hyperintense, exhibit strong enhancement, and often have a dural "tail." The major differential diagnosis is atypical or anaplastic meningioma.[11,45]

CIC-rearranged sarcoma corresponds to similar soft-tissue tumors. Multiple *CIC*-fusion partners have been identified. Round-cell sarcomas with myxoid features are typical. These tumors can occur at any age but are most common in adolescents and young adults. They are highly aggressive and are designated as WHO CNS grade 4 lesions.[11,45]

Primary intracranial sarcoma, *DICER1*-mutant, is a highly-malignant CNS sarcoma that is part of the expanding spectrum of *DICER1* and type 1 neurofibromatosis syndromes. This intracranial sarcoma primarily occurs in children and young adults, exhibiting malignant spindle cell morphology often with focal rhabdomyoblastic differentiation.[11,45]

Hematolymphoid Tumors

Other than grouping lymphomas and histiocytic tumors together as hematolymphoid tumors, no significant changes occurred in the 2021 WHO.
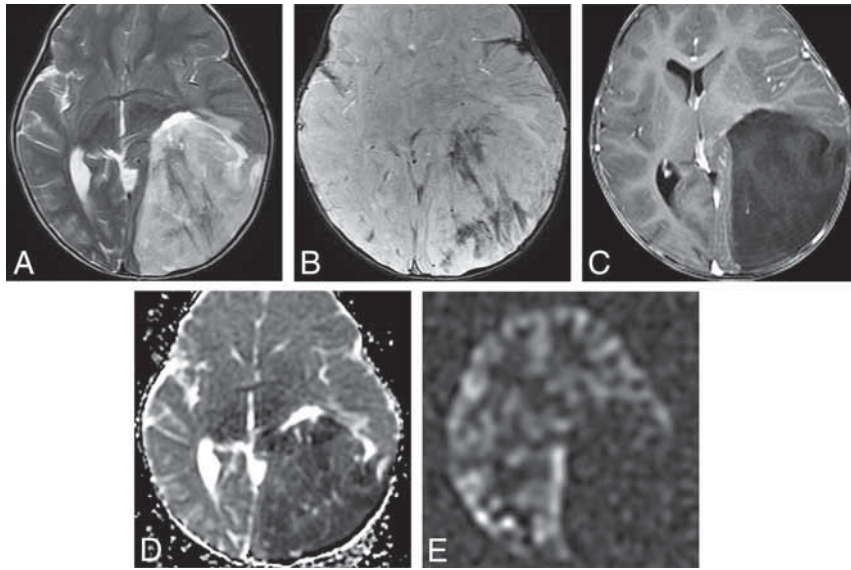
FIG 10. Embryonal tumor with multilayered rosettes in a 1-year-old girl. *A*, An axial T2-weighted scan shows a large, left parieto-occipital mass with little surrounding edema. *B*, The mass exhibits hemorrhage on susceptibility-weighted imaging and no enhancement following contrast administration (*C*). *D*, Strikingly restricted diffusion is seen on the ADC map. *E*, Arterial spin-labeling perfusion shows decreased perfusion in the tumor.

Germ Cell Tumors

No significant 2021 changes were made in germ cell neoplasms.

Tumors of the Sellar Region

Pituitary adenomas are now designated as pituitary adenoma/pituitary neuroendocrine tumors to correspond to systemic neuroendocrine tumors. Pituitary neuroendocrine tumors are now also classified according to adenohypophyseal cell lineages, rather than just by the hormone produced. Pituicytoma, granular cell tumor of the sellar region and spindle cell oncocytoma remain unchanged from WHO 2016, and though they are classified as separate tumor types, they are considered a related group of tumor types with possibly morphologic variations of the same tumor.[11,46]

One new tumor, pituitary blastoma, has been added to the 2021 WHO Classification of sellar region tumors. Pituitary blastomas are rare embryonal sellar neoplasms of infants (median age, 8 months) that are associated with somatic or germline *DICER1* mutations. Pituitary blastomas are hypophyseal tumors that resemble a 10- to 12-week embryonic-stage pituitary gland. Primitive blastemal cells similar to those in pleuropulmonary blastomas, neuroendocrine cells, and Rathke-type epithelium in rosettes/glandular structures are characteristic. Pituitary blastomas are designated WHO CNS grade 4 neoplasms.[11,45]

Summary

The 2021 5th edition WHO Classification of CNS neoplasms (the series popularly known as the Blue Books) builds on the trend of molecular tumor classification first introduced in the 2016 (4-plus) edition. Gliomas are divided into adult-type diffuse gliomas, pediatric-type diffuse low-grade gliomas, pediatric-type diffuse high-grade gliomas, and circumscribed astrocytic gliomas. WHO

grades are now expressed in Arabic numbers instead of Roman numerals. The 5th edition introduces 14 new gliomas and glioneuronal tumors and 8 other new tumors into the neuropathologic lexicon.[36] The critical importance of identifying mutations other than the canonical *IDH1* R132H mutation in diffuse gliomas, especially in patients younger than 55 years of age, is emphasized. Neuroradiologists must familiarize themselves with the updated WHO Classification of CNS neoplasms to function appropriately as part of the modern neuro-oncology clinical team.

Disclosure forms provided by the authors are available with the full text and PDF of this article at www.ajnr.org.

REFERENCES

1. Louis DN, Aldape K, Brat DJ, et al. **Announcing cIMPACT-NOW: the Consortium to Inform Molecular and Practical Approaches to CNS Tumor Taxonomy.** *Acta Neuropathol* 2017;133:1–3 CrossRef Medline
2. Louis DN, Aldape K, Brat DJ, et al. **cIMPACT-NOW (the Consortium to Inform Molecular and Practical Approaches to CNS Tumor Taxonomy): a new initiative in advancing nervous system tumor classification.** *Brain Pathol* 2017;27:851–52 CrossRef Medline
3. Louis DN, Wesseling P, Paulus W, et al. **cIMPACT-NOW update 1: not otherwise specified (NOS) and not elsewhere classified (NEC).** *Acta Neuropathol* 2018;135:481–84 CrossRef Medline
4. Louis DN, Giannini C, Capper D, et al. **cIMPACT-NOW update 2: diagnostic clarifications for diffuse midline glioma, H3K27M-mutant and diffuse astrocytoma/anaplastic astrocytoma, IDH-mutant.** *Acta Neuropathol* 2018;135:639–42 CrossRef Medline
5. Brat DJ, Aldape K, Colman H, et al. **cIMPACT-NOW update 3: recommended diagnostic criteria for "diffuse astrocytic glioma, IDH-wildtype, with molecular features of glioblastoma, WHO grade IV."** *Acta Neuropathol* 2018;136:805–10 CrossRef Medline
6. Ellison DW, Hawkins C, Jones DTW, et al. **cIMPACT-NOW update 4: diffuse gliomas characterized by MYB, MYBL1, or FGFR1 alterations or BRAF V600E mutation.** *Acta Neuropathol* 2019;137:683–87 CrossRef Medline
7. Brat DJ, Aldape K, Colman H, et al. **cIMPACT-NOW update 5: recommended grading criteria and terminologies for IDH-mutant astrocytomas.** *Acta Neuropathol* 2020;139:603–08 CrossRef Medline
8. Louis DN, Wesseling P, Aldape K, et al. **cIMPACT-NOW update 6: new entity and diagnostic principle recommendations of the cIMPACT-UTRECHT meeting on future CNS tumor classification and grading.** *Brain Pathol* 2020;30:844–56 CrossRef Medline
9. Ellison DW, Aldape KD, Capper D, et al. **cIMPACT-NOW update 7: advancing the molecular classification of ependymal tumors.** *Brain Pathol* 2020;30:863–66 CrossRef Medline
10. Louis DN, Ellison DW, Brat DJ, et al. **cIMPACT-NOW: a practical summary of diagnostic points from Round 1 updates.** *Brain Pathol* 2019;29:469–72 CrossRef Medline
11. WHO Classification of Tumours Editorial Board. World Health Organization Classification of Tumours of the Central Nervous System. 5th ed: Lyon: International Agency for Research on Cancer; 2021

12. Batchala PP, Muttikkal TJ, Donahue JH, et al. **Neuroimaging-based classification algorithm for predicting 1p/19q-codeletion status in IDH-mutant lower grade gliomas.** *AJNR Am J Neuroradiol* 2019;40:426–42 CrossRef Medline

13. Patel SH, Poisson LM, Brat DJ, et al. **T2-FLAIR mismatch, an imaging biomarker for IDH and 1p/19q status in lower-grade gliomas: a TCGA/TCIA project.** *Clin Cancer Res* 2017;23:6078–85 CrossRef Medline

14. Doig D, Kachramanoglou C, Dumba M, et al. **Characterisation of isocitrate dehydrogenase gene mutant WHO grade 2 and 3 gliomas: MRI predictors of 1p/19q co-deletion and tumour grade.** *Clin Radiol* 2021;76:785 CrossRef Medline

15. Chen Y, Tian T, Guo X, et al. **Polymorphous low-grade neuroepithelial tumor of the young: case report and review focus on the radiological features and genetic alterations.** *BMC Neurol* 2020;20:123 CrossRef Medline

16. Benson JC, Summerfield D, Carr C, et al. **Polymorphous low-grade neuroepithelial tumor of the young as a partially calcified intraaxial mass in an adult.** *AJNR Am J Neuroradiol* 2020;41:573–78 CrossRef Medline

17. Ryall S, Zapotocky M, Fukuoka K, et al. **Integrated molecular and clinical analysis of 1,000 pediatric low-grade gliomas.** *Cancer Cell* 2020;37:569–83 CrossRef Medline

18. Ross JL, Velazquez Vega J, Plant A, et al. **Tumor immune landscape of paediatric high-grade gliomas.** *Brain* 2021;144:2594–2609 CrossRef Medline

19. Roux A, Pallud J, Saffroy R, et al. **High-grade gliomas in adolescents and young adults highlight histomolecular differences from their adult and pediatric counterparts.** *Neuro Oncol* 2020;22:1190–1202 CrossRef Medline

20. Yekula A, Gupta M, Coley N, et al. **Adult H3K27M-mutant diffuse midline glioma with gliomatosis cerebri growth pattern: case report and review of the literature.** *Int J Surg Case Rep* 2020;68:124–28 CrossRef Medline

21. Aboian MS, Solomon DA, Felton E, et al. **Imaging characteristics of pediatric diffuse midline gliomas with histone H3 K27M mutation.** *AJNR Am J Neuroradiol* 2017;38:795–800 CrossRef Medline

22. Muñoz Pérez JP, Muchart J, Santa-María López V, et al. **Targeted therapy for pediatric low-grade glioma.** *Childs Nerv Syst* 2021;37:2511–20 CrossRef Medline

23. Bender K, Perez E, Chirica M, et al. **High-grade astrocytoma with piloid features (HGAP): the Charite experience with a new central nervous system tumor entity.** *J Neurooncol* 2021;153:109–20 CrossRef Medline

24. Chen W, Soon YY, Pratiseyo PD, et al. **Central nervous system neuroepithelial tumors with MN1-alteration: an individual patient data meta-analysis of 73 cases.** *Brain Tumor Pathol* 2020;37:145–53 CrossRef Medline

25. Hirose T, Nobusawa S, Sugiyama K, et al. **Astroblastoma: a distinct tumor entity characterized by alterations of the X chromosome and MN1 rearrangement.** *Brain Pathol* 2018;28:684–94 CrossRef Medline

26. Mhatre R, Sugur HS, Nandeesh BN, et al. **MN1 rearrangement in astroblastoma: study of eight cases and review of literature.** *Brain Tumor Pathol* 2019;36:112–20 CrossRef Medline

27. Deng MY, Sill M, Sturm D, et al. **Diffuse glioneuronal tumour with oligodendroglioma-like features and nuclear clusters (DGONC): a molecularly defined glioneuronal CNS tumour class displaying recurrent monosomy 14.** *Neuropathol Appl Neurobiol* 2020;46:422–30 CrossRef Medline

28. Lucas CH, Villanueva-Meyer JE, Whipple N, et al. **Myxoid glioneuronal tumor, PDGFRA p.K385-mutant: clinical, radiologic, and histopathologic features.** *Brain Pathol* 2020;30:479–94 CrossRef Medline

29. Chiang JC, Harreld JH, Tanaka R, et al. **Septal dysembryoplastic neuroepithelial tumor: a comprehensive clinical, imaging, histopathologic, and molecular analysis.** *Neuro Oncol* 2019;21:800–08 CrossRef Medline

30. Lecler A, Broquet V, Bailleux J, et al. **Advanced multiparametric magnetic resonance imaging of multinodular and vacuolating neuronal tumor.** *Eur J Neurol* 2020;27:1561–69 CrossRef Medline

31. Nunes RH, Hsu CC, da Rocha AJ, et al. **Multinodular and vacuolating neuronal tumor of the cerebrum: a new "leave me alone" lesion with a characteristic imaging pattern.** *AJNR Am J Neuroradiol* 2017;38:1899–1904 CrossRef Medline

32. Lecler A, Bailleux J, Carsin B, et al; ENIGMA Investigation Group (EuropeaN Interdisciplinary Group for MVNT Analysis). **Multinodular and vacuolating posterior fossa lesions of unknown significance.** *AJNR Am J Neuroradiol* 2019;40:1689–94 CrossRef Medline

33. Kupp R, Ruff L, Terranova S, et al. **ZFTA-translocations constitute ependymoma chromatin remodeling and transcription factors.** *Cancer Discov* 2021;11:2216–29 CrossRef Medline

34. Wang G, Jia Y, Ye Y, et al. **Identification of key methylation differentially expressed genes in posterior fossa ependymoma based on epigenomic and transcriptome analysis.** *J Transl Med* 2021;19:174 CrossRef Medline

35. Witt H, Mack SC, Ryzhova M, et al. **Delineation of two clinically and molecularly distinct subgroups of posterior fossa ependymoma.** *Cancer Cell* 2011;20:143–57 CrossRef Medline

36. Raffeld M, Abdullaev Z, Pack SD, et al. **High level MYCN amplification and distinct methylation signature define an aggressive subtype of spinal cord ependymoma.** *Acta Neuropathol Commun* 2020;8:101 CrossRef Medline

37. Reis J, Stahl R, Zimmermann H, et al. **Advanced MRI findings in medulloblastomas: relationship to genetic subtypes, histopathology, and immunohistochemistry.** *J Neuroimaging* 2021;31:306–16 CrossRef Medline

38. Coltin H, Sundaresan L, Smith KS, et al. **Subgroup and subtype-specific outcomes in adult medulloblastoma.** *Acta Neuropathol* 2021;142:859–71 CrossRef Medline

39. Skowron P, Farooq H, Cavalli FM, et al. **The transcriptional landscape of SHH medulloblastoma.** *Nat Comm* 2021;12:1749 CrossRef Medline

40. Cai C. **SWI/SNF deficient central nervous system neoplasms.** *Semin Diagn Pathol* 2021;38:167–74 CrossRef Medline

41. Tauziede-Espariat A, Pierron G, Seigfried A, et al. **The EP300:BCOR fusion extends the genetic alteration spectrum defining the new tumoral entity of "CNS tumors with BCOR internal tandem duplication."** *Acta Neuropathol Commun* 2020;8:178 CrossRef Medline

42. Shih RY, Koeller KK. **Embryonal tumors of the central nervous system: from the radiologic pathology archives.** *Radiographics* 2018;38:525–41 CrossRef Medline

43. Korshunov A, Okonechnikov K, Schmitt-Hoffner F, et al. **Molecular analysis of pediatric CNS-PNET revealed nosologic heterogeneity and potent diagnostic markers for CNS neuroblastoma with FOXR2-activation.** *Acta Neuropathol Commun* 2021;9:20 CrossRef Medline

44. Thomas C, Wefers A, Bens S, et al. **Desmoplastic myxoid tumor, SMARCB1-mutant: clinical, histopathological and molecular characterization of a pineal region tumor encountered in adolescents and adults.** *Acta Neuropathol* 2020:277–86 CrossRef Medline

45. Louis DN, Perry A, Wesseling P, et al. **The 2021 WHO Classification of Tumors of the Central Nervous System: a summary.** *Neuro Oncol* 2021;23:1231–51 CrossRef Medline

46. Lopes MB. **The 2017 World Health Organization Classification of Tumors of the Pituitary Gland: a summary.** *Acta Neuropathol* 2017;134:521–55 CrossRef Medline

PET/MRI in Pediatric Neuroimaging: Primer for Clinical Practice

C. Pedersen, M. Aboian, J.E. McConathy, H. Daldrup-Link, and A.M. Franceschi

ABSTRACT

SUMMARY: Modern pediatric imaging seeks to provide not only exceptional anatomic detail but also physiologic and metabolic information of the pathology in question with as little radiation penalty as possible. Hybrid PET/MR imaging combines exquisite soft-tissue information obtained by MR imaging with functional information provided by PET, including metabolic markers, receptor binding, perfusion, and neurotransmitter release data. In pediatric neuro-oncology, PET/MR imaging is, in many ways, ideal for follow-up compared with PET/CT, given the superiority of MR imaging in neuroimaging compared with CT and the lower radiation dose, which is relevant in serial imaging and long-term follow-up of pediatric patients. In addition, although MR imaging is the main imaging technique for the evaluation of spinal pathology, PET/MR imaging may provide useful information in several clinical scenarios, including tumor staging and follow-up, treatment response assessment of spinal malignancies, and vertebral osteomyelitis. This review article covers neuropediatric applications of PET/MR imaging in addition to considerations regarding radiopharmaceuticals, imaging protocols, and current challenges to clinical implementation.

ABBREVIATIONS: DOPA = dioxyphenylalanine; DOTATATE = [tetrazetan-D-Phe1,Tyr3]-octreotate; FET = fluoroethyltyrosine; mFBG = meta-fluorobenzyl-guanidine; MIBG = metaiodobenzylguanidine; LCH = Langerhans cell histiocytosis; max = maximum; MET = methionine; SUV = standard uptake value

Serial imaging and radiation dose reduction should remain balanced in pediatric imaging. Repeat PET/CTs, especially in pediatric neuro-oncology, result in a considerable cumulative radiation dose and may increase the risk of secondary cancer.[1-3] The risk of radiation-induced malignancy is increased at exposures of >50–100 mSv.[2] A retrospective review of 78 pediatric patients found that the average cumulative dose from PET/CT during a 5-year period amounted to 78.9 mSV.[3] Meanwhile, reduction in the cumulative dose by PET/MR imaging has been reported to be as high as 50%–70% in pediatric lymphoma.[4-6] Further dose reduction may be achieved by lowering radiopharmaceutical doses with artificial intelligence–based algorithms, which is an area of active research and product development.[7,8]

Hybrid PET/MR imaging is particularly promising in pediatric neuroimaging because it allows functional and soft-tissue characterization with a low radiation dose and comparable agreement with PET/CT reported in several recent studies.[5,6,9] Unlike PET applications in body imaging, the CT component of brain PET/CT typically provides little clinically useful information beyond attenuation correction, but it does contribute to the radiation dose. PET can be used to differentiate high-grade from low-grade tumors at the initial work-up, provide prognosis for patient progression-free survival and overall survival, identify the site for optimal biopsy, and determine the extent of tumor to optimize resection and radiation therapy.[10] PET is also useful to evaluate tumor recurrence posttreatment in the setting of equivocal MR imaging findings and to detect transformation of tumor to a higher-grade malignancy.[10] MR imaging allows DWI and FLAIR sequences, which are valuable in brain tumor assessment, and also whole-body evaluation of metastatic disease.[11-13] MR imaging–based attenuation correction methods for PET are more complex than for CT but are possible and typically involve tissue-segmentation techniques.[14]

PET/MR imaging can be performed with a sequential or synchronous system. In a synchronous system, the solid-state PET detectors are located between the body and gradient coils in the 3T MR imaging gantry, which allows truly synchronous data acquisition. In a sequential system, PET and MR imaging are performed separately with transportation of the patient between scanners. A sequential system is technically easier to achieve because

FIGURE. Diffuse astrocytoma in 4-year-old child demonstrates a nonenhancing FLAIR hyperintense mass involving the gray and white matter of the left frontal lobe (*A* and *B*). There is no evidence of reduced diffusion or hypointense signal on ADC (*C* and *D*). The inferior aspect of the lesion demonstrates a subtle decrease in FDG uptake compared with the contralateral side (*E*), while the superior portion demonstrates relative hypermetabolism on FDG-PET (*F*).

most US hospitals currently own separate MR imaging and PET machines, but 1 major drawback is the asynchronous nature of the scans, potentially giving rise to misregistration artifacts, longer scan times, and longer sedation requirements.[15,16] Therefore, a synchronous PET/MR imaging system is generally preferable in pediatric neuroimaging.[4]

Reduction in sedation need and sedation time is best achieved by decreasing the overall MR imaging scan time, eg, by specifically tailored protocols and sequence design.[17,18] In 1 study, the use of a rapid brain-tailored protocol in 1308 pediatric emergency department encounters decreased head CT use by >20% without a missed diagnosis on follow-up imaging.[19] Sequence design may be optimized with SyntheticMR (https://syntheticmr.com/company/), which allows reconstruction of multiple sequences for qualitative and quantitative analysis from a single acquisition[20] and has been applied to multiple disease processes including cancer, neurodegenerative disorders, and stroke.[21,22]

Combining PET and MR imaging results in imaging time reduction, decreases sedation time and need, and, overall, has the potential to increase throughput of scans.[4] Cost analysis of savings from increased throughput of patients remains an area of future investigation.

PET/MR Imaging in Pediatric Neuro-Oncology
CNS cancer is the leading cause of death in children and adolescents.[23] Standard-of-care treatment for pediatric brain tumors is maximum safe resection, targeted radiation therapy, and chemotherapy. PET may help differentiate high-grade from low-grade

tumors, prognosticate progression-free and overall survival, identify an optimal biopsy site, and determine tumor extent to optimize resection and radiation therapy.[10] Postoperative MR imaging may be equivocal or miss small residual lesions. In this setting, PET can be used to evaluate tumor recurrence and detect transformation to a higher tumor grade.

[18F] FDG-PET. FDG is a positron-emitting analog of glucose that uses glucose transporters to transport labeled FDG into the cells. Once the FDG is inside the cell, it gets phosphorylated by hexokinase, resulting in intracellular retention.[24] This method allows imaging of cellular glucose uptake and thus allows for assessment of cellular glucose metabolism. A higher level of FDG uptake has been shown to correlate with a higher tumor grade and lead to survival prediction in primary brain tumors such as gliomas.[10] Disadvantages of FDG-PET include high normal brain parenchymal uptake, which may lead to poor visualization of low-grade tumors, and limitations in tumor-margin assessment (Figure). Prominent FDG uptake can also be seen in inflammatory lesions, so careful multimodal lesion evaluation is recommended.[25] FDG-PET is particularly valuable when differentiating posttreatment changes from tumor recurrence in the clinical setting because the former is not expected to be FDG-avid (Online Supplemental Data).[24]

Amino Acid PET. Amino acids are critical substrates in cellular metabolic pathways for synthesis of proteins and nucleotides and generation of adenosine triphosphate, all essential for cell function and growth. Up-regulation of amino acid transporters is an early step in carcinogenesis.[26,27] The main advantage of amino acid–based tracer imaging is very low background uptake by normal brain parenchyma, allowing better lesion detection and improved tumor-border visualization. Natural and modified amino acids have been used to study amino acid metabolism of tumors, with the most commonly used tracers including ^{11}C-methionine (MET), [18F] dioxyphenylalanine (DOPA), [18F] fluoroethyltyrosine ([18F] FET), and [18F] fluciclovine (Online Supplemental Data).[26,28,29] ^{11}C-MET is a natural amino acid labeled with a carbon-11 radionuclide that has a very short half-life of 20 minutes and is, thus, limited to centers with an on-site cyclotron. The main benefit of ^{11}C-MET in pediatrics is the low radiation dose that is administered, but the inconvenience of a short half-life outweighs the benefits. [18F] FET and [18F] DOPA are modified amino acids that use the same pathway as natural amino acids but are labeled with [18F], which has led to more widespread use due to a longer half-life (110 minutes). Both tracers can be analyzed on static imaging, but interpretation of

dynamic PET is more established for [18F] FET.[30,31] One of the main applications of [18F] FET-PET in pediatric neuro-oncology is the definition of residual tumor after resection. In a study evaluating residual brain tumors in 27 pediatric patients, [18F] FET-PET found at least 1 residual tumor not clearly identified on MR imaging, which significantly altered management.[32] There are also promising results for the differentiation of radiation necrosis from tumor recurrence and the definition of tumor hypermetabolic regions, though most of the studies are performed in adults.[33]

[18F] FDG- and [11C]-MET-PET were compared in 27 children with newly diagnosed brain tumors with diverse histology.[34] Twenty-two of 23 patients had increased uptake on MET-PET. High-grade tumors demonstrated a significantly elevated mean standard uptake value (SUVmean) and maximum SUV (SUVmax) compared with low-grade tumors. When the same patients were imaged with FDG-PET, 52% of tumors were hypermetabolic; 38%, eumetabolic; and 10%, hypometabolic. Because FDG uptake was higher in high-grade tumors, it was proposed that FDG-PET may provide information on tumor grade, while MET-PET provides superior information on tumor location and border delineation.

An emerging amino acid PET tracer in pediatrics [18F] fluciclovine PET, also known as Axumin PET, is an FDA-approved tracer for imaging metastatic prostate cancer, but it is also showing promising results in neuro-oncology.[29,35-38] It has lower background uptake compared with [11C]-MET and is transported by both L-type amino acid transporter 1 and system alanine-serine-cysteine amino acid transporter-2 into the cell. Upcoming trials in pediatric brain tumors will elucidate the role and applications of this tracer in clinical neuro-oncology.

Head and Neck Tumors

Orbital Malignancies. Hybrid PET/MR imaging in pediatric orbital disease is still under evaluation. Orbital involvement by lymphoma and other lymphoproliferative malignancies can be evaluated using [18F] FDG-PET, while malignancies of the optic nerves can be evaluated by both [18F] FDG and amino acid tracers.[39] Uveal melanoma has been described as FDG-avid, while intraorbital retinoblastoma demonstrates heterogeneous FDG avidity.[39,40] Meningiomas may originate along the optic nerve sheath or extend into the orbit through the sphenoid bone or foramen rotundum and can be evaluated using somatostatin receptor analogs such as gallium-68 [tetra-zetan-D-Phe1,Tyr3]-octreotate (DOTATATE).[41]

Rhabdomyosarcoma in the Head and Neck. Rhabdomyosarcoma in the head and neck region requires multimodal evaluation. The primary tumor is best evaluated with high-resolution MR imaging including noncontrast and non-fat-suppressed T1 and postcontrast T1 while [18F] FDG-PET can help delineate metastases and detect tumor recurrence (Online Supplemental Data). Recent literature indicates that FDG-PET is superior to conventional imaging in characterization of metastatic lesions and prediction of treatment response and patient outcomes.[42,43] Notably, chest CT is currently still required to evaluate pulmonary metastases in these patients. While MR imaging and PET are making progress, the sensitivity of CT for pulmonary metastases remains superior.

Neuroendocrine Malignancies. Neuroblastoma originates in primitive neural crest cells of the sympathetic nervous system and is the most common solid extracranial tumor of childhood. Most cases are diagnosed before 5 years of age and up to 50% of patients present with metastatic disease, commonly involving lymph nodes, bone, liver, and skin (Online Supplemental Data).[44]

Iodine-123-metaiodobenzylguanidine (123I-MIBG) imaging is based on iodine accumulation in tumor cells and is the primary imaging technique for staging and treatment-response assessment and provides the foundation for targeted therapy with 131I-MIBG.[45,46] 23I-MIBG SPECT and SPECT/CT can be acquired advantageously to assist with tracer-uptake identification. In 1 meta-analysis, 123I-MIBG had lower per-lesion accuracy but was more specific compared with [18F] FDG-PET. MR imaging is a valuable for initial local staging and treatment response and lends itself well to the multivariate presentations of neuroblastoma. The sensitivity of MR imaging was superior to that of MIBG in 1 study, though less specific.[47] Whole-body MR imaging demonstrated good sensitivity for lymph node metastases, though with lower specificity compared with [18F] FDG-PET, partly due to difficulty in distinguishing treated and viable disease.[48]

More recently, 124I-MIBG-PET has demonstrated a favorable dosimetry profile and allows high-resolution images with increased accuracy for the detection of metastatic lesions in the head, neck, and spine compared with conventional 123I-MIBG SPECT in several studies.[49,50]

[18F] FDG-PET is generally preferred in non-MIBG-avid neuroblastomas, in aggressive and dedifferentiated tumors with loss of iodine uptake, and when high background activity complicates the evaluation of spinal involvement.[51,52] FDG-PET has good accuracy in metastatic lesion detection compared with 123I and 131I-MIBG scans.[11,43,44] Novel PET tracers such as [18F] DOPA have shown high accuracy and good agreement with MIBG in patients with relapse.[53-55] [18F] meta-fluorobenzylguanidine ([18F] mFBG) has been developed as a radiotracer that can provide MIBG-equivalent whole-body staging on PET/MR imaging.[56,57] Thus, [18F] mFBG PET/MR imaging may combine local and whole-body staging in 1 session, which is particularly helpful in pediatric patients who typically require anesthesia for medical imaging.

Additional imaging agents for neuroblastoma include 68Ga-DOTATATE, which is a somatostatin receptor analog approved for the detection of neuroendocrine tumors expressing somatostatin receptors such as neuroblastoma.[58] Somatostatin receptor analogs may be combined with peptide receptor radionuclide therapy for refractory neuroblastoma, eg, 177Lu-DOTATATE, because the tumor expresses somatostatin receptors, which allow select targeting.[59]

Thyroid Cancer. Thyroid nodules are less common in children than in adults but carry a higher risk of malignancy.[60] [18F] FDG-PET is not used routinely for thyroid nodules but may be useful in staging non-radioiodine-avid metastatic disease. MR imaging of the neck in this setting helps evaluate the thyroid resection bed for local recurrence and depicts anatomically complex regions such as the skull base and spine.[60]

PET/MR Imaging in Pediatric Spine Imaging

[18F] FDG-PET may provide useful information in treatment-response assessment of spinal malignancies, tumor staging, and follow-up. The role of FDG-PET in neuroblastomas was covered above (Online Supplemental Data). Nononcologic spinal imaging applications of PET/MR imaging include Langerhans cell histiocyt-osis (LCH) and spinal infection. Furthermore, [18F] DOPA may detect hormonally active beta cells in patients with congenital hyperinsulinism.

Pediatric Spinal Malignancy. Astrocytomas are the most common primary intramedullary tumor in children and young adults. Most are slow-growing, low-grade tumors, while about 10%–15% are high-grade and may demonstrate elevated tracer uptake on [18F]-FDG- and 11C-MET-PET. The classic imaging presentation is an eccentrically located infiltrating tumor with fusiform spinal cord expansion, variable enhancement, and often an associated cyst or syrinx. Ependymomas arise from ependymal cells of the central canal and typically present as an enhancing mass with surrounding edema, associated cysts, and hemorrhage. Due to their central location, even a small ependymoma may cause partial obstruction of the central canal and lead to formation of a syrinx.

Ewing sarcoma is the second most common primary malignant osseous tumor and typically occurs between 10 and 20 years of age. Primary vertebral Ewing sarcoma may present as either a lytic, sclerotic, or mixed lytic and sclerotic mass and may involve any part of the spine. Paravertebral Ewing sarcoma may extend directly through the neuroforamina, and spinal invasion is common.[61] Necrosis, cystic change, hemorrhage, and robust enhancement are common imaging findings. These tumors demonstrate avid tracer uptake on all 3 phases of technetium Tc99m methylene diphosphonate bone scans. [18F] FDG-PET may be used for staging purposes and to evaluate residual disease following treatment (Online Supplemental Data).

Sacrococcygeal teratomas are the most common congenital tumor in the fetus and neonate and can be classified into 4 types depending on their location within and outside the pelvis. They are often large tumors composed of different tissues with a variable appearance on T1, T2, and postcontrast images. About a third are immature or malignant. [18F] FDG-PET may aid in staging and posttreatment follow-up of malignant sacrococcygeal tumors.

Lymphoma

Lymphoma is one of the most common indications for PET imaging in pediatric oncology (Online Supplemental Data). The Deauville or Lugano criteria are endorsed by the Children's Oncology Group and rely on semiquantitative measurements of glucose metabolism, which is helpful to avoid radiation therapy of non-FDG-avid residual soft-tissue masses.[4] Current clinical practice includes PET/CT before, during, and after initiation of therapy, with a resultant high cumulative radiation dose. Meanwhile, PET/MR imaging provides excellent soft-tissue contrast and is either equivalent or superior for malignant lymph node detection.[4,62,63] There is a high correlation between FDG-PET/MR imaging tumor SUV compared with PET/CT, though 1 study reported systematically lower SUVs on PET/MR imaging compared with PET/CT.[4,63,64] The greatest benefit of PET/MR imaging in lymphoma is radiation-dose reduction.[6,64] PET/MR imaging for lymphoma in children is typically acquired as a whole-body scan from head to toe.[13]

Langerhans Cell Histiocytosis

LCH is a proliferative process of histiocytes in children and young adults with a predilection for the vertebral bodies, which may result in vertebral body collapse (vertebra plana). The prognosis depends on disease extension, and [18F] FDG-PET is used to evaluate metastatic disease and residual tumor following resection (Online Supplemental Data).[65]

Vertebral Osteomyelitis

Clinical manifestations of osteomyelitis are diverse and depend on location, causative microorganism, immune status, comorbidities of the host, and route of contamination. Conventional radiographs are nonspecific and only show late findings of osteomyelitis. CT provides excellent resolution and good osseous evaluation but is limited in the evaluation of soft tissues, which are commonly involved in osteomyelitis. Three-phase bone scintigraphy is based on hydroxyapatite deposition and is sensitive for detection of osteomyelitis (83%), though not specific (45%).[66] A leukocyte (white blood cell) scan is based on leukocyte recruitment and is more specific (88%) with reasonable sensitivity (73%) but requires cumbersome labeling of white blood cells that might not be routinely available. MR imaging and PET/CT have excellent sensitivity for vertebral osteomyelitis.[67-69] MR imaging provides excellent evaluation of surrounding soft tissues and is more sensitive than PET/CT for the evaluation of small epidural abscesses. FDG-PET excels in the detection of distant sites of infection. Thus, MR imaging is used as the primary imaging tool to evaluate uncomplicated unifocal cases, while FDG-PET may be considered for possible multifocal disease. PET/MR imaging fared better than PET/CT in a small study,[70] though larger prospective studies are yet to confirm these results.

Congenital Hyperinsulinism

Congenital hyperinsulinism is characterized by persistent hypoglycemia in infancy due to abnormal insulin secretion. Genetic analysis and [18F] DOPA-PET help differentiate focal and diffuse histologic subtypes, which, in medically refractory cases, may undergo focal pancreatic resection or total pancreatectomy, respectively.

[18F] DOPA-PET is based on L-3,4-DOPA uptake in pancreatic islet cells by amino acid transporters, where it is converted to dopamine by DOPA decarboxylase.[71] DOPA decarboxylase activity is high in focal and diffuse forms of congenital hyperinsulinism. Thus, [18F] DOPA can be used as an indirect marker of aromatic amino acid decarboxylase activity due to the increased detection of [18F] DOPA in B-cells with a high rate of insulin synthesis and secretion.[72] In focal congenital hyperinsulinism, [18F] DOPA uptake is greater in the focally abnormal part of the pancreas, while diffuse forms of congenital hyperinsulinism show higher uptake in the pancreatic head compared with other parts of the pancreas. SUV suggests focal disease with >1.5-fold localized [18F] DOPA uptake compared with background pancreatic uptake.[73] Euglycemia must be maintained during scanning, and glucagon therapy should be stopped 2 days before scanning due to potential interference with B-cell activity.[74]

CONCLUSIONS

Hybrid PET/MR imaging is a promising technique in pediatric neuroimaging and provides functional and anatomic information in combination with a reduction in the radiation dose, sedation time, and sedation events. Availability and technical implementation are still limited, but the improved diagnostic capabilities are quite attractive and applicable to a wide range of oncologic and nononcologic pediatric pathologies.

ACKNOWLEDGMENTS

REFERENCES

1. Mathews JD, Forsythe AV, Brady Z, et al. **Cancer risk in 680,000 people exposed to computed tomography scans in childhood or adolescence: data linkage study of 11 million Australians.** *BMJ* 2013;346:f2360 CrossRef Medline
2. Pearce MS, Salotti JA, Little MP, et al. **Radiation exposure from CT scans in childhood and subsequent risk of leukaemia and brain tumours: a retrospective cohort study.** *Lancet* 2012;380:499–505 CrossRef Medline
3. Chawla SC, Federman N, Zhang D, et al. **Estimated cumulative radiation dose from PET/CT in children with malignancies: a 5-year retrospective review.** *Pediatr Radiol* 2010;40:681–86 CrossRef Medline
4. Daldrup-Link H. **How PET/MR can add value for children with cancer.** *Curr Radiol Rep* 2017;5:15 CrossRef Medline
5. Schafer JF, et al. **Simultaneous whole-body PET/MR imaging in comparison to PET/CT in pediatric oncology: initial results.** *Radiology* 2014;273:220–31 CrossRef Medline
6. Ponisio MR, McConathy J, Laforest R, et al. **Evaluation of diagnostic performance of whole-body simultaneous PET/MRI in pediatric lymphoma.** *Pediatr Radiol* 2016;46:1258–68 CrossRef Medline
7. Schmall JP, Surti S, Otero HJ, et al. **Investigating low-dose image quality in whole-body pediatric (18)F-FDG scans using TOF-PET/MRI.** *J Nucl Med* 2021;62:123–30 CrossRef Medline
8. Kaplan S, Zhu YM. **Full-dose PET image estimation from low-dose PET image using deep learning: a pilot study.** *J Digit Imaging* 2019;32:773–78 CrossRef Medline
9. Klenk C, Gawande R, Uslu L, et al. **Ionising radiation-free whole-body MRI versus F-18-fluorodeoxyglucose PET/CT scans for children and young adults with cancer: a prospective, non-randomised, single-centre study.** *Lancet Oncol* 2014;15:275–85 CrossRef Medline
10. Padma MV, Said S, Jacobs M, et al. **Prediction of pathology and survival by FDG PET in gliomas.** *J Neurooncol* 2003;64:227–37 CrossRef Medline
11. Ishiguchi H, Ito S, Kato K, et al. **Diagnostic performance of (18)F-FDG PET/CT and whole-body diffusion-weighted imaging with background body suppression (DWIBS) in detection of lymph node and bone metastases from pediatric neuroblastoma.** *Ann Nucl Med* 2018;32:348–62 CrossRef Medline
12. Maggialetti N, Ferrari C, Minoia C, et al. **Role of WB-MR/DWIBS compared to 18F-FDG PET/CT in the therapy response assessment of lymphoma.** *Radiol Med* 2016;121:132–43 CrossRef Medline
13. Pareek A, Muehe AM, Theruvath AJ, et al. **Whole-body PET/MRI of pediatric patients: the details that matter.** *J Vis Exp* 2017;57128 CrossRef Medline
14. Tudisca C, Nasoodi A, Fraioli F. **PET-MRI: clinical application of the new hybrid technology.** *Nucl Med Commun* 2015;36:666–78 CrossRef Medline
15. Brendle CB, Schmidt H, Fleischer S, et al. **Simultaneously acquired MR/PET images compared with sequential MR/PET and PET/CT: alignment quality.** *Radiology* 2013;268:190–99 CrossRef Medline
16. Broski SM, Goenka AH, Kemp BJ, et al. **Clinical PET/MRI: 2018 Update.** *AJR Am J Roentgenol* 2018;211:295–313 CrossRef Medline
17. Barkovich MJ, Xu D, Desikan RS, et al. **Pediatric neuro MRI: tricks to minimize sedation.** *Pediatr Radiol* 2018;48:50–55 CrossRef Medline
18. Patel DM, Tubbs RS, Pate G, et al. **Fast-sequence MRI studies for surveillance imaging in pediatric hydrocephalus.** *J Neurosurg Pediatr.* 2014;13:440–47 CrossRef Medline
19. Ramgopal S, Karim SA, Subramanian S, et al. **Rapid brain MRI protocols reduce head computerized tomography use in the pediatric emergency department.** *BMC Pediatr* 2020;20:14 CrossRef Medline
20. Andica C, Hagiwara A, Hori M, et al. **Review of synthetic MRI in pediatric brains: Basic principle of MR quantification, its features, clinical applications, and limitations.** *J Neuroradiol* 2019;46:268–75 CrossRef Medline
21. Haacke EM, Chen Y, Utriainen D, et al. **STrategically Acquired Gradient Echo (STAGE) imaging, part III: technical advances and clinical applications of a rapid multi-contrast multi-parametric brain imaging method.** *Magn Reson Imaging* 2020;65:15–26 CrossRef Medline
22. Tanenbaum LN, Tsiouris AJ, Johnson AN, et al. **Synthetic MRI for clinical neuroimaging: results of the Magnetic Resonance Image Compilation (MAGiC) prospective, multicenter, multireader trial.** *AJNR Am J Neuroradiol* 2017;38:1103–10 CrossRef Medline
23. Siegel RL, Miller KD, Jemal A. **Cancer statistics, 2020.** *CA Cancer J Clin* 2020;70:7–30 CrossRef Medline
24. Langleben DD, Segall GM. **PET in differentiation of recurrent brain tumor from radiation injury.** *J Nucl Med* 2000;41:1861–67 Medline
25. Love C, Tomas MB, Tronco GG, et al. **FDG PET of infection and inflammation.** *Radiographics* 2005;25:1357–68 CrossRef Medline
26. Youland RS, Kitange GJ, Peterson TE, et al. **The role of LAT1 in (18) F-DOPA uptake in malignant gliomas.** *J Neurooncol* 2013;111:11–88 CrossRef Medline
27. Lu X. **The role of large neutral amino acid transporter (LAT1) in cancer.** *Curr Cancer Drug Targets* 2019;19:863–76 CrossRef Medline
28. Dunet V, Rossier C, Buck A, et al. **Performance of 18F-fluoro-ethyl-tyrosine (18F-FET) PET for the differential diagnosis of primary brain tumor: a systematic review and meta-analysis.** *J Nucl Med* 2012;53:207–14 CrossRef Medline
29. Albano D, Tomasini D, Bonù M, et al. **(18)F-fluciclovine ((18)F-FACBC) PET/CT or PET/MRI in gliomas/glioblastomas.** *Ann Nucl Med* 2020;34:81–86 CrossRef Medline
30. Röhrich M, Huang K, Schrimpf D, et al. **Integrated analysis of dynamic FET PET/CT parameters, histology, and methylation profiling of 44 gliomas.** *Eur J Nucl Med Mol Imaging* 2018;45:1573–84 CrossRef Medline
31. Zaragori T, Ginet M, Marie P-Y, et al. **Use of static and dynamic [(18)F]-F-DOPA PET parameters for detecting patients with glioma recurrence or progression.** *EJNMMI Res* 2020;10:56 CrossRef Medline
32. Marner L, Nysom K, Sehested A, et al. **Early postoperative (18)F-FET PET/MRI for pediatric brain and spinal cord tumors.** *J Nucl Med* 2019;60:1053–58 CrossRef Medline
33. Chiaravalloti A, Filippi L, Ricci M, et al. **Molecular imaging in pediatric brain tumors.** *Cancers (Basel)* 2019;11:1853 CrossRef Medline
34. Utriainen M, Metsähonkala L, Salmi TT, et al. **Metabolic characterization of childhood brain tumors: comparison of 18F-fluorodeoxyglucose and 11C-methionine positron emission tomography.** *Cancer* 2002;95:1376–86 CrossRef Medline
35. Bogsrud TV, Londalen A, Brandal P, et al. **18F-fluciclovine PET/CT in suspected residual or recurrent high-grade glioma.** *Clin Nucl Med* 2019;44:605–11 CrossRef Medline
36. Henderson F, Brem S, O'Rourke DM Jr, et al. **(18)F-fluciclovine PET to distinguish treatment-related effects from disease progression in recurrent glioblastoma: PET fusion with MRI guides neurosurgical sampling.** *Neurooncol Pract* 2020;7:152–57 CrossRef Medline

37. Kondo A, Ishii H, Aoki S, et al. **Phase IIa clinical study of [(18)F]flu-ciclovine: efficacy and safety of a new PET tracer for brain tumors.** *Ann Nucl Med* 2016;30:608–18 CrossRef Medline

38. Michaud L, Beattie BJ, Akhurst T, et al. **18 F-Fluciclovine (18 F-FACBC) PET imaging of recurrent brain tumors.** *Eur J Nucl Med Mol Imaging* 2020;47:1353–67 CrossRef Medline

39. Kalemaki MS, Karantanas AH, Exarchos D, et al. **PET/CT and PET/MRI in ophthalmic oncology (Review).** *Int J Oncol* 2020;56:417–29 CrossRef Medline

40. Moll AC, Hoekstra OS, Imhof SM, et al. **Fluorine-18 fluorodeoxy-glucose positron emission tomography (PET) to detect vital retino-blastoma in the eye: preliminary experience.** *Ophthalmic Genet* 2004;25:31–35 CrossRef Medline

41. Pelak MJ, d'Amico A, Pecka KM. **The prognostic usability of Ga68-DOTA-TATE PET-CT in irradiated meningioma.** *Neuro-Oncology* 2016;18(Suppl 5):iv14–15 CrossRef

42. Dong Y, Zhang X, Wang S, et al. **18F-FDG PET/CT is useful in ini-tial staging, restaging for pediatric rhabdomyosarcoma.** *Q J Nucl Med Mol Imaging* 2017;61:438–46 CrossRef Medline

43. Eugene T, Corradini N, Carlier T, et al. **¹⁸F-FDG-PET/CT in initial staging and assessment of early response to chemotherapy of pedi-atric rhabdomyosarcomas.** *Nucl Med Commun* 2012;33:1089–95 CrossRef Medline

44. Berthold F, Spix C, Kaatsch P, et al. **Incidence, survival, and treat-ment of localized and metastatic neuroblastoma in Germany 1979-2015.** *Paediatr Drugs* 2017;19:577–93 CrossRef Medline

45. Bar-Sever Z, Biassoni L, Shulkin B, et al. **Guidelines on nuclear medi-cine imaging in neuroblastoma.** *Eur J Nucl Med Mol Imaging* 2018;45:2009–24 CrossRef Medline

46. Mueller WP, Coppenrath E, Pfluger T. **Nuclear medicine and multi-modality imaging of pediatric neuroblastoma.** *Pediatr Radiol* 2013;43:418–27 CrossRef Medline

47. Pfluger T, Schmied C, Porn U, et al. **Integrated imaging using MRI and 123I metaiodobenzylguanidine scintigraphy to improve sensi-tivity and specificity in the diagnosis of pediatric neuroblastoma.** *AJR Am J Roentgenol* 2003;181:1115–24 CrossRef Medline

48. Goo HW. **Whole-body MRI of neuroblastoma.** *Eur J Radiol* 2010;75:306–14 CrossRef Medline

49. Aboian MS, Huang Sy, Hernandez-Pampaloni M, et al. **I-MIBG PET-CT to monitor metastatic disease in children with relapsed neuroblastoma.** *J Nucl Med* 2021;62:43–47 CrossRef Medline

50. Huang Sy, Bolch WE, Lee C, et al. **Patient-specific dosimetry using pretherapy [(1)(2)(4)I]m-iodobenzylguanidine ([(1)(2)(4)I]mIBG) dynamic PET/CT imaging before [(1)(3)(1)I]mIBG targeted radio-nuclide therapy for neuroblastoma.** *Mol Imaging Biol* 2015;17:284–94 CrossRef Medline

51. Papathanasiou ND, Gaze MN, Sullivan K, et al. **18F-FDG PET/CT and 123I-metaiodobenzylguanidine imaging in high-risk neuro-blastoma: diagnostic comparison and survival analysis.** *J Nucl Med* 2011;52:519–25 CrossRef Medline

52. Dhull VS, Sharma P, Patel C, et al. **Diagnostic value of 18F-FDG PET/CT in paediatric neuroblastoma: comparison with 131I-MIBG scintigraphy.** *Nucl Med Commun* 2015;36:1007–13 CrossRef Medline

53. Lopci E, Piccardo A, Nanni C, et al. **18F-DOPA PET/CT in neuro-blastoma: comparison of conventional imaging with CT/MR.** *Clin Nucl Med* 2012;37:e73–78 CrossRef Medline

54. Piccardo A, Lopci E, Conte M, et al. **Comparison of 18F-DOPA PET/CT and 123I-MIBG scintigraphy in stage 3 and 4 neuroblastoma: a pilot study.** *Eur J Nucl Med Mol Imaging* 2012;39:57–71 CrossRef Medline

55. Piccardo A, Puntoni M, Lopci E, et al. **Prognostic value of (1)(8)F-DOPA PET/CT at the time of recurrence in patients affected by neu-roblastoma.** *Eur J Nucl Med Mol Imaging* 2014;41:1046–56 CrossRef Medline

56. Pandit-Taskar N, Zanzonico P, Staton KD, et al. **Biodistribution and dosimetry of (18)F-meta-fluorobenzylguanidine: a first-in-human PET/CT imaging study of patients with neuroendocrine malignan-cies.** *J Nucl Med* 2018;59:147–53 CrossRef Medline

57. Zhang H, Huang R, Cheung NK, et al. **Imaging the norepinephrine transporter in neuroblastoma: a comparison of [18F]-MFBG and 123I-MIBG.** *Clin Cancer Res* 2014;20:2182–91 CrossRef Medline

58. Gains JE, Aldridge MD, Mattoli MV, et al. **68Ga-DOTATATE and 123I-mIBG as imaging biomarkers of disease localisation in meta-static neuroblastoma: implications for molecular radiotherapy.** *Nucl Med Commun* 2020;41:1169–77 CrossRef Medline

59. Gains JE, Bomanji JB, Fersht NL, et al. **177Lu-DOTATATE molecular radiotherapy for childhood neuroblastoma.** *J Nucl Med* 2011;52:1041–47 CrossRef Medline

60. Iakovou I, Giannoula E, Sachpekidis C. **Imaging and imaging-based management of pediatric thyroid nodules.** *J Clin Med* 2020;9:384 CrossRef Medline

61. Ilaslan H, Sundaram M, Unni KK, et al. **Primary Ewing's sarcoma of the vertebral column.** *Skeletal Radiol* 2004;33:506–13 CrossRef Medline

62. Lyons K, Seghers V, Sorensen JIL, et al. **Comparison of standardized uptake values in normal structures between PET/CT and PET/MRI in a tertiary pediatric hospital: a prospective study.** *AJR Am J Roentgenol* 2015;205:1094–101 CrossRef Medline

63. Sher AC, Seghers V, Paldino MJ, et al. **Assessment of sequential PET/MRI in comparison with PET/CT of pediatric lymphoma: a prospec-tive study.** *AJR Am J Roentgenol* 2016;206:623–31 CrossRef Medline

64. Hirsch FW, Sattler B, Sorge I, et al. **PET/MR in children. Initial clin-ical experience in paediatric oncology using an integrated PET/MR scanner.** *Pediatr Radiol* 2013;43:860–75 CrossRef Medline

65. Jessop S, Crudgington D, London K, et al. **FDG PET-CT in pediatric Langerhans cell histiocytosis.** *Pediatr Blood Cancer* 2020;67:e28034 CrossRef Medline

66. Wang GL, Zhao K, Liu ZF, et al. **A meta-analysis of fluorodeoxyglu-cose-positron emission tomography versus scintigraphy in the eval-uation of suspected osteomyelitis.** *Nucl Med Commun* 2011;32:1134–42 CrossRef Medline

67. Kouijzer IJE, Scheper H, de Rooy JWJ, et al. **The diagnostic value of (18)F-FDG-PET/CT and MRI in suspected vertebral osteomyelitis: a prospective study.** *Eur J Nucl Med Mol Imaging* 2018;45:798–805 CrossRef Medline

68. Termaat MF, Raijmakers PG, Scholten HJ, et al. **The accuracy of diag-nostic imaging for the assessment of chronic osteomyelitis: a system-atic review and meta-analysis.** *J Bone Joint Surg Am* 2005;87:2464–71 CrossRef Medline

69. Demirev A, Weijers R, Geurts J, et al. **Comparison of [18 F]FDG PET/CT and MRI in the diagnosis of active osteomyelitis.** *Skeletal Radiol* 2014;43:665–72 CrossRef Medline

70. Hulsen DJ, Geurts J, Arts JJ, et al. **Hybrid FDG-PET/MR imaging of chronic osteomyelitis: a prospective case series.** *Eur J Hybrid Imaging* 2019;3:7 CrossRef Medline

71. Jager PL, Chirakal R, Marriott CJ, et al. **6-L-18F-fluorodihydrophe-nylalanine PET in neuroendocrine tumors: basic aspects and emerg-ing clinical applications.** *J Nucl Med* 2008;49:573–86 CrossRef Medline

72. de Lonlay P, Simon-Carre A, Ribeiro MJ, et al. **Congenital hyperinsu-linism: pancreatic [18F]fluoro-L-dihydroxyphenylalanine (DOPA) positron emission tomography and immunohistochemistry study of DOPA decarboxylase and insulin secretion.** *J Clin Endocrinol Metab* 2006;91:933–40 CrossRef Medline

73. Mohnike K, Blankenstein O, Minn H, et al. **[18F]-DOPA positron emission tomography for preoperative localization in congenital hyperinsulinism.** *Horm Res* 2008;70:65–72 CrossRef Medline

74. Ribeiro MJ, Boddaert N, Bellanné-Chantelot C, et al. **The added value of [18F]fluoro-L-DOPA PET in the diagnosis of hyperinsu-linism of infancy: a retrospective study involving 49 children.** *Eur J Nucl Med Mol Imaging* 2007;34:2120–28 CrossRef Medline

Navigating Supply Chain Disruptions of Iodinated Contrast Agent for Neuroimaging and How Business Intelligence Can Help the Decision Process

R. Bammer and S.A. Amukotuwa

ABSTRACT

SUMMARY: A recent coronavirus disease 2019–related shutdown of the main production facility of iohexol in China has led to massive shortages of iodinated contrast material across the globe. This shortage has also jeopardized neuroimaging. In this article, we describe remedies to reduce iodinated contrast material use for stroke imaging, which is its primary use in neuroimaging, that we have implemented in our hospital network.

ABBREVIATIONS: BI = Business Intelligence; CE = contrast-enhanced; coronavirus disease = COVID; ECR = endovascular clot retrieval; ICM = iodinated contrast material; Tmax = time-to-maximum

The latest knock-on effect of the coronavirus disease 2019 (COVID-19) pandemic is a global shortage of iodinated contrast medium (ICM) triggered by the shutdown of GE Healthcare's main production facility of iohexol (Omnipaque; GE Healthcare) during the latest lockdown in Shanghai at the end of March 2022. The combination of the company's Just-in-Time inventory management and lean production strategies that afforded competitive pricing (~\$0.13/mL for our institution) and GE's large global market share of ICM has led to a massive disruption in the global supply of ICM, which caught many of us by surprise. With stock levels dwindling and unclear information on when the factory will return to full capacity or make up for the production shortfall, many hospitals are scrambling to source more ICM from elsewhere. This unusual sudden demand, in turn, leads to an additional squeeze on the ICM supply chain. Several professional interest groups, including the American College of Radiology[1] and the American Society of Hospital Pharmacists,[2] have issued guidance documents on how to address the current ICM shortage, including various strategies for conservation of contrast material for those diagnostic tests and interventions that are time-critical and without which patients would die or have considerable morbidity. A recent clinical perspective in the *American Journal of Roentgenology* highlighted several broad strategies to conserve ICM at imaging facilities.[3] This

perspective focusses on the most frequent indication for contrast-enhanced (CE) CT in neuroimaging: Code Stroke.

Overcoming the ICM Shortage

Here, we report the status quo and ICM shortage remedies implemented on May 13, 2022, at our institution and provide guidance on imaging protocol changes. A bottom-up analysis using our own Business Intelligence (BI) tools showed that the minimum contrast usage after the intervention could be as low as 10% of our precrisis ICM usage. We hope that some of the insights from our intervention can also be of use to others in the neuroradiology community.

Our institution is the largest public hospital network in Australia and comprises a tertiary referral center, which is also a comprehensive stroke center, 2 large peripheral metropolitan hubs, and an oncology center, all located in the southeastern metropolitan area of Melbourne. Our estimated catchment is approximately 2.75 million people. Across our network, our annual expenditure on CT contrast agents is \$465,000. We use approximately 15.9 L of ICM per day, of which 15 L is Omnipaque; the remainder is iodixanol (Visipaque; GE Healthcare), which is primarily used in the catheterization laboratory.

Evidence from our department's BI tools shows that before the ICM shortage, cardiac, chest, and abdominal CT imaging accounted for ~70% of all contrast agent usage, while Code Stroke accounted for 10% and was, therefore, by far the largest user of ICM in the diagnostic (noninterventional) neuroimaging category (Fig 1). If available at other institutions, we recommend that readers use similar BI tools to analyze the case mix at their institutions because it might differ from ours. A breakdown of the biggest ICM users via BI tools can be helpful in assessing
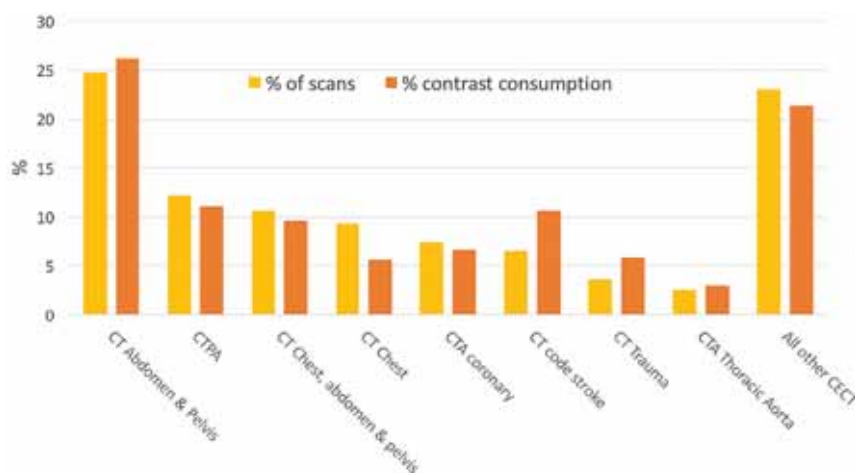
FIG 1. The most common use of an iodinated contrast agent in CT imaging (CT PA indicates CT pulmonary angiography).

which sectors are the most frequent users of contrast agent and are, therefore, most likely to yield significant reduction of ICM usage if targeted with ICM-reducing interventions.

As of May 16, 2022, our current inventory would have lasted for another 2.5 weeks based on our normal operational ICM consumption rate (note some Australian hospitals have already exhausted their supply and depend on support from the Department of Health and other hospitals). We, therefore, urgently needed strategies to conserve ICM.

The ICM shortage remedies that we implemented fall into 5 major categories:

1) Mandate "CT with contrast" ordered by an attending physician or specialist advanced trainee and have a communication plan for referring physicians to employ appropriate use criteria for contrast-based CT examinations.
2) Modify protocols to scan without contrast agent.
3) Use alternative imaging modalities in lieu of CE CT.
4) Optimize CT scan protocols to use less ICM.
5) Prioritize inpatient imaging over outpatient studies.

The order in which the 5 categories are implemented depends on the organ systems imaged. For example, at our institution, applying category 2 (ie, switching to unenhanced CTs for chest, abdomen, and pelvis studies) was one of the easiest and most effective measures to implement in body radiology, yielding a substantial reduction ICM usage.

For diagnostic neuroimaging, the other 4 categories were the preferred interventions, which we will discuss in more detail next. Code Stroke is the primary user of ICM in diagnostic neuroradiology, accounting for approximately 60% of all ICM use in neuroradiology CTs (71% if only emergent studies are considered). Evidence from our BI tools also showed the use (from most-to-least volume use in diagnostic neuroimaging) of ICM for CTA for SAH and parenchymal hematoma to identify aneurysms and vascular malformations (10%); CTA for identifying carotid disease (9%); CE CT of the brain (7%); and CE CT imaging of the neck (5.5%); but the volumes were, even in aggregate, much less than our institution's use for Code Stroke. Hence, the remainder of this document will focus solely on Code Stroke.

Category 1: Mandate CE CTs Ordered by Attending Referring Stroke Neurology Physicians Only. Within the past 12 months, we have observed a considerable increase (40%) in orders for Code Stroke multimodal (head CT, CTA of head and neck, and CTP) studies from our emergency and stroke services across the network. Aside from a general increase of Code Stroke CTs performed globally due to the broad adoption of endovascular clot retrieval (ECR),[4] at our institution, this increase has also aligned with implementation of ordering imaging studies directly via our electronic medical records and overcrowding of our emergency departments.[5] Facilitated by the ease of electronic medical record–based ordering, we have noticed that junior doctors have a lower threshold for ordering multimodal CT scans than more senior clinicians. Our emergency departments have an overreliance on imaging for ruling out strokes to facilitate patient discharge.

In the first 48 hours since we mandated that imaging tests need to be ordered by an attending stroke neurologist, the number of multimodal CTs was reduced to 43% of the average daily volume ordered in the 12 weeks before our intervention. Most interesting, the ratio of positive findings to the number Code Stroke CT scans ordered increased to 25%, which is in stark contrast to the 8% rate during the 12 weeks prior.

Category 2: Modify Scanning Protocols to Scan without Contrast Agent. It is well-known that the diagnostic sensitivity and specificity of unenhanced CT is relatively poor, particularly in the hyperacute phase of a stroke.[6] Specific indications such as sulcal effacement, the insular ribbon sign, and loss of gray/white contrast are more apparent in established infarcts, while the hyperdense vessel sign strongly depends on clot composition. Assessing the true size of the irreversibly damaged tissue can also be fraught with poor sensitivity and variability due to poor contrast and reader subjectivity. Even when augmented by artificial intelligence, eg, artificial intelligence–driven ASPECTS,[7] identifying the site of occlusion or assessing how much salvageable tissue remains is often not possible without perfusion or angiographic imaging. Generally, ASPECTS is useful to rule out patients receiving ECR, but unenhanced CT and ASPECTS are not well-suited to rule in patients. Moreover, angiographic assessment of the neck and intracranial vessels is still needed to establish the presence of large-vessel occlusion. The risk of patients missing out on potentially beneficial treatment is too high. Therefore, we cannot advocate foregoing the use of ICM in the acute stroke work-up. If CT is the technique to use for a Code Stroke, we still perform multimodal CT albeit with a lesser amount of ICM. For even more conservative approaches, an unenhanced CT (with ASPECTS) can be augmented by a CTA, preferably with a reduced ICM injection volume.
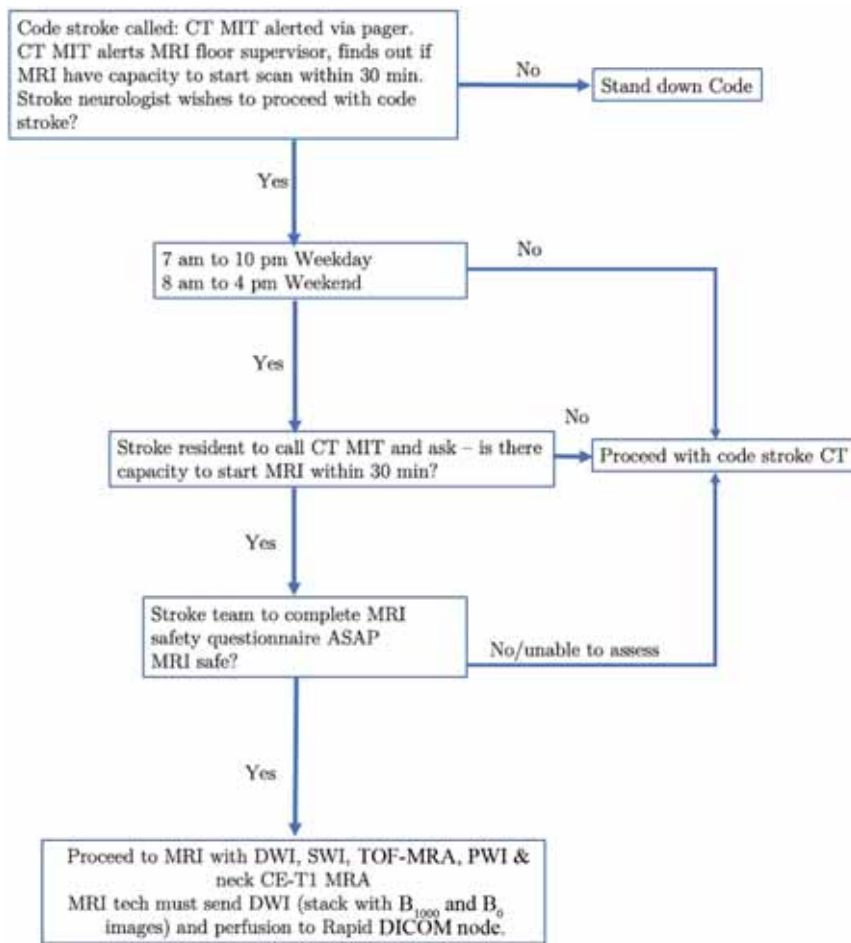
FIG 2. MR imaging/CT decision tree for Code Stroke. ASAP indicates as soon as possible.

Category 3: Use Alternative Imaging Modalities in Lieu of CE CT.
DWI has exquisite diagnostic sensitivity for detecting acute stroke lesions and is considered the definitive test.[6] Gradient-echo or susceptibility-weighted imaging as well as FLAIR or even b_0 DWI and prebolus DSC-PWI allow one to detect hemorrhage with sensitivities that are comparable with or superior to CT.[8-10] Moreover, DSC-PWI is equally well established to determine tissue-at-risk as CTP.

Two shortcomings of MR imaging use are the typical MR imaging contraindications (eg, pacemakers and stimulators, aneurysm clips, and so forth) and 24/7 availability. In addition, inpatient MRIs are frequently used for other complex examinations, making access logistically more challenging. Moreover, MR imaging is considered a rather lengthy examination, typically lasting 20–30 minutes, whereas the door-to-CT time at our institution is ≤10 minutes and the duration of the multimodal CT is around 5 minutes.

In response to the ICM shortage, we have worked with our entire stroke care and MR imaging team to implement an acute stroke (fast) MR imaging protocol and workflow, which we have tested successfully, to achieve short door-to-MRI scan turnaround times, but our goal was to reduce ICM usage and not to fully replace multimodal CT. Our default is still multimodal CT, for example after-hours when our MRIs are not staffed with on-site personnel,

when patients' contraindications to MR imaging cannot be safely excluded either by reviewing screening forms with the patient or next of kin or via a fast mobile x-ray, or when the patient is unlikely to fit into the scanner bore (>120 kg). The decision flow chart under which our team is operating is shown in Fig 2. Because stroke is a time-critical emergency and delay to treatment must be avoided, this workflow factors in how quickly a slot in one of our MRIs can be made available. For example, if a lengthy scan on a complex ICU patient, a patient with a conditional pacemaker, or a patient with cord compression is underway on our inpatient MR imaging scanners, the patient is automatically diverted to CT.

The primary purpose of sending patients to urgent stroke MR imaging is to identify patients with large-vessel occlusion who qualify for ECR. On the basis of the experience of the authors who have designed the CT and MR imaging protocols for several clinical trials,[11-13] we have set up 5-minute acute stroke MR imaging protocols akin to the protocols used in Endovascular Therapy Following Imaging Evaluation for Ischemic Stroke 3 (DEFUSE 3).[14] These minimalistic protocols are tailored to determine the following: 1) infarct core (DWI); 2) the presence of hemorrhage (SWI); 3) large-vessel occlusion (3D TOF-MRA); 4) at-risk tissue (time-to-maximum [Tmax] from DSC-PWI); and 5) proximal occlusion (CE T1WI MRA). They are tuned for speed and not for resolution yet provide sufficient quality for stroke diagnosis. We also use the residual equilibrium contrast agent circulating through the blood stream immediately after the DSC-PWI instead of using a second bolus injection for the CE MRA, which is sufficient to visualize the large neck vessels and saves time. Specifically, we use a 1- minute axial 3D Dixon volumetric interpolated breath-hold examination (DIXON VIBE) sequence with 2-mm section resolution covering the arch to skull base. Alternatively, the single bolus can be divided into DSC-PWI and CE MRA if the overall use of gadolinium-based contrast agent is a concern.

Most current MR imaging systems have parallel imaging and other acceleration techniques available. To achieve stroke protocols in <5 minutes still requires accepting lower resolution and thicker slices and perhaps a bit more distortion on the EPI scans than found on the longer protocols. Figure 3 shows typical results for a fast (Avanto 1.5T; Siemens) MR imaging protocol. An example of an MR imaging protocol (3T Verio; Siemens) can be found in the Online Supplemental Data. The key to successful implementation is to understand that the role of MR imaging in the acute setting is to find ECR candidates with salvageable tissue and to rule out brain
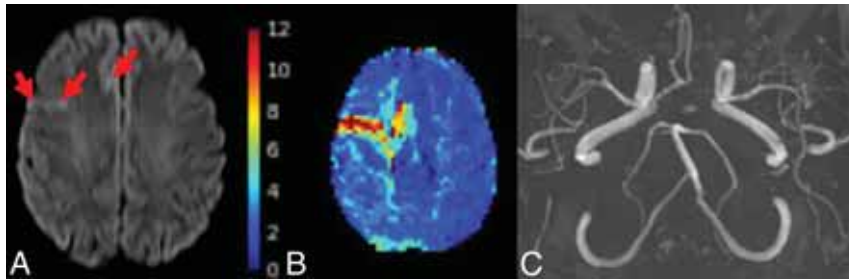
FIG 3. Acute fast Code Stroke MR imaging. A 51-year-old woman with new left-sided weakness, last seen well 12 hours earlier. Abbreviated MR imaging protocol with fast DWI, PWI, SWI, TOF-MRA, and T1 neck was performed. *A*, DWI shows small foci of cortical restricted diffusion in the right frontal lobe in the MCA and anterior cerebral artery territories. *B*, The Tmax map shows severe delay in the distribution of the right MCA M3 and anterior cerebral artery A4 branches. *C*, TOF-MRA MIP shows no large-vessel occlusion. An M3 occlusion is evident on source images.

hemorrhage. Most embolic infarcts can also be depicted on a 30- to 40-second DWI, and the PWI allows detection of mid-to-distal vessel occlusions using Tmax maps.[15] In fact, small emboli and distal vessel occlusions are often not detected on CT and CTA, though CTP has helped to increase diagnostic sensitivity.[16,17] Patients who do not have a stroke but have imaging findings suggestive of an alternative pathology can undergo a more comprehensive MR imaging examination later if further sequences or better spatial resolution is required for diagnosis.

We had not previously used MR imaging as the first-line technique for Code Stroke and have encountered some initial issues in overcoming the logistic challenges in an already-busy inpatient MR imaging service. If MR imaging is not a part of your institution's usual Code Stroke process, it is vital to have a clear communication plan to ensure short door-to-scanner and door-to-needle times when implementing this change. This includes clear instructions to the stroke and emergency department teams, such as when to send patients to MR imaging and not to CT and which new phone numbers and pagers to call. The neuroradiologist acts as a change manager and fulfills a crucial role in motivating an MR imaging team to embrace this new challenge.

Category 4: Optimize CT Scan Protocols to Use Less ICM. There are different vectors along which scan protocols can be altered to reduce ICM usage. Next, we will discuss those interventions that we have instituted in our network.

1) Shift multimodal stroke imaging to wide-detector CTs (when available). We shifted most of our patients with Code Stroke to our 320-detector-row CT (Aquilion One; Toshiba) scanner and set up a straightforward "burst mode" CTP protocol with 140-mm z-coverage. This change allows whole-brain CTA to be reconstructed from the CTP. Five seconds into the CTP scan, we acquired a bone mask at a higher SNR for subtraction (310 mA, 0.75-second rotation time, 80 kV[peak]), which was followed by a dynamic scan (29 cycles, 2-second cycle time, 150 mA, 0.75-second rotation time, 80 kVp) that started 10 seconds after the bolus injection. We used only 40 mL of Omnipaque at a flow rate of 6 mL/sec followed by a 60-mL saline chaser at the same flow rate. This acquisition allows us to compute all perfusion parameter maps (eg, CBF and Tmax) relevant for mismatch analysis. While the time series data were

sent off to compute the perfusion parameter maps, we identified the timeframe with the peak arterial concentration at the ipsilateral side, and using 0.5- or 1.0-mm slice collimation allowed us to also reconstruct an intracranial angiogram from this CTP timeframe. A sample CTP protocol can be found in the Online Supplemental Data.

Immediately following the CTP, while iodine was still recirculating, a CT from the aortic arch to circle of Willis was performed that was topped up with another 20- to 40-mL iodine bolus to visualize the neck vessel, to rule out any proximal occlusions, and assess arterial access; we found the venous overlay acceptable. To boost the CTA contrast, we reduced the tube voltage of our standard head and neck CTA to 80 kVp. Figure 4 shows an example of such a scan. Alternatively, Oei et al[18,19] implemented an interleaved CTP and arch to the circle of Willis CTA approach on the Toshiba 320. At the peak arterial concentration, the CTP was interrupted for 4 seconds to allow an arch to the circle of Willis CTA, after which the table was returned and the CTP was completed. We have not implemented the Oei approach mainly because it requires manual triggering of the CTA and is difficult to protocol, which is a concern when we must train a large CT technologist workforce.

2) We have also adjusted our other protocols (eg, Discovery CT750 HD GSI; GE Healthcare), similar to our wide-detector CTs. First, we have reduced the injected iodine for CTP from 60 to 40 mL. Note that all our CTP protocols were already at the lowest setting (70 or 80 kVp) to get closest to the K-edge of iodine. Second, similar to the wide detector protocol above (1), we performed CTA immediately after CTP to use residual contrast. Third, we reduced our CTA iodine injection volume from 70 to 30–40 mL and lowered the tube voltage settings of our standard CTA to 80 kVp (Fig 5). An example the CTP protocol can be found in the Online Supplemental Data. Because the injected volume for the CTA is smaller, we have noticed that some of the iodine may be held up in upper limb and axillary veins and is not fully pushed into the central circulation. We, therefore, advise using a large volume of saline chaser (eg, 60mL) to ensure that all the ICM is safely pushed out of the injector tubing and arm veins into the central circulation.

The compactness of the bolus usually also depends on the injection flow rate. With smaller injection volumes, it is, therefore, good to use higher flow rates. Some dispersion will occur in any case when passing through the lung circulation. Nevertheless, a sharper bolus means more iodine per unit of blood volume and thus more attenuation. Due to the shorter bolus, the triggering of the CTA requires proper fluoro triggering because the CTA will be more sensitive to incorrect timing. Lowering the trigger threshold by 15%–20% can avoid missing the bolus. For taller patients, a larger (40–50mL) bolus will still be needed. Here, the blood volume in which the iodine is distributed in the central circulation depends not only on the patient's weight but also his or her height,
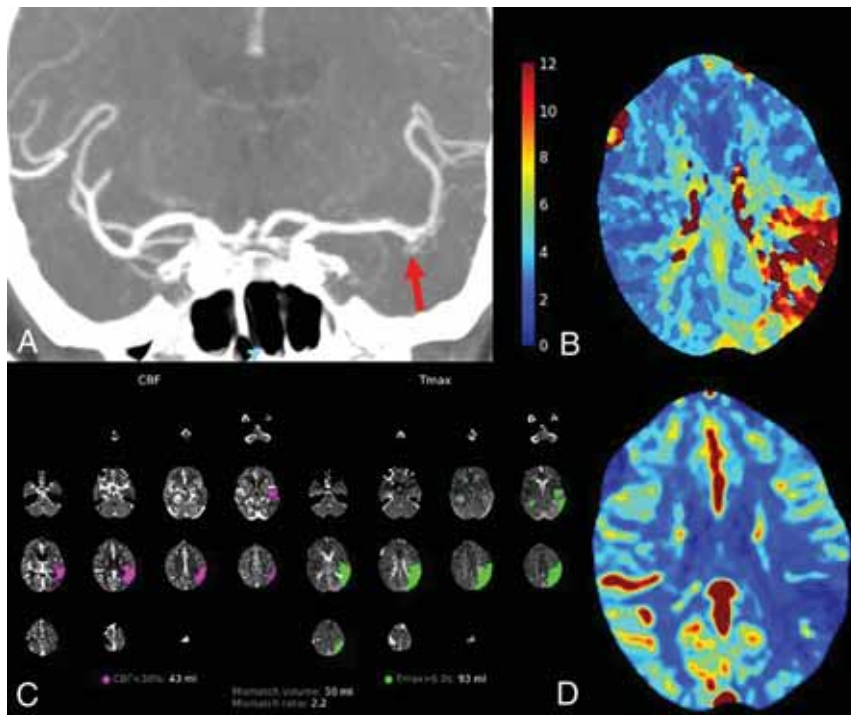
FIG 4. Sample of 40-mL CTP/CTA obtained on a Toshiba 320 scanner. Images from a 79-year-old woman who presented with sudden-onset expressive dysphasia. *A*, MIP CTA images reconstructed from the CTP acquisition at peak arterial opacification demonstrate good opacification of medium and distal intracranial arteries. Proximal occlusion of the left MCA inferior to the M2 division (*arrow*) is evident. *B* and *D*, Selected slices of Tmax and relative CBF maps show marked territorial Tmax delay and reduced rCBF. The subarachnoid space over the right frontal lobe is focally dilated. *C*, CTP, relative CBF, and Tmax mismatch maps show that there is some salvageable penumbra. Diagnostic-quality CTP was maintained despite contrast dose reduction.
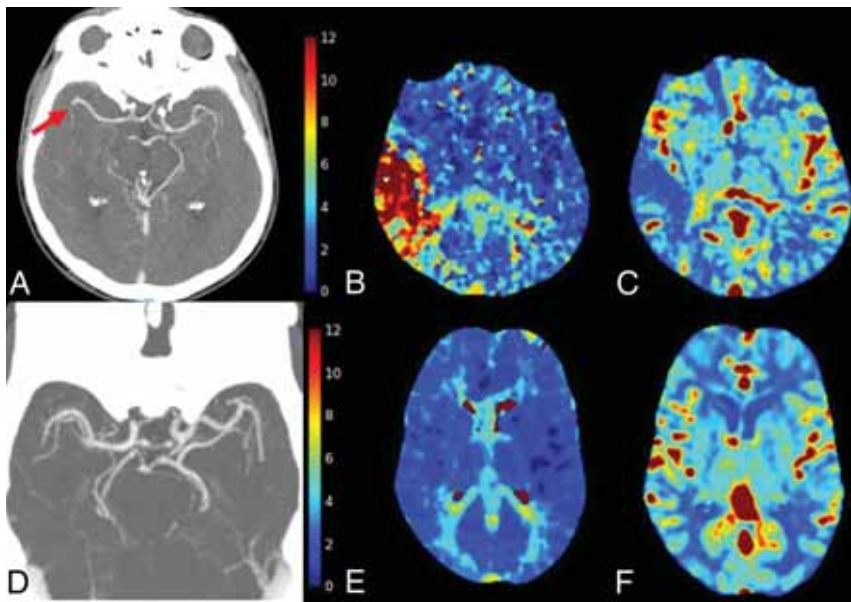
FIG 5. Examples of 20-mL CTA performed on small-detector-width CT (Discovery 750; GE Healthcare). *A*, Axial CTA MIP demonstrates occlusion of the inferior M2 division of the right MCA (*arrow*) in a 75-year-old man with sudden-onset abnormal left-sided movements. *B* and *C*, A single section of Tmax and rCBF maps shows territorial Tmax delay and a small area of severely reduced relative CBF. *D*, Sample of an axial CTA MIP in a different patient, a 71-year-old woman with right-sided weakness. The patient had a low weight (50 kg), accounting for the superior arterial opacification with the same contrast load. *E* and *F*, Selected Tmax and relative CBF images show that the CTP quality is excellent.

connected through the body mass index. For a more optimized weight-based volume calculation, especially in patients with obesity, the interested reader is directed to the Lemmens-Bernstein-Brodsky formula.[20] Reviewing the time density curve from the preceding CTP study, mainly the time of arrival and the width of the arterial input function (eg, >20 seconds), also helps to identify patients with poor cardiac output or ejection fraction, another factor that sometimes impacts CTAs. In our experience, roughly 20% of patients with Code Stroke present with poor cardiac output. For such patients, it is also prudent to use at least 40 mL of ICM to ensure sufficient vessel opacification.

Dual-energy CT scanning also allows acquiring images at a lower kilovolt(peak) and thus bringing the acquisition closer to the K-edge of iodine. Consequently, less iodine is needed to create comparable vascular contrast than at high kilovolt(peak) settings. We are cognizant, however, that dual-energy CT scanners are less prevalent in the global installation base of CT scanners and are largely limited to academic centers and referral centers. While we have implemented dual-energy scanning on our body CT protocols, we have not done so for neuroimaging protocols.

At our institution, we have decided against foregoing CTP and just relying on an unenhanced CT and CTA because CTP provides important diagnostic information beyond large-vessel occlusions. We have shown that distal vessel occlusions and other diseases causing hemodynamic abnormalities can be detected much faster and with greater confidence than on CTA alone.[16,17] This added diagnostic capability is critical to our clinical referrers, who rely on it to guide decisions on distal vessel thrombectomy, thrombolysis beyond 4.5 hours, and patient discharge instead of admission for further work-up if CTP findings are normal. We think that after reducing the ICM of our multimodal CT Code Stroke protocol from 130 to 60 mL; directing Code Stroke in-hours to MR imaging; and having attendings instead of trainees requesting CE studies, our ICM for CTP studies can be well-justified in the interest

of patient care. Before the ICM shortage, our daily contrast usage for Code Stroke work-up was approximately 1.0 L per day. In the 96 hours since all the aforementioned interventions were implemented, the new daily ICM consumption for Code Stroke work-up has been 0.12 L (88% reduction). The average number of Code Stroke CTs decreased from 8 per day to 2 per day. Overall, ICM consumption for all CT studies was reduced by 72% in our network within the same period. At this time, we have no evidence that we have missed strokes that were later seen with DWI.

Category 5: Prioritize Inpatient and Emergency Imaging over Outpatient Studies. Patients with Code Stroke present at our institutions through the emergency department or stroke service as inpatients and receive priority. Deferment of imaging is not an option for patients with acute ischemic stroke who are at high risk of death and significant morbidity without treatment. For transient symptoms, work-up within 48 hours of presentation is recommended by the American Heart Association/American Stroke Association guidelines.[21] We will continue to offer these patients urgent outpatient brain MRIs but replace CTA with carotid sonography within 48 hours to conserve ICM.

The other emergent, time-critical ICM-consuming neuroimaging study for which CT is preferred over MR imaging because of access is brain CTA for SAH. We will divert these to MR imaging with TOF-MRA when our ICM supplies become critically low. Most diagnostic neuroradiology work-up is via MR imaging, and when reviewing our BI data, we found negligible use of ICM for our outpatient work.

Of course, the implementation of protocol and workflow changes requires buy-in from all health care professionals involved in the patient experience. In our opinion, it is of paramount importance to have a proper change-management process in place that involves all stakeholders. Due to the relatively sudden onset of the crisis and several of the implemented changes being quite substantial and demanding for some staff, we cannot emphasize enough how important it is to have frequent and clear communication of changes and "champions" identified when trying to establish these alterations. Moreover, if you lead the change process, it is also critical to ensure that the changes are adequately followed through and risks are properly anticipated, identified, and managed.

The silver lining is that this crisis has shown us that for many examinations, we can get by with substantially less contrast material without sacrificing diagnostic capability. It has also highlighted the role and value of alternative tests. This begs the question: Why have these approaches not been used earlier? After all, significant annual costs are associated with current ICM volumes. Nevertheless, it cannot be assumed that there will be an overall cost-savings from this period of reduced ICM usage. This is a multifaceted problem. Many tests will be moved to MR imaging, for which the contrast agent is more expensive, and there are opportunity costs when either displacing other patients or stretching MR imaging capacity to accommodate more patients. It also needs to be shown how these new measures will affect diagnostic accuracy as well as their overall effect on patient and health economics outcomes.

Summary

The supply chain disruptions of ICM due to COVID-19 lockdowns in March 2022 in China caught most of us by surprise. A few larger customers were forewarned by the vendor and could replenish their supplies in time, but most hospitals were caught off guard. With this Practice Perspectives, we wanted to share with the *American Journal of Neuroradiology* readership the measures that our institution has put in place to weather this shortage. In such unprecedented times, we wanted to lend our experience from protocolling many stroke studies to the broader community. We are cognizant that there are multiple ways to reduce ICM and ours is just one of many versions.* An interesting question arises from this ICM crisis and the forced ICM austerity measures: Will we ever return to the large volumes of ICM use? Maybe this reset was long overdue. Many of the CTA protocols, for example, were grandfathered in from times when CT scanners were slower and the bolus outran the table movements. Times have change, and if start of CTA acquisition timed correctly, a narrow, less voluminous bolus can be easily chased by a modern scanner.

REFERENCES

1. American College of Radiology. **Statement from the ACR Committee on Drugs and Contrast Media Brief Statement on Nomenclature for Symptoms Associated with Gadolinium-Based Contrast Agent Exposure (SAGE).** May 13, 2022. https://www.acr.org/-/media/ACR/Files/Clinical-Resources/SAGE-Paragraph-_-FINAL.pdf. Accessed May 13, 2022

2. American Society of Hospital Pharmacists. **Considerations for Imaging Contrast Shortage Management and Conservation.** 2022. https://www.ashp.org/drug-shortages/shortage-resources/considerations-for-imaging-contrast-shortage-management. Accessed May 13, 2022

3. Cavallo J, Pahade J. **Practice management strategies for imaging facilities facing an acute iodinated contrast media shortage.** *AJR Am J Roentgenol* 2022 May 13. [Epub ahead of print] CrossRef Medline

4. Wang JJ, Pelzl CE, Boltyenkov A, et al. **Updated trends, disparities, and clinical impact of neuroimaging utilization in ischemic stroke in the Medicare population: 2012 to 2019.** *J Am Coll Radiology* 2022 April 26. [Epub ahead of print] CrossRef Medline

5. Cunningham M, Dow A. **It feels like you're just trying to save disasters from happening.** *The Sydney Morning Herald* May 8, 2022

6. Mullins ME, Schaefer PW, Sorensen AG, et al. **CT and conventional and diffusion-weighted MR imaging in acute stroke: study in 691 patients at presentation to the emergency department.** *Radiology* 2002;224:353–60 CrossRef Medline

7. Maegerlein C, Fischer J, Monch S, et al. **Automated calculation of the Alberta Stroke Program Early CT Score: feasibility and reliability.** *Radiology* 2019;291:141–48 CrossRef Medline

8. Amukotuwa SA, Fischbein NJ, Albers GW, et al. **Comparison of T2*GRE and DSC-PWI for hemorrhage detection in acute ischemic stroke patients: pooled analysis of the EPITHET, DEFUSE 2, and SENSE 3 stroke studies.** *Int J Stroke* 2020;15:216–25 CrossRef Medline

9. Verma RK, Kottke R, Andereggen L, et al. **Detecting subarachnoid hemorrhage: comparison of combined FLAIR/SWI versus CT.** *Eur J Radiol* 2013;82:1539–45 CrossRef Medline

10. Kidwell CS, Chalela JA, Saver JL, et al. **Comparison of MRI and CT for detection of acute intracerebral hemorrhage.** *JAMA* 2004;292:1823–30 CrossRef Medline

11. Saver JL, Goyal M, Bonafe A, et al. **Stent-retriever thrombectomy after intravenous t-PA vs. t-PA alone in stroke.** *N Engl J Med* 2015;372:2285–95 CrossRef Medline

12. Nogueira RG, Jadhav AP, Haussen DC, et al. **Thrombectomy 6 to 24 hours after stroke with a mismatch between deficit and infarct.** *N Engl J Med* 2018;378:11–21 CrossRef Medline

13. Albers GW, Marks MP, Kemp S, et al. **Thrombectomy for stroke at 6 to 16 hours with selection by perfusion imaging.** *N Engl J Med* 2018;378:708–18 CrossRef Medline

14. Albers GW, Lansberg MG, Kemp S, et al. **A multicenter randomized controlled trial of endovascular therapy following imaging evaluation for ischemic stroke (DEFUSE 3).** *Int J Stroke* 2017;12:896–905 CrossRef Medline

15. Campbell BC, Christensen S, Levi CR, et al. **Comparison of computed tomography perfusion and magnetic resonance imaging perfusion-diffusion mismatch in ischemic stroke.** *Stroke* 2012;43:2648–53 CrossRef Medline

16. Amukotuwa SA, Wu A, Zhou K, et al. **Distal medium vessel occlusions can be accurately and rapidly detected using Tmax maps.** *Stroke* 2021;52:3308–17 CrossRef Medline

17. Amukotuwa SA, Wu A, Zhou K, et al. **Time-to-maximum of the tissue residue function improves diagnostic performance for detecting distal vessel occlusions on CT angiography.** *AJNR Am J Neuroradiol* 2021;42:65–72 CrossRef Medline

18. Oei MT, Meijer FJ, van der Woude WJ, et al. **Interleaving cerebral CT perfusion with neck CT angiography, Part I: proof of concept and accuracy of cerebral perfusion values.** *Eur Radiol* 2017;27:2649–56 CrossRef Medline

19. Oei MT, Meijer FJ, van der Woude WJ, et al. **Interleaving cerebral CT perfusion with neck CT angiography, Part II: clinical implementation and image quality.** *Eur Radiol* 2017;27:2411–18 CrossRef Medline

20. Lemmens HJ, Bernstein DP, Brodsky JB. **Estimating blood volume in obese and morbidly obese patients.** *Obes Surg* 2006;16:773–76 CrossRef Medline

21. Kleindorfer DO, Towfighi A, Chaturvedi S, et al. **2021 Guideline for the Prevention of Stroke in Patients with Stroke and Transient Ischemic Attack: A Guideline From the American Heart Association/American Stroke Association.** *Stroke* 2021;52:e364–67 CrossRef Medline

Survey of the American Society of Neuroradiology Membership on the Use and Value of Intracranial Vessel Wall MRI

M. Mossa-Basha, C. Zhu, C. Yuan, L. Saba, D.A. Saloner, M. Edjlali, N.V. Stence, D.M. Mandell, J.M. Romero, Y. Qiao, D.J. Mikulis, and B.A. Wasserman

ABSTRACT

BACKGROUND AND PURPOSE: Intracranial vessel wall MR imaging is an emerging technique for intracranial vasculopathy assessment. Our aim was to investigate intracranial vessel wall MR imaging use by the American Society of Neuroradiology (ASNR) members at their home institutions, including indications and barriers to implementation.

MATERIALS AND METHODS: The ASNR Vessel Wall Imaging Study Group survey on vessel wall MR imaging use, frequency, applications, MR imaging systems and field strength used, protocol development approaches, vendor engagement, reasons for not using vessel wall MR imaging, ordering-provider interest, and impact on clinical care, was distributed to the ASNR membership between April 2 and August 30, 2019.

RESULTS: There were 532 responses; 79 were excluded due to nonresponse and 42 due to redundant institutional responses, leaving 411 responses. Fifty-two percent indicated that their institution performs vessel wall MR imaging, with 71.5% performed at least 1–2 times/month, most frequently on 3T MR imaging, and 87.7% using 3D sequences. Protocols most commonly included were T1-weighted pre- and postcontrast and TOF-MRA; 60.6% had limited contributions from vendors or were still in protocol development. Vasculopathy differentiation (94.4%), cryptogenic stroke (41.3%), aneurysm (38.0%), and atherosclerosis (37.6%) evaluation were the most common indications. For those not performing vessel wall MR imaging, interpretation (53.1%) or technical (46.4%) expertise, knowledge of applications (50.5%), or limitations of clinician (56.7%) or radiologist (49.0%) interest were the most common reasons. If technical/expertise obstacles were overcome, 56.4% of those not performing vessel wall MR imaging indicated that they would perform it. Ordering providers most frequently inquiring about vessel wall MR imaging were from stroke neurology (56.5%) and neurosurgery (25.1%), while 34.3% indicated that no providers had inquired.

CONCLUSIONS: More than 50% of neuroradiology groups use vessel wall MR imaging for intracranial vasculopathy characterization and differentiation, emphasizing the need for additional technical and educational support, especially as clinical vessel wall MR imaging implementation continues to grow.

ABBREVIATIONS: ASNR = American Society of Neuroradiology; IP = Internet Protocol; MR-VWI = vessel wall MR imaging

Intracranial vessel wall MR imaging (MR-VWI) is capable of detecting,[1,2] differentiating,[3-5] and characterizing intracranial vasculopathies[6-10] and may be able to help predict patient outcomes.[11,12] Because this technique has been adopted by a growing number of institutions worldwide, the American Society of Neuroradiology (ASNR) Vessel Wall Imaging Study Group was developed to disseminate vessel wall imaging techniques, educate the general neuroradiology community on its implementation and interpretation, and influence vendors to improve vessel wall imaging techniques.[13] Numerous barriers to the implementation of MR-VWI may exist at many institutions, including technology, expertise, knowledge, workflow limitations, and/or vendor relation

limitations. The goal of the current survey study was to poll the membership of the ASNR to determine whether institutions were performing MR-VWI, and if not, what barriers exist to its implementation and use. For institutions already performing MR-VWI, our goal was to evaluate applications of the technique, which sequences were being used, how the techniques were developed, levels of clinician interest, and vendor collaborations for technique development. To our knowledge, this is the first study to evaluate institutional use of MR-VWI across a United States–based neuroradiologic society. The survey can help inform the ASNR Vessel Wall Imaging Study Group on the needs of the neuroradiologic community on how to best educate and facilitate the performance of MR-VWI, as well as guide vendors on technical needs for broader MR-VWI use.

MATERIALS AND METHODS

The survey was discussed at ASNR Vessel Wall Imaging Study Group meetings and developed through input by multiple Study Group members. Through an iterative review process, the final survey was developed on the SurveyMonkey.com platform. The survey was built with logic, and if a respondent indicated that they did not perform MR-VWI, he or she skipped to the last 4 questions of the MR-VWI portion of the survey, focused on barriers to MR-VWI performance and ordering-provider interest (the questions in the survey are provided in the Online Supplemental Data). Respondents who indicated that their institution did perform MR-VWI were expected to answer each MR-VWI question of the survey. After institutional review board review, the survey received institutional review board exemption. The anonymous survey was first sent to the ASNR Vessel Wall Imaging Study Group and was opened to the group from March 30 through April 17, 2018. After approval from the ASNR Executive Committee, the survey was then sent to the ASNR membership on April 2, 2019. A second reminder was sent to the membership on August 14, 2019. Responses were gathered between April 2 and August 30, 2019, after which the survey was closed. Individuals could respond to the survey only once.

After collection of survey responses, response quality was assessed, with exclusion of surveys in which the respondent spent <20 seconds on the survey and responded to ≤1 question. Internet Protocol (IP) addresses of the respondents were reviewed to determine the institution of origin for the response. For institutions with multiple responses, partially completed responses were excluded. If there was >1 complete response for an institution, the study investigators reviewed the institutional responses to assess accuracy on the basis of their knowledge of the protocol and clinical performance based on publications, presentations, and/or personal knowledge of the specific institution at the time of the survey. If this issue was not unresolved, discussion with MR-VWI leaders at the particular institution was performed for clarification on their approach at the time. Redundant institutional responses were removed to reduce bias arising from multiple responses from individual institutions that would result in overestimation of the approaches of larger institutions. IP addresses without institutional associations were not excluded. IP addresses were also used to determine the region from which the response came. Responses were grouped into continent, country, and, for US responses, region of the country, divided on the basis of US Census definitions.[14] Institutions were categorized as academic, private practice, hybrid, or federal.

RESULTS

Respondents

The survey was distributed to 5552 ASNR members, and 1854 individuals opened the e-mails. There were a total of 46 respondents from the ASNR Vessel Wall Imaging Study Group and 486 respondents from the ASNR membership, for a total of 532 responses. The response rate was 9.6%. Respondents, on average, spent 11 minutes on the survey, and there was an 86% completion rate. We subsequently excluded survey responses for which <20 seconds was spent on the survey and the respondent answered 1 or no questions ($n = 79$), leaving 453 complete responses. We subsequently excluded redundant institutional responses ($n = 42$), leading to 411 included responses.

Of the 411 included responses, 81.3% were from North America, 7.5% from Europe, 5.8% from Asia, 3.6% from South America, 1.0% from Australia, and 0.7% from Africa. Among countries, the United States had the most included responses with 314, followed by Canada ($n = 16$), Brazil ($n = 12$), and South Korea ($n = 5$) (see Table 1 for a complete list of country response and included counts). For the 314 US responses, 30.3% were from the South, 24.5% from the Midwest, 24.5% from the East, and 20.7% from the West. Of the 114 responses with institutional IP addresses, 52.6% were academic, 38.6% private practice, 5.3% federal, and 3.5% hybrid institutions.

Table 1: Countries of origin of total and included respondents

Country	Responses	Included
US	353	314
Canada	17	16
Brazil	13	12
South Korea	6	5
the Netherlands	5	5
Italy	4	4
China	4	4
France	4	4
Britain	4	4
Australia	4	4
India	4	4
Israel	3	3
Spain	3	3
Germany	3	3
Japan	3	3
Colombia	2	2
Chile	2	2
Portugal	2	2
Switzerland	2	2
Jamaica	2	2
Turkey	2	2
Emirates	1	1
Zambia	1	1
Mexico	1	1
South Africa	1	1
Bangladesh	1	1
Albania	1	1
Philippines	1	1
Thailand	1	1
Ireland	1	1
Hungary	1	1
Greece	1	1
Total	453	411

MR-VWI Use

Of included respondents, 52.1% (214/411) indicated that their institution performed MR-VWI. Among those that used MR-VWI, the most common frequency was 1–2 times per month, representing 29.9% (64/214) of respondents, followed by 25.7% (55/214) indicating that they performed MR-VWI at least twice per week, while 15.4% (33/214) indicated that they performed MR-VWI once per week. Overall, 71.5% indicated MR-VWI was performed at least 1–2 times per month (Fig 1).

Of respondents, 56.3% (120/213) indicated that MR-VWI was performed as an add-on to the MR imaging stroke protocol ordered by clinicians, 51.6% (110/213) indicated that MR-VWI was performed as a stand-alone examination ordered by clinicians, and 46.5% (99/213) of respondents stated that at their institution, MR-VWI was added on the basis of the protocoling radiologist's decision. See Fig 2 for full details.
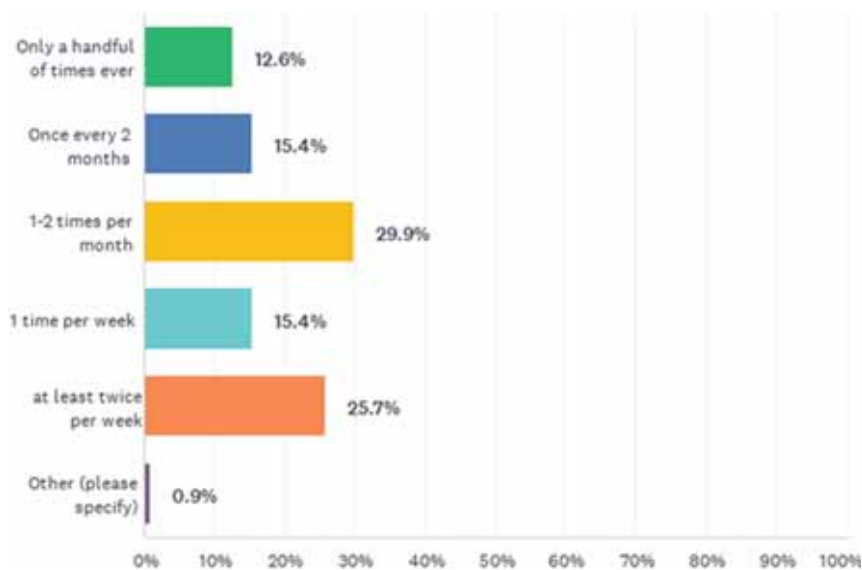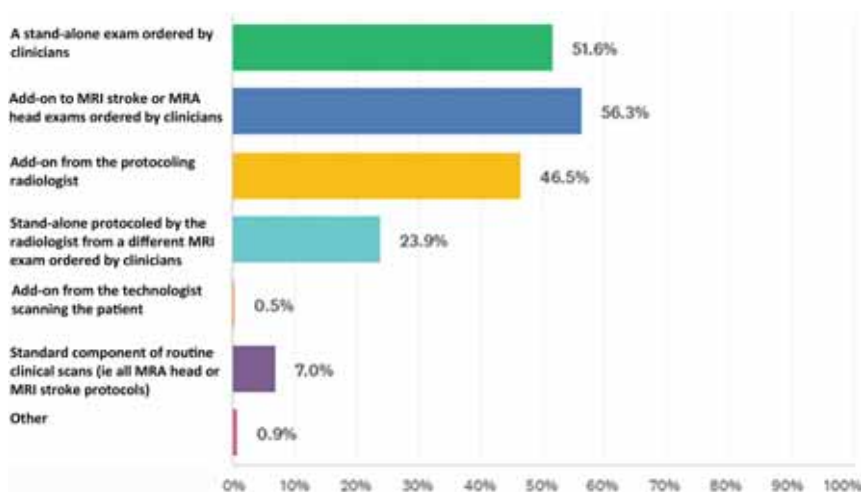
Intracranial vasculopathy differentiation was the most common clinical indication for MR-VWI, indicated by 94.4% (201/213) of respondents. This was followed by cryptogenic stroke evaluation (41.3%; 88/213), aneurysm characterization for rupture risk or culprit aneurysm (38.0%; 81/213), and atherosclerosis characterization for culprit plaque (37.6%; 80/213). Full responses are shown in Fig 3.

In the United States, 47.3% of respondents indicated that their institution performed MR-VWI. Regionally, Eastern respondents indicated the highest frequency of use (58.4%), followed by the West (55.4%), South (45.8%), and Midwest (31.2%). For respondents outside the United States, 67% indicated that their institution performed MR-VWI. These included 80.6% European, 62.5% Asian and South American, and 66% African; none of the Australian respondents indicated MR-VWI use. In addition, 75% of Canadian and 50% of Jamaican respondents performed MR-VWI.

Among institution types, 61.7% of academic institutions' responses indicated that they performed MR-VWI, compared with 52.3% of private practice, 66% of federal institutions, and 100% of hybrid practices. These were among 114 responses with institutional IP addresses.

Vendor Involvement

Two hundred fifty-seven total responses indicated that MR-VWI was performed on 3T MR imaging systems, compared with 80 responses indicating use of 1.5T MR imaging systems and 3 indicating the use of 7T systems. MR-VWI was most frequently performed on 3T Siemens MR imaging systems (59.9%; 127/212), followed by 3T GE Healthcare MR imaging systems (34.0%; 72/212) and 3T Philips Healthcare MR imaging systems (26.9%; 57/212). See the Online Supplemental Data for further details. Of responses, 71.2% indicated that they performed MR-VWI on only 3T MR imaging systems; 7.1%, on 1.5T systems only; and 21.7%, on both 3T and 1.5T systems at their respective institutions.

Of respondents, 42.0% indicated that their institution had a research agreement with the vendor, 36.8% indicated they did not, and 21.2% were not sure. For those with a vendor research agreement, 31.9% sought help from the vendor for development of their MR-VWI protocol, and 38.8% did not, while 29.4% were not sure. For those that developed a protocol in collaboration with the vendor that was satisfactory to their clinical needs, 49.2% did so with Siemens; 30.5%, with GE Healthcare; and 28.0%, with

FIG 1. How often do you perform intracranial vessel wall MR imaging? Respondents = 214.

FIG 2. Is intracranial vessel wall MR imaging being clinically performed as? (choose all that apply) Respondents = 213.
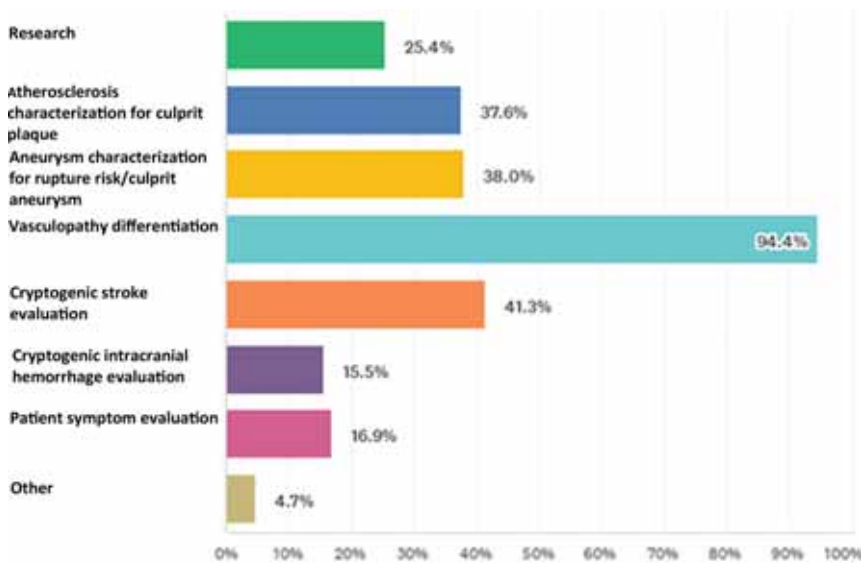
FIG 3. For what primary purpose does your institution perform intracranial vessel wall imaging? (choose all that apply) Respondents = 213.
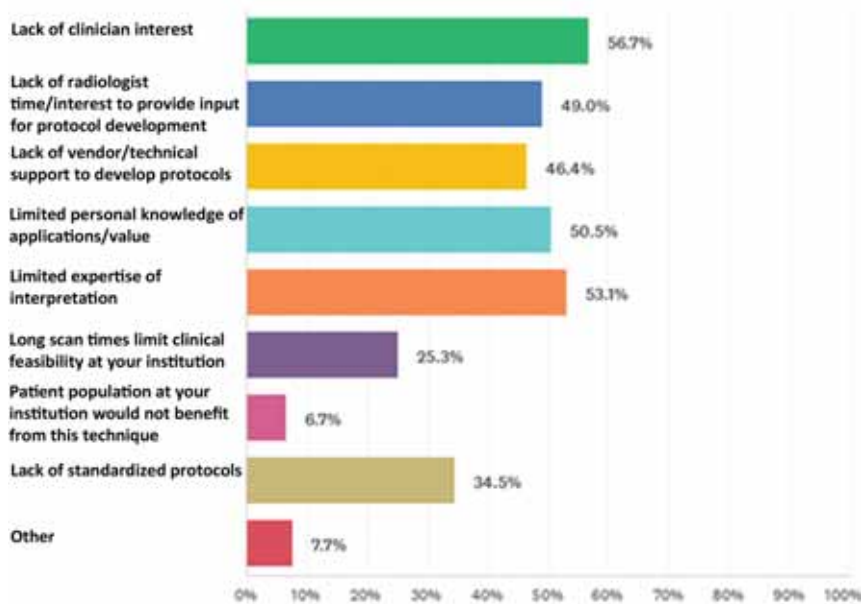
FIG 4. If your institution does not perform intracranial vessel wall MR imaging (only respond to this question if you do not use intracranial vessel wall imaging), what barriers does your institution face for implementation? (choose all that apply) Respondents = 194.

Philips Healthcare (Online Supplemental Data). Of respondents, 38.0% indicated limited contributions from the vendors in the development of their clinical protocols, 28.2% indicated initial difficulties when working with the vendor with an eventual solution reached, and 22.5% are still looking for a collaborative solution with their MR imaging vendor; 16.2% indicated an excellent experience working with the vendor on developing an MR-VWI protocol (Online Supplemental Data). In the free-text response, 12 respondents indicated unhappiness with their vendor engagement on

protocol development. For those that responded that they did not seek vendor support for protocol building, 40.3% indicated limited vendor contributions, while for those that indicated that they had limited vendor contribution, 48% indicated that they did not seek help from the vendor and 20.4% did, while 31.5% were not sure.

MR-VWI Protocol

Of respondents, 51.2% indicated that they exclusively used 3D MR-VWI protocols and 12.3% used only 2D protocols; 36.5% performed combined 2D/3D protocols; 60.6% pursued their approach to protocols on the basis of published literature, conference lectures, and/or guidance from the ASNR Vessel Wall Imaging Study Group; 29.6% designed their protocols on the basis of the limitations of their MR imaging equipment; 30.5% focused on workflow time constraints to guide protocol approach; 59.2% developed their protocol in-house; 38.9% obtained the protocol from the vendor; and 19.9% received the protocol from another institution (Online Supplemental Data).

Institutions most frequently used postcontrast T1-weighted MR-VWI sequences (89.1%), T1-weighted MR-VWI (88.6%), and T2-weighted (39.3%) sequences, respectively. For MRA techniques, TOF-MRA (76.3%) and contrast-enhanced MRA (36.5%) were used (Online Supplemental data).

Obstacles to Use of MR-VWI

One hundred ninety-seven respondents (47.9%) indicated that their institution was not performing MR-VWI. Of those respondents, 56.7% indicated that the reason was due to lack of ordering-provider interest, while 53.1% indicated that it was due to limited radiologist expertise in interpretation, 50.5% due to limited personal knowledge of applications and value, 49.0% due to lack of radiologists' time or interest in providing input for protocol development, and 46.4% due to lack of vendor or technical support for protocol development. See Fig 4 for full details.

For those facing technical or expertise obstacles for performance of MR-VWI, 56.4% indicated that they would use the technique if these obstacles were overcome; 6.4% indicated that they still would not (Online Supplemental data); and 37.3% were unsure.
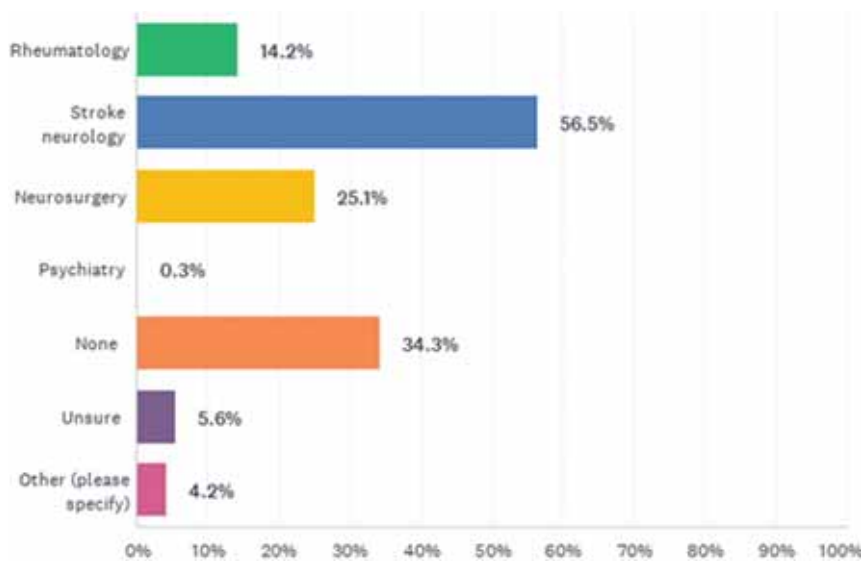
FIG 5. Have your clinicians approached the radiologists in your group in regard to performing intracranial vessel wall imaging? If so, which clinician groups? (choose all that apply) Respondents = 359.

Ordering Provider Interest in MR-VWI

Respondents indicated that the following ordering-provider specialties approached radiology departments with interest in MR-VWI performance (respondents could indicate >1 specialty): stroke neurology (56.5%), neurosurgery (25.1%), and rheumatology (14.2%); 34.3% indicated that no ordering providers had expressed interest in MR-VWI (Fig 5).

For respondents indicating that neurology was the only clinical service that ordered examinations, the most common reason was for vasculopathy differentiation (71.1%), followed by cryptogenic stroke (33.0%). For respondents who received requests from neurology and neurosurgery, vasculopathy differentiation remained the most common (83.3%), followed by aneurysm (60.0%) and atherosclerosis (41.7%) characterization for vulnerability. For those who received requests from neurology, neurosurgery, and rheumatology, vasculopathy differentiation was most common (80.8%), followed by aneurysm characterization (57.7%) and cryptogenic stroke (50.0%). See Table 2 for further details.

MR-VWI Impact on Patient Management

Of respondents, 40.6% believed that MR-VWI had led to an impact on patient management at their institution, 37.5% believed it had not impacted patient care, and 21.9% were unsure.

DISCUSSION

MR-VWI is a technique that has gained use across >50% of radiology departments that took part in this survey. The technique has shown value in vasculopathy characterization[6,7,9,10] and differentiation,[3-5] prediction of outcomes,[11,12] and association with patient symptoms.[6,15] To our knowledge, the current survey study is the first assessing use, approaches, vendor relations, and indications for performance of MR-VWI. Of ASNR member respondents, 52.1% indicated that they were performing MR-VWI for intracranial

vasculopathy differentiation, cryptogenic stroke etiology evaluation, and atherosclerosis with aneurysm characterization for vulnerability being the most common indication. Almost 72% of respondents indicated that MR-VWI was performed at their institution at least 1–2 times per month, with 41.1% performing the technique at least once per week. Respondents most frequently indicated a successful interaction with Siemens in protocol development; however, <45% indicated development of a protocol with more than limited contributions from the vendor, and 16% indicated an excellent experience. However, these responses are because almost half of those that indicated limited vendor contribution never sought vendor help for protocol development, indicating the need for increased radiologist-to-vendor outreach and engagement. The most common approach to protocols was the use of 3D sequences, indicated by >87% of respondents with protocols developed in-house. The most common protocol constructions were based on recommendations or approaches outlined by the ASNR Vessel Wall Imaging Study Group, published literature, or lectures at national meetings. The most common barriers to MR-VWI implementation were lack of ordering-provider interest, lack of expertise in interpretation, limited personal knowledge of MR-VWI value or applications, lack of time or interest by the radiologist in providing protocol input, and lack of vendor or technical support for protocol development.

Protocols most commonly included T1-weighted, T1-weighted postcontrast, T2-weighted MR-VWI sequences, and TOF-MRA and contrast-enhanced MRA for luminal imaging, respectively. T1-weighted pre- and postcontrast high-resolution sequences are central to MR-VWI performance because assessment of enhancement contributes to vasculopathy differentiation,[3,5] determination of culprit status of atherosclerosis[9,16] and aneurysms,[15] association with increased aneurysm vulnerability scores,[8] symptoms,[6] risk of growth,[7] associations with recurrent stroke,[12,17] association with subsequent vasospasm development,[11] and identifying appropriate biopsy targets.[18] T2-weighted MR-VWI is less frequently used, likely in many groups, due to time constraints; however, T2-weighted sequences have shown additional value in differentiating vasculopathies.[4] While luminal stenosis measurements are more accurate on MR-VWI compared with TOF-MRA,[2,19] TOF-MRA is frequently included in MR-VWI protocols because it provides easier identification of stenoses, luminal irregularities, and aneurysms. Contrast-enhanced MRA is also frequently used because it provides more accurate depiction of slow or turbulent flow than TOF-MRA.

The reluctance to implement MR-VWI with little experience or training is well-founded, considering the high frequency of interpretive pitfalls encountered with these examinations.[20] A majority of those not performing MR-VWI (56.4%) indicated that if

Table 2: Institutional indications for MR-VWI performance relative to ordering provider interest

Ordered by	Research	Atheroma Risk	Aneurysm Risk	Differentiate Vasculopathy	Cryptogenic Stroke
Neurology only (*n* = 97) (No.) (%)	12 (12.4)	24 (24.7)	11 (11.3)	69 (71.1)	32 (33.0)
Neurology and neurosurgery (*n* = 60) (No.) (%)	16 (26.7)	25 (41.7)	36 (60)	50 (83.3)	23 (38.3)
Neurology, neurosurgery, and rheumatology (*n* = 26) (No.) (%)	15 (57.7)	10 (38.5)	15 (57.7)	21 (80.8)	13 (50)
Neurosurgery only (*n* = 5) (3 blank for reasons) (No.) (%)	1 (20)	0 (0)	1 (20)	2 (40)	1 (20)

technical or expertise barriers were overcome, their institution would perform MR-VWI. Therefore, both vendor involvement with users and user willingness to reach out to vendors are fundamental to the implementation of MR-VWI in clinical practice. This requirement was highlighted in the survey by most respondents indicating limited or no contribution from the vendors in the development of successful clinical protocols, yet nearly half of the respondents that indicated limited vendor contribution never sought help from their vendors. Increased societal engagement with vendors is also necessary to share expert opinions on technical and clinical approaches and the value and applications of MR-VWI and to help optimize technique development and implementation. In addition, there are various technical parameters to be manipulated in the MR-VWI sequences, including spatial resolution, the timing between injection and postcontrast sequence acquisition, and specific sequence preparation to decrease slow-flow artifacts. The sheer number of options and variables contributes to general uncertainty in how to construct the optimal MR-VWI sequence.

This survey conveys the high level of interest from ordering providers and neuroradiologists in MR-VWI and its potential in the diagnosis and characterization of intracranial vascular diseases. Considering that many respondents indicated a lack of knowledge of MR-VWI applications and imaging interpretation and limited technical expertise, MR-VWI could be even further incorporated into clinical practice with improved education from national and international societies, journals, and study groups. This education can be accomplished through an increased representation of MR-VWI at national and international radiology conferences, through conference sessions on MR-VWI, MR-VWI cases of the day at conferences and on societal webpages, case presentations from experts on social media, peer-reviewed educational publications in radiology and nonradiology clinical journals and webinars, and engagement through institutional multidisciplinary conferences. Through improved knowledge by radiologists of appropriate applications of MR-VWI and correct examination interpretation, ordering providers will better understand the potential diagnostic impact of the technique.

Improved and automated reconstruction, segmentation, quantitation, and disease identification algorithms can also facilitate adoption of MR-VWI. Tools that are agnostic about vendor platforms and techniques could improve generalization and use. Software solutions that make MR-VWI interpretation more standardized, efficient, reproducible, and definitive would facilitate development of standard interpretation approaches and contribute to the development of improved imaging guidelines. These tools could also facilitate the development of automated, quantitative metrics that could help differentiate vasculopathies and stratify patient risk of vasculopathy complications, including stroke and subarachnoid hemorrhage, as well as tracking treatment responses. Because these tools would reduce the burden on radiologists' expertise and technical homogeneity, neuroradiology and ordering-provider teams would more readily rely on MR-VWI and its output.

Stroke neurologists were the most common ordering provider with interest in MR-VWI. Considering nearly one-third of respondents indicated that no ordering providers had inquired about MR-VWI at their institution, further education of relevant providers on the value of MR-VWI through their societies via educational sessions at annual meetings, webinars, targeted publications, and education through institutional multidisciplinary conferences can even further increase interest in the technique and lead to increased institutional adoption.

The current survey has a number of limitations. First, it was a voluntary survey of a national society with a relatively low response rate; thus, selection bias based on those more motivated to respond to the survey due to interest may be present. In addition, neuroradiologists or radiologists who interpret neuroradiology studies but are not members of ASNR would not have had an opportunity to respond. This process leads to a limited sampling of the total population of neuroradiologists. Second, this survey was performed in 2019, and due to the rapid evolution of MR imaging technology and the relatively quick adoption of MR-VWI, the responses of some respondents may have changed during the past 2 years. Third, the survey was anonymous; thus, we did not request names or institutions of respondents. While we did use IP addresses of respondents to mitigate redundant institutional responses, this was not available for all institutions, so it is still possible that >1 response could have come from some institutions, potentially presenting bias toward larger institutions.

CONCLUSIONS

Intracranial vessel wall MR imaging is a technique that is used by >50% of institutions as indicated by this survey of the American Society of Neuroradiology membership, primarily for intracranial vasculopathy differentiation, cryptogenic stroke, and atherosclerosis and aneurysm risk assessment. Approximately half of respondents reported limited expertise in interpretation, half reported limited knowledge of applications, and half reported technical limitations in protocol development as barriers to implementation. In addition, one-third expressed no provider interest in intracranial vessel wall MR imaging. These survey results highlight the need for further education of neuroradiologists and relevant ordering providers by national and international societies and the ASNR Vessel Wall Imaging Study Group and increased engagement with vendors to overcome technical limitations in protocol implementation,

especially as the increasing adoption of vessel wall MR imaging across practices continues.

REFERENCES

1. Mossa-Basha M, Watase H, Sun J, et al. **Inter-rater and scan-rescan reproducibility of the detection of intracranial atherosclerosis on contrast-enhanced 3D vessel wall MRI.** *Br J Radiol* 2019;92:20180973 CrossRef Medline

2. Tian X, Tian B, Shi Z, et al. **Assessment of intracranial atherosclerotic plaques using 3D black-blood MRI: comparison with 3D time-of-flight MRA and DSA.** *J Magn Reson Imaging* 2021;53:469–78 CrossRef Medline

3. Mossa-Basha M, de Havenon A, Becker KJ, et al. **Added value of vessel wall magnetic resonance imaging in the differentiation of Moyamoya vasculopathies in a non-Asian cohort.** *Stroke* 2016;47:1782–88 CrossRef Medline

4. Mossa-Basha M, Hwang WD, De Havenon A, et al. **Multicontrast high-resolution vessel wall magnetic resonance imaging and its value in differentiating intracranial vasculopathic processes.** *Stroke* 2015;46:1567–73 CrossRef Medline

5. Mossa-Basha M, Shibata DK, Hallam DK, et al. **Added value of vessel wall magnetic resonance imaging for differentiation of nonocclusive intracranial vasculopathies.** *Stroke* 2017;48:3026–33 CrossRef Medline

6. Fu Q, Wang Y, Zhang Y, et al. **Qualitative and quantitative wall enhancement on magnetic resonance imaging is associated with symptoms of unruptured intracranial aneurysms.** *Stroke* 2021;52:213–22 CrossRef Medline

7. Gariel F, Ben Hassen W, Boulouis G, et al. **Increased wall enhancement during follow-up as a predictor of subsequent aneurysmal growth.** *Stroke* 2020;51:1868–72 CrossRef Medline

8. Hartman JB, Watase H, Sun J, et al. **Intracranial aneurysms at higher clinical risk for rupture demonstrate increased wall enhancement and thinning on multicontrast 3D vessel wall MRI.** *Br J Radiol* 2019;92:20180950 CrossRef Medline

9. Qiao Y, Anwar Z, Intrapiromkul J, et al. **Patterns and implications of intracranial arterial remodeling in stroke patients.** *Stroke* 2016;47:434–40 CrossRef Medline

10. Li X, Sun B, Wang L, et al. **Association of type 2 diabetes mellitus and glycemic control with intracranial plaque characteristics in patients with acute ischemic stroke.** *J Magn Reson Imaging* 2021;54:655–66 CrossRef Medline

11. Mossa-Basha M, Huynh TJ, Hippe DS, et al. **Vessel wall MRI characteristics of endovascularly treated aneurysms: association with angiographic vasospasm.** *J Neurosurg* 2018;131:859–67 CrossRef Medline

12. Shi Z, Li J, Zhao M, et al. **Progression of plaque burden of intracranial atherosclerotic plaque predicts recurrent stroke/transient ischemic attack: a pilot follow-up study using higher-resolution MRI.** *J Magn Reson Imaging* 2021;54:560–70 CrossRef Medline

13. Mandell DM, Mossa-Basha M, Qiao Y, et al; Vessel Wall Imaging Study Group of the American Society of Neuroradiology. **Intracranial Vessel Wall MRI: Principles and Expert Consensus Recommendations of the American Society of Neuroradiology.** *AJNR Am J Neuroradiol* 2017;38:218–29 CrossRef Medline

14. US Census Bureau. **Census Regions and Divisions of the United States.** https://www2.census.gov/geo/pdfs/maps-data/maps/reference/us_regdiv.pdf. 2020. Accessed December 28, 2021

15. Edjlali M, Guédon A, Ben Hassen W, et al. **Circumferential thick enhancement at vessel wall MRI has high specificity for intracranial aneurysm instability.** *Radiology* 2018;289:181–87 CrossRef Medline

16. Qiao Y, Zeiler SR, Mirbagheri S, et al. **Intracranial plaque enhancement in patients with cerebrovascular events on high-spatial-resolution MR images.** *Radiology* 2014;271:534–42 CrossRef Medline

17. Sun B, Wang L, Li X, et al. **Intracranial atherosclerotic plaque characteristics and burden associated with recurrent acute stroke: a 3D quantitative vessel wall MRI study.** *Front Aging Neurosci* 2021;13:706544 CrossRef Medline

18. Zeiler SR, Qiao Y, Pardo CA, et al. **Vessel wall MRI for targeting biopsies of intracranial vasculitis.** *AJNR Am J Neuroradiol* 2018;39:2034–36 CrossRef Medline

19. Sarikaya B, Colip C, Hwang WD, et al. **Comparison of time-of-flight MR angiography and intracranial vessel wall MRI for luminal measurements relative to CT angiography.** *Br J Radiol* 2021;94:20200743 CrossRef Medline

20. Kang N, Qiao Y, Wasserman BA. **Essentials for interpreting intracranial vessel wall MRI results: state of the art.** *Radiology* 2021;300:492–505 CrossRef Medline

Commentary on the Survey of the American Society of Neuroradiology Membership on the Use and Value of Intracranial Vessel Wall MRI

The American Society of Neuroradiology (ASNR) Vessel Wall Imaging (MR-VWI) Study Group and all the ASNR members that took the time to respond to their questions should be applauded for this MR-VWI survey. The survey is a comprehensive assessment of the use and perceived value of MR-VWI and was sent to all ASNR members via e-mail. Although the response rate was low at 9% of those surveyed and therefore unlikely to be truly representative of the community, the responses obtained perfectly illustrate many of the important issues involved in the implementation and adoption of new technologies and imaging techniques.

Adoption of intracranial MR-VWI by clinical neuroradiologists has been slow since suppression of luminal flow signal to evaluate the vessel wall was first described in the mid-1990s. Incremental improvements in MR imaging hardware, particularly the increased use of head coils containing more channels, along with refinement of MR imaging sequences, has resulted in superior images and shorter imaging times than were possible previously, making the technique more suitable for clinical use. Imaging times were not addressed by the survey but are still relatively long for clinical use. Most pre- and postcontrast 3D T1 sequences take between 5 and 7 minutes each at 3T, with imaging times longer at up to 9 minutes for each sequence using a 16-channel head coil at 1.5T. Hopefully effort directed at further technique refinement will result in a decrease in these imaging times, allowing greater patient throughput and a decreased number of scans affected by motion artifacts. Decreased scan time and superior 3D image resolution at 3T are likely the reason most respondents are using 3T or a combination of 3T and 1.5T MR imaging for MR-VWI, with only 3 respondents having access to 7T imaging.

The ASNR MR-VWI Study Group has previously published consensus recommendations for current clinical practice in the *American Journal of Neuroradiology*, using evidence from research studies. From the results of this survey, it seems as though the recommendations of the group have been widely adopted, with 61% of respondents using MR-VWI, basing protocols on published literature, conference lectures, and/or guidance from the ASNR MR-VWI Study Group.

Responses also suggest that MR-VWI has been successfully adopted across different types of practices with use rates only slightly higher in the academic (62%) compared with private practice (52%) settings. Results suggest that the survey responders may be biased toward those most likely to practice subspeciality neurovascular radiology at the highest level. This statement is supported by the high number (42%) of respondents who indicated that their institution had a research agreement with a vendor, with an even higher number (59%) having the expertise to develop their MR-VWI protocol in-house.

Vendor support is very important for optimizing imaging techniques across different imaging platforms in all types of clinical settings, especially when there is no local MR-VWI protocol expertise. The results of the survey suggest that vendors could do more to support neuroradiologists with MR-VWI, with relatively few (39%) of those performing MR-VWI obtaining their protocol from their vendors and 38% indicating limited contributions from vendors in the development of their clinical protocols. I was somewhat surprised that only 31% of those with a vendor research agreement sought support from their vendors for MR-VWI protocol development, given the widespread availability of support for such endeavors, possibly due to these centers already having in-house experts.

When provided, support was higher from Siemens than from the other vendors at 49%. Improved vendor support should be encouraged and should result in more widespread adoption of MR-VWI. Of those not performing MR-VWI, 46% stated that this was due to lack of vendor or technical support for protocol development. Even when vendor support was available, there was certainly room for improvement, with 28% indicating initial difficulties working with their vendors with an eventual solution reached and 23% still looking for a collaborative solution with their vendors. This vendor issue appears to be a wasted opportunity for all concerned, particularly at a time when standardized vendor-neutral protocols and collection and analysis of large,

standardized data sets are of increasing importance for population-based research and development of artificial intelligence.

More widespread education of our clinical colleagues is going to be important in ensuring increased patient access to MR-VWI so that they can benefit from the additional information obtained. Of the 48% of responders not performing MR-VWI, 57% indicated that the reason is a lack of ordering-provider interest. The authors of the study have some very sensible suggestions as to how this should be improved, and we should all try to implement their suggestions.

Currently MR-VWI is performed most often as an addition to an MR imaging stroke protocol, with the most common indications being differentiation of vasculopathy, aneurysm characterization, and cryptogenic stroke. Research studies have also shown MR-VWI to be a useful technique for diagnosis, and this is supported by clinical experience, with 41% of responders stating that MR-VWI has had a positive impact on patient care at their institution. Effort should, therefore, be made by the ASNR MR-VWI Study Group and others to increase exposure of neuroradiologists to the technique so that we may all become experts at reading these often-complex studies. More widespread familiarity with MR-VWI, including the pitfalls in image interpretation, will lead to improved patient care, more widespread adoption of MR-VWI, and, hopefully, increased research output related to this useful technique.

J. Becker
Associate Professor
Mayo Clinic, Arizona

RAPID CT Perfusion–Based Relative CBF Identifies Good Collateral Status Better Than Hypoperfusion Intensity Ratio, CBV-Index, and Time-to-Maximum in Anterior Circulation Stroke

A. Potreck, E. Scheidecker, C.S. Weyland, U. Neuberger, C. Herweh, M.A. Möhlenbruch, M. Chen, S. Nagel, M. Bendszus, and F. Seker

ABSTRACT

BACKGROUND AND PURPOSE: Information of collateral flow may help to determine eligibility for thrombectomy. Our aim was to identify CT perfusion–based surrogate parameters of good collateral status in acute anterior circulation ischemic stroke.

MATERIALS AND METHODS: In this retrospective study, we assessed the collateral status of 214 patients who presented with acute ischemic stroke due to occlusion of the MCA M1 segment or the carotid terminus. Collaterals were assessed on dynamic CTA images analogous to the multiphase CTA score by Menon et al. CT perfusion parameters (time-to-maximum, relative CBF, hypoperfusion intensity ratio, and CBV-index) were assessed with RAPID software. The Spearman rank correlation and receiver operating characteristic analyses were performed to identify the parameters that correlate with collateral scores and good collateral supply (defined as a collateral score of ≥ 4).

RESULTS: The Spearman rank correlation was highest for a relative CBF $< 38\%$ volume ($\rho = -0.66$, $P < .001$), followed by the hypoperfusion intensity ratio ($\rho = -0.49$, $P < .001$), CBV-index ($\rho = 0.51$, $P < .001$), and time-to-maximum > 8 seconds ($\rho = -0.54$, $P < .001$). Good collateral status was better identified by a relative CBF $< 38\%$ at a lesion size <27 mL (sensitivity of 75%, specificity of 80%) compared with a hypoperfusion intensity ratio of <0.4 (sensitivity of 75%, specificity of 62%), CBV-index of >0.8 (sensitivity of 60%, specificity of 78%), and time-to-maximum > 8 seconds (sensitivity of 68%, specificity of 76%).

CONCLUSIONS: Automated CT perfusion analysis allows accurate identification of collateral status in acute ischemic stroke. A relative CBF $< 38\%$ may be a better perfusion-based indicator of good collateral supply compared with time-to-maximum, the hypoperfusion intensity ratio, and the CBV-index.

ABBREVIATIONS: AUC = area under the curve; HIR = hypoperfusion intensity ratio; IQR = interquartile range; mCTA = multiphase CTA; rCBF = relative CBF; sCTA = single-phase CTA; Tmax = time-to-maximum

According to the latest guidelines of the American Stroke Association, information on collateral flow may help to determine eligibility for mechanical thrombectomy in some candidates.[1] Although a multitude of different methods and collateral grading systems have been described,[2] the guidelines do not recommend a specific method. In CT imaging, collaterals can be assessed on single-phase or multiphase CT angiography. Single-phase CTA (sCTA) collateral scores may underestimate the collateral supply

because they rely on the spatial extent of collateral enhancement during a single phase only. In contrast, multiphase CTA (mCTA) or dynamic CTA, which is postprocessed from CTP data, provides information on both the spatial extent and delay in collateral filling.[3-5] In the past, collateral grading based on mCTA was found to predict final infarct volume and clinical outcome better than sCTA-based collateral assessment.[4,6]

In recent years, various methods of automated assessment of collateral status have been proposed.[7,8] Lee et al,[9] for instance, reported that the perfusion delay, as indicated by the time-to-maximum (Tmax) parameter, correlates with sCTA collateral status. Furthermore, novel perfusion-based parameters, such as the hypoperfusion intensity ratio (HIR) and the CBV-index were introduced.[10-12] The HIR is calculated by dividing the volume of tissue with a perfusion delay of Tmax > 10 seconds by the volume of tissue with Tmax > 6 seconds. The CBV-index indicates the

mean CBV within the volume of tissue with a perfusion delay of Tmax > 6 seconds divided by the mean CBV of healthy tissue.[10,13] These parameters were found to correlate with infarct growth during interhospital transfer for thrombectomy[14] and with clinical outcome after thrombectomy.[13] Whether the HIR or CBV-index identifies collateral status better than other perfusion parameters remains to be investigated.

The aim of this study was, therefore, to identify and compare CTP-based surrogate parameters (Tmax, CBF, HIR, and CBV-index) of collateral supply on dynamic CTA.

MATERIALS AND METHODS

Patient Data

At our comprehensive stroke center, all patients transferred to the angiography suite for thrombectomy are registered in a prospective institutional registry. This registry was screened retrospectively for patients with an occlusion of the carotid terminus or the M1 segment of the MCA and acquisition of volume CTP between April 2014 and March 2020. The study was approved by the local ethics board of Heidelberg University, and informed consent was waived.

CTP Imaging

CTP imaging was performed on a 64-multislice CT (Somatom Definition AS; Siemens) with a z-axis coverage of 8 cm. A contrast bolus of 36 mL of iobitridol (Xenetix 350; Guerbet) followed by a saline flush of 20 mL was applied at a flow rate of 6.0 mL/s. Acquisition parameters for CTP were 80 kV and 180 mAs, and acquisition duration was 44 seconds at a repetition rate of 1.5 seconds. CTP data were reconstructed with a section thickness of 5 mm.[8]

Perfusion Analysis

Fully automated perfusion analysis was performed using RApid processing of PerfusIon and Diffusion (RAPID software, Version 5.0.4; iSchemaView). The volumes with Tmax > 6 seconds, > 8 seconds, > 10 seconds; the volumes with relative CBF (rCBF) < 30%, < 34%, < 38% (as predefined in the RAPID software reports); and the HIR and CBV-index were analyzed. When patients had no lesions with Tmax > 6 seconds, the HIR and CBV-index were undefined by RAPID. In these cases, the HIR and CBV-index were set to 0 and 1.0, respectively.

Assessment of Dynamic CTA Collateral Status

CTP images were postprocessed using syngo.CT Dynamic Angio (Siemens Healthcare, Erlangen, Germany).[15] First, an arterial input function and a venous output function were defined by manually placing ROIs within an arterial vessel in the unaffected hemisphere and within a vein or dural sinus. Analogously to Menon et al,[4] 3 phases were determined. CTA images of the arterial phase were then created by MIP of the temporal volumes ± 2 seconds from the peak of the arterial input function, whereas CT images of the venous phase were created by temporal MIP of the acquisitions ± 2 seconds from the peak of the venous output function. CTA images for a late venous phase were created by temporal MIP of the acquisitions 6–12 seconds after the venous peak. Therefore, dynamic CTA phases were comparable with conventional

multiphase CTA as described by Menon et al,[4] in which arterial, venous, and late venous CTA images were acquired 8 seconds apart with an acquisition time for each volume of 3.6 seconds.[4]

Collateral status on dynamic CTA was assessed by an experienced reader who was blinded to clinical data and perfusion analysis. Collaterals were scored analogous to the mCTA collateral scoring system by Menon et al[4] using a 6-point ordinal scale (ranging from absent collateral supply [collateral sore = 0] to excellent collateral supply [score = 5]). Good collaterals were defined as collateral scores of 4–5 (Fig 1).[3,4]

Statistical Analysis

Statistical analysis was performed with R statistical and computing software (http://www.r-project.org). Group differences were assessed by the Fisher exact test for nominal variables and the Mann-Whitney U test for continuous variables. Correlation between perfusion indices and collateral scores was assessed by the Spearman rank correlation. Receiver operating characteristic curves were analyzed for the identification of good collaterals (scores = 4–5). Differences of the area under the curve (AUC) were assessed by the DeLong test.[16] Optimal thresholds to identify good collateral status were chosen according to the Youden index. The statistical significance level was set to $P < .05$. Medians are provided with their interquartile range (IQR), and means, with their SDs. All confidence intervals are provided as 95% CI.

RESULTS

Baseline Patient Characteristics

Two-hundred thirty-seven patients met the inclusion criteria. Of these, 1 patient had to be excluded due to an incomplete perfusion acquisition. Six patients were excluded from the analysis due to severe head motion during image acquisition, and 16 patients were excluded due to bolus delay or insufficient contrast enhancement. In all cases included in the analysis, the first pass of the contrast agent bolus was captured completely. Furthermore, 1 patient with an acute space-occupying subdural hematoma was excluded because the RAPID software falsely classified the hematoma as an infarct core.

Altogether, collateral scores and CTP analyses of 214 patients (122 women, 57%) were included in the analysis. In all cases, the first pass of contrast bolus was completely captured. The occlusion site was the MCA M1-segment in 169 (79%) patients and the carotid terminus in 45 (21%) patients. The median time from symptom onset or last seen well to imaging was 187 minutes (IQR, 96–364 minutes). The median NIHSS score at admission was 16 (IQR, 11–20), and the median ASPECTS on acute CT imaging was 9 (IQR, 7–10). Baseline patient characteristics are summarized in the Online Supplemental Data.

Collateral Scores and Perfusion Indices

The collateral score was 0 in 6 patients (3%), 1 in 16 patients (7%), 2 in 26 patients (12%), 3 in 55 (26%) patients, 4 in 58 (27%) patients, and 5 in 53 (25%) patients.

The mean infarct core (rCBF < 30%) was 24 mL (95% CI 19–28 mL) and mean lesion size of Tmax > 6 seconds was 111 mL (95% CI 102–119 mL). The mean CBV-index was 0.68 (95% CI

0.65–0.70), and the mean HIR was 0.37 (95% CI 0.34–0.40). In 4 patients (2%), a lesion size of Tmax > 6 seconds was 0 mL; therefore, the RAPID software was unable to calculate the HIR and CBV-index. These parameters were set manually to HIR = 0 and CBV-index = 1.0.

On a group level, all perfusion parameters differed significantly between patients with good-versus-poor collaterals (P < .001; Table 1 and Fig 2). Furthermore, all perfusion indices correlated directly with collateral scores on the Spearman rank correlation analysis (Table 2). The highest (negative) correlation was found for volumes with rCBF < 38%, followed by Tmax > 8 seconds, CBV-index, and HIR.

Receiver operating characteristic analysis for good collateral status revealed similar results (Fig 3). With an AUC of 0.83, rCBF performed the best (Table 2). There were significant differences in the AUC between rCBF < 38% and Tmax > 6 seconds (P = .01), Tmax > 8 seconds (P = .04), Tmax > 10 seconds (P = .02), CBV-index (P = .008), and HIR (P < .001), respectively. According to the Youden index, good collateral status was identified on rCBF < 38% maps when the lesion size was <27 mL (sensitivity of 75%, specificity of 80%, and accuracy 77%) and the resulting contingency table was significant (P < .001; Table 3).

DISCUSSION

The aim of this study was to identify CTP-based surrogate parameters of collateral supply. We found that all CTP parameters, particularly Tmax delay, CBF lesion size, CBV-index, and HIR, correlated with collateral supply. The highest correlation was observed for rCBF < 38%.

Compared with previous studies, our study confirms that the HIR and CBV-index correlate well with collateral status. We found that HIR <0.4 identifies good collateral status with a sensitivity of 75% and specificity of 62%. Guenego et al[11] reported a sensitivity of 79% and specificity of 56% for the same threshold. Lyndon et al[17] compared the HIR with mCTA collateral status in 52 patients and found an optimum cutoff value of HIR >0.45 to identify poor collateral status.

However, the comparison of HIR, CBV-index, Tmax, and CBF in our study revealed that CBF, particularly the volume with rCBF < 38%, may be an even better predictor of good collateral status. In our analysis, good collateral supply was identified best by a volume with rCBF < 38% of <27 mL, with a sensitivity of 75% at a specificity of 80%.

Noticeably, the RAPID software uses rCBF for the identification of the ischemic core as well, but at a threshold of rCBF < 30%. It additionally provides rCBF volumes with thresholds at 34% and 38%. So far, data analyzing and comparing the clinical relevance of these thresholds is scarce. Muehlen et al[18] reported

FIG 1. Noncontrast CT, conventional CTA, and dynamic CTA for 2 exemplary patients with acute ischemic stroke. Patient A (*left column*) underwent imaging within 293 minutes from symptom onset, and patient B (*right column*), within 284 minutes from symptom onset. Both patients had an ASPECTS of 10 on noncontrast CT (subfigures *A1* and *B1*). Conventional CTA reveals an acute occlusion of the M1 segment of the left MCA (indicated by the *arrows* on subfigures *A2* and

B2) for both patients. On dynamic CTA, patient A had good collateral supply, and arterial contrast-enhancement was almost synchronous, compared with the unaffected right hemisphere (early arterial phase [*A3*]; parenchymal phase [*A4*]; late venous phase [*A5*]). In contrast, patient B exhibited poor collateral supply on dynamic CTA with delayed and reduced arterial enhancement (reduced and delayed contrast-enhancement by 2 phases compared with the contralateral hemisphere [*B3–B5*]).

Table 1: CTP parameters in patients with good-versus-poor collaterals[a]

Perfusion Parameter	All Patients	Patients with Poor Collaterals (Score, 0–3)	Patients with Good Collaterals (Score, 4–5)	P Value
Tmax > 6 sec (mL)	111 (102–119)	135 (124–145)	88 (77–99)	<.001
Tmax > 8 sec (mL)	74 (67– 82)	97 (88–107)	53 (44–63)	<.001
Tmax > 10 sec (mL)	48 (43–54)	66 (58–74)	32 (25–39)	<.001
rCBF < 30%, mL	24 (19–28)	41 (33–49)	8 (5–11)	<.001
rCBF < 34%, mL	30 (25–35)	50 (41–58)	11 (8–14)	<.001
rCBF < 38%, mL	36 (31–42)	59 (50–68)	15 (12–19)	<.001
CBV-index	0.68 (0.65–0.70)	0.60 (0.56–0.63)	0.76 (0.72–0.78)	<.001
HIR	0.37 (0.34–0.40)	0.46 (0.42–0.50)	0.29 (0.24–0.33)	<.001

[a] Data are given as mean values and 95% confidence intervals.
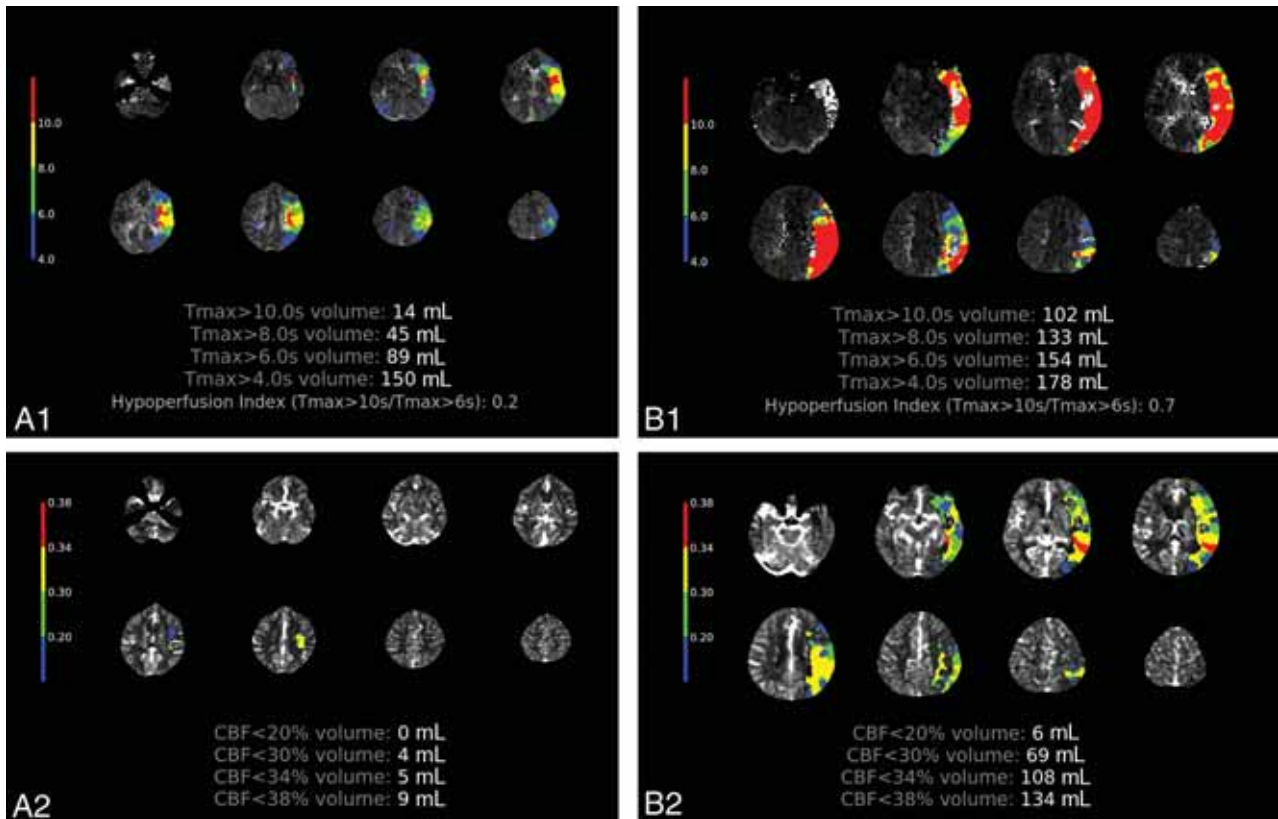
FIG 2. Tmax maps (*A1* and *B1*) and CBF maps (*A2* and *B2*) for 2 patients with either good (patient A, *left column*) or poor collateral supply (patient B, *right column*). Tmax lesion sizes, HIR, and CBF lesion sizes are all considerably smaller for patient A with good collateral supply compared with patient B with poor collateral supply. See Fig 1 for the corresponding noncontrast CT, CTA, and dynamic CTA for the same patients.

that rCBF < 38% correlates best with the final infarct volume. However, compared with a threshold of rCBF < 30%, it was associated with a higher risk of infarct overestimation.[18]

Taken together, our findings indicate a strong interaction between collateral status and infarct core size. CBF measures blood flow velocity, which is found to depend on collaterals in the case of an upstream occlusion. We found that an rCBF < 38% indicates poor collateral status best, while rCBF < 30% may be the critical threshold for an irreversible tissue injury.

The major strength of this study is the relatively large cohort size with 214 patients. Additionally, collateral scores were assessed on dynamic CTA images, accounting for both the spatial extent and the delay of collateral supply. None of the previous studies correlated HIR with collateral status assessed on dynamic CTA. Furthermore,

we used the RAPID software, which is an established perfusion postprocessing tool, to determine the CTP parameters in this study.[19]

Thus, several factors such as bolus shape, scanner protocol, and generation and postprocessing software can influence CTP analysis. Moreover, CTP analysis is susceptible to patient-specific factors and head motion.[20] Compared with the drawbacks of collateral assessment on CTA, including the reduced temporal resolution and need for a visual assessment, quantitative collateral grading based on perfusion data may still allow a more uniform and systematic collateral assessment.

Further limitations result from the monocentric, retrospective study design. Due to this retrospective design, we could include only patients who were transferred to the angiography suite and registered in our institutional thrombectomy database. As a result,

Table 2: Results from the Spearman rank correlation analysis for collateral score as a function of perfusion parameters (ρ [95% CI] and _P_ value) and from ROC analysis for the identification of good collateral status[a]

Perfusion Parameter	ρ (95% CI)	_P_ Value	AUC (95% CI)	Cutoff Value	Sensitivity	Specificity	Accuracy
Tmax >6 sec (mL)	−0.50 (−0.61 to −0.39)	<.001	0.75 (0.68–0.81)[b]	124 mL	56%	82%	69%
Tmax >8 sec (mL)	−0.54 (−0.64 to −0.43)	<.001	0.77 (0.71–0.83)[b]	74 mL	68%	76%	72%
Tmax >10 sec (mL)	−0.50 (−0.60 to−0.39)	<.001	0.77 (0.71–0.83)[b]	53 mL	64%	80%	72%
rCBF < 30% (mL)	−0.61 (−0.71 to −0.52)	<.001	0.81 (0.75–0.87)	14 mL	72%	82%	77%
rCBF < 34% (mL)	−0.64 (−0.73 to −0−55)	<.001	0.83 (0.77–0.88)	25 mL	67%	87%	77%
rCBF < 38% (mL)	−0.66 (−0.74 to −0.57)	<.001	0.83 (0.78–0.89)	27 mL	75%	80%	77%
CBV-index	+0.51 (0.40–0.63)	<.001	0.76 (0.69–0.81)[b]	0.8	60%	78%	69%
HIR	−0.49 (−0.60−0.37)	<.001	0.73 (0.66–0.79)[b]	0.4	75%	62%	65%

[a] Overall, the volume with an rCBF < 38% performed best. Optimal cutoff values to identify good collateral supply were estimated according to the Youden index.
[b] Significant differences in AUC compared with the AUC for the volume with rCBF < 38%.
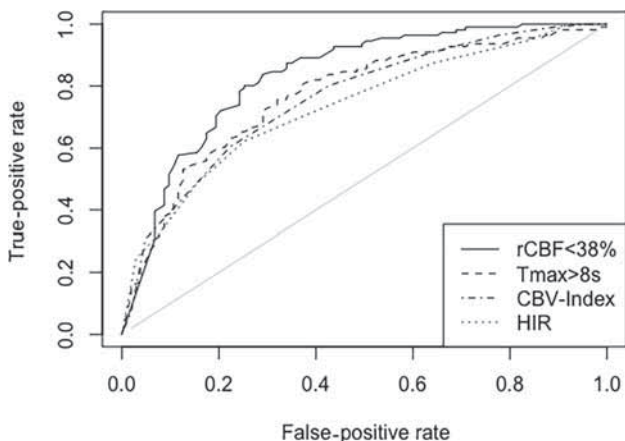
FIG 3. Receiver operating characteristics for rCBF < 38% (_solid line_), Tmax > 8 seconds (_dashed line_), the CBV-index (_dot-dashed line_), and HIR (_dotted line_) for the identification of good collateral status. The AUC was highest for rCBF < 38% with an AUC of 0.83.

Table 3: Contingency table for collateral status compared with volume with rCBF < 38%[a]

Volume with rCBF <38%: Collateral Status	<27 mL	≥27 mL	Total
Good collateral status (score 4—5)	89	22	111
Poor collateral status (score 0–3)	26	77	103
Total	115	99	214

[a] Good collateral status was significantly associated with a smaller rCBF < 38% lesion size (Fisher exact test was significant with _P_ < .001).

there is a potential selection bias toward patients with better collateral status and smaller infarct sizes. Only 10% of the patients showed absent or nearly absent collaterals (scores = 0–1). Nonetheless, the proportion of patients with poor collaterals (48% with scores of 0–3) was higher compared with other studies such as that of Lyndon et al.[17] Therefore, a potential selection bias should not affect the validity of the results.

Another minor limitation is the absence of a collateral score based on DSA, which is still considered the criterion standard for collateral assessment. Depending on the occlusion location and the anatomy of the circle of Willis, however, DSA may underestimate collateral supply unless images from the contralateral ICA and vertebral artery are obtained. Collateral scoring and perfusion parameters are based on the same source data in our study, which could be regarded as a limitation.

CONCLUSIONS

Automated CTP analysis allows accurate identification of collateral supply in acute ischemic stroke. The volume of rCBF < 38% may be a more precise perfusion-based indicator of good collateral status than Tmax, HIR, or CBV-index.

REFERENCES

1. Powers WJ, Rabinstein AA, Ackerson T, et al; American Heart Association Stroke Council. **Guidelines for the Early Management of Patients with Acute Ischemic Stroke: 2019 Update to the 2018 Guidelines for the Early Management of Acute Ischemic Stroke—A Guideline for Healthcare Professionals From the American Heart Association/American Stroke Association.** _Stroke_ 2019;50: e344–18 CrossRef Medline

2. McVerry F, Liebeskind DS, Muir KW. **Systematic review of methods for assessing leptomeningeal collateral flow.** _AJNR Am J Neuroradiol_ 2012;33:576–82 CrossRef Medline

3. Seker F, Pereira-Zimmermann B, Pfaff J, et al. **Collateral scores in acute ischemic stroke.** _Clin Neuroradiol_ 2020;30:789–93 CrossRef Medline

4. Menon BK, d'Esterre CD, Qazi EM, et al. **Multiphase CT angiography: a new tool for the imaging triage of patients with acute ischemic stroke.** _Radiology_ 2015;275:510–20 CrossRef

5. Scheidecker E, Pereira-Zimmermann B, Potreck A, et al. **Role of diabetes in collateral status assessed in CT perfusion-derived dynamic CTA in anterior circulation stroke.** _Neuroradiology_ 2022;64:1195–99 CrossRef Medline

6. Lu SS, Zhang X, Xu XQ, et al. **Comparison of CT angiography collaterals for predicting target perfusion profile and clinical outcome in patients with acute ischemic stroke.** _Eur Radiol_ 2019;29:4922–29 CrossRef Medline

7. Potreck A, Seker F, Hoffmann A, et al. **A novel method to assess pial collateralization from stroke perfusion MRI: subdividing Tmax into anatomical compartments.** _Eur Radiol_ 2017;27:618–26 CrossRef Medline

8. Seker F, Pfaff J, Potreck A, et al. **Correlation of Tmax volumes with clinical outcome in anterior circulation stroke.** _Brain Behav_ 2017;7: e00772 CrossRef Medline

9. Lee MJ, Son JP, Kim SJ, et al. **Predicting collateral status with magnetic resonance perfusion parameters: probabilistic approach with a Tmax-derived prediction model.** _Stroke_ 2015;46:2800–07 CrossRef Medline

10. Mlynash M, Lansberg MG, Kemp S, et al. **Abstract WP79: Combination of Tmax and Relative CBV Perfusion Parameters More Accurately Predicts CTA Collaterals Than a Single Perfusion Parameter in DEFUSE 3.** _Stroke_ 2019;50(Suppl 1) CrossRef

11. Guenego A, Fahed R, Albers GW, et al. **Hypoperfusion intensity ratio correlates with angiographic collaterals in acute ischaemic stroke with M1 occlusion.** *Eur J Neurol* 2020;27:864–70 CrossRef Medline

12. Wang CM, Chang YM, Sung PS, et al. **Hypoperfusion index ratio as a surrogate of collateral scoring on CT angiogram in large vessel stroke.** *J Clin Med* 2021;10:1296 CrossRef Medline

13. Olivot JM, Mlynash M, Inoue M, et al; DEFUSE 2 Investigators. **Hypoperfusion intensity ratio predicts infarct progression and functional outcome in the DEFUSE 2 cohort.** *Stroke* 2014;45:1018–23 CrossRef Medline

14. Guenego A, Mlynash M, Christensen S, et al. **Hypoperfusion ratio predicts infarct growth during transfer for thrombectomy.** *Ann Neurol* 2018;84:616–20 CrossRef Medline

15. Frölich AM, Schrader D, Klotz E, et al. **4D CT angiography more closely defines intracranial thrombus burden than single-phase CT angiography.** *AJNR Am J Neuroradiol* 2013;34:1908–13 CrossRef Medline

16. DeLong ER, DeLong DM, Clarke-Pearson DL. **Comparing the areas under two or more correlated receiver operating characteristic curves: a nonparametric approach.** *Biometrics* 1988;44:837–45 CrossRef Medline

17. Lyndon D, van den Broek M, Niu B, et al. **Hypoperfusion intensity ratio correlates with CTA collateral status in large-vessel occlusion acute ischemic stroke.** *AJNR Am J Neuroradiol* 2021;42:1380–86 CrossRef Medline

18. Muehlen I, Sprügel M, Hoelter P, et al. **Comparison of two automated computed tomography perfusion applications to predict the final infarct volume after thrombolysis in cerebral infarction 3 recanalization.** *Stroke* 2022;53:1657–64 CrossRef Medline

19. Albers GW, Marks MP, Kemp S, et al. **Thrombectomy for stroke at 6 to 16 hours with selection by perfusion imaging.** *N Engl J Med* 2018;378:708–18 CrossRef Medline

20. Potreck A, Seker F, Mutke MA, et al. **What is the impact of head movement on automated CT perfusion mismatch evaluation in acute ischemic stroke?** *J Neurointerv Surg* 2021;14:623–33 CrossRef Medline

Quantitative Collateral Assessment on CTP in the Prediction of Stroke Etiology

F. Shi, Q. Zeng, X. Gong, W. Zhong, Z. Chen, S. Yan, and M. Lou

ABSTRACT

BACKGROUND AND PURPOSE: Patients with stroke etiology of large-artery atherosclerosis were thought to have better collateral circulation compared with patients with other stroke etiologies. We aimed to investigate the association between stroke etiology and collateral circulation with a new quantitative collateral assessment method.

MATERIALS AND METHODS: This retrospective study reviewed data from consecutive patients with proximal anterior artery occlusion who underwent CTP before reperfusion therapy. CBF maps were derived from CTP. A new indicator, maximum CBF of collateral vessels within the Sylvian fissure ($cCBF_{max}$), was applied to quantitatively assess the collateral status. The relationship between collateral status and stroke etiology was investigated.

RESULTS: A total of 296 patients were finally analyzed. The median $cCBF_{max}$ was significantly higher in patients with large-artery atherosclerosis than in those without it (92 [interquartile range, 65–123] mL/100 g/min versus 62 [interquartile range, 46–82] mL/100 g/min; $P < .001$). Multivariable analysis revealed that a higher $cCBF_{max}$ score was independently associated with large-artery atherosclerosis etiology (OR, 1.010; 95% CI, 1.002–1.018; $P = .017$) after adjustment. The area under the curve, sensitivity, and specificity of the final model in predicting the etiology of large-artery atherosclerosis were 0.870, 89.7%, and 75.2%, respectively.

CONCLUSIONS: Patients with large-artery atherosclerosis had a more adequate collateral perfusion supply with the new quantitative collateral assessment. The new quantitative collateral measurement might contribute to the prediction of stroke etiology in the acute clinical scenario for patients with acute ischemic stroke.

ABBREVIATIONS: AIS = acute ischemic stroke; AUC = area under the curve; $cCBF_{max}$ = maximum CBF of collateral vessels within the Sylvian fissure; CE = cardioembolism; IQR = interquartile range; LAA = large-artery atherosclerosis; ROC = receiver operating characteristic

Intracranial large-artery occlusion is a common cause of acute ischemic stroke (AIS), which often leads to a poor prognosis.[1,2] Endovascular therapy could greatly improve the recanalization rate of the occluded arteries and has been recommended as a standard therapy for patients with acute proximal large-artery

occlusion.[3] The success of endovascular therapy was influenced by the stroke etiology.[4,5] The secondary prevention strategies would also depend on stroke etiologies. Therefore, prediction of stroke etiology might provide potentially pivotal information for neurologists and neurointerventionists to guide management in the acute clinical scenario and enable early initiation of appropriate secondary prevention.

Collateral circulation in patients with AIS can maintain perfusion and may influence the timing of ischemic brain tissue—that is, collateral circulation contributes to improving the prognosis of patients with ischemic stroke. Several clinical trials such as the Endovascular Treatment for Small Core and Anterior Circulation Proximal Occlusion with Emphasis on Minimizing CT to Recanalization Times (ESCAPE) and Extending the Time for Thrombolysis in Emergency Neurological Deficits—Intra-Arterial (EXTEND-IA) revealed that collateral assessment in the acute clinical stage could help select optimal candidates for reperfusion therapy.[6,7] Large-artery atherosclerosis (LAA) and cardioembolism (CE) are the 2 common causes of intracranial large-artery occlusion. It

has been assumed that atherosclerosis develops chronically, which might lead to better cerebral collateral flow. However, previous studies have presented inconsistent results on the association between stroke etiology and collateral circulation in patients with AIS.[8,9]

Most collateral assessments used in previous research were qualitative collateral grading methods. A qualitative collateral method based on the extent of the reconstitution of the MCA up to the distal end of its occlusion via leptomeningeal collaterals has been proposed before.[10] Recently, we developed a new technique for quantitative assessment of collateral perfusion to the distal end of the occlusion within the Sylvian fissure with CTP.[11] This method was found to be reliable and was also superior to existing qualitative indices of collateral flow.[11] Thus, we aimed to explore the association between stroke etiology and collateral circulation with the new quantitative collateral assessment method.

MATERIALS AND METHODS

Ethics Statement

This protocol was approved by the human ethics committee of the Second Affiliated Hospital of Zhejiang University, School of Medicine. The investigations were conducted according to the principles expressed in the Declaration of Helsinki. Written informed consent was obtained from all patients.

Patients

This retrospective study reviewed our prospectively collected database, Comparison Influence to Prognosis of CTP and MRP in AIS Patients; ClinicalTrials.gov identifier: NCT03367286 (CIPPIS), for consecutive patients with AIS who received intravenous thrombolysis with or without mechanical thrombectomy from May 2009 to July 2018. We then enrolled patients who met the following criteria: 1) They had a diagnosis of AIS confirmed by DWI or CT, 2) underwent CTP within 8 hours after stroke onset, and 3) had occlusion of the MCA-M1 segment with or without the ICA confirmed on reconstructed CTA images from CTP. Patients who had poor image quality due to motion artifacts or incomplete images were excluded. Some of the patients were reported in our previous research based on the database.[11]

Clinical Data

Baseline clinical variables were recorded, including demographics, risk factors (smoking, hypertension, diabetes mellitus, hyperlipidemia, or a history of stroke/TIA or atrial fibrillation), prior antiplatelet use, onset-to-needle time, baseline NIHSS score, and radiologic data. The stroke etiologies were determined according to the Trial of Org 10172 in Acute Stroke Treatment (TOAST) to categorize the etiology into LAA, CE, undetermined etiology, and another determined cause.[12] The protocol for the work-up of the TOAST criteria is shown in the Online Supplemental Data. The stroke etiology was determined by 2 experienced neurologists according to the TOAST criteria, with rater discrepancies settled by consensus discussion before quantitative collateral measurement.

Baseline Imaging Protocol

All patients underwent baseline CTP on a 64-section CT scanner (Somatom Definition Flash; Siemens), including noncontrast (120 kV, 320 mA, contiguous 5-mm axial sections, matrix of 512×512, FOV of 240×240 mm^2, 7-second acquisition time, 25 slices) and volumetric perfusion (100 mm in the z-axis, 4-second delay after the start of contrast medium injection, 74.5-second total imaging duration, 80 kV, 120 mA, 1.5-mm section thickness, 32×1.2 mm collimation, matrix of 512×512, FOV of 240×240 mm^2, 2574 slices) scanned in accordance with our stroke imaging protocol.[11]

Imaging Analysis

Pretreatment relative CBF of <30% at CTP was calculated for the baseline infarct core volume.[13] A threshold of time-to-peak of the residual function of >6 seconds was used for volumetric measurement of the pretreatment hypoperfused volume on CTP.[14] The occlusion location was determined on reconstructed CTA derived from CTP. According to the TAN collateral score, collaterals were classified as good if they were seen in ≥50% of the MCA territory and poor in <50% of the territory on CTA.[15] The circle of Willis variants were assessed on CTA according to a previously reported method (type 1: a missing or hypoplastic ipsilateral anterior cerebral artery A1 segment; type 2: a missing or hypoplastic contralateral A1 segment; type 3: a fetal ipsilateral posterior cerebral artery; type 4: an impaired ipsilateral posterior circulation including a missing or hypoplastic ipsilateral the communicating posterior artery or P1 segments).[16]

Quantitative Collateral Assessment

The arterial input function and venous outflow function from the MCA territory and the superior sagittal sinus of the nonischemic hemisphere were automatically selected by MIStar (Version 3.2; Apollo Medical Imaging Technology) and manually adjusted if necessary. Voxel-based quantitative analysis was performed using the MIStar software.

In this study, we performed a quantitative collateral assessment as described previously.[11] To achieve the quantitative collateral assessment, the image sections visualized to contain the visible vessels within the ipsilateral Sylvian fissure on temporally fused MIP CTP images with 10-mm-thick slabs were identified and then outlined by manually drawing the ROI on each image section (Fig 1). For patients without visible vessels within the Sylvian fissure, the ROI was drawn in an area where one would expect to see vessels. Each ROI was then copied to the corresponding CBF map derived from CTP images with a 10-mm-thick MIP. The highest CBF value from all sections was recorded as the maximum CBF of collateral vessels within the Sylvian fissure ($cCBF_{max}$).

Statistical Analysis

Continuous variables were reported as medians with interquartile range (IQR), and categoric variables were reported as proportions. For categoric variables, the χ^2 test was used to compare differences among groups. For continuous variables, the Mann-Whitney U test was used to compare the difference between the 2 groups. Receiver operating characteristic (ROC) analyses were performed to assess the discriminative ability, and the area under the curve (AUC) was calculated. Optimal cutoff values were derived from ROC curves, and sensitivity and specificity were calculated on the
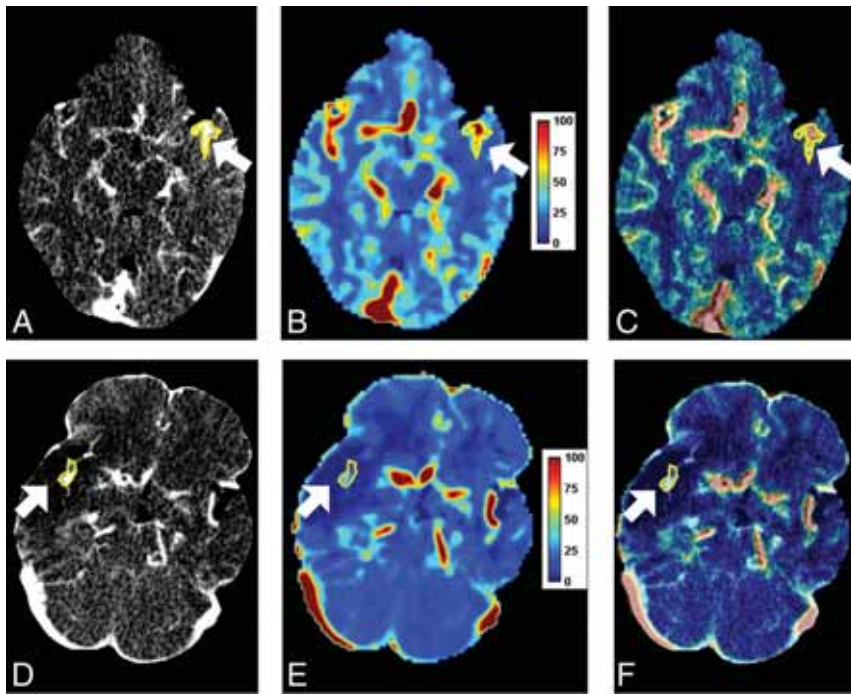
FIG 1. Graphic representation of the quantitative collateral measurement of a patient with LAA with a $cCBF_{max}$ value of 123 mL/100 g/min (*A–C*) and a patient without LAA with a $cCBF_{max}$ value of 51 mL/100 g/min (*D–F*). The patient with LAA had occlusion of the left M1 segment and ICA (*A*). The patient without LAA had occlusion of the right M1 segment of the MCA (*D*). ROIs (*white arrows*) were drawn by outlining the entire visible vessels within the ipsilateral Sylvian fissure on temporally fused MIP CTP images, each ROI was then copied to the corresponding CBF map derived from CTP images with a 10-mm-thick MIP, and the highest CBF value from all sections was recorded as $cCBF_{max}$ (*B* and *E*). The relatively high CBF regions in the ipsilateral Sylvian fissure overlapped well with the collateral vessels (*C* and *F*).

basis of these best cutoff values. The variables with *P* values < .1 on univariable analysis were included in the multivariable models. Multivariable logistic regression with the stepwise method was performed to assess independent predictors of stroke etiology. All statistical analyses were performed using SPSS, Version 22.0 (IBM). *P* < .05 was considered statistically significant.

RESULTS

During the study, 314 patients met the inclusion criteria; then, 18 patients were excluded due to insufficient imaging quality ($n = 14$) and incomplete images ($n = 4$). A total of 296 patients were finally analyzed, with a median age of 73 (IQR, 62–80) years, a median NIHSS score of 14 (IQR, 10–18), and a median onset-to-needle time of 221 (IQR, 149–302) minutes (Online Supplemental Data). According to the TOAST criteria, the stroke etiologies of these patients were CE ($n = 157$), LAA ($n = 58$), undetermined etiology ($n = 80$), and other determined cause ($n = 1$). The median $cCBF_{max}$ was 67 (IQR, 47–91) mL/100 g/min. The median ROI sizes of the patients without visible vessels within the Sylvian fissure were not significantly different compared with those of the patients with visible vessels (1.7 [IQR, 1.2–2.2] mL versus 1.9 [IQR, 1.3–2.5] mL, $P = .576$).

The $cCBF_{max}$ was negatively associated with age ($\rho = -0.262$, $P < .001$), baseline NIHSS score ($\rho = -0.396$, $P < .001$), baseline

infarct core volume ($\rho = -0.531$, $P < .001$), and baseline hypoperfusion volume ($\rho = -0.386$, $P < .001$). The median $cCBF_{max}$ was significantly lower in patients with atrial fibrillation than in those without atrial fibrillation (61 [IQR, 42–80] mL/100 g/min versus 71 [IQR, 51–108] mL/100 g/min; $P < .001$) and lower in patients with hypertension than in those without hypertension (63 [IQR, 46–87] mL/100 g/min versus 70 [IQR, 51–96] mL/100 g/min, $P = .046$). There was no significant association between onset-to-imaging time and $cCBF_{max}$ ($\rho = 0.019$, $P = .758$). Similar findings were observed in the LAA group ($\rho = 0.069$, $P = .619$), CE group ($\rho = 0.017$, $P = .838$), or the undetermined etiology group ($\rho = -0.112$, $P = .343$). The locations of the occlusions were significantly associated with median $cCBF_{max}$ scores (57 [IQR, 37–80] mL/100 g/min versus 67 [IQR, 51–87] mL/100 g/min versus 82 [IQR, 54–135] mL/100 g/min for M1+ICA and proximal M1 and distal M1 segments; $P = .001$). We found a trend toward the association between the circle of Willis variants and $cCBF_{max}$ scores ($P = .054$).

In our study, the patients were then dichotomized as the LAA group ($n = 58$) and the non-LAA group ($n = 238$) (Online Supplemental Data). Patients in the LAA group were significantly younger ($P < .001$) and more often male ($P < .001$) and had a higher proportion of smokers ($P < .001$) compared with those in non-LAA group. Patients in LAA group were inclined to have higher rates of diabetes mellitus ($P = .056$). Meanwhile, patients with LAA were found to have lower median baseline NIHSS scores (9 [IQR, 5–13] versus 15 [IQR, 11–18]; $P < .001$) and lower median baseline infarct core volumes (43.1 [IQR, 11.9–78.5] mL versus 59.5 [IQR, 31.4–108.5] mL; $P = .003$), respectively. When collaterals were dichotomized into good and poor according to the TAN score, patients with LAA more often had significantly good collaterals than the patients without LAA (74.1% versus 58.8%, $P = .031$). The sensitivity and specificity of good collaterals determined by the TAN score for predicting LAA were 41.2% and 74.1%, respectively.

Sample illustrations of the quantitative collateral measurement for patients with and without LAA are shown in Fig 1. The median $cCBF_{max}$ score was significantly higher in patients with LAA than in those without it (92 [IQR, 65–123] mL/100 g/min versus 62 [IQR, 46–82] mL/100 g/min; $P < .001$). The ROC analysis revealed an optimal cutoff $cCBF_{max}$ of 89 mL/100 g/min in predicting the LAA etiology from the other etiologies, and the AUC, sensitivity, and specificity were 0.691, 53.4%, and 80.7%, respectively (Fig 2*A*).

Then, age, sex, baseline NIHSS score, smoking, diabetes mellitus, baseline infarct core volume, and $cCBF_{max}$ scores were included
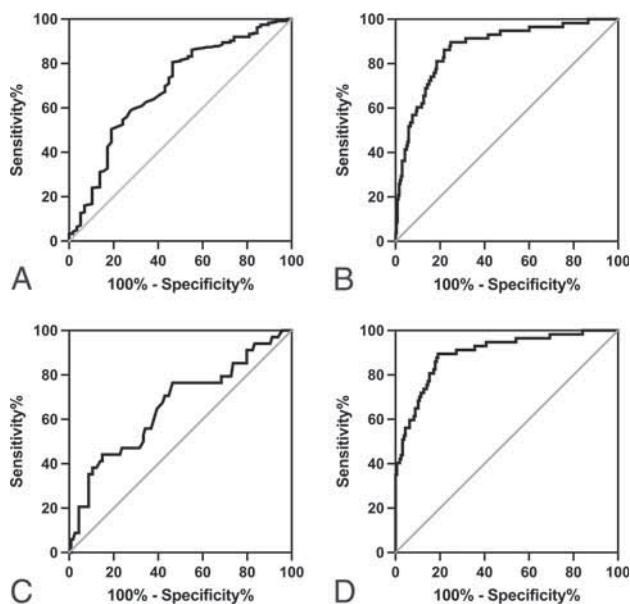
FIG 2. ROC curves (*black line*) of $cCBF_{max}$ in differentiating an LAA etiology from other etiologies (*A*) and from CE (*C*). The ROC curves generated from binary logistic regression models in distinguishing LAA etiology from other etiologies (*B*) and from CE (*D*).

in multivariable stepwise regression analysis. It was revealed that higher $cCBF_{max}$ (OR, 1.010; 95% CI, 1.002–1.018; $P = .017$), younger age (OR, 0.964; 95% CI, 0.940–0.990; $P = .007$), male sex (OR, 10.584; 95% CI, 3.696–30.311; $P < .001$), and lower baseline NIHSS scores (OR, 0.878; 95% CI, 0.821–0.939; $P < .001$) were independently associated with LAA etiology (Online Supplemental Data). The ROC curve generated from the final model in distinguishing the LAA etiology from other etiologies revealed that the AUC, sensitivity, and specificity were 0.870, 89.7% and 75.2%, respectively (Fig 2*B*).

Among patients with the 2 commonly determined etiologies, there were 58 patients with LAA and 157 with CE. The median $cCBF_{max}$ score was significantly higher in patients with LAA than in patients with CE (92 [IQR, 65–123] mL/100 g/min versus 60 [IQR, 44–76] mL/100 g/min; $P < .001$). The optimal cutoff, AUC, sensitivity, and specificity of $cCBF_{max}$ in distinguishing LAA from CE were 89 mL/100 g/min, 0.728, 53.4%, and 87.3%, respectively (Fig 2*C*). Multivariable analysis showed that a higher $cCBF_{max}$ was independently associated with LAA etiology (OR, 1.025; 95% CI, 1.010–1.041; $P = .001$) after adjustment, shown in the Online Supplemental Data. The ROC curve generated from the model in distinguishing LAA from CE showed that AUC, sensitivity, and specificity were 0.921, 88.5%, and 85.6%, respectively (Fig 2*D*).

DISCUSSION

Prediction of stroke etiology is important-but-difficult in the acute stage. In this study, we found that patients with AIS with an LAA etiology might have a more extensive collateral circulation than patients with other etiologies. The new quantitative collateral measurement might contribute to the prediction of stroke etiology in the acute clinical scenario for patients with AIS.

Stroke with an LAA etiology has been associated with better collateral circulation. Guglielmi et al[17] found that patients with ischemic stroke due to cervical carotid atherosclerosis had better collateral circulation graded on a 4-point scale.[9] Hassler et al[9] showed that pre-existing carotid artery stenosis was associated with better collateral status by the TAN score.[8] Most collateral assessment methods used in those previous studies were qualitative-grading collateral methods. A systematic review revealed a wide variation in the methods of grading collateral circulation.[18] Previous studies indicated that quantitative assessment might minimize the observer subjectivity.[19-21]

Recently, we have developed a quantitative parameter of collateral status at CTP ($cCBF_{max}$), which compared favorably with existing qualitative metrics of collateral perfusion.[11] Thus, in the current study, we evaluated the differential value in stroke etiologies with this new quantitative collateral parameter. The proportions of LAA and CE in this study were similar to those in the previous studies.[9,17] A previous histologic study found that the features of the clots in patients with undetermined etiology were more like those of patients with cardiogenic thrombi.[22] Therefore, the patients were further dichotomized into LAA and non-LAA groups in the current study. Then, we found that patients with AIS with an LAA etiology had higher $cCBF_{max}$ values, indicating better collateral supply.

The exact mechanism for the better collateral supply of stroke with an LAA etiology is not totally clear. One possible mechanism might be that atherosclerosis developed chronically, possibly promoting cerebral collateral circulation. Previously, in rat models, it was found that improved cerebral collateral circulation was significantly associated with chronic cerebral hypoperfusion.[23] In patients with carotid artery stenosis, the collateral circulation was associated with carotid stenosis and increased with the degree of stenosis.[8,9] From a pathophysiologic perspective, in patients with carotid artery stenosis, an increased degree of stenosis and repeat arterio-arterial microembolism from carotid plaques might lead to recurrent focal cerebral tissue ischemia.[9,24] It was reported that chronic hypoperfusion was associated with better collateral circulation.[23] Collateral circulation could maintain perfusion, and greater collateral circulation might contribute to a better baseline condition such as a lower baseline NIHSS score and baseline infarct core volume.

Stroke etiology has a crucial role for clinicians involved in acute ischemic stroke management. Different devices and procedures were introduced for patients with different etiologies.[25] Patients with an LAA etiology more often had stent retriever refractoriness and some other complications; those patients were more likely to require adjunctive therapies.[4,5,26-28] Recently, CTP was increasingly performed before reperfusion therapy. On the basis of the CBF maps derived from CTP images, $cCBF_{max}$ could quantitatively assess the collateral status. Our results revealed that $cCBF_{max}$ might help to facilitate prediction of stroke etiology in the acute clinical stage. Therefore, 1 CTP scan could provide the quantitative information of infarct core volume, penumbra volume, and collateral circulation, which might contribute to the selection of the optimal candidates for reperfusion therapy, especially for those beyond the time window.

In our study, we found that the collateral circulation did not change with the time. A previous study found that collateral circulation might show a better response at later time windows—that is, the time window of clinical benefit might be longer if collateral circulation was maintained.[29] Besides, this quantitative collateral method might be helpful for management in patients with stroke with an unknown onset time. Future studies with a large sample size are needed to clarify the relationship between collaterals and time.

This study had some limitations. First, this was a retrospective study, which might have a potential risk of selection bias, though data were prospectively collected using a stroke registry protocol. Second, in this study, we included patients with proximal anterior artery occlusion; thus, the results were inapplicable to the patients with occlusion of small arteries or posterior circulation. Third, we did not include other imaging markers such as clot characteristics, and these might be related to stroke etiology. Further studies with a list of factors are needed to confirm our findings. Finally, the sample size of this study was modest. The prediction of this quantitative collateral method for stroke etiology should be investigated in a large sample size and randomized prospective clinical trials in the future.

CONCLUSIONS

On the basis of CBF maps derived from CTP images, quantitative assessment of $cCBF_{max}$ revealed that patients with LAA had more sufficient collateral perfusion supply to the ischemic brain tissue than patients with other stroke origins, which might contribute to prediction of stroke etiology in the acute clinical scenario and early initiation of appropriate secondary prevention.

Disclosure forms provided by the authors are available with the full text and PDF of this article at www.ajnr.org.

REFERENCES

1. Saver JL, Jahan R, Levy EI, et al. **Solitaire flow restoration device versus the Merci Retriever in patients with acute ischaemic stroke (SWIFT): a randomised, parallel-group, noninferiority trial.** *Lancet* 2012;380:1241–49 CrossRef Medline

2. Gorelick PB, Wong KS, Bae HJ, et al. **Large artery intracranial occlusive disease: a large worldwide burden but a relatively neglected frontier.** *Stroke* 2008;39:2396–99 CrossRef Medline

3. Powers WJ, Rabinstein AA, Ackerson T, et al. **Guidelines for the Early Management of Patients with Acute Ischemic Stroke: 2019 Update to the 2018 Guidelines for the Early Management of Acute Ischemic Stroke—A Guideline for Healthcare Professionals From the American Heart Association/American Stroke Association.** *Stroke* 2019;50:e344–418 CrossRef Medline

4. Baek JH, Kim BM, Kim DJ, et al. **Importance of truncal-type occlusion in stentriever-based thrombectomy for acute stroke.** *Neurology* 2016;87:1542–50 11 CrossRef Medline

5. Matias-Guiu JA, Serna-Candel C, Matias-Guiu J. **Stroke etiology determines effectiveness of retrievable stents.** *J Neurointerv Surg* 2014;6:e11 CrossRef Medline

6. Goyal M, Demchuk AM, Menon BK, et al; ESCAPE Trial Investigators. **Randomized assessment of rapid endovascular treatment of ischemic stroke.** *N Engl J Med* 2015;372:1019–30 CrossRef Medline

7. Campbell BC, Mitchell PJ, Kleinig TJ, et al; EXTEND-IA Investigators. **Endovascular therapy for ischemic stroke with perfusion-imaging selection.** *N Engl J Med* 2015;372:1009–18 CrossRef Medline

8. Sallustio F, Motta C, Pizzuto S, et al. **CT angiography-based collateral flow and time to reperfusion are strong predictors of outcome in endovascular treatment of patients with stroke.** *J NeuroIntervent Surg* 2017;9:940–43 CrossRef Medline

9. Hassler E, Kneihsl M, Deutschmann H, et al. **Relationship between stroke etiology and collateral status in anterior circulation large vessel occlusion.** *J Neurol* 2020;267:3362–70 CrossRef Medline

10. Miteff F, Levi CR, Bateman GA, et al. **The independent predictive utility of computed tomography angiographic collateral status in acute ischaemic stroke.** *Brain* 2009;132:2231–38 CrossRef Medline

11. Shi F, Gong X, Liu C, et al. **Acute stroke: prognostic value of quantitative collateral assessment at perfusion CT.** *Radiology* 2019;290:760–68 CrossRef Medline

12. Adams HP Jr, Bendixen BH, Kappelle LJ, et al. **Classification of subtype of acute ischemic stroke: initions for use in a multicenter clinical trial—TOAST. Trial of Org 10172 in Acute Stroke Treatment.** *Stroke* 1993;24:35–41 CrossRef Medline

13. Campbell BC, Christensen S, Levi CR, et al. **Cerebral blood flow is the optimal CT perfusion parameter for assessing infarct core.** *Stroke* 2011;42:3435–40 CrossRef Medline

14. Lin L, Bivard A, Levi CR, et al. **Comparison of computed tomographic and magnetic resonance perfusion measurements in acute ischemic stroke: back-to-back quantitative analysis.** *Stroke* 2014;45:1727–32 CrossRef Medline

15. Tan IY, Demchuk AM, Hopyan J, et al. **CT angiography clot burden score and collateral score: correlation with clinical and radiologic outcomes in acute middle cerebral artery infarct.** *AJNR Am J Neuroradiol* 2009;30:525–31 CrossRef Medline

16. Westphal LP, Lohaus N, Winklhofer S, et al. **Circle of Willis variants and their association with outcome in patients with middle cerebral artery-M1-occlusion stroke.** *Eur J Neurol* 2021;28:3682–91 CrossRef Medline

17. Guglielmi V, LeCouffe NE, Zinkstok SM, et al; MR-CLEAN Registry Investigators. **Collateral circulation and outcome in atherosclerotic versus cardioembolic cerebral large vessel occlusion.** *Stroke* 2019;50:3360–68 CrossRef Medline

18. McVerry F, Liebeskind DS, Muir KW. **Systematic review of methods for assessing leptomeningeal collateral flow.** *AJNR Am J Neuroradiol* 2012;33:576–82 CrossRef Medline

19. Kawano H, Bivard A, Lin L, et al. **Relationship between collateral status, contrast transit, and contrast density in acute ischemic stroke.** *Stroke* 2016;47:742–49 CrossRef Medline

20. Beyer SE, von Baumgarten L, Thierfelder KM, et al. **Predictive value of the velocity of collateral filling in patients with acute ischemic stroke.** *J Cereb Blood Flow Metab* 2015;35:206–12 CrossRef Medline

21. Cao W, Campbell BC, Dong Q, et al. **Relative filling time delay based on CT perfusion source imaging: a simple method to predict outcome in acute ischemic stroke.** *AJNR Am J Neuroradiol* 2014;35:1683–87 CrossRef Medline

22. Ahn SH, Hong R, Choo IS, et al. **Histologic features of acute thrombi retrieved from stroke patients during mechanical reperfusion therapy.** *Int J Stroke* 2016;11:1036–44 CrossRef Medline

23. Busch HJ, Buschmann IR, Mies G, et al. **Arteriogenesis in hypoperfused rat brain.** *J Cereb Blood Flow Metab* 2003;23:621–28

24. Khan MB, Hafez S, Hoda MN, et al. **Chronic remote ischemic conditioning is cerebroprotective and induces vascular remodeling in a VCID model.** *Transl Stroke Res* 2018;9:51–63 CrossRef Medline

25. Zaidat OO, Yoo AJ, Khatri P, et al; Cerebral Angiographic Revascularization Grading (CARG) Collaborators; STIR Revascularization Working Group; STIR Thrombolysis in Cerebral Infarction (TICI) Task Force. **Recommendations on angiographic revascularization grading standards for acute ischemic stroke: a consensus statement.** *Stroke* 2013;44:2650–63 CrossRef Medline

26. Toyoda K, Koga M, Hayakawa M, et al. **Acute reperfusion therapy and stroke care in Asia after successful endovascular trials.** *Stroke* 2015;46:1474–81 CrossRef Medline

27. Gascou G, Lobotesis K, Machi P, et al. **Stent retrievers in acute ischemic stroke: complications and failures during the perioperative period.** *AJNR Am J Neuroradiol* 2014;35:734–40 CrossRef Medline

28. Kang DH, Kim YW, Hwang YH, et al. **Instant reocclusion following mechanical thrombectomy of in situ thromboocclusion and the role of low-dose intra-arterial tirofiban.** *Cerebrovasc Dis* 2014;37:350–55 CrossRef Medline

29. Agarwal S, Bivard A, Warburton E, et al. **Collateral response modulates the time-penumbra relationship in proximal arterial occlusions.** *Neurology* 2018;90:e316–22 CrossRef Medline

Assessment of Heating on Titanium Alloy Cerebral Aneurysm Clips during 7T MRI

S. Tsutsui, T. Matsuda, K. Takeda, M. Sasaki, Y. Kubo, K. Setta, S. Fujiwara, K. Chida, and K. Ogasawara

ABSTRACT

BACKGROUND AND PURPOSE: Patients with cerebral aneurysms often undergo MR imaging after microsurgical clipping. Ultra-high-field MR imaging at 7T may provide high diagnostic capability in such clinical situations. However, titanium alloy clips have safety issues such as adverse interactions with static magnetic fields and radiofrequency-induced heating during 7T MR imaging. The purpose of this study was to quantitatively assess temperature increases on various types of titanium alloy aneurysm clips during 7T MR imaging.

MATERIALS AND METHODS: Five types of titanium alloy aneurysm clips were tested, including combinations of short, long, straight, angled, and fenestrated types. Each clip was set in a phantom filled with gelled saline mixed with polyacrylic acid and underwent 7T MR imaging with 3D T1WI with a spoiled gradient recalled acquisition in the steady-state technique. Temperature was chronologically measured at the tips of the clip blade and head, angled part of the clip, and 5 mm from the tip of the clip head using MR imaging–compatible fiber-optic thermometers.

RESULTS: Temperature increases at all locations for right-angled and short straight clips were <1°C. Temperature increases at the angled part for the 45° angled clip and the tip of the clip head for the straight fenestrated clip were >1°C. Temperature increases at all locations for the long straight clip were >2°C.

CONCLUSIONS: Temperature increases on the right-angled and short straight clips remained below the regulatory limit during 7T MR imaging, but temperature increases on the 45° angled, straight fenestrated, and long straight clips exceeded this limit.

ABBREVIATIONS: ASTM = American Society for Testing and Materials; B1+rms = root mean square of the MRI effective component of the B_1 field; SAR = specific absorption rate; SPGR = echo-spoiled gradient echo; TI = temperature increase

Patients with cerebral aneurysms often undergo MR imaging after microsurgical clipping of the aneurysm. The most common indication for MR imaging after microsurgical clipping is follow-up of the clipped aneurysm and screening for de novo aneurysms.[1] MR imaging is also used to assess the presence of cerebral infarction caused by the microsurgical clipping itself or cerebral vasospasm due to SAH.[2,3] In addition, MR imaging is used to detect other intracerebral lesions such as brain tumors or cerebrovascular diseases, including cerebral small-vessel disease, which can develop many years after microsurgical clipping.[4] MR imaging at 1.5T and 3T has been used as a primary diagnostic tool in such clinical situations. Ultra-high-field MR imaging at

7T is becoming clinically available.[5-7] In particular, this imaging technique provides high diagnostic capability and superior evaluation of cerebral microaneurysms,[8] the aneurysm dome and neck,[9] smaller peripheral blood vessels,[10] or perforating arteries.[11] These capabilities are equal to angiography via arterial catheterization[12] and are superior to lower-field MR imaging.[9,10,13]

Titanium alloy clips have safety issues such as adverse interactions with static magnetic fields (eg, displacement force and torque) and radiofrequency-induced heating at 7T.[14,15] In terms of the former, a short straight clip is reported to be potentially safe when exposed to the 7T MR imaging environment.[14] Other investigators have suggested that commercially available aneurysm clips are likely to be safe for patients exposed to an 8T MR imaging system regardless of materials (eg, pure titanium or titanium alloy) and shape.[16] For radiofrequency-induced heating, the International Electrotechnical Commission guidelines recommend that the MR imaging equipment should limit the temperature rise in body core temperature and the absolute temperature in local tissues to 0.5°C and 39°C, respectively, for normal operating mode, and to 1°C and 40°C, respectively, for the first level

controlled.[17] Realistic simulation models have shown that tissue temperature remained below the regulatory limit for short straight clips but exceeded this limit for long straight clips.[15,18] However, a variety of aneurysm clips, including short, long, straight, angled, and fenestrated types, are widely used in neurosurgical settings.

The purpose of the present study was to quantitatively assess temperature increases (TIs) on various types of titanium alloy aneurysm clips during 7T MR imaging.

MATERIALS AND METHODS

This study was based on the American Society for Testing and Materials (ASTM) F2182-19e2 "Standard Test Method for Measurement of Radio Frequency Induced Heating On or Near Passive Implants During Magnetic Resonance Imaging."[19]

Test Objects
Five types of aneurysm clips were tested, including combinations of short, long, straight, angled, and fenestrated (Fig 1). All clips were made of titanium alloy. Clip length was in the following ascending order: right-angled < short straight < 45°angled < straight fenestrated < long straight.

Phantom
This test used a T-shaped plastic head/torso phantom filled with gelled saline (ie, 1.32 g/L of sodium chloride plus 10 g/L of polyacrylic acid in distilled water) (Fig 2A). The weight of the gelled saline in the phantom was 11.1 kg. Two phantoms with the same specifications (including shape and components) were provided. Measured conductivity and relative permittivity in the 2 phantoms were identical (conductivity, 0.517 S/m; relative permittivity, 82.12).

MR Imaging
MR imaging was performed using a 7T MR imaging platform (Discovery MR950; GE Healthcare) with a 2-channel transmit and 32-channel receive head coil (NM008-32-7GE-MR950; Nova Medical). This MR imaging system was used for research only and had received neither approval from the US FDA nor CE certification. ASTM standard protocol F2182-19e2 recommends that a protocol producing relatively high radiofrequency power should be used to achieve the temperature rise to be investigated.[19] The echo-spoiled gradient echo (SPGR) technique can change the flip angle, ie, radiofrequency power, and can use a short TR. Thus, SPGR allows easy control of the radiofrequency power. All aneurysm clips were thus scanned using 3D T1WI with an SPGR technique using the following sequence parameters: TE, 0.9 ms; TR, 4.0 ms; FOV, 24.0 cm; section thickness, 2.0 mm; matrix, 64 × 64; number of excitations, 50; number of slices, 102; and scan time, 20 minutes.

The ASTM standard protocol F2182-19e2 recommends performing MR imaging using the maximum value of sequence parameters related to heating such as flip angle, estimated specific absorption rate (SAR), and root mean square of the MR imaging effective component of the B_1 field (B1+rms).[19,20] Transmitter adjustment was performed automatically by the MR imaging system, with head-averaged SAR and B1+rms calculated as 1.6 W/kg and 3.28 μT, respectively, when the flip angle was set at 37°.
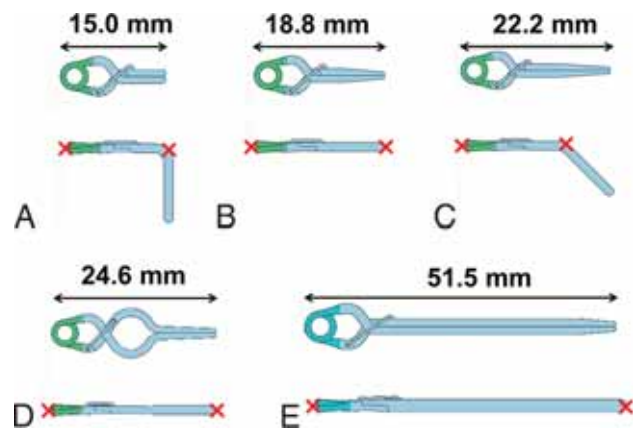
FIG 1. Schematic drawings of aneurysm clips tested in the present study. Upper row, top view; lower, row, lateral view. *Red cross marks* denote locations at which the temperature was measured. *A*, 17–001-22: No. 22, right-angled type. *B*, 17-001-02: No. 2, short straight type. *C*, 17-001-49: No. 49, 45°-angled type. *D*, 17-001-30: No. 30, straight fenestrated type. *E*, 17-001-92: No. 92, long straight type.
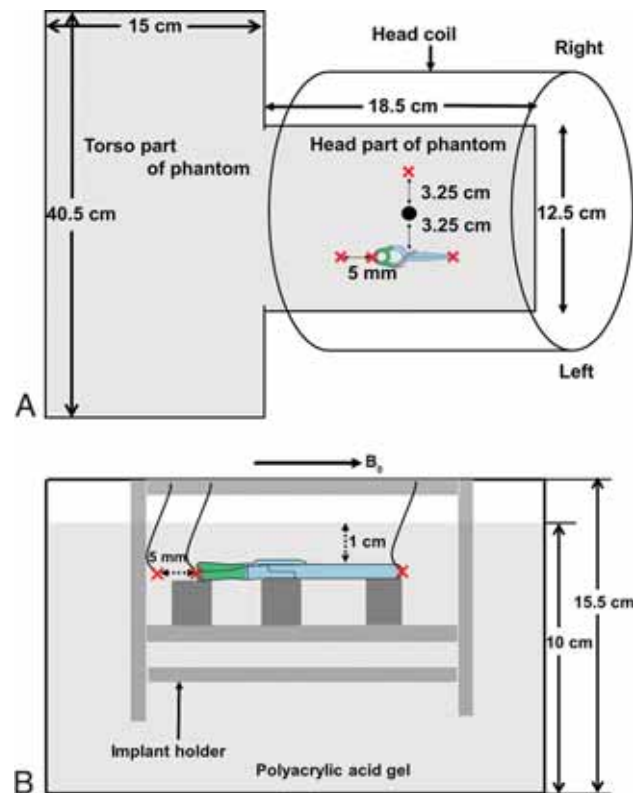
FIG 2. Schematic drawings of an aneurysm clip and fiber-optic thermometer probes in the T-shaped plastic head/torso phantom filled with gelled saline. An aneurysm clip and 4 thermometer probes are set parallel to the static magnetic field (B_0) with the implant holder in the phantom so that they are placed 1 cm below the surface of the gelled saline. The *closed circle* denotes the isocenter of the magnetic field. *Cross marks* denote locations at which temperature is measured. *A*, Upper view of the whole phantom. *B*, Lateral view of the head part of the phantom.

Measurement of Temperature
The temperature in the phantom during MR imaging was measured using 4 MR imaging–compatible fiber-optic thermometer probes with temperature resolutions of 0.1°C and accuracies of

±0.2°C (Neoptix Reflex; Neoptix). Two phantoms, tested clips, thermometer probes, forceps, and digital vernier calipers were left inside the MR imaging room for ≥12 hours before each temperature measurement to equalize the intraphantom temperature with the ambient temperature (19°C–20°C). The MR imaging fan was turned off during scanning.

ASTM standard protocol F2182-19e2 recommends that implants be placed at greater heating positions in the phantom.[19] In the present study, the location of maximum B_1 was assumed to represent the hottest location. In a pilot study, the location of maximum B_1 was determined from 3D actual flip angle imaging.[21] That pilot study demonstrated that the point 3.25 cm to the left of the isocenter was the location of maximum B_1, and each aneurysm clip was thus placed at this point (Fig 2*A*).

The temperature of each aneurysm clip set in the phantom was measured using thermometer probes in contact with the clip at the following 2 locations: tip of the clip blade and tip of the clip head for the short straight clip, straight fenestrated clip, and long straight clip; and tip of the clip head and angled part of the clip for the right-angled clip and 45°-angled clip (Fig 1). The third and fourth thermometer probes were set 5 mm from the tip of the clip head and 3.25 cm to the right of the isocenter as a reference, respectively (Fig 2). One investigator removed the implant holder from the phantom and set an aneurysm clip and thermometer probes using forceps. Another investigator confirmed the condition of contact with the thermometer probes and clip. The former investigator measured the distance between the third thermometer probe and the tip of the clip head using digital Vernier Calipers (https://www.sigmaaldrich.com), and the latter investigator confirmed this distance. Temperatures at the 3 locations for each clip were measured simultaneously in a single MR image. An aneurysm clip and 3 thermometer probes were set parallel to the static magnetic field with an implant holder made of acrylic resin in the phantom so that they were placed at 1 cm under the surface of the gelled saline (Fig 2*B*). Immediately after the end of temperature measurement, 2 investigators confirmed the condition of contact with the clip and measured the distance between the third thermometer probe and the tip of the clip head in the same fashion.

Before temperature measurement of each aneurysm clip, the temperature in the other phantom without aneurysm clips was measured as a control on the same day. This control temperature measurement was performed in the same fashion except for the absence of the clip. Temperature measurements including a combination of absence and presence of an aneurysm clip were performed twice for each clip, and the interval between these 2 conditions for temperature measurement was 2 days. Temperature measurement was performed for only 1 aneurysm clip per day. Each temperature was measured every 2 seconds from 15 minutes before the start of MR imaging to 15 minutes after the end of MR imaging. The SAR averaged for each 6 minutes during MR imaging was also obtained using the scanner console.

Analysis of Temperature

First, for the control temperature without an aneurysm clip, the temperature difference for 5 minutes before the start of MR imaging was averaged as the baseline, and this baseline temperature was subtracted from the temperature at each time point during and after MR imaging. The value at each time point was thus defined as a temperature increase (TI [degree Celsius]), and the maximum TI was determined for each location.

Next, the control temperature without an aneurysm clip was subtracted from the temperature of the aneurysm clip at each time point. The maximum TI for the location of each aneurysm clip was also determined in the same fashion. When the maximum TI was >1°C, sequence parameters related to heating such as flip angle, estimated SAR, and B1+rms were determined to decrease the maximum TI to ≤1°C.

RESULTS

The temperature was successfully measured at all time points. The actual averaged SAR measured for each 6 minutes during MR imaging on the scanner console was 3.0 W/kg.[22] This value was higher than head estimated SAR (1.6 W/kg) calculated before measuring the temperature of aneurysm clips but was close to the 3.2 W/kg proposed by the International Electrotechnical Commission as the upper limit.[17]

The mean (SD) times required to set an aneurysm clip and thermometer probes in the implant holder (the time when the implant holder was outside the phantom) were 5.2 (SD, 0.2) minutes and 5.1 (SD, 0.3) minutes for the first and second measurements, respectively. Two investigators confirmed that the condition of contact with the thermometer probes and target clip and the distance between the third thermometer probe and the tip of the clip head remained unchanged from before to after the temperature measurement for all measurements with aneurysm clips.

The maximum TIs in controls measured twice at each location without aneurysm clips are shown in Table 1. Differences in the maximum TI between these 2 measurements (second measurement – first measurement) ranged from −0.5°C to +0.4°C. The maximum TIs at all locations ranged from 1.7°C to 3.3°C (mean, 2.7 [SD, 0.4]°C). The maximum TIs at the reference point were lower than those at other locations except at 5 mm from the tip of the clip head for the long straight clip.

For all 5 types of aneurysm clips, the TI began to increase with the greatest slope 100–400 seconds after the start of scanning, kept increasing during scanning, and peaked between 660 and 1200 seconds after the start of scanning (Fig 3; Online Supplemental Data). The temperature then plateaued for 60 or 120 seconds after the end of MR imaging and subsequently decreased.

The maximum TIs measured twice at each location are shown in Table 2. Differences in the maximum TI between these 2 measurements (second measurement – first measurement) ranged from −0.2°C to +0.2°C, with the exception of 2 locations for the long straight clip where the absolute value of the difference was ≥0.3°C. The maximum TIs at all locations for the right-angled and short straight clips were <1°C. The maximum TIs at the angled part of the 45°-angled clip and the tip of the clip head for the straight fenestrated clip were >1°C. The maximum TIs at all locations for the long straight clip were >2°C. The maximum TIs at 5 mm from the tip of the head for the long straight clip were >3°C.

For the 45°-angled, straight fenestrated, and long straight clips with a maximum TI of >1°C, sequence parameters related to

Table 1: Maximum increase in control temperature measured twice at each location without aneurysm clips

Type of Clip/Location	1st Measurement	2nd Measurement	Difference (2nd Measurement − 1st Measurement) (°C)
Right-angled (No. 22)			
Tip of clip head	+3.0°	+2.7°	−0.3
Angled part of clip	+3.1°	+3.0°	−0.1
5 mm from tip of clip head	+3.1°	+3.1°	0
Reference	+2.3°	+2.4°	0.1
Short straight (No. 2)			
Tip of clip head	+2.9°	+2.6°	−0.3
Tip of clip blade	+3.3°	+2.9°	−0.4
5 mm from tip of clip head	+3.2°	+3.1°	−0.1
Reference	+2.9°	+2.4°	−0.5
45°-angled (No. 49)			
Tip of clip head	+2.5°	+2.7°	0.2
Angled part of clip	+2.8°	+3.1°	0.3
5 mm from tip of clip head	+2.8°	+3.0°	0.2
Reference	+2.1°	+2.5°	0.4
Straight fenestrated (No. 30)			
Tip of clip head	+2.5°	+2.9°	0.4
Tip of clip blade	+ 3.0°	+3.1°	0.1
5 mm from tip of clip head	+ 2.8°	+2.9°	0.1
Reference	+ 2.1°	+2.1°	0
Long straight (No. 92)			
Tip of clip head	+ 2.5°	+2.5°	0
Tip of clip blade	+ 2.7°	+2.8°	0.1
5 mm from tip of clip head	+ 1.9°	+1.7°	−0.2
Reference	+ 2.4°	+2.1°	−0.3
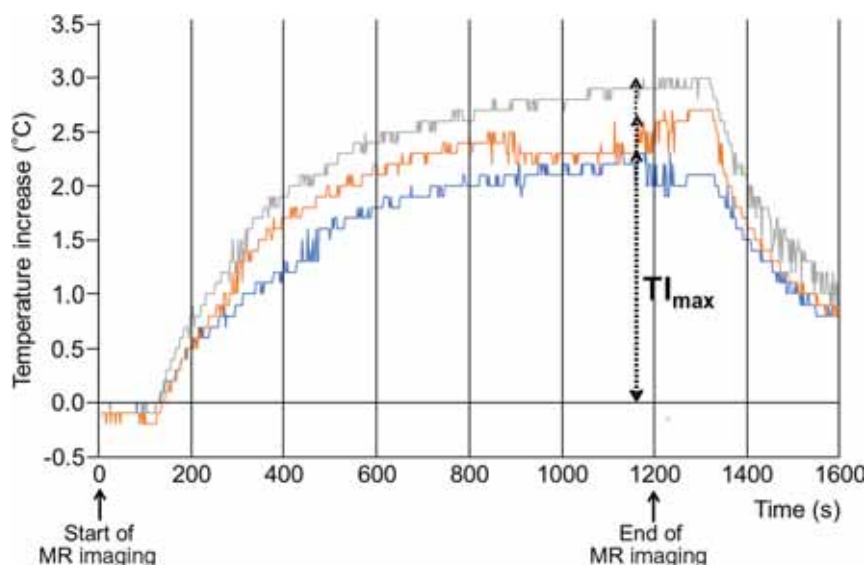
FIG 3. Chronological changes in the TI at 3 locations for the long straight clip. TI (degrees Celsius) indicates the difference between temperatures before MR imaging and during or after MR scanning (latter-former). *Blue, orange,* and *gray lines* denote the TI at tip of the clip head, tip of the clip blade, and 5 mm from the tip of the clip blade, respectively. TI_{max} indicates maximum TI at each location.

DISCUSSION

The present study demonstrated that the TI on the right-angled and short straight clips remained below the regulatory limit during 7T MR imaging, but the TI on the 45°-angled, straight fenestrated, and long straight clips exceeded this limit.

For all aneurysm clips, the temperature kept increasing and subsequently plateaued while MR imaging was still underway. The temperature surrounding an aneurysm clip is increased by the radiofrequency during MR imaging but is decreased by the conduction of heat to the gelled saline in the phantom. Combinations of these former and latter effects might have resulted in the present chronological changes in the TI. MR images with the higher energy of radiofrequency than the SPGR used in the present study (eg, fast spin-echo) may induce higher temperatures.

The ASTM F2182-19e2 suggested that marked heating during MR imaging may occur at sharp edges, points, ends of devices, corners, and near the ends of implants.[19] In vitro and in silico assessment of radiofrequency-induced heating around the aneurysm clips demonstrated the highest temperatures at both ends of the short straight clip or near the ends of implants.[15] The temperature of

heating such as flip angle, the estimated SAR, and B1+rms were determined to decrease the TI to <1°C. Such values were calculated as <26°, <0.8 W/kg, and <2.3 μT, respectively, for the 45°-angled and straight fenestrated clips and <14°, <0.2 W/kg, and <1.24 μT, respectively, for the long straight clip.

Table 2: Maximum increase in temperature measured twice at each location for each aneurysm clip

Type of Clip/Location	1st Measurement (°C)	2nd Measurement (°C)	Difference (2nd Measurement – 1st Measurement) (°C)
Right-angled (No. 22)			
Tip of clip head	+0.3	+0.4	0.1
Angled part of clip	+0.8	+0.7	−0.1
5 mm from tip of clip head	+0.7	+0.6	−0.1
Reference	0	+0.2	0.2
Short straight (No. 2)			
Tip of clip head	+0.4	+0.6	0.2
Tip of clip blade	+0.3	+0.5	0.2
5 mm from tip of clip head	+0.4	+0.4	0
Reference	+ 0.1	0	−0.1
45°-angled (No. 92)			
Tip of clip head	+0.4	+0.6	0.2
Angled part of clip	+1.0[a]	+1.2[a]	0.2
5 mm from tip of clip head	+0.8	+0.9	0.1
Reference	+0.1	0	−0.1
Straight fenestrated (No. 30)			
Tip of clip head	+1.1[a]	+0.9	−0.2
Tip of clip blade	+0.7	+0.5	−0.2
5 mm from tip of clip head	+0.7	+0.5	−0.2
Reference	0	+0.2	0.2
Long straight (No. 92)			
Tip of clip head	+2.3[a]	+2.1[a]	−0.2
Tip of clip blade	+2.8[a]	+2.2[a]	(−0.6)[b]
5 mm from tip of clip head	+3.0[a]	+3.3[a]	(0.3)[b]
Reference	0	0	0

[a] Maximum increase in temperature >+1°C.
[b] Maximal differences.

each aneurysm clip was thus measured at the tip of the clip blade, tip of the clip head, angled part of the clip, and at 5 mm from the tip of the clip head. The TI was <1°C at all locations for the right-angled and short straight clips, >1°C at 1 location for the 45°-angled and straight fenestrated clips, and >1°C at all locations for the long straight clip. These results for the short and long straight clips were comparable with those obtained from in vitro and in silico assessments of radiofrequency-induced heating around aneurysm clips.[15,18] The latter assessment also showed that the temperature rose with increasing length of the clip until the length approached 50 mm and the worst-case length was 50 mm.[18] When implant length approximates half of a wavelength of radiofrequency on MR imaging, antenna resonance effects may result in substantial increases in temperature.[19,23] Half of the wavelength of radiofrequency is 55 mm at 7T[24,25] and better approximates the length of the long straight clip (51.5 mm) than other types of clip, a finding that may explain our results.

The present study also showed that for the 45°-angled, straight fenestrated, and long straight clips with a TI of >1°C, when sequence parameters related to heating such as flip angle, estimated SAR, and B1+rms were reduced, the TI decreased below 1°C. However, flip angle reduction involves a reduction in signal intensity,[26] and a reduction in the estimated SAR or B1+rms results in a reduced number of slices, prolonging the acquisition time.[20] These limitations may preclude clinical use of 7T MR imaging for patients with aneurysmal clips.

The present study has serious limitations. First, the MR imaging system used in the present study was only for research purposes and had not obtained approval from the US FDA and did not have CE certification. However, because the magnitude of the B1+ field was measured during the prescan immediately before each test, the relationship between B1+rms and the degree of temperature rise was considered accurate.[27] Second, the thermometer probe placement on the aneurysm clip might have differed subtly between the first and second measurements, even though 2 investigators confirmed the condition of contact with thermometer probes and clips and the distances between the relevant parts before and after temperature measurement for all measurements. Differences in the maximum TI between these 2 measurements ranged from −0.2°C to +0.2°C, with the exception of 2 locations for the long straight clip where the maximum TIs were >2°C.

The accuracies of the thermometer probes used in the present study were ±0.2°C. Differences in positioning of the thermometer probe may have been minimal for the 4 types of aneurysm clips but may have considerably affected temperature measurement for the long straight clip. Third, aneurysm clips parallel to the static magnetic field might not always represent the worst-case orientation for temperature elevation. The electric field distribution and associated currents can differ substantially. Electric field polarization was not measured in the present study. Furthermore, the actual electric field distribution for the human head at 7T is difficult to predict.[28] This issue is because radiofrequency wavelengths at 7T are shorter and tissue compartments within the human head are widely heterogeneous, so current distributions in radiofrequency field distributions result in complicated heating patterns.[28] In addition, the location of maximum B1 determined from 3D actual flip angle imaging in the present study might not always have been the hottest location.[15] Fourth, natural convection in wet tissue and conduction in blood vessels may buffer the TI when these conditions are present at or near the implant location.[19]

Thus, the TI measured in a phantom is likely to overestimate the actual TI seen in an implant in situ.[19] In the brain, CBF and CSF flow may reduce temperature rises compared with phantom measurements. Further studies regarding temperature measurements in animal brains during MR imaging at ≥7T would be of benefit.

CONCLUSIONS

The present study demonstrated that the TIs for right-angled and short straight clips remained below the regulatory limit during 7T MR imaging, but the TIs for the 45°-angled, straight fenestrated, and long straight clips exceeded this limit.

REFERENCES

1. Gönner F, Lövblad KO, Heid O, et al. **Magnetic resonance angiography with ultrashort echo times reduces the artefact of aneurysm clips.** *Neuroradiology* 2002;44:755–58 CrossRef Medline

2. Grandin CB, Cosnard G, Hammer F, et al. **Vasospasm after subarachnoid hemorrhage: diagnosis with MR angiography.** *AJNR Am J Neuroradiol* 2000;21:1611–17 Medline

3. Leclerc X, Fichten A, Gauvrit JY, et al. **Symptomatic vasospasm after subarachnoid haemorrhage: assessment of brain damage by diffusion and perfusion-weighted MRI and single-photon emission computed tomography.** *Neuroradiology* 2002;44:610–16 CrossRef Medline

4. Villain A, Boulouis G, Ben Hassen W, et al. **Small-vessel disease in patients with subarachnoid hemorrhage: prevalence and associations with vasospasm occurrence, severity and clinical outcomes.** *Neuroradiol J* 2019;32:438–44 CrossRef Medline

5. Kollia K, Maderwald S, Putzki N, et al. **First clinical study on ultra-high-field MR imaging in patients with multiple sclerosis: comparison of 1.5T and 7T.** *AJNR Am J Neuroradiol* 2009;30:699–702 CrossRef Medline

6. Fujimoto K, Uwano I, Sasaki M, et al. **Acetazolamide-loaded dynamic 7T MR quantitative susceptibility mapping in major cerebral artery steno-occlusive disease: comparison with PET.** *AJNR Am J Neuroradiol* 2020;41:785–91 CrossRef Medline

7. Sato Y, Ogasawara K, Yoshida K, et al. **Preoperative visualization of the marginal tentorial artery as an unusual collateral pathway in a patient with symptomatic bilateral vertebral artery occlusion undergoing arterial bypass surgery: a 7.0-T magnetic resonance imaging study.** *Surg Neurol Int* 2014;5:157 CrossRef Medline

8. Matsushige T, Kraemer M, Schlamann M, et al. **Ventricular microaneurysms in Moyamoya angiopathy visualized with 7T MR angiography.** *AJNR Am J Neuroradiol* 2016;37:1669–72 CrossRef Medline

9. Wrede KH, Matsushige T, Goericke SL, et al. **Non-enhanced magnetic resonance imaging of unruptured intracranial aneurysms at 7 Tesla: comparison with digital subtraction angiography.** *Eur Radiol* 2017;27:354–64 CrossRef Medline

10. von Morze C, Xu D, Purcell DD, et al. **Intracranial time-of-flight MR angiography at 7T with comparison to 3T.** *J Magn Reson Imaging* 2007;26:900–04 CrossRef Medline

11. Conijn MM, Hendrikse J, Zwanenburg JJ, et al. **Perforating arteries originating from the posterior communicating artery: a 7.0-Tesla MRI study.** *Eur Radiol* 2009;19:2986–92 CrossRef Medline

12. Wrede KH, Dammann P, Monninghoff C, et al. **Non-enhanced MR imaging of cerebral aneurysms: 7 Tesla versus 1.5 Tesla.** *PLoS One* 2014;9:e84562 CrossRef Medline

13. De Cocker LJ, Lindenholz A, Zwanenburg JJ, et al. **Clinical vascular imaging in the brain at 7T.** *Neuroimage* 2018;168:452–58 CrossRef Medline

14. Dula AN, Virostko J, Shellock FG. **Assessment of MRI issues at 7T for 28 implants and other objects.** *AJR Am J Roentgenol* 2014;202:401–05 CrossRef Medline

15. Noureddine Y, Kraff O, Ladd ME, et al. **In vitro and in silico assessment of RF-induced heating around intracranial aneurysm clips at 7 Tesla.** *Magn Reson Med* 2018;79:568–81 CrossRef Medline

16. Kangarlu A, Shellock FG. **Aneurysm clips: evaluation of magnetic field interactions with an 8.0 T MR system.** *J Magn Reson Imaging* 2000;12:107–11 CrossRef Medline

17. International Electrotechnical Commission. **Particular requirements for the basic safety and essential performance of magnetic resonance equipment for medical diagnosis international standard IEC 60601 medical electrical equipment.** 2015; Part 2–33. https://webstore.iec.ch/publication/22705. Accessed April 30, 2022

18. Noureddine Y, Kraff O, Ladd ME, et al. **Radiofrequency induced heating around aneurysm clips using a generic birdcage head coil at 7 Tesla under consideration of the minimum distance to decouple multiple aneurysm clips.** *Magn Reson Med* 2019;82:1859–75 Medline

19. American Society for Testing and Materials (ASTM) International: F2182-19e2. **Standard Test Method for Measurement of Radio Frequency Induced Heating On or Near Passive Implants During Magnetic Resonance Imaging.** 2019. https://www.astm.org/f2182-19e02.html. Accessed April 30, 2022

20. Boutet A, Elias GJB, Gramer R, et al. **Safety assessment of spine MRI in deep brain stimulation patients.** *J Neurosurg Spine* 2020 Feb 4. [Epub ahead of print] CrossRef Medline

21. Yarnykh VL. **Actual flip-angle imaging in the pulsed steady state: a method for rapid three-dimensional mapping of the transmitted radiofrequency field.** *Magn Reson Med* 2007;57:192–20 CrossRef Medline

22. National Electrical Manufacturers Association (NEMA). **Characterization of the Specific Absorption Rate (SAR) for Magnetic Resonance Imaging Systems.** 2016. https://standards.globalspec.com/std/10166401/NEMA%20MS%208. Accessed April 30, 2022

23. Shellock FG. **Radiofrequency energy-induced heating during MR procedures: a review.** *J Magn Reson Imaging* 2000;12:30–36 CrossRef Medline

24. Collins CM, Smith MB. **Signal-to-noise ratio and absorbed power as functions of main magnetic field strength, and definition of "90 degrees:" RF pulse for the head in the birdcage coil.** *Magn Reson Med* 2001;45:684–91 CrossRef Medline

25. Ladd ME. **High-field-strength magnetic resonance: potential and limits.** *Top Magn Reson Imaging* 2007;18:139–52 CrossRef Medline

26. Schmitz BL, Aschoff AJ, Hoffmann MH, et al. **Advantages and pitfalls in 3T MR brain imaging: a pictorial review.** *AJNR Am J Neuroradiol* 2005;26:2229–37 Medline

27. Baker KB, Tkach JA, Nyenhuis JA, et al. **Evaluation of specific absorption rate as a dosimeter of MRI-related implant heating.** *J Magn Reson Imaging* 2004;20:315–20 CrossRef Medline

28. Fagan AJ, Amrami KK, Welker KM, et al. **Magnetic resonance safety in the 7T environment.** *Magn Reson Imaging Clin N Am* 2020;28:573–82 CrossRef Medline

Diffuse Calvarial Hyperostosis and Spontaneous Intracranial Hypotension: A Case-Control Study

J.C. Babcock, D.R. Johnson, J.C. Benson, D.K. Kim, P.H. Luetmer, D.P. Shlapak, C.P. Cross, M.P. Johnson, J.K. Cutsforth-Gregory, and C.M. Carr

ABSTRACT

BACKGROUND AND PURPOSE: Diagnosing spontaneous intracranial hypotension and associated CSF leaks can be challenging, and additional supportive imaging findings would be useful to direct further evaluation. This retrospective study evaluated whether there was a difference in the prevalence of calvarial hyperostosis in a cohort of patients with spontaneous intracranial hypotension compared with an age- and sex-matched control population.

MATERIALS AND METHODS: Cross-sectional imaging (CT of the head or brain MR imaging examinations) for 166 patients with spontaneous intracranial hypotension and 321 matched controls was assessed by neuroradiologists blinded to the patient's clinical status. The readers qualitatively evaluated the presence of diffuse or layered calvarial hyperostosis and measured calvarial thickness in the axial and coronal planes.

RESULTS: A significant difference in the frequency of layered hyperostosis (31.9%, 53/166 subjects versus 5.0%, 16/321 controls, $P < .001$, OR = 11.58) as well as the frequency of overall (layered and diffuse) hyperostosis (38.6%, 64/166 subjects versus 13.2%, 42/321 controls, $P < .001$, OR = 4.66) was observed between groups. There was no significant difference in the frequency of diffuse hyperostosis between groups (6.6%, 11/166 subjects versus 8.2%, 26/321 controls, $P = .465$). A significant difference was also found between groups for calvarial thickness measured in the axial ($P < .001$) and coronal ($P < .001$) planes.

CONCLUSIONS: Layered calvarial hyperostosis is more prevalent in spontaneous intracranial hypotension compared with the general population and can be used as an additional noninvasive brain imaging marker of spontaneous intracranial hypotension and an underlying spinal CSF leak.

ABBREVIATION: SIH = spontaneous intracranial hypotension

Spontaneous intracranial hypotension (SIH) classically presents with orthostatic headaches and results from a CSF leak in the absence of trauma or iatrogenic injury.[1] The CSF leak may arise from within the thecal sac, at the neural foramen, or just lateral to it in the case of CSF-venous fistulas and nerve root sleeve tears. Recently, imaging techniques such as digital subtraction myelography and CT dynamic myelography have improved the detection and localization of the dural tears and CSF-venous fistulas that cause SIH,[2] and effective treatments are available, including recently described endovascular techniques.[3] Unfortunately, SIH can be a challenging diagnosis because presenting symptoms vary widely.[4] In patients with equivocal clinical symptoms or radiographic evidence of SIH, additional supportive findings on conventional imaging modalities would be useful to guide further imaging and clinical work-up. A recent study described an association between calvarial hyperostosis and SIH.[5] We performed a matched case-control study in a large group of patients with SIH to further investigate this association.

MATERIALS AND METHODS

A retrospective case-control study was conducted following institutional review board approval with waived consent for Health Insurance Portability and Accountability Act compliance.

Case Identification

Our institutional electronic medical record was queried to identify adult patients 18 years of age or older who underwent digital subtraction myelography, conventional myelography, or dynamic CT myelography for the indication of "CSF leak." The results of the query included patients who underwent one of the aforementioned imaging studies between May of 2018 (the time of the institution of the latest electronic medical record) and November
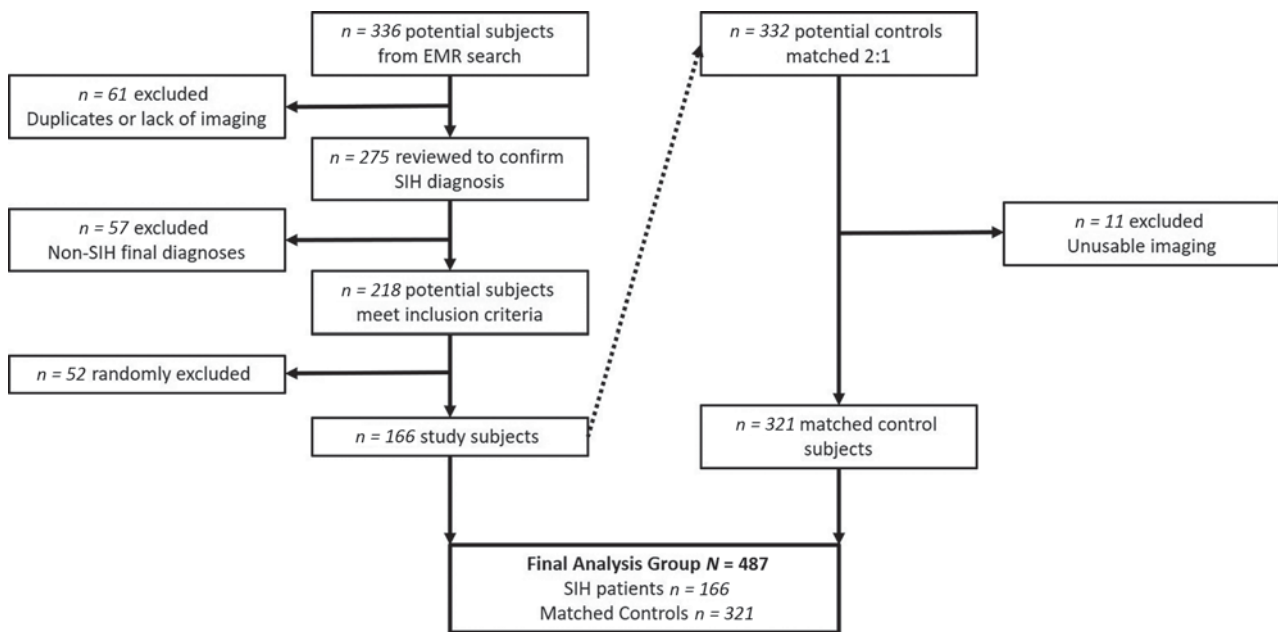
FIG 1. Flow chart defining the process of selecting the subject inclusion cohort. EMR indicates electronic medical record.

2020 (the time of the query). Only subjects with a final clinical diagnosis of SIH were included, as determined by 2 neurologists using modified diagnostic criteria supported by clinical history and radiographic findings in a fashion similar to that used in previous studies.[6] Patients without cross-sectional head imaging (CT or MR imaging) available for review and patients with a history suggestive of posttraumatic/postsurgical CSF leak or an alternative explanation of symptoms were excluded. This process identified 218 eligible cases, of which 166 were randomly selected to exceed the 157 cases needed per power calculations (Fig 1).

Control Matching

Following the case-identification process, controls were matched 2:1 based on age, sex, and study type using the Greedy Matching Algorithm,[7] meaning that once a match was made it was never broken. All subjects were first matched to 1 control; then second control matching began. Sex and study type were matched exactly, and age was matched within 5 years. Study indication and disposition status varied among control examinations because the ability to match additional variables was limited. Available head imaging (CT or MR imaging) varied in the subject population, with either one or both available for each subject. The most recent available head imaging study was selected for analysis. If both MR imaging and CT were available in close succession, the CT head examination was preferentially selected for analysis to allow better spatial resolution and intrinsic contrast for the calvarial measurement. The matching process was designed to identify like control examinations for comparison (ie, CTs were matched to CTs, and MRIs to MRIs). If a control imaging study was found to be inadequate for analysis during image review, for example due to low-quality imaging in which hyperostosis could not be assessed, the control study was excluded and not replaced.

Image Analysis

Six fellowship-trained neuroradiologists from our institution with experience ranging between 1 and 29 years postfellowship

evaluated the cases and controls for hyperostosis. An equal distribution of subject and control examinations was assigned to each neuroradiologist, randomized by a medical record number. All neuroradiologists were blinded to the control or subject status of each examination. Following predetermined instructions, each reader recorded 4 observations: 1) qualitative presence of diffuse hyperostosis (present or absent), 2) qualitative presence of layered hyperostosis (present or absent), 3) calvarial thickness measurement (millimeters) in the axial plane, and 4) calvarial thickness measurement (millimeters) in the coronal plane. Diffuse and layered hyperostosis was considered to be mutually exclusive.

Diffuse hyperostosis was subjectively identified by the presence of generalized thickening of the calvaria without discrete layering (Fig 2B). Layered hyperostosis can be thought of as a subtype of diffuse calvarial thickening in which there is distinct expansion of the inner bone table (Fig 2C), previously reported as having a "layer-cake" appearance.[5] To standardize calvarial thickness measurements, readers were given specific instructions. In the axial plane, maximal calvarial thickness was recorded at the level of the foramen of Monro 25°–35° off midline in either direction to avoid the frontal sinuses (Fig 3A, -B). In the coronal plane, a measurement was recorded where the calvaria was thickest 35°–45° off midline in either direction at the level of the vertex (Fig 3C, -D).

Statistical Methods

This study was designed to achieve 80% power to detect an OR of 5 for calvarial hyperostosis in patients with SIH versus matched controls, assuming a type I error rate of 0.05 and estimating a 3% prevalence of calvarial hyperostosis in the general population. Using a 2:1 control-to-subject ratio, we determined that 157 subjects and 314 matched controls were required.

Patient characteristics for the analysis cohort, including a sample among matching variables, were summarized using percentage for categoric variables and mean (SD) for continuous

variables. Categoric variables were compared between groups using the Pearson χ^2 test, and continuous variables were compared using the 2-sample t test.

The association between calvarial hyperostosis and SIH was analyzed using conditional logistic regression to account for the matched data. P values $< .05$ were considered statistically significant. Sample size calculations were conducted using PASS 2021 (NCSS); matching was performed using SAS software, Version 9.4 (SAS Institute); and data analysis was completed using R, Version 3.6.2 (http://www.r-project.org/).

RESULTS

Patient Characteristics

There were no statistically significant differences in the mean patient age ($P = .902$), sex ($P = .796$), or examination type ($P = .886$) between the matched subject and control patient populations (Table 1). The median time from symptom onset to head imaging used for this study in the subject population was 26 months (interquartile range, 9–66). There was no statistically significant difference in the duration from symptom onset to the time of imaging among the SIH cohort based on the presence of diffuse hyperostosis, the presence of layered hyperostosis, or absence of hyperostosis (Table 2). Small numeric differences

FIG 2. Hyperostosis examples. Normal calvarial thickness (*A*). Axial bone kernel and bone window CT image with a representative example of normal calvarial thickness. Diffuse calvarial hyperostosis (*B*). Axial bone kernel and bone window CT image demonstrates diffuse thickening of the calvaria. Layered calvarial hyperostosis (*C*). Axial bone kernel and bone window CT image demonstrates calvarial thickening with discrete enlargement of the inner and outer tables (*white arrows*), producing a layered appearance.

between the matched cohorts resulted from subject exclusion, for example in the case of inadequate imaging.

Subjective Hyperostosis Evaluation

Layered hyperostosis was present in 53/166 (31.9%) patients with SIH and 16/321 (5.0%) controls ($P < .001$). The OR for the presence of layered hyperostosis in patients with SIH in comparison with the control cohort was 11.58 (95% CI, 5.48–24.46). Diffuse hyperostosis was present in 11/166 (6.6%) patients with SIH and 26/321 (8.2%) controls ($P = .46$). The OR for the presence of diffuse hyperostosis in patients with SIH in comparison with the control cohort was 0.75 (95% CI, 0.36–1.59). Hyperostosis of either variety was present in 64/166 (38.6%) patients with SIH and 42/321 (13.2%) controls ($P < .001$). The OR for the presence of hyperostosis of either variety in patients with SIH in comparison with the control cohort was 4.66 (95% CI, 2.79–7.79). Two of 321 control images (0.6%) could not be assessed due to inadequate image resolution.

Quantitative Calvarial Measurements

In the SIH patient group, the mean axial calvarial thickness was 7.3 (SD 2.6) mm with a range of 1.3–17.9 mm. In the control group, mean axial calvarial thickness was 6.4 (SD 1.9) mm with a range of 1.5–12.2 mm ($P < .001$, OR = 1.20; 95% CI, 1.09–1.32). Measurements of 1/166 (0.6%) patients with SIH and 2/321 (0.6%) control examinations could not be obtained due to inadequate image resolution.

With respect to coronal calvarial thickness, the mean measurement in patients with SIH was 7.4 (SD 2.0) mm with a range of 1.3–14.1 mm, and in the control group, the mean coronal calvarial thickness was 6.6 (SD 1.7) mm with a range of 2.6–13.9 mm ($P < .001$, OR = 1.32; 95% CI, 1.16–1.49). Fifty-five of 487 (11.2%) calvarial measurements could not be obtained due to the absence of a coronal plane in the image set or inadequate image resolution for retrospective reconstruction of coronal images; One of 166 (0.6%)

FIG 3. Example of calvarial thickness measurements obtained in the same patient in the axial and coronal planes. Full-field (*A*) and zoomed (*B*) axial bone kernel and bone window CT images demonstrate a sample axial thickness measurement obtained 25°–35° off midline. Full-field (*C*) and zoomed (*D*) coronal bone kernel and bone window CT images demonstrate a sample coronal thickness measurement obtained 35°–45° off midline.

patients and 54/321 (16.8%) control examinations were affected.

DISCUSSION

This matched case-control study demonstrates that calvarial thickness differs between patients with SIH and the general population by both subjective and objective evaluation. Furthermore, our data indicate that the layer-cake phenotypic appearance is strongly associated with SIH, similar to prior observations,[5] approaching a frequency of nearly 1 in 3 in our population of patients with SIH, with an OR exceeding 11. Diffuse hyperostosis was not significantly associated with SIH in this study.

According to the Monro-Kellie hypothesis, the sum of intracranial CSF, blood, and brain parenchymal volumes must remain constant, and a change in one component necessitates reciprocal change in the others,[8] such as engorgement of the

Table 1: Subject and control group demographics

	Subject (n = 166)	Control (n = 321)	P Value
Age (mean) (SD)	54.5 (12.8)	54.4 (12.9)	.902
Male sex	63 (38.0%)	118 (36.8%)	.796
CT studies	46 (27.7%)	87 (27.1%)	.886
MR imaging studies	120 (72.3%)	234 (72.9%)	

Table 2: Symptom duration of the SIH cohort[a]

	Present	Absent	P Value
Overall hyperostosis[b]	n = 64	n = 102	.171
	36 months (12–78)	22 months (8–49)	
Diffuse hyperostosis	n = 11	n = 155	.798
	36 months (7–80)	25 months (9–64)	
Layered hyperostosis	n = 53	n = 113	.197
	36 months (12–77)	22 months (8–51)	

[a] Numbers in parentheses are interquartile range (25th and 75th percentiles) of symptom duration in months.
[b] Diffuse and layered.
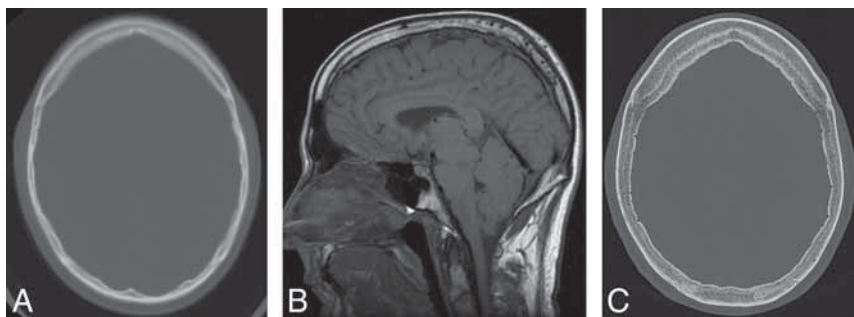
FIG 4. Development of hyperostosis in a 67-year-old man with 2 decades of waxing and waning SIH symptoms with a history of remote CSF leak at C2–C4. *A*, Axial CT head image at 45 years of age shows qualitatively normal calvarial thickness. *B*, Sagittal T1-weighted MR image at 48 years of age demonstrates severe brain sag and a suggestion of developing layered hyperostosis. Diffuse pachymeningeal thickening and enhancement are also present (not shown). *C*, The most recent axial head CT at 67 years of age demonstrates new layered calvarial hyperostosis.

venous structures or development of extra-axial fluid collections in response to a spinal CSF leak.[9,10] Classically, consideration of the Monro-Kellie hypothesis regards the overall intracranial volume as fixed and does not consider the calvaria as a distinct compartment that can potentially undergo change. Calvarial thickening, however, is a means by which the volume of the container could change in response to the loss of the interior contents.

The phenomenon of increased calvarial thickness has previously been reported in pediatric patients with ventricular shunts.[11] In 1 such case, Moseley et al[12] described calvarial remodeling with thickening of discrete inner and outer tables, analogous to the layer-cake appearance. We have observed notable change in calvarial thickness during serial examinations in some of our patients with SIH. One patient with chronic waxing and waning symptoms attributed to a spinal CSF leak developed calvarial thickening during 2 decades (Fig 4). The findings of this study support the phenomenon of increasing bone deposition specifically along the inner table of calvaria in the setting of intracranial volume loss, rather than generalized remodeling or thickening (diffuse hyperostosis pattern). However, the mechanism of this process remains unclear.

Rebound intracranial hypertension following successful treatment of various types of CSF leak may occur in about one-quarter of patients, most often within 1 week posttreatment, and it is generally self-limited in nature and responsive to acetazolamide.[13] The causes of rebound intracranial hypertension remain to be proven.[14] A new headache pattern despite improved or resolving imaging stigmata of CSF hypovolemia suggests rebound intracranial hypertension. Occasionally, papilledema may be appreciated by fundoscopy or MR imaging. While rare, rebound intracranial hypertension and papilledema can be prolonged in course and refractory to conservative measures. We have anecdotally observed multiple patients with hyperostosis developing severe rebound intracranial hypertension after successful treatment of a spinal CSF leak. One such patient with layered calvarial hyperostosis (Fig 5) ultimately required ventriculoperitoneal shunt placement due to papilledema refractory to maximal acetazolamide and optic nerve sheath fenestration.

It may be valuable to further investigate the frequency of posttreatment rebound intracranial hypertension in patients with and without hyperostosis in a dedicated systemic study.

Implications of Findings

SIH is often disabling, so it is gratifying to have improved imaging techniques for localizing spinal CSF leaks, such as CT dynamic myelography and digital subtraction myelography. Yet these examinations are invasive, uncomfortable, resource-intensive, and not available at many centers.[9,15] Because some

FIG 5. A 53-year-old man who developed refractory papilledema and rebound intracranial hypertension following repair of a CSF-venous fistula at T8–T9 at 51 years of age. Rebound intracranial hypertension symptoms began 3 weeks following treatment. Sagittal T1-weighted (*A*) and axial FLAIR (*B*) MR images at 29 years of age demonstrate brain sag with normal baseline qualitative calvarial thickness, respectively. Sagittal T1-weighted (*C*) and axial T2-weighted (*D*) MR images at 51 years of age demonstrate improvement in brain sag with new posterior globe flattening indicative of papilledema, respectively. *E*, Preoperative stereotactic CT image before ventriculoperitoneal shunt placement demonstrates new layered calvarial hyperostosis.

patients with spinal CSF leaks lack brain sag, pachymeningeal enhancement, and other classic signs of SIH, additional objective radiographic signs that increase the pretest probability of finding a leak and for selecting appropriate patients for invasive myelography are advantageous. Our study supports a relationship between layered calvarial hyperostosis and SIH, so in the proper clinical setting, it would be reasonable to offer further work-up for a CSF leak when layered calvarial hyperostosis is observed.

Study Limitations

Although the neuroradiologists were blinded to the control-versus-subject status of the examination at the time of measurement, other qualitative imaging findings were sometimes present to suggest the diagnosis of SIH (eg, brain sag or pachymeningeal enhancement on MR imaging), potentially biasing the reader to presume a subject status. Due to limitations in the availability of a coronal plane or adequate resolution on some examinations (predominantly outside examinations), analysis was performed without many coronal plane calvarial measurements. Additionally, calvarial thickness in any given individual may be variable, possibly introducing measurement error despite a systematic approach in the study design. There is likely some degree of selection bias in the acquisition of the SIH inclusion cohort based on the indication of CSF leak when searching the myelogram imaging database. Additionally, it is plausible that our SIH cohort represents a

subselection of patients refractory to conservative treatment with longer symptom duration, given that we are a referral center. During the subject-to-control matching process, a small number of unsuitable control examinations (postoperative examinations or significant intracranial pathology) were matched and could not be used for analysis. Finally, although 6 neuroradiologists participated in this study, there was no formal analysis regarding interobserver agreement for subjective classification of diffuse or layered calvarial hyperostosis.

CONCLUSIONS

Layered calvarial hyperostosis is present much more frequently in the setting of SIH than in the general population. In the proper clinical context, this finding should prompt further investigation for spinal CSF leak.

Disclosure forms provided by the authors are available with the full text and PDF of this article at www.ajnr.org.

REFERENCES

1. Schievink WI. **Spontaneous intracranial hypotension.** *N Engl J Med* 2021;385:2173–78 CrossRef Medline
2. Schievink WI, Maya M, Prasad RS, et al. **Spontaneous spinal cerebrospinal fluid-venous fistulas in patients with orthostatic headaches and normal conventional brain and spine imaging.** *J Headache Pain* 2021;61:387–91 CrossRef Medline
3. Brinjikji W, Savastano L, Atkinson J, et al. **A novel endovascular therapy for CSF hypotension secondary to CSF-venous fistulas.** *AJNR Am J Neuroradiol* 2021;42:882–87 CrossRef Medline
4. Schievink WI. **Spontaneous spinal cerebrospinal fluid leaks and intracranial hypotension.** *JAMA* 2006;295:2286–96 CrossRef Medline
5. Johnson DR, Carr CM, Luetmer PH, et al. **Diffuse calvarial hyperostosis in patients with spontaneous intracranial hypotension.** *World Neurosurg* 2021;146:e848–53 CrossRef Medline
6. Schievink W, Maya M, Louy C, et al. **Diagnostic criteria for spontaneous spinal CSF leaks and intracranial hypotension.** *AJNR Am J Neuroradiol* 2008;29:853–56 CrossRef Medline
7. Bergstralh E, Kosanke J. **Computerized Matching of Cases to Controls. Technical Report Number 56.** *Mayo Foundation* 1995; 3:56
8. Mokri B. **The Monro-Kellie hypothesis: applications in CSF volume depletion.** *Neurology* 2001;56:1746–48 CrossRef Medline
9. Dobrocky T, Grunder L, Breiding PS, et al. **Assessing spinal cerebrospinal fluid leaks in spontaneous intracranial hypotension with a scoring system based on brain magnetic resonance imaging findings.** *JAMA Neurol* 2019;76:580–87 CrossRef Medline
10. Dobrocky T, Rebsamen M, Rummel C, et al. **Monro-Kellie hypothesis: increase of ventricular CSF volume after surgical closure of a spinal dural leak in patients with spontaneous intracranial hypotension.** *AJNR Am J Neuroradiol* 2020;41:2055–61 CrossRef Medline

11. Lucey BP, March GP, Hutchins GM. **Marked calvarial thickening and dural changes following chronic ventricular shunting for shaken baby syndrome.** *Arch Pathol Lab Med* 2003;127:94–97 CrossRef Medline

12. Moseley JE, Rabinowitz JG, Dziadiw R. **Hyperostosis cranii ex vacuo.** *Radiology* 1966;87:1105–07 CrossRef Medline

13. Schievink WI, Maya MM, Jean-Pierre S, et al. **Rebound high-pressure headache after treatment of spontaneous intracranial hypotension.** *Neurol Clin Pract* 2019;9:93–100 CrossRef Medline

14. Mokri B. **Intracranial hypertension after treatment of spontaneous cerebrospinal fluid leaks.** *Mayo Clin Proc* 2002;77:1241–46 CrossRef Medline

15. Farb R, Nicholson P, Peng P, et al. **Spontaneous intracranial hypotension: a systematic imaging approach for CSF leak localization and management based on MRI and digital subtraction myelography.** *AJNR Am J Neuroradiol* 2019;40:745–53 CrossRef Medline

Alterations of Microstructure and Sodium Homeostasis in Fast Amyotrophic Lateral Sclerosis Progressors: A Brain DTI and Sodium MRI Study

M.M. El Mendili, A.-M. Grapperon, R. Dintrich, J.-P Stellmann, J.-P. Ranjeva, M. Guye, A. Verschueren, S. Attarian, and W. Zaaraoui

ABSTRACT

BACKGROUND AND PURPOSE: While conventional MR imaging has limited value in amyotrophic lateral sclerosis, nonconventional MR imaging has shown alterations of microstructure using diffusion MR imaging and recently sodium homeostasis with sodium MR imaging. We aimed to investigate the topography of brain regions showing combined microstructural and sodium homeostasis alterations in amyotrophic lateral sclerosis subgroups according to their disease-progression rates.

MATERIALS AND METHODS: Twenty-nine patients with amyotrophic lateral sclerosis and 24 age-matched healthy controls were recruited. Clinical assessments included disease duration and the Revised Amyotrophic Lateral Sclerosis Functional Rating Scale. Patients were clinically differentiated into fast ($n = 13$) and slow ($n = 16$) progressors according to the Revised Amyotrophic Lateral Sclerosis Functional Rating Scale progression rate. 3T MR imaging brain protocol included ^{1}H TI-weighted and diffusion sequences and a ^{23}Na density-adapted radial sequence. Quantitative maps of diffusion with fractional anisotropy, mean diffusivity, and total sodium concentration were measured. The topography of diffusion and sodium abnormalities was assessed by voxelwise analyses.

RESULTS: Patients with amyotrophic lateral sclerosis showed significantly higher sodium concentrations and lower fractional anisotropy, along with higher sodium concentrations and higher mean diffusivity compared with healthy controls, primarily within the corticospinal tracts, corona radiata, and body and genu of the corpus callosum. Fast progressors showed wider-spread abnormalities mainly in the frontal areas. In slow progressors, only fractional anisotropy measures showed abnormalities compared with healthy controls, localized in focal regions of the corticospinal tracts, the body of corpus callosum, corona radiata, and thalamic radiation.

CONCLUSIONS: The present study evidenced widespread combined microstructural and sodium homeostasis brain alterations in fast amyotrophic lateral sclerosis progressors.

ABBREVIATIONS: AD = axial diffusivity; ALS = amyotrophic lateral sclerosis; ALSFRS-R = Revised Amyotrophic Lateral Sclerosis Functional Rating Scale; ATP = adenosine triphosphate; CST = corticospinal tract; FA = fractional anisotropy; HC = healthy controls; MD = mean diffusivity; MNI152 = Montreal Neurological Institute 152; RD = radial diffusivity; TBSS = tract-based spatial statistics; TSC = total sodium concentration

Amyotrophic lateral sclerosis (ALS) is a relentlessly progressive neurodegenerative disorder leading to paralysis and ultimately death. As a heterogeneous condition, ALS is characterized by

variable clinical presentations and progression of symptoms depending on various factors such as age at disease onset, the site of onset, genetic factors, and the presence of nonmotor symptoms, especially cognitive impairment.[1-4] ALS outcome varies drastically, with a median survival time from onset ranging from 24 months (Northern Europe) to 48 months (South Asia).[5] For 1.1% of cases of ALS, the median survival time from onset is 18 months and can go up to 10 years in 5%–13.3% of cases, demonstrating the heterogeneity of the disease.[3,6] While disability is commonly scored by the Revised Amyotrophic Lateral Sclerosis Functional Rating Scale (ALSFRS-R), the Amyotrophic Lateral Sclerosis Functional Rating Scale (ALSFRS) disease-progression rate is also considered an important marker of the disease to predict disability progression and patient survival.[7-9]

Conventional MR imaging (eg, T2*, FLAIR, and proton density–weighted imaging) lacks sensitivity and specificity to detect

abnormalities in ALS and is mainly used to exclude ALS mimics.[10] Although conventional MR imaging could detect signal abnormalities in ALS such as hyperintensity in the white matter (WM) along the corticospinal tract (CST), they are rare and nonspecific and their exploration is not recommended for diagnosis.[10-13] In contrast, nonconventional MR imaging has gradually characterized features of neurodegeneration in ALS.[14] To a large extent, DTI studies have reported microstructure alterations in upper motor neurons and extramotor WM tracts.[15] Notably, DTI has shown an increased burden of WM pathology, concordant with neuropathologic staging and correlating with disease aggressiveness.[14,16-18] Recently, a sodium MR imaging study provided the first evidence of increased total sodium concentration (TSC) located in the CST of patients with ALS, reflecting disturbance of sodium homeostasis involved in metabolic failure, contributing to the neurodegenerative process.[19]

Mitochondrial dysfunction can mediate cell death by reducing adenosine triphosphate (ATP) production and impairing sodium and calcium homeostasis. If ATP availability becomes insufficient to allow ion pumps to maintain the appropriate ion gradients, changes in electrical properties and the excitability of motor neurons occur. Thus, investigating sodium concentration disturbances with sodium MR imaging could provide relevant functional information on neuron energetic status and cell viability, while DTI efficiently explores microstructural disorders. The combination of sodium and diffusion imaging could, therefore, enable the exploration of complementary processes leading to neuronal injury. Besides, one may assume that brain regions presenting combined sodium homeostasis and microstructural alterations depend on disease aggressiveness. The present study aimed to investigate the topography of brain regions showing combined microstructural and sodium homeostasis alterations in ALS subgroups according to their disease-progression rates.

MATERIALS AND METHODS
Ethics and Institutional Review Board Approval
This prospective study was approved by the local ethics committee (Comité de Protection des Personnes Sud Méditerranée 1), and written informed consent was obtained from all participants.

Study Participants and Procedures
Twenty-nine patients with ALS (9 women; mean, 54 [SD, 10] years of age; mean disease duration, 1.6 [SD, 1.2] years) were recruited from the ALS reference center of our university hospital along with 24 age- and sex-matched healthy controls (HC) with no history of neurologic or neuropsychiatric disorder (11 women; mean, 51 [SD, 11] years of age). The inclusion criteria were a diagnosis of ALS according to the revised El Escorial criteria.[20] The exclusion criteria were no current or past history of neurologic disease other than ALS, and no frontotemporal dementia, respiratory insufficiency, or substantial bulbar impairment incompatible with an MR imaging examination. Patients were clinically assessed immediately after MR imaging and scored on the ALSFRS-R.[21] Patients were clinically differentiated into fast and slow progressors according to their ALFSRS-R rate of progression, defined as ([48 ALSFRS-R]/disease duration). A threshold of 0.5 ALSFRS-R per month was set to differentiate fast from slow progressors.[22]

MR Imaging Acquisition
MR imaging was performed on a 3T Verio system (Siemens Healthineers) using a 32-channel phased-array ^{1}H head coil (Siemens Healthineers) and a ^{23}Na ^{1}H volume head coil (RAPID Biomedical).

^{1}H-MR imaging protocol included a 3D T1-weighted MPRAGE sequence (TE/TR/TI = 3/2300/900 ms, 160 slices, voxel size = $1 \times 1 \times 1$ mm^3, acquisition time = 6 minutes) and a single-shot echo-planar imaging DTI sequence (64 encoding directions, b = 1000 s/mm^2 and B$_0$, TE = 95 ms, TR = 10,700 ms, 60 contiguous slices, voxel size = $2 \times 2 \times 2$ mm^3, acquisition time = 12 minutes).

The ^{23}Na MR imaging protocol included a 3D density-adapted radial sequence (TR/TE = 120/0.2 ms, 17,000 projections with 369 samples per projection, voxel size = $3.6 \times 3.6 \times 3.6$ mm^3, acquisition time = 34 minutes).[23] Two tubes (50 mmol/L within 2% agar gel) placed within the FOV served as a reference for quantification.[24]

Data Processing
Anatomic. T1WIs were normalized to the Montreal Neurological Institute 152 (MNI152) template using SyN-ANTS (https://github.com/ANTsX/ANTs) nonlinear registration.[25]

DTI. Diffusion images were denoised using a local principal component analysis method that reduces signal fluctuations solely rooted in thermal noise.[26] Images were further corrected for eddy currents and head motion using affine registration to the associated non-diffusion-weighted images.[27] Fractional anisotropy (FA), mean diffusivity (MD), axial diffusivity (AD), and radial diffusivity (RD) maps were computed by fitting a tensor model.[27] FA images were aligned to the FMRIB58_FA (https://fsl.fmrib.ox.ac.uk/fsl/fslwiki/FMRIB58_FA) target, which is in MNI152 standard space, using a nonlinear registration.[27] Aligned FA images were averaged, then a "thinning" (non-maximum-suppression perpendicular to the local tract structure) was applied to create a skeletonized mean FA image. The resulting image was thresholded (FA = 0.2) to suppress areas of low mean FA values and/or high intersubject variability.[28] For each subject's FA image, the maximum FA value perpendicular to each voxel of the skeleton was projected onto the mean FA skeleton. Similarly, skeletonized MD, AD, and RD images were generated in the MNI152 space using Tract-Based Spatial Statistics (TBSS) FSL tools (https://fsl.fmrib.ox.ac.uk/fsl/fslwiki/TBSS) before voxelwise analysis.

Sodium Imaging. Sodium images were reconstructed offline, denoised, and then normalized relative to the reference tube signals to compute quantitative TSC maps of the whole brain.[19,24] TSC maps were rigidly aligned to their corresponding T1WI. Linear and nonlinear transformations were concatenated then used to bring TSC maps into the MNI152 standard space, and spatially normalized TSC maps were smoothed with a Gaussian kernel ($8 \times 8 \times 8$ mm) before voxelwise analysis.

Statistical Analysis
Statistical analysis was performed using FSL (FMRIB Software Library v6.0; https://fsl.fmrib.ox.ac.uk/fsl/fslwiki/)[27] and SPSS, Version 23 (IBM).

Demographic and clinical data[a]

	ALS	Fast	Slow	HC	P Value
Number	29	13	16	24	–
Age (yr)	54.3 (10.2)	56 (9.9)	52.9 (10.6)	51 (10.7)	.244[b,c]
					.152[b,d]
					.586[b,e]
					.388[b,f]
Sex	9F/20M	6F/7M	3F/13M	11F/13M	.394[g,c]
					.101[g,d]
					1.000[g,e]
					.172[g,f]
Disease duration (mo)	18.8 (14.5)	19.4 (13.9)	18.4 (15.4)	–	–[c],–[d],–[e] .660[h,f]
Site of onset					
Spinal	22 (6 UL, 16 LL)	10 (3 UL, 7 LL)	12 (3 UL, 9 LL)	–	–
Bulbar	7	3	4	–	–
Revised El Escorial criteria					
Definite	7	7	0	–	–
Probable	7	3	6	–	–
Probable laboratory					
Supported	6	1	5	–	–
Possible	9	2	5	–	–
Disease progression rate	0.84 (0.87)	1.54 (0.93)	0.27 (0.09)	–	–[c],–[d],–[e] .001[h,f]
ALSFRS-R (/48)	38.72 (5.55)	37.31 (4.81)	40.46 (6.09)	–	–[c],–[d],–[e] .067[h,f]

Note:—F indicates female; Fast, fast progressors; LL, lower limb; M, male; mo, month; yr, year; Slow, slow progressors; –, not applicable; UL, upper limb.
[a] Values are expressed as mean (SD), unless otherwise indicated.
[b] Student t test.
[c] ALS versus HC.
[d] Fast versus HC.
[e] Slow versus HC.
[f] Fast versus slow.
[g] χ^2 test.
[h] Kruskal-Wallis test.

Group Comparisons. Differences in age, disease duration, and the ALSFRS-R score between groups were assessed by using the Student t test or the Kruskal-Wallis test when applicable. Differences in sex between groups were assessed using the χ^2 test.

Voxelwise Analysis. Differences in diffusion (FA, MD, RD, AD) and sodium (TSC) maps between groups (patients with ALS versus HC, fast versus HC, slow versus HC, fast versus slow) were assessed using permutation inference statistics (5000 permutations) combined with t testing. Threshold-free cluster enhancement with a significance interval of P values $< .05$ was used to correct for multiple comparisons (ie, family-wise error correction).[28] Common regions with significant group differences in both diffusion and TSC maps were identified from the Johns Hopkins University White Matter Tractography Atlas and labels and the Harvard-Oxford structural atlas and sorted by overlap with the corresponding tracts and cortical and subcortical regions.

RESULTS

Demographic and clinical measures of our population are reported in the Table. Figure 1 shows an example of FA and TSC images in a healthy control and fast and slow progressors. There were no significant differences in age or sex between patients with ALS and fast and slow progressors and HC (all P values $> .05$). There were no significant differences in disease duration or in ALSFRS-R between fast and slow progressors. The mean disease-progression rate was 1.54 (SD, 0.93) ALSFRS-R per month for fast progressors and 0.27 (SD, 0.09) ALSFRS-R per month for slow progressors.

ALS versus HC

Statistical maps resulting from voxelwise analysis and TBSS comparing patients with ALS with HC for TSC, FA, and MD are presented in Fig 2.

TSC. Patients with ALS showed significantly higher TSC compared with HC, mainly at the level of the body and genu of the corpus callosum, CSTs, bilateral corona radiata, and thalamic radiation for WM and middle frontal, precentral, postcentral, and cingulate gyri and anterior division for grey matter (GM). These clusters had a mean TSC of 58.15 (SD, 4.54) mM in patients with ALS and 53.41 (SD, 3.22) mM in HC. No clusters of significantly lower TSC in patients with ALS compared with HC were found.

DTI. Patients with ALS showed significantly lower FA compared with HC, mainly at the level of the bilateral corona radiata, body of the corpus callosum, forceps minor, genu of corpus callosum, and CSTs. Patients with ALS showed significantly higher MD compared with HC, mainly at the level of the bilateral corona radiata, body of the corpus callosum, CSTs, internal and external capsule, and longitudinal fasciculus. No clusters of significantly higher FA or lower MD in patients with ALS compared with HC were found.

Overlap between TSC and DTI. As reported in Fig 2, compared with HC, patients with ALS showed significantly higher TSC and lower FA and higher TSC and higher MD, mainly at the level of the corpus callosum, CSTs, and bilateral corona radiata. No clusters of significantly higher FA and lower TSC or lower TSC and
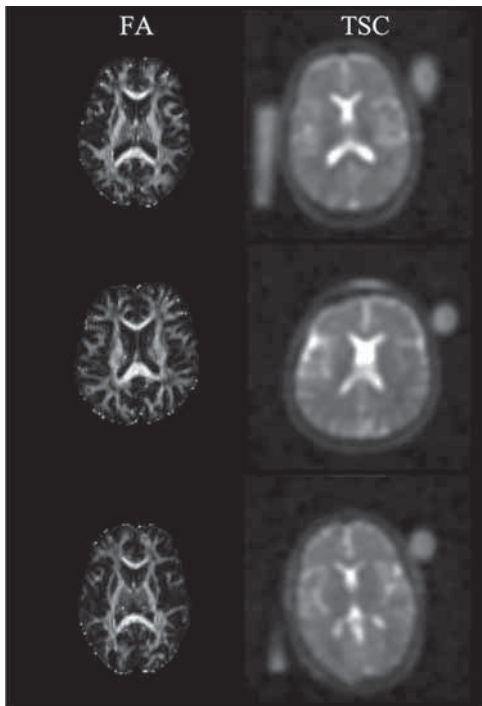
FIG 1. Example of FA and TSC maps in a healthy control (*upper row*), a fast progressor with ALS (*middle row*), and a slow progressor with ALS (*lower row*).

lower MD in those with ALS compared with HC were found. A complete list of the significant clusters emerging from the voxelwise analysis is reported in the Online Supplemental Data.

Fast Progressors versus HC

Statistical maps resulting from voxelwise analysis comparing fast ALS progressors with HC for TSC, FA, and MD are presented in Fig 3.

TSC. Fast progressors showed significantly higher TSC compared with HC, mainly at the level of the body and genu of the corpus callosum, thalamic radiation, bilateral corona radiata, forceps minor, and CSTs for WM; and precentral, postcentral, cingulate, precingulate, middle frontal, superior frontal gyri, thalamus, and caudate for GM and deep GM (Fig 3). These clusters had a mean TSC of 59.23 (SD, 5.03) mM in fast progressors and 53.12 (SD, 3.12) mM in HC. No clusters of significantly lower TSC in fast progressors compared with HC were found.

DTI. Fast progressors showed significantly lower FA compared with HC mainly in the bilateral corona radiata, body and genu of the corpus callosum, forceps minor, external capsule, uncinate fasciculus, and CSTs (Fig 3). Fast progressors showed significantly higher MD compared with HC mainly at the level of the bilateral corona radiata, body and genu of the corpus callosum, forceps minor, CSTs, internal capsule, longitudinal fasciculus, fronto-occipital fasciculus, thalamic radiation, and external capsule (Fig 3).
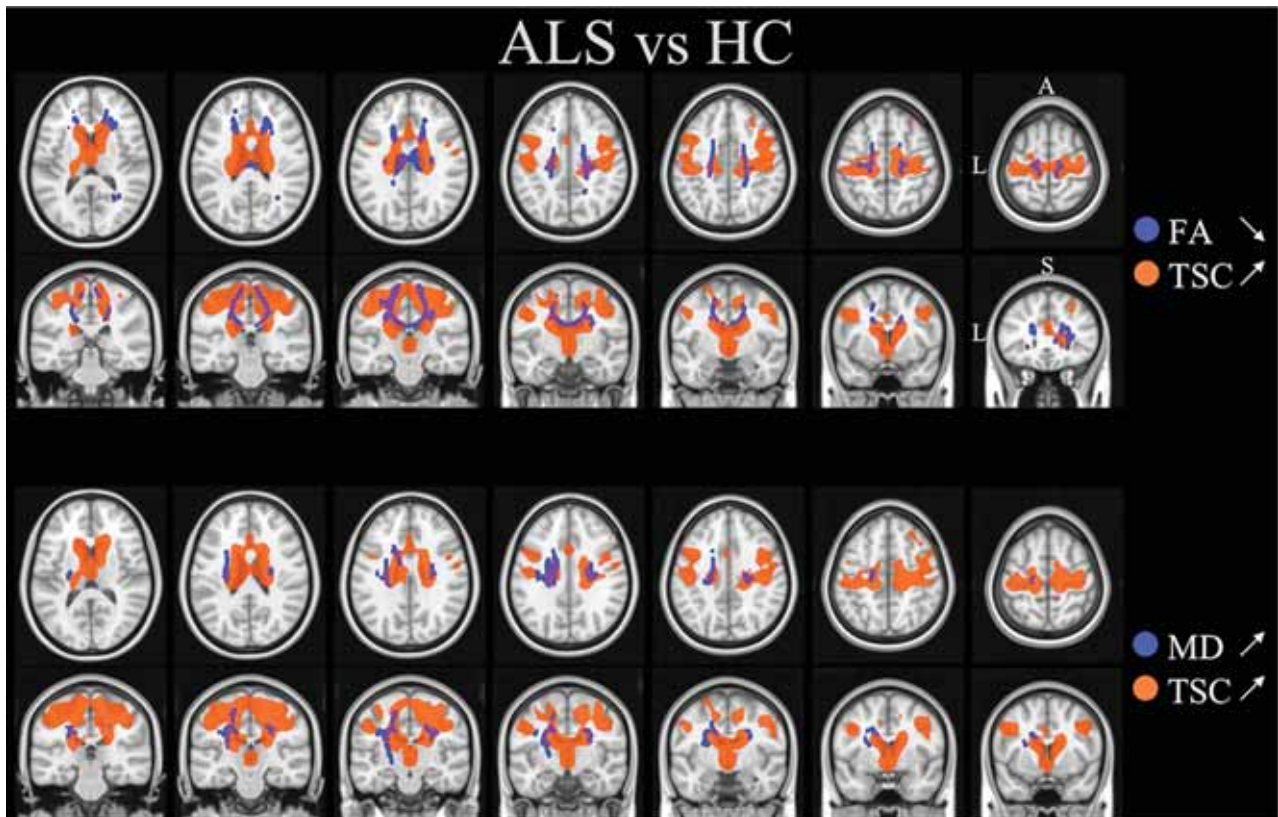
FIG 2. Significant clusters resulting from the comparison of patients with ALS and HC using voxelwise analysis of TSC (increased in ALS) and TBSS for FA (decreased in ALS) and for MD (increased in ALS). A indicates anterior; L, left; S, superior.
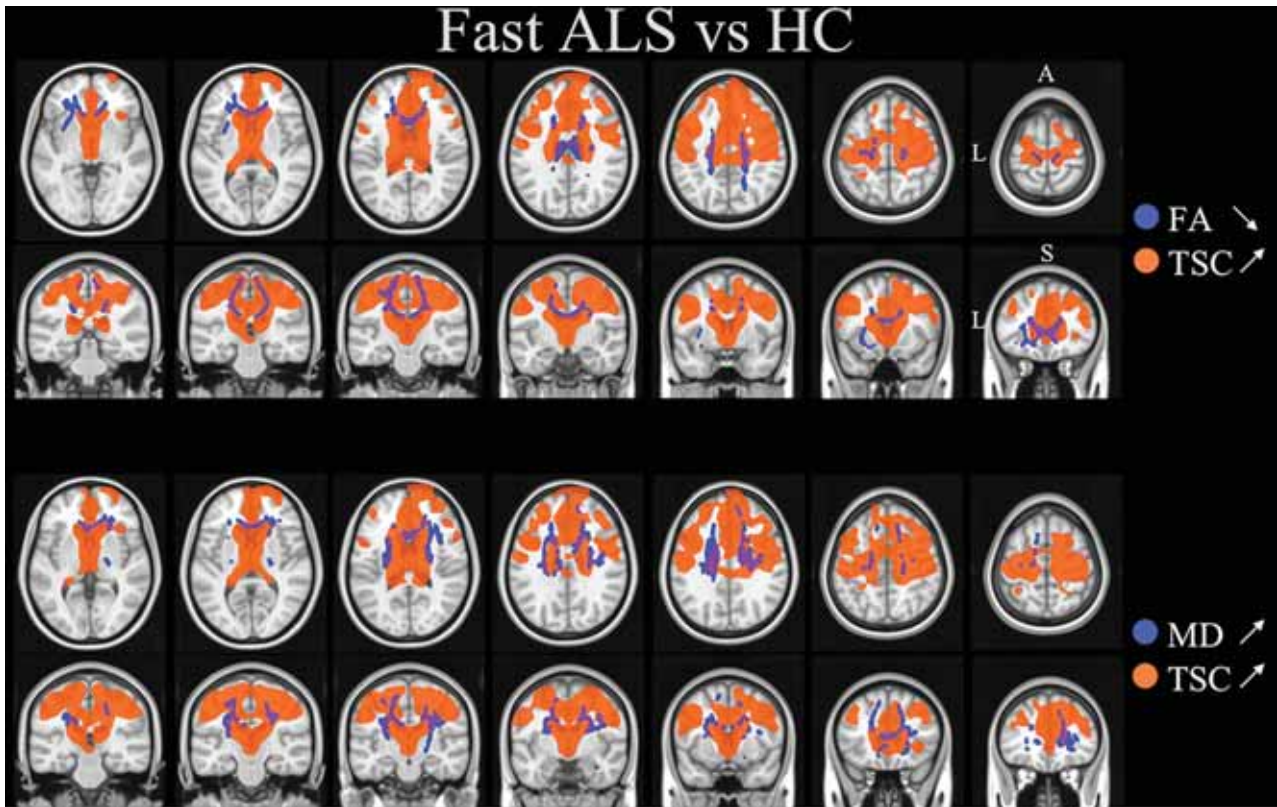
FIG 3. Significant clusters resulting from the comparison between fast ALS progressors and HC using voxelwise analysis for TSC (increased in fast ALS) and TBSS for FA (decreased in fast ALS) and MD (increased in fast ALS). A indicates anterior; L, left; S, superior.
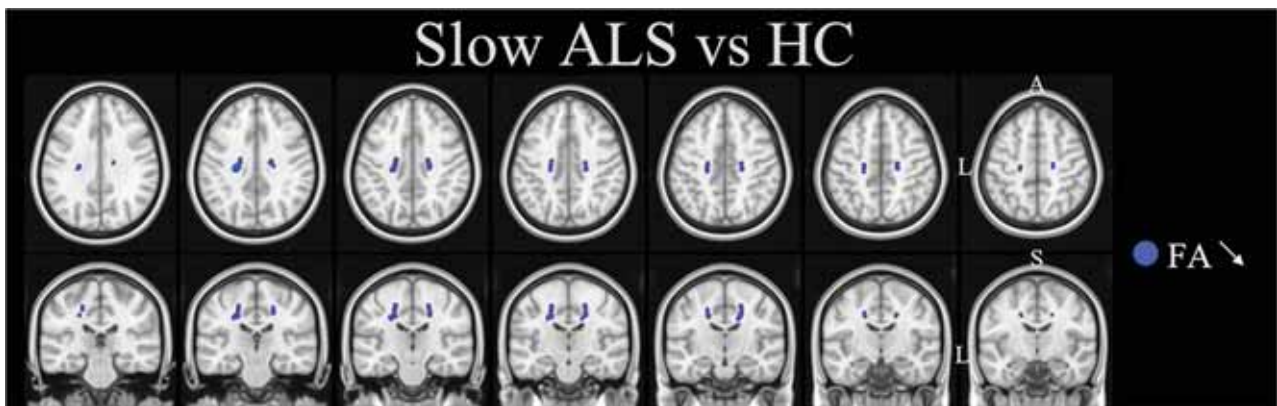
FIG 4. Significant clusters resulting from the comparison between slow ALS progressors and HC using TBSS for FA (decreased in slow ALS). A indicates anterior; L, left; S, superior.

No clusters of significantly higher FA or lower MD in fast progressors compared with HC were found.

Overlap between TSC and DTI. As reported in Fig 3, compared with HC, fast progressors showed significantly higher TSC and lower FA and higher TSC and higher MD, mainly at the level of the corona radiata, body and genu of the corpus callosum, forceps minor, and CSTs. No clusters of significantly higher FA and lower TSC or lower TSC and lower MD in fast progressors compared with HC were found. A complete list of the significant clusters emerging from the voxelwise analysis is reported in the Online Supplemental Data.

Slow Progressors versus HC
Only FA showed significantly lower values in slow progressors compared with HC, mainly at the level of the bilateral superior corona radiata, CSTs, body of the corpus callosum, and thalamic radiation (Fig 4). A complete list of the significant clusters emerging from TBSS analysis is reported in the Online Supplemental Data.

Fast versus Slow Progressors
No significant differences in TSC and DTI metrics were found between fast and slow progressors. Results from TBSS analysis for RD and AD are reported in the Online Supplemental Data.

DISCUSSION

The present study highlighted brain regions with combined microstructural and sodium homeostasis disturbances corresponding to clinically relevant regions involved in ALS, namely, the CST and the corpus callosum.[29] We opted for whole-brain voxel-to-voxel analyses to highlight the focal tissue involvement that would be masked by a global approach such as an ROI. Our results are in accordance with DTI studies that confirmed the impairment of the CST (subcortical to brainstem) as a main hallmark in ALS, even in patients with no upper motor neuron signs at the time of MR imaging but who developed pyramidal symptoms later.[16,30,31] Furthermore, callosal impairment has also been stressed by several studies, especially the motor-related regions of the corpus callosum.[10,32] A recent meta-analysis DTI study analyzing 14 studies with 396 patients with ALS reported 2 clusters of brain microstructural impairment.[33] The first cluster was located in the left corona radiata, extending to the body and splenium of the corpus callosum, left superior longitudinal fasciculus, posterior limb of the internal capsule, right corona radiata, and bilateral cingulate gyrus. The second cluster was located in the right corticospinal tract, which extended to the right cerebral peduncle. Most interesting, these 2 clusters were found in our study to be the site of microstructural impairment but also sodium homeostasis disturbances, a marker of neurodegeneration related to mitochondrial dysfunction and energy failure.[19-34]

Considering that heterogeneous disease-progression rates impact prognosis and might affect the responsiveness to future treatments, there has been recent effort to study patient stratification.[35,36] Stratifying patients by disease progression, we characterized widespread, combined microstructural and ionic alterations in fast progressors, while slow progressors showed only restricted microstructure damage. These results are important because they reflect diverse pathophysiologic processes in patients with no difference in age or disease duration or disability scale (ALSFRS-R) but who experienced different disease-progression rates. A few studies have investigated WM and GM alterations in fast and slow progressors.[16,17,30] A DTI study reported that fast progressors with lower-motor-neuron ALS had a substantial impairment in the CST and frontal and prefrontal brain regions compared with HC, while slow progressors showed less severe alterations.[17] In addition, patients with high disease aggressiveness showed a distinct pattern of supratentorial WM density decreases relative to those with low aggressiveness but no significant differences in GM density suggesting axonal loss.[30]

In our study, we found sodium alterations that reflect mitochondrial dysfunction and subsequent energy failure, both of which are key factors in the induction of pathologic processes in ALS.[37,38] In vitro experiments demonstrated that axonal degeneration caused by experimental anoxia within the brain is a calcium ion (Ca^{2+})-dependent process that can be triggered by a sustained sodium ion (Na+) influx driving reverse Na^+–Ca^{2+} exchange and importing damaging levels of Ca^{2+} within the axons.[39] This early work suggested that ATP depletion and consequent Na^+-(potassium) K^+-ATPase failure might result in a breakdown of ionic gradients because Na^+ ions enter the axon via persistently activated Na+ channels. An additional study reported that axons may degenerate because nitric oxide (NO) can inhibit mitochondrial respiration, resulting in energy failure and intra-axonal accumulation of sodium. Most interesting, axons could be protected from NO-mediated damage by using Na^+ channel blockers.[40]

Limitations

The cross-sectional design of the study did not allow us to assess the course of the disease between fast and slow progressors and investigate whether fast progressors are an ALS phenotype, as suggested in some studies,[16,17] or a maladaptive condition. In the present study, fast and slow progressors were differentiated using a threshold of 0.47 for the disease-progression rate. This choice was based on the results of a previous study,[22] which found that this threshold was a significant predictor of survival in ALS. Nevertheless, because no consensus is available, this may be open to discussion. Another limitation is related to the restricted number of patients, which prevented better staging between subgroups and might explain the lack of a significant difference between fast and slow progressors. Finally, a neuropsychological assessment would have helped to explain whether clusters found in the frontotemporal lobe of fast progressors were due to cognitive deficits. Future multicentric and longitudinal imaging studies will be of interest to identify early markers of neurodegeneration and predict the course of the disease of individual patients.[41]

CONCLUSIONS

The present brain DTI and sodium MR imaging study evidenced combined microstructural and sodium homeostasis alterations in ALS. These alterations were in accordance with disease aggressiveness. Fast progressors showed more widespread brain tissue damage than slow progressors compared with HC. Our study highlights the relevance of a multinuclear MR imaging approach to stratify patients according to their disease aggressiveness.

Disclosure forms provided by the authors are available with the full text and PDF of this article at www.ajnr.org.

REFERENCES

1. Chiò A, Moglia C, Canosa A, et al. **Cognitive impairment across ALS clinical stages in a population-based cohort.** *Neurology* 2019;93:e984–94 CrossRef Medline
2. Chiò A, Logroscino G, Traynor BJ, et al. **Global epidemiology of amyotrophic lateral sclerosis: a systematic review of the published literature.** *Neuroepidemiology* 2013;41:118–30 CrossRef Medline
3. Chiò A, Calvo A, Moglia C, et al; PARALS Study Group. **Phenotypic heterogeneity of amyotrophic lateral sclerosis: a population-based study.** *J Neurol Neurosurg Psychiatry* 2011;82:740–46 CrossRef Medline
4. Volk AE, Weishaupt JH, Andersen PM, et al. **Current knowledge and recent insights into the genetic basis of amyotrophic lateral sclerosis.** *Med Genet* 2018;30:252–58 CrossRef Medline
5. Marin B, Boumédiene F, Logroscino G, et al. **Variation in worldwide incidence of amyotrophic lateral sclerosis: a meta-analysis.** *Int J Epidemiol* 2017;46:57–74 CrossRef Medline
6. Pupillo E, Messina P, Logroscino G, et al; SLALOM Group. **Long-term survival in amyotrophic lateral sclerosis: a population-based study.** *Ann Neurol* 2014;75:287–97 CrossRef Medline
7. Kimura F, Fujimura C, Ishida S, et al. **Progression rate of ALSFRS-R at time of diagnosis predicts survival time in ALS.** *Neurology* 2006;66:265–67 CrossRef Medline
8. Kollewe K, Mauss U, Krampfl K, et al. **ALSFRS-R score and its ratio: a useful predictor for ALS-progression.** *J Neurol Sci* 2008;275:69–73 CrossRef Medline

9. Daghlas SA, Govindarajan R; Pooled Resource Open-Access ALS Clinical Trials Consortium. **Relative effects of forced vital capacity and ALSFRS-R on survival in ALS.** *Muscle Nerve* 2021;64:346–51 CrossRef Medline

10. Filippini N, Douaud G, Mackay CE, et al. **Corpus callosum involvement is a consistent feature of amyotrophic lateral sclerosis.** *Neurology* 2010;75:1645–52 CrossRef Medline

11. Winhammar JM, Rowe DB, Henderson RD, et al. **Assessment of disease progression in motor neuron disease.** *Lancet Neurol* 2005;4:229–38 CrossRef Medline

12. Gupta A, Nguyen TB, Chakraborty S, et al. **Accuracy of conventional MRI in ALS.** *Can J Neurol Sci* 2014;41:53–57 CrossRef Medline

13. Jin J, Hu F, Zhang Q, et al. **Hyperintensity of the corticospinal tract on FLAIR: a simple and sensitive objective upper motor neuron degeneration marker in clinically verified amyotrophic lateral sclerosis.** *J Neurol Sci* 2016;367:177–83 CrossRef Medline

14. Kassubek J, Müller HP. **Advanced neuroimaging approaches in amyotrophic lateral sclerosis: refining the clinical diagnosis.** *Expert Rev Neurother* 2020;20:237–49 CrossRef Medline

15. Basaia S, Filippi M, Spinelli EG, et al. **White matter microstructure breakdown in the motor neuron disease spectrum: recent advances using diffusion magnetic resonance imaging.** *Front Neurol* 2019;10:193 CrossRef Medline

16. Steinbach R, Gaur N, Roediger A, et al. **Disease aggressiveness signatures of amyotrophic lateral sclerosis in white matter tracts revealed by the D50 disease progression model.** *Hum Brain Mapp* 2021;42:737–52 CrossRef Medline

17. Müller HP, Agosta F, Riva N, et al. **Fast progressive lower motor neuron disease is an ALS variant: a two-centre tract of interest-based MRI data analysis.** *Neuroimage Clin* 2018;17:145–52 CrossRef Medline

18. Brettschneider J, Del Tredici K, Toledo JB, et al. **Stages of pTDP-43 pathology in amyotrophic lateral sclerosis.** *Ann Neurol* 2013;74:20–38 CrossRef Medline

19. Grapperon AM, Ridley B, Verschueren A, et al. **Quantitative brain sodium MRI depicts corticospinal impairment in amyotrophic lateral sclerosis.** *Radiology* 2019;292:422–28 CrossRef Medline

20. Brooks BR, Miller RG, Swash M, et al; World Federation of Neurology Research Group on Motor Neuron Diseases. **El Escorial revisited: revised criteria for the diagnosis of amyotrophic lateral sclerosis.** *Amyotroph Lateral Scler Other Motor Neuron Disord* 2000;1:293–99 CrossRef Medline

21. Cedarbaum JM, Stambler N, Malta E, et al. **The ALSFRS-R: a revised ALS functional rating scale that incorporates assessments of respiratory function—BDNF ALS Study Group (Phase III).** *J Neurol Sci* 1999;169:13–21 CrossRef Medline

22. Labra J, Menon P, Byth K, et al. **Rate of disease progression: a prognostic biomarker in ALS.** *J Neurol Neurosurg Psychiatry* 2016;87:628–32 CrossRef Medline

23. Nagel AM, Laun FB, Weber MA, et al. **Sodium MRI using a density-adapted 3D radial acquisition technique.** *Magn Reson Med* 2009;62:1565–73 CrossRef Medline

24. Ridley B, Marchi A, Wirsich J, et al. **Brain sodium MRI in human epilepsy: disturbances of ionic homeostasis reflect the organization of pathological regions.** *Neuroimage* 2017;157:173–83 CrossRef Medline

25. Avants BB, Tustison NJ, Stauffer M, et al. **The Insight ToolKit image registration framework.** *Front Neuroinform* 2014;8:44 CrossRef Medline

26. Manjón JV, Coupé P, Concha L, et al. **Diffusion weighted image denoising using overcomplete local PCA.** *PLoS One* 2013;8:e73021 CrossRef Medline

27. Jenkinson M, Beckmann CF, Behrens TE, et al. **FSL.** *Neuroimage* 2012;62:782–90 CrossRef Medline

28. Smith SM, Jenkinson M, Johansen-Berg H, et al. **Tract-Based Spatial Statistics: voxelwise analysis of multi-subject diffusion data.** *Neuroimage* 2006;31:1487–505 CrossRef Medline

29. Bede P, Iyer PM, Schuster C, et al. **The selective anatomical vulnerability of ALS: "disease-defining" and "disease-defying" brain regions.** *Amyotroph Lateral Scler Frontotemporal Degener* 2016;17:561–70 CrossRef Medline

30. Steinbach R, Prell T, Gaur N, et al. **Patterns of grey and white matter changes differ between bulbar and limb onset amyotrophic lateral sclerosis.** *Neuroimage Clin* 2021;30:10267 CrossRef Medline

31. Sach M, Winkler G, Glauche V, et al. **Diffusion tensor MRI of early upper motor neuron involvement in amyotrophic lateral sclerosis.** *Brain* 2004;127:340–50 CrossRef Medline

32. Chapman MC, Jelsone-Swain L, Johnson TD, et al. **Diffusion tensor MRI of the corpus callosum in amyotrophic lateral sclerosis.** *J Magn Reson Imaging* 2014;39:641–47 CrossRef Medline

33. Zhang F, Chen G, He M, et al. **Altered white matter microarchitecture in amyotrophic lateral sclerosis: a voxel-based meta-analysis of diffusion tensor imaging.** *Neuroimage Clin* 2018;19:122–29 CrossRef Medline

34. Huhn K, Engelhorn T, Linker RA, et al. **Potential of sodium MRI as a biomarker for neurodegeneration and neuroinflammation in multiple sclerosis.** *Front Neurol* 2019;10:84 CrossRef Medline

35. Schuster C, Hardiman O, Bede P. **Survival prediction in amyotrophic lateral sclerosis based on MRI measures and clinical characteristics.** *BMC Neurol* 2017;17:73 CrossRef Medline

36. Spinelli EG, Riva N, Rancoita PMV, et al. **Structural MRI outcomes and predictors of disease progression in amyotrophic lateral sclerosis.** *Neuroimage Clin* 2020;27:102315 CrossRef Medline

37. Sassani M, Alix JJ, McDermott CJ, et al. **Magnetic resonance spectroscopy reveals mitochondrial dysfunction in amyotrophic lateral sclerosis.** *Brain* 2020;143:3603–18 CrossRef Medline

38. Vandoorne T, De Bock K, Van Den Bosch L. **Energy metabolism in ALS: an underappreciated opportunity?** *Acta Neuropathol* 2018;135:489–509 CrossRef Medline

39. Stys PK, Waxman SG, Ransom BR. **Ionic mechanisms of anoxic injury in mammalian CNS white matter: role of Na+ channels and Na(+)-Ca2+ exchanger.** *J Neurosci* 1992;12:430–39 CrossRef Medline

40. Kapoor R, Davies M, Blaker PA, et al. **Blockers of sodium and calcium entry protect axons from nitric oxide-mediated degeneration.** *Ann Neurol* 2003;53:174–80 CrossRef Medline

41. Meier JM, van der Burgh HK, Nitert AD, et al. **Connectome-based propagation model in amyotrophic lateral sclerosis.** *Ann Neurol* 2020;87:725–38 CrossRef Medline

Quantifying Brain Iron in Hereditary Hemochromatosis Using R2* and Susceptibility Mapping

S.K. Sethi, S. Sharma, S. Gharabaghi, D. Reese, Y. Chen, P. Adams, M.S. Jog, and E.M. Haacke

ABSTRACT

BACKGROUND AND PURPOSE: Brain iron dyshomeostasis is increasingly recognized as an important contributor to neurodegeneration. Hereditary hemochromatosis is the most commonly inherited disorder of systemic iron overload. Although there is an increasing interest in excessive brain iron deposition, there is a paucity of evidence showing changes in brain iron exceeding that in healthy controls. Quantitative susceptibility mapping and R2* mapping are established MR imaging techniques that we used to noninvasively quantify brain iron in subjects with hereditary hemochromatosis.

MATERIALS AND METHODS: Fifty-two patients with hereditary hemochromatosis and 47 age- and sex-matched healthy controls were imaged using a multiecho gradient-echo sequence at 3T. Quantitative susceptibility mapping and R2* data were generated, and regions within the deep gray matter were manually segmented. Mean susceptibility and R2* relaxation rates were calculated for each region, and iron content was compared between the groups.

RESULTS: We noted elevated iron levels in patients with hereditary hemochromatosis compared with healthy controls using both R2* and QSM methods in the caudate nucleus, putamen, pulvinar thalamus, red nucleus, and dentate nucleus. Additionally, the substantia nigra showed increased susceptibility while the thalamus showed an increased R2* relaxation rate compared with healthy controls, respectively.

CONCLUSIONS: Both quantitative susceptibility mapping and R2* showed abnormal levels of brain iron in subjects with hereditary hemochromatosis compared with controls. Quantitative susceptibility mapping and R2* can be acquired in a single MR imaging sequence and are complementary in quantifying deep gray matter iron.

ABBREVIATIONS: CN = caudate nucleus; GP = globus pallidus; DGM = deep gray matter; DN = dentate nucleus; FDRI = field-dependent relaxation rate increase; HC = healthy controls; HH = hereditary hemochromatosis; PUT = putamen; PT = pulvinar of the thalamus; QSM = quantitative susceptibility mapping; RN = red nucleus; SN = substantia nigra; SWIM = susceptibility weighted imaging and mapping; THA = thalamus

Brain iron deposition in subjects with hereditary hemochromatosis (HH) has received very little attention to date, and very few descriptions of brain imaging showing iron deposition for these patients have been reported in the literature.[1-3] Hemochromatosis is an inherited disorder of parenchymal iron overload characterized by several genetic mutations as its causative factor.[4,5] The most common mutation in White patients that leads to HH involves the *HFE* gene.[5,6] Clinically, it manifests as

iron deposition in several organs including the liver, skin, pancreas, joints, bones, and heart.[4,7] Hepatic iron deposition in subjects with HH is thought to reflect total body iron stores.[8] Noninvasive imaging methods using MR imaging have been used to quantify hepatic iron deposition in subjects with HH.[8,9] These methods can also be applied to imaging brain iron.

Both R2* mapping and quantitative susceptibility mapping (QSM) are highly sensitive and stable methods for assessing brain iron in the form of ferritin, particularly in the deep GM where it is concentrated.[10,11] Furthermore, R2* and QSM have been validated in histologic studies.[12,13] R2* maps can be used to calculate putative iron via the magnetization transverse relaxation rates in the gradient-echo images, and QSM reconstructs local susceptibility differences from the filtered phase data.[14] Furthermore, both methods can be calculated from the same gradient recalled-echo scan within a clinically acceptable imaging time. Iron quantification using R2* mapping and QSM has been extensively investigated

in patients with neurodegenerative disorders including Parkinson's disease, multiple sclerosis, neurodegeneration with brain iron accumulation, and several other disorders.[15-17] Therefore, we chose to apply these methods in a unique cohort of subjects with hemochromatosis as well as age-matched healthy controls (HC) to characterize cerebral iron deposition in deep gray matter (DGM) nuclei. Having baseline levels of iron may be useful for diagnosis and longitudinally tracking the course of the disease or the efficacy of therapeutic interventions.

MATERIALS AND METHODS

Subjects

We enrolled 52 subjects (30 men; mean age, 58.23 [SD, 12.29] years and 22 women; mean age, 58.00 [SD, 14.91] years) with HH and 47 age- and sex-matched healthy controls (19 men; mean age, 53.32 [SD, 12.82] years and 28 women; mean age, 54.46 [SD,13.38] years; Table 1). No age differences were seen between these groups ($t = -1.56$, $P = .12$). The demographic details of the 52 subjects who underwent MR imaging are given in Table 2.

MR Imaging and QSM Processing

All subjects were imaged using a 3T Discovery MR750 system with a 32-channel head coil (GE Healthcare). Images were collected with the following parameters using a spoiled multiecho gradient recalled-echo sequence: 6 echoes with a TE from 5 to 30 ms and an echo spacing of 5 ms, flip angle = 7°, TR = 36 ms, FOV = 220 mm × 220 mm, matrix size = 366 × 366, section thickness = 2 mm. Images were interpolated to an in-plane display resolution 0.43 mm × 0.43 mm. The scan time was 7 minutes 20 seconds.

QSM data were reconstructed for each echo individually using an in-house algorithm with the following steps: The FSL Brain Extraction Tool (http://fsl.fmrib.ox.ac.uk/fsl/fslwiki/BET)[18] was used to isolate the brain tissue (threshold = 0.2, erode = 4, and island = 2000); a 3D phase unwrapping algorithm (3DSRNCP)[19]

was used to unwrap the original phase data; and the sophisticated harmonic artifact reduction (SHARP)[20] filter was used to remove unwanted background fields (threshold = 0.05 and deconvolution kernel size = 6). A truncated k-space division-based inverse filtering technique (threshold = 0.1) with an iterative approach (iteration threshold = 0.1 and number of iterations = 4) was used to reconstruct the susceptibility map.[21] The resulting susceptibility map was constructed from the QSM data from TE_2–TE_6 using a method that uses a weighted averaging of each TE based on its SNR.[22] R2* maps were generated using a previously established conventional method.[23] We did not use the first echo data because it caused reconstruction errors when combining it with the others.

ROIs in the DGM were traced by 2 experienced raters on the QSM images (due to high contrast) using Signal Processing In NMR (SPIN) Software (SpinTech MR imaging) and reviewed by a neurologist/radiologist (S.S.). Full width at half maximum thresholding was used to delineate the boundary. Manual adjustments were performed if the algorithm failed. Interrater agreement was established using an intraclass correlation coefficient for absolute agreement.[24]

We analyzed the following structures: caudate nucleus (CN), globus pallidus (GP), putamen (PUT), pulvinar of the thalamus (PT), red nucleus (RN), substantia nigra (SN), thalamus (THA), and dentate nucleus (DN). The ROIs were then overlaid on the R2* data. Subsequently, mean susceptibility and R2* values for each region were calculated and compared between patients with HH and healthy controls. All reported structural measurements were averaged bilaterally. Statistical analysis was performed using SPSS, Version 22 (IBM). Demographic details of the study subjects are described as mean (SD) for continuous variables and as frequency for categoric variables. Comparative analysis of the mean R2* and the susceptibility of DGM nuclei between study groups was performed using unpaired t tests. The significance level was set at .05.

RESULTS

A total of 52 patients with HH and 47 HCs were included in the MR imaging analyses. R2* and susceptibility results are shown in Tables 3 and 4. In both analyses, we noted multiple structures with elevated iron in the HH group compared with the HC group. These structures included the CN, PUT, PT, RN, and the DN. QSM showed elevated iron in the SN, while R2* showed elevated iron in the THA.

Examples of how increases in iron manifest (appearing as hyperintense regions) in both methods for patients with HH and HC are shown in Fig 1. One of the subjects with extreme iron deposition also had iron increases in the cuneus and cingulate sulcus (Fig 1C, -G). In this same patient, the iron was so high (approaching 1 part per million in some cases) that we could not reconstruct the R2* values for the whole regions of the CN and PUT due to lack of signal in the magnitude images. This case also showed elevated iron within the SN and the GP. We plotted iron content in

Table 1: Mean age of subjects with HH and healthy controls

Subjects with HH (n = 52)	No.	Mean Age (yr)	95% CI	P Value
Men				
HH	30	58.23 (SD, 12.29)	−12.29–2.52	.19
HC	19	53.32 (SD, 12.82)		
Women				
HH	22	58.00 (SD, 14.91)	−11.59–4.52	.38
HC	28	54.46 (SD, 13.38)		

Table 2: Demographics of patients with HH who underwent MR imaging

Demographics of Patients with HH	
Age at HH diagnosis (mean) (yr)	51.09 (SD, 12.92) (n = 52)
Handedness	Right: 50, left: 2
Family history of HH	Yes: 30, no: 21, unknown: 1
Average duration from time of diagnosis to MR imaging (yr)	7.29 (SD, 5.22) (n = 51)
Genetic diagnosis (n = 60)	C282Y homozygous: 41
	H63D homozygous: 2
	C282Y heterozygous: 2
	H63D heterozygous: 1
	Compound heterozygous: 3
	Unknown status: 3

Table 3: Comparative analysis of mean susceptibility (parts per billion) in the DGM nuclei between patients with HH and HC[a]

	Group Statistics					T Test for Equality of Means					95% CI of the Difference	
Structure	Diagnosis	No.	Mean	SD	Standard Error of the Mean	t	df	Significant (2-Tailed)	Mean Difference	Standard Error Difference	Lower	Upper
CN	HC	47	24.43	8.7	1.3	−2.08	97	.040[a]	−6.86	3.30	−13.41	−0.31
	HH	52	31.29	21.0	2.9							
GP	HC	47	85.48	20.1	2.9	1.09	97	.278	4.57	4.19	−3.74	12.89
	HH	52	80.91	21.4	3.0							
PUT	HC	47	33.06	14.4	2.1	−3.37	97	.001[b]	−19.63	5.83	−31.20	−8.07
	HH	52	52.70	37.5	5.2							
THA	HC	47	3.45	3.6	0.5	−1.78	97	.079	−1.58	0.89	−3.36	0.19
	HH	52	5.04	5.1	0.7							
PT	HC	47	36.40	13.5	2.0	−2.66	97	.009[b]	−9.79	3.68	−17.09	−2.48
	HH	52	46.19	21.7	3.0							
RN	HC	47	94.91	24.1	3.5	−4.32	97	<.001[c]	−23.40	5.41	−34.15	−12.66
	HH	52	118.32	29.2	4.1							
SN	HC	47	129.69	22.8	3.3	−2.26	97	.026[a]	−11.66	5.15	−21.88	−1.43
	HH	52	141.35	27.9	3.9							
DN	HC	47	92.53	24.2	3.5	−5.10	97	<.001[c]	−32.09	6.30	44.59	−19.59
	HH	52	124.62	36.5	5.1							

[a] P < .05.
[b] P < .01.
[c] P < .001.

Table 4: Comparative analysis of R2* (s⁻¹) in the deep gray matter nuclei between subjects with HH and HC

	Group Statistics					T Test for Equality of Means					95% Confidence Interval of the Difference	
Structure	Diagnosis	No.	Mean	SD	Standard Error of the Mean	t	df	Significant (2-Tailed)	Mean Difference	Standard Error Difference	Lower	Upper
CN	HC	47	25.23	3.0	0.4	2.89	97	.005[a]	−2.94	1.02	−4.95	−0.92
	HH	52	28.17	6.3	0.9							
GP	HC	47	40.12	4.6	0.7	1.88	97	.064	−2.22	1.18	−4.57	0.13
	HH	52	42.35	6.8	0.9							
PUT	HC	47	29.67	4.9	0.7	4.19	97	<.001[b]	−5.98	1.43	−8.81	−3.15
	HH	52	35.65	8.6	1.2							
THA	HC	47	21.01	1.5	0.2	−3.59	97	.001[a]	−1.31	0.37	−2.04	−0.59
	HH	52	22.32	2.1	0.3							
PT	HC	47	24.15	3.0	0.4	−4.36	97	<.001[b]	−3.20	0.73	−4.66	−1.74
	HH	52	27.35	4.2	0.6							
RN	HC	47	36.26	5.3	0.8	−2.65	97	.009[a]	−3.46	1.31	−6.05	−0.87
	HH	52	39.72	7.4	1.0							
SN	HC	47	36.60	4.5	0.7	−1.94	97	.056	−2.02	1.04	-4.08	0.05
	HH	52	38.62	5.7	0.8							
DN	HC	47	32.23	5.2	0.8	−3.95	97	<.001[b]	−6.28	1.59	−9.43	−3.13
	HH	52	38.50	9.7	1.3							

[a] P <.01.
[b] P <.001.

Figs 2 and 3 to highlight the group differences between the 2 cohorts.

DISCUSSION

R2* mapping and QSM are complementary MR imaging postprocessing techniques for detecting abnormal iron in the DGM in subjects with hemochromatosis. Furthermore, they are also sensitive for discriminating HH from HC as noted by the low P values for numerous structures (Table 3). These methods have the potential to detect abnormal brain iron in patients with HH.

HH is the most common inherited disorder of systemic iron excess in populations of Northern European descent.[25] HFE C282Y mutations are the most frequent cause of HH.[26-28] As a result of HFE mutations, iron accumulates in excess in several organs, in particular the liver, skin, pancreas, endocrine organs, and heart.[29] Brain iron deposition has been controversial in HH because the presence of an intact blood-brain barrier is proposed to protect against brain iron overload.[30,31] However, recent findings suggest that HFE is expressed strategically at the blood-brain barrier in the endothelium, and several authors have argued that this expression of HFE would lead to excessive brain iron deposition because HFE mutations are associated with high iron accumulation in several other organs.[32-36] The present study validated this finding of excess brain iron deposition in a fraction of the HH
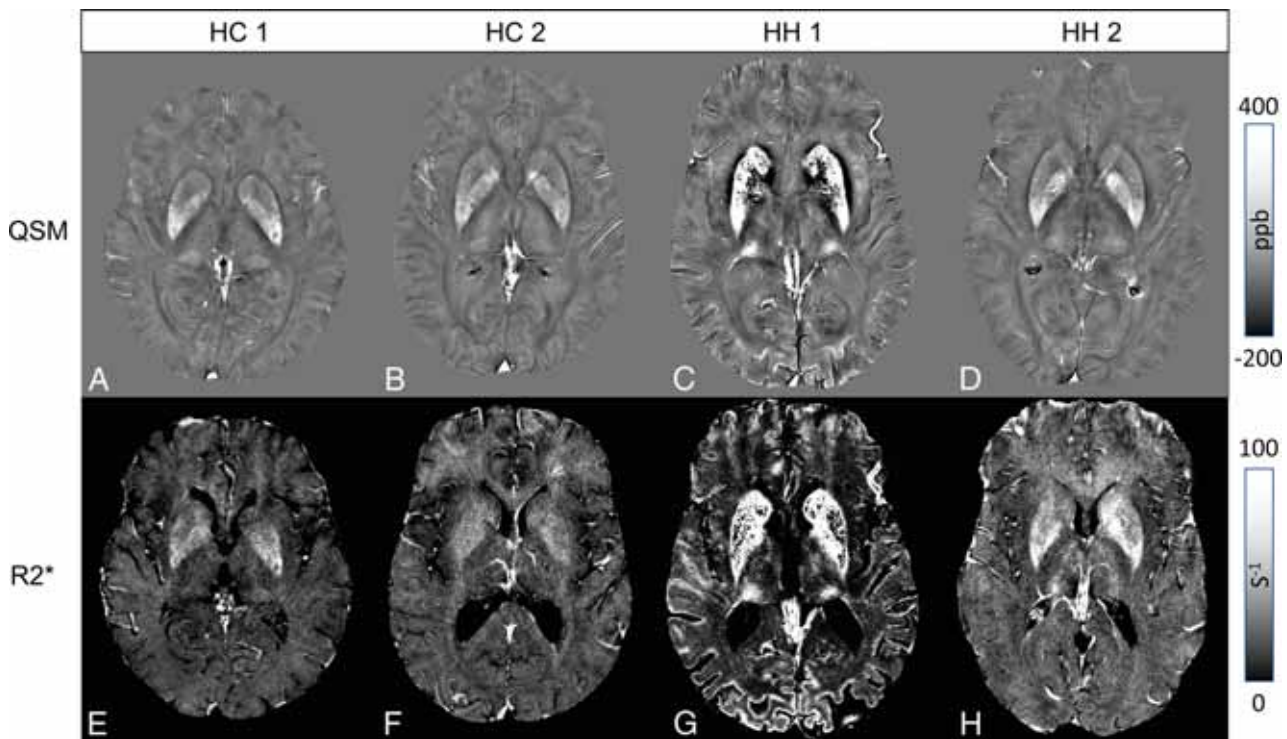
FIG 1. *Upper row*: QSM showing 2 HC (*A* and *B*) and 2 subjects with HH (*C* and *D*). *Lower row*: Corresponding R2* maps. Elevated striatal and PT iron is depicted in both subjects with HH (*C* and *D*, *F* and *G*). For 1 subject (*C* and *F*), high iron can be seen in the cuneus and striatal cortex.

cases using both QSM and R2*, whose postprocessing is derived from 1 spoiled gradient recalled-echo MR imaging sequence.

Kalpouzos et al[37] studied the influence of brain iron overload and the link to the genetic polymorphisms associated with iron dysregulation (C282Y and H63D) in healthy subjects. They hypothesized that elevated iron content in these structures would negatively influence cognitive outcome. Using QSM, we found that carriers of the C282Y allele had higher levels of iron only in the PUT compared with noncarriers. Both brain iron and transferrin saturation, a serum marker of elevated iron, are associated with status, but the authors suggested a beneficial effect of *HFE*-positive carrier status relating to brain iron and executive function. Conversely, subjects with *HFE*-negative status showed a correlation between brain iron and working memory, a finding similar to that in Bartzokis et al.[2] They observed a correlation between iron measured via susceptibility and transferrin saturation, though age did not magnify the effect of *HFE*-positive status on brain and blood iron. Subjects with iron overload were not part of the cohort. Our work showed elevated iron content in the rest of the DGM (SN, DN, CN, RN, THA, and PT) in either QSM, R2*, or both in the cohort with the C282Y allele with a hemochromatosis diagnosis. Another recent article using the same data set addressed the influence of regional brain iron deposition as measured with QSM and development of specific movement disorders in subjects with HH. Therefore, we did not include any correlative analysis with clinical data in the current article.[38]

The field-dependent relaxation rate increase (FDRI) method has been used to demonstrate higher iron accumulation in the brain of male cohorts who are carriers of gene variants of iron metabolism, namely *HFE* H63D and transferrin C2, compared with noncarriers.[1] Berg et al[39] reported increased iron in the basal ganglia using CT, MR imaging, and sonography; however, the sample size was only 14 subjects. Additionally, multiple case reports with movement disorders have been associated with HH and MR imaging signal changes related to iron.[40] Large-scale studies using quantitative MR imaging are scarce; however, Bartzokis et al[1] have mapped basal ganglia iron FDRI and found increased iron in the DGM in subjects lacking at least 1 gene for HH. One of the key differences between FDRI and R2* is that FDRI measures R2 relaxation (relaxation from spin-spin interactions) but R2* includes both spin-spin interactions and the effects from field inhomogeneities induced by local increases in iron. FDRI is cumbersome to acquire data because it requires scans from multiple systems and field strengths to calculate R2 (1/R2). Additionally, it is subject to scanner variability.[41]

Measurements from the 3 methods (FDRI, R2*, and QSM)[17,42,45] correlate with postmortem iron measurements from the seminal work by Hallgren and Sourander.[43] FDRI is believed to be impervious to the presence of myelin as R2* and phase are; however, gray matter is not well-myelinated so the confounding effects from myelin may be negligible.[41] Furthermore, smaller changes in iron as well as heterogeneity within structures can be more easily detected using R2* and QSM, with the latter being the most sensitive.[17] We noted a discrepancy in the results for the GP, THA, and the SN when comparing QSM and R2* results in discriminating groups. The GP is a known source of physiologic mineralization and calcification, which may explain the discrepant (though nonsignificant) results between the 2 measures. QSM can discriminate between paramagnetic signal like nonheme iron and diamagnetic signal from mineralization and
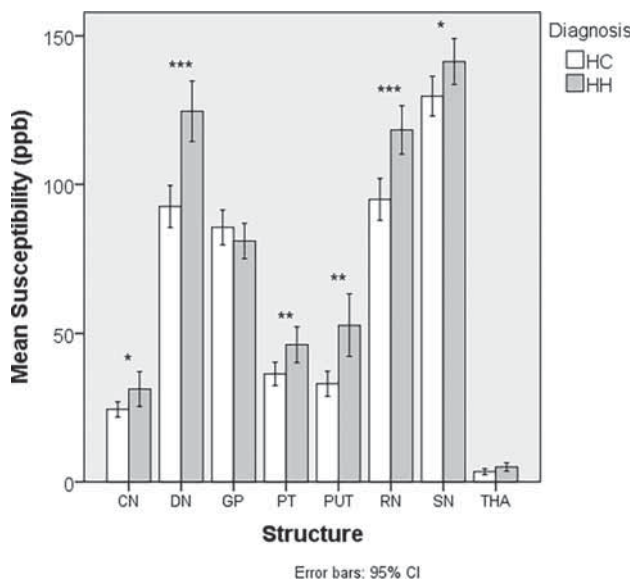
FIG 2. Comparison of susceptibility (parts per billion) between patients with HH and HC. *Asterisk* indicates $P < .05$; *double asterisks, $P < .01$; triple asterisks, $P < .001$.*

FIG 3. Comparison of R2* (s^{-1}) between patients with HH and HC. *Double asterisks* indicate $P < .01$; *triple asterisks, $P < .001$.*

calcification, whereas R2* mapping cannot. When comparing the QSM and R2* plots in Figs 2 and 3 for the GP, we did not see a clear separation between the groups on the QSM plot, demonstrating the additive effect of both diamagnetic and paramagnetic substances on R2* values.[44] The differences in the results between the methods when evaluating the THA and SN may be due to the heterogeneity of iron both within the group, because there were some cases with excessive iron, as well as within the structures themselves. Therefore, future analyses may consider using thresholding approaches to reduce within-structure variance.[45]

The susceptibility and R2* results for the HC are in accordance with multiple articles.[46-48] Work from Ghassaban et al[48] compared iron content between subjects with Parkinson disease and aged HC using similar methods and found that QSM is more sensitive at detecting iron generally using the same processing algorithm with thinner sliced data. Although we did not compare the sensitivity or specificity of QSM and R2* in discriminating patients with HH and HC on the basis of on iron content, Feng et al[49] have also reported less variation in QSM results compared with R2*. Yi and Sethi[47] have shown repeatability with multisite, multiscanner data using iterative SWIM reconstruction methods in a large, multi-site cohort of subjects. Although iterative SWIM can mitigate streaking artifacts inherent in truncated k-space division susceptibility mapping, the weighted combination of SWIMs by TE may lessen these effects while providing good SNR. Using a structurally constrained iterative SWIM approach may reduce noise and streaking artifacts even further.[22]

Although QSM and R2* are generally highly stable measurements, they are still subject to multiple sources of error from collection and errors propagated from the different processing steps.[10] Susceptibility is a relative measurement in that the values reported are changes compared with the surrounding tissue. We did not use a reference area such as WM or CSF, and whether the effect size of iron deposition in hemochromatosis is large enough
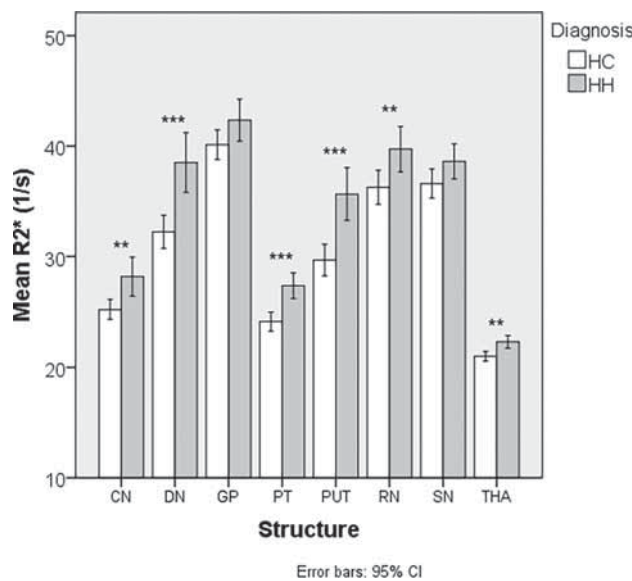
compared to the magnitude of iron in a reference area remains to be seen. It is possible that the THA, being close in susceptibility to WM ($\sim$0 parts per billion), may have been affected by these shifts in QSM that led to similar susceptibility values between patients with HH and HC. R2* has an advantage because it does not need a reference region to normalize measurements. On the other hand, for abnormally high iron, the lack of signal in the images will cause the algorithm to fail. In this particular study, we capitalized on the multiecho nature of the sequence and created not only R2* maps but also QSM with higher SNR as opposed to a single-echo approach. If scanning time is an issue, then single-echo approaches for QSM may be run to save time.[44] Additionally, short TEs (10–15 ms) may be beneficial to collect data to avoid phase aliasing for subjects with abnormally high iron content.

This study has several limitations: 1) Manual demarcation of ROIs may generate unwanted sources of error from inter-rater variation; therefore, using an automated deep gray matter segmentation technique may help mitigate these errors.[48] 2) This study is cross-sectional in nature and only provides a snapshot of iron content in time for an individual. Future study designs should be longitudinal; this approach may yield estimates of change and provide information about the cause-and-effect relationship of iron deposition with respect to disease progression or treatment models. 3) Not all subjects with HH had abnormal iron, and there was overlap with some of the HC.

CONCLUSIONS

Subjects with HH have abnormal brain iron in the DGM compared with controls. QSM and R2* are complementary ways to noninvasively quantify putative iron content from 1 MR imaging sequence. Future study designs should involve multiple time points to track iron deposition longitudinally.

REFERENCES

1. Bartzokis G, Lu PH, Tishler TA, et al. **Prevalent iron metabolism gene variants associated with increased brain ferritin iron in healthy older men.** *J Alzheimers Dis* 2010;20:333–41 CrossRef Medline

2. Bartzokis G, Lu PH, Tingus K, et al. **Gender and iron genes may modify associations between brain iron and memory in healthy aging.** *Neuropsychopharmacology* 2011;36:1375–84 CrossRef Medline

3. Hagemeier J, Ramanathan M, Schweser F, et al. **Iron-related gene variants and brain iron in multiple sclerosis and healthy individuals.** *Neuroimage Clin* 2018;17:530–40 CrossRef Medline

4. Brissot P, Cavey T, Ropert M, et al. **Genetic hemochromatosis: pathophysiology, diagnostic and therapeutic management.** *Presse Med* 2017;46:e288–95 CrossRef Medline

5. Powell LW, Seckington RC, Deugnier Y. **Haemochromatosis.** *Lancet* 2016;388:706–16 CrossRef Medline

6. Milman NT, Schioedt FV, Junker AE, et al. **Diagnosis and treatment of genetic HFE-hemochromatosis: the Danish aspect.** *Gastroenterology Res* 2019;12:221–32 CrossRef Medline

7. Nielsen JE, Jensen LN, Krabbe K. **Hereditary haemochromatosis: a case of iron accumulation in the basal ganglia associated with a parkinsonian syndrome.** *J Neurol Neurosurg Psychiatry* 1995;59:318–21 CrossRef Medline

8. Golfeyz S, Lewis S, Weisberg IS. **Hemochromatosis: pathophysiology, evaluation, and management of hepatic iron overload with a focus on MRI.** *Expert Rev Gastroenterol Hepatol* 2018;12:767–78 CrossRef Medline

9. Labranche R, Gilbert G, Cerny M, et al. **Liver iron quantification with MR imaging: a primer for radiologists.** *Radiographics* 2018;38:392–412 CrossRef Medline

10. Wang R, Xie G, Zhai M, et al. **Stability of R2* and quantitative susceptibility mapping of the brain tissue in a large scale multi-center study.** *Sci Rep* 2017;7:45261 CrossRef Medline

11. Ropele S, Wattjes MP, Langkammer C, et al. **Multicenter R2* mapping in the healthy brain.** *Magn Reson Med* 2014;71:1103–07 CrossRef Medline

12. Wang C, Foxley S, Ansorge O, et al. **Methods for quantitative susceptibility and R2* mapping in whole post-mortem brains at 7T applied to amyotrophic lateral sclerosis.** *Neuroimage* 2020;222:117216 CrossRef Medline

13. Zheng W, Nichol H, Liu S, et al. **Measuring iron in the brain using quantitative susceptibility mapping and X-ray fluorescence imaging.** *Neuroimage* 2013;78:68–74 CrossRef Medline

14. Haacke EM, Liu S, Buch S, et al. **Quantitative susceptibility mapping: current status and future directions.** *Magn Reson Imaging* 2015;33:1–25 CrossRef Medline

15. Yan F, He N, Lin H, et al. **Iron deposition quantification: applications in the brain and liver.** *J Magn Reson Imaging* 2018;48:301–17 CrossRef Medline

16. Ghassaban K, Liu S, Jiang C, et al. **Quantifying iron content in magnetic resonance imaging.** *Neuroimage* 2019;187:77–92 CrossRef Medline

17. Haacke EM, Cheng NY, House MJ, et al. **Imaging iron stores in the brain using magnetic resonance imaging.** *Magn Reson Imaging* 2005;23:1–25 CrossRef Medline

18. Smith S. **Fast robust automated brain extraction.** *Hum Brain Mapp* 2002;17:143–55 CrossRef Medline

19. Abdul-Rahman HS, Gdeisat MA, Burton DR, et al. **Fast and robust three-dimensional best path phase unwrapping algorithm.** *Appl Opt* 2007;46:6623–35 CrossRef Medline

20. Schweser F, Deistung A, Lehr BW, et al. **Quantitative imaging of intrinsic magnetic tissue properties using MRI signal phase: an approach to in vivo brain iron metabolism?** *Neuroimage* 2011;54:2789–807 CrossRef Medline

21. Tang J, Liu S, Neelavalli J, et al. **Improving susceptibility mapping using a threshold-based K-space/image domain iterative reconstruction approach.** *Magn Reson Med* 2013;69:1396–1407 CrossRef Medline

22. Gharabaghi S, Liu S, Wang Y, et al. **Multi-echo quantitative susceptibility mapping for Strategically Acquired Gradient Echo (STAGE) imaging.** *Front Neurosci* 2020;14:581474 CrossRef Medline

23. Chen Y, Liu S, Wang Y, et al. **STrategically Acquired Gradient Echo (STAGE) imaging, Part I: creating enhanced T1 contrast and standardized susceptibility weighted imaging and quantitative susceptibility mapping.** *Magn Reson Imaging* 2018;46:130–39 CrossRef Medline

24. Sethi SK, Kisch SJ, Ghassaban K, et al. **Iron quantification in Parkinson's disease using an age-based threshold on susceptibility maps: the advantage of local versus entire structure iron content measurements.** *Magn Reson Imaging* 2019;55:145–52 CrossRef Medline

25. Brissot P, Pietrangelo A, Adams PC, et al. **Haemochromatosis.** *Nat Rev Dis Prim* 2018;4:18016 CrossRef Medline

26. Brissot P, Troadec MB, Loréal O, et al. **Pathophysiology and classification of iron overload diseases; update 2018.** *Transfus Clin Biol* 2019;26:80–88 CrossRef Medline

27. Pietrangelo A. **Hereditary hemochromatosis: pathogenesis, diagnosis, and treatment.** *Gastroenterology* 2010;139:393–408 CrossRef Medline

28. Kawabata H. **The mechanisms of systemic iron homeostasis and etiology, diagnosis, and treatment of hereditary hemochromatosis.** *Int J Hematol* 2018;107:31–43 CrossRef Medline

29. Katsarou MS, Papasavva M, Latsi R, et al. *Hemochromatosis: Hereditary Hemochromatosis and HFE gene.* Elsevier; 2019

30. Russo N, Edwards M, Andrews T, et al. **Hereditary haemochromatosis is unlikely to cause movement disorders.** *J Neurol* 2004;251:849–52 CrossRef Medline

31. Wade QW, Chiou B, Connor JR. Iron uptake at the blood-brain barrier is influenced by sex and genotype. In: Wade QW, Chiou B, Connor JR. *Adv Pharmacol* 2019;84:123–45 CrossRef

32. Nandar W, Connor JR. **HFE gene variants affect iron in the brain.** *J Nutr* 2011;141:729S–39S CrossRef Medline

33. Connor JR, Milward EA, Moalem S, et al. **Is hemochromatosis a risk factor for Alzheimer's disease?** *J Alzheimers Dis* 2001;3:471–77 CrossRef Medline

34. Hänninen MM, Haapasalo J, Haapasalo H, et al. **Expression of iron-related genes in human brain and brain tumors.** *BMC Neurosci* 2009;10:36 CrossRef Medline

35. Bastin JM, Jones M, O'Callaghan CA, et al. **Kupffer cell staining by an HFE-specific monoclonal antibody: Implications for hereditary haemochromatosis.** *Br J Haematol* 1998;103:931–41 CrossRef Medline

36. Johnstone D, Milward EA. **Molecular genetic approaches to understanding the roles and regulation of iron in brain health and disease.** *J Neurochem* 2010;113:1387–402 CrossRef Medline

37. Kalpouzos G, Mangialasche F, Falahati F, et al. **Contributions of HFE polymorphisms to brain and blood iron load, and their links to cognitive and motor function in healthy adults.** *Neuropsychopharmacol Rep* 2021;41:393–404 CrossRef Medline

38. Sharma S, Sethi SK, Reese D, et al. **Brain iron deposition and movement disorders in hereditary haemochromatosis without liver failure: a cross-sectional study.** *Eur J Neurol* 2022;29:1417–26 CrossRef Medline

39. Berg D, Hoggenmüller U, Hofmann E, et al. **The basal ganglia in haemochromatosis.** *Neuroradiology* 2000;42:9–13 CrossRef Medline

40. Kumar N, Rizek P, Sadikovic B, et al. **Movement disorders associated with hemochromatosis.** *Can J Neurol Sci* 2016;43:801–08 CrossRef Medline

41. Daugherty A, Raz N. **Age-related differences in iron content of subcortical nuclei observed in vivo: a meta-analysis.** *Neuroimage* 2013;70:113–21 CrossRef Medline

42. Pfefferbaum A, Adalsteinsson E, Rohlfing T, et al. **MRI estimates of brain iron concentration in normal aging: comparison of field-dependent (FDRI) and phase (SWI) methods.** *Neuroimage* 2009;47:493–500 CrossRef Medline

43. Hallgren B, Sourander P. **The effect of age on the non-haemin iron in the human brain.** *J Neurochem* 1958;3:41–51 CrossRef Medline

44. Langkammer C, Schweser F, Krebs N, et al. **Quantitative susceptibility mapping (QSM) as a means to measure brain iron? A post mortem validation study.** *Neuroimage* 2012;62:1593–99 CrossRef Medline

45. Liu M, Liu S, Ghassaban K, et al. **Assessing global and regional iron content in deep gray matter as a function of age using susceptibility mapping.** *J Magn Reson Imaging* 2016;44:59–71 CrossRef Medline

46. Acosta-Cabronero J, Betts MJ, Cardenas-Blanco A, et al. **In vivo MRI mapping of brain iron deposition across the adult lifespan.** *J Neurosci* 2016;36:364–74 CrossRef Medline

47. Li Y, Sethi SK, Zhang C, et al. **Iron content in deep gray matter as a function of age using quantitative susceptibility mapping: a multi-center study.** *Front Neurosci* 2021;14:607705 CrossRef Medline

48. Ghassaban K, He N, Sethi SK, et al. **Regional high iron in the substantia nigra differentiates Parkinson's disease patients from healthy controls.** *Front Aging Neurosci* 2019;11:106 CrossRef Medline

49. Feng X, Deistung A, Reichenbach JR. **Quantitative susceptibility mapping (QSM) and R_2^* in the human brain at 3 T.** *Z Med Phys* 2018;28:36–48 CrossRef Medline

Flow Diversion for ICA Aneurysms with Compressive Neuro-Ophthalmologic Symptoms: Predictors of Morbidity, Mortality, and Incomplete Aneurysm Occlusion

D.P.O. Kaiser, G. Boulouis, S. Soize, V. Maus, S. Fischer, D. Lobsien, J. Klisch, H. Styczen, C. Deuschl, N. Abdullayev, C. Kabbasch, A. Jamous, D. Behme, K. Janot, G. Bellanger, C. Cognard, L. Pierot, M. Gawlitza, and the Compressive Aneurysm Study Group

ABSTRACT

BACKGROUND AND PURPOSE: Flow diversion is an effective treatment for aneurysms of the ICA with compression-related neuro-ophthalmologic symptoms, especially when treatment is initiated early after symptom onset and aneurysm occlusion is complete. However, non-negligible complication rates have been reported. Our aim was to identify risk factors for morbidity/mortality and incomplete aneurysm occlusion.

MATERIALS AND METHODS: We performed a secondary analysis of a previous publication, which included all patients treated with flow diversion for an unruptured aneurysm of the ICA with compression-related symptoms.

RESULTS: Fifty-four patients with 54 aneurysms (48 women, 88.9%; mean age, 59.2 [SD, 15.9] years; range, 21–86 years) treated with flow diversion were included. We observed morbidity and mortality rates of 7.4% and 3.7%. Increasing age (OR per decade, 3.2; 95% CI, 1.23–8.49; $P = .02$) and dual-antiplatelet therapy with ticagrelor (OR, 13.9; 95% CI, 1.16–165.97; $P = .04$) were significantly associated with morbidity/mortality. After a median follow-up of 13.3 [SD, 10.5] months, the rates of complete aneurysm occlusion, neck remnant, and aneurysm remnant were 74%, 14%, and 12%. Incomplete occlusion at follow-up was less frequently observed in aneurysms treated with additional coil embolization (OR, 0.1; 95% CI, 0.01–0.86; $P = .04$).

CONCLUSIONS: Although a promising treatment for compressive ICA aneurysms, flow diversion carries a relevant risk for complications and incomplete aneurysm occlusion. Our results may help identify patients in which flow diversion may not be the ideal treatment method. Additional coil embolization increased the likelihood of complete aneurysm occlusion at follow-up.

ABBREVIATIONS: CN = cranial nerve; FD = flow diverter; PVO = parent vessel occlusion

Intracranial aneurysms of the ICA may cause mass effect and induce neuro-ophthalmologic disorders by compressing cranial nerves (CNs). Visual impairment or diplopia induced by CN palsy is disabling and often leads to urgent treatment of the underlying aneurysms, which are often large and/or rapidly growing.[1]

Since their introduction, flow diverters (FDs) have revolutionized endovascular treatment paradigms, particularly for unruptured intracranial aneurysms. FDs have a positive effect on resolving the mass effect of aneurysms by reducing intrasaccular filling and promoting collapse and healing, while preserving the vessel in contrast to parent vessel occlusion (PVO).[2] However, the literature on the use of FDs in ICA aneurysms causing compressive neuro-ophthalmologic symptoms is scarce.[2-6] In a recent study, we have shown that FDs are very effective for this indication

Table 1: Factors associated with morbidity/mortality

	Morbidity/Mortality (n = 6)	No Morbidity/Mortality (n = 48)	Univariate Analysis P Value	Multivariate Analysis OR (95% CI)	P Value
Patient characteristics					
Female sex	6/6 (100%)	42/48 (87.5%)	.36		
Age (yr)	Mean, 73.8 (SD, 13.4)	Mean, 57 (SD, 15.3)	.03	3.27 (1.23–8.49)[a]	.02
Hypertension	6/6 (100%)	19/48 (39.6%)	.05		NS[b]
Current smoker	1/6 (16.7%)	11/48 (22.9%)	.73		
Previous smoker	2/6 (33.3%)	12/48 (25%)	.66		
Diabetes mellitus	1/6 (16.7%)	1/48 (2.1%)	.08		
Family history	0/6 (0%)	2/48 (4.2%)	.61		
Aneurysm characteristics					
Aneurysm size (mm)	Mean, 19.4 (SD, 8.4)	Mean, 15.8 (SD, 7.4)	.28		
Left-sided aneurysm	3/6 (50%)	33/48 (68.8%)	.36		
Intradural aneurysm	5/6 (83.3%)	28/48 (58.3%)	.24		
Fusiform aneurysm	3/6 (50%)	18/48 (37.5%)	.55		
Aneurysmal thrombus	2/6 (33.3%)	14/48 (29.2%)	.83		
Treatment-related data					
Ticagrelor	5/6 (83.3%)	19/48 (39.6%)	.04	13.9 (1.16–165.97)	.04
≥2 flow diverters	1/6 (16.7%)	2/48 (4.2%)	.21		
Additional coiling	3/6 (50%)	16/48 (33.3%)	.42		

Note:—NS indicates not significant.
[a] Age was grouped into decades for regression analysis.
[b] Variable not included in the regression mode.

regarding both clinical and anatomic outcome. Recovery of CN palsies was associated with early initiation of treatment after symptom onset and with complete aneurysm occlusion.[7] However, we observed a non-negligible risk of permanent neurologic deficits and death. Furthermore, a substantial number of aneurysms were not completely occluded at follow-up.

By analyzing the factors associated with treatment-related morbidity/mortality and incomplete aneurysm occlusion, we aimed to define patient and aneurysm characteristics for which flow diversion should be indicated with caution and other treatment strategies may be preferable.

MATERIALS AND METHODS
Study Design and Cohort
We conducted a retrospective, observational, binational multicenter study with data from 9 hospitals in Germany and France. We included consecutively treated patients between January 1, 2015, and December 31, 2020, with unruptured intracranial aneurysms of the ICA and associated compression-induced neuropathy of the oculomotor nerves (ie, CNs III, IV, VI) and/or the optic pathway. Treatment was performed using flow diversion alone or in conjunction with coil embolization. The study methods are described in detail in our previous publication.[7] The present work is a secondary analysis of the data set.

Ethics
The study was approved by the ethics committee of Dresden/Germany (Ethikkommission an der Technischen Universität Dresden) and was conducted in accordance with the Declaration of Helsinki. Patient consent was waived due to the retrospective nature of the study. The contributing centers obtained ethics committee approval in accordance with regional or national standards.

Patient and Aneurysm Characteristics
We collected the following patient characteristics: age, sex, and the presence of high blood pressure, diabetes mellitus, family history of intracranial aneurysms/nontraumatic SAH, and other relevant comorbidities. We collected information on the patients' current and previous smoking habits.

Target aneurysms were classified as either saccular or fusiform and were rated as located in the intra- or extradural space. We measured the maximum aneurysm sac diameter and assessed the presence of intra-aneurysmal thrombus.

Morbidity/Mortality and Imaging Outcomes
We assessed treatment-related mortality and morbidity. Morbidity was defined as neurologic deficits at last follow-up not present at the initial patient presentation. Hemorrhagic and ischemic complications were defined as cross-sectional imaging evidence of hemorrhage or infarction associated with a permanent neurologic deficit or death.

Imaging outcomes obtained by DSA, MRA, or CTA were graded by the respective contributing center according to the widely accepted classification: "aneurysm remnant," "neck remnant," and "complete occlusion."[8] If retreatment of the target aneurysm was performed with an FD, final clinical and imaging results of the patient were assessed at the last follow-up, and these patients were not excluded from the analysis.

Statistical Analysis
Frequency counts are presented as percentages. Continuous and ordinally scaled variables were tested for normal distribution using the Kolmogorov-Smirnov test and are presented as mean (SD). Continuous parameters were compared using the Student t test. Contingency analyses for categoric variables were performed

Table 2: Factors associated with incomplete aneurysm occlusion at last anatomic follow-up

Variable	Incomplete Occlusion (n = 13)	Complete Occlusion (n = 37)	Univariate Analysis P Value	Multivariate Analysis OR (95% CI)	P Value
Patient characteristics					
Female sex	10/13 (76.9%)	34/37 (91.9%)	.15		
Age (yr)	Mean, 62.3 (SD, 19.1)	Mean, 55.8 (SD, 13.5)	.19		
Hypertension	5/13 (38.5%)	17/37 (45.9%)	.64		
Current smoker	1/13 (7.7%)	11/37 (29.7%)	.11		
Previous smoker	2/13 (15.4%)	11/37 (29.7%)	.31		
Diabetes mellitus	1/13 (7.7%)	1/37 (2.7%)	.43		
Family history	1/13 (7.7%)	1/37 (2.7%)	.43		
Aneurysm characteristics					
Aneurysm size (mm)	Mean, 17.3 (SD, 6.7)	Mean, 15.4 (SD, 7.5)	.42		
Left-sided aneurysm	10/13 (76.9%)	25/37 (67.6%)	.52		
Intradural aneurysm	5/13 (38.5%)	26/37 (70.3%)	.04	0.28 (0.05–1.56)	.15
Fusiform aneurysm	8/13 (61.5%)	9/37 (24.3%)	.02	5.2 (0.97–27.56)	.05
Aneurysmal thrombus	5/13 (38.5%)	10/37 (27%)	.44		
Treatment-related data					
Ticagrelor	5/13 (38.5%)	17/37 (45.9%)	.64		
≥2 flow diverters	1/13 (26%)	0/37 (0%)	.09		NS[a]
Additional coiling	2/13 (10.5%)	17/37 (45.9%)	.05	0.1 (0.01–0.86)	.04
Follow-up					
Last anatomic follow-up (mo)	Mean, 9 (SD, 7)	Mean, 14.6 (SD, 11.1)	.097	0.88 (0.78–0.99)	.03

Note:—NS indicates not significant.

[a] Variable not included into the regression model.

using the χ^2 test. Multivariate analyses were performed using a logistic regression analysis with stepwise backward selection, with an entry and exit threshold of 0.20. Factors with a $P < .10$ at univariate analysis were included in the regression analysis. Age was grouped into decades for multivariate analysis. The OR is presented with its 95% CI. Statistical significance was defined as a P value $< .05$. Statistical analysis was performed using SPSS 27 (IBM).

RESULTS
Study Demographics
Fifty-four patients with 54 aneurysms were identified and included in the analysis (48 women, 88.9%). The mean age was 59.2 (SD, 15.9) years with a range from 21 to 86 years. Detailed demographics are described in the Online Supplemental Data. In the current analysis, we excluded 1 patient of the previous data set who was retreated with carotid artery deconstruction after asymptomatic intra-aneurysmal migration of the proximal end of an FD construct (2 devices) and balloon test occlusion in the first week after the index procedure.[7,9]

Procedural Characteristics
We treated 51 patients (94.4%) with a single FD; 1 patient (1.9%) was treated with a construct of 2; and 2 patients (3.7%), with a construct of 3 devices. We used the following devices: Derivo (Acandis), FRED (MicroVention), p64 (phenox), Pipeline Embolization Device (Medtronic), and Surpass (Stryker Neurovascular). Additional coiling during the procedure was performed in 19 patients (35.2%). Five patients (9.3%) underwent retreatment with implantation of additional FD stents. All patients received periprocedural dual-antiplatelet therapy started before the intervention and continued it for at least 3 months after the intervention. Ticagrelor was used as a second medication

in addition to acetylsalicylic acid or clopidogrel in 24 (44.4%) patients; the remaining patients received acetylsalicylic acid/clopidogrel in combination.

Morbidity/Mortality
During follow-up, 2 patients (3.7%) had hemorrhagic complications with permanent neurologic deficits, and 1 patient (1.9%) died from a hemorrhagic complication. Two patients (3.7%) experienced ischemic complications with permanent deficits. One patient (1.9%) died within the first month after the intervention from an unknown cause. Due to absence of other identifiable causes, we considered this death to be treatment-related. With total morbidity and mortality rates of 7.4% and 3.7%, respectively, the cumulative treatment-related morbidity/mortality rate was 11.1%.

Risk Factors for Morbidity/Mortality
In univariate analysis, 2 factors were significantly associated with morbidity/mortality: older age (mean, 73.8 [SD, 13.4] years versus 57 [SD, 15.3] years; $P = .03$) and ticagrelor intake (5/6 [83.3%] versus 19/48 [39.6%]; $P = .04$). A tendency toward a significant association with morbidity/mortality was furthermore observed for hypertension (6/6 [100%] versus 19/48 [39.6%]; $P = .05$). In multivariate analysis, age (OR per decade of age, 3.2; 95% CI, 1.23–8.49; $P = .02$) and ticagrelor intake (OR, 13.9; 95% CI, 1.16–165.97; $P = .04$) were significantly associated with morbidity/mortality. Data are presented in Table 1. We assessed the association of ticagrelor intake with ischemic and hemorrhagic morbidity/mortality by univariate analysis (Online Supplemental Data) and found no statistically significant differences ($P = .19$).

Anatomic Outcomes
Vascular imaging follow-up was available for 50 patients at a mean of 13.3 (SD, 10.5) months after the initial procedure. Rates of

complete aneurysm occlusion, neck remnant, and aneurysm remnant were 74% (37/54), 14% (7/54), and 12% (6/54), respectively.

Risk Factors for Incomplete Aneurysm Occlusion

In univariate analysis, incomplete aneurysm occlusion occurred significantly more frequently in fusiform aneurysm morphology (8/13 [61.5%] versus 9/37 [24.3%]; $P = .02$) and less frequently in an intradural aneurysm location (5/13 [38.5%] versus 26/37 [70.3%]; $P = .04$). In the multivariate analysis, additional coil embolization (OR, 0.1; 95% CI, 0.01–0.86; $P = .04$) and a longer time interval from treatment to last anatomic follow-up (OR, 0.88; 95% CI, 0.78–0.99; $P = .03$) were less frequently associated with incomplete aneurysm occlusion. Fusiform aneurysm morphology (OR, 5.2; 95% CI, 0.97–27.56; $P = .05$) showed a nonsignificant trend toward incomplete occlusion in multivariate analysis. Data are presented in Table 2.

DISCUSSION

In this study, we found patient-, aneurysm-, and treatment-related factors that were associated with a higher likelihood of morbidity/mortality and incomplete aneurysm occlusion in flow diversion treatment of patients with neuro-ophthalmologic symptoms due to compressive ICA aneurysms. Our findings may help to identify patients in which flow diversion may not be the ideal treatment method and risk factors that can potentially be avoided in advance.

As pointed out in our previous study, flow diversion for compressive ICA aneurysms with ophthalmologic symptoms is associated with a high risk of complications.[7] With morbidity and mortality rates of 7.4% and 3.7%, respectively, the cumulative treatment-related morbidity/mortality rate was 11.1% in our study population. This is considerably higher compared with the findings of the Pipeline Embolization Device for Uncoilable or Failed Aneurysms (PUFS) trial (morbidity/mortality rate of 5.6%,[10] but it is in line with data from the International Retrospective Study of the Pipeline Embolization Device (IntrePED) trial, in which neurologic morbidity/mortality was observed in 9.2% of patients with unruptured aneurysms of the ICA measuring >10 mm.[11] In our study, 2 factors were associated with treatment-related morbidity/mortality in multivariate analysis: patient age and ticagrelor intake.

Patient age has been previously described as a risk factor for morbidity/mortality in a subgroup analysis of the IntrePED data.[12] In that study, mortality rates after flow diversion were significantly higher in patients older than 70 years of age (7.4%). Moreover, in a multivariate analysis, the authors found a significant association of increasing age with neurologic mortality, combined neurologic morbidity and mortality, all-cause mortality, and intracranial hemorrhage. The mean patient age in the IntrePED trial was 57.7 (SD, 13.8) years. In our study, the mean patient age was comparable, with 58.9 (SD, 15.9) years, and the risk of morbidity/mortality increased 3.2 times per decade of age. These results indicate that in elderly patients, FDs for compressive ICA aneurysms should be considered only after careful weighing of the risk-benefit ratio and discussion of alternative options with the patient. Most important, treatment decisions should take into account that chances of complete symptom recovery may decrease with increasing age, fusiform aneurysm

morphology, and a longer delay between the onset of ocular symptoms and endovascular treatment.[7]

A valuable, well-established alternative to flow diversion for ICA aneurysms is PVO. In a study from 2016, symptoms improved or resolved after PVO in 88% of 62 patients with large or giant ICA aneurysms and cranial nerve dysfunction; the rate of permanent neurologic complications was 1.1% (1/88).[13] Another study reported improved or resolved symptoms in 72% of 32 patients with ophthalmologic symptoms; major persistent ischemic symptoms (mRS > 1) occurred in 5.5% of 56 patients with ICA aneurysms treated with PVO.[14] However, the oldest patient in that study was 66 years of age; thus, the cohort is not comparable with ours. One must additionally take into account that PVO is not feasible in about one-third of patients without prior bypass surgery in case of a failed occlusion test.[13] On the other hand, surgical clipping is also an effective, well-established alternative for symptomatic aneurysms of the para- and supraclinoid ICA, including the posterior communicating artery.[5,6,15] In summary, all available methods should be discussed for each treatment indication, and we believe that conservative management should be preferred in elderly patients with low chances of symptom recovery and a low, or rather nonexistent, risk of SAH, particularly from extradural aneurysms.

The association of ticagrelor intake with morbidity/mortality is surprising because several studies have reported a favorable efficacy and safety profile of ticagrelor in neuroendovascular procedures.[16-19] We did not observe statistically significant differences regarding hemorrhagic or ischemic complications depending on the antiplatelet medication. Our finding should encourage further studies to seek an explanation. However, we suppose that the association is rather related to a center-based selection bias.

Ophthalmologic symptom relief is related to complete aneurysm occlusion.[7] We observed increased rates of complete occlusion at follow-up when additional coil embolization was performed. The literature on this aspect is currently ambiguous, with studies showing increased rates of complete aneurysm occlusion[20,21] and studies reporting similar results after flow diversion with additional coiling.[22] Of note, additional coil embolization had no effect on clinical symptom recovery in our previous study.[7]

We observed increased rates of incomplete aneurysm occlusion after flow diversion for fusiform aneurysm morphology, but this finding was not significant in multivariate analysis. Fusiform aneurysm morphology is also a risk factor for incomplete ophthalmologic recovery.[7] A postmortem histopathologic study of 4 giant fusiform aneurysms revealed that endothelialization of an FD may not occur at all and that thrombus organization may not be initiated inside these aneurysms for as long as 1 year.[23] Altogether, incomplete healing after flow diversion of fusiform aneurysms with persisting mass effect and nonorganized intra-aneurysmal thrombus may be a hypothesis for our observation. The association between longer follow-up and complete occlusion is obvious, and progressive aneurysm occlusion with time has been described.[24]

Our study has limitations, its retrospective nature being the most important one. It also has decreased external validity because anatomic results are self-reported, and the severity and relevance of complications were not adjudicated by an independent clinical event committee. Further limitations are the nonstandardized

follow-up protocols and antiplatelet regimens. These limitations should be addressed in a large, prospective, consecutive patient cohort investigating this subject under controlled circumstances.

CONCLUSIONS

Flow diversion for compressive ICA aneurysms with ophthalmologic symptoms, though a promising technique, is associated with a significant complication rate. The most important risk factor for morbidity/mortality may be increasing patient age. Because relief of neuro-ophthalmologic symptoms is linked to complete aneurysm occlusion, risk factors for incomplete occlusion after flow diversion should be considered when making individual treatment decisions. Additional coil embolization increased the likelihood of complete aneurysm occlusion at follow-up in our study cohort.

Collaborators

Compressive Aneurysm Study Group: Pierre-François Manceau (Department of Neuroradiology, Hôpital Maison Blanche, 45 Rue Cognacq-Jay, Champagne-Ardenne University, Reims 51092, France; e-mail: pf.manceau@gmail.com); Maher Sahnoun (Department of Neuroradiology, Hôpital Maison Blanche, 45 Rue Cognacq-Jay, Champagne-Ardenne University, Reims 51092, France; e-mail: maher_sahnoun@yahoo.fr); Christophe Gelmini, (Department of Neuroradiology, Hôpital Maison Blanche, 45 Rue Cognacq-Jay, Champagne-Ardenne University, Reims 51092, France; e-mail: cgelmini@chu-reims.fr); Richard Bibi (Department of Interventional Neuroradiology, CHRU de Tours, Tours, France; e-mail: R.bibi@chu-tours.fr); Denis Herbreteau (Department of Interventional Neuroradiology, CHRU de Tours, Tours, France; e-mail: denis.herbreteau@univ-tours.fr); Heloïse Ifergan (Department of Interventional Neuroradiology, CHRU de Tours, Tours, France; e-mail: h.ifergan@chu-tours.fr); Nourou Dine Adeniran Bankolle (Department of Interventional Neuroradiology, CHRU de Tours, Tours, France; e-mail: bkadenir@gmail.com); and Jennifer Linn (Institute of Neuroradiology, University Hospital Carl Gustav Carus, Dresden, Germany; e-mail: jennifer.linn@ukdd.de).

REFERENCES

1. Micieli JA, Newman NJ, Barrow DL, et al. **Intracranial aneurysms of neuro-ophthalmologic relevance.** *J Neuroophthalmol* 2017;37:421–39 CrossRef Medline
2. Szikora I, Marosfoi M, Salomváry B, et al. **Resolution of mass effect and compression symptoms following endoluminal flow diversion for the treatment of intracranial aneurysms.** *AJNR Am J Neuroradiol* 2013;34:935–39 CrossRef Medline
3. Binyamin TR, Dahlin BC, Waldau B. **Resolution of third nerve palsy despite persistent aneurysmal mass effect after flow diversion embolization of posterior communicating artery aneurysms.** *J Clin Neurosci* 2016;31:207–09 CrossRef Medline
4. Sahlein DH, Fouladvand M, Becske T, et al. **Neuroophthalmological outcomes associated with use of the Pipeline Embolization Device: analysis of the PUFS trial results.** *J Neurosurg* 2015;123:897–905 CrossRef Medline
5. Silva MA, See AP, Dasenbrock HH, et al. **Vision outcomes in patients with paraclinoid aneurysms treated with clipping, coiling, or flow diversion: a systematic review and meta-analysis.** *Neurosurg Focus* 2017;42:E15 CrossRef Medline
6. Silva MA, See AP, Khandelwal P, et al. **Comparison of flow diversion with clipping and coiling for the treatment of paraclinoid aneurysms in 115 patients.** *J Neurosurg* 2019;130:1505–12 CrossRef Medline
7. Boulouis G, Soize S, Maus V, et al; Compressive Aneurysm Study Group. **Flow diversion for internal carotid artery aneurysms with compressive neuro-ophthalmologic symptoms: clinical and anatomical results in an international multicenter study.** *J Neurointerv Surg* 2021 Nov 18. [Epub ahead of print] CrossRef Medline
8. Raymond J, Guilbert F, Weill A, et al. **Long-term angiographic recurrences after selective endovascular treatment of aneurysms with detachable coils.** *Stroke* 2003;34:1398–1403 CrossRef Medline
9. Gawlitza M, Soize S, Manceau P-F, et al. **Delayed intra-aneurysmal migration of a flow diverter construct after treatment of a giant aneurysm of the cavernous internal carotid artery.** *J Neuroradiol* 2020;47:233–36 CrossRef Medline
10. Becske T, Kallmes DF, Saatci I, et al. **Pipeline for uncoilable or failed aneurysms: results from a multicenter clinical trial.** *Radiology* 2013;267:858–68 CrossRef Medline
11. Kallmes DF, Hanel R, Lopes D, et al. **International retrospective study of the Pipeline Embolization Device: a multicenter aneurysm treatment study.** *AJNR Am J Neuroradiol* 2015;36:108–115 CrossRef Medline
12. Brinjikji W, Kallmes DF, Cloft HJ, et al. **Age-related outcomes following intracranial aneurysm treatment with the Pipeline Embolization Device: a subgroup analysis of the IntrePED registry.** *J Neurosurg* 2016;124:1726–30 CrossRef Medline
13. Bechan RS, Majoie CB, Sprengers ME, et al. **Therapeutic internal carotid artery occlusion for large and giant aneurysms: a single center cohort of 146 patients.** *AJNR Am J Neuroradiol* 2016;37:125–29 CrossRef Medline
14. Labeyrie MA, Lenck S, Bresson D, et al. **Parent artery occlusion in large, giant, or fusiform aneurysms of the carotid siphon: clinical and imaging results.** *AJNR Am J Neuroradiol* 2015;36:140–45 CrossRef Medline
15. Gaberel T, Borha A, di Palma C, et al. **Clipping versus coiling in the management of posterior communicating artery aneurysms with third nerve palsy: a systematic review and meta-analysis.** *World Neurosurg* 2016;87:498–506.e4 CrossRef Medline
16. Chien SC, Chen CC, Chen CT, et al. **Ticagrelor versus clopidogrel in stent-assisted coil embolization of unruptured intracranial aneurysms.** *Interv Neuroradiol* 2021 Nov 18. [Epub ahead of print] CrossRef Medline
17. Moore JM, Adeeb N, Shallwani H, et al. **A multicenter cohort comparison study of the safety, efficacy, and cost of ticagrelor compared to clopidogrel in aneurysm flow diverter procedures.** *Neurosurgery* 2017;81:665–71 CrossRef Medline
18. Park KY, Ozaki T, Kostynskyy A, et al. **Ticagrelor versus clopidogrel in the dual antiplatelet regimen for intracranial stenting or flow-diverter treatment for unruptured cerebral aneurysms: a single-center cohort study.** *AJNR Am J Neuroradiol* 2021;42:1638–44 CrossRef Medline
19. Soize S, Foussier C, Manceau P-F, et al. **Comparison of two preventive dual antiplatelet regimens for unruptured intracranial aneurysm embolization with flow diverter/disrupter: a matched-cohort study comparing clopidogrel with ticagrelor.** *J Neuroradiol* 2019;46:378–83 CrossRef Medline

20. Zhang Q, Shao Q, Chang K, et al. **Safety and efficacy of coils in conjunction with the Pipeline Flex Embolization Device for the treatment of cerebral aneurysms.** *Front Neurol* 2021;12:651465 CrossRef Medline

21. Lin N, Brouillard AM, Krishna C, et al. **Use of coils in conjunction with the Pipeline Embolization Device for treatment of intracranial aneurysms.** *Neurosurgery* 2015;76:142–49 CrossRef Medline

22. Sweid A, Atallah E, Herial N, et al. **Pipeline-assisted coiling versus Pipeline in flow diversion treatment of intracranial aneurysms.** *J Clin Neurosci* 2018;58:20–24 CrossRef Medline

23. Szikora I, Turányi E, Marosfoi M. **Evolution of flow-diverter endothelialization and thrombus organization in giant fusiform aneurysms after flow diversion: a histopathologic study.** *AJNR Am J Neuroradiol* 2015;36:1716–20 CrossRef Medline

24. Becske T, Brinjikji W, Potts MB, et al. **Long-term clinical and angiographic outcomes following Pipeline Embolization Device treatment of complex internal carotid artery aneurysms: five-year results of the Pipeline for Uncoilable or Failed Aneurysms trial.** *Neurosurgery* 2017;80:40–48 CrossRef Medline

The Safety and Efficacy of Flow Diversion versus Conventional Endovascular Treatment for Intracranial Aneurysms: A Meta-analysis of Real-world Cohort Studies from the Past 10 Years

S. Li, C. Zeng, W. Tao, Z. Huang, L. Yan, X. Tian, and F. Chen

ABSTRACT

BACKGROUND: Although the flow diverter has advantages in the treatment of intracranial aneurysms, pooled studies that directly compare it with conventional endovascular treatments are rare.

PURPOSE: Our aim was to compare the safety and efficacy of flow-diverter and conventional endovascular treatments in intracranial aneurysms.

DATA SOURCES: We performed a comprehensive search of the literature using PubMed, EMBASE, and the Cochrane Database.

STUDY SELECTION: We included only studies that directly compared the angiographic and clinical outcomes of flow-diverter and conventional endovascular treatments.

DATA ANALYSIS: Random effects or fixed effects meta-analysis was used to pool the cumulative rate of short- and long-term angiographic and clinical outcomes.

DATA SYNTHESIS: Eighteen studies with 1001 patients with flow diverters and 1133 patients with conventional endovascular treatments were included; 1015 and 1201 aneurysm procedures were performed, respectively. The flow-diverter group had aneurysms of a larger size (standard mean difference, 0.22; 95% CI, 0.03–0.41; $P = .026$). There was a higher risk of complications in the flow-diverter group compared with the conventional endovascular group (OR, 1.4; 95% CI, 1.01–1.96; $P = .045$) during procedures. The follow-up angiographic results of flow-diverter treatment indicated a higher rate of complete occlusion (OR, 2.55; 95% CI, 1.70–3.83; $P < .001$) and lower rates of recurrence (OR, 0.24; 95% CI, 0.12–0.46; $P < .001$) and retreatment (OR, 0.31; 95% CI, 0.21–0.47; $P < .001$).

LIMITATIONS: Limitations include a retrospective, observational design in some studies, high heterogeneity, and selection bias.

CONCLUSIONS: Compared with the conventional endovascular treatments, the placement of a flow diverter may lead to more procedure-related complications, but there is no difference in safety, and it is more effective in the long term.

ABBREVIATIONS: BAC = balloon-assisted coiling; CEV = conventional endovascular; FD = flow diverter; IA = intracranial aneurysm; SAC = stent-assisted coiling; SMD = standard mean difference

Rapid technologic advances in endovascular treatments have been transforming the treatment modalities of intracranial aneurysms (IAs) in recent years. The Guglielmi detachable coil (Stryker), introduced in the early 1990s, provided an alternative to traditional surgical clipping in the treatment of IAs.[1] After that, reconstructive techniques such as balloon-assisted coiling (BAC) and stent-assisted coiling (SAC), were initially used.[2,3] Most recently, low-profile visualized intraluminal support (LVIS; MicroVention), a self-expandable, recyclable, braided stent, has also been widely adopted in clinical practice.[4]

Compared with these standard and conventional stent methods, flow diverters (FDs), like the Pipeline Embolization Device (PED; Medtronic) approved by the US Food and Drug Administration in 2011,[5,6] have greater metal coverage and have broader indications for the treatment of complex aneurysms, such as large and giant ICA aneurysms and fusiform, dissecting, and blood blister–like aneurysms.[7,8] However, the high rate of

aneurysm rupture, procedural mortality, and morbidity after placement of FDs has also raised many concerns.[9] It is crucial to assess the risk-benefit ratio for treatment with FDs by comparing it with conventional endovascular (CEV) treatments. However, early pooled analyses focused on only single-arm studies without directly comparing them. In our present work, we conducted a meta-analysis directly comparing the short- and long-term angiographic and clinical outcomes of the 2 methods in the past decade since the introduction of FDs.

MATERIALS AND METHODS
Search Strategy and Selection Criteria
Our searches of PubMed, EMBASE, and the Cochrane Database followed the principles of the common evidence medicine framework Patient Population, Intervention, Control, and Outcome: Did adult patients with intracranial aneurysms (patient population) who underwent an FD procedure (intervention) have better clinical outcomes, higher rates of aneurysm occlusion, and lower rates of mortality and procedure-related complications (outcomes) compared with patients who underwent the CEV (control) treatments from January 2010 to December 2020? Titles, abstracts, and keywords were searched using combinations of the terms including the following: "intracranial aneurysm," "cerebral aneurysm," "endovascular," "flow diverter," "flow diverting," "Pipeline," "PED," "Surpass," and "Tubridge." For detailed strategies, see the Online Supplemental Data. This meta-analysis was conducted according to the Preferred Reporting Items for Systematic Reviews and Meta-Analyses.[10] The systematic review protocol was registered in the International Prospective Register of Systematic Reviews (PROSPERO, ID: CRD42021282218). References generated from these searches were imported into the reference manager EndNote X9 (Thompson), and 2 authors (C.Z. and W.T.) systematically screened the references independently according to the inclusion criteria. Any discrepancies were resolved after discussion with the third author (S.L.). The inclusion criteria were the following: 1) direct comparison of FD and CEV treatment, including coiling alone, stent alone, SAC, BAC, and LVIS; 2) patients 18 years of age or older with intracranial aneurysms; and 3) detailed follow-up of angiographic and clinical outcomes. The exclusion criteria were the following: 1) fewer than 10 participants in either group; 2) no report of outcome variables; and 3) studies primarily focused on animals. Additionally, studies were included only if they were original articles published in English. Review articles, abstracts, case reports, systematic reviews and meta-analyses, letters to the editor, reviews, editorials, commentaries, studies on animal models, and basic science studies were not considered.

Data Extraction and Quality Assessment
A review and the data extraction of all included studies were performed by 3 authors (C.Z., W.T., and S.L.) independently. Any disagreements were resolved by consensus in meetings with all authors. Extracted study and patient characteristics included the author, year of publication, sex, age, hypertension, aneurysm size, number of participants in each group, follow-up duration, and the study design type, ie, whether the patient was matched by age, sex, aneurysm size, or aneurysm morphology. The periprocedural mortality, procedure-related complications such as ischemia and

hemorrhage, the immediate occlusion rates, and good outcomes (mRS 0–2) were extracted for each study. The follow-up angiographic and clinical outcomes were also included.

The quality of included studies was assessed using the Newcastle-Ottawa Scale for cohort studies.[11] This scale rates studies on the basis of 3 major aspects: selection, comparability, and ascertainment of the outcome of interest. We indicated high-quality choices by adding stars to the questions in each aspect if available. More stars indicated higher-quality studies. We included all eligible studies regardless of their assessed quality.

Statistical Analysis
All statistical analyses were performed using R version 4.1.0 (http://www.r-project.org). Dichotomous data from included studies were used to generate ORs, and continuous data were used for standard mean difference (SMD) with 95% confidence intervals by the DerSimonian and Laird models using the inverse-variance weighting method. A random effects model was used if the outcome had high heterogeneity and was noted as $I^2 > 50\%$; otherwise, the fixed-effects model was applied. The sources of heterogeneity were explored by subgroup analyses, meta-regression, and sensitivity analyses by the sequential exclusion of 1 study at a time. Publication bias was evaluated using a funnel plot based on the Egger regression test. Statistical significance was identified with $P < .05$.

RESULTS
Selected Studies
A total of 18 articles met the eligibility criteria for the meta-analysis after the full-text screening of 1001 patients with FDs and 1133 with CEV treatments, including 1015 and 1201 aneurysm procedures in the FD and CEV groups, respectively.[12 -29] The flow chart and selection process are shown in Fig 1. Among the selected studies, 15 used the PED, 1 used Pipeline or Surpass stent (Stryker Neurovascular), and 2 studies used the Tubridge (MicroPort Medical Company) as the only endovascular tool in the FD group. The Surpass and Pipeline stents without embolization tools were used in 2 studies in combination with other FD devices. Many different methods were applied in the conventional group. Detailed descriptions of the included studies are listed in the Online Supplemental Data. Eight matched studies were identified using propensity score matching analysis or other methods by matching patient age, sex, aneurysm size, or aneurysm morphology. All selected studies scored at least 6 stars in the Newcastle-Ottawa Scale grading system, indicating the high quality of these cohort studies (Table 1).

Patient Characteristics
Four usual variables were selected, including age, sex, hypertension, and the diameter of the aneurysm. There were no significant differences between the FD and CEV groups in terms of age (SMD, −0.23; 95% CI, −0.55–0.09; $P = .166$), proportion of women (OR, 1.02; 95% CI, 0.79–1.32; $P = .864$), and hypertension rates (OR, 1.19; 95% CI, 0.82–1.72; $P = .357$). Compared with the CEV group, the FD group had larger aneurysms (SMD, 0.22; 95% CI, 0.03–0.41; $P = .026$) (Online Supplemental Data).

Procedural Outcomes

Results were inconclusive about the risk of periprocedural mortality in the FD group compared with the conventional group (OR, 1.81; 95% CI, 0.73–4.48; $P = .197$), and there was no significant difference in the risk of periprocedural ischemia (OR, 0.85; 95% CI, 0.53–1.36; $P = .505$) and hemorrhage (OR, 1.51; 95% CI, 0.80–2.86; $P = .204$). Intriguingly, the combination of procedure-related complications (including ischemia, hemorrhage, mortality, and visual impairment) was statistically significant, with the FD group having a higher risk of procedural complications than the CEV group (OR, 1.4; 95% CI, 1.01–1.96; $P = .045$) (Online Supplemental Data). No significant differences were observed about immediate occlusions (OR, 0.27; 95% CI, 0.04–1.69; $P = .16$) (Online Supplemental Data). Subsequently, similar rates of good outcomes (mRS 0–2) at discharge were observed between the 2 groups (OR, 0.43; 95% CI, 0.15–1.23; $P = .117$) (Online Supplemental Data).

Long-term Angiographic and Clinical Outcomes

In contrast to the results of immediate occlusions, the follow-up angiographic results after flow diversion indicated higher rates of complete occlusion (OR, 2.55; 95% CI, 1.70–3.83; $P < .001$) but with a high heterogeneity of $I^2 = 68\%$ (Fig 2). Moreover, during follow-up, the FD group had lower recurrence rates
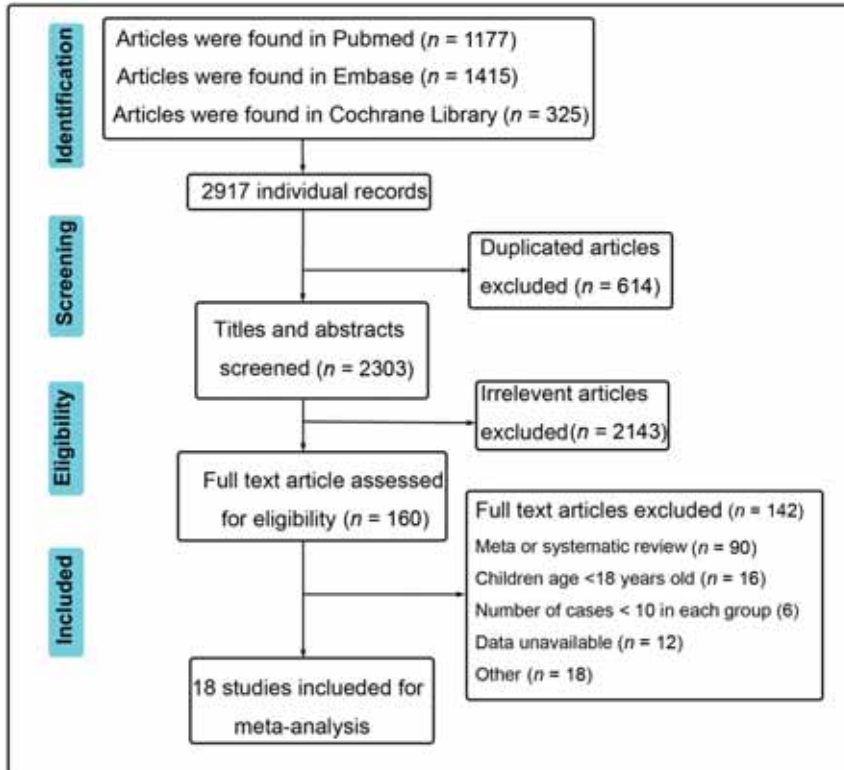
FIG 1. The flow chart of selecting eligible studies in the present work.

Table 1: The quality assessments based on Newcastle-Ottawa Scale for included cohort studies

| Author | Year | Selection | | | | Comparability | Outcome | | | Quality Scores |
		A	B	C	D	E	F	G	H	
Chalouhi et al[15]	2013	*	*	*	*	*	*	*	*	8
Zhang et al[29]	2016	*	*	*		*	*	*	*	7
Lanzino et al[20]	2012	*	*	*	*	*	*		*	7
Chalouhi et al[14]	2014	*	*	*	*	*	*	*	*	8
Chalouhi et al[13]	2017	*	*	*	*	*	*	*	*	8
Salem et al[24]	2020	*	*	*	*	*	*	*	*	8
Durst et al[17]	2016	*	*	*		*	*	*	*	7
Yupeng Zhang et al[28]	2019	*	*	*		*	*	*	*	7
Lu et al[22]	2019	*	*	*			*	*	*	6
Silva et al[25]	2019	*	*	*	*		*	*	*	7
Adeeb et al[12]	2017	*	*	*			*	*	*	6
Petr et al[23]	2016	*	*	*	*		*	*	*	7
Zanaty et al[27]	2014	*	*	*	*		*	*	*	7
Di Maria et al[16]	2015	*	*	*	*		*	*	*	7
Kim et al[19]	2014	*	*	*	*		*	*	*	7
Enriquez-Marulanda et al[18]	2019	*	*	*	*		*	*	*	7
Liu et al[21]	2018	*	*	*	*		*	*	*	7
Wang et al[26]	2019	*	*	*			*	*	*	6

Note:—Asterisk indicates that the included study meet the quality assessment criteria.
A, Representativeness of the exposed cohort.
B, Selection of the nonexposed cohort.
C, Ascertainment of exposure.
D, Demonstration that the outcome of interest was not present at the start of the study.
E, Comparability of cohorts on the basis of the design or analysis.
F, Assessment of outcome.
G, Was follow-up long enough for outcomes to occur?
H, Adequacy of follow-up of cohorts.
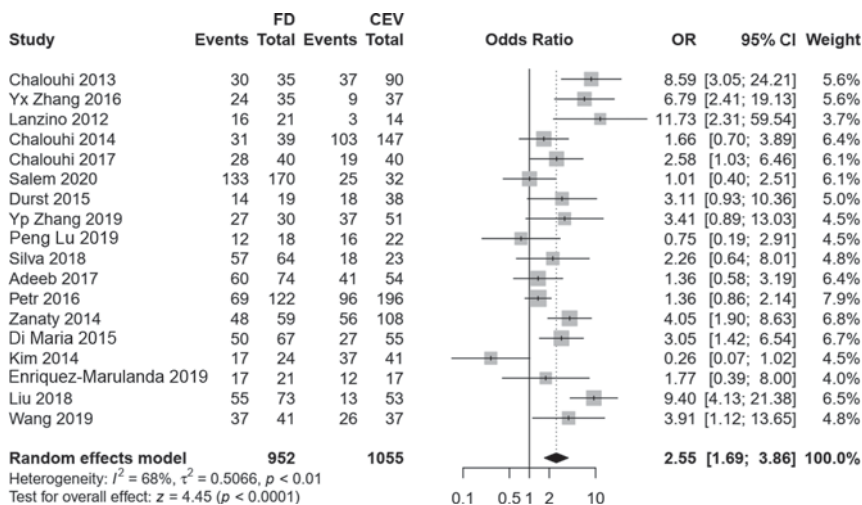
FIG 2. The complete occlusion rate of FD and CEV treatments at the last follow-up.
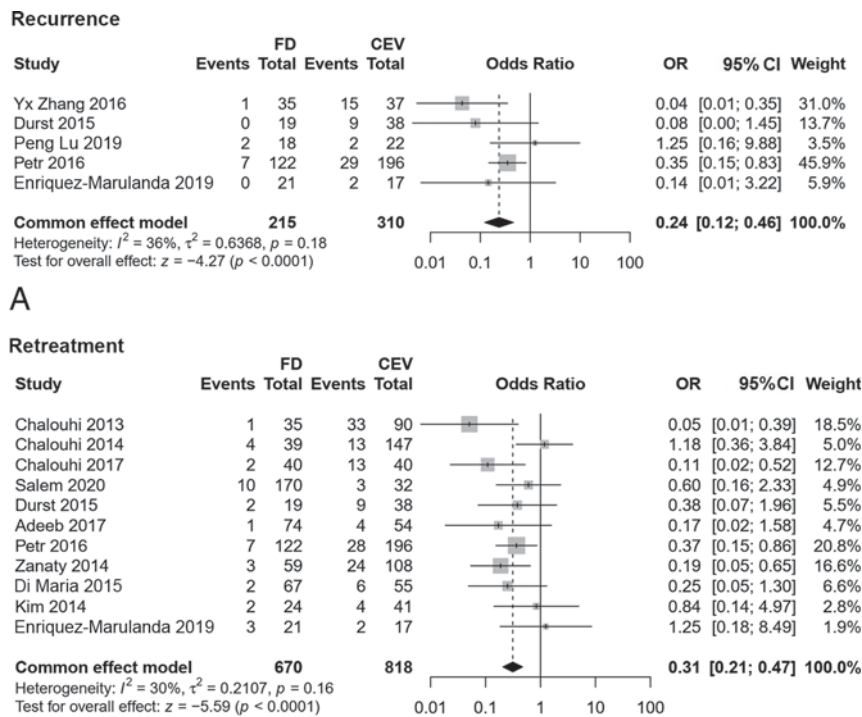
FIG 3. The comparison of recurrence (*A*) and retreatment (*B*) of FD and CEV treatment.

after removal of the aneurysms under angiography (OR, 0.24; 95% CI, 0.12–0.46; *P* < .001) and retreatment (OR, 0.31; 95% CI, 0.21–0.47; *P* < .001) (Fig 3). There were no statistical differences of delayed complications (OR, 1.14; 95% CI, 0.46–2.84; *P* = .775) and follow-up clinical outcomes (OR, 1.24; 95% CI, 0.82–1.88; *P* = .304) between the FD and CEV groups (Online Supplemental Data). Table 2 summarizes all the results of this meta-analysis.

Subgroup, Meta-regression, and Sensitivity Analysis
To discover the source of heterogeneity in follow-up occlusions, we conducted subgroup analyses, meta-regression, and sensitivity

analyses. First, we divided the included studies into 2 groups, matched and non-matched. In the subgroup analysis, the matched group indicates that the FD group had a higher rate of follow-up occlusion (OR, 3.33; 95% CI, 1.86–5.98; *P* < .001) and the I^2 decreased to 58%, but in the nonmatched group, the I^2 increased to 73% (Online Supplemental Data). Because no evident changes were observed after dividing the study designs into subgroups, we further divided these studies into 3 groups according to reported aneurysm sizes: large aneurysm group (diameter, >10 mm), small aneurysm (<4 mm), and both. In our analysis, the I^2 decreased to 0% and 6% in the large and small groups, respectively, but remained at 60% in studies that did not distinguish among the sizes of aneurysms (Fig 4). Therefore, we postulated that the source of heterogeneity of the follow-up occlusion rate was due to aneurysm size. We also conducted a meta-regression that showed that neither the published years (β, −0.1043; 95% CI, −0.287–0.078; *P* = .262) nor age (β, 0.0544; 95% CI, −0.065–0.174; *P* = .373) affected the outcome (Online Supplemental Data). Furthermore, the sensitivity analysis showed that the results of follow-up occlusions were not influenced by the leaving-one-out method (Online Supplemental Data). Finally, the funnel plot revealed that there was no publication bias, with all studies exhibiting symmetric distributions (Online Supplemental Data).

DISCUSSION
CEV treatments, including coiling alone,[30] SAC,[31] and BAC,[32] have been widely used in the treatment of intracranial aneurysms. Aneurysms unfavorable for simple coiling require deployment of a stent across the aneurysm neck to prevent coil migration, while the high bleeding risk due to dual-antiplatelet therapy during the perioperative period can lead to a poor prognosis.[33] In contrast, dual-antiplatelet medication was not obligatory for the BAC embolization technique, which was accompanied by low thrombosis formation, first reported by Moret et al[34] in 1997. However, the risk of recurrence and retreatment of aneurysms treated by coil embolization can reach 20% and 10%, respectively, based on a meta-analysis across all aneurysm sizes.[35] The role of conventional and standard endovascular tools in the treatment of IAs was challenged when FD devices were introduced. The PED,[36] as the first commercially available FD on the US market, presented its safety and

Table 2: Summaries of all results of present work

Variables	Studies, No.	FD, No.	CEV, No.	OR/SMD	95% CI	I²	P Value
Age	9	361	522	−0.23[a]	−0.55–0.09	78%	.166
Female	17	910	1076	1.02	0.79–1.32	7%	.864
Hypertension	6	272	210	1.19	0.82–1.72	0%	.357
Diameter of aneurysm	10	464	712	0.22[a]	0.03–0.41	52%	.026
Periprocedural death	17	910	1076	1.81	0.73–4.48	0%	.197
Periprocedural ischemia	16	848	1053	0.85	0.53–1.36	0%	.505
Periprocedural hemorrhage	16	848	1053	1.51	0.80–2.8	0%	.204
Procedure-related complications	17	910	1076	1.4	1.01–1.96	0%	.045
Immediate occlusion	7	302	405	0.27	0.04–1.69	92%	.16
mRS at discharge	6	249	263	0.43	0.15–1.23	0%	.117
Follow-up occlusion	18	952	1055	2.55	1.70–3.83	68%	<.001
Recurrence	5	215	310	0.24	0.12–0.46	38%	<.001
Retreatment	11	670	818	0.31	0.21–0.47	33%	<.001
Delayed complications	11	582	708	1.14	0.46–2.84	59%	.775
mRS at follow-up	14	763	883	1.24	0.82–1.88	0%	.304

[a] Represents the SMD result.
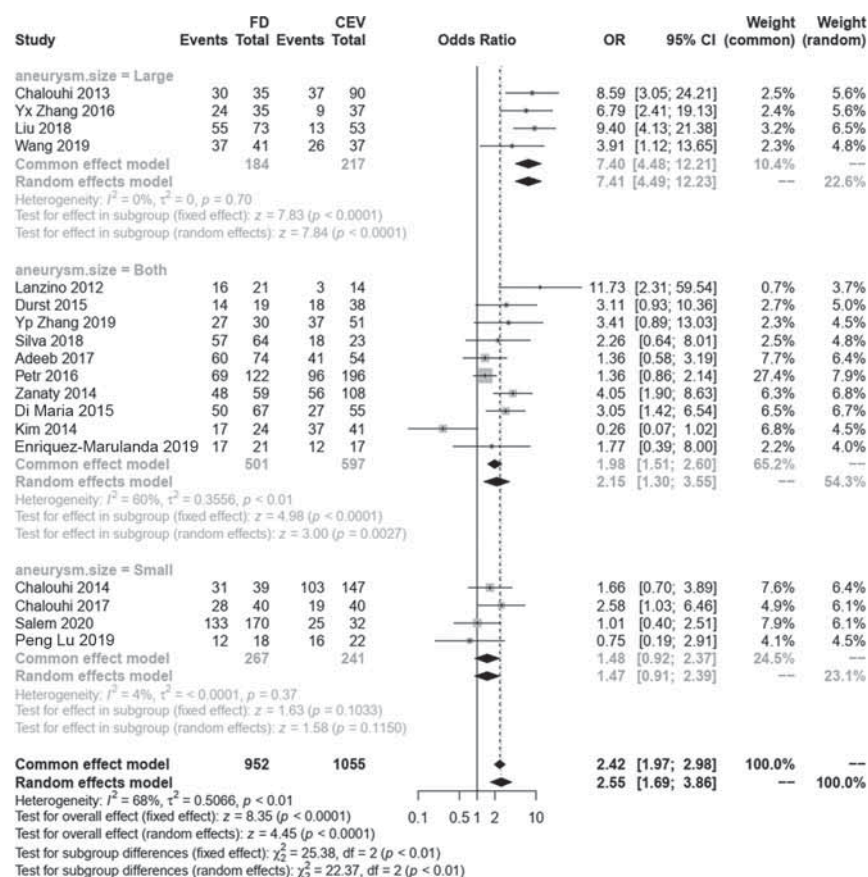
FIG 4. The subgroup analysis based on the aneurysm size to find the source of heterogeneity for the follow-up complete occlusion rate.

In the present study, a total of 18 studies from the past decade, including 2000 patients (2200 aneurysms), were selected. The covariates age, sex, and risk factors, such as hypertension, did not show statistical difference, but we observed that the size of aneurysms in the FD group were larger than that of CEV group. Originally, the FD was intended for treatment of complex and large or giant aneurysms,[15] and across time, the FD was indicated for small aneurysms.[14] Furthermore, due to major injuries caused by clipping or bypass microsurgeries, patients and surgeons preferred the FD to remove large/giant aneurysms out of the circulation while protecting the perforating artery.However, the conventional treatments for large/giant aneurysms may cause stent malposition and endoleaks, leading to recurrence and retreatment. Thus, in the real world, the CEV group had smaller aneurysms than the FD group.

Both short- and long-term angiographic and clinical outcomes are commonly reported, including procedure-related complications, immediate occlusion rates, mRS scores at discharge, occlusion rates at the last follow-up, delayed complications, and mRS scores at the last follow-up. For these observed variables, only the occlusion rate at the last follow-up was reported in all included cohorts; therefore, a funnel plot of this variable was depicted to detect the publication bias of all the studies. We extracted only the complete occlusion data according to the Raymond classification, except for Wang et al,[26] who selected the O'Kelly-Marotta grading scale as the standard criterion. Aggregation of the data about ischemia, hemorrhage, and cranial nerve deficits and other complications

effectiveness in the clinic.[37] Failures or complications associated with the FD were also reported, such as remaining filling, postprocedural rupture, postprocedural thrombosis, and ischemic stroke.[38,39] Thus, the feasibility, safety, and efficacy of the FD versus conventional standard treatments are still elusive and controversial. To our knowledge, this is the first meta-analysis that directly compares both techniques, without considering aneurysm size and location, in terms of immediate and long-term angiographic and clinical outcomes.

indicated that the risk of procedure-related complications due to the FD was higher than that of the CEV group, which was consistent with an early meta-analysis.[40] Rupture with poor prognoses was reported in about 81.3% of patients experiencing death or poor neurologic outcomes after FD treatment.[41,42] Using a numeric method, Cebral et al[43] found that the increased pressure in aneurysms following FD treatment may contribute to rupture, which was proved by another simulation study.[44] An early single-arm meta-analysis found that procedure-related permanent morbidity and mortality rates reached 5% and 4%, respectively, in FD treatments. High rates of intraparenchymal hemorrhage, postprocedural SAH, and ischemic stroke were also reported.[45] Our meta-analysis provides more representative data by directly comparing the safety of FD and CEV treatments.

The long-term follow-up angiographic results indicated the superiority of the FD with a higher complete occlusion rate and lower recurrence and retreatment rates. In series studies, complete occlusion was noted in 63% of aneurysms in early postmarket results,[8] 82.6% of aneurysms in the study were not restricted to the circle of Willis,[46] and 93.9% of aneurysms had a stent placed within an FD.[47] The occlusion rate at the last follow-up treatment with an FD can even reach 100%.[48] In this pooled study, the complete occlusion rate of the FD group was 2.5-fold that of the CEV group. Nevertheless, high heterogeneity was also observed. After the subgroup meta-regression and sensitivity analyses, we found that the heterogeneity was due to aneurysm size, which implied that a study adjusting for aneurysm diameter may be better when exploring the effectiveness and safety of flow-diverting in the future. Accompanied by a high complete occlusion rate, the rates of recurrence and retreatment in the FD group were lower than those in the CEV group. However, in terms of long-term clinical outcomes, there were no significant differences between the 2 groups.

The significant findings of this work were the following: 1) aneurysms treated with an FD were larger than those in the CEV group; 2) the procedure-related complications occurred more often during FD placement; 3) compared with the FD group, the CEV group had a lower rate of complete obliteration during angiography; and 4) the recurrence and retreatment rates of the FD group were lower than those of the CEV group.

There are some limitations to our study. First, as we determined, aneurysm size influenced the analysis and contributed to the heterogeneity of the results. It is better to divide this variable into small, medium, and large groups. In addition, the status (ruptured or unruptured),[49,50] anatomic location,[51] and aneurysm type[52] may also affect the final results, but we neglected to include these factors in our study. This omission is because research studies that directly compare FD and CEV treatments are rare, and these factors were not taken into consideration in the original studies. However, these confounding effects were resolved as much as possible by subgrouping analyses and meta-regression. Second, the findings of recurrence and retreatment differences were based on data from a small subset of the included studies. A large data set is needed to verify these results. Third, multiple FDs and CEV treatments included may

introduce heterogeneity. Last, the periprocedural risk that occurs with retreatment was not pooled because such results were not recorded in the original articles.

CONCLUSIONS

Our meta-analysis directly compared the effectiveness and safety of FD and CEV treatment in the immediate and long term. Compared with the CEV treatment, the placement of an FD may lead to more procedure-related complications, but there is not a difference of safety and it is more effective in the long term.

Disclosure forms provided by the authors are available with the full text and PDF of this article at www.ajnr.org.

REFERENCES

1. Guglielmi G, Viñuela F, Dion J, et al. **Electrothrombosis of saccular aneurysms via endovascular approach, Part 2: preliminary clinical experience.** *J Neurosurg* 1991;75:8–14 CrossRef Medline
2. Higashida RT, Smith W, Gress D, et al. **Intravascular stent and endovascular coil placement for a ruptured fusiform aneurysm of the basilar artery: case report and review of the literature.** *J Neurosurg* 1997;87:944–49 CrossRef Medline
3. Moret J, Cognard C, Weill A, et al. **Reconstruction technic in the treatment of wide-neck intracranial aneurysms: long-term angiographic and clinical results—apropos of 56 cases.** *J Neuroradiol* 1997;24:30–44 Medline
4. Zhang X, Zhong J, Gao H, et al. **Endovascular treatment of intracranial aneurysms with the LVIS device: a systematic review.** *J Neurointerv Surg* 2017;9:553–57 CrossRef Medline
5. Becske T, Kallmes DF, Saatci I, et al. **Pipeline for uncoilable or failed aneurysms: results from a multicenter clinical trial.** *Radiology* 2013;267:858–68 CrossRef Medline
6. Nelson PK, Lylyk P, Szikora I, et al. **The Pipeline Embolization Device for the intracranial treatment of aneurysms trial.** *AJNR Am J Neuroradiol* 2011;32:34–40 CrossRef Medline
7. Chalouhi N, Jabbour P, Singhal S, et al. **Stent-assisted coiling of intracranial aneurysms: predictors of complications, recanalization, and outcome in 508 cases.** *Stroke* 2013;44:1348–53 CrossRef Medline
8. Kan P, Siddiqui AH, Veznedaroglu E, et al. **Early postmarket results after treatment of intracranial aneurysms with the Pipeline Embolization Device: a U.S. multicenter experience.** *Neurosurgery* 2012;71:1080–87; discussion 7–8 CrossRef Medline
9. Li W, Tian Z, Zhu W, et al. **Hemodynamic analysis of postoperative rupture of unruptured intracranial aneurysms after placement of flow-diverting stents: a matched case-control study.** *AJNR Am J Neuroradiol* 2019;40:1916–23 CrossRef Medline
10. Moher D, Liberati A, Tetzlaff J, et al; PRISMA Group. **Preferred reporting items for systematic reviews and meta-analyses: the PRISMA statement.** *PLoS Med* 2009;6:e1000097 CrossRef Medline
11. Stang A. **Critical evaluation of the Newcastle-Ottawa scale for the assessment of the quality of nonrandomized studies in meta-analyses.** *Eur J Epidemiol* 2010;25:603–05 CrossRef Medline
12. Adeeb N, Griessenauer CJ, Foreman PM, et al. **Comparison of stent-assisted coil embolization and the Pipeline Embolization Device for endovascular treatment of ophthalmic segment aneurysms: a multicenter cohort study.** *World Neurosurg* 2017;105:206–12 CrossRef Medline
13. Chalouhi N, Daou B, Barros G, et al. **Matched comparison of flow diversion and coiling in small, noncomplex intracranial aneurysms.** *Neurosurgery* 2017;81:92–97 CrossRef Medline
14. Chalouhi N, Starke RM, Yang S, et al. **Extending the indications of flow diversion to small, unruptured, saccular**

aneurysms of the anterior circulation. *Stroke* 2014;45:54–58 CrossRef Medline

15. Chalouhi N, Tjoumakaris S, Starke RM, et al. **Comparison of flow diversion and coiling in large unruptured intracranial saccular aneurysms.** *Stroke* 2013;44:2150–54 CrossRef Medline

16. Di Maria F, Pistocchi S, Clarençon F, et al. **Flow diversion versus standard endovascular techniques for the treatment of unruptured carotid-ophthalmic aneurysms.** *AJNR Am J Neuroradiol* 2015;36:2325–30 CrossRef Medline

17. Durst CR, Starke RM, Clopton D, et al. **Endovascular treatment of ophthalmic artery aneurysms: ophthalmic artery patency following flow diversion versus coil embolization.** *J Neurointerv Surg* 2016;8:919–22 CrossRef Medline

18. Enriquez-Marulanda A, Salem MM, Ascanio LC, et al. **No differences in effectiveness and safety between Pipeline Embolization Device and stent-assisted coiling for the treatment of communicating segment internal carotid artery aneurysms.** *Neuroradiol J* 2019;32:344–52 CrossRef Medline

19. Kim LJ, Tariq F, Levitt M, et al. **Multimodality treatment of complex unruptured cavernous and paraclinoid aneurysms.** *Neurosurgery* 2014;74:51–61; discussion 61; quiz 61 CrossRef Medline

20. Lanzino G, Crobeddu E, Cloft HJ, et al. **Efficacy and safety of flow diversion for paraclinoid aneurysms: a matched-pair analysis compared with standard endovascular approaches.** *AJNR Am J Neuroradiol* 2012;33:2158–61 CrossRef Medline

21. Liu JM, Zhou Y, Li Y, et al. **Parent artery reconstruction for large or giant cerebral aneurysms using the Tubridge flow diverter: a multicenter, randomized, controlled clinical trial (PARAT).** *AJNR Am J Neuroradiol* 2018;39:807–16 CrossRef Medline

22. Lu P, Zhang Y, Niu H, et al. **Comparison of endovascular treatment for middle cerebral artery aneurysm with a low-profile visualized intraluminal support stent or Pipeline Embolization Device.** *Exp Ther Med* 2019;18:2072–78 CrossRef Medline

23. Petr O, Brinjikji W, Cloft H, et al. **Current trends and results of endovascular treatment of unruptured intracranial aneurysms at a single institution in the flow-diverter era.** *AJNR Am J Neuroradiol* 2016;37:1106–13 CrossRef Medline

24. Salem MM, Ravindran K, Enriquez-Marulanda A, et al. **Pipeline Embolization Device versus stent-assisted coiling for intracranial aneurysm treatment: a retrospective propensity score-matched study.** *Neurosurgery* 2020;87:516–22 CrossRef Medline

25. Silva MA, See AP, Khandelwal P, et al. **Comparison of flow diversion with clipping and coiling for the treatment of paraclinoid aneurysms in 115 patients.** *J Neurosurg* 2019;130:1505–08 CrossRef Medline

26. Wang J, Jia L, Duan Z, et al. **Endovascular treatment of large or giant non-saccular vertebrobasilar aneurysms: Pipeline Embolization Devices versus conventional stents.** *Front Neurosci* 2019;13:1253 CrossRef Medline

27. Zanaty M, Chalouhi N, Starke RM, et al. **Flow diversion versus conventional treatment for carotid cavernous aneurysms.** *Stroke* 2014;45:2656–61 CrossRef Medline

28. Yupeng Zhang Y, Liang F, Zhang Y, et al. **Exploring the feasibility of Pipeline Embolization Device compared with stent-assisted coiling to treat non-saccular, unruptured, intradural vertebral artery aneurysms.** *Front Neurol* 2019;10:275 Medline

29. Zhang Y, Zhou Y, Yang P, et al. **Comparison of the flow diverter and stent-assisted coiling in large and giant aneurysms: safety and efficacy based on a propensity score-matched analysis.** *Eur Radiology* 2016;26:2369–77 CrossRef Medline

30. Park HK, Horowitz M, Jungreis C, et al. **Endovascular treatment of paraclinoid aneurysms: experience with 73 patients.** *Neurosurgery* 2003;53:14–23; discussion 24 CrossRef Medline

31. Hetts SW, Turk A, English JD, et al; Matrix and Platinum Science Trial Investigators. **Stent-assisted coiling versus coiling alone in unruptured intracranial aneurysms in the Matrix and Platinum Science Trial: safety, efficacy, and mid-term outcomes.** *AJNR Am J Neuroradiol* 2014;35:698–705 CrossRef Medline

32. Malek AM, Halbach VV, Phatouros CC, et al. **Balloon-assist technique for endovascular coil embolization of geometrically difficult intracranial aneurysms.** *Neurosurgery* 2000;46:1397–406; discussion 406–07 CrossRef Medline

33. Amenta PS, Dalyai RT, Kung D, et al. **Stent-assisted coiling of wide-necked aneurysms in the setting of acute subarachnoid hemorrhage: experience in 65 patients.** *Neurosurgery* 2012;70:1415–29; discussion 29 CrossRef Medline

34. Moret J, Cognard C, Weill A, et al. **The "Remodelling Technique" in the treatment of wide neck intracranial aneurysms. angiographic results and clinical follow-up in 56 cases.** *Interv Neuroradiol* 1997;3:21–35 CrossRef Medline

35. Ferns SP, Sprengers ME, van Rooij WJ, et al. **Late reopening of adequately coiled intracranial aneurysms: frequency and risk factors in 400 patients with 440 aneurysms.** *Stroke* 2011;42:1331–37 CrossRef Medline

36. Nossek E, Chalif DJ, Chakraborty S, et al. **Concurrent use of the Pipeline Embolization Device and coils for intracranial aneurysms: technique, safety, and efficacy.** *J Neurosurg* 2015;122:904–11 CrossRef Medline

37. Xiang J, Ma D, Snyder KV, et al. **Increasing flow diversion for cerebral aneurysm treatment using a single flow diverter.** *Neurosurgery* 2014;75:286–94; discussion 94 CrossRef Medline

38. Bonney PA, Connor M, Fujii T, et al. **Failure of flow diverter therapy: predictors and management strategies.** *Neurosurgery* 2020;86:S64–73 CrossRef Medline

39. Townsend RK, Wolfe SQ, Anadani M, et al. **Endovascular management of acute postprocedural flow diverting stent thrombosis.** *J Neurointerv Surg* 2020;12:67–71 CrossRef Medline

40. Domingo RA, Tripathi S, Perez-Vega C, et al. **Treatment of posterior circulation non-saccular aneurysms with flow diversion versus stent-assisted coiling: a systematic review and meta-analysis.** *J Neurointerv Surg* 2021;13:159–63 CrossRef Medline

41. Rouchaud A, Brinjikji W, Lanzino G, et al. **Delayed hemorrhagic complications after flow diversion for intracranial aneurysms: a literature overview.** *Neuroradiology* 2016;58:171–77 CrossRef Medline

42. Turowski B, Macht S, Kulcsár Z, et al. **Early fatal hemorrhage after endovascular cerebral aneurysm treatment with a flow diverter (SILK-Stent): do we need to rethink our concepts?** *Neuroradiology* 2011;53:37–41 CrossRef Medline

43. Cebral JR, Mut F, Raschi M, et al. **Aneurysm rupture following treatment with flow-diverting stents: computational hemodynamics analysis of treatment.** *AJNR Am J Neuroradiol* 2011;32:27–33 CrossRef Medline

44. Hassan T, Ahmed YM, Hassan AA. **The adverse effects of flow-diverter stent-like devices on the flow pattern of saccular intracranial aneurysm models: computational fluid dynamics study.** *Acta Neurochir (Wien)* 2011;153:1633–40 CrossRef Medline

45. Brinjikji W, Murad MH, Lanzino G, et al. **Endovascular treatment of intracranial aneurysms with flow diverters: a meta-analysis.** *Stroke* 2013;44:442–47 CrossRef Medline

46. Pistocchi S, Blanc R, Bartolini B, et al. **Flow diverters at and beyond the level of the circle of Willis for the treatment of intracranial aneurysms.** *Stroke* 2012;43:1032–38 CrossRef Medline

47. Ocal O, Peker A, Balci S, et al. **Placement of a stent within a flow diverter improves aneurysm occlusion rates.** *AJNR Am J Neuroradiol* 2019;40:1932–38 CrossRef Medline

48. Mazur MD, Kilburg C, Wang V, et al. **Pipeline Embolization Device for the treatment of vertebral artery aneurysms: the fate of covered branch vessels.** *J Neurointerv Surg* 2016;8:1041–47 CrossRef Medline

49. Bhatia KD, Kortman H, Orru E, et al. **Periprocedural complications of second-generation flow diverter treatment using Pipeline Flex for unruptured intracranial aneurysms: a systematic review and meta-analysis.** *J Neurointerv Surg* 2019;11: 817–24 CrossRef Medline

50. Cagnazzo F, di Carlo DT, Cappucci M, et al. **Acutely ruptured intracranial aneurysms treated with flow-diverter stents: a systematic review and meta-analysis.** *AJNR Am J Neuroradiol* 2018;39:1669–75 CrossRef Medline

51. Cagnazzo F, Perrini P, Dargazanli C, et al. **Treatment of unruptured distal anterior circulation aneurysms with flow-diverter stents: a meta-analysis.** *AJNR Am J Neuroradiol* 2019;40:687–93 CrossRef Medline

52. Rouchaud A, Brinjikji W, Cloft HJ, et al. **Endovascular treatment of ruptured blister-like aneurysms: a systematic review and meta-analysis with focus on deconstructive versus reconstructive and flow-diverter treatments.** *AJNR Am J Neuroradiol* 2015;36:2331–39 CrossRef Medline

Glymphatic System in Ocular Diseases: Evaluation of MRI Findings

P. Manava, C. Eckrich, F. Luciani, J. Schmidbauer, M.M. Lell, and K. Detmar

ABSTRACT

BACKGROUND AND PURPOSE: There is growing evidence of leakage of gadolinium in an impaired blood-retina barrier. We investigated gadolinium enhancement in different eye compartments and correlated the enhancement with specific ophthalmologic diseases.

MATERIALS AND METHODS: In a prospective clinical study (ClinicalTrials.gov Identifier: NCT05035251), 95 patients (63 with and 32 without ophthalmologic disease) were examined before and after gadolinium administration (20 and 120 minutes) with heavily T2-weighted FLAIR. The cohort was divided according to the location of pathology into anterior and posterior eye compartment groups. Relative signal intensity increase in the anterior eye chamber, vitreous body with retina, optic nerve sheath, and the Meckel cave was analyzed and correlated with the final clinical diagnosis.

RESULTS: In patients with a disorder in the anterior eye compartment, significant signal intensity increases were found in the central anterior eye chamber (P 20 minutes = .000, P 120 minutes = .000), lateral anterior eye chamber (P 20 minutes = .001, P 120 minutes = .005), and vitreous body with retina (P 20 minutes = .02) compared with the control group. Patients with pathologies in the posterior eye compartment showed higher signal intensity levels in the central anterior eye compartment (P 20 minutes = .041) and vitreous body with retina (P 120 minutes = .006).

CONCLUSIONS: Increased gadolinium enhancement was found in the central and lateral anterior eye compartments and the vitreous body with retina in patients with anterior eye compartment disorders 20 and 120 minutes after contrast application, suggesting impairment of the blood-aqueous barrier. In patients with a disorder in the posterior eye compartment, pathologic enhancement indicated disruption of the blood-retinal barrier that allows gadolinium to diffuse into the vitreous body with retina from posterior to anterior, opposite to the known physiologic glymphatic pathway.

ABBREVIATIONS: AC = anterior eye chamber; AEC = anterior eye compartment; Gd = gadolinium; GLOS = gadolinium leakage in ocular structures; PEC = posterior eye compartment; SI = signal intensity; VB = vitreous body with retina

The physiologic pathway of CSF involves production by the choroid plexus, followed by circulation through the CSF spaces and absorption via arachnoid villi, allowing CSF to pass through the capillary walls into the interstitial fluid of the surrounding brain tissue.[1]

Previous reports also revealed pulsatile fluid movement with local exchange among CSF, interstitial fluid, and blood. Key elements of this homeostasis are astrocytes, aquaporins, and membrane transporters enabling exchange at the blood-brain barrier, providing a bidirectional drainage pathway. These findings have important effects for the understanding of physiologic processes in the CNS, such as the distribution of trophic factors, CNS waste clearance, and drug application.[2] The optic nerve and retina have similar paravascular clearance systems as parts of the CNS.[3]

The diffusion of gadolinium (Gd) in the glymphatic pathway through the blood-brain barrier, the CSF barrier, and the blood-ocular barrier has been demonstrated in several reports,[2,4-8] especially in delayed imaging with a signal increase in different CSF compartments (anterior eye compartment [AEC], the Meckel cave, suprasellar cistern, internal auditory canal, and ambient cistern).[8] These findings reinforce the hypothesis that in the glymphatic pathway, Gd diffuses physiologically into the CSF through the choroid plexus and the aqueous chamber of the eye because there is a higher permeability for Gd in these compartments than in the blood-brain barrier and the blood-retina barrier.[7,9]

As part of the CNS, the optic nerve is exposed to pressure equivalent to the intracranial pressure.[3] At the lamina cribrosa, 2 different pressure types meet, the low-pressure compartment of the retrobulbar CSF space and the high-pressure compartment of the intraocular space.[3] These findings could suggest a high probability of an association between the development of glaucoma relating to the composition of CSF and the pressure surrounding the optic nerve.[10] Even small amounts of Gd can be detected with heavily T2-weighted FLAIR; this sequence performed at different time points helps to demonstrate the kinetics of Gd distribution in different compartments of the CSF.[2,11]

Gd within the CSF and the anterior AEC is part of a physiologic excretion process.[2] In contrast, an increase in Gd in the vitreous body with retina (VB) has been described as gadolinium leakage in ocular structures (GLOS) in patients with acute ischemic stroke and small-vessel diseases caused by impairment of the blood-retinal barrier.[4,12] GLOS was observed in patients with uveitis[6] and optic neuritis.[5] Glymphatic dysfunction was also suggested as a possible pathomechanism for idiopathic intracranial hypertension.[13]

The aims of our study were to find specific enhancement patterns and to evaluate the Gd kinetics of the glymphatic system in various ocular diseases in this specifically optimized MR imaging sequence for delayed Gd imaging.

MATERIALS AND METHODS
Patients
Ninety-five patients were enrolled between March 2019 and May 2020. The patient cohort included 63 patients with ophthalmologic diseases and 32 patients without any ophthalmologic disease (control group).

Only patients with a clinical indication for Gd administration were included in this study. MR imaging of the whole brain was performed to exclude central pathologies. Patient details are summarized in Table 1 and the Online Supplemental Data.

The following ophthalmic examinations were performed in each patient with ophthalmologic disease: inspection of the eyelids with surrounding tissues and the palpebral fissure in an external examination, visual acuity, visual field (Goldmann), pupil function, refraction, ocular motility, close inspection with a slit lamp of the anterior eye structures and ocular adnexa, tonometry, fundus examination, fluorescein angiography, and optical coherence tomography.

The different ophthalmologic pathologies were categorized as the following:

Disorder in the AEC: uveitis anterior, episcleritis, herpetic keratouveitis, uveitis intermedia, uveitis anterior and intermedia ($n = 15$ patients); and a disorder in the posterior (retinal) eye compartment (PEC): nonarteritic anterior ischemic optic neuropathy, arteritic anterior ischemic optic neuropathy, vitreous hemorrhage, optic nerve atrophy, retrobulbar neuritis, central retinal vein occlusion, central retinal artery occlusion, sudden vision loss not otherwise specified, uveitis posterior, vitritis, amaurosis fugax attacks, temporal arteritis, glaucoma, panuveitis, papillitis, papillophlebitis, and Graves ophthalmopathy ($n = 48$ patients).

The control group included patients with vertigo, extracranial tumors, depression, and dementia ($n = 32$ patients) without a medical history of ophthalmic diseases who underwent MR imaging of the whole brain to exclude central pathologies.

MR Imaging Protocol
All patients underwent MR imaging on a 1.5T unit (Espree; Siemens). The sequence parameters of the heavily T2-weighted FLAIR were as follows: TE = 566 ms, TR = 9000 ms, TI = 2500 ms, number of averages = 2, number of phase-encoding steps = 219, echo-train length = 321, flip angle = 120°, fat saturation, voxel size = 0.5 × 0.5 × 2 mm, acquisition time = 6 minutes and 21 seconds. Three scans were obtained, first as baseline before intravenous contrast administration of gadoteric acid (DotaVision 0.5 mmol/mL; B-E Imaging; 0.2 mL/kg of body weight) and then with delays of 15 and 120 minutes after contrast administration.

Image Analysis
Image analysis was performed on a PACS workstation by 2 observers (10 and 25 years of experience in cerebral MR imaging) independently. Whole-brain imaging was analyzed on a patient basis to exclude central pathologies. ROIs for signal intensity (SI) measurements were drawn in different CSF spaces in the baseline scan and with coregistration copied onto the first and second follow-ups after intravenous contrast administration. The sizes of the ROIs depended on the target structure. We measured the following structures: the lateral and central aqueous chambers (anterior eye chamber [AC] lateral and AC central) and the VB of the eye, the distal optic nerve sheath, the Meckel cave, lateral ventricles, and basal cisterns (Figs 1 and 2).

SI measurements were normalized to the SI of the brain parenchyma.[14] The relative SI increase was calculated with the following ratio: relative SI increase = $(SI_{post} - SI_{baseline})/SI_{baseline}$.

Table 1: Patient characteristics

	OP ($n = 63$)	Nonop ($n = 32$)	P Value
Sex			
Male	36 (38%)	20 (21%)	$\chi^2 = .811$
Female	27 (28%)	12 (13%)	
Weight (mean) (kg)	80.31 (SD, 15.19)	80.67 (SD, 14.72)	.912
Age (mean) (yr)	60.87 (SD, 16.18)	60.09 (SD, 16.67)	.825
Gd (mean) (mL)	15.31 (SD, 2.65)	14.91 (SD, 3.00)	.508
Comorbidity			
Arterial hypertension	35 (56%)	10 (31%)	$\chi^2 = .015$
Diabetes mellitus	12 (19%)	6 (19%)	$\chi^2 = .89$
Nicotine abuse	5 (8%)	3 (9%)	$\chi^2 = .368$
Obesity	6 (9%)	1 (3%)	$\chi^2 = .238$
Atherosclerosis	16 (17%)	4 (13%)	$\chi^2 = .102$
OSAS	2 (3%)	1 (3%)	$\chi^2 = .959$
Rheumatoid arthritis	9 (14%)	3 (9%)	$\chi^2 = .449$

Note:—OP indicates ophthalmologic pathology; Nonop, no ophthalmologic pathology; OSAS, obstructive sleep apnea syndrome.
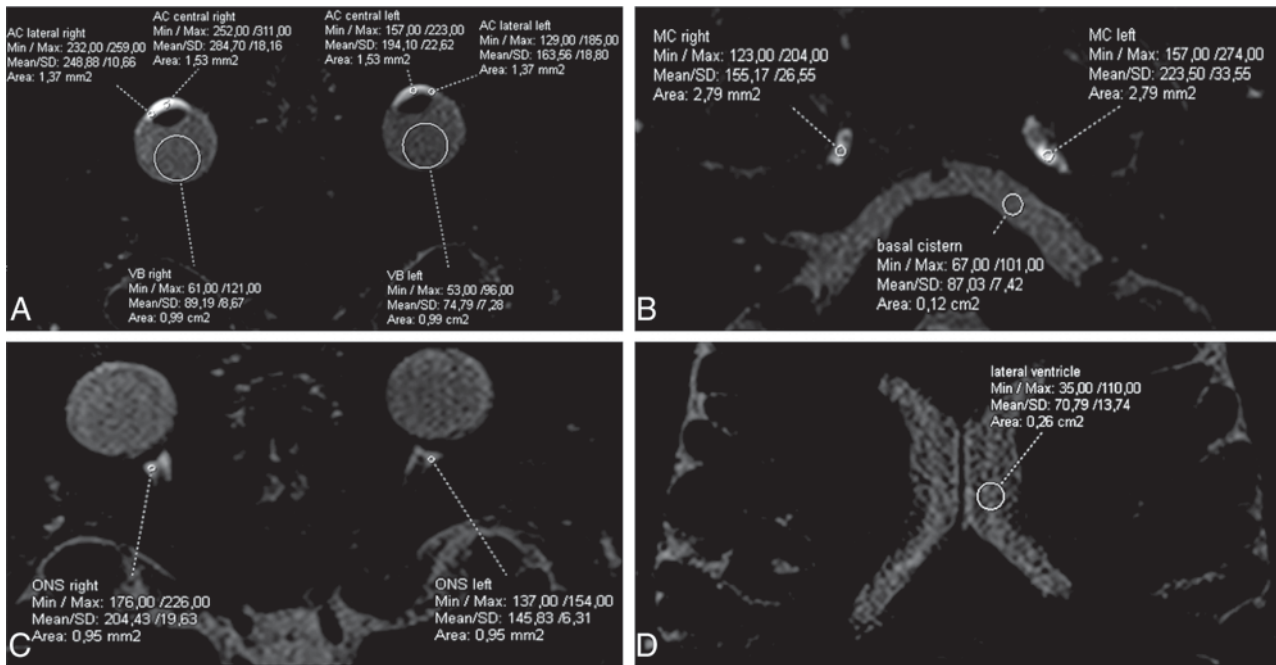
FIG 1. Examples of ROIs in the lateral and central eye chamber and the VB (*A*), the optical nerve sheath (ONS) (*B*), the Meckel Cave (MC), and the basal cistern (*C*) and lateral ventricles (*D*). Min indicates minimum; Max, maximum.
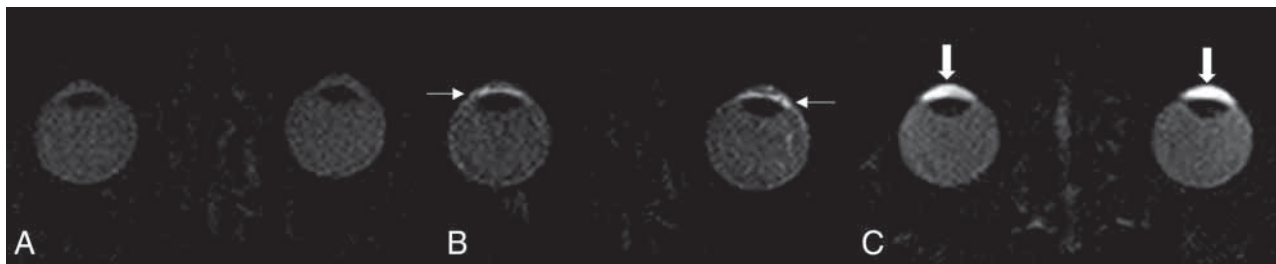
FIG 2. Image demonstrating contrast agent kinetics after injection of gadolinium in healthy patients: native scan (*A*), scan 20 minutes after Gd injection demonstrating the physiologic permeability of Gd in the lateral eye chamber (*small arrow*) (*B*), and physiologic, symmetric enhancement in the central eye chamber and the VB in the late scan after 120 minutes (*C*) (*thick arrows*).

Statistics

Mean values of the measured relative SI increase (SD, 1-fold) were used for analyses in commercially available software (SPSS Statistics, Version 22; IBM). The Levene test was used to assess the normality of the data distribution. Data with a Gaussian distribution were evaluated by ANOVA with a post hoc analysis of Gabriel (equality of variances, different case numbers) for the 3 groups (AEC, PEC, control group) for the 2 relative SI increases (after 20 and 120 minutes). A χ^2 test was used for analysis of patient characteristics (sex and the presence of comorbidities such as arterial hypertension, diabetes mellitus, nicotine abuse, obesity, atherosclerosis, obstructive sleep apnea syndrome (OSAS), rheumatoid arthritis). The level of significance was set at $P < .05$.

Similar to previous reports,[7,8] each side was investigated individually, resulting in 95 left and 95 right eyes. Sixty-four eyes composed the control group; 30 eyes had a disorder in the AEC, and 96 had one in the PEC. The disorder was documented separately for each eye.

RESULTS

Patient weight, age, and applied volume of Gd (in milliliters) did not differ between the study and control groups (Table 1). The measured ocular tension of patients with ophthalmologic diseases in the right eye was 14.46 (SD, 0.385) mm Hg, and that in the left eye was 14.52 (SD 0.39) mm Hg. In our study cohort, a higher number of patients with an ophthalmologic disease had arterial hypertension than in the control group ($\chi^2 = .015$) (Table 1).

In patients with a disorder in the AEC, the average relative SI increase in the central eye chamber after 20 minutes was 0.84 (SD, 0.79), and after 120 minutes, it was 3.40 (SD, 2.21), with significant differences ($p_{20min} < .001$, $p_{120min} = .000$) compared with the control group, which showed mean relative SI increase 0.27 (SD, 0.5) after 20 minutes and 1.79 (SD, 1.39) after 120 minutes.

Similar results were found in the lateral AC with mean relative SI increase of 0.86 (SD, 0.92) after 20 minutes and 1.93 (SD, 1.43) after 120 minutes, with statistically significant differences ($p_{20min} = .001$, $p_{120min} = .005$) compared with the control group, with mean
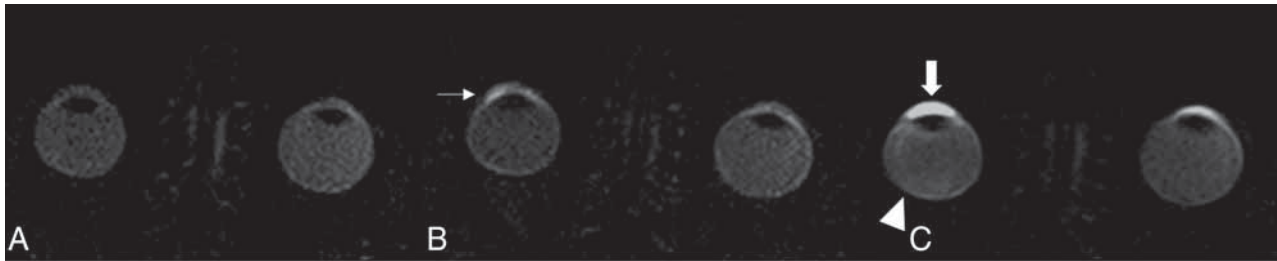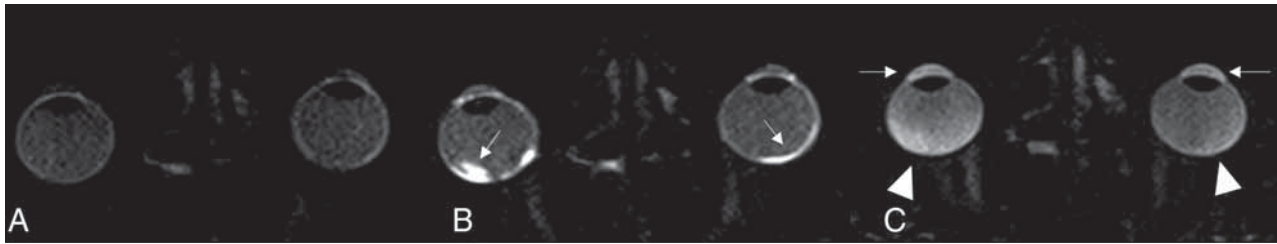
FIG 3. Example of a patient with a disorder in the AEC on the right; native scan (*A*), scan 20 minutes after gadolinium injection demonstrating a higher permeability of Gd in the lateral eye chamber (*small arrow*) and increased Gd enhancement in the in the central eye chamber on the right (*thick arrow*) (*B*), and the VB (*arrowhead*) in the late scan after 120 minutes in the right eye (*C*).

Table 2: Relative SI of the control group and patients with a disorder in the AEC and PEC compared with the control group[a]

ROI, Groups	No.	Mean		SD		SD Error		p_{20}	p_{120}
		20 min	120 min	20 min	120 min	20 min	120 min		
AC central									
Control	64	0.27	1.79	0.5	1.39	0.06	0.17		
AEC	30	0.84	3.40	0.79	2.21	0.14	0.40	.000	.001
PEC	96	0.51	2.49	0.66	1.80	0.07	0.18	.055	.041
AC lateral									
Control	64	0.29	1.10	0.62	0.99	0.08	0.12		
AEC	30	0.86	1.93	0.92	1.43	0.17	0.26	.001	.005
PEC	96	0.50	1.40	0.68	1.26	0.07	0.13	.201	.241
VB									
Control	64	0.04	0.16	0.26	0.43	0.03	0.05		
AEC	30	0.11	0.42	0.20	0.49	0.04	0.09	.020	.090
PEC	96	0.04	0.44	0.26	0.64	0.03	0.07	.169	.006
Distal optic nerve									
Control	64	0.31	1.46	1.16	1.23	0.14	0.15		
AEC	30	0.44	1.77	0.57	1.21	0.10	0.22	.860	.699
PEC	96	0.33	1.78	0.76	1.65	0.08	0.17	.999	.308
MC									
Control	64	0.45	1.61	0.71	1.15	0.09	0.14		
AEC	30	0.72	2.10	0.71	1.16	0.13	0.21	.138	.184
PEC	96	0.53	1.81	0.53	1.26	0.05	0.13	.812	.647
Basel cistern									
Control	32	0.004	0.24	0.29	0.22	0.05	0.04		
AEC	15	0.15	0.38	0.22	0.38	0.06	0.09	.340	.898
PEC	48	0.85	0.37	0.33	0.63	0.05	0.09	.576	.461
Lateral ventricles									
Control	32	0.04	0.27	0.34	0.39	0.06	0.07		
AEC	15	0.21	0.40	0.24	0.28	0.06	0.07	.210	.650
PEC	48	0.08	0.31	0.27	0.43	0.04	0.06	.945	.922

Note:—AC central indicates central aqueous chamber of the eye; AC lateral, lateral aqueous chamber of the eye; MC, Meckel cave.
[a] Reported values are estimated mean (SD), errors of SD, and P values.

relative SI increase of 0.29 (SD, 0.62) after 20 minutes and 1.1 (SD, 0.99) after 120 minutes.

In the VB, the mean relative SI increase of 0.11 (SD, 0.20) after 20 minutes was significantly different ($p_{20min} = .02$), while mean relative SI increase of 0.42 (SD, 0.49) after 120 minutes was similar ($p_{120min} = .09$) to that in the control group, with mean relative SI increase of 0.04 (SD, 0.26) after 20 minutes and 0.16 (SD, 0.43) after 120 minutes (Fig 3).

The mean enhancements in the optical nerve were not significantly different from those in the control group (Table 2).

Patients with disorders in the PEC had higher levels of contrast enhancement in the central AC (mean relative SI_{120min} = 2.49, SD_{120min} = 1.80, p_{120min} = .041) compared with the control

group (mean relative SI_{120min} = 1.79, SD_{120min} = 1.39) and in the VB (mean relative SI_{120min} = 0.44, SD_{120min} = 0.64, p_{120min} = .006) after 120 minutes compared with the control group (mean relative SI_{120min} = 0.16, SD_{120min} = 0.43). Other regions, including the lateral AC, showed no differences compared with the control group (Table 2 and Figs 4 and 5).

The mean relative SI increase in the central eye chamber in patients with disease in the AEC were different from those in patients with disease in the PEC 20 minutes after administration of contrast medium (difference in the mean relative SI = 0.33, p_{20min} = .030) and 120 minutes after administration (p_{120min} = .034). The other target measurements did not show significant differences between 20 minutes and 120 minutes.

FIG 4. Example of a patient with a disorder in the PEC (retinal). Native scan (*A*), 20 minutes after gadolinium injection demonstrating a pathologic permeability of Gd at the blood-retinal barrier (*small arrows*) (*B*), and accumulation of Gd in the VB after 120 minutes (*arrowhead*) demonstrating an opposite pathway of Gd (*C*). The physiologic enhancement in the anterior eye segment can also be seen in *C*, independent of the pathology of the posterior eye segment.
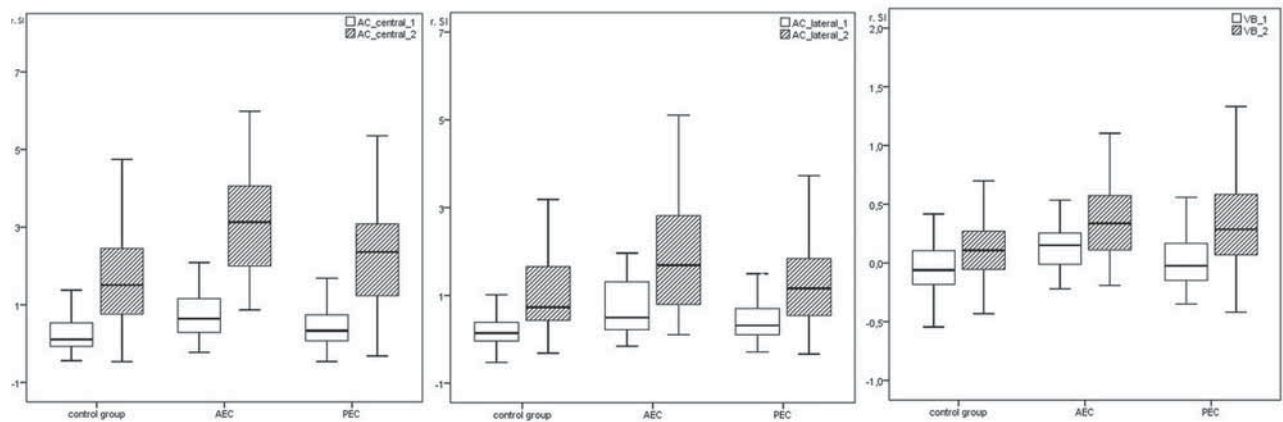
FIG 5. Relative SI 20 minutes (*white boxplot*) and 120 minutes (*gray boxplot*) after contrast application in the AC central (AC_central_1 = 20 minutes, AC_central_2 = 120 minutes), AC lateral (AC_lateral_1 = 20 minutes, AC_lateral = 120 minutes), and VB (VB_1 = 20 minutes, VB_2 = 120 minutes) in the control group and in patients with disorders in the AECs and PECs.

DISCUSSION

Recently published studies have demonstrated perfusion of Gd into the CSF with possible entry points at the choroid plexus and the aqueous chamber of the eye.[7] Additionally, in patients with stroke, GLOS was observed as an impairment of the blood-retinal barrier,[12] and Gd was documented in the VB. Furthermore, GLOS has been reported as not related to stroke but also associated with age and vascular risk factors.[12] The hypothesis of an ocular drainage glymphatic pathway for Gd has been postulated to flow from the orbit along the optical nerve into the basal CSF cistern,[10] with an entry point at the root of the iris into the anterior chamber through a known physiologic passage of the blood-aqueous barrier,[7] allowing plasma components to diffuse out of the uveal vessels.[15]

In the control group, as well as in unaffected eyes, we confirmed this pattern with increasing Gd accumulation with time in an anterior-to-posterior direction, starting from the lateral eye chamber at the blood-aqueous barrier over the central anterior chamber of the eye and continuing to the posterior eye chamber over the VB. Patients with ocular disease (such as uveitis anterior, episcleritis, glaucoma, diabetic retinopathy, arteritic anterior ischemic optic neuropathy, nonarteritic anterior ischemic optic neuropathy, uveitis posterior, vitritis, and age-related macular degeneration (Online Supplemental Data) demonstrated deviations in Gd dynamics.

Patients with disorders in the AEC showed significantly higher enhancement in the VB and AC 20 and 120 minutes after contrast application compared with the control group and the patients with PEC. These findings could be explained by an alteration of the physiologic permeability of the blood-aqueous barrier due to AEC disease. The increased permeability of Gd in the AC in cases with a pathology in the AEC resulted in a higher passage of Gd from anterior to posterior, reflecting a significantly higher enhancement in the VB.

We also found significantly higher SI in the VB in delayed imaging (after 120 minutes) in patients with a disorder of the PEC. These patients demonstrated Gd accumulation from a posterior-to-anterior direction, in contrast to those with AEC disease. This reversed enhancement pattern of the VB could be interpreted as a disruption of the blood-retinal barrier compared with the findings in cases with optic neuritis[5] and uveitis.[6] Previous studies did not report Gd diffusion through the blood-retinal barrier in healthy patients,[2,7,8,16] which is in accordance with our findings in eyes without PEC disease. GLOS has been related to patients with stroke[12] and patients with small-vessel disease, referring to age-related and vascular risk factor diseases.[4] Our study focused on the ophthalmic diseases and not on patients with stroke. We tried to find specific patterns according to the ophthalmic disease, classifying the diseases according to the vascular perfusion patterns of the eye. In our study cohort, a

significantly higher number of patients with an ophthalmologic disease had arterial hypertension than in the control group, indicating a vascular risk factor. We present similar findings to the reports of impairment of the blood-retina barrier in patients with uveitis[6] and optical neuritis[5] in a larger number of cases and furthermore in comparison with cases with diseases in the AEC.

Limitations

The relatively large number of different ocular diseases within the 2 groups and the relatively small number of patients included in the study cohort might be considered a limitation, but the time-consuming scan protocol posed an obstacle to increasing the cohort.

Although a pathophysiologic link between glymphatic dysfunction and glaucoma has been suggested and animal models indicating abnormal glymphatic circulation in glaucoma support this hypothesis, we did not find significant differences in Gd accumulation in specific areas compared with the control group.[17] Most likely, this finding is an effect of the small number of patients with glaucoma in our cohort. The delay time of 120 minutes after intravenous injection of Gd should not be problematic because Gd passing into the AEC through the aqueous chamber has been reported as early as 12 minutes.[7] In this study, MR imaging was performed unattached to the treatment and duration of illness.

Our study shows the diagnostic potential of contrast-enhanced MR imaging to objectively and noninvasively monitor blood-aqueous and blood-retinal barrier function. Although we could not find significant alterations in Gd dynamics at the optic nerve head in patients with glaucoma, we detected an inverse enhancement pattern in patients with diseases in the PEC, indicating an effect of the blood-retinal barrier and a higher permeability of Gd at the blood-aqueous barrier in the AEC.

CONCLUSIONS

Gd accumulation in the anterior and posterior eye compartments is significantly higher in patients with ocular diseases. Patients with AEC diseases demonstrated increased Gd accumulation compared with the control group and patients with PEC disease; furthermore, the level of enhancement increased from the early to the late phase. Patients with PEC diseases also showed increasing levels of enhancement with time, but they demonstrated a reversed (posterior-to-anterior) enhancement pattern, indicating a disruption of the blood-retinal barrier.

Disclosure forms provided by the authors are available with the full text and PDF of this article at www.ajnr.org.

REFERENCES

1. Brinker T, Stopa E, Morrison J, et al. **A new look at cerebrospinal fluid circulation.** *Fluids Barriers CNS* 2014;11:10 CrossRef Medline
2. Deike-Hofmann K, Reuter J, Haase R, et al. **Glymphatic pathway of gadolinium-based contrast agents through the brain: overlooked and misinterpreted.** *Invest Radiol* 2018;54:229–37 CrossRef Medline
3. Wostyn P, De Groot V, Van Dam D, et al. **The glymphatic hypothesis of glaucoma: a unifying concept incorporating vascular, biomechanical, and biochemical aspects of the disease.** *Biomed Res Int* 2017;2017:5123148 CrossRef Medline
4. Galmiche C, Moal B, Marnat G, et al. **Delayed gadolinium leakage in ocular structures: a potential marker for age- and vascular risk factor-related small vessel disease?** *Invest Radiol* 2021;56:425–32 CrossRef Medline
5. Förster A, Böhme J, Groden C, et al. **Gadolinium leakage in ocular structures in optic neuritis.** *J Clin Neurosci* 2019;68:268–70 CrossRef Medline
6. Herrera DA, Franco S, Bustamante S, et al. **Contrast-enhanced T2-FLAIR MR imaging in patients with uveitis.** *Int Ophthalmol* 2017;37:507–12 CrossRef Medline
7. Deike-Hofmann K, von Lampe P, Schlemmer HP, et al. **The anterior eye chamber: entry of the natural excretion pathway of gadolinium contrast agents?** *Eur Radiol* 2020;30:4633–40 CrossRef Medline
8. Taoka T, Naganawa S. **Gadolinium-based contrast media, cerebrospinal fluid and the glymphatic system: possible mechanisms for the deposition of gadolinium in the brain.** *Magn Reson Med Sci* 2018;17:111–19 CrossRef Medline
9. Pardridge WM. **CSF, blood-brain barrier, and brain drug delivery.** *Expert Opin Drug Deliv* 2016;13:963–75 CrossRef Medline
10. Wostyn P, Van Dam D, Audenaert K, et al. **A new glaucoma hypothesis: a role of glymphatic system dysfunction.** *Fluids Barriers CNS* 2015;12:16 CrossRef Medline
11. Naganawa S, Kawai H, Taoka T, et al. **Heavily T2-weighted 3D-FLAIR improves the detection of cochlear lymph fluid signal abnormalities in patients with sudden sensorineural hearing loss.** *Magn Reson Med Sci* 2016;15:203–11 CrossRef Medline
12. Hitomi E, Simpkins AN, Luby M, et al. **Blood-ocular barrier disruption in patients with acute stroke.** *Neurology* 2018;90:e915–23 CrossRef Medline
13. Jones O, Cutsforth-Gregory J, Chen J, et al. **Idiopathic intracranial hypertension is associated with a higher burden of visible cerebral perivascular spaces: the glymphatic connection.** *AJNR Am J Neuroradiol* 2021;42:2160–64 CrossRef Medline
14. Shinohara RT, Sweeney EM, Goldsmith J, et al. **Statistical normalization techniques for magnetic resonance imaging.** *Neuroimage Clin* 2014;6:9–19 CrossRef Medline
15. Bill A. **Capillary permeability to and extravascular dynamics of myoglobin, albumin and gammaglobulin in the uvea.** *Acta Physiol Scand* 1968;73:204–19 CrossRef Medline
16. Jacobsen HH, Ringstad G, Jørstad ØK, et al. **The human visual pathway communicates directly with the subarachnoid space.** *Invest Ophthalmol Vis Sci* 2019;60:2773– 80 CrossRef Medline
17. Jacobsen HH, Sandell T, Jørstad ØK, et al. **In vivo evidence for impaired glymphatic function in the visual pathway of patients with normal pressure hydrocephalus.** *Invest Ophthalmol Vis Sci* 2020;61:24 CrossRef Medline

Adding MR Diffusion Imaging and T2 Signal Intensity to Neck Imaging Reporting and Data System Categories 2 and 3 in Primary Sites of Postsurgical Oral Cavity Carcinoma Provides Incremental Diagnostic Value

A. Jajodia, G. Mandal, V. Yadav, J. Khoda, J. Goyal, S. Pasricha, S. Puri, and A. Dewan

ABSTRACT

BACKGROUND AND PURPOSE: The NI-RADS lexicon doesn't use ADC parameters and T2 weighted signal for ascribing categories. We explored ADC, DWI, and T2WI to examine the diagnostic accuracy in primary sites of postsurgical oral cavity carcinoma in the Neck Imaging Reporting and Data System (NI-RADS) categories 2 and 3.

MATERIALS AND METHODS: We performed a retrospective analysis in clinically asymptomatic post-surgically treated patients with oral cavity squamous cell carcinoma who underwent contrast-enhanced MRI between January 2013 and January 2016. Histopathology and follow-up imaging were used to ascertain the presence or absence of malignancy in subjects with "new enhancing lesions," which were interpreted according to the NI-RADS lexicon by experienced readers, including NI-RADS 2 and 3 lesions in the primary site. NI-RADS that included T2WI and DWI (referred to as NI-RADS A) and ADC (using the best cutoff from receiver operating characteristic curve analysis, NI-RADS B) was documented in an Excel sheet to up- or downgrade existing classic American College of Radiology NI-RADS and calculate diagnostic accuracy.

RESULTS: Sixty-one malignant and 23 benign lesions included in the study were assigned American College of Radiology NI-RADS 2 ($n = 33$) and NI-RADS 3 ($n = 51$) categories. The recurrence rate was 90% (46/51) for NI-RADS three, 45% (15/33) for NI-RADS 2, and 73% (61/84) overall. T2WI signal morphology was intermediate in 45 subjects (53.5%) and restricted DWI in 54 (64.2%). Sensitivity, specificity, positive predictive value, negative predictive value, and accuracy of the American College of Radiology NI-RADS were the following: NI-RADS (75.4%, 78.3%, 90.1%, 54.5%, and 76.1%); NI-RADS A (79.1%, 81.2%, 91.9%, 59.1%, and 79.6%); and NI-RADS B (88.9%, 72.7%, 91.4%, 66.7%, and 85.1%), respectively.

CONCLUSIONS: Adding MR imaging diagnostic characteristics like T2WI, DWI, and ADC to the American College of Radiology NI-RADS improved diagnostic accuracy and sensitivity.

ABBREVIATIONS: ACR = American College of Radiology; AUC = area under the ROC curve; CE = contrast-enhanced CT; HNSCC = head and neck squamous cell carcinoma; NI-RADS = Neck Imaging Reporting and Data System; NPV = negative predictive value; PPV = positive predictive value; ROC = receiver operating characteristic

Head and neck squamous cell carcinomas (HNSCCs) recur in up to 15%–50% of patients, most frequently in the first 2–3 years after treatment, and surveillance imaging is critical during this period to detect recurrence as quickly as possible, contributing to optimistic salvage treatment choices.[1] Salvage surgery may be undertaken in the setting of recurrent disease, and if this is not practicable, chemotherapy and a biologic agent may be used.[2] Patients with recurrences of early-stage HNSCC who undergo salvage surgery have a 70% 2-year relapse-free survival rate, as opposed to others with advanced-stage HNSCC, who have a 22% 2-year relapse-free survival rate.[3]

The National Comprehensive Cancer Network suggests post-treatment baseline imaging after 6 months of therapy for advanced HNSCC but does not formally advocate imaging for asymptomatic patients.[4] Few studies show a clear benefit or survival advantage to using ubiquitous surveillance imaging after the initial baseline assessment.[5] However, the ideal timing and frequency for using PET with contrast-enhanced (CE) CT in the posttreatment context have not yet been established.[6]

The American College of Radiology (ACR) in 2016 released the first iteration of a standardized reporting system dubbed the Neck Imaging Reporting and Data System (NI-RADS).[7] The lexicon defines NI-RADS 2b lesions as deep soft-tissue lesions with ill-defined
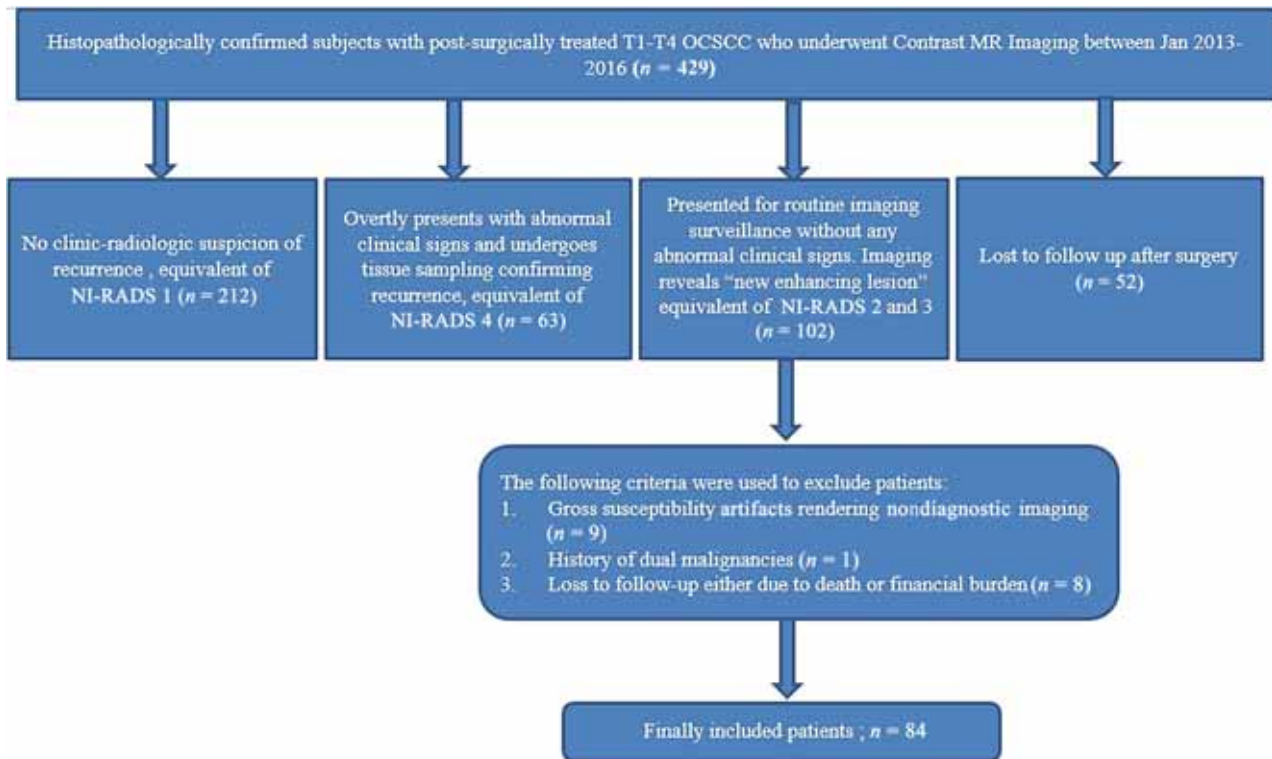
FIG 1. Flow chart of the enrolling process of the study and reasons for patient exclusion. OCSCC indicates oral cavity squamous cell carcinoma.

or mildly enhancing soft tissue or soft tissue with only mild FDG uptake. These are indeterminate lesions and should have a short-term-interval follow-up. Depending on the degree of suspicion for treatment failure, NI-RADS 3 lesions should have a short-term-interval follow-up or biopsy. In past studies, recurrence rates in NI-RADS 2b and NI-RADS 3 lesions were 5.6% and 60%–80%, respectively.[8]

The template was initially designed for CECT with a concentration on PET/CT for detecting recurrence; MR imaging has been recently explored in various studies.[9-11] ADC has potential value for distinguishing recurring tumors and posttreatment changes in head and neck squamous cell carcinoma.[12] Although DWI has become a routine sequence in head and neck imaging, it is not yet a criterion in NI-RADS;[13] until recently, when a study[11] evaluated the additive role of T2WI DWI in the NI-RADS MR imaging lexicon. Past studies[5,8,11,14,15] have appraised MR imaging in NI-RADS but with numerous limitations like heterogeneous imaging with a more miniature representation of MR imaging[8] and a smaller amount of oral cavity squamous cell carcinoma as a subsite,[14,15] small NI-RADS 3 in a representative sample population,[14] and lack of a fixed interval for inclusion in the sample population.[15]

We aimed to explore the incremental diagnostic accuracy using ADC, DWI, and T2WI in NI-RADS categories 2 and 3 in primary sites of postsurgical oral cavity carcinoma.

MATERIALS AND METHODS
Patient Selection
After institutional review board approval, a retrospective analysis was performed in patients with post-surgically treated oral cavity squamous cell carcinoma who presented between January 2013 and January 2016 to the surgical outpatient services as a part of the

institution-based protocol for surveillance contrast-enhanced MR imaging. The final cohort consisted of clinically asymptomatic patients who were determined to have "new enhancing lesions" on surveillance imaging. A time interval of >3 months and <2 years from the point of surgery and/or completion of chemoradiation was considered suitable clinically for inclusion. If imaging surveillance examination findings are worrisome but not conclusive of recurrence, a multidisciplinary meeting every week determines the decision to shorten the next surveillance interval. A routine follow-up imaging study was performed every 8–12 weeks for the new enhancing lesion.

Occult recurrence was without troubling symptoms or physical examination evidence consistent with posttreatment changes. Suspicious clinical examination results include new palpable abnormalities on physical examination or a suspicious finding by surgeons performing flexible fiber optic endoscopy. Clinically asymptomatic patients determined to have new enhancing lesions on surveillance imaging were assessed for tissue-sampling feasibility. Histopathology was the criterion standard to confirm the presence or absence of malignancy. If not feasible due to any reason, the new enhancing lesion was assigned "benign" if it resolved or shrank spontaneously in the absence of therapy within 6–12 months as determined by a follow-up imaging study. New enhancing lesions were labeled malignant if confirmed histopathologically or on follow-up imaging. Only NI-RADS categories 2 and 3 were included in the study. Figure 1 summarizes the flow chart of the study enrolling process and reasons for patient exclusion.

In the stipulated study period, a total of 84 patients were enrolled. Informed consent was waived after approval from the institutional review board and the scientific committee.

Imaging Study and Image Analysis

We used a 1.5T Avanto (Siemens) machine with a circular polarization surface coil to perform traditional diffusion-weighted scans. The patients had DWIs performed using a multisection spin-echo single-shot EPI sequence. An average of 15 sections was obtained in the axial plane, covering the study area. The parameters for the imaging were as follows: TR/TE of 10,000/108 ms, a FOV of 23 × 23 cm, a 128 × 128 matrix, a section thickness of 5 mm, and a 1- to 2-mm gap between sections when they met. Diffusion-probing gradients were used in all 3 orthogonal directions (x, y, and z). With a diffusion-weighted factor, factor b, the MR images were obtained at 0, 400, and 800 s/mm^2. They were obtained with a factor of $b = 0$. Radiologists reviewed DWIs and decided whether they were good enough to be used for more study, paying attention to how susceptibility artifacts could distort the image. Finally, T1WIs (TR/TE of 800/15 ms) were performed after the patients had gadolinium-based contrast injected into their veins. Before giving the patients contrast and getting their permission, the renal function parameters were checked.

New enhancing lesions were in proximity to the primary tumor site, visualized as areas of T2 prolongation that could be edema, fibrous-inflammatory reaction, neoplasm, and different levels of mass effect. While the initial radiologic report used nonstandardized formats because they were studied before 2016, new enhancing lesions were graded and interpreted following the NI-RADS lexicon by experienced readers (20 years' experience). Our focus in this study was only on NI-RADS 2 and 3 lesions in the primary site.

Using a previously described methodology,[11] we manually placed 3 polygonal ROIs on the highest b-value (800) images, either on the same or subsequent axial sections, according to the size and extent of the primary foci, and a head and neck radiologist with 20 years of experience in the interpretation of oral cavity squamous cell carcinoma MR images automatically copied them on the appropriate ADC maps. In the presence of enhancement, ROIs were placed on the most enhancing regions of new enhancing lesions, excluding necrotic areas, using contrast-enhanced T1WI and T2WI in the same axial sections. The average ADC mean value was determined using the 3 measurements for each target.

A review of related literature[11,13,16] helped us classify T2WI signal morphology as iso- to hypo-intense, intermediate and hyperintense to muscle signal intensity. Similar to a previous study,[11] if the T2WI had an intermediate tumor signal with corresponding diffusion restriction (diffusion restriction was defined as the presence of high signal intensity on DWI [b-value = 800 s/mm^2] and low signal intensity on the ADC map in the corresponding tumor, an upgrade was assigned to the NI-RADS category. Similarly, a downgrade was assigned in the absence of both features. The best cutoff for the study population was determined by the Youden index of the receiver operating characteristic (ROC) curve for ADC values. The new NI-RADS taking into account T2WI and DWI (referred to as NI-RADS A for purposes of simplicity) and ADC (choosing the best cutoff yielded by ROC, referred to as NI-RADS B) was documented in an Excel (Microsoft) sheet for calculation of diagnostic accuracy.

Statistical Analysis

SPSS 22.0 (IBM) was used for statistical evaluation. The 2-sided Fisher exact test was used to calculate P values for categoric variables, while the differences in medians test were used to obtain P values for continuous variables.

A Diagnostic Test Calculator (http://araw.mede.uic.edu/cgi-bin/testcalc.pl) was used to calculate specificity, sensitivity, and positive and negative likelihood ratios for different diagnostic categories. The statistical program MedCalc 12.2.1 (MedCalc Software) was used to generate ROC curves and compare the areas under the ROC curves (AUCs). ROC and AUC were used to predict malignancy. The AUC, a measure of the diagnostic accuracy of the individual parameter, is shown with 95% CIs. ROC curves were compared using the DeLong test. A 2-tailed $P < .05$ was considered statistically significant.

RESULTS

Among the 84 subjects enrolled in the study with a median age of 59 years (range, 32–83 years), 61 had a malignant new enhancing lesion and 23 had benign lesions. The histologic findings of 61 malignant and 23 benign lesions were verified by tissue sampling in 69 subjects and follow-up imaging within 8–12 weeks in the remaining 15 subjects. The follow-up imaging revealed unequivocal progression in 5 cases, which were labeled "malignant," while resolution in the remaining 10 cases was labeled benign. The histopathology of the benign lesions was granulation tissue ($n = 5$), fibrous elements ($n = 3$), abscess ($n = 3$), and osteoradionecrosis ($n = 2$). The median time to recurrence in our study was 8 months (range, 5–37 months). Surgery with or without radiation therapy as a part of management for recurrence was performed in 24/61 subjects after discussion in a multidisciplinary tumor board committee. The remaining 30 subjects were managed by radiation with or without chemotherapy, while 7 were provisionally started on oral metronomic therapy.

Thirty-three subjects were assigned ACR NI-RADS 2, while 51 were assigned the NI-RADS 3 category based on the lexicon and previous studies. Our recurrence rate was 90% (46/51) for NI-RADS-3, 45% (15/33) for NI-RADS-2, and 73% (61/84) overall.

The median ADC of lesions was 1.12×10^{-3} mm^2/s (range = $0.48–2.18 \times 10^{-3}$ mm^2/s), and T2WI signal morphology was hypointense ($n = 10$, 11.9%), intermediate ($n = 45$, 53.5%), and hyperintense ($n = 29$, 34.5%). DWI was interpreted as positive for restriction in 54 (64.2%) patients. There was a statistically significant difference between the benign and malignant new enhancing lesions concerning the ACR NI-RADS category and DWI, T2WI, and ADC values, as elaborated in Table 1.

The ROC curve produced an AUC that measured the overall diagnostic accuracy (Fig 2), with the best diagnostic performance by DWI (AUC = 0.793). ROC analysis showed an AUC of 0.72 (0.611–0.811 CI) for ADC, with a cutoff ADC mean of $>1.3 \times 10^{-3}$ mm^2/s, which showed the highest sensitivity, specificity, positive predictive value (PPV), and negative predictive value (NPV) (88.5%, 56.5%, 84.3%, and 65.1%, respectively). There were 34/37 (92%) correct upgrades and 9 incorrect downgrades in NI-RADS A, with 32/35 (91%) correct upgrades and 8 correct downgrades in NI-RADS B. The addition of T2 signal morphology and ADC

yielded higher diagnostic accuracy than ACR NI-RADS. NI-RADS A and NI-RADS B had a higher diagnostic performance (sensitivity, specificity, PPV, NPV, and accuracy of 79.1%, 81.2%, 91.9%, 59.1%, and 79.6%; and 88.9%, 72.7%, 91.4%, 66.7%, and 85.1%, respectively) compared with the ACR NI-RADS (75.4%, 78.3%,

90.1%, 54.5%, and 76.1%). The diagnostic parameters alone and in combination are summarized in Table 2.

DISCUSSION

Our study shows that a definite incremental sensitivity is achieved with concomitant diagnostic accuracy by incorporating T2WI, DWI, and ADC metrics into the existing ACR NI-RADS lexicon descriptors. There was a noticeable improvement in the false-positives, which would help the surgeon obviate unnecessary biopsies, and the false-negatives that would correctly identify actual disease without delay, which is essential to provide the window of salvage opportunities.

Our study had a 72% recurrence rate in our population of asymptomatic patients. The recurrence rate was 54% (46/84) in NI-RADS 3 and 17% (15/84) in NI-RADS 2, similar to findings in a previous study,[14] which documented 54.6% in a large subset of 618 subjects. Our study is quintessential because it deals with a subset of the population who were clinically occult and asymptomatic, which was a shortfall in the previous studies.[5]

Table 1: Baseline characteristics of study population (n = 84)

	Recurrence	No Recurrence	P Value
NI-RADS			<.001
NI-RADS 2	15	18	
NI-RADS 3	46	5	
DWI			<.001
Present	49	5	
Absent	12	18	
T2WI			.02
Hypo	4	6	
Intermediate	37	8	
High	20	9	
ADC ($\times 10^{-3}\,mm^2/s$)			<.001
>1.3	7	13	
<1.3	54	10	

Note:—Hypo indicates Hypo-intense.

Variable	AUC	95% CI[b]
DWI	0.793	0.691 to 0.874
ACR NI-RADS	0.768	0.664 to 0.853
ADC	0.720	0.611 to 0.812
T2WI	0.536	0.424 to 0.646
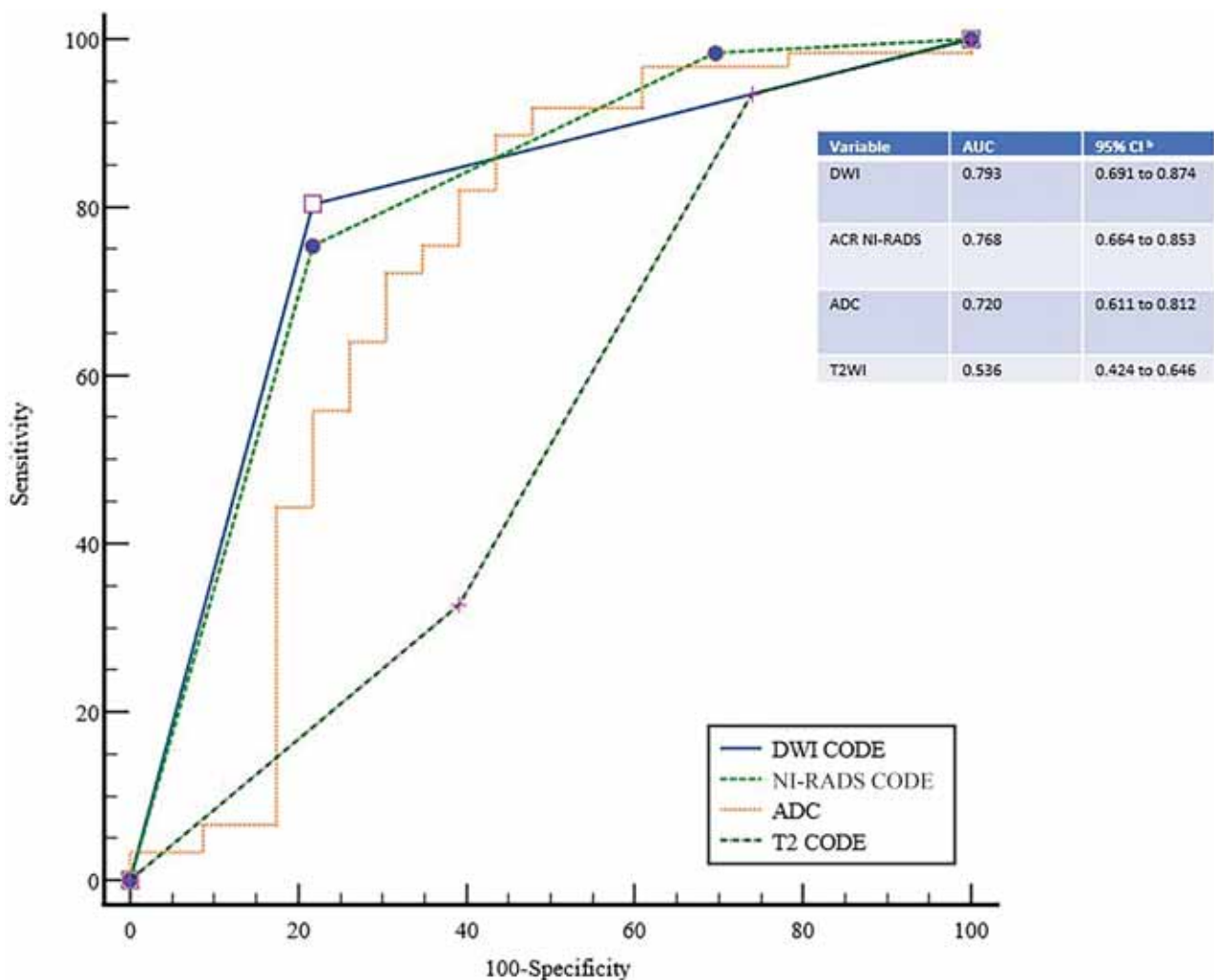
FIG 2. ROC comparison curves for ACR NI-RADS, TW2I, DWI, and ADC show the highest diagnostic accuracy with DWI (0.793), followed by ACR NI-RADS (0.768), ADC (0.720), and T2WI (0.536), with a statistically significant difference between DWI and T2WI (P value = .002) and ACR NI-RADS and T2WI (P value = .005).

Table 2: Diagnostic parameters for different criteria included in the study

Criteria	Specificity	Sensitivity	PPV	NPV	Accuracy
NI-RADS	78.3	75.4	90.1%	54.5%	76.1%
NI-RADS A	81.2	79.1	91.9%	59.1%	79.6%
NI-RADS B	72.7	88.9	91.4%	66.7%	85.1%
ADC	56.5	88.5	84.3%	65.1%	79.7%
DWI	78.3	80.3	90.7%	60.1%	79.7%
T2 signal	65.2	60.7	82.2%	38.5%	61.9%
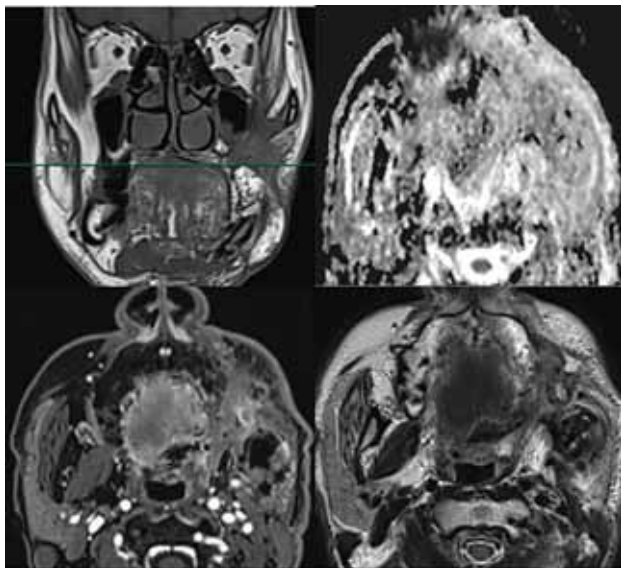
FIG 3. A post-surgically treated case of left buccal mucosa squamous cell carcinoma in a symptomatic 45-year-old male subject with a mild-to-moderate new enhancing lesion in the deep tissue along the superior margin of the flap occult to clinical examination, interpreted as NI-RADS 2. Corresponding ADC shows low values ($<1.3 \times 10^{-3}$ mm^2/s) with intermediate gray T2WI. It was a histopathologically-confirmed malignancy.

In a previous study,[5] more than one-third of all imaging-detected recurrences occurred in patients with no clinical symptoms, with a median time of 4–11 months,[15] similar to our findings, re-emphasizing the critical nature of extending the current National Comprehensive Cancer Network imaging surveillance guidelines beyond the first 6 months of treatment. It has been found that more than one-third of the recurrences identified on imaging were clinically indistinguishable from recurrences that were clinically occult, and 80% of those occurred >6 months after therapy.[5]

Previous studies[14,15] documented an overall PPV of 54%–56% for NI-RADS 3 posttreatment PET/CT, which was considered low. Compared with these previous studies, our diagnostic parameters using MR imaging had a high PPV (90%). We observed that the PPV did not show any improvement among the DWI, ACR NI-RADS, NI-RADS A, and NI-RADS B diagnostic categories but exhibited a high PPV compared with previous studies using CECT/PET/CT (90% versus 56%). We hypothesize that this high PPV could be due to our institutional imaging protocol because a study found that CECT alone was more likely to correctly identify recurrence than CECT PET (91.7% versus 40.0%).[14] However, this finding lowers the NPV of the NI-RADS 2 category, which is undesirable (67% NPV versus 91% PPV), as we found in our results.

NI-RADS favors NPV over PPV to potentially capture treatable lesions, even if it comes at the cost of performing additional biopsies. One possible explanation for our findings was that our experienced readers were overly cautious, favoring specificity over sensitivity. NI-RADS can serve as an assessment tool, with which individual radiologists or groups of radiologists can use the PPV and NPV to evaluate their own performance. We found improved detection of recurrence using ADC and T2WI/DWI parameters in conventional NI-RADS (88% and 79% versus 75%).[14] The overall diagnostic accuracy for NI-RADS at the primary site was 0.786, comparable with ours (AUC = 0.768). Although a previous study[11] showed higher specificity than ours (90.7 versus 56.5%) for a comparable sensitivity (92% versus 88%) for the diagnostic parameter ADC, it included most non-surgical candidates not specific to subsite of oral cavity subsite specific patients. Our study highlights the importance of imaging in this subsite, which is more subject to misreading due to the complex altered anatomy in post-surgically treated cases.

Among the 9 false, downgrades in NI-RADS A in our study, 5 subjects were due to superadded infection amounting to abscess formation in 3 and osteoradionecrosis of the mandible in 2, keeping with the previous literature.[6] The use of ADC and deploying NI-RADS B correctly identified 5 of these, as depicted in representative cases in Fig 3. Functional imaging like DWI and ADC parameters derived from DWI have shown promise in identifying true disease recurrence with higher specificity than conventional PET/CT, with a reported pooled sensitivity and specificity of 85% and 93% for PET/CT.[8] However, in our institution, the cost and radiation[17] factors propel the multidisciplinary team to use PET/CT in reserve cases. The cost-effectiveness and overall survival advantage have not been discussed here because they are beyond the scope of this study and will be addressed in future studies.

One potential limitation in our study was the lack of inter-reader agreement, but studies[18] have found that assigning NI-RADS categories to findings and impressions has moderate-to-solid interreader and intrareader reliability, even when readers with different levels of experience from different institutions read the studies. We could not determine how early imaging can detect recurrences or its effect on an outcome. This determination would need controls that were beyond the scope of the study. Our study focused on the primary site without addressing the neck. Abnormal and palpable lymphadenopathy in a post-surgically treated population by clinical examination would be subjected to sonography-guided tissue sampling for confirmation without MR imaging. Last, although our study has a clinically occult population, some subjects had trismus due to postsurgical and radiation therapy. This would mean an improper or unjust "clinically occult" classification on our part in this subset of patients. Last, further differentiation and suggestions for follow-up imaging for NI-RADS categories 2b and 3 would be suitable, as mentioned in a previous study,[10] but we did not have a large enough sample size to arrive at these conclusions.

CONCLUSIONS

Improved diagnostic accuracy was achieved in classic ACR NI-RADS by including MR imaging diagnostic parameters like T2WI, DWI, and ADC, with a gain in sensitivity. Standardization

of associated treatment recommendations and their relevance to patient outcomes should validate performance and emphasize the radiologist's added value in in patient care. Before implementing the NI-RADS imaging template, a standardized approach to develop a consensus surveillance imaging algorithm should be undertaken.

Disclosure forms provided by the authors are available with the full text and PDF of this article at www.ajnr.org.

REFERENCES

1. Chang JH, Wu CC, Yuan KS, et al. **Locoregionally recurrent head and neck squamous cell carcinoma: incidence, survival, prognostic factors, and treatment outcomes.** *Oncotarget* 2017;8:55600–12 CrossRef Medline

2. Ritoe SC, Krabbe PFM, Kaanders JH, et al. **Value of routine follow-up for patients cured of laryngeal carcinoma.** *Cancer* 2004;101:1382–89 CrossRef Medline

3. Goodwin WJ. **Salvage surgery for patients with recurrent squamous cell carcinoma of the upper aerodigestive tract: when do the ends justify the means?** *Laryngoscope* 2000;110:1–18 CrossRef Medline

4. Wierzbicka M, Napierała J. **Updated National Comprehensive Cancer Network Guidelines for Treatment of Head and Neck Cancers 2010-2017.** *Otolaryngol Pol* 2017;71:1–6 CrossRef Medline

5. Gore A, Baugnon K, Beitler J, et al. **Posttreatment imaging in patients with head and neck cancer without clinical evidence of recurrence: should surveillance imaging extend beyond 6 months?** *AJNR Am J Neuroradiol* 2020;41:1238–44 CrossRef Medline

6. Baugnon KL. **NI-RADS to predict residual or recurrent head and neck squamous cell carcinoma.** *Neuroimaging Clin N Am* 2022;32:1–18 CrossRef Medline

7. Aiken AH, Farley A, Baugnon KL, et al. **Implementation of a novel surveillance template for head and neck cancer: Neck Imaging Reporting and Data System (NI-RADS).** *J Am Coll Radiol* 2016;13:743–46.e1 CrossRef Medline

8. Dinkelborg P, Ro SR, Shnayien S, et al. **Retrospective evaluation of NI-RADS for detecting postsurgical recurrence of oral squamous cell carcinoma on surveillance CT or MRI.** *AJR Am J Roentgenol* 2021;217:198–206 CrossRef Medline

9. Aiken AH, Rath TJ, Anzai Y, et al. **ACR Neck Imaging Reporting and Data Systems (NI-RADS): a white paper of the ACR NI-RADS committee.** *J Am Coll Radiol* 2018;15:1097–1108 CrossRef Medline

10. Elsholtz FH, Erxleben C, Bauknecht HC, et al. **Reliability of NI-RADS criteria in the interpretation of contrast-enhanced magnetic resonance imaging considering the potential role of diffusion-weighted imaging.** *Eur Radiol* 2021;31:6295–6304 CrossRef Medline

11. Ashour MM, Darwish EA, Fahiem RM, et al. **MRI posttreatment surveillance for head and neck squamous cell carcinoma: proposed MR NI-RADS criteria.** *AJNR Am J Neuroradiol* 2021;42:1123–29 CrossRef Medline

12. Hwang I, Choi SH, Kim YJ, et al. **Differentiation of recurrent tumor and posttreatment changes in head and neck squamous cell carcinoma: application of high b-value diffusion-weighted imaging.** *AJNR Am J Neuroradiol* 2013;34:2343–48 CrossRef Medline

13. Ailianou A, Mundada P, De Perrot T, et al. **MRI with DWI for the detection of posttreatment head and neck squamous cell carcinoma: why morphologic MRI criteria matter.** *AJNR Am J Neuroradiol* 2018;39:748–55 CrossRef Medline

14. Krieger DA, Hudgins PA, Nayak GK, et al. **Initial performance of NI-RADS to predict residual or recurrent head and neck squamous cell carcinoma.** *AJNR Am J Neuroradiol* 2017;38:1193–99 CrossRef Medline

15. Wangaryattawanich P, Branstetter BF, Ly JD, et al. **Positive predictive value of neck imaging reporting and data system categories 3 and 4 posttreatment FDG-PET/CT in head and neck squamous cell carcinoma.** *AJNR Am J Neuroradiol* 2020;41:1070–75 CrossRef Medline

16. King AD, Keung CK, Yu KH, et al. **T2-weighted MR imaging early after chemoradiotherapy to evaluate treatment response in head and neck squamous cell carcinoma.** *AJNR Am J Neuroradiol* 2013;34:1237–41 CrossRef Medline

17. Pryor DI, Porceddu SV, Scuffham PA, et al. **Economic analysis of FDG-PET-guided management of the neck after primary chemoradiotherapy for node-positive head and neck squamous cell carcinoma.** *Head Neck* 2013;35:1287–94 CrossRef Medline

18. Hsu D, Rath TJ, Branstetter BF, et al. **Interrater reliability of NI-RADS on posttreatment PET/contrast-enhanced CT scans in head and neck squamous cell carcinoma.** *Radiol Imaging Cancer* 2021;3:e200131 CrossRef Medline

Do We Need Gadolinium-Based Contrast Agents for Routine MRI Surveillance of Unoperated Pituitary Macroadenoma?

 A.A. Alali, P.B. Hanagandi, and P.J. Maralani

ABSTRACT

BACKGROUND AND PURPOSE: The use of gadolinium-based contrast agents contributes to the cost of MR imaging and prolongs image-acquisition time. There are also recent concerns regarding gadolinium deposition, particularly in patients who require frequent follow-up MRIs. The purpose of this study was to assess whether gadolinium-based contrast agents are needed during MR imaging follow-up for unoperated pituitary macroadenoma.

MATERIALS AND METHODS: A total of 105 patients with unoperated pituitary macroadenoma who underwent follow-up MR imaging of the sella were included in this retrospective study. The craniocaudal dimension, cavernous sinus invasion grading, and optic pathway compression were assessed independently on coronal T2WI and compared with coronal T1-weighted images with gadolinium-based contrast agents (T1 postcontrast images). The agreement between the T2WI and T1 postcontrast images for the craniocaudal dimension was assessed using the intraclass correlation coefficient; for the cavernous sinus invasion and optic pathway compression, it was assessed using κ statistics.

RESULTS: There was excellent agreement for the craniocaudal dimensions between T2WI and T1 postcontrast images (intraclass correlation coefficient = 0.96, $P < .001$; 95% CI, 0.84–0.99). Additionally, there was almost-perfect agreement between cavernous sinus invasion and optic pathway compression between T2WI and T1 postcontrast images, with κ = 0.95 and 0.84, respectively ($P < .001$).

CONCLUSIONS: MR imaging of the sella without the use of gadolinium-based contrast agents could potentially be considered for the follow–up of unoperated pituitary macroadenomas. This choice can reduce the MR imaging examination cost and acquisition time and avoids potential adverse effects of gadolinium-based contrast agents.

ABBREVIATIONS: GBCA = gadolinium-based contrast agent; ICC = intraclass correlation coefficient; T1C = T1 postcontrast images

Pituitary adenoma is a benign slow-growing tumor with an estimated prevalence of 14.4% in postmortem and 22.5% in imaging studies.[1] Macroadenomas represent up to 31% of pituitary adenomas in epidemiologic studies.[2,3] Patients with macroadenoma who are not candidates for upfront surgery or elect not to have surgery require MR imaging follow-up to assess tumor size, cavernous sinus invasion, and mass effect on the optic pathways with commonly used gadolinium-based contrast agents (GBCAs).

GBCAs increase the cost of MR imaging, prolong scan time, and require insertion and discontinuation of intravenous access,

which further contribute to scan costs. GBCAs are also associated with adverse reactions at a rate of 0.07%–2.4%.[4,5] Additionally, repeat GBCA administration can lead to permanent gadolinium deposition in the brain.[6-10] The clinical significance of these deposits is unknown. For these reasons, the risks must be weighed against benefits before administering GBCA.

The purpose of this study was to assess whether GBCAs are needed for routine MR imaging follow-up of unoperated pituitary macroadenomas. We hypothesized that coronal T2WI and coronal post-GBCA T1-weighted images (T1C) have the same performance for assessment of craniocaudal dimension, cavernous sinus invasion, and optic pathway compression in patients with unoperated pituitary macroadenomas.

MATERIALS AND METHODS

This retrospective, single-center study was approved by local institutional review board (King Abdullah International Medical Research Center) with a waiver of informed consent. The initial

search of our data base including patients 14 years of age and older with a diagnosis of pituitary macroadenoma who underwent MR imaging of the sella between January 2010 and September 2021 revealed 119 consecutive patients. Five were excluded because they did not have GBCA-enhanced scans, and 9 were excluded because they had prior pituitary surgery. A total of 105 patients were included in the study (Fig 1).

MR Imaging Scanning Settings
The patients were scanned on 3T Achieva (Philips Healthcare), 1.5T Espree (Siemens), or 3T Discovery (GE Healthcare) scanners. The imaging parameters for coronal T1C and coronal T2WI are detailed in Table 1. Gadoterate meglumine (Dotarem; Guerbet) was used as the GBCA for all patients.

Image Analysis
The first routine MR imaging follow-up of the sella was used for analysis to ensure that the dedicated pituitary protocol was performed for all patients. All scans were anonymized, and we constructed 2 separate batches: One contained only coronal T2WIs, and the other one contained only coronal T1Cs. To avoid potential bias, we analyzed the T1C batch 1 month after the T2WI batch analysis was completed. Analysis was performed by a neuroradiologist with 4 years of experience (A.A.A., reader 1), who was blind to all clinical data.

For each case, the maximum craniocaudal dimension of the macroadenoma was measured. The cavernous sinus invasion was assessed using the Knosp classification (Fig 2).[11] The optic pathway (prechiasmatic optic nerves, optic chiasm, or optic tracts) compression was assessed and classified into 3 categories: no contact, abutment without displacement, and compression with displacement.

To assess interrater reliability, we randomly chose 31 patients, and another neuroradiologist with 10 years of experience (P.B.H., reader 2) reviewed them independently using the same method as reader 1.

Statistical Analysis
Descriptive statistics were used for continuous variables including mean (SD) and range. A difference of ≥ 2 mm along the craniocaudal dimension between the baseline and follow-up examination was considered notable growth or shrinkage. The agreement between the coronal T2WI and T1C for the craniocaudal dimension was assessed using the intraclass correlation coefficient (ICC).[12] The agreement of the cavernous sinus invasion and optic pathway compression was assessed using κ statistics.[13]

All P values were 2-sided, and a $P < .05$ was considered statistically significant. Statistical analysis was performed using STATA, Version 17 (StataCorp).

RESULTS
A total of 105 patients, including 57 women (54.28%) and 48 men (45.71%), with pituitary macroadenoma were included in this study, with a mean age of 48.5 (SD,15.79) years (range, 16–87 years).

Analysis of Interval Growth
The mean time between the baseline and analyzed scans was 10.41 (SD, 5.96) months (range, 2–36 months). Thirty-eight/105 patients had routine brain MR imaging without dedicated sellar sequences as their baseline scan. To assess interval growth, we excluded these, with the remaining 67 patients
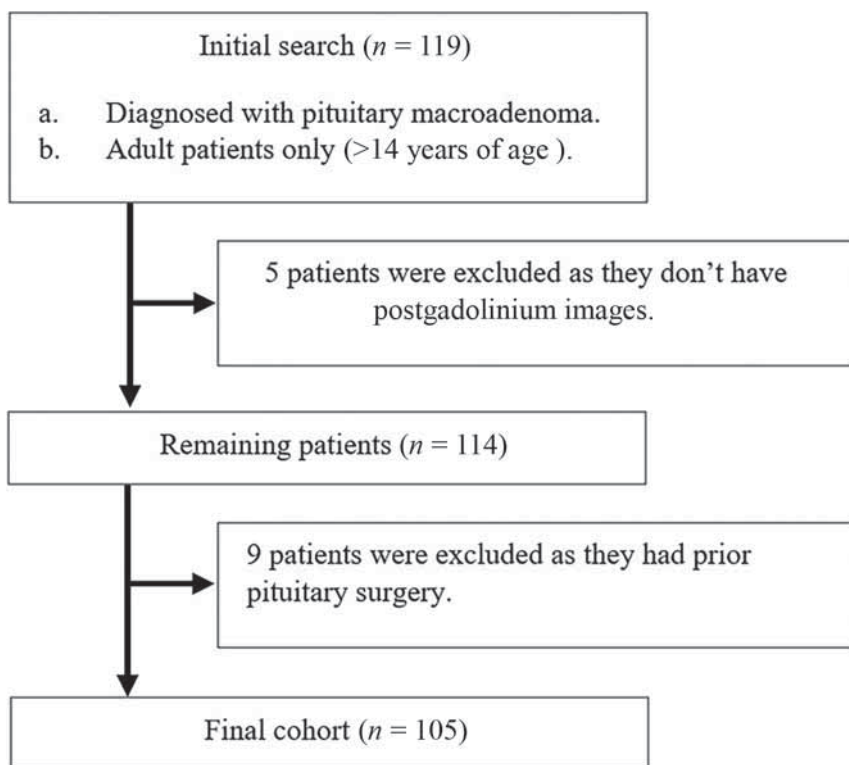
FIG 1. Flow chart shows patient selection.

Table 1: MR imaging parameters

Scanner	Coronal Sequence	TR (ms)	TE (ms)	Flip Angle	FOV (mm)	Section Thickness (mm)	Voxel Size (mm)	Image Matrix	Acquisition Time (Min)
Philips	T1WI	450	10	90°	130	2.5 or 3	$0.7 \times 0.7 \times 2.5$	184×184	3:45
	T2WI	3000	80	90°	130	2.5 or 3	$0.7 \times 0.7 \times 2.5$	184×185	2:32
GE	T1WI	471	9	111°	150	2.5 or 3	$0.6 \times 0.8 \times 2.5$	256×192	2:35
	T2WI	2800	103.9	111°	150	2.5 or 3	$0.5 \times 0.8 \times 2.5$	320×192	3:06
Siemens	T1WI	400	8.6	150°	140	2.5 or 3	$0.8 \times 0.5 \times 2.5$	179×256	2:50
	T2WI	3200	96	150°	140	2.5 or 3	$0.8 \times 0.5 \times 2.5$	184×256	2:25
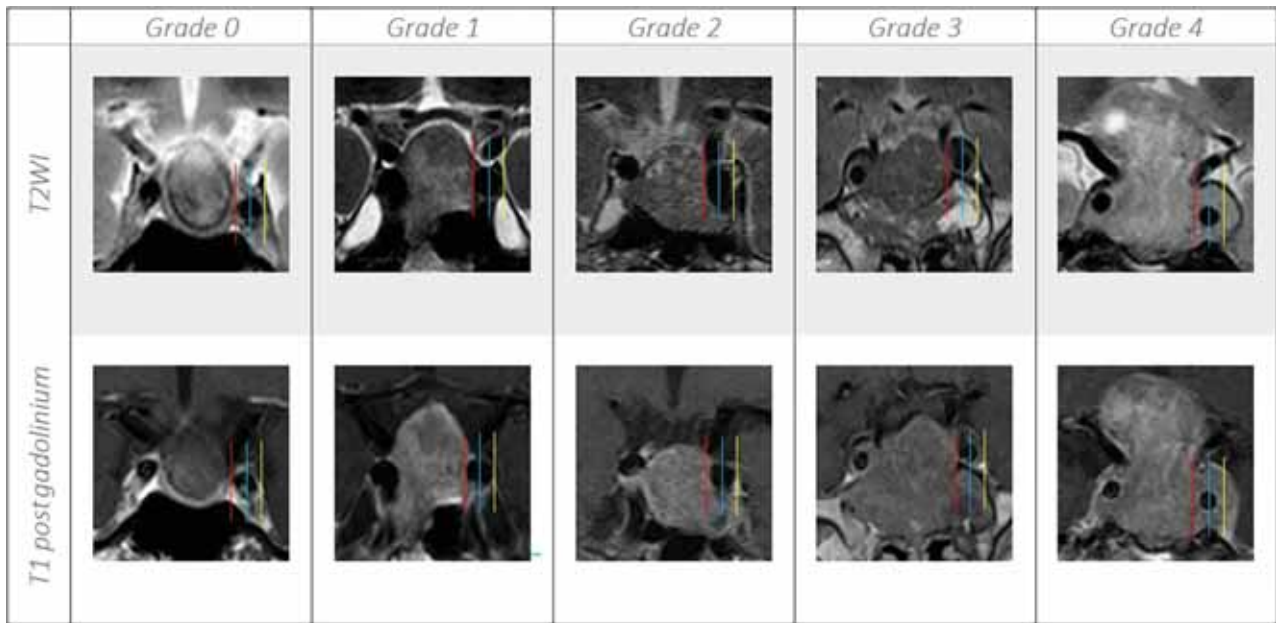
FIG 2. Coronal T2WI versus TIC show the different grades of cavernous sinus invasion using the Knosp classification; grade 0, the lesion does not extend beyond the medial carotid line (*red line*); grade 1, the lesion extends to the medial line but does not reach the intercarotid line (*blue line*); grade 2, the tumor extends beyond the intercarotid line but does not extend beyond the lateral line (*yellow line*); grade 3, the tumor extends to the lateral line more so on the left (*yellow line*); and grade 4, there is complete encasement of the cavernous carotid artery.

with dedicated MR imaging of the sella for both the baseline scans and the scans included in this study.

Thirty-four/67 (50.74%) patients were stable in their craniocaudal dimension: 16/67 (23.88%) increased and 17/67 (25.37%) decreased at almost-perfect agreement between the T2WI and T1C with a κ of 0.9 ($P < .001$). Analysis of the interval change revealed no significant difference in the craniocaudal dimensions between the T2WI and T1C ($P = .85$) and also excellent agreement between T2WI and T1C (ICC = 0.98, $P < .001$; 95% CI, 0.96–0.98).

By means of T2WI, the average growth or regression of the craniocaudal dimension from baseline to the follow-up scan was 3.8 (SD, 2.1) mm (range, 2–8 mm) and 6 (SD, 4.3) mm (range, 2–14 mm), respectively.

Analysis of the Craniocaudal Dimension

The mean craniocaudal dimension of macroadenomas on T2WI was 23.13 (SD, 10.73) mm (range, 9–55 mm) compared with 23.14 (SD, 10.79) mm (range, 8–55 mm) on the T1C ($P = .99$) (ICC = 0.96; $P < .001$; 95% CI, 0.84–0.99) (Table 2).

Analysis of the Cavernous Sinus Invasion

There were 16 patients classified as Knosp zero, 28 as Knosp one, 33 as Knosp two, 15 as Knosp 3, and 13 as Knosp 4, with almost-perfect agreement between the T2WI and T1C with $\kappa = 0.95$ ($P < .001$).

Analysis of the Optic Pathway Compression

The macroadenoma showed no contact with the optic pathway in 32 (30.47%) patients, while there was abutment of the optic pathway without displacement in 18 (17.14%) and mass effect and displacement in 55 (52.38%) patients (Fig 3). There was almost perfect agreement between the T2WI and T1C regarding the optic pathway compression with $\kappa = 0.84$ ($P < .001$).

Subgroup Analysis of Macroadenoma with Internal Heterogeneity

A total of 47 (44.76%) of 105 patients demonstrated a heterogeneous appearance on the T2WI sequence. Subgroup analysis of the heterogeneous macroadenomas revealed no significant difference in the craniocaudal dimensions ($P = .98$), but it did have excellent agreement between the sequences, (ICC = 0.99, $P < .001$; 95% CI 0.998–0.999). Analysis of the heterogeneous macroadenomas revealed less but still almost-perfect agreement between T2WI and T1C for cavernous sinus invasion with $\kappa = 0.94$ ($P < .001$) and substantial agreement for optic pathway compression with $\kappa = 0.74$ ($P < .001$).

Interrater Reliability

There were 31 patients randomly chosen and reviewed independently by both reader 1 and reader 2 for the craniocaudal dimensions, cavernous sinus invasions, and optic pathway compression using coronal T2WI. Analysis of this subset revealed excellent interrater reliability between the 2 readers for craniocaudal dimensions (ICC = 0.95, $P = .001$; 95% CI, 0.61–0.99) and substantial agreement for cavernous sinus invasion with $\kappa = 0.76$ ($P < .001$). There was also substantial agreement for the optic pathway compression with $\kappa = 0.77$ ($P < .001$).

DISCUSSION

In this study, we demonstrated that coronal T2WI and T1C perform similarly for assessment of craniocaudal length, cavernous sinus invasion, and optic pathway compression in patients with unoperated pituitary macroadenomas. MR imaging follow-up in this group of patients without the use of GBCA can provide safety improvement for patients and operational cost-savings.

Table 2: Summary statistics comparing the craniocaudal dimension of pituitary macroadenoma, cavernous sinus invasion, and optic pathway compression on T2WI versus T1C

	Coronal T2WI	Coronal T1C	Agreement ICC/κ
Craniocaudal dimension			
Mean	23.1 (SD, 10.7) mm	23.1 (SD, 10.8) mm	ICC = 0.96
Range	9–55 mm	8–55 mm	
Knosp Classification (No.) (%)			
0	16 (15.2)	16 (15.2)	κ = 0.95
1	28 (26.7)	27 (25.7)	
2	33 (31.4)	33 (31.4)	
3	15 (14.3)	16 (15.2)	
4	13 (12.4)	13 (12.4)	
Optic pathway compression (No.) (%)			
No contact	32 (30.5)	34 (32.4)	κ = 0.84
Abutment without displacement	18 (17.1)	20 (19)	
Compression with displacement	55 (52.4)	51 (48.6)	
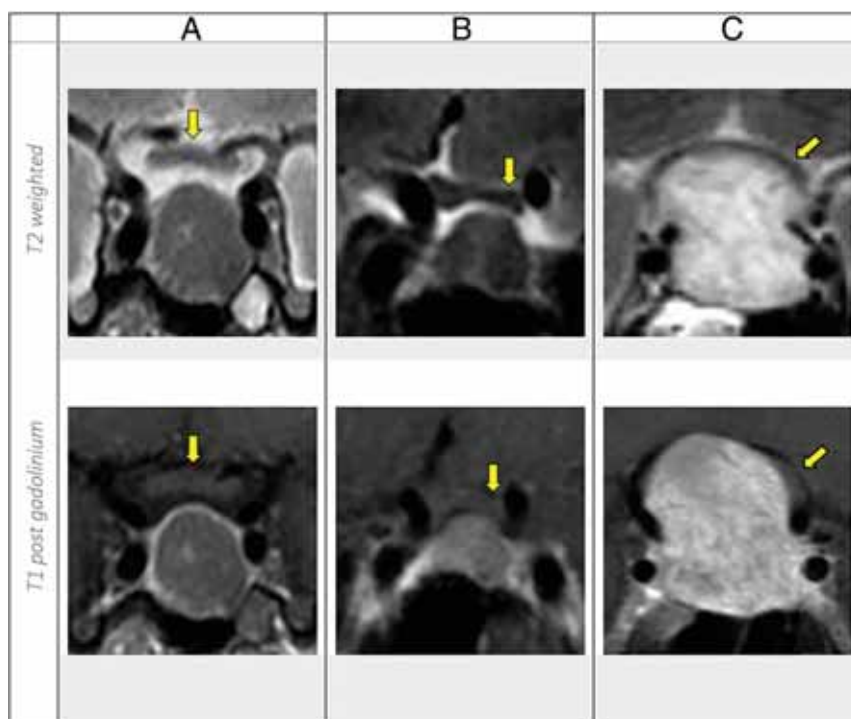
FIG 3. Coronal T2WI versus T1C show the optic pathway (depicted by *yellow arrows*) compression classification. *A*, There is no contact. *B*, The pituitary macroadenoma is abutting the left aspect of the optic chiasm without displacement. *C*, There are mass effect and displacement of the optic pathway.

Surgery is the standard of care for pituitary macroadenomas, particularly if symptomatic and large. However, up to 30% of pituitary macroadenomas are managed conservatively instead of with surgery for several reasons:[14] Some patients are not surgical candidates due to comorbidities. The benefits of upfront surgery for nonfunctioning asymptomatic pituitary macroadenoma or prolactin-secreting macroadenoma without optic pathway compression for patients undergoing medical treatment remains questionable.[15] Local practice patterns may also affect the decision to pursue upfront surgery rather than imaging follow-up in patients with pituitary macroadenoma. In addition, up to 24% of macroadenomas demonstrate evidence of growth with time if untreated.[16]

Therefore, there is a subgroup of patients with pituitary macroadenoma that do not undergo upfront surgery but need serial imaging follow-up annually or, in those patients in whom there is a high demonstrated growth rate, even more frequently.[17,18]

On the basis of our results, administration of GBCA has no added value to the follow-up MR imaging examinations for unoperated pituitary macroadenomas to assess tumor size. We assessed cavernous sinus invasion because it affects the surgical approach, risks, and outcomes.[19] Cavernous sinus invasion is associated with increased risk of residual disease and the need for future interventions[20] following surgery. This knowledge is necessary for risk-benefit assessment in patients with macroadenoma who are on conservative imaging surveillance. Visual pathway compression is also significant because the presence of visual impairment is a potential indication for surgery,[21] affecting surgical outcomes.[22,23] In addition, our results demonstrated no added value of performing coronal T1C compared with coronal T2WI in the assessment of heterogeneous-versus-non-heterogeneous macroadenomas.

Multiple prior studies have also demonstrated a lack of added clinical value of using GBCA for routine follow–up scans of benign intracranial tumors such as meningiomas[24] and vestibular schwannomas.[25] The contrast-enhanced scans are associated with increased cost, including the GBCAs themselves, longer scan times, and additional support staff for IV access insertion and removal. They are also associated with more patient discomfort and the potential for adverse reactions to GBCA. In addition, repeat GBCA administrations lead to permanent deposition of gadolinium in the brain, and, in particular, in the dentate nucleus and globus pallidus.[6-10] Although the current study was designed to compare T2WI and T1C, in practice the non-contrast-enhanced MR imaging of the sella includes T1-weighted images, which provide more information with regard to internal hemorrhage and the presence of fluid-fluid levels, a posterior pituitary bright spot, and bone marrow in the clivus compared with T2WI alone (Fig 4).

Limitations

The retrospective single-center nature of this study and limited sample size are sources of bias. Volumetric assessment of pituitary macroadenoma is the most accurate measure of its size. However,

| Sag T1 pre gad | Sag T2 | Sag T1 post gad |

| Coronal T2 | Coronal T1 post gad |
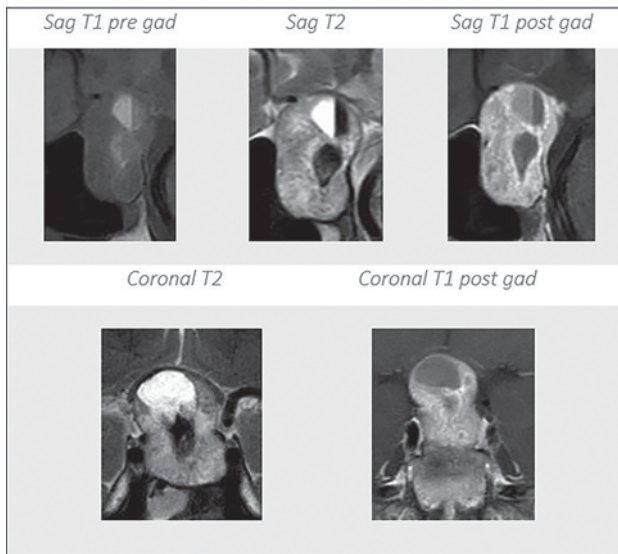
FIG 4. MR imaging of the sella shows internal hemorrhage with the hematocrit level on different sequences. Sag indicates sagittal; pre gad, pregadolinium; post gad, postgadolinium.

this is not applicable to daily clinical practice, and we, therefore, assessed the craniocaudal dimension due to its importance to optic pathway compression. Last, because local practice patterns can affect whether a patient with macroadenoma will undergo upfront surgery, different practices may have different numbers of patients to whom the results of this study could be applicable.

CONCLUSIONS

Our study suggests that non-contrast-enhanced MR imaging of the sella could potentially be considered for the follow–up scans of unoperated pituitary macroadenomas. The results need to be validated in larger, multicenter studies.

Disclosure forms provided by the authors are available with the full text and PDF of this article at www.ajnr.org.

REFERENCES

1. Ezzat S, Asa SL, Couldwell WT, et al. **The prevalence of pituitary adenomas: a systematic review.** *Cancer* 2004;101:613–19 CrossRef Medline
2. Aljabri KS, Bokhari SA, Assiri FY, et al. **The epidemiology of pituitary adenomas in a community-based hospital: a retrospective single center study in Saudi Arabia.** *Ann Saudi Med* 2016;36:341–45 CrossRef Medline
3. Hussein SH, Wahedi TS, Johani NA, et al. **Clinical and epidemiological characteristics of pituitary tumours in a single centre in Saudi Arabia.** *Hormones (Athens)* 2018;17:261–67 CrossRef Medline
4. Committee on Drugs and Contrast Media. **ACR Manual on Contrast Media.** 2021: American College of Radiology. 2021. https://www.acr.org/-/media/ACR/Files/Clinical-Resources/Contrast_Media.pdf.
5. Granata V, Cascella M, Fusco R, et al. **Immediate adverse reactions to gadolinium-based MR contrast media: a retrospective analysis on 10,608 examinations.** *Biomed Res Int* 2016;2016:3918292 CrossRef Medline
6. Stojanov D, Aracki-Trenkic A, Benedeto-Stojanov D. **Gadolinium deposition within the dentate nucleus and globus pallidus after repeated administrations of gadolinium-based contrast agents: current status.** *Neuroradiology* 2016;58:433–41 CrossRef Medline
7. Kanda T, Ishii K, Kawaguchi H, et al. **High signal intensity in the dentate nucleus and globus pallidus on unenhanced T1-weighted MR images: relationship with increasing cumulative dose of a gadolinium-based contrast material.** *Radiology* 2014;270:834–41 CrossRef Medline
8. Kanda T, Osawa M, Oba H, et al. **High signal intensity in dentate nucleus on unenhanced T1-weighted MR images: association with linear versus macrocyclic gadolinium chelate administration.** *Radiology* 2015;275:803–09 CrossRef Medline
9. Quattrocchi CC, Mallio CA, Errante Y, et al. **Gadodiamide and dentate nucleus T1 hyperintensity in patients with meningioma evaluated by multiple follow-up contrast-enhanced magnetic resonance examinations with no systemic interval therapy.** *Invest Radiol* 2015;50:470–72 CrossRef Medline
10. Gulani V, Calamante F, Shellock FG, et al; International Society for Magnetic Resonance in Medicine. **Gadolinium deposition in the brain: summary of evidence and recommendations.** *Lancet Neurol* 2017;16:564–70 CrossRef Medline
11. Knosp E, Steiner E, Kitz K, et al. **Pituitary adenomas with invasion of the cavernous sinus space: a magnetic resonance imaging classification compared with surgical findings.** *Neurosurgery* 1993;33:610–17; discussion 617–18 CrossRef Medline
12. Koo TK, Li MY. **A guideline of selecting and reporting intraclass correlation coefficients for reliability research.** *J Chiropr Med* 2016;15:155–63 CrossRef Medline
13. Landis JR, Koch GG. **The measurement of observer agreement for categorical data.** *Biometrics* 1977;33:159–74 CrossRef Medline
14. Levy MJ, Robertson IJ, Khalk N, et al. **Long-term follow-up of a large prospective cohort of patients with nonfunctioning pituitary adenomas: the outcome of a conservative management policy.** *Clin Endocrinol (Oxf)* 2018;89:354–59 CrossRef Medline
15. Ogiwara T, Nagm A, Nakamura T, et al. **Significance and indications of surgery for asymptomatic nonfunctioning pituitary adenomas.** *World Neurosurg* 2019;128:e752–59 CrossRef Medline
16. Molitch ME. **Pituitary tumours: pituitary incidentalomas.** *Best Pract Res Clin Endocrinol Metab* 2009;23:667–75 CrossRef Medline
17. Kim JH, Dho YS, Kim YH, et al. **Developing an optimal follow-up strategy based on the natural history of nonfunctioning pituitary adenomas.** *J Neurosurg* 2019;131:500–06 CrossRef Medline
18. Dekkers OM, Pereira AM, Romijn JA. **Treatment and follow-up of clinically nonfunctioning pituitary macroadenomas.** *J Clin Endocrinol Metab* 2008;93:3717–26 CrossRef Medline
19. Ajlan A, Achrol AS, Albakr A, et al. **Cavernous sinus involvement by pituitary adenomas: clinical implications and outcomes of endoscopic endonasal resection.** *J Neurol Surg B Skull Base* 2017;78:273–82 CrossRef Medline
20. Woodworth GF, Patel KS, Shin B, et al. **Surgical outcomes using a medial-to-lateral endonasal endoscopic approach to pituitary adenomas invading the cavernous sinus.** *J Neurosurg* 2014;120:1086–94 CrossRef Medline
21. Fahlbusch R, Honegger J, Buchfelder M. **Surgical management of acromegaly.** *Endocrinol Metab Clin North Am* 1992;21:669–92 CrossRef Medline
22. Powell M. **Recovery of vision following transsphenoidal surgery for pituitary adenomas.** *Br J Neurosurg* 1995;9:367–73 CrossRef Medline
23. Hisanaga S, Kakeda S, Yamamoto J, et al. **Pituitary macroadenoma and visual impairment: postoperative outcome prediction with contrast-enhanced FIESTA.** *AJNR Am J Neuroradiol* 2017;38:2067–72 CrossRef Medline
24. Boto J, Guatta R, Fitsiori A, et al. **Is contrast medium really needed for follow-up MRI of untreated intracranial meningiomas?** *AJNR Am J Neuroradiol* 2021;42:1421–28 CrossRef Medline
25. Buch K, Juliano A, Stankovic KM, et al. **Noncontrast vestibular schwannoma surveillance imaging including an MR cisternographic sequence: is there a need for postcontrast imaging?** *J Neurosurg* 2018;131:549–54 CrossRef Medline

Comparison of the Utility of High-Resolution CT-DWI and T2WI-DWI Fusion Images for the Localization of Cholesteatoma

X. Fan, C. Ding, and Z. Liu

ABSTRACT

BACKGROUND AND PURPOSE: Cholesteatoma is an aggressive disease that may lead to hearing impairment. This study aimed to compare the utility of high-resolution CT and TSE-DWI fusion images with that of T2WI and TSE-DWI fusion images in the localization of middle ear cholesteatoma.

MATERIALS AND METHODS: Seventy-one patients with middle ear cholesteatoma were retrospectively recruited. High-resolution CT, T2WI with fat suppression, and TSE-DWI scans were obtained, and image fusion was performed using a 3D reconstruction post-processing workstation to form CT-DWI and T2WI-DWI fusion images. The quality of the 2 fused images was subjectively evaluated using a 5-point Likert scale with the horizontal semicircular canal transverse position as the reference. Receiver operating characteristic analysis was performed, and the diagnostic efficacies of CT-DWI and T2WI-DWI fusion images in localizing middle ear cholesteatoma were calculated.

RESULTS: The overall quality of T2WI-DWI fusion images was slightly higher than that of CT-DWI fusion images ($P < .001$), and the semicircular canal was slightly less clear on T2WI-DWI than on CT-DWI ($P < .001$). No statistical difference was found in the diagnostic confidence between them. In the localization of middle ear cholesteatoma, the accuracy, sensitivity, and specificity of T2WI-DWI fusion images and CT-DWI fusion images were equivalent for involvement of the attic, tympanic cavity, mastoid antrum, and mastoid process, with no statistically significant differences.

CONCLUSIONS: T2WI-DWI fusion images could replace CT-DWI in the preoperative selection of surgical options for middle ear cholesteatoma.

ABBREVIATION: HRCT = high-resolution CT

C holesteatoma is an aggressive disease that can lead to conductive hearing impairment, facial palsy, labyrinthine fistula, brain abscess, and sigmoid sinus thrombosis when the lesion expands and invades adjacent structures.[1] Currently, surgical resection is the only treatment for cholesteatoma. The choice of a surgical approach varies according to the location and extent of cholesteatoma involvement;[2] therefore, precise preoperative localization is crucial.[3,4] DWI is commonly used by head and neck specialists as an imaging sequence to detect cholesteatoma,[5] especially in the diagnosis of recurrent or residual lesions.[6] Previous studies have shown that TSE-DWI has the advantages of causing fewer artifacts and providing higher lesion visibility for the diagnosis of cholesteatoma;[7] however, it is not effective in showing the

landmarks of temporal bone anatomy and is not reliable for preoperative localization or determination of the surgical approach.

High-resolution CT (HRCT) is the examination of choice for cholesteatoma. This technique displays clear anatomic details of the temporal bone region. The fusion of DWI and HRCT images has been reported in previous studies[8-12] in which cholesteatoma lesions with high signal intensity on DWI were superimposed on the corresponding HRCT temporal bone structures to improve preoperative cholesteatoma detection, assessment, and localization; however, DWI and HRCT are 2 different imaging techniques, and the fusion process is cumbersome. Kanoto et al[13] and Watanabe et al[14] showed that DWI with MR cisternography can increase the accuracy of anatomic localization. However, MR cisternography sequences of the ear require additional scanning time, which may cause motion artifacts due to patient discomfort from the prolonged body position, leading to image-quality degradation.

T2WI with fat suppression is a routine MR imaging sequence that can clearly show the key anatomic landmarks of the ear in
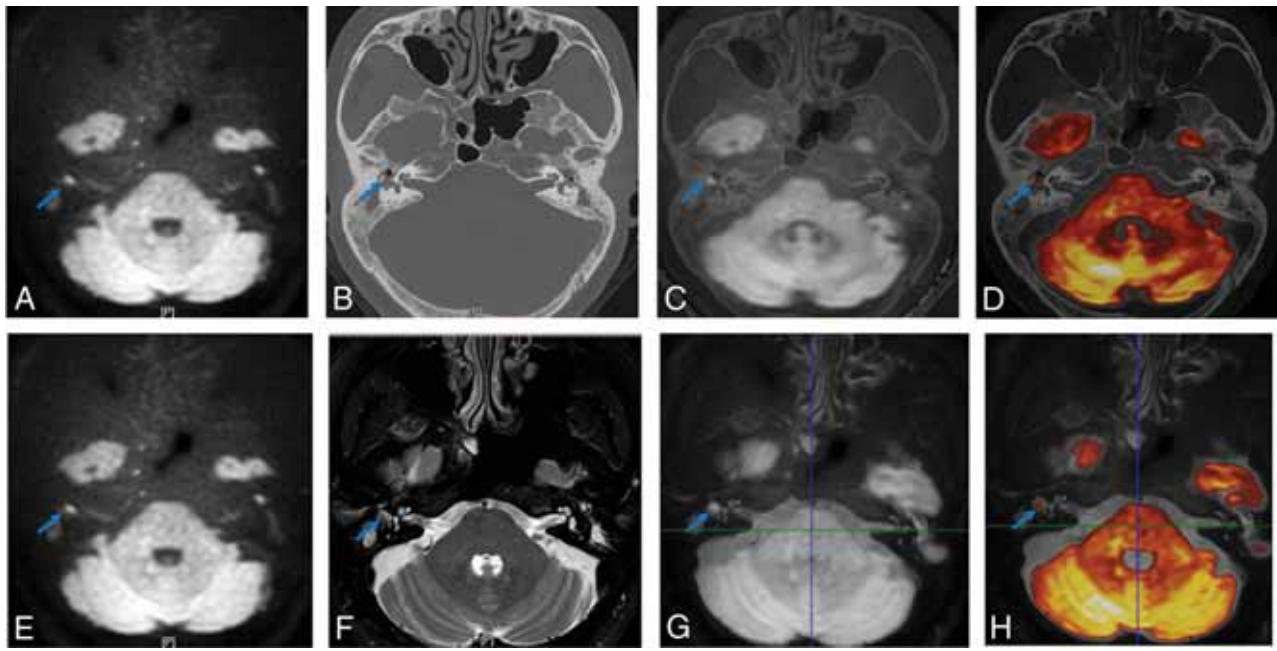
FIG 1. TSE-DWI images (*A* and *E*) were fused with HRCT (*B*) and T2WI fat-suppression images (*F*), respectively, to generate CT-DWI (*C*) and T2WI-DWI (*G*) fusion images, converting the colors to increase the visibility of the lesion (*blue arrow*) (*D* and *H*).

cholesteatoma surgery (ie, the cochlea and semicircular canal structures). DWI and T2WI fusion techniques are effective in localizing cholesteatoma;[15] however, they use specific T2 MR cisternography sequences instead of T2WI fat-suppression sequences in conventional ear MR imaging. Therefore, the aim of this study was to compare the image quality and localization efficacy of T2WI fat-suppression and DWI fusion images with those of HRCT and DWI fusion images in patients with middle ear cholesteatoma.

MATERIALS AND METHODS

Case Data

The clinical data of patients with initial suspicion of cholesteatoma who subsequently underwent an operation and were pathologically diagnosed as having a cholesteatoma were retrospectively collected from September 2019 to November 2021 in our otology department. Clinical data included the patient's sex and age, otoscopic findings, the presence of otopyorrhea and the odor of the secretion, and the presence of facial palsy, headache, and vertigo. The inclusion criteria for this study were the following: 1) initial clinical suspicion of cholesteatoma; 2) none of the affected ears undergoing any surgical treatment before the examination; 3) HRCT, T2WI fat-suppression sequence, and TSE-DWI examination before the operation; and 4) surgical treatment and pathologically confirmed cholesteatoma. The exclusion criteria were the following: 1) previous otologic surgery; 2) insufficient HRCT, thin-layer T2WI, or TSE-DWI image quality for image fusion; and 3) contraindication to MR imaging such as metal implants and pacemakers. This study was approved by our institutional ethics committee (2019PS069J).

Equipment and Scanning Protocol

A 256–detector row CT scanner (Philips Healthcare) was used for this study, and HRCT images were acquired with the

collimation set to 20×0.625; ear HRCT scan mode (spiral sweep; pitch, 0.25; matrix, 768×768; peak, 120 kV; 200 mA/s; reconstruction layer thickness, 1 mm; interval, 0.5 mm; rotation time, 0.4 seconds; filter function, Y-Sharp [YE]; window width, 4000; window position, 700). MR imaging signals were acquired using a 3T superconducting MR imaging scanner (Ingenia; Philips Healthcare) and a 32-channel head and neck phased-array coil with the following parameters: 1) axial T2-weighted TSE and fat suppression (TR, 3000 ms; TE, 80 ms; matrix, 308×192; section thickness, 2 mm; intersection interval, 0.2 mm); and 2) axial MR imaging DWIs ($b=0$ and 1000 s/mm^2; TR, 3000 ms; TE, 72 ms; matrix, 118×87; section thickness, 1.5 mm; intersection interval, 1 mm). HRCT and MR imaging scans were taken from the superior edge of the petrous bone to the inferior edge of the mastoid process. All raw images were transferred in DICOM format to a 3D reconstruction postprocessing workstation (Philips) for image analysis.

Image Quality Analysis

In this study, HRCT, T2WI fat-suppression, and TSE-DWI images were jointly uploaded to the 3D reconstruction postprocessing workstation for image fusion. The fusion process was performed by experienced otolaryngologists and head and neck radiologists. HRCT, T2WI fat-suppression, and TSE-DWI were changed to the same random number code, and the HRCT was reconstructed to have the same FOV and layer thickness as the T2WI fat-suppression and TSE-DWI images. The fusion images were then automatically generated and manually fine-tuned to form CT-DWI and T2WI-DWI fusion according to the structure of the internal auditory canal and temporal bone. The fusion images were converted to color to increase the visualization of the lesion (Fig 1). Due to the high keratin content of the cholesteatoma, the temporal bone region shows marked high signal

intensity on the TSE-DWI sequence (b=1000 s/mm^2).[7] On the basis of these signal characteristics, the red area of the temporal bone on both fusion images was defined as a cholesteatoma, and the gray area was defined as the absence of cholesteatoma (Fig 2). Two experts independently scored the quality of both CT-DWI and T2WI-DWI fusion images subjectively, including the overall quality of fusion images, lateral semicircular canal display, lesion clarity, and diagnostic confidence. The lateral semicircular canal transverse position was used as the reference, and the 2 fusion images were scored separately using the Likert 5-point tabulation (Table 1). A score of ≥3 was considered acceptable, and the weighted κ test was performed to measure the consistency of the 2 experts' scores.

Evaluation of Efficacy in Cholesteatoma Localization

The location of the cholesteatoma was recorded in detail in all surgical patients. Patients with a subjective score of <3 for both fused images were excluded from further localization diagnosis. In this study, 4 anatomic regions of the middle ear (attic, tympanic cavity, mastoid antrum, and mastoid cavity) were used for localization as proposed by Kanoto et al:[13] 1) attic: superior to the horizontal semicircular canal and anterior to the posterior margin of the horizontal semicircular canal; 2) the tympanic cavity: inferior to the horizontal semicircular canal and anterior to the posterior margin of the horizontal semicircular canal; 3) the mastoid antrum: superior to the horizontal semicircular canal and posterior to the posterior border of the horizontal semicircular canal; and 4) mastoid cells: inferior to the horizontal semicircular canal and posterior to the posterior border of the horizontal semicircular canal.

For each lesion, 2 experienced head and neck radiologists independently evaluated the presence or absence of a cholesteatoma at each site of the temporal bone. Both specialists were blinded to the patient's surgical data and findings. The diagnostic efficacy of

FIG 2. Left middle ear mastoid region. *A*, CT-DWI fusion image of a cholesteatoma in red (*blue arrowhead*) and inflammatory tissue in gray (*green arrow*). *B*, T2WI-DWI fusion image of cholesteatoma in red (*blue arrowhead*) and inflammatory tissue in gray (*green arrow*).

the 2 fusion images for localization of the 4 anatomic regions was assessed using the intraoperative location of the cholesteatoma in the temporal bone region, which is considered the reference standard. To prevent recall bias, we assessed the 2 fusion images at 1-week intervals in a randomized order.

Statistical Analysis

All data were statistically analyzed using SPSS 22.0 (IBM) and MedCalc statistical software, Version 19.6 (MedCalc Software). After we tested for normality, data conforming to a normal distribution were expressed as mean (SD), and comparisons were performed using an independent samples t test; $P < .05$ was considered statistically significant. Two experts were used for the statistical analysis of the diagnostic agreement of the fused graphs, using the weighted κ test. The weighted κ coefficients were defined as follows: poor (0.00–0.30), fair (0.31–0.50), moderate (0.51–0.70), good (0.71–0.90), and excellent (0.91–1.00). The Wilcoxon rank-sum test was used to compare the overall quality scores of CT-DWI and T2WI-DWI fusion images. The accuracy, sensitivity, and specificity of CT-DWI and T2WI-DWI fusion image data were calculated, and the diagnostic efficacy of the 2 fusion images was compared by receiver operating characteristic analysis.

RESULTS

Basic Patient Information

All 106 patients with initial clinical suspicion of cholesteatoma underwent an operation, including 75 patients with pathologically confirmed cholesteatoma, of which 4 cases were excluded due to image artifacts in TSE-DWI, T2WI, and HRCT. A total of 71 patients were included. The mean interval between CT and MR imaging in these patients was 2.08 (SD, 3.47) days, with the shortest interval being 0 days and the longest interval being 23 days. The mean interval between MR imaging and an operation was 4.77 (SD, 3.36) days, with a minimum interval of 1 day and a maximum interval of 18 days. The measured mean lesion diameter in the cholesteatoma group was 10.17 (SD, 6.51) mm (range, 2.0–35.0 mm).

Subjective Evaluation of CT-DWI and T2WI-DWI Fusion Images

The subjective evaluation of fusion image quality by the 2 experts was consistent, with κ values of >0.80 (Table 2). Although the overall quality of both CT-DWI and T2WI-DWI fusion images was higher (Fig 3*A*), the overall quality of CT-DWI fusion images was slightly lower than that of T2WI-DWI ($P < .001$). Both experts were well able to distinguish the landmark anatomic structures of the middle ear region on CT-DWI and T2WI-DWI. Using the horizontal semicircular canal as a reference, both experts could clearly distinguish the anterior and posterior branch margins of the horizontal semicircular canal in the transverse position on the fusion images (Fig 3*B*); however, the score of the clarity of the
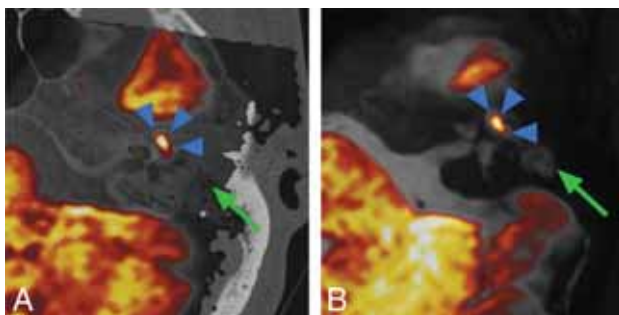
Table 1: Subjective evaluation of fusion image quality

Score	Overall Quality of the Fusion Image	Semicircular Canal Display	Clarity of the Lesion	Diagnostic Confidence
1	Unacceptable	Difficult to identify edges	Severe blurring of contours	Very poor
2	Poor, evaluation moderately limited	Blurred edges, but identifiable	Blurred contours	Poor
3	Moderate, evaluation mildly limited	Margins recognizable	Contours recognizable	Moderate
4	Good, evaluation less limited	Edges visible, no distortion	Contour edges visible	Good
5	Very good	Clear edges	Clear contours	Very good

semicircular canal display was slightly higher on CT-DWI than on T2WI-DWI ($P < .001$). Both CT-DWI and T2WI-DWI fusion images had higher subjective scores for lesion significance and diagnostic confidence of cholesteatoma localization in the middle ear mastoid (Fig 3C, -D) without statistical differences (lesion significance, $P = .62$; diagnostic confidence, $P = .59$). However, in 10 cases, the outline of the red portion in the temporal bone region on both fusion images was blurred due to small cholesteatoma size, with a score of <3.

Evaluation of the Diagnostic Efficacy of Cholesteatoma Localization

Patients with cholesteatomas with 2 fusion scores of <3 were excluded, and 61 patients with cholesteatomas were finally included for the localization of 4 key anatomic landmarks in the middle ear. CT-DWI and T2WI-DWI fusion images showed no statistical difference in area under the curve for the 4 anatomic regions, as detailed in Table 3. Except for the tympanic cavity, the accuracy of T2WI-DWI fusion images for localization of the attic,

tympanic sinus, and mastoid process was slightly higher than that of CT-DWI fusion images (Figs 4 and 5).

DISCUSSION

The results of this study showed that the T2WI-DWI fusion produced images of good overall quality, with high sensitivity, specificity, and accuracy for landmark localization of cholesteatoma, without substantial differences from CT-DWI fusion images, therefore meeting the requirements for preoperative surgical evaluation and selection of the surgical approach.

It has been demonstrated that CT-DWI fusion images improve the accuracy of the preoperative diagnosis of cholesteatoma by combining the diagnostic ability of DWI with the localization capacity of CT.[8,9,11] In this study, the overall image quality of T2WI-DWI fusion images was higher than that of CT-DWI fusion images. This is likely due to the interval between the preoperative CT and DWI examinations and the continuous growth of the cholesteatoma, resulting in imprecise matching of the lesion displayed in the 2 images. T2WI-DWI fusion images can well avoid the problem of temporal inconsistency between the 2 images. These images are based on 2 sequences from the same MR imaging scan using the same machine and scan position, thus shortening the processing time for image fusion and reducing manual alignment bias caused by the fusion of images from both CT and DWI techniques. Moreover, MR imaging fusion

Table 2: Comparison of subjective evaluation agreement between CT-DWI and T2WI-DWI fusion images[a]

	CT-DWI, Interobserver κ (95% CI)	T2WI-DWI, Interobserver κ (95% CI)
Overall quality of fusion image	0.82 (0.71–0.93)	0.87 (0.73–1.00)
Semicircular canal display	0.88 (0.77–0.98)	0.81 (0.70–0.92)
Clarity of the lesion	0.94 (0.88–0.99)	0.93 (0.88–0.99)
Diagnostic confidence	0.93 (0.86–0.99)	0.91 (0.85–0.97)

[a] κ indicates weighted κ coefficients.
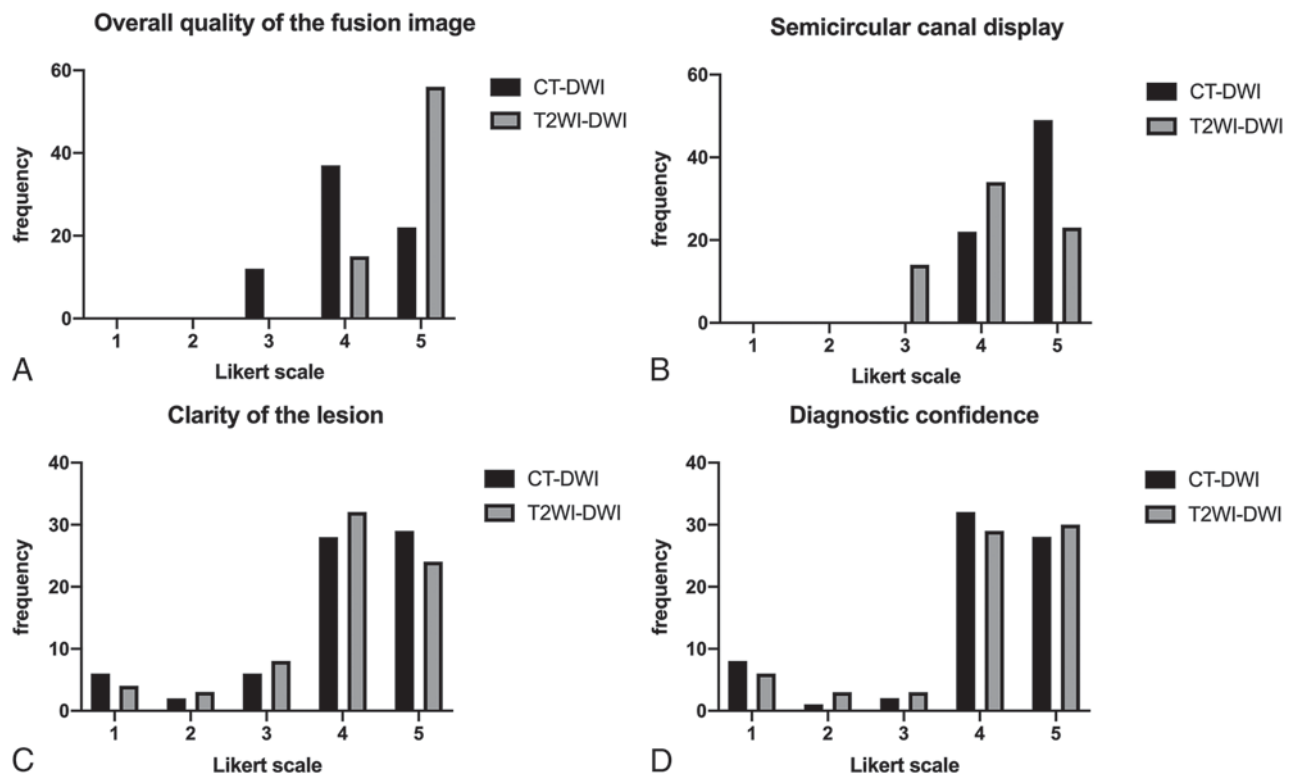
FIG 3. Subjective evaluation of CT-DWI and T2WI fusion image quality.

Table 3: Diagnostic efficacy of middle ear mastoid localization in CT-DWI fusion and T2WI-DWI fusion images

	Sensitivity	Specificity	AUC	AUC 95% CI	P Value
Attic					.32
CT-DWI	0.98	0.75	0.87	0.76–0.94	
T2WI-DWI	1.00	0.75	0.88	0.77–0.95	
Tympanic cavity					.30
CT-DWI	0.84	0.86	0.85	0.74–0.93	
T2WI-DWI	0.84	0.72	0.78	0.66–0.88	
Mastoid antrum					.70
CT-DWI	0.76	0.87	0.82	0.70–0.90	
T2WI-DWI	0.79	0.87	0.83	0.71–0.91	
Mastoid cavity					.16
CT-DWI	0.75	0.85	0.80	0.68–0.89	
T2WI-DWI	0.82	0.82	0.85	0.74–0.93	

Note:—AUC indicates area under the curve.
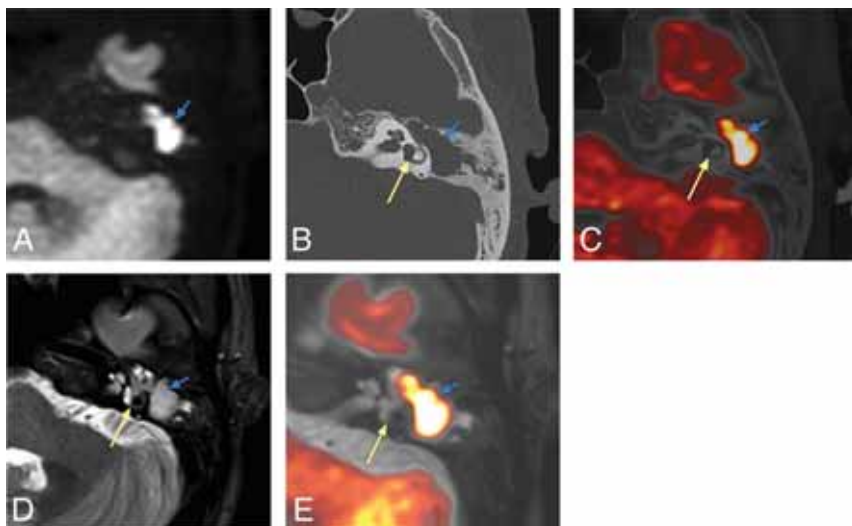
FIG 4. Pathologically confirmed cholesteatoma. The attic and mastoid antrum are filled with cholesteatoma during the operation. *A*, TSE-DWI: a high signal intensity area (*blue arrow*) is seen in the mastoid of the left middle ear with clear borders and poorly displayed semicircular canal. *B*, HRCT: a soft-tissue density shadow is seen within the middle ear mastoid cavity (*blue arrow*), and the anterior and posterior pedicles of the horizontal semicircular canal are clearly displayed (*yellow arrow*). CT-DWI fusion image (*C*) shows the cholesteatoma exceeding the posterior branch of the horizontal semicircular canal, involving the mastoid antrum. *D*, T2WI shows a non-specific high-intensity-signal shadow in the mastoid process of the left middle ear. *E*, T2WI-DWI: the horizontal semicircular canal is clear, the cholesteatoma shows yellow changes, and the lesion involves the attic and mastoid antrum.

images do not pose the same ionizing radiation hazard as CT examinations, which makes them applicable to a wider range of people.

TSE-DWI and its corresponding T2WI fusion images can clearly show important anatomic landmarks, such as the lateral semicircular canal and the cochlea. Although T2WI is not sufficient to match the CT display of fine anatomy and cholesteatoma bone erosion,[16] the horizontal semicircular canal display and the relationship between the lesion and the horizontal semicircular canal are the otologist's main concern because they influence the choice of the surgical approach. When the cholesteatoma lesion is confined to the attic or tympanic cavity and does not extend to the posterior limb of the lateral semicircular canal, it is resected using only the transcanal endoscopic approach; involvement of

the mastoid antrum or mastoid process requires conversion to mastoidectomy (microscopic ear surgery) or the combined microscopic and endoscopic approach to resect the lesion.[17-21] Although the semicircular canal was scored slightly lower in the T2WI-DWI fusion images than in the CT-DWI fusion images, there was no statistical difference between the 2 in terms of the clarity of the cholesteatoma margins and diagnostic confidence. The sensitivity and accuracy of T2WI-DWI fusion images for involvement of the mastoid antrum and mastoid were slightly higher than those of CT-DWI fusion images in this study, though there was no statistical difference between them.

Compared with T2WI-DWI, CT-DWI had higher image resolution and more clearly showed the fine structures; however, it did not improve the ability to detect cholesteatoma involvement of the mastoid antrum and mastoid cavity. Therefore, T2WI-DWI fusion images can competently assess whether the mastoid antrum and mastoid process are preoperatively involved. The diagnostic accuracy of the present study for mastoid antrum involvement (83%) was slightly lower than that of the study by Benson et al[15] (93.3%), probably due to the thicker layer (2 mm) of the T2WI fat-suppression sequence routinely used in the present study. Benson et al[15] used a thinner layer (0.6 mm) with the T2 sampling perfection with application-optimized contrasts by using different flip angle evolution (SPACE sequence; Siemens) technique, and the thinner scan thickness allowed a clearer display of the cholesteatoma border. The sensitivity and specificity for the mastoid region in this study was slightly lower than those reported in other studies,[17] probably due to the absence of a combined T1WI sequence to exclude cholesterol granulomas.

The accuracy of T2WI-DWI fusion images in this study was slightly superior to that of CT-DWI for localization of the attic. This is probably because the cholesteatoma lesion was smaller, and a large amount of inflammatory tissue surrounding the lesion showed a substantially high intensity signal in the TSE-DWI sequence, thus obscuring the location of the red lesion in the CT-DWI fusion images. In contrast, the inflammatory tissue showed high signal intensity on the T2WI suppressed images, which were fused with the DWI, giving rise to complete T2WI-DWI images for the evaluation of the cholesteatoma. The accuracy of CT-DWI and T2WI-DWI fusion images for attic localization in this
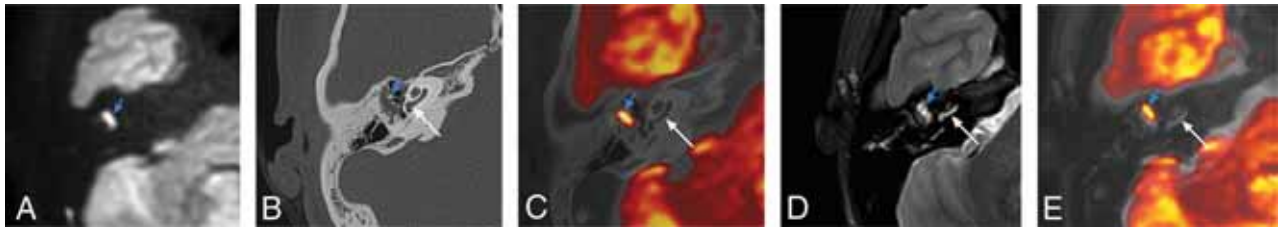
FIG 5. Surgical confirmation of a cholesteatoma in the tympanic cavity. *A*, TSE-DWI: a clear high-intensity-signal area (*blue arrow*) with a clear border in the right middle ear. *B*, HRCT: soft-tissue density shadow (*blue arrow*) in the middle ear with an unclear border and clear cochlear structures (*yellow arrows*). CT-DWI fusion image (*C*) clearly shows the cholesteatoma in the tympanic cavity. *D*, T2WI shows a nonspecific high-intensity-signal shadow in the mastoid process of the right middle ear. *E*, T2WI-DWI shows a clear cochlea with the cholesteatoma, localized in the tympanic cavity with reddish-yellow changes.

study was slightly higher than that reported by Felici et al.[11] This difference is probably because our study included only unoperated patients, whereas Felici et al[11] included patients with postoperative recurrence of cholesteatoma. In such patients, the structures were relatively less easy to identify, which is also consistent with the results of Benson et al.[15] When the cholesteatoma is located in the tympanic cavity, the diagnostic yield of T2WI-DWI fusion images is slightly lower than that of CT-DWI fusion images. This may be because CT-DWI images can clearly distinguish the boundary between the external auditory canal and the tympanic cavity, whereas T2WI-DWI cannot, easily leading to the confusion of lesions within the external auditory canal with lesions in the tympanic cavity.

This study has the following shortcomings and limitations. First, all included patients had surgically and pathologically confirmed cholesteatoma, and only the localization accuracy for cholesteatoma was evaluated; the diagnostic efficacies of the 2 fusion techniques for cholesteatoma were not compared. Second, only patients with an initial cholesteatoma were included to evaluate whether T2WI-DWI can replace CT-DWI as the procedure of choice for patients with cholesteatomas, and the localization of lesions in patients with recurrent disease has not been evaluated. Numerous studies have shown that DWI sequences can replace secondary surgical exploration to evaluate patients for cholesteatoma recurrence.[6] Whether T2WI-DWI fusion images can be used to guide the surgical options in patients with suspected recurrence is a prospective topic for future research. Third, image fusion is postprocessed on a separate workstation with more workflow; however, many PACS vendors are beginning to incorporate autoregistration and image fusion into their postprocessing functions, which can minimize procedural errors during image transfer and reduce reliance on third-party applications.[22,23] As PACS advanced postprocessing functions become more sophisticated, image-fusion techniques will become an efficient workflow and gain wider adoption. Finally, T1WI sequences have great advantages for excluding cholesterol granuloma,[17] and T1WI sequences may be added in future studies for synergistic diagnosis[24,25] to reduce false-positive rates.

CONCLUSIONS

In this study, we compared T2WI-DWI fusion images with CT-DWI fusion images in terms of image quality and localization of middle ear cholesteatoma. The T2WI-DWI fusion image can clearly assess the involvement of cholesteatoma on the attic, tympanic cavity, mastoid antrum, and mastoid process, which can assist clinicians in the preoperative assessment and in the selection of the best surgical plan and optimal surgical approach. In the past, otologists could only choose the plan preoperatively on the basis of HRCT imaging and surgical experience; the choice, to a certain extent, could cause subjective bias. The development of T2WI-DWI fusion imaging can provide technical support for cholesteatoma diagnosis and operative treatment.

Disclosure forms provided by the authors are available with the full text and PDF of this article at www.ajnr.org.

REFERENCES

1. Yung M, Tono T, Olszewska E, et al. **EAONO/JOS Joint Consensus Statements on the Definitions, Classification and Staging of Middle Ear Cholesteatoma.** *J Int Adv Otol* 2017;13:1–8 CrossRef Medline
2. Chiao W, Chieffe D, Fina M. **Endoscopic management of primary acquired cholesteatoma.** *Otolaryngol Clin North Am* 2021;54:129–45 CrossRef Medline
3. Anschuetz L, Presutti L, Marchioni D, et al. **Discovering middle ear anatomy by transcanal endoscopic ear surgery: a dissection manual.** *J Vis Exp* 2018;56390 CrossRef Medline
4. Prasad SC, Piras G, Piccirillo E, et al. **Surgical strategy and facial nerve outcomes in petrous bone cholesteatoma.** *Audiol Neurootol* 2016;21:275–85 CrossRef Medline
5. Lingam R, Bassett P. **A meta-analysis on the diagnostic performance of non-echoplanar diffusion-weighted imaging in detecting middle ear cholesteatoma: 10 years on.** *Otol Neurotol* 2017;38:521–28 CrossRef Medline
6. Muzaffar J, Metcalfe C, Colley S, et al. **Diffusion-weighted magnetic resonance imaging for residual and recurrent cholesteatoma: a systematic review and meta-analysis.** *Clin Otolaryngol* 2017;42:536–43 CrossRef Medline
7. Wiesmueller M, Wuest W, May MS, et al. **Comparison of readout-segmented echo-planar imaging and single-shot TSE DWI for cholesteatoma diagnostics.** *AJNR Am J Neuroradiol Neuroradiol* 2021;42:1305–12 CrossRef Medline
8. Alzahrani M, Alhazmi R, Belair M, et al. **Postoperative diffusion weighted MRI and preoperative CT scan fusion for residual cholesteatoma localization.** *Int J Pediatr Otorhinolaryngol* 2016;90:259–63 CrossRef Medline
9. Locketz GD, Li PM, Fischbein NJ, et al. **Fusion of computed tomography and PROPELLER diffusion-weighted magnetic resonance imaging for the detection and localization of middle ear cholesteatoma.** *JAMA Otolaryngol Head Neck Surg* 2016;142:947–53 CrossRef Medline
10. Campos A, Mata F, Reboll R, et al. **Computed tomography and magnetic resonance fusion imaging in cholesteatoma preoperative assessment.** *Eur Arch Otorhinolaryngol* 2017;274:1405–11 CrossRef Medline

11. Felici F, Scemama U, Bendahan D, et al. **Improved assessment of middle ear recurrent cholesteatomas using a fusion of conventional CT and non-EPI-DWI MRI.** *AJNR Am J Neuroradiol* 2019;40:1546–51 CrossRef Medline

12. Yamashita K, Hiwatashi A, Togao O, et al. **High-resolution three-dimensional diffusion-weighted MRI/CT image data fusion for cholesteatoma surgical planning: a feasibility study.** *Eur Arch Otorhinolaryngol* 2015;272:3821–24 CrossRef Medline

13. Kanoto M, Sugai Y, Hosoya T, et al. **Detectability and anatomical correlation of middle ear cholesteatoma using fused thin slice non-echo planar imaging diffusion-weighted image and magnetic resonance cisternography (FTS-nEPID).** *Magn Reson Imaging* 2015;33:1253–57 CrossRef Medline

14. Watanabe T, Ito T, Furukawa T, et al. **The efficacy of color mapped fusion images in the diagnosis and treatment of cholesteatoma using transcanal endoscopic ear surgery.** *Otol Neurotol* 2015;36:763–68 CrossRef Medline

15. Benson JC, Carlson ML, Yin L, et al. **Cholesteatoma localization using fused diffusion-weighted images and thin-slice T2 weighted images.** *Laryngoscope* 2021;131:E1662–67 CrossRef Medline

16. Cavaliere M, Di Lullo AM, Russo C, et al. **Computed-tomography-structured reporting in middle ear opacification: surgical results and clinical considerations from a large retrospective analysis.** *Front Neurol* 2021;12:615356 CrossRef Medline

17. Baba A, Kurihara S, Fukuda T, et al. **Non-echoplanar diffusion weighed imaging and T1-weighted imaging for cholesteatoma mastoid extension.** *Auris Nasus Larynx* 2021;48:846–51 CrossRef Medline

18. Migirov L, Wolf M, Greenberg G, et al. **Non-EPI DW MRI in planning the surgical approach to primary and recurrent cholesteatoma.** *Otol Neurotol* 2014;35:121–25 CrossRef Medline

19. Abdul-Aziz D, Kozin ED, Lin BM, et al. **Temporal bone computed tomography findings associated with feasibility of endoscopic ear surgery.** *Am J Otolaryngol* 2017;38:698–703 CrossRef Medline

20. Tolisano AM, Killeen DE, Hunter JB, et al. **The Antrum-Malleus-Tegmen score: a pilot study assessing preoperative radiographic predictors for transcanal endoscopic cholesteatoma dissection.** *Otol Neurotol* 2019;40:e901–08 CrossRef Medline

21. Das A, Mitra S, Ghosh D, et al. **Endoscopic versus microscopic management of attic cholesteatoma: a randomized controlled trial.** *Laryngoscope* 2020;130:2461–66 CrossRef Medline

22. Colleran GC, Kwatra N, Oberg L, et al. **How we read pediatric PET/CT: indications and strategies for image acquisition, interpretation and reporting.** *Cancer Imaging* 2017;17:28 CrossRef Medline

23. Berkowitz SJ, Wei JL, Halabi S. **Migrating to the modern PACS: challenges and opportunities.** *Radiographics* 2018;38:1761–72 CrossRef Medline

24. Fukuda A, Morita S, Harada T, et al. **Value of T1-weighted magnetic resonance imaging in cholesteatoma detection.** *Otol Neurotol* 2017;38:1440–44 CrossRef Medline

25. Moustin D, Veillon F, Karch-Georges A, et al. **Importance of signal intensity on T1-weighted spin-echo sequence for the diagnosis of chronic cholesteatomatous otitis.** *Eur Arch Otorhinolaryngol* 2020;277:1601–08 CrossRef Medline

Brain Injury in Fetuses with Vein of Galen Malformation and Nongalenic Arteriovenous Fistulas: Static Snapshot or a Portent of More?

C. Jaimes, F. Machado-Rivas, K. Chen, M.A. Bedoya, E. Yang, and D.B. Orbach

ABSTRACT

BACKGROUND AND PURPOSE: Brain injury in fetuses with vein of Galen malformations and nongalenic AVFs is a rare complication whose appearance, course, and prognosis are poorly studied. We sought to characterize the MR imaging features and examine associations with postnatal outcome.

MATERIALS AND METHODS: This was a retrospective analysis of fetal MRIs of subjects with vein of Galen malformation and nongalenic arteriovenous fistulas. Two pediatric neuroradiologists independently reviewed examinations to determine the presence of abnormalities on structural imaging (T1 volumetric interpolated breath-hold examination and T2-HASTE), DWI, and T2*-weighted images; discrepancies were adjudicated by a third reviewer. Radiologic progression of injury was determined by additional fetal or neonatal MRIs. A simple composite score evaluating poor neonatal clinical outcome as either intubation or death by postnatal day 2 was also queried. A body fetal imager evaluated the presence of systemic findings of right heart strain.

RESULTS: Forty-nine fetal MR imaging examinations corresponding to 31 subjects (27 vein of Galen malformations and 4 nongalenic AVF cases) were analyzed. Injury was observed in 8 subjects (26%) with 14 fetal examinations; the mean gestational age at identification of injury was 32.2 (SD 4.9) weeks. Structural abnormalities were present in all subjects with injury; restricted diffusion, in 5/7 subjects with available data; and T2* abnormalities, in all subjects with available data ($n = 7$). Radiologic progression was documented in all cases with follow-up imaging ($n = 7$). All subjects with fetal brain injury had a poor neonatal clinical outcome.

CONCLUSIONS: Brain injury in fetuses with vein of Galen malformation and nongalenic AVFs shows a combination of structural abnormalities, restricted diffusion, and blooming on T2* images. Injury appears to portend a poor prognosis, with relentless progression and a likely association with adverse neonatal outcomes.

ABBREVIATIONS: NG-AVF = nongalenic AVF; VOGM = vein of Galen malformation; VIBE = volumetric interpolated breath-hold examination

Congenital AVMs are a rare group of disorders that result from either persistent primitive anastomoses or formation of pathologic connections in the early embryonic and fetal stages. The most common of these conditions is a vein of Galen malformation (VOGM), which results from persistent communication

http://dx.doi.org/10.3174/ajnr.A7533

between the embryonic choroidal arteries and the median prosencephalic vein of Markowski.[1] Other lesions, such as pial arteriovenous fistulas, occur more rarely and are collectively referred to as nongalenic AVFs (NG-AVFs).[2] These conditions are increasingly identified prenatally and are referred to subspecialized centers for counseling and treatment planning.[3]

VOGMs and NG-AVFs result in direct communication between the arterial and vascular beds, creating high-flow intracranial shunts and secondary high-cardiac-output states. Even though the hemodynamic repercussions of a high-output state do manifest prenatally, end-organ injury is rare. For example, most fetuses will show an elevated volume load in the right heart chambers, but only rarely will overt cardiac failure ensue.[4] Parenchymal brain injury, while also rare in utero, is, nevertheless, sometimes identified in fetuses that undergo MR imaging. Due to the overall low incidence of VOGMs and NG-AVFs and the challenges associated with serial imaging in fetal life, little is known about the evolution and significance of

Table 1: Fetal brain parenchymal injury and progression

MRI Feature	% (No.)
Fetal brain parenchymal injury (*n* = 8)	26 (8/31)
Structural abnormality (*n* = 8)	100 (8/8)
Low volume	88 (7/8)
Ventriculomegaly	50 (4/8)
Signal abnormality (T1WI or T2WI)	88 (7/8)
DWI abnormality (*n* = 5)	71 (5/7)[a]
DWI data available for only 7 of 8 subjects	
T2* Abnormality (*n* = 5)	100 (5/5)[a]
T2* data available for only 5 of 8 subjects	
Progression (*n* = 7)	100 (7/7)[a]

[a] Repeat scan data are available for only 7 of 8 subjects.

parenchymal injury in fetuses with high-flow intracranial vascular shunts.

The purpose of this study was to characterize the MR imaging features of parenchymal injury in fetuses with VOGM and NG-AVFs, to investigate their clinical context, and to explore its prognostic significance. We hypothesized that parenchymal injury would show relentless progression and that it would be associated with poor neonatal outcomes.

MATERIALS AND METHODS
Sample Recruitment
We performed a retrospective institutional review board–approved and Health Insurance Portability and Accountability Act–compliant study. We queried the institution's electronic health record for cases of VOGM or NG-AVFs between 2007 and 2021 that had fetal brain and body MR imaging. We excluded cases with nondiagnostic image quality or cases with other CNS/body abnormalities nonattributable to the VOGM or NG-AVF. For each subject, we recorded gestational age and sex. Additionally, we reviewed postnatal records and classified the outcome into good and adverse outcomes; the adverse outcome was defined as a composite measure derived from the patient's need for intubation or emergent embolization or death by postnatal day 2.

Fetal Brain Evaluation
Cases were reviewed independently by 2 board-certified pediatric neuroradiologists with experience in fetal neuroimaging. The discrepancies were adjudicated by blinded and independent review of the images by a third, board-certified neuroradiologist/Committee on Advanced Subspecialty Training (CAST)-credentialed neurointerventional radiologist with 15 years of experience in pediatric endovascular interventions, including VOGM management.

Images were reviewed to confirm the diagnosis of VOGM or NG-AVF. The studies were additionally reviewed to determine the presence of parenchymal injury. Sequences available were reviewed, including structural images (T2 HASTE, steady-state free precession, and T1-volumetric interpolated breath-hold examination [VIBE]), diffusion-weighted images (or diffusion tensor images), and T2*/gradient-echo sequences. All images were scored in a binary manner as having either normal or abnormal findings. For structural images, the radiologists evaluated the following: 1) signal abnormality

(T2 hyperintensity, T2 hypointensity, and T1 hyperintensity), 2) low volume, and 3) ventriculomegaly. DWI was evaluated for the presence of restricted diffusion, and the T2*gradient-echo imaging was evaluated for the presence of abnormal parenchymal blooming.

Progression of the brain injury was evaluated in all subjects with a repeat fetal scan by a single reviewer. If no fetal scan was available, an immediate postnatal MR imaging was evaluated to assess chronic changes. The increased extent of the injury that was documented prenatally or development of new areas of parenchymal injury was regarded as progression.

Fetal Body Evaluation
Images were reviewed by a board-certified pediatric radiologist with expertise in fetal imaging. Only structural images were analyzed (T2 HASTE, steady-state free precession, and T1-VIBE). The radiologist evaluated the presence of the following: 1) ascites, 2) pleural effusion, 3) pericardial effusion, 4) cardiomegaly, 5) scalp edema, 6) body wall edema, and 7) anasarca.

Statistical Analysis
Measures of central tendency were used to describe the population. Percentages were used to describe the scoring of brain parenchymal injury and progression. To evaluate associations between fetal brain parenchymal injury and fetal body MR imaging in a cross-sectional fashion, we estimated the prevalence odds ratio for each variable. To evaluate associations between brain parenchymal injury and postnatal clinical outcomes at 2 days of life in a retrospective cohort, we estimated the relative risk. All statistical analyses were performed in STATA (StataCorp) with an α threshold of .05.

RESULTS
Study Sample
A total of 49 fetal MR imaging examinations were analyzed. Of these, 46 (94%) had T2 HASTE sequences, 39 (80%) had steady-state free precession, 37 (76%) had T1 VIBE, 34 (69%) had DWI, and 31 (63%) had T2* images. The examinations corresponded to 31 subjects (27 with VOGM and 4 with AVFs), of which 18 were male and 13 female. The mean gestational age for the first examination was 32.3 (SD 4.7) weeks (minimum, 20.4 weeks; maximum, 37.6 weeks), and 14 subjects underwent at least 1 additional fetal MR imaging examination (mean interval, 3.9 [SD, 3.2] weeks; minimum, 0.9 weeks; maximum, 12.7 weeks).

Brain Injury
Findings consistent with brain injury were observed in 8 subjects (26%) in 14 individual fetal MR imaging examinations. The mean gestational age at the time of identification of brain injury for each subject (presenting MR imaging) was 32.2 (SD 4.9) weeks. Findings are summarized in Table 1, and a case-by-case outline is presented in Table 2.

Abnormalities on structural imaging were identified in all fetuses with brain injury (*n* = 8) (Fig 1). Mild or moderate diffuse parenchymal volume loss was identified in 7 subjects (88%) and was noted in the presenting examination in 5 subjects (63%). Ventriculomegaly was present in 4 fetuses (50%) and was

Table 2: Subject demographics and MR imaging examination findings

Subject	Dx	GA (wk)	Structural Abnormality	Low Volume	Ventriculomegaly	Signal Abnormality	DWI Abnormality	T2* Abnormality	Documented Progression
1	VOGM	36.9	Yes	Yes	Yes	Yes			
2	NG-AVF	28.6	Yes	No	No	Yes	Yes	Yes	Fetal
		29.4	Yes	No	No	Yes	No	Yes	
3	VOGM	20.4	Yes	No	No	Yes			Fetal
		21.9	Yes	Yes	No	Yes	No	Yes	
4	VOGM	32.3	Yes	Yes	No	No	No		Postnatal[a]
5	VOGM	35.3	Yes	Yes	Yes	Yes	Yes	Yes	Postnatal[a]
6	VOGM	29.3	Yes	Yes	No	Yes	No	Yes	Fetal
		31.7	Yes	Yes	Yes	Yes	No	Yes	
		33	Yes	No	No	Yes	Yes	Yes	
7	VOGM	26.7	No	No	No	No	Yes		Fetal
		30.3	Yes	Yes	Yes	Yes	No		
8	NG-AVF	32.0	Yes	Yes	No	Yes	Yes	Yes	Fetal
		35.0	Yes	Yes	No	Yes	No	Yes	

Note:—Dx indicates diagnosis; GA, gestational age; wk, weeks.
[a] Immediate postnatal exam.
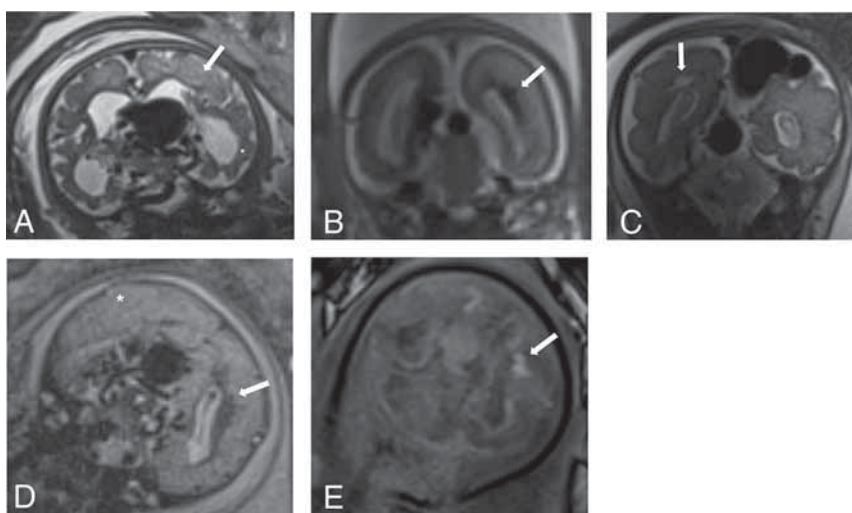
FIG 1. Structural abnormalities in fetuses with brain injury on T2- and T1-weighted images. *A*, Coronal T2 HASTE in a 35.3-week fetus (subject 5, scan 1) shows localized T2 prolongation (*arrow*), volume loss, and ventriculomegaly. *B*, Coronal T2 HASTE in a 21.9-week fetus (subject 3, scan 2) shows T2 hypointensity in the periventricular region (*arrow*). *C*, Coronal T2 HASTE shows periventricular cystic change (*arrow*) in a 29.4-week fetus (subject 2, scan 2). Coronal T2 HASTE (*D*) and coronal T1 VIBE (*E*) in a 33-week fetus (subject 6, scan 3) show generalized T2 prolongation and cerebral edema (*asterisk*), periventricular T2 hypointensity (*arrow in D*), and corresponding T1 hyperintensity (*arrow in E*).

identified in the presenting examination in 2 subjects (25%). Signal abnormalities, including T2 prolongation, T2 hypointensity in periventricular regions (radiating periventricular abnormalities and/or the germinal matrix), and T1 hyperintensity in the periventricular regions were identified in 7 fetuses (88%) and in the presenting examination in 6 subjects (75%). T2 prolongation was identified in the presenting examination of 50% of subjects; T2 hypointense signal, in 50%; and T1 hypointensity, in 25%. An individual fetus often had >1 pattern of signal abnormality on structural images.

Five of the 8 fetuses with brain injury had T2*-weighted sequences available, and abnormalities in T2* were identified in all; in every case, the abnormality was appreciable in the presenting examination. The patterns observed included engorgement of the periventricular (medullary) veins (60%), "blooming" in the germinal matrix (20%), and generalized signal drop throughout the parenchyma (40%) (Fig 2). Subject 8 had both patterns, with generalized blooming ipsilateral to the AVF and contralateral engorgement of the periventricular veins.

Restricted diffusion was identified in 5 of 7 fetuses who had available data (71%) and was identified in the presenting scan in 3 subjects (43%). Four cases showed patchy bilateral areas of restricted diffusion and 1 case (20%) showed generalized restricted diffusion in the gray and white matter of both cerebral hemispheres (Fig 3).

The abnormalities in this cohort of fetuses with brain injury were confined to the supratentorial brain, completely sparing the posterior fossa. In all fetuses with VOGM with injury ($n = 6$) and in 1 fetus with NG-AVF whose shunt drained to a midline vein (subject 2), the injury was bilateral and symmetric. In a single fetus with a NG-AVF with dominant left-hemispheric drainage (to the vein of Labbe) (subject 8), the pattern of injury was markedly asymmetric, with severe involvement of the left hemisphere and only minimal periventricular changes on structural imaging and T2* in the right periventricular region (Online Supplemental Data).

Progression of Brain Injury
We observed progression of the fetal brain parenchymal injury in all cases that had at least 1 abnormality and for whom a repeat scan was available (Fig 4). The mean interval between examinations for this subgroup was 3.1 (SD 2.1) weeks, including 2 cases of documented progression in the immediate postnatal period.

In subject 8 (NG-AVF with left hemispheric venous drainage), progression included the worsening of the severe injury that was

noted in the left hemisphere on the baseline MR imaging as well as development of subtle areas of injury in the periventricular regions of the contralateral hemisphere.

Body MR Imaging Associations

We observed a trend of increased odds of concurrent body abnormalities in subjects who had brain parenchymal injury relative to those without parenchymal injury, but the trend did not reach statistical significance (all $P > .47$) (Online Supplemental Data).

Similarly, we observed a nonsignificant trend of increased odds of fetal body abnormalities in subjects who had an adverse composite outcome compared with those who did not (all $P > .09$) (Online Supplemental Data).

Postnatal Outcomes

All subjects (8/8) who had brain parenchymal injury on fetal MR imaging met the composite outcome of death or intubation at 2 days of life, while this was the case for only 30% of subjects (7/23) who did not manifest fetal brain injury. These findings indicate a tripling of the risk of meeting the composite outcome in patients with fetal brain parenchymal injury (relative risk, 3.29; 95% CI, 1.77–6.1; $P < .001$).

DISCUSSION

Parenchymal injury in fetuses with high-flow intracranial vascular malformations is a rare complication, as opposed to neonates with these conditions in whom parenchymal injuries frequently accrue. The increase in the use of fetal MR imaging to evaluate patients with VOGM and NG-AVF has led to an increase in the recognition of this form of end-organ damage and its evolution. Our retrospective analysis of fetuses with VOGM and NG-AVF shows that brain injury occurs in a minority of the affected patients; it is limited to the supratentorial space; and it is almost always bilateral and symmetric. Abnormalities were detected in structural images, T2*-weighted images, and DWI. Our results also indicate that parenchymal injury is a marker of an aggressive disease course, with documented radiologic progression in all cases that underwent serial imaging and with a strong association with adverse neonatal clinical outcomes.

Fetal MR imaging is a valuable tool to determine prognosis and counsel parents of patients with VOGM who are diagnosed prenatally. Despite advances in neurointerventional techniques and critical care, up to 40% of patients with VOGM who require urgent embolization die in the neonatal period, and half of the survivors have severe neurologic sequelae.[5] Stratifying the risk of death or disability on the basis of prenatal examinations remains challenging, though the caliber of the venous sinus draining the main varix may be a strong predictor;[6] nevertheless, the strongest prognostic evidence rests on clinical evaluation in the first hours and days after birth. We believe that the presence of prenatal brain injury is a marker of an aggressive pathophysiologic cascade and that this understanding can aid in parental counseling. Lecce et al[5] reported that brain injury on a postnatal MR imaging was a predictor of adverse outcomes, and it would be reasonable to attribute at least a similar if not greater prognostic value to prenatal injury. Furthermore, our results support the likely association between prenatal brain injury and adverse neonatal outcome; this would suggest that these fetuses are likely to present in the neonatal period with low Bicêtre scores and overlap with the populations reported by Lecce et al, as nonsurvivors or survivors with significant neurologic impairment.[6]
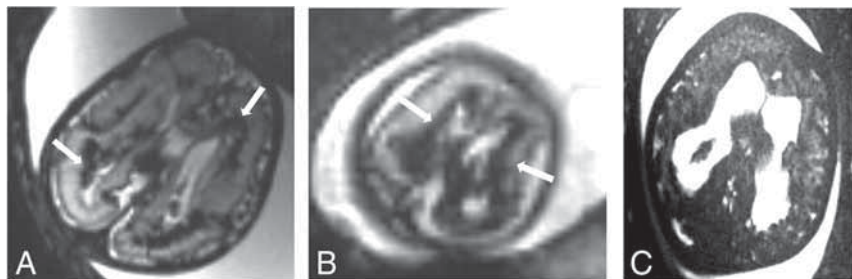
FIG 2. Abnormalities on T2*-weighted echo-planar sequences in fetuses with brain injury. *A*, Axial image in a 28.6-week fetus (subject 2, scan 1) shows blooming in the periventricular regions (*arrows*). *B*, Axial image in a 21.9-week fetus (subject 3, scan 2) shows blooming in the periventricular regions following the expected distribution of the proliferative compartments (germinal matrix [*arrows*]). *C*, Axial image in a 35.3-week fetus (subject 5, scan 1) shows generalized signal drop throughout the parenchyma.
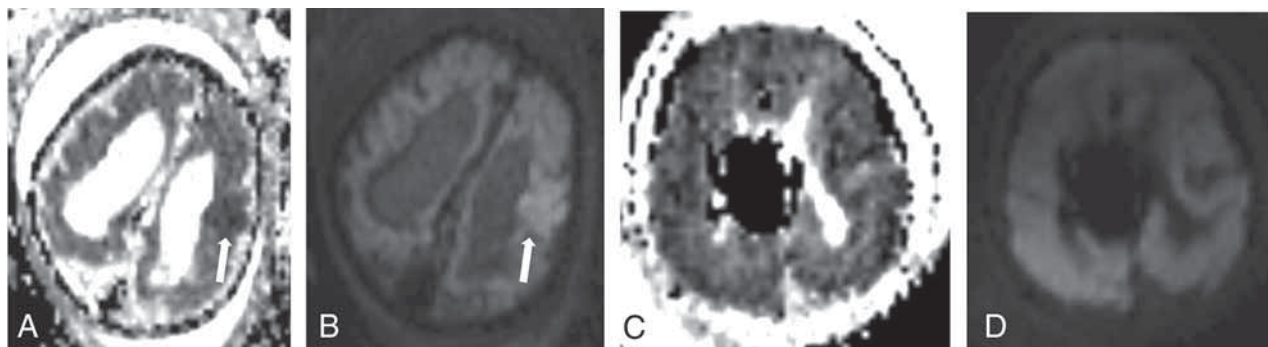
FIG 3. Diffusion abnormalities in fetuses with brain injury. ADC (*A*) and diffusion trace (*B*) in a 35.3-week fetus (subject 5, scan 1) show localized restricted diffusion in the left frontal lobe (*arrows*). ADC (*C*) and diffusion trace (*D*) in a 33-week fetus (subject 6, scan 3) show generalized restricted diffusion throughout the parenchyma (manual ROI measurements revealed ADC in C < 700 mm^2/s in the deep gray nuclei and white matter).
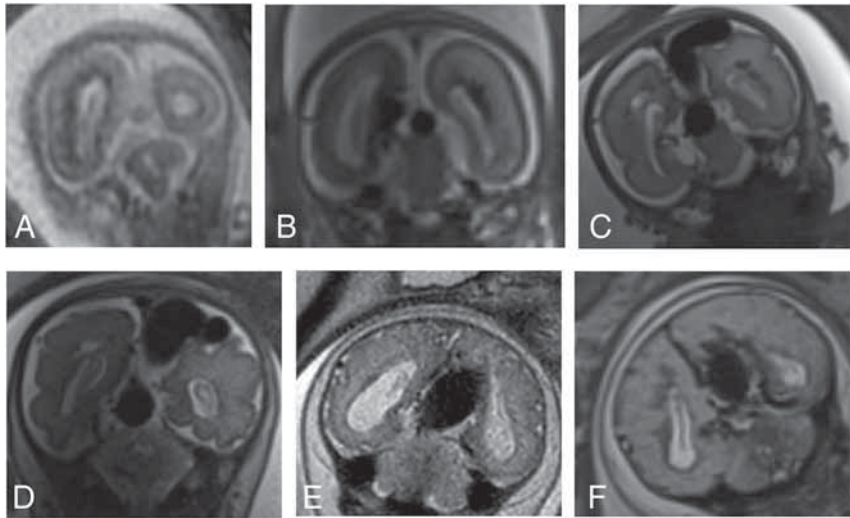
FIG 4. Progression of brain injury in 3 patients who underwent serial fetal MRIs. *A* and *B*, Subject 3, scan 1 and 2, at 20.4 weeks and then at 21.9 weeks when there is evidence of increased periventricular T2 hypointensity. *C* and *D*, Subject 2, scan 1 and 2, at 28.6 weeks and then at 29.4 weeks when there is evidence of a cystic change in the periventricular white matter and worsening of the T2 signal abnormality. *E* and *F*, Subject 6, scan 2 and 3, at 31.7 weeks and then at 33 weeks when there is generalized brain swelling and effacement of the extra-axial CSF in a pattern consistent with diffuse injury.

We observed a heterogeneous MR imaging appearance of prenatally diagnosed brain injury that probably reflects a complex pathophysiology with varying degrees of acuity and with cumulative injury. Prior reports have postulated that diffuse and progressive acute injury to the parenchyma in subjects with VOGM, referred to as "melting brain syndrome," is secondary to elevated venous pressure and chronic hypoxia.[7,8] The pattern of MR imaging abnormalities observed in our cohort is consistent with this hypothesis. For example, the areas of periventricular T2 prolongation could be attributable to either venous congestion or injury of varying chronicity, the restricted diffusion could represent acute venous ischemia, and the areas of T1 hyperintensity could represent late subacute areas of injury. Similarly, the T2*-weighted findings are consistent with a venous pattern of injury, including findings of venous congestion in the medullary veins and parenchyma and occasionally areas of hemorrhage. The bilateral and symmetric distribution of injury in patients with drainage via midline veins in contrast to the asymmetric injury in the fetus with lateralized venous drainage of a NG-AVF further supports a venous hemodynamic etiology as a contributing factor or causative mechanism.

Parenchymal injury showed a relentless course toward progression in our cohort of affected fetuses. This finding is consistent with observations in neonates and infants with VOGM; in these patients, the occurrence of even focal brain parenchymal injury is considered an urgent indication for intervention. If an intervention does not alleviate the adverse hemodynamic conditions, the injury may progress to "melting brain," and the prognosis is poor.[9] Recognizing that fetal brain injury differs from a static insult is fundamental to counseling parents and to the subsequent management of the fetus. If the abnormalities are subtle or equivocal, a repeat MR imaging in a short interval can confirm the presence of injury. If the abnormalities are overt, one should expect them to progress during the remainder of the pregnancy and probably result in substantial neurocognitive sequelae if the patient survives. Our results also show that brain parenchymal injury is a relatively rare occurrence (26% of the sample), which differs from the rate (40%) reported by Paladini et al.[10] The reason for this discrepancy is difficult to resolve due to the substantial differences between studies including the following: 1) random differences in populations and referral patterns, 2) modalities used, 3) definitions of brain injury, and 4) the duration of time during which the study populations were identified (dating back to 1999 in the study by Paladini et al).

This study has several limitations. First, a small sample size limits the power of the statistical analysis performed and increases the chance of type II error. This also precludes subgroup analysis and exploratory analysis with other demographic variables (sex, morphologic features of the malformation, and so forth). A second limitation is the retrospective design. Use of MRIs acquired at several institutions (outside records) during a 10-year period yields a variable quality of the MR imaging examinations as well as variability in protocols. Follow-up examinations were performed at variable intervals, and data from other outside records that were not uploaded onto the PACS (eg, fetal echocardiograms) may be incomplete or be unreliable. Third, our analysis is limited to neonatal clinical outcomes and does not have longer-term data or structured neurologic testing. Fourth, our sample may be subject to a selection bias. Our hospital is a tertiary referral center for subspecialized pediatric care, possibly resulting in overrepresentation of severe clinical presentations; the observed prevalence of brain injury in 25% of our cases could be overestimated as a result.

Last, for this first study, we chose to focus on the significance of prenatal signs and a limited set of clinical outcomes in the immediate neonatal period (death or intubation within 2 days postnatally due to heart failure). National-level outcome data from the same expert, high-volume center contrasting neonates with VOGM and this degree of heart failure with those who can be treated electively postneonatally (Lecce et al[5] compared with Gopalan et al[9]) makes clear that this distinction represents a major bifurcation in outcome, with high mortality and a high rate of severe neurocognitive injuries in the former group. No doubt, future effort should focus on long-term outcomes and associations with interventions.

CONCLUSIONS

Parenchymal brain injury is a complication seen in a minority of fetuses with VOGM and NG-AVFs. A combination of sequences, including DWI and T1-, T2-, and T2*-weighted sequences can help identify and characterize the injury. Findings of brain injury

appear to portend a poor prognosis, with relentless progression and a likely association with adverse neonatal outcomes.

REFERENCES

1. Raybaud C. **Normal and abnormal embryology and development of the intracranial vascular system.** *Neurosurg Clin N Am* 2010;21:399–426 CrossRef Medline
2. Yu J, Shi L, Lv X, et al. **Intracranial non-galenic pial arteriovenous fistula: a review of the literature.** *Interv Neuroradiol* 2016;22:557–68 CrossRef Medline
3. Cordova EG, Levy P, Kheir JN, et al. **Vein of Galen malformation.** *Neoreviews* 2020;21:e678–86 CrossRef Medline
4. Godfrey ME, Tworetzky W, Morash D, et al. **Cardiac findings in the fetus with cerebral arteriovenous malformation are associated with adverse outcome.** *Fetal Diagn Ther* 2017;41:108–14 CrossRef Medline
5. Lecce F, Robertson F, Rennie A, et al. **Cross-sectional study of a United Kingdom cohort of neonatal vein of Galen malformation.** *Ann Neurol* 2018;84:547–55 CrossRef Medline
6. Arko L, Lambrych M, Montaser A, et al. **Fetal and neonatal MRI predictors of aggressive early clinical course in vein of Galen malformation.** *AJNR Am J Neuroradiol* 2020;41:1105–11 CrossRef Medline
7. Hergan F, Huisman TA. "**Melting brain**" as complication of a vein of Galen aneurysmal malformation diagnosed by fetal MRI. *Clin Obstet Gynecol Reprod Med* 2018;4:1–3 CrossRef
8. Wagner MW, Vaught AJ, Poretti A, et al. **Vein of Galen aneurysmal malformation: prognostic markers depicted on fetal MRI.** *Neuroradiol J* 2015;28:72–75 CrossRef Medline
9. Gopalan V, Rennie A, Robertson F, et al. **Presentation, course, and outcome of postneonatal presentations of vein of Galen malformation: a large, single-institution case series.** *Dev Med Child Neurol* 2018;60:424–29 CrossRef Medline
10. Paladini D, Deloison B, Rossi A, et al. **Vein of Galen aneurysmal malformation (VGAM) in the fetus: retrospective analysis of perinatal prognostic indicators in a two-center series of 49 cases.** *Ultrasound Obstet Gynecol* 2017;50:192–99 CrossRef Medline

Asymmetry Matters: Diffusion Tensor Tractography of the Uncinate Fasciculus in Children with Verbal Memory Deficits

S.A. Mohammad, N.H. Nashaat, A.A.M.B. Okba, A. Kilany, A.S. Abdel-Rahman, A.M. Abd-Elhamed, and E.R. Abdelraouf

ABSTRACT

BACKGROUND AND PURPOSE: Verbal declarative memory performance relies on frontotemporal connectivity. The uncinate fasciculus is a major association tract connecting the frontal and temporal lobes. Hemispheric asymmetries contribute to various cognitive and neurobehavioral abilities. Here we investigated microstructural alterations and hemispheric asymmetry of the uncinate fasciculus and their possible correlation to memory performance of children with learning disorders attributed to verbal memory deficits.

MATERIALS AND METHODS: Two groups of right-handed children with learning disorders attributed to verbal memory deficits and typically developing children ($n = 20$ and 22, respectively) underwent DTI on a 1.5T scanner. Tractography of the uncinate fasciculus in both hemispheres was performed, and fractional anisotropy and diffusivity indices (radial diffusivity, axial diffusivity, and trace) were obtained. The asymmetry index was calculated. Verbal memory was assessed using subsets of the Stanford Binet Intelligence Scale, 4th edition, a dyslexia assessment test, and the Illinois test of Psycholinguistic Abilities. Correlation between diffusion metrics and verbal memory performance was investigated in the learning disorders group. Also, hemispheric differences in each group were tested, and between-group comparisons were performed.

RESULTS: Children with learning disorders showed absence of the normal left-greater-than-right asymmetry of fractional anisotropy and the normal right-greater-than-left asymmetry of radial diffusivity seen in typically developing children. Correlation with verbal memory subsets revealed that the higher the fractional anisotropy and asymmetry index, the better the rapid naming performance ($P < .05$) was.

CONCLUSIONS: These findings demonstrated microstructural aberrations with reduction of hemispheric asymmetry of the uncinate fasciculus, which could disrupt the normal frontotemporal connectivity in children with learning disorders attributed to verbal memory deficits. This outcome gives more understanding of pathologic mechanisms underlying this disorder.

ABBREVIATIONS: AD = axial diffusivity; AI = asymmetry index; FA = fractional anisotropy; LD = learning disorder; RD = radial diffusivity; UF = uncinate fasciculus; TDC = typically developing children; VMD = verbal memory deficits

Memory is considered a critical component of the learning process. Children rely on their memory for acquiring and processing new information, which is needed for proper school performance.[1] Verbal memory is concerned with the processing of language and verbally presented information. A higher proficiency at verbal memory–related tasks was found to be associated with better educational outcomes. Verbal memory was reported to be defective in children with various types of learning disorders (LDs).[2,3]

Different brain systems have been found to control different types of memory. Connections between diverse brain regions are essential for the process of encoding memory, in addition to its consolidation and retrieval.[1,4] Verbal declarative memory is thought to rely primarily on medial temporal lobe structures including the hippocampus. Functional neuroimaging studies have found that the left medial temporal lobe supports the ability to encode verbal information with activation of the left hemispheric prefrontal regions during semantic retrieval.[5,6] Increased memory performance has been correlated with elevated functional connectivity between the temporal lobes and prefrontal cortex.[7] Moreover, the 2 cerebral hemispheres were found to have functional and anatomic asymmetries that contribute to cognitive and neurobehavioral abilities; this hemispheric lateralization of function was found to be associated with increased cognitive ability.

Aberrations in hemispheric asymmetries have been reported in dyslexia, autism spectrum disorder, and schizophrenia.[8-12]

The uncinate fasciculus (UF) is a long association tract connecting the inferior frontal and mesial temporal lobes (regions that are implicated in encoding and retrieval of verbal memory). Left hemispheric dominance of the UF has been reported in healthy individuals.[13-16] In developing children and adolescents, the proficiency of verbal memory performance has been linked to white matter integrity of the left UF in DTI studies.[17,18]

Furthermore, DTI has been used to explore the correlations between white matter microstructure and different aptitudes reflecting cognitive performance, not only in typically developing children (TDC) but also in children with other neuropathologic conditions such as temporal lobe epilepsy and traumatic brain insult.[12,19-22] In addition, frontotemporal connectivity has been investigated using DTI in schizophrenia, dementia, and bipolar disorder, which are known to be associated with memory deficits.[8,15,23] However, to the best of our knowledge, there were no prior reports investigating frontotemporal connectivity and hemispheric asymmetry in children with LDs manifesting verbal memory deficits (VMD) without reading or writing disorders.

We hypothesized that frontotemporal connectivity expressed by UF integrity and hemispheric asymmetry might be altered in children with LDs manifesting VMD compared with TDC. To test this hypothesis, we investigated microstructural alterations of the UF in terms of fractional anisotropy (FA) and diffusivity indices using DTI. In addition, we tested the correlation between DTI markers and verbal memory performance in children with LDs.

MATERIALS AND METHODS

Participants
The study was conducted after approval of the ethics committee. A cross-sectional study included a convenient sample of children with poor scholastic achievement, which was related only to VMD. They were diagnosed as having an LD with executive functioning deficits, which included memory performance.[24] They were visiting the Learning Disability and Neurorehabilitation Research Clinic at the Medical Research Center of Excellence, National Research Center. In addition, control subjects were recruited from the patients' relatives. They included age- and sex-matched TDC, having the same social and ethnic origins. All participants were right-handed, native Arabic speakers, enrolled in the national educational system. Children with impairment in reading and writing and dyscalculia, sensory deficits, intellectual disability, associated neuropsychiatric disorders, or abnormalities on electroencephalography were excluded from the study group. Control subjects with a history of developmental language disorders, delayed developmental milestones, or having received language therapy sessions in early childhood were excluded as well. Also, any participant with contraindications to MR imaging was excluded.

A total of 45 subjects were initially included. Three subjects were excluded due to poor image quality. Finally, 20 children with LDs related to VMD and 22 TDC (matched in age, sex, and handedness) were enrolled in the study. The age of children in both groups ranged from 7 to 11 years; the mean ages were 9.3 (SD, 1.3) years and 9.1 (SD, 1.3) years for cases and control groups, respectively.

Clinical Measures
The aptitudes of the children with LDs were evaluated by the Arabic version of the Stanford-Binet Intelligence Scale, 4th edition, for intelligence quotient assessment,[25] the Arabic Dyslexia Assessment Test,[26] and the Arabic version of the Illinois Test of Psycholinguistic Abilities.[27] The items that represented verbal memory in these tests were rapid naming, semantic fluency of the Arabic Dyslexia Assessment Test (representing long-term memory), the Digit Span Backward (representing working memory), and the Auditory Sequential Memory Test of the Illinois Test of Psycholinguistic Abilities (representing short-term memory). The higher the scores of rapid naming, the worse the performance of this subtest was. The opposite applied to the other subtests in which higher scores were associated with better performance.

MR Imaging Protocol
All children were scanned with a 1.5T scanner (Achieva; Philips Healthcare) using an 8-channel sensitivity encoding head coil (sensitivity encoding acceleration factor of 8). The DTIs were acquired in 32 noncollinear directions along with baseline B_0 images using a single-shot echo-planar sequence. Axial images were acquired parallel to the anterior/posterior commissure line with a 2-mm section thickness. The FOV was 230×230 mm, and in-plain resolution was 2.5×2.5 mm^2. The head position was maintained using padding.

Image Analysis
DTI images were analyzed in Windows on a PC using DTIStudio software (Version 3.0.3; Johns Hopkins University), produced by this laboratory (H. Jiang and S. Mori, the Johns Hopkins Medical Institute [http://lbam.med.jhmi.edu]). Participants with scans that showed obvious head-motion artifacts were excluded from the study. The raw DWIs were then coregistered to B_0 images using the Automatic Image Registration tool (AIR; https://www.nitrc.org/projects/air/) with affine transformation and trilinear interpolation. FA and color FA and different diffusivity indices, radial diffusivity (RD), axial diffusivity (AD), and trace maps, were calculated in native space.[28]

Tractography
Tractography was performed using the fiber assignment by continuous tracking method following the previously described high-reproducibility protocol described by Wakana et al.[29] The UF was extracted from both hemispheres using 2 manually drown ROIs (Online Supplemental Data).[29] Tractography started at FA = 0.25. It ended at FA = 0.25 and a turning angle = 70°. The average FA, RD, AD, and trace were then calculated.

Moreover, the asymmetry index (AI) was calculated using the formula $(2 \times [\text{Right} - \text{Left}]/[\text{Right} + \text{Left}]) \times 100$ to further quantify the differences between the measured variables of both hemispheres. A positive AI value indicated that the measured variable of the right hemisphere was greater than the corresponding left variable (rightward asymmetry), while a negative value corresponded to the opposite (leftward asymmetry).[11,12]
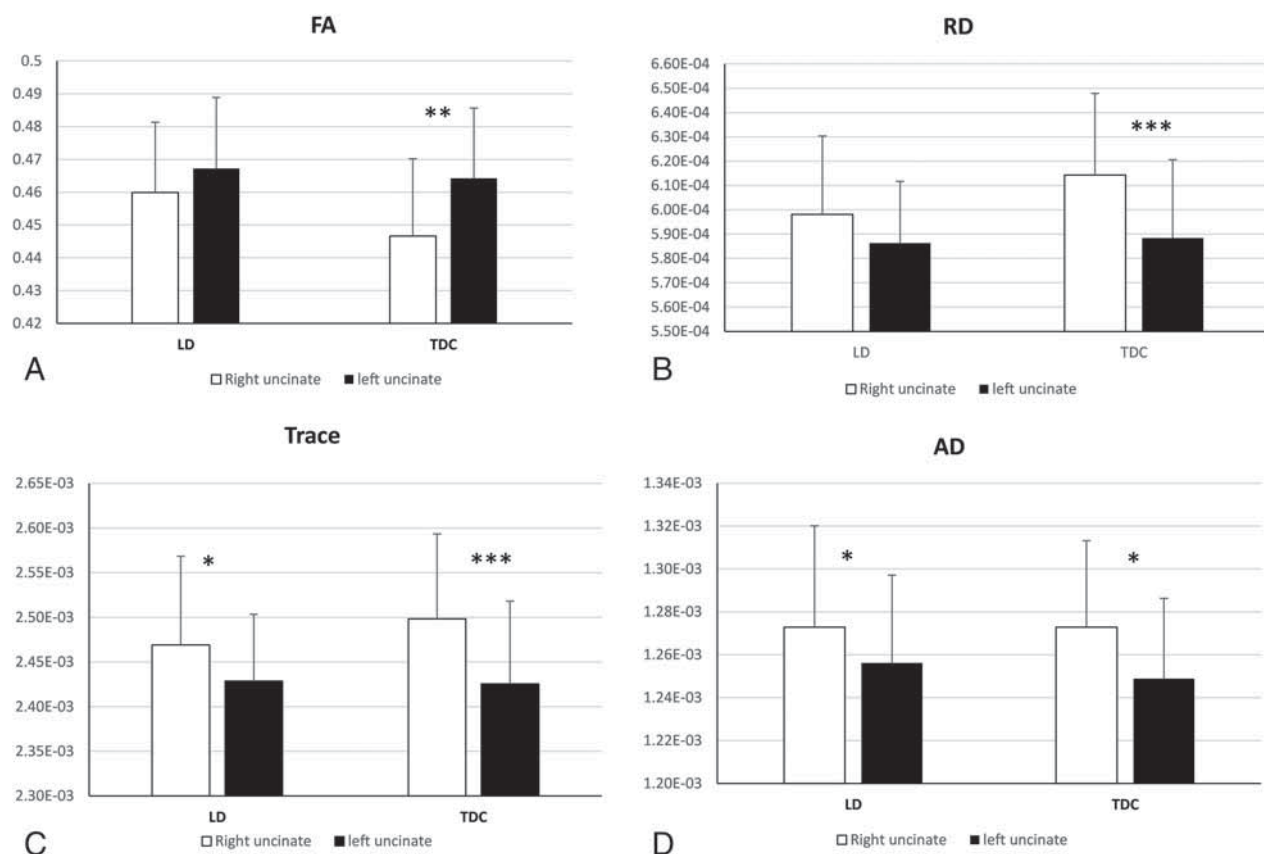
FIG 1. The UF asymmetries were calculated by comparing FA, RD (mm²s-1), AD (mm²s-1), and trace (mm²s-1) in both hemispheres. Rightward asymmetry was defined as having a higher value in the right brain than in the left, while leftward asymmetry was defined as left-greater-than-right values. The *asterisk* indicates $P < .05$; *double asterisks*, $P < .01$; *triple asterisks*, $P < .001$).

Statistical Analysis

FA, diffusivity indices (RD, AD, trace), and AI were correlated to the raw scores of rapid naming, semantic fluency, Digit Span Backward, and the Auditory Sequential Memory Test using the Spearman rank correlation test. To test hemispheric asymmetry in each group, we compared each tract value between both hemispheres using a paired Student t test. All the measured FA, diffusivity indices, and AI for each tract were compared between both groups using the Student t test.

RESULTS

All participants with LDs manifested rapid naming and semantic fluency deficits (mean raw scores: 66.2 [SD, 24.3] and 9.3 [SD, 0.9], respectively) with intelligent quotient ranges of 89–107 (mean, 96.7 [SD, 51]). The percentage of children with deficits in the Digit Span Backward was 65%, and in the Auditory Sequential Memory Test, it was 35%. Correlation with clinical tests revealed a significant negative correlation between rapid naming and both FA of the right uncinate fasciculus and its AI ($r = -0.5$, $P = .02$ and $r = -0.52$, $P = .01$, respectively). In other words, the higher the FA and AI, the lower the rapid naming score was with better performance. Otherwise, no significant statistical correlations were detected.

In TDC, the mean FA of the left UF was significantly higher than that of the right UF ($P = .004$), while RD, trace, and AD were found to be significantly lower ($P < .001$, $P < .001$, and $P =$

.016, respectively). However, in children with LDs, there was no significant statistical difference between the right and left hemispheres regarding FA or RD. On the other hand, hemispheric differences regarding the AD and trace were still preserved ($P = .04$ and .03, respectively) (Fig 1 and the Table).

Compared with TDC, the AI was found to be lower in children with LDs (Fig 2). Also, the UF of both cerebral hemispheres of the LD group showed higher FA, higher AD, but lower trace and RD. However, these differences failed to reach statistical significance (Table).

DISCUSSION

Despite the existence of growing literature exploring the relation between frontotemporal connectivity and cognitive aptitudes in healthy subjects and individuals with neuropsychiatric abnormalities,[8-12] microstructural aberrations of the UF and hemispheric asymmetry in children with LDs related to VMD have not yet been comprehensively investigated. Our findings support the hypothesis of the existence of white matter microstructural alterations in terms of reduced hemispheric asymmetry in right-handed children with LDs related to VMD, in addition to significant statistical correlations with certain verbal memory subsets. These alterations in hemispheric asymmetry together with the correlation results might be useful in understanding the pathogenesis of VMD in children with LDs.

Diffusion metrics of the uncinate fasciculus[a]

	LD				TDC			
	Right (mean) (SD)	Left (mean) (SD)	P Value	AI (mean) (SD)	Right (mean) (SD)	Left (mean) (SD)	P Value	AI (mean) (SD)
FA	0.46 (0.02)	0.47 (0.02)	.09	−1.58 (4.02)	0.45 (0.02)	0.46 (0.02)	.004	−3.9 (5.69)
RD	5.98E-04 (3.2E-05)	5.86E-04 (2.5E-05)	.06	1.95 (4.54)	6.14E-04 (3.35E-05)	5.88E-04 (3.22E-05)	<.001	4.32 (4.85)
AD	1.27E-03 (4.73 E-05)	1.26E-03 (4.09−05)	.04	1.3 (2.64)	1.27E-03 (4.03E-05)	1.25E-03 (3.74E-05)	.016	1.66 (3.00)
Trace	2.47E-03 (9.9E-05)	2.43E-03 (7.5E-05)	.03	1.61 (3.19)	2.50E-03 (9.50E-05)	2.43E-03 (9.25E-05)	<.001	2.96 (3.24)

[a] AD (mm^{2}s-1), RD (mm^{2}s-1), trace (mm^{2}s-1).
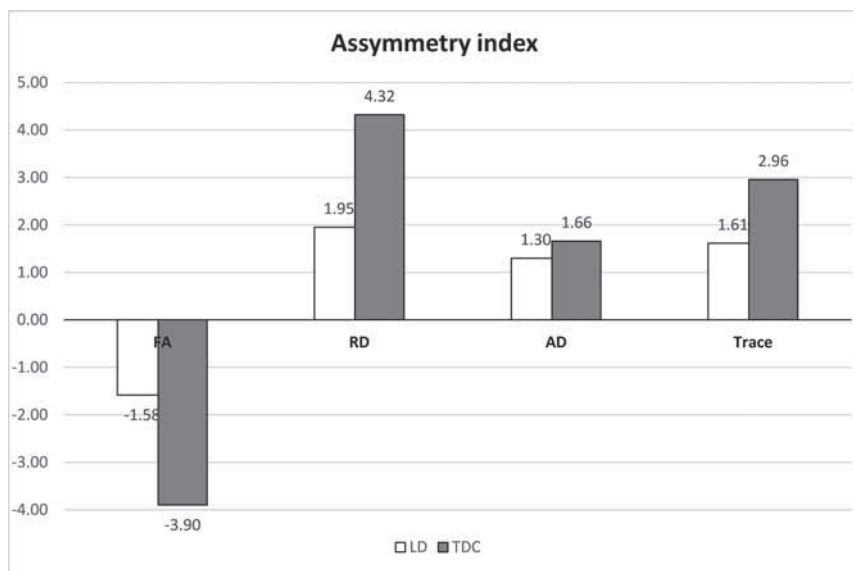
FIG 2. AIs of the UF in both groups (FA, AD, RD, and trace).

All participants of the LD group manifested deficits in subtests related to long-term memory, highlighting its role in the performance of these children and necessitating its targeting in the rehabilitation programs designed to increase performance in executive functions. Furthermore, the percentage of participants showing deficits in verbal working memory was more than in those having deficits in short-term memory. Nonetheless, similar memory deficits were previously reported in children with dyslexia,[3] underscoring the contribution of memory performance in all kinds of LDs.

The rapid naming performance showed a significant correlation with the FA of the right UF and its AI, indicating the reliance of participants with LDs in this study on the right-sided connections. The more the FA and AI, the better was the performance of rapid naming. Learning and memory are complex interacting cognitive functions. Declarative memory, which is a form of long-term memory, incorporates semantic and episodic memory. Semantic memory is considered a child's database of knowledge about the world.[30] Data in formal educational situations in school-aged children are acquired through direct experience and are further extended through several processes. The latter include self-generation of new factual knowledge via integration of information acquired in separate-yet-related episodes of new learning. These operations are related to working memory integrity. Therefore, brain structures sharing in verbal memory processing are essential for the proficiency of learning.[2]

The uncinate fasciculus can be divided into 3 segments (temporal, insular segment, and frontal) (Online Supplemental Data). The temporal segment originates partly from the entorhinal cortex, perirhinal cortex, and anterior temporal lobe. The entorhinal and perirhinal cortices are believed to be related to episodic memory function, object memory, and perception, respectively, while the anterior temporal lobe has been linked to semantic memory.[15] While the role of the UF in object naming and semantic processing has been proposed; more recently, its role in object naming has been suggested to be the most relevant function.[31] Furthermore, verbal memory (as evaluated by list learning) was found to be instantly impaired following left UF resection in 18 right-handed individuals.[32] Similarly, a decrease in UF integrity has been associated with semantic dementia and memory impairment in temporal lobe epilepsy.[12,23] Our finding of the significant correlation between the UF and rapid naming scores enforces the previously suggested link between them.

By means of DTI voxel-based morphometry, the UF was dissected into a longer superior segment and a shorter inferior segment. The former showed a higher FA in the left hemisphere, while the latter showed a greater FA in the right.[20,33] Using diffusion tensor tractography in our study, we averaged FA and diffusivity indices from all voxels occupied by this tract. Consequently, the mean values were influenced by the longer superior portion, which was found to be left-lateralized. Leftward asymmetry of the UF was also documented by other research groups.[8,16,20] Higher FA could reflect higher myelination and higher fiber numbers and/or density in the left hemisphere in TDC. Moreover, we have found that the left hemisphere had lower diffusivity values in terms of RD, AD, and trace. RD was found to reflect myelination, while AD reflects axonal integrity.[34]

In the control group (TDC), the hemispheric asymmetries of FA and the diffusivity indices of the UF may reflect structural differences between cerebral hemispheres. In the second and third trimesters of gestation, structural asymmetries have been found in the Sylvian fissure, the surrounding frontal operculum, and the planum temporal.[33,35,36] These structural asymmetries were found to be associated

with functional asymmetries as well. Production and processing of language are predominantly controlled by the left hemisphere, while visuospatial processing has right-hemispheric dominance in most individuals.[37] Decreased hemispheric asymmetry has been linked to autism spectrum disorder and developmental dyslexia.[38] Moreover, the lateralization hypothesis of schizophrenia signifying developmental aberrations in brain lateralization has been developed.[36] Similarly, the reduced asymmetry in the UF in children with LDs related to VMD can suggest an analogous mechanism with significant structural and functional aberrations that could be developmental in origin. Children with LDs in our study were found to have lost hemispheric asymmetry of the UF in terms of FA and RD, while the differences between UFs of both hemispheres in terms of AD and trace were preserved. To the best of our knowledge, this pattern of alterations of diffusion metrics has not been previously published.

Compared with the control group (TDC), UFs of both cerebral hemispheres in children with LDs showed higher FA, higher AD, but lower RD and trace. However, the difference was statistically insignificant. These possible aberrations in anisotropy and diffusivity could be attributed to an increase in myelination, axonal diameter, packing density, or branching. More FA and less diffusivity are not always indications of better function. These changes could represent compensatory mechanisms secondary to the dysfunction of memory-related cortical areas. Similarly, FA was found to be abnormally higher in the right superior longitudinal fasciculus of patients with Williams syndrome compared with control subjects.[39]

The study is possibly limited by the relatively small number of participants; however, to the best of our knowledge, this is the first study to investigate UF hemispheric asymmetry in children with LDs related to VMD. We recruited children who were perfectly matched in age, sex, and handedness to ensure that the DTI metrics were truly reflecting alterations in brain structure related to the disease rather than just differences in brain structure due to language hemispheric dominance. Also, a considerable percentage of included children with LDs had long-term memory impairment in addition to other types of verbal memory deficits. Nevertheless, memory performance and tasks interlace even in the models describing the memory.[1] Thus, it would be difficult to recruit children with only 1 type of memory deficit.

CONCLUSIONS

The present findings indicated microstructural aberrations of the UF with reduction of hemispheric asymmetry in right-handed children with LDs attributed to memory deficits. These changes could influence the normal frontotemporal connectivity and, consequently, disrupt the proper functioning of memory performance of such children. The results of this study give more understanding of neuropathologic mechanisms underlying this disorder.

Disclosure forms provided by the authors are available with the full text and PDF of this article at www.ajnr.org.

REFERENCES

1. Brem AK, Ran K, Pascual-Leone A. **Learning and memory.** *Handb Clin Neurol* 2013;116:693–737 CrossRef Medline

2. Bauer PJ, Blue SN, Xu A, et al. **Productive extension of semantic memory in school-aged children: relations with reading comprehension and deployment of cognitive resources.** *Dev Psychol* 2016;52:1024–37 CrossRef Medline

3. Nashaat N, Hasan H, Kilany A, et al. **Correlation between reading and spelling performance of Egyptian children with reading disorder and their cognitive and linguistic abilities.** *Journal of Indian Association for Child and Adolescent Mental Health* 2017;13:82–106

4. Thompson RF, Kim JJ. **Memory systems in the brain and localization of a memory.** *Proc Natl Acad Sci U S A* 1996;93:13438–44 CrossRef Medline

5. Kelley WM, Miezin FM, McDermott KB, et al. **Hemispheric specialization in human dorsal frontal cortex and medial temporal lobe for verbal and nonverbal memory encoding.** *Neuron* 1998;20:927–36 CrossRef Medline

6. Gotts SJ, Jo HJ, Wallace GL, et al. **Two distinct forms of functional lateralization in the human brain.** *Proc Natl Acad Sci U S A* 2013;110: E3435–44 CrossRef Medline

7. Menon V, Boyett-Anderson JM, Reiss AL. **Maturation of medial temporal lobe response and connectivity during memory encoding.** *Brain Res Cogn Brain Res* 2005;25:379–85 CrossRef Medline

8. Kubicki M, Westin CF, Maier SE, et al. **Uncinate fasciculus findings in schizophrenia: a magnetic resonance diffusion tensor imaging study.** *Am J Psychiatry* 2002;159:813–20 CrossRef Medline

9. Mohammad SA, Sakr HM, Bondok SM, et al. **Fronto-temporal connectivity in never-medicated patients with first-episode schizophrenia: a DTI study.** *Egypt Journal of Radiology and Nuclear Medicine* 2016;47:255–62 CrossRef

10. Song JW, Mitchell PD, Kolasinski J, et al. **Asymmetry of white matter pathways in developing human brains.** *Cereb Cortex* 2015;25:2883–93 CrossRef Medline

11. Carper RA, Treiber JM, DeJesus SY, et al. **Reduced hemispheric asymmetry of white matter microstructure in autism spectrum disorder.** *J Am Acad Child Adolesc Psychiatry* 2016;55:1073–80 CrossRef Medline

12. Zhao X, Zhou ZQ, Xiong Y, et al. **Reduced interhemispheric white matter asymmetries in medial temporal lobe epilepsy with hippocampal sclerosis.** *Front Neurol* 2019;10:394 CrossRef Medline

13. Powell HW, Parker GJ, Alexander DC, et al. **Hemispheric asymmetries in language-related pathways: a combined functional MRI and tractography study.** *Neuroimage* 2006;32:388–99 CrossRef Medline

14. Hasan KM, Iftikhar A, Kamali A, et al. **Development and aging of the healthy human brain uncinate fasciculus across the lifespan using diffusion tensor tractography.** *Brain Res* 2009;1276:67–76 CrossRef Medline

15. Von Der Heide RJ, Skipper LM, Klobusicky E, et al. **Dissecting the uncinate fasciculus: disorders, controversies and a hypothesis.** *Brain* 2013;136:1692–1707 CrossRef Medline

16. Mohammad SA, Nashaat NH. **Age-related changes of white matter association tracts in normal children throughout adulthood: a diffusion tensor tractography study.** *Neuroradiology* 2017;59:715–24 CrossRef Medline

17. Peters BD, Szeszko PR, Radua J, et al. **White matter development in adolescence: diffusion tensor imaging and meta-analytic results.** *Schizophr Bull* 2012;38:1308–17 CrossRef Medline

18. Schaeffer DJ, Krafft CE, Schwarz NF, et al. **The relationship between uncinate fasciculus white matter integrity and verbal memory proficiency in children.** *Neuroreport* 20142;25:921–25 CrossRef Medline

19. Mabbott DJ, Rovet J, Noseworthy MD, et al. **The relations between white matter and declarative memory in older children and adolescents.** *Brain Res* 2009;1294:80–90 CrossRef Medline

20. Eluvathingal TJ, Hasan KM, Kramer L, et al. **Quantitative diffusion tensor tractography of association and projection fibers in normally developing children and adolescents.** *Cereb Cortex* 2007;17:2760–68 CrossRef Medline

21. Diehl B, Busch RM, Duncan JS, et al. **Abnormalities in diffusion tensor imaging of the uncinate fasciculus relate to reduced memory in temporal lobe epilepsy.** *Epilepsia* 2008;49:1409–18 CrossRef Medline

22. Chung S, Wang X, Fieremans E, et al. **Altered relationship between working memory and brain microstructure after mild traumatic brain injury.** *AJNR Am J Neuroradiol* 2019;40:1438–44 CrossRef Medline

23. Matsuo K, Mizuno T, Yamada K, et al. **Cerebral white matter damage in frontotemporal dementia assessed by diffusion tensor tractography.** *Neuroradiology* 2008;50:605–11 CrossRef Medline

24. Cortiella C, Horowitz SH. **The state of learning disabilities: facts, trends, and emerging issues.** August 13 2014. https://www.ncld.org/wp-content/uploads/2014/11/2014-State-of-LD.pdf. Accessed March 1, 2022

25. Melika L. *Stanford Binet Intelligence Scale. 4th Arabic Version.* 2nd ed. Victor Kiorlos Publishing, Cairo; 1998

26. Aboras Y, Abdou R, Kozou H. **Development of an Arabic test for assessment of dyslexia in Egyptian children.** *Bull Alexandria Fac Med* 2008;44:653–62

27. El-Sady S, El-Shobary A, Rifaie N, et al. **Illinois Test of Psycholinguistic Abilities.** [master's thesis]. Ain Shams University, Department of Otorhinolaryngology, Phoniatrics Unit; 1996

28. Jiang DT, van Zijl PC, Kim J, et al. **DtiStudio: resource program for diffusion tensor computation and fiber bundle tracking.** *Comput Methods Programs Biomed* 2006;81:106–16 CrossRef Medline

29. Wakana S, Caprihan A, Panzenboeck MM, et al. **Reproducibility of quantitative tractography methods applied to cerebral white matter.** *Neuroimage* 2007;36:630–44 CrossRef Medline

30. Martin-Ordas G, Atance CM, Caza JS. **How do episodic and semantic memory contribute to episodic foresight in young children?** *Front Psychol* 2004;5:732 CrossRef Medline

31. Papagno C. **Naming and the role of the uncinate fasciculus in language function.** *Curr Neurol Neurosci Rep* 2011;11:553–59 CrossRef Medline

32. Papagno C, Miracapillo C, Casarotti A, et al. **What is the role of the uncinate fasciculus? Surgical removal and proper name retrieval.** *Brain* 2011;134:405–14 CrossRef Medline

33. Park HJ, Westin CF, Kubicki M, et al. **White matter hemisphere asymmetries in healthy subjects and in schizophrenia: a diffusion tensor MRI study.** *Neuroimage* 2004;23:213–23 CrossRef Medline

34. Song SK, Sun SW, Ramsbottom MJ, et al. **Dysmyelination revealed through MRI as increased radial (but unchanged axial) diffusion of water.** *Neuroimage* 2002;17:1429–36 CrossRef Medline

35. Wada JA, Clarke R, Hamm A. **Cerebral hemispheric asymmetry in humans: cortical speech zones in 100 adults and 100 infant brains.** *Arch Neurol* 1975;32:239–46 CrossRef Medline

36. Crow TJ, Ball J, Bloom SR, et al. **Schizophrenia as an anomaly of development of cerebral asymmetry: a postmortem study and a proposal concerning the genetic basis of the disease.** *Arch Gen Psychiatry* 1989;46:1145–50 CrossRef Medline

37. O'Regan L, Serrien DJ. **Individual differences and hemispheric asymmetries for language and spatial attention.** *Front Hum Neurosci* 2018;12:380 CrossRef Medline

38. Waldie KE, Haigh CE, Badzakova-Trajkov G, et al. **Reading the wrong way with the right hemisphere.** *Brain Sci* 2013;3:1060–75 CrossRef Medline

39. Hoeft F, Barnea-Goraly N, Haas BW, et al. **More is not always better: increased fractional anisotropy of superior longitudinal fasciculus associated with poor visuospatial abilities in Williams syndrome.** *J Neurosci* 2007;27:11960–65 CrossRef Medline

Brain Abnormalities in Patients with Germline Variants in *H3F3*: Novel Imaging Findings and Neurologic Symptoms Beyond Somatic Variants and Brain Tumors

C.A.P.F. Alves, O. Sherbini, F. D'Arco, D. Steel, M.A. Kurian, F.C. Radio, G.B. Ferrero, D. Carli, M. Tartaglia, T.B. Balci, N.N. Powell-Hamilton, S.A. Schrier Vergano, H. Reutter, J. Hoefele, R. Günthner, E.R. Roeder, R.O. Littlejohn, D. Lessel, S. Lüttgen, C. Kentros, K. Anyane-Yeboa, C.B. Catarino, S. Mercimek-Andrews, J. Denecke, M.J. Lyons, T. Klopstock, E.J. Bhoj, L. Bryant, and A. Vanderver

ABSTRACT

BACKGROUND AND PURPOSE: Pathogenic somatic variants affecting the genes *Histone 3 Family 3A and 3B* (*H3F3*) are extensively linked to the process of oncogenesis, in particular related to central nervous system tumors in children. Recently, *H3F3* germline missense variants were described as the cause of a novel pediatric neurodevelopmental disorder. We aimed to investigate patterns of brain MR imaging of individuals carrying *H3F3* germline variants.

MATERIALS AND METHODS: In this retrospective study, we included individuals with proved *H3F3* causative genetic variants and available brain MR imaging scans. Clinical and demographic data were retrieved from available medical records. Molecular genetic testing results were classified using the American College of Medical Genetics criteria for variant curation. Brain MR imaging abnormalities were analyzed according to their location, signal intensity, and associated clinical symptoms. Numeric variables were described according to their distribution, with median and interquartile range.

RESULTS: Eighteen individuals (10 males, 56%) with *H3F3* germline variants were included. Thirteen of 18 individuals (72%) presented with a small posterior fossa. Six individuals (33%) presented with reduced size and an internal rotational appearance of the heads of the caudate nuclei along with an enlarged and squared appearance of the frontal horns of the lateral ventricles. Five individuals (28%) presented with dysgenesis of the splenium of the corpus callosum. Cortical developmental abnormalities were noted in 8 individuals (44%), with dysgyria and hypoplastic temporal poles being the most frequent presentation.

CONCLUSIONS: Imaging phenotypes in germline *H3F3*-affected individuals are related to brain features, including a small posterior fossa as well as dysgenesis of the corpus callosum, cortical developmental abnormalities, and deformity of lateral ventricles.

Histones are nuclear proteins that bind to DNA in the nucleus and help condense it into chromatin.[1] Histones are dynamically decorated with posttranslational modifications, which regulate the processes of DNA repair, gene expression, mitosis, and meiosis. Abnormal dysregulation of these posttranslational modifications has been linked to cancer, neurodevelopmental syndromes, psychiatric disorders, and cardiovascular disease.[2-5] Therefore, histone biology is critical to understanding the pathophysiology of many diseases and developing treatments.

Pathogenic somatic variants affecting *H3F3* have been extensively linked to the epigenetic process of oncogenesis. In particular, when these variants involve 2 critical amino acids, p.Lys27 and p.Gly34, they are linked to central nervous system in children (p.Lys27 is linked to diffuse midline gliomas, and p.Gly34 is linked to supratentorial hemispheric gliomas).[6-8] Currently, these variants represent a major molecular feature for accurate classification of these neoplasms according to the World Health Organization.[9]

Expanding the correlation of this gene with human disease, Bryant et al[10] have recently demonstrated that *H3F3* plays a major role during embryogenesis, and causative pathogenic variants in these genes are associated with neurocognitive delay along with other symptoms such as seizures and hypotonia. In the present study, we sought to investigate the value of brain MR imaging in individuals carrying *H3F3A* or *H3F3B* germline variants, looking for an imaging pattern that would be recognizable for diagnostic purposes.

MATERIALS AND METHODS

Individual Population

This study included individuals with proved *H3F3* pathogenic and likely pathogenic variants that are causative of disease and with available clinical MR imaging scans of the brain. Individuals and their families were collected prospectively from the Myelin Disorders Bioregistry Project with approval from the institutional review board at Children's Hospital of Philadelphia (institutional review board approval No. IRB 14–011236). Written informed consent for the collection of clinical information, neuroimaging, and genetic information was obtained for each study participant.

Abstraction of Clinical Data

Clinical and demographic data were retrieved from available medical records of affected individuals. Genetic testing reports were reviewed, or variants were provided by the referring provider and classified using the American College of Medical Genetics criteria for variant curation. All clinical and molecular data were reviewed by a board-certified clinical and/or clinical molecular geneticist.

MR Imaging Technique

We retrospectively reviewed all available brain MR imaging studies of the included subjects. Images were acquired at either 1.5T or 3T MR using different imaging protocols including at least sagittal and axial T1WI and T2WI. MR images not allowing adequate visual assessment were excluded.

Imaging Analysis

MR images of all individuals were reviewed independently by 2 pediatric neuroradiologists (C.A.P.F.A. and F.D.) with final consensus agreement in searching for structural features involving the posterior fossa, major commissural structures, and cortex, along with abnormalities in the ventricular system, basal ganglia, and thalamus. Additional evaluation, measurements, and ratios of the posterior fossa and corpus callosum, both evaluated in the sagittal midline, were performed to confirm the size abnormalities.[11-15] Detailed analysis of characteristics of white matter myelination was also performed.

Table 1: Demographic, genetic, and clinical information of individuals with disease-causing missense variants[a]

Characteristics	Individuals (n = 18)
Age at last evaluation (yr)	4.46 (1.9–12.1)
Sex: female/male	(8:10)
H3F3 variant	
H3F3A	11 (61)
H3F3B	7 (39)
Microcephaly	8 (44)
Seizures	10 (56)
Febrile	5 (50)
Nonfebrile	5 (50)
Sitting (n = 17)	
Normal	1 (6)
Delayed	12 (71)
Not achieved	4 (23)
Walking	
Normal	2 (11)
Delayed	10 (56)
Not achieved	6 (33)
Speaking	
Normal	1 (6)
Delayed	7 (38)
Not achieved	10 (56)

[a] Categoric variables are described as number (percentage). Continuous variables are described as median (1Q–3Q).

Statistical Analysis

Statistical analyses were performed using R statistical and computing software (http://www.r-project.org) and R studio (http://rstudio.org/download/desktop). A 2-tailed $P < .05$ was considered statistically significant. The Shapiro-Wilk test was used to assess the normality of continuous variables, which were presented as median and first and third quartiles (1Q–3Q). Categoric variables were presented as counts and percentages. Mann-Whitney *U* or Student *t* tests were used to compare continuous variables, and the Fisher exact test was used to compare categoric variables between clinical data and MR imaging findings. For statistical analysis, individuals were divided into 2 groups, nonachievement milestones versus normal achievement plus development delay. Delayed and normal developmental milestones were grouped together due to the small number of subjects with normal development. Delayed milestones were defined as sitting after 6 months, walking after 20 months, and first word after 12 months of age.

RESULTS

On the basis of the inclusion criteria, a cohort of 18 individuals (mean age, 4.5 years; range, 1.9–12.1 years; 10 males/8 females) with proved *H3F3* variants causative of disease were included in this study. All individuals underwent brain MR imaging. These individuals had 1 of 2 genotypes: *H3F3A* variants ($n = 11$) or *H3F3B* variants ($n = 7$). The details of each individual's demographic, clinical, and genetic information are given in Table 1 and the Online Supplemental Data. The overall imaging findings are described in Table 2.

Posterior Fossa

Thirteen of 18 individuals (72%) presented with a verticalized tentorium and low insertion of the torcula, along with features

Table 2: Abnormal imaging information of individuals with disease-causing *H3F3* missense variants[a]

Imaging Features	Individuals (n = 18)
Small posterior fossa	13 (72)
Cerebellum	2 (11)
Brainstem	2 (11)
Thalamus	0
Caudate	8 (44)
Putamen	0
Globus pallidum	0
Corpus callosum	5 (28)
Fourth ventricle	6 (33)
Lateral ventricle	7 (38)
White matter	2
Cortex	8 (44)
Optic nerves and chiasm	1 (6)
Temporal lobes/hippocampus	8 (44)
Clivus/sella	4 (22)

[a] Categoric variables are described as number (percentage).

suggestive of a small posterior fossa and hypoplasia of the occipital bone, later confirmed with additional posterior fossa measurements and ratios (Online Supplemental Data).[13-15] The occipital bone, measured by the supraoccipital line, of those patients with a small posterior fossa was disproportionally small, and it was significantly smaller ($P = .001$) compared with the subjects with a normal posterior fossa. Of those, 7 individuals (7/13 54%) had posterior fossa structures (brainstem and cerebellum) that appeared crowded (Fig 1A–D). A low disposition of the cerebellar tonsils fitting in the Chiari I deformity criteria[15] was observed in 4 individuals. Further mild malformative features of the brainstem were observed in 2 children: both with abnormal anterior-posterior pattern of malformations, one with disproportional predominance of the midbrain (Online Supplemental Data) and the other with disproportional size reduction of the midbrain compared with the medulla oblongata (Online Supplemental Data). Hypoplasia of the clivus and signs of platybasia were noted in 3 individuals.

Major Commissures
Malformative features of the corpus callosum, accompanied or not accompanied by anterior commissure hypoplasia, were present in 5 individuals (28%). The involvement of the splenium of the corpus callosum was the most remarkable feature, being absent or elongated and hypoplastic according to the patient's age in all 5 cases. Agenesis of the body and splenium of the corpus callosum was observed in 1 case (5.5%) (Fig 1A–D and Online Supplemental Data).

Cortex
The cerebral cortex of 8 individuals (44%) presented with malformative features. Six of them showed variable degrees of diffuse dysgyria, (Fig 2A–D) 1 anterior pachygyria, and 1 diffuse simplified cortical appearance. Along with the cortical abnormalities, all 8 individuals also had bilateral temporal lobe hypoplasia (Fig 2E–H).

Basal Ganglia and Lateral Ventricles
Six individuals (33%) presented with a relatively reduced size and/or internal rotational appearance of the heads of the caudate nuclei. These features resulted in a characteristic deformity of the lateral
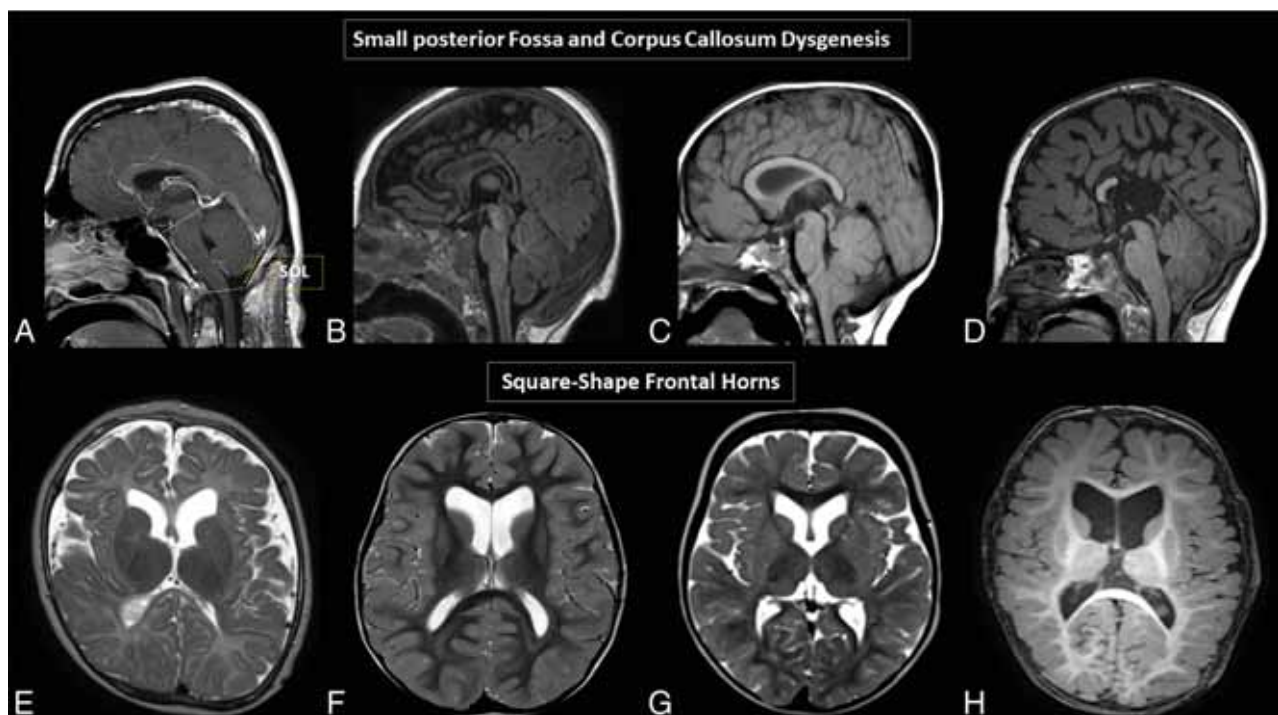
FIG 1. Brain MR images. *A* and *D*, Variable degrees of corpus callosum deformities, particularly involving the body and splenium, noting partial agenesis in *D*. Deformed morphology of the posterior fossa, with variable degrees of low insertion of the torcula and size reduction of the supraoccipital line (SOL). Note the crowded appearance of the structures in the posterior fossa along with low disposition of the cerebellar tonsils, fitting in the Chiari I deformity criteria in C and *D*. *E–H*, Variable degrees of reduced size and/or internal rotational appearance of the head of the caudate nuclei, resulting in an enlarged and squared appearance of the frontal horns.
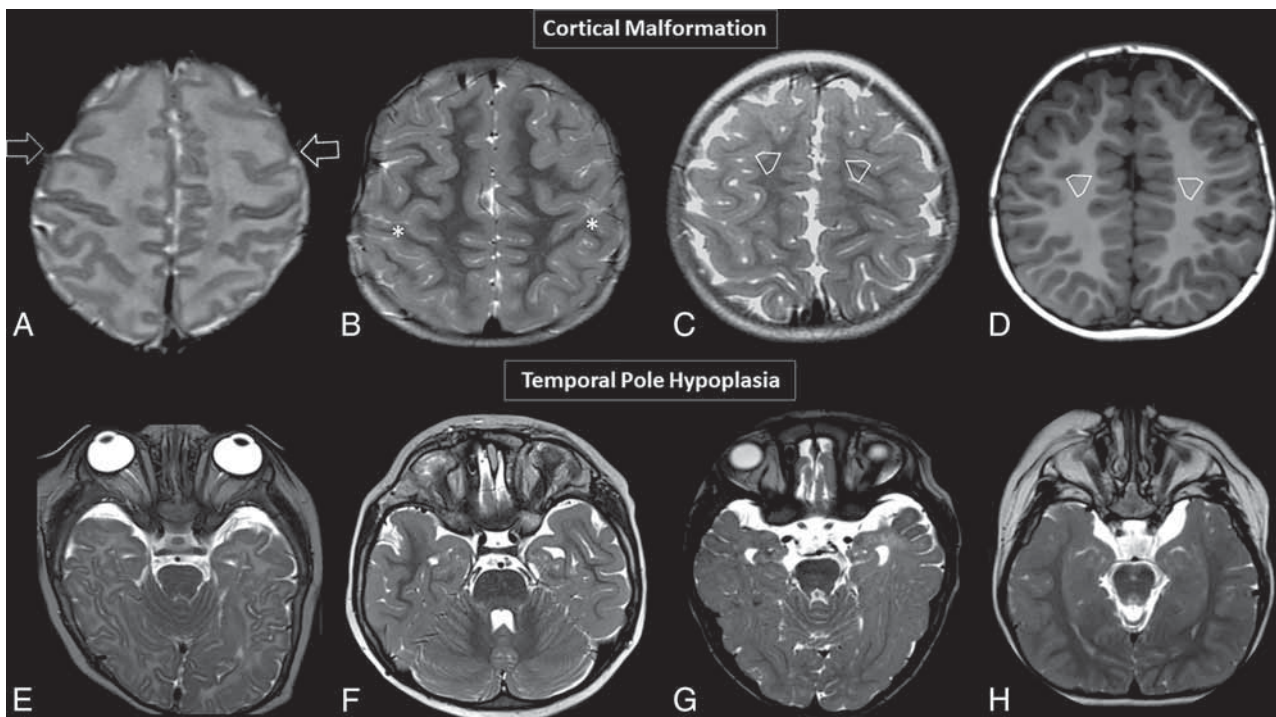
Cortical Malformation

Temporal Pole Hypoplasia

FIG 2. Brain MR images. Axial T2WI (*A–C*) and axial T1WI (*D*) showing 4 different patients with variable degrees of diffuse abnormal orientation and morphology of the gyri and sulci. Note particular abnormal morphology involving both frontal lobes (*open arrows*, *A*), a deformed periro-landic region (*asterisks*, *B*), and abnormal gyration of the medial frontal lobes in *C* and *D* (*open arrowheads*, *C* and *D*). Axial T2WI (*E–H*) shows 4 different patients with temporal pole hypoplasia.

ventricles, with an enlarged and squared appearance of the frontal horns (Fig 1*E–H*).

Clinical Correlation

Our entire cohort (*n* = 18) presented with at least 1 clinical symptom, including microcephaly, the presence of seizures, and delayed or not delayed achieved development milestones (Table 1).

No statistically significant ($P < .05$) correlation between clinical symptoms (absence of achievement of gross motor and speaking milestones, presence of seizures) and main imaging findings (small posterior fossa, basal ganglia abnormalities, and corpus callosum and cortical malformations) was found. However, all individuals included in our cohort except for 1 had severe clinical symptoms and marked abnormalities involving the brain. Moreover, 50% of individuals presenting with seizures also had malformative features involving the cortex (Online Supplemental Data).

DISCUSSION

Somatic variants in *H3F3* are well-known promoters of oncogenesis;[16-19] however, the role of germline variants remain underrecognized. The recent discovery of disease-associated missense variants in *H3F3* that cause a neurodevelopmental disorder, but not cancer, profoundly impacts histone biology research.[10] In the present study, we sought to investigate the value of brain MR imaging of individuals carrying *H3F3* germline variants, assessing imaging patterns and the neurodegenerative clinical symptoms. We found a constellation of malformative features of the brain, including a small posterior fossa, along with changes in the basal ganglia, cortex, and corpus callosum.

Neuroimaging plays an important role in the diagnosis of pediatric glial tumors related to pathogenic somatic variants affecting *Histone 3 Family 3A and 3B*.[9,16,20-22] Because some recent studies have demonstrated the critical importance of histone turnover in neuronal transcription and plasticity in the mammalian brain[23-25] and Bryant et al[10] have demonstrated the role of germline variants of *H3F3* during embryogenesis as a causative factor of neurocognitive delay in young individuals, we have investigated the potential presentation of malformative features in the brain MR imaging of these individuals and how these would impact the patient's prognosis.

Individuals with disease-causing germline variants in histone 3.3 in our cohort had a characteristic clinical background, usually presenting with neurocognitive delay, seizures, and microcephaly. On neuroimaging, our cohort also shared some similar features; the most prevalent was a small posterior fossa (13/18 individuals), with some of them presenting with Chiari I deformity and malformative features affecting the brainstem or cerebellum. There is a wide spectrum of congenital abnormalities associated with a small posterior fossa, including developmental malformations caused by a genetic defect[26-28] as well as disruptive causes due to injury of a structure with normal developmental potential.[29-32] Understanding the spectrum of congenital posterior fossa anomalies and their diagnostic criteria is of paramount importance for optimal therapy, accurate prognosis, and correct genetic counseling.[29]

We have encountered further neuroimaging findings in our cohort of individuals with disease-causing germline missense variants in *H3F3*. The findings included enlarged frontal horns of the lateral ventricles, reflecting reduced size and/or an internal

rotational appearance of the nuclei of the caudate heads, dysgenesis of the corpus callosum, and malformations of cortical development, such as dysgyria. Cortical malformation implies abnormalities in both the migration of neurons to the cortex and abnormal cortical organization[33,34] and may underlie the relatively high frequency of epilepsy in those individuals.[35,36]

No statistical significance ($P < .05$) was found correlating milestones delay (in sitting, walking, and speaking the first word) or the presence of seizures with the main imaging findings, including a small posterior fossa, basal ganglia abnormalities, and corpus callosum and cortical malformations. Fifty percent of individuals presenting with seizures also had malformative features involving the cortex, suggesting a potential correlation between both.

Despite presenting promising findings, our study also had limitations, including the retrospective nature of our study design. Our cohort was biased because all individuals included in our study except for 1 had severe clinical symptoms and significant abnormalities involving the brain, making correlative analysis more difficult. The other limitation was that we had a relatively small sample size of individuals who had brain MR imaging assessment, though it represents almost half of the 43 reported individuals in the literature. On the other hand, we found consistent neuroimaging findings among our cohort, which is helpful for guiding appropriate genetic investigations of these individuals. Our imaging findings may reflect the spectrum of abnormalities seen in individuals with germline variants in histone 3.3; however, these results need to be validated in a larger cohort with broader disease severity.

CONCLUSIONS

The current series, including a subset of individuals previously reported in the original work of Bryant et al,[10] represents the largest cohort of neuroradiologically characterized subjects carrying disease-causing *H3F3* germline variants. The identified constellation of neuroimaging findings, namely a small posterior fossa, reduced size and/or a rotational appearance of the nuclei of the caudate heads, dysgenesis of the corpus callosum, and malformations of cortical development, offer novel diagnostic pattern able to guide the diagnosis of *H3F3*-related disorder.

REFERENCES

1. Mariño-Ramírez L, Kann MG, Shoemaker BA, et al. **Histone structure and nucleosome stability.** *Expert Rev Proteomics* 2005;2:719–29 CrossRef Medline
2. Zhao Z, Shilatifard A. **Epigenetic modifications of histones in cancer.** *Genome Biol* 2019;20:245 CrossRef Medline
3. Kim JH, Lee JH, Lee IS, et al. **Histone lysine methylation and neurodevelopmental disorders.** *Int J Mol Sci* 2017;18:1404 CrossRef Medline
4. Peter CJ, Akbarian S. **Balancing histone methylation activities in psychiatric disorders.** *Trends Mol Med* 2011;17:372–79 CrossRef Medline
5. Bagchi RA, Weeks KL. **Histone deacetylases in cardiovascular and metabolic diseases.** *J Mol Cell Cardiol* 2019;130:151–59 CrossRef Medline
6. Sturm D, Witt H, Hovestadt V, et al. **Hotspot mutations in H3F3A and IDH1 define distinct epigenetic and biological subgroups of glioblastoma.** *Cancer Cell* 2012;22:425–37 CrossRef Medline
7. Aboian MS, Solomon DA, Felton E, et al. **Imaging characteristics of pediatric diffuse midline gliomas with histone H3 K27M mutation.** *AJNR Am J Neuroradiol* 2017;38:795–800 CrossRef Medline
8. Kurokawa R, Baba A, Kurokawa M, et al. **Neuroimaging features of diffuse hemispheric glioma, H3 G34-mutant: a case series and systematic review.** *J Neuroimaging* 2022;32:17–27 CrossRef Medline
9. Louis DN, Perry A, Wesseling P, et al. **The 2021 WHO Classification of Tumors of the Central Nervous System: a summary.** *Neuro Oncol* 2021;23:1231–51 CrossRef Medline
10. Bryant L, Li D, Cox SG, et al. **Histone H3.3 beyond cancer: germline mutations in Histone 3 Family 3A and 3B cause a previously unidentified neurodegenerative disorder in 46 patients.** *Sci Adv* 2020;6:eabc9207 CrossRef Medline
11. Garel C, Cont I, Alberti C, et al. **Biometry of the corpus callosum in children: MR imaging reference data.** *AJNR Am J Neuroradiol* 2011;32:1436–43 CrossRef Medline
12. Jandeaux C, Kuchcinski G, Ternynck C, et al. **Biometry of the cerebellar vermis and brain stem in children: MR imaging reference data from measurements in 718 children.** *AJNR Am J Neuroradiol* 2019;40:1835–41 CrossRef Medline
13. Marin-Padilla M, Marin-Padilla TM. **Morphogenesis of experimentally induced Arnold–Chiari malformation.** *J Neurol Sci* 1981;50:29–55 CrossRef Medline
14. Nishikawa M, Sakamoto H, Hakuba A, et al. **Pathogenesis of Chiari malformation: a morphometric study of the posterior cranial fossa.** *J Neurosurg* 1997;86:40–47 CrossRef Medline
15. Poretti A, Ashmawy R, Garzon-Muvdi T, et al. **Chiari type 1 deformity in children: pathogenetic, clinical, neuroimaging, and management aspects.** *Neuropediatrics* 2016;47:293–307 CrossRef Medline
16. Schwartzentruber J, Korshunov A, Liu XY, et al. **Driver mutations in histone H3.3 and chromatin remodelling genes in paediatric glioblastoma.** *Nature* 2012;482:226–31 CrossRef Medline
17. Weinberg DN, Allis CD, Lu C. **Oncogenic mechanisms of histone H3 mutations.** *Cold Spring Harb Perspect Med* 2017;7:a026443 CrossRef Medline
18. Khuong-Quang DA, Buczkowicz P, Rakopoulos P, et al. **K27M mutation in histone H3.3 defines clinically and biologically distinct subgroups of pediatric diffuse intrinsic pontine gliomas.** *Acta Neuropathol* 2012;124:439–47 CrossRef Medline
19. Feng J, Hao S, Pan C, et al. **The H3.3 K27M mutation results in a poorer prognosis in brainstem gliomas than thalamic gliomas in adults.** *Hum Pathol* 2015;46:1626–32 CrossRef Medline
20. Castel D, Philippe C, Calmon R, et al. **Histone H3F3A and HIST1H3B K27M mutations define two subgroups of diffuse intrinsic pontine gliomas with different prognosis and phenotypes.** *Acta Neuropathol* 2015;130:815–27 CrossRef Medline
21. Aboian MS, Tong E, Solomon DA, et al. **Diffusion characteristics of pediatric diffuse midline gliomas with histone H3-K27M mutation using apparent diffusion coefficient histogram analysis.** *AJNR Am J Neuroradiol* 2019;40:1804–10 CrossRef Medline
22. Piccardo A, Tortora D, Mascelli S, et al. **Advanced MR imaging and 18F-DOPA PET characteristics of H3K27M-mutant and wild-type pediatric diffuse midline gliomas.** *Eur J Nucl Med Mol Imaging* 2019;46:1685–94 CrossRef Medline
23. Maze I, Wenderski W, Noh K-M, et al. **Critical role of histone turnover in neuronal transcription and plasticity.** *Neuron* 2015;87:77–94 CrossRef Medline
24. Deal RB, Henikoff JG, Henikoff S. **Genome-wide kinetics of nucleosome turnover determined by metabolic labeling of histones.** *Science* 2010;328:1161–64 CrossRef Medline
25. Dion MF, Kaplan T, Kim M, et al. **Dynamics of replication-independent histone turnover in budding yeast.** *Science* 2007;315:1405–08 CrossRef Medline

26. Hennekam RC, Biesecker LG, Allanson JE, et al; Elements of Morphology Consortium. **Elements of morphology: general terms for congenital anomalies.** *Am J Med Genet A* 2013;161A:2726–33 CrossRef Medline

27. Doherty D, Millen KJ, Barkovich AJ. **Midbrain and hindbrain malformations: advances in clinical diagnosis, imaging, and genetics.** *Lancet Neurol* 2013;12:381–93 CrossRef Medline

28. Boycott KM, Flavelle S, Bureau A, et al. **Homozygous deletion of the very low density lipoprotein receptor gene causes autosomal recessive cerebellar hypoplasia with cerebral gyral simplification.** *Am J Hum Genet* 2005;77:477–83 CrossRef Medline

29. Bosemani T, Orman G, Boltshauser E, et al. **Congenital abnormalities of the posterior fossa.** *Radiographics* 2015;35:200–20 CrossRef Medline

30. Limperopoulos C, Soul JS, Gauvreau K, et al. **Late gestation cerebellar growth is rapid and impeded by premature birth.** *Pediatrics* 2005;115:688–95 CrossRef Medline

31. Messerschmidt A, Prayer D, Brugger PC, et al. **Preterm birth and disruptive cerebellar development: assessment of perinatal risk factors.** *Eur J Paediatr Neurol* 2008;12:455–60 CrossRef Medline

32. Steggerda SJ, Leijser LM, Wiggers-de Bruïne FT, et al. **Cerebellar injury in preterm infants: incidence and findings on US and MR images.** *Radiology* 2009;252:190–99 CrossRef Medline

33. Barkovich AJ, Kuznieky RI, Jackson GD, et al. **Classification system for malformations of cortical development: update 2001.** *Neurology* 2001;57:2168–78 CrossRef Medline

34. Barkovich AJ, Kuznieky RI, Jackson GD, et al. **A developmental and genetic classification for malformations of cortical development.** *Neurology* 2005;65:1873–87 CrossRef Medline

35. Shorvon S, Guerrini R, Trinka E, et al. *The Causes of Epilepsy: Diagnosis and Investigation.* Cambridge University Press; 2019

36. Barkovich AJ, Guerrini R, Kuznieky RI, et al. **A developmental and genetic classification for malformations of cortical development: update 2012.** *Brain* 2012;135:1348–69 CrossRef Medline

Imaging Findings and Clinical Analysis of Primary Intracranial Pure Yolk Sac Tumors in Children and Adolescents: A Retrospective Study from China

W. Dai, H. Liu, Y. Chen, and Z. Chen

ABSTRACT

BACKGROUND AND PURPOSE: Primary intracranial pure yolk sac tumor is very rare. Our aim was to summarize the characteristics of primary intracranial pure yolk sac tumors from the clinical and imaging aspects in a retrospective study.

MATERIALS AND METHODS: We studied 5 patients with primary intracranial pure yolk sac tumors in Guangzhou Women and Children's Medical Center from January 2015 to June 2021. A comprehensive literature search was performed on the electronic database of the China National Knowledge Infrastructure (1990 to June 2021). Clinical data based on age, sex, treatment, CT, and MR imaging findings were collected and analyzed.

RESULTS: A total of 25 patients were included in the study, 21 boys and 4 girls. Twenty-one patients underwent plain MR imaging and an enhanced examination, 9 patients underwent DWI, and 12 patients underwent plain CT and/or an enhanced examination. The tumors were posterior fossa in 9 cases and supratentorial in 16 cases. All tumors showed marked enhancement after enhanced scanning by MR imaging or CT. The signal on DWI was similar to that of the cerebral cortex, and the ADC map was similar to or slightly higher than that of the cerebral cortex. Among the cases, 13 were followed up from 2 months to 5 years. There was no recurrence or metastasis in 9 patients with postoperative chemotherapy or chemoradiotherapy followed up for 1.5–5 years. Four patients died 2 months to 1.5 years after only an operation, or chemoradiotherapy but no operation.

CONCLUSIONS: There are some relatively specific imaging findings of primary intracranial yolk sac tumors that could assist in their diagnosis. Surgery combined with radiation therapy and/or chemotherapy can achieve a better prognosis.

ABBREVIATIONS: AFP = α-fetoprotein; YST = yolk sac tumor

Yolk sac tumor (YST), also known as endodermal sinus tumor, is a highly malignant tumor originating from primitive germ cells.[1] It usually occurs in the gonads (testes, ovaries) but can be found outside the gonads in rare cases. YST can be divided into pure and mixed types.[2] Primary intracranial YST is very rare, accounting for 2%–5% of intracranial tumors and 6.5% of intracranial germ cell tumors,[3] with a peak onset at 10–12 years.[4] Most patients with primary intracranial YST have a poor prognosis, with 1-, 3-, and 5-year survival rates of 65.2%, 47.3%, and 40.5%, respectively.[4]

Due to the extremely low incidence of primary intracranial pure YSTs, imaging reports are even rarer. At present, there are mainly just some case reports.[5-7] In the present study, we retrospectively analyzed 5 cases of pure intracranial YST from our center and reviewed all previously reported intracranial pure YST cases in China. The purpose of our study was to summarize the typical clinical characteristics and imaging appearance of primary, intracranial pure YSTs to better understand their characteristics.

MATERIALS AND METHODS
Clinical Patients
We studied 5 cases of primary, intracranial pure YST in Guangzhou Women and Children's Medical Center from January 2010 to June 2021 (Online Supplemental Data). Patients were diagnosed by surgical pathology and immunohistochemistry. Blood serum was obtained to measure α-fetoprotein (AFP) levels. This study was approved by the ethics committee of Guangzhou Women and Children's Medical

Center (KY 2020–57900). Informed consent was obtained from all of the parents or legal guardians.

The Preferred Reporting Items for Systematic Reviews and Meta-Analyses guidelines were used to collect the data. The terms "primary intracranial yolk sac tumor," "primary intracranial endodermal sinus tumor," and "malignant germ cell tumor" were searched using the electronic database of the China National Knowledge Infrastructure (1990 to June 2021). A total of 20 qualified cases were obtained (Online Supplemental Data).

The inclusion criteria of the cases in the literature were as follows: 1) younger than 18 years of age, 2) first onset, 3) primary intracranial, 4) pure yolk sac tumor, and 5) published in journals and magazines. Exclusion criteria were the following: 1) 18 years of age or older, 2) metastatic yolk sac tumor, 3) YST complicated by other components (mixed type), 4) cases with incomplete clinical or imaging data, and 5) the case not Chinese.

Imaging Protocols

Four patients in our center underwent scanning on a Magnetom Skyra 3T scanner (Siemens). In 4 cases, MR imaging–enhanced head scans were performed, and DWI scans were performed in 3 cases. The scans had the following parameters: T1WI: TR/TE = 500~600 ms/8~10 ms; T2WI: TR/TE = 3500–4200/100–120 ms; T1WI gradient-echo fat-suppression sequence: TR/TE = 250–500/5–10 ms; DWI: TR/TE = 3500–4200/60–80 ms, b-value = 800 seconds/mm^2. All the sequence parameters were as follows: thickness/gap = 5/1 mm, FOV = 240 × 240 mm, matrix = 320 × 320. The dose of contrast agent was 0.1 mmol/kg.

Two cases in our center underwent head contrast-enhanced CT. The CT scanning protocol consisted of the axial plane using a 64-section spiral CT machine (tube voltage = 120 kV, automatic current conditions, thickness = 1 mm, layer spacing = 1 mm, matrix = 512 × 512, and a standard algorithm reconstruction image

with a 5-mm-layer-thickness multiplanar reconstruction and volume rendering). Contrast-enhanced CT was performed following intravenous injection of 2 mL/kg of nonionic contrast medium.

For uncooperative children, chloral hydrate (0.5 mL/kg) was administered orally for sedation, and they were scanned when in quiet sleep.

In the literature,[8-22] 17 patients underwent contrast-enhanced MR imaging, and 6 patients underwent DWI scans. Two patients underwent plain head CT scans, and 8 patients underwent enhanced head CT scans.

Image Analysis

All cases were reviewed by 2 pediatric neuroradiologists, and consensus was reached after discussion in case of disagreement. Information was collected about the lesion location, size, morphology, signal or density, enhancement characteristics, and surrounding edema, mass effect, hydrocephalus, and so forth.

RESULTS

Clinical Data Characteristics

Among the 25 cases, 21 were boys and 4 were girls, from 1 year and 10 months of age to 17 years of age, with a median age of 10 years (Table). Before surgery, the serum AFP was increased in 6 cases, all of which were >1000 ng/mL (normal value = 0–8.1 ng/mL) and the serum AFP gradually decreased to normal after surgery. In a case with tumor recurrence, the AFP increased significantly after surgery. The tumor was resected in 23 cases, and only a biopsy was performed in 2 cases. Thirteen cases were followed up from 2 months to 5 years. Three patients were followed up after surgery combined with radiation and chemotherapy for 1.5 years, 4 years, and 5 years, respectively, without recurrence. One patient was followed up for 2 years after surgical resection without recurrence. Two patients died 2 months after

Clinical manifestations of 25 patients with primary, intracranial, pure YST

| No.	Sex	Age (yr)	Clinical Manifestations
1	Boy	11	Headache with vomiting
2	Boy	4	Gait instability
3	Boy	2 and 10 mo	Headache with vomiting
4	Boy	1 and 10 mo	Headache with vomiting
5	Boy	10	Headache with vomiting
6	Boy	3	Vomiting with convulsions
7	Boy	11	Headache with vomiting
8	Boy	2.5	Headache with vomiting and gait instability
9	Boy	2	Gait instability
10	Boy	3	Headache with vomiting and gait instability
11	Girl	12	Headache with vomiting
12	Boy	13	Headache with vomiting and gait instability
13	Boy	2	Gait instability
14	Girl	10	Headaches, sleepiness, and blurred vision
15	Boy	9	Headache with blurred vision
16	Boy	10	Headache with seizures
17	Boy	14	Side limb weakness
18	Boy	14	Headache with vomiting
19	Boy	1 and 11 mo	Headache with vomiting and gait instability
20	Girl	10	Headaches, sleepiness, and blurred vision
21	Boy	5	Headache with vomiting
22	Boy	10	Headache
23	Girl	11	Headache
24	Boy	15	Headache and vomiting with diplopia and precocious puberty
25	Boy	17	Headache with vomiting and gait instability
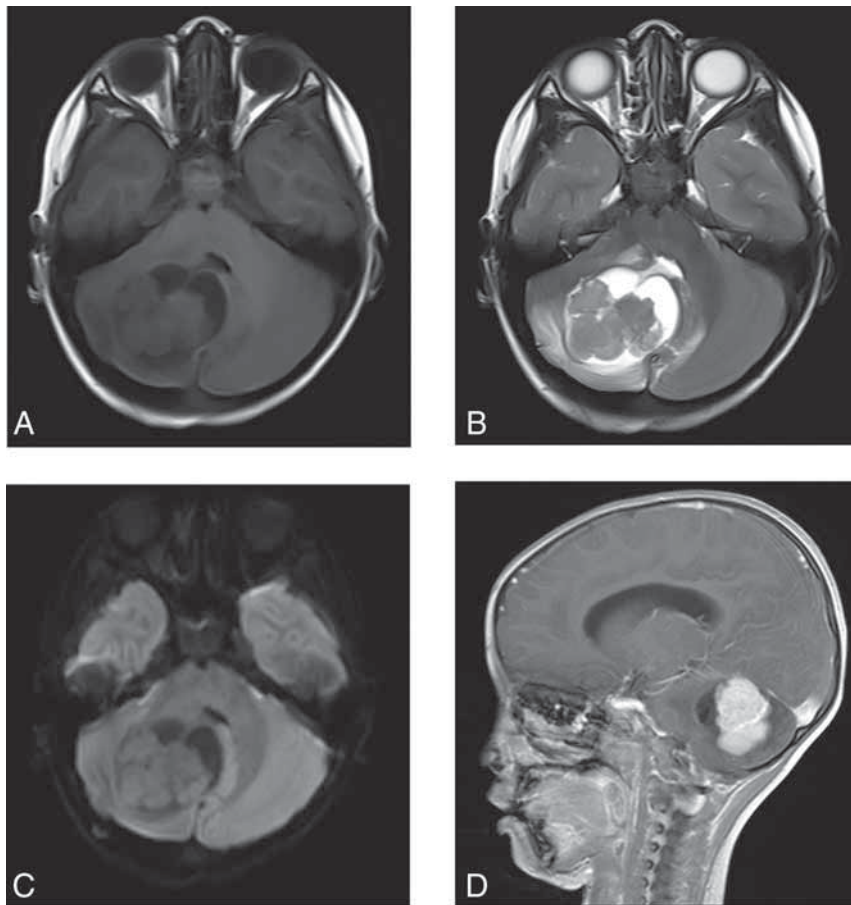
FIG 1. A 4-year-old boy with a right cerebellar hemisphere YST. *A*, MR image shows the tumor located in the right cerebellar hemisphere. It is solid with cystic changes. *B*, There is a small amount of edema around the tumor, and the fourth ventricle is compressed. *C*, DWI shows isosignal of solid components of the mass. *D*, The tumor shows serpiginous enhancement.

Thirteen cases of tumors were solid, of which 11 cases had relatively uniform signals, with multiple faint microcysts showing slightly low signals on T1WI and slightly high signals on T2WI; 2 cases had uniform signals, with slightly high signals on T1WI and slightly high signals on T2WI. Eight cases were cystic solid lesions (Fig 1), dominated by solid components; cystic components could be seen around or in the center of the tumor. Solid components showed slightly lower signals on T1WI and slightly higher signals on T2WI. After enhanced scanning, the solid components of the solid tumors and cystic solid tumors were significantly enhanced, with multiple, thick, serpiginous enhancement (Fig 1) and multiple unenhanced microscopic cystic components, which were increased compared with plain scanning. The was no enhancement of the cystic components. In 2 cases, the signal was uniform and the tumor enhancement was uniform. Nine DWI signals were equisignal (compared with the cerebral cortex) (Figs 1 and 2), and 7 ADC signals were equisignal or slightly high (compared with the cerebral cortex).

In 12 patients, 1 patient had slightly low density, 3 patients had isodense, and 8 patients had uniform or slightly high density. Three patients had peritumor or central cystic changes, and 3 patients had peritumor calcification. Ten cases had obvious enhancement, among which 6 cases had irregular enhancement (Fig 3).

Pathologic Features

The gross specimen of the tumor was tough and rich in blood supply. Microscopically, the tumor tissue was distributed in a loose network. The tumor cells were rich in cytoplasm, red-stained or transparent, and the nuclei were large, round, or oval, with obvious atypia and abundant nuclear mitosis. Eosinophilic and Schiller-Duval bodies were seen locally, and hemorrhagic necrosis was seen in the stroma. Immunohistochemical results were as follows: AFP (+), glypican-3 (+), cytokeratin (+), sal-like protein 4 (+), focal (+), Ki67 (20∼70% (+), CD30 (−), octamer-binding transcription factor 4(−).

DISCUSSION

Primary intracranial pure YST is a rare and highly malignant germ cell tumor that is usually located in the pineal and the saddle regions. Primary YST occurring in the posterior fossa is even rarer.[23] In this study, the incidence of primary intracranial YST was significantly higher in boys (21/25, 84%), which was slightly higher than that in a report about the prevalence of YST in children and adolescents (males 132/191, 69%).[2] However, this report

surgery, and 2 patients died 6 months and 1.5 years after radiation therapy and chemotherapy. Four patients were followed up with surgery combined with chemotherapy for 1.5 years, 2 years, 3 years, and 3 years, respectively, without recurrence. One patient did not receive chemotherapy after surgery due to family economic reasons. After 6 months of outpatient follow-up, his blood AFP increased significantly and tumor recurrence was found by MR imaging examination. Surgical treatment was performed again, and standard chemotherapy was performed after surgery. There were no signs of a second recurrence after 4 years of follow-up.

Imaging Findings

Of the 25 patients with primary intracranial YST, 9 cases were located in the posterior fossa and 16 cases were located in the supratentorial lateral ventricle. In 25 cases, the maximum diameter line was 2.5–7.0 cm, the boundary was relatively clear, and there were different degrees of mass effect with no edema or only mild edema around the tumor. There were 19 cases with different degrees of obstructive hydrocephalus in the supratentorial ventricle and 6 cases without hydrocephalus. Sixteen cases were quasi-circular, and 9 cases were irregular. Nine cases were cystic solid with solid components, and 16 cases were solid.
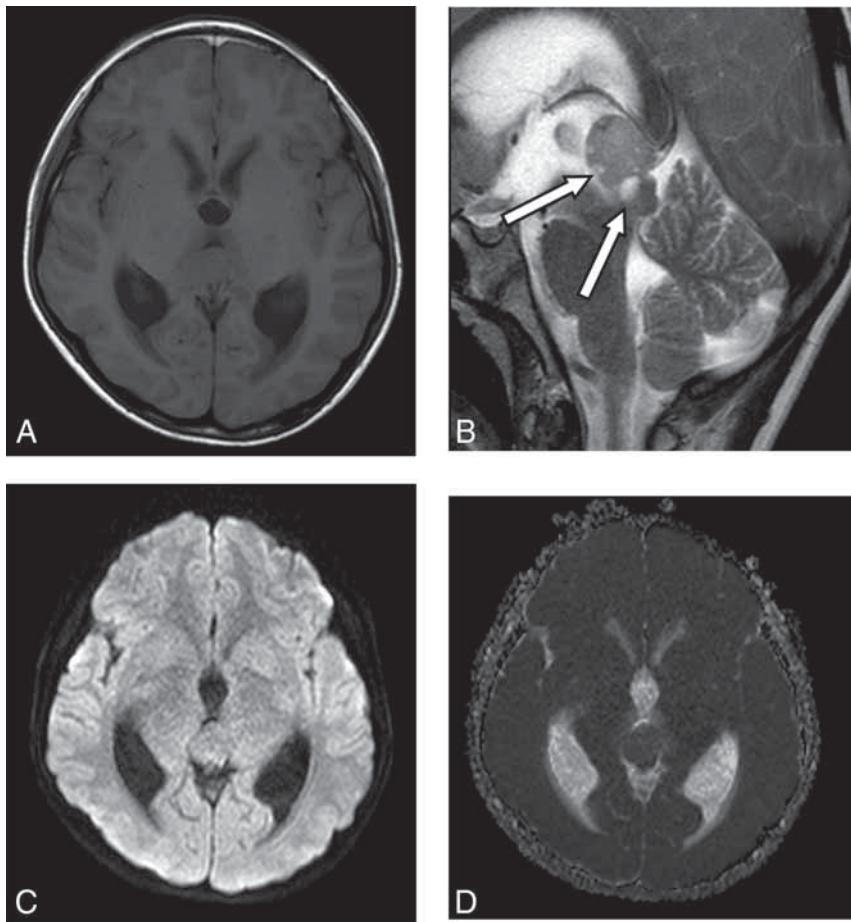
FIG 2. An 11-year-old boy with a pineal region YST. *A,* MR image shows the tumor located in the pineal region with a slightly low signal associated with supratentorial dilation of the ventricle. *B,* The T2 sequence shows multiple, fine cysts with hypersignal (*arrows*). *C* and *D,* The DWI sequence and ADC map show that the tumor signal is the same as that of the cerebral cortex.
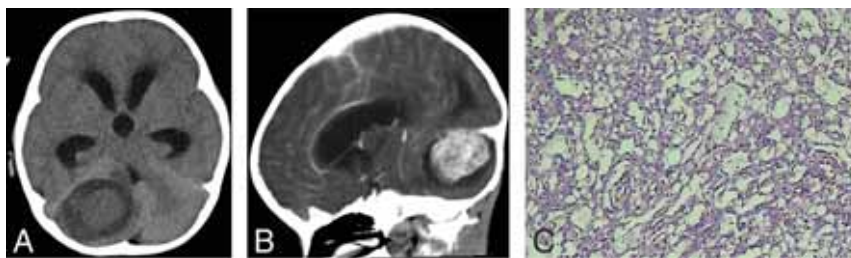

FIG 3. A boy, 2 years and 10 months of age, with a right cerebellar hemisphere YST. *A,* CT shows a slightly hypodense mass lesion accompanied by peritumoral edema. *B,* Enhanced CT shows heterogeneous density. *C,* H&E staining shows a typical Schiller-Duval body and loose, vacuolated network structures and prominent nucleoli with more atypia cells.

sample size collected in this study. To date, primary intracranial pure YST in the posterior fossa has not been reported in any girls worldwide, possibly indicating that it only occurs in boys, but more cases need to be confirmed in the future.

Due to the low incidence and high degree of malignancy of intracranial YST, there are no relevant treatment guidelines at present. However, recent studies suggest that surgical resection followed by chemoradiotherapy and/or chemotherapy can improve the survival rate of patients with intracranial, primary YST.[23,25,26] In this study, 13 patients were followed up, and there was no recurrence or metastasis in patients with surgery combined with chemoradiotherapy or surgery combined with chemotherapy for 1.5–5 years (8/13, 62%), while patients with surgery alone or chemoradiotherapy alone died after 2 months to 1.5 years (4/13, 3%). This finding suggests that surgical resection combined with standard chemotherapy or radiation therapy and chemotherapy can improve the survival rate of children with primary, intracranial, pure YST, a finding consistent with that in previous literature reports.

Because YST originates from the endoderm, it retains the ability to synthesize AFP in the fetus, and AFP levels are high in most patients. Therefore, elevated blood AFP levels are considered a sensitive indicator for the diagnosis of YST.[27] In this study, the blood AFP of 6 children was significantly increased before surgery and decreased to the normal level after surgery, and in 1 case, AFP was also significantly increased after recurrence. Therefore, we believe that the serum AFP level should be checked regularly after surgery to detect recurrences early.

The imaging findings of intracranial primary YST are considered nonspecific,[28-30] but the imaging findings of this group of cases have certain characteristics. Intracranial primary YST presented as a round mass (16/25, 64%) with a clear boundary and an obvious mass effect, but the surrounding edema was usually mild and CT showed slightly higher, equal, or slightly lower density. On MR imaging, the solid components of intracranial primary YST showed equal or slightly lower T1WI signals and slightly higher T2WI signals, and a small part showed slightly higher T1WI signals, which may be related to the presence of mucous components in the tumor or the rich capillary and sinusoid

covered YST in multiple systemic systems and did not discuss the incidence of intracranial YST separately. To date, no more than 20 cases of posterior fossa YST have been reported in PubMed,[23,24] all of which were male and mostly in Asian races, mainly in Japan, China, and South Korea. In this study, tumors in 9 patients (9/25, 36%), all of whom were male, were located in the posterior cranial fossa. The high proportion of tumors occurring in the posterior cranial fossa may also be related to the

structures in the tumor. In this study, 21 cases of MR imaging and 6 cases of CT were significantly enhanced with uneven enhancement, in which there were many microcystic or cystic components and many large, twisted blood vessels in the solid enhancement components, suggesting that the tumor was rich in blood supply, which was consistent with the pathologic features reported in the literature.[16]

Four cases had uniform enhancement after CT enhancement, which may be because the soft-tissue resolution of CT is lower than that of MR imaging, and tiny cystic components in the tumor were not visible. Combined with the cases in this study and relevant literature,[28,31,32] we believe that cystic changes, especially multiple microvesicles and multiple thickening and twisting tumor vessels, are one of the imaging features of primary intracranial pure YST, corresponding to pathologic changes.

DWI shows the disorderly diffusion movement of free water by calculating the ADC value, which is manifest as a high signal on DWI and a low ADC value, reflecting the size of the extracellular space, number of cells, and the ratio of cytoplasm to extracellular space.[33] In most malignant tumors,[34-36] due to the dense distribution of tumor cells, large nuclei, small extracellular intervals, and limited diffusion of free water movement, DWI showed a high signal and a reduced ADC value, suggesting limited diffusion. Similar to previous reports,[28,32] 9 cases in this study had equal signals on DWI and equal or slightly higher signals on ADC, suggesting that diffusion was not limited. It is speculated that this finding may be related to the loose network structure of tumor tissue and the large extracellular space. Therefore, we believe that DWI can be used to differentiate most malignancies, such as lymphoma, medulloblastoma, and atypical teratoma/rhabdomyoid tumor.

YST in the pineal region is mainly differentiated from pineal tumors, germ cell tumors, and non-germ cell tumors. YST in the cerebellum is mainly differentiated from medulloblastoma, astrocytoma, and atypical teratoma/rhabdomyoid tumor. Combined with laboratory AFP levels are helpful in the diagnosis of YST. In addition, although AFP is a characteristic marker of YST, it is not specific and can also be expressed in other germ cell–derived tumors and many non-germ cell tumors. It is still difficult to distinguish intracranial YST from other mixed germ cell tumors with YST components on imaging.

The limitation of this study is its retrospective analysis. Some cases are from the literature, and the clinical and imaging data are limited, a feature that needs further improvement. In addition, we studied only cases of Chinese children, so there may be some biases for non-Chinese cases.

CONCLUSIONS

Primary intracranial pure YST is extremely rare and is mostly seen in boys. The imaging findings of this disease have certain characteristics, such as multiple microsacs in the tumor; significant enhancement, and multiple thick, serpiginous enhancement; equal signal on DWI; and equal or slightly higher signal on ADC combined with the serum AFP level, which is helpful for the diagnosis of this disease, but the diagnosis depends on pathologic and immunohistochemical examinations.

REFERENCES

1. Ueno T, Tanaka YO, Nagata M, et al. **Spectrum of germ cell tumors: from head to toe.** *Radiographics* 2004;24:387–404 CrossRef Medline
2. Shi Q, Wang FH, Gao Q, et al. **Clinicopathological analysis of yolk sac tumor in children and adolescents.** *Chinese Journal of Woman and Child Health Research* 2019;30(3):342–46
3. Nagasawa DT, Lagman C, Sun M, et al. **Pineal germ cell tumors: two cases with review of histopathologies and biomarkers.** *J Clin Neurosci* 2017;38:23–31 CrossRef Medline
4. Echevarría ME, Fangusaro J, Goldman S. **Pediatric central nervous system germ cell tumors: a review.** *Oncologist* 2008;13:690–99 CrossRef Medline
5. Kuang H, Zhang C, Gong H, et al. **Primary cerebellar endodermal sinus tumor: a case report.** *Oncol Lett* 2014;8:1713–16 CrossRef Medline
6. Wu N, Chen Q, Chen M, et al. **Primary yolk sac tumor in the cerebellar hemisphere: a case report and literature review of the rare tumor.** *Front Oncol* 2021;5:739733 CrossRef Medline
7. Tsugu H, Oshiro S, Ueno Y, et al. **Primary yolk sac tumor within the lateral ventricle.** *Neurol Med Chir (Tokyo)* 2009;49:528–31 CrossRef Medline
8. Du S, Guan JH, Li Y. **Yolk sac tumor in fourth ventricle (report of one case and review of literature).** *J Clin Neurosurg* 2020;17:339–42
9. Zhang L, Lei JQ. **Rare intracranial yolk sac tumor: report of one case.** *J Chin Clin Med Imaging* 2012;23:564
10. Liu YH, Zheng ZC, Zhang J. **One case of the primary endodermal sinus tumor under tentorium cerebelli.** *J Pract Radiol* 1998;14:761
11. Jiao Z, Jiang R, Li Z, et al. **Cerebellar endodermal sinus tumor in children: report of two cases.** *Clinical Rational Drug Use* 2012;5:160
12. Lan YX, Chen F, Shen XJ, et al. **Third ventricle yolk sac tumor: Case report.** *Chin J Med Imaging Technol* 2016;32:1632
13. Li XJ, Huang MH, Wang JH, et al. **Yolk sac tumor in brain: a case report.** *Journal of Naval General Hospital* 2009;22:190–91
14. Zhou W, Zhu YC, Wang JL, et al. **Intracranial yolk sac carcinoma in a child: a case report. University Medical Science Edition.** *Journal of Soochow* 2009;29:196
15. Guo YF, Chen JL, Zhang Y, et al. **Analysis to MRI features of intracranial yolk sac tumour.** *Journal of Clinical Radilolgy* 2019;38:37–39
16. Chen LW, Zhong Q. **MRI findings of yolk sac tumor of lateral ventricle: a case report.** *Chin J Radiol* 2017;51:464
17. Xu SM, Guan XL, Sun HM, et al. **Primary endodermal sinus tumor of cerebellum: a case report.** *Chin J Appl Clin* 2015;30:1678–79
18. Xie K, Zhang Y, Cheng JL, et al. **Primary yolk sac tumor of saddle area: report of one case.** *J Chin Med Imaging* 2017;28:377–78
19. Wang SX, Fang GG. **One case: imagine findings of cerbellar endodermal sinus tumor in child.** *J Pract Radiol* 2006;22:380–81
20. Chang XS, Zhen P, Zeng J. **Primary endodermal sinus tumor of cerebellar vermis: a case report.** *Chinese Journal of Coal Industry Medicine* 2005;8:919
21. Wang SH, Luo LS, Yan XC, et al. **One case of primary pineal yolk sac tumor.** *Journal of Gannan Medical University* 2001;04:368
22. Zhang XP, Zhang GJ, Ding XH, et al. **One case of intracranial endodermal sinus tumor.** *Chin J Neurosurg* 1994;10:243
23. Raynald Yang, H, Zhang X, et al. **Primary intracranial pure endodermal sinus tumor: a retrospective series of 6 cases in a single center and a systematic review of overall survival.** *Neurochirurgie* 2021;67:587–98 CrossRef Medline
24. Jung Koh E, Kim SK, Park SH, et al. **Two male infants each with a cerebellar mass.** *Brain Pathol* 2019;29:143–44 CrossRef Medline
25. Xu ZN, Yue XY, Cao XC, et al. **Multidisciplinary treatment of primary intracranial yolk sac tumor: a case report and literature review.** *Medicine (Baltimore)* 2021;100:e25778 CrossRef Medline

26. da Silva NS, Cappellano AM, Diez B, et al. **Primary chemotherapy for intracranial germ cell tumors: results of the third international CNS germ cell tumor study.** *Pediatr Blood Cancer* 2010;54:377–83 CrossRef Medline

27. Matsutani M, Sano K, Takakura K, et al. **Primary intracranial germ cell tumors: a clinical analysis of 153 histologically verified cases.** *J Neurosurg* 1997;86:446–55 CrossRef Medline

28. Ji Q, Ding C, Liu C, et al. **Yolk sac tumor of the fourth ventricle in a 3-year-old boy: imaging features.** *Childs Nerv Syst* 2020;36:3123–28 CrossRef Medline

29. Zhao S, Shao G, Guo W, et al. **Intracranial pure yolk sac tumor in the anterior third ventricle of an adult: a case report.** *Exp Ther Med* 2014;8:1471–72 CrossRef Medline

30. Macvanski M, Ristić-Balos D, Vasić B, et al. **Intracranial yolk sac tumor in an adult patient: MRI, diffusion-weighted imaging and 1H MR spectroscopy features.** *Vojnosanit Pregl* 2012;69:277–80 CrossRef Medline

31. Yamaoka T, Togashi K, Koyama T, et al. **Yolk sac tumor of the ovary: radiologic-pathologic correlation in four cases.** *J Comput Assist Tomogr* 2000;24:605–09 CrossRef Medline

32. Li Y, Zheng Y, Lin J, et al. **Radiological-pathological correlation of yolk sac tumor in 20 patients.** *Acta Radiol* 2016;57:98–106 CrossRef Medline

33. Koh DM, Collins DJ. **Diffusion-weighted MRI in the body: applications and challenges in oncology.** *AJR Am J Roentgenol* 2007;188:1622–35 CrossRef Medline

34. Dai WC, Liu HS, Chen XW, et al. **Imaging findings of atypical teratoid/rhabdoid tumor of central nervous system with clinical correlation.** *Chin J Radiol* 2017;51(8):612–15

35. Schneider JF, Confort-Gouny S, Viola A, et al. **Multiparametric differentiation of posterior fossa tumors in children using diffusion-weighted imaging and short echo-time 1H-MR spectroscopy.** *J Magn Reson Imaging* 2007;26:1390–98 CrossRef Medline

36. Kao HW, Chiang SW, Chung HW, et al. **Advanced MR imaging of gliomas: an update.** *Biomed Res Int* 2013;2013:970586 CrossRef Medline

Arterioectatic Spinal Angiopathy of Childhood: Clinical, Imaging, Laboratory, Histologic, and Genetic Description of a Novel CNS Vascular Pathology

T. Abruzzo, R. van den Berg, S. Vadivelu, S.W. Hetts, M. Dishop, P. Cornejo, V. Narayanan, K.E. Ramsey, C. Coopwood, E.G. Medici-van den Herik, S.D. Roosendaal, M. Lawton, and S. Bernes

ABSTRACT

SUMMARY: Pediatric patients with myelopathy expressing intradural spinal vascular ectasia without arteriovenous shunting were studied at four tertiary referral neuropediatric centers. Patients were identified by retrospective review of institutional records and excluded if spinal vascular pathology could be classified into a previously described category of spinal vascular malformation. Four patients meeting the study criteria were enrolled in the study. Clinical, magnetic resonance imaging, catheter-directed angiography, laboratory, histological and genetic data were analyzed to characterize the disease process and elucidate underlying pathomechanisms. Our study revealed a highly lethal, progressive multi-segmental myelopathy associated with a unique form of non-inflammatory spinal angiopathy featuring diffuse enlargement and tortuosity of spinal cord arteries, spinal cord hyperemia, and spinal cord edema (Arterioectatic Spinal Angiopathy of Childhood). The condition was shown to mimic venous congestive myelopathy associated with pediatric spinal cord arteriovenous shunts on MRI but to have distinct pathognomonic findings on catheter-directed angiography. Clinicopathological, genetic, and neuroimaging features, which are described in detail, closely overlap with those of mitochondrial disease.

ABBREVIATIONS: AESA = arterioectatic spinal angiopathy; AV = arteriovenous; CPA = cerebral proliferative angiopathy; RMA = radiculomedullary artery; WES = whole exome sequencing

Spinal cord arteriovenous (AV) shunts, including AV malformations (AVM) and AV fistulae (AVF) are a rare but treatable cause of myelopathy.[1-4] Marked ectasia of the spinal cord vasculature on MR imaging is traditionally considered pathognomonic. In children with spinal cord AV shunts, subarachnoid hemorrhage is the clinical presentation in two-thirds, while venous congestive myelopathy is the presentation in one-third.[1,2] Notably, venous congestive myelopathy due to a spinal cord AV shunt is more common in children younger than 2 years of age and features cord edema that spares the cord periphery.[3] A definitive diagnosis relies on demonstration of an AV shunt by catheter-directed DSA. Children with venous congestive myelopathy due to a spinal cord AV shunt most often present with progressive episodic neurologic decline, culminating in complete loss of spinal cord function within months to years.[1-4] If the diagnosis is established early, treatment of the underlying AV shunt by embolization or microsurgical ligation leads to neurologic stabilization with varying degrees of functional recovery.[1,5]

Recognized forms of spinal cord vascular malformations include AV shunt lesions and nonshunting lesions. While multiple classification systems have been proposed, none account for spinal cord vascular ectasia in the absence of an AV shunt.[6] The authors of this report have encountered pediatric patients with myelopathy presenting with striking enlargement of the spinal cord vasculature and vasogenic edema of the central spinal cord in the absence of AV shunting. In this report, we describe this previously uncharacterized spinal angiopathy and review the literature to identify cases that have phenotypic overlap. Experiences with different treatment strategies are presented, and alternate theories of pathogenesis are considered.

MATERIALS AND METHODS

This study received institutional review board (Cincinnati Children's Hospital Medical Center) approval for exempt research and a waiver of informed consent. Neuropediatric specialists at 4 tertiary referral

centers retrospectively reviewed their records to identify children with myelopathy who underwent catheter-directed DSA to evaluate abnormally enlarged spinal cord vessels found on MR imaging. Patients were excluded if DSA showed an AV shunt or vascular abnormality that could be classified into a known category of spinal vascular malformation. Clinical, laboratory, MR imaging, DSA, histopathologic, and genetic data were retrospectively analyzed at each study site. Descriptive analysis of anonymized data submitted by each site was performed.

Presenting clinical features, clinical course, and laboratory findings were assessed by electronic medical record review at the site where the patient's care was provided. Spinal MR imaging studies and catheter-directed spinal DSA studies of each patient were also reviewed by study investigators at the site where patient care was provided. When available, brain MR imaging, cerebral MR spectroscopy, and catheter-directed cerebral DSA studies were similarly reviewed.

Results of standardized genetic testing performed on blood samples were reviewed at the site where the corresponding patient's care was provided. In 1 case, whole exome sequencing (WES) and deletion analysis of nuclear and mitochondrial DNA from blood and nuclear DNA from radiculomedullary artery (RMA) tissue, performed at ×150 and ×159 resolution, respectively, were reviewed. In this case, targeted nuclear sequence analysis was also performed, covering multiple gene superfamilies (*RHO*, *RHEB*, and *RAS*) and individual genes implicated in the pathogenesis of AVMs (*MEK*, *PTEN*, *NOTCH1*, and so forth).[7] In another case, WES of nuclear DNA from blood was performed. Genetic panels for hereditary hemorrhagic telangioectasia and capillary malformation AVM syndrome were used to examine nuclear DNA from blood samples of 3 patients.

The authors performed a literature review to identify spinal vascular pathology that phenotypically overlaps with the angiopathy described in this report. We searched the PubMed database for English language reports published between January 1953 and January 2022 using the search terms "ectasia," "dolichoectasia," "arteriopathy," and "arteriovenous" crossed with the term "spinal."

RESULTS

Each of 4 participating sites identified 1 patient that met the study criteria, contributing a total of 4 patients (2 females) in a record review period that spanned 14–35 years; median, 18 (SD, 8) years. Every patient in this series presented before the advent of the Severe Acute Respiratory Syndrome coronavirus disease 2019 (SARS-CoV-2) pandemic. Presenting clinical features of each patient are detailed in the Online Supplemental Data. The first symptoms of myelopathy presented at a median age of 17.5 (SD, 8.5) months (range, 11–24 months). All patients initially presented with delayed onset or regression of ambulatory motor skills and hypotonia. Physical findings included cutaneous vascular birth marks in 2, eczema in 1, and bilateral cataracts in 1. Three of 3 patients with a perinatal history had complications including preeclampsia, prematurity, postmaturity, or breech presentation. One was noted to have a neonatal history of subdural hygromas. In 1 case, there was a maternal family history of recurrent spontaneous abortion.

Laboratory study results for each patient are detailed in the Online Supplemental Data. Two patients underwent electromyography and nerve-conduction studies, with normal results. CSF analysis showed normal protein and glucose levels and cell counts in all patients. CSF from 2 patients was submitted for comprehensive studies including lactate, amino acids, pyruvate, neurotransmitters, myelin basic protein, aquaporin 4, immunoglobulin G, oligoclonal bands, neopterin, and biopterin. CSF lactate was abnormally elevated in one, and CSF pyruvate was abnormally elevated in another. Hematology lab studies revealed microcytic anemia in 1 patient. Two had abnormally elevated serum transaminase levels late in their clinical course.

Spinal MR imaging results for each patient are detailed in the Online Supplement Data and are highlighted in Fig 1. On T2-weighted images, abnormally ectatic and tortuous pial blood vessels surrounded the spinal cord and conus medullaris. There was abnormal T2 signal hyperintensity in the central spinal cord (anterior > posterior) and cord tumefaction in all patients. T2 signal hyperintensity longitudinally involved the entire cord and extended into the ventral medulla. Variable cord parenchymal enhancement was present in 2 patients.

Brain MR imaging studies were performed in all patients. The results are detailed in the Online Supplemental Data and are highlighted in Fig 2. In 2 patients, there was mild diffuse encephalomalacia and ex vacuo enlargement of the cerebral ventricles and cortical sulci without signal abnormality. In another, there was signal abnormality in the anterior pons, pontine raphe, and middle cerebellar peduncles. Cerebral MR spectroscopy was performed in 3 patients. An abnormal lactate peak in the cerebral periventricular white matter was demonstrated in 1. Diffuse ectasia of the intracranial arteries shown on T2-weighted images of the brain was reported in 1 patient and unreported in 3 patients.

The results of catheter-directed spinal DSA are detailed in the Online Supplemental Data and highlighted in Fig 3. In all patients, catheter-directed DSA showed marked ectasia and tortuosity of the anterior spinal artery. In 3 of 4 patients, DSA of the dominant lower thoracic RMA showed the descending ramus of the anterior spinal artery to be much larger than the ascending ramus. Multiple RMAs were markedly ectatic in each patient, though the dominant lower thoracic RMA was most ectatic. In every patient, the central sulcal penetrators were markedly enlarged, producing a conspicuous pattern resembling the steps of a spiral staircase cycling between "on end" and "elongated" orientations in frontal-projection angiograms (Fig 3). By comparison, the posterolateral spinal arteries and radiculopial arteries were only modestly enlarged. Extrinsic spinal cord veins were modestly enlarged. Intrinsic spinal cord veins were not demonstrably enlarged. All patients demonstrated spinal cord hyperemia with brisk parenchymal venous drainage. In all patients, the prompt and diffuse angiographic appearance of the medullary and perimedullary veins followed the angiographic appearance of a hyperemic spinal cord parenchymal blush. There was no angiographic documentation of direct arterial-to-venous shunting (ie, AVF or AVM) in any patient.

Catheter-directed cerebral angiography was performed in 1 patient. Results detailed and shown in the Online Supplemental Data describe moderate diffuse intracranial arterial ectasia.
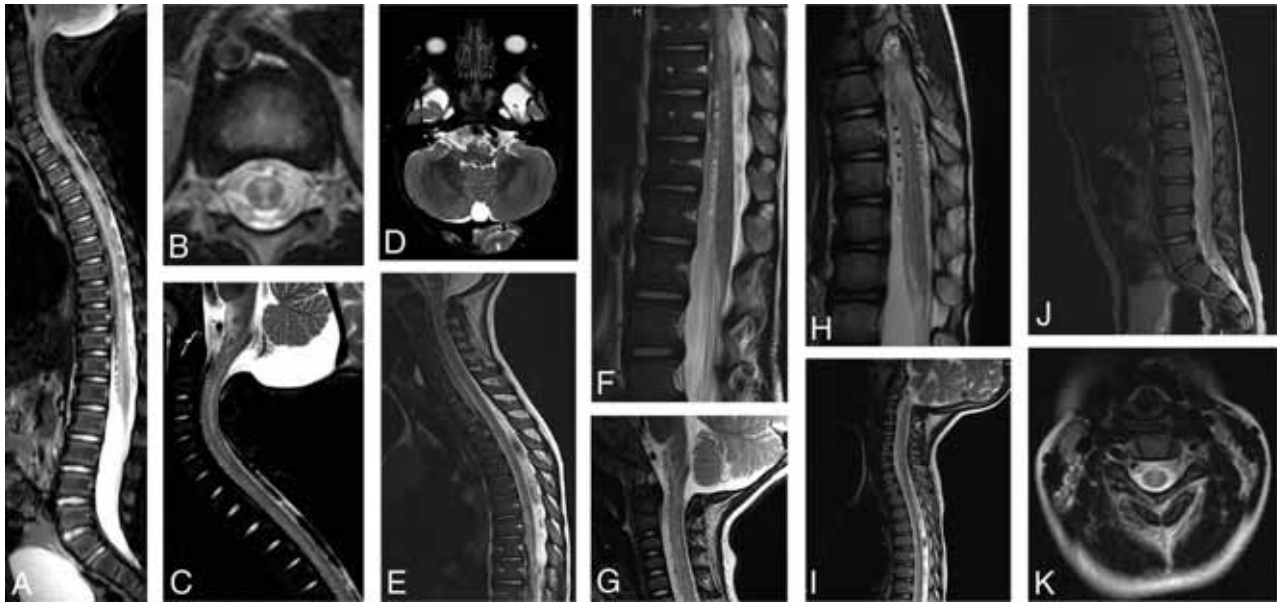
FIG 1. Spine MR imaging findings. *A*, Midline T2-weighted sagittal MR image of the spine in patient 1 shows abnormal T2-weighted hyperintense signal in the thoracic spinal cord and conus medullaris. Spinal cord volume expansion is also present. There is conspicuous abnormal perimedullary vascular ectasia anterior to the conus medullaris and thoracic spinal cord. *B*, Axial T2-weighted image of the midthoracic spine shows the distribution of abnormal T2-weighted signal hyperintensity within the central and anterior spinal cord. *C*, Midline T2-weighted sagittal MR image of the cervical spine reveals abnormal T2-weighted hyperintense signal in the central cervical spinal cord and ventral medulla. There is diffuse spinal cord swelling affecting the region of the cervical enlargement. *D*, Axial T2-weighted image of the brain at the level of the medulla shows T2-signal hyperintensity in the pyramids, more conspicuous on the left. *E*, Midline T2-weighted sagittal MR image of the cervical and thoracic spine in patient 4 shows abnormal T2-weighted hyperintense signal in the ventral cervical and thoracic spinal cord and medulla. There is spinal cord volume expansion, prominent in the region of the cervical enlargement, and abnormal perimedullary vascular ectasia anterior to the thoracic spinal cord. *F*, Midline T2-weighted sagittal MR image of the lower thoracic and lumbar spine reveals abnormal T2-weighted hyperintense signal in the anterior spinal cord. There is diffuse spinal cord swelling, severely affecting the region of the lumbar enlargement. Note marked ectasia of the perimedullary vessels anterior to the spinal cord. *G*, Midline T2-weighted sagittal MR image of the cervical spine in patient 3 shows abnormal T2-weighted hyperintense signal in the central and anterior cervical spinal cord as well as in the ventral medulla. Mild expansion of cervical spinal cord volume is also present. Conspicuous abnormal perimedullary vascular ectasia anterior to the cervical spinal cord is demonstrated. *H*, Midline T2-weighted sagittal MR image of the lower thoracic spine reveals abnormal T2-weighted hyperintense signal in the central and anterior thoracic spinal cord and conus medullaris, with mild associated volume expansion. Note marked perimedullary vascular ectasia surrounding the spinal cord. *I*, Midline T2-weighted sagittal MR image of the cervical and thoracic spine in patient 2 shows abnormal T2-weighted hyperintense signal in the cervical and thoracic spinal cord. The region of the cervical enlargement is severely affected and shows mild volume expansion. *J*, Midline T2-weighted sagittal image of the lower thoracic and lumbar spine shows abnormal T2-weighted signal hyperintensity within the anterior spinal cord. There is conspicuous perimedullary vascular ectasia anterior to the conus medullaris. *K*, Axial T2-weighted MR image of the cervical spine reveals abnormal T2-weighted hyperintense signal in the central cervical spinal cord.

The clinical course for each patient is detailed in the Online Supplemental Data. All patients developed a spastic gait disorder with bilateral lower-extremity paraparesis. Three of 4 progressed to quadriparesis within 7–34 months. One patient also had loss of head control and respiratory depression within 15 months. This patient died of aspiration pneumonia. Another died with lactic acidosis and progressive encephalopathy (Online Supplemental Data). Two patients remained ambulatory at last follow-up 1–4 years after onset. Two patients had marked transient exacerbations of neurologic deficits after febrile illness or general anesthesia. One patient was treated with vitamin E and carnitine to augment mitochondrial function but had no improvement. One patient treated with steroids failed to improve. This patient was also treated with microsurgical ligation of the dominant RMA in an attempt to reduce spinal cord hyperemia and edema. After a few days of neurologic worsening corresponding to the effects of anesthesia, the patient returned to neurologic baseline but died of complications from aspiration pneumonia 5 weeks later. Histopathologic

examination of the resected RMA showed normal vessel wall architecture without evidence of inflammation (Fig 4).

Testing with negative results for hereditary hemorrhagic telangioectasia (3-gene panel: endoglin, *SMAD4*, and activin receptor-like kinase) was performed on blood samples from 3 patients. Genetic testing for capillary malformation AVM syndrome (2-gene panel including ephrin B4 and *RASA1*) with negative results was performed on blood samples from 2 patients. WES of nuclear DNA from blood revealed a pathologic mutation in 1 allele of the *TFRC* gene in 1 patient. WES and targeted sequence analysis did not reveal confirmatory evidence of pathologic mutations in blood or RMA tissue in another patient. Mitochondrial DNA testing in the same patient did not reveal evidence of a pathologic mutation.

Our literature search yielded 1154 publications. Three reports warranted full-text review after abstract evaluation.[8-10] One report described a "spinal arterial malformation" without a venous component in a child with hereditary hemorrhagic telangioectasia based on findings at surgery.[8] Two additional references describing "spinal
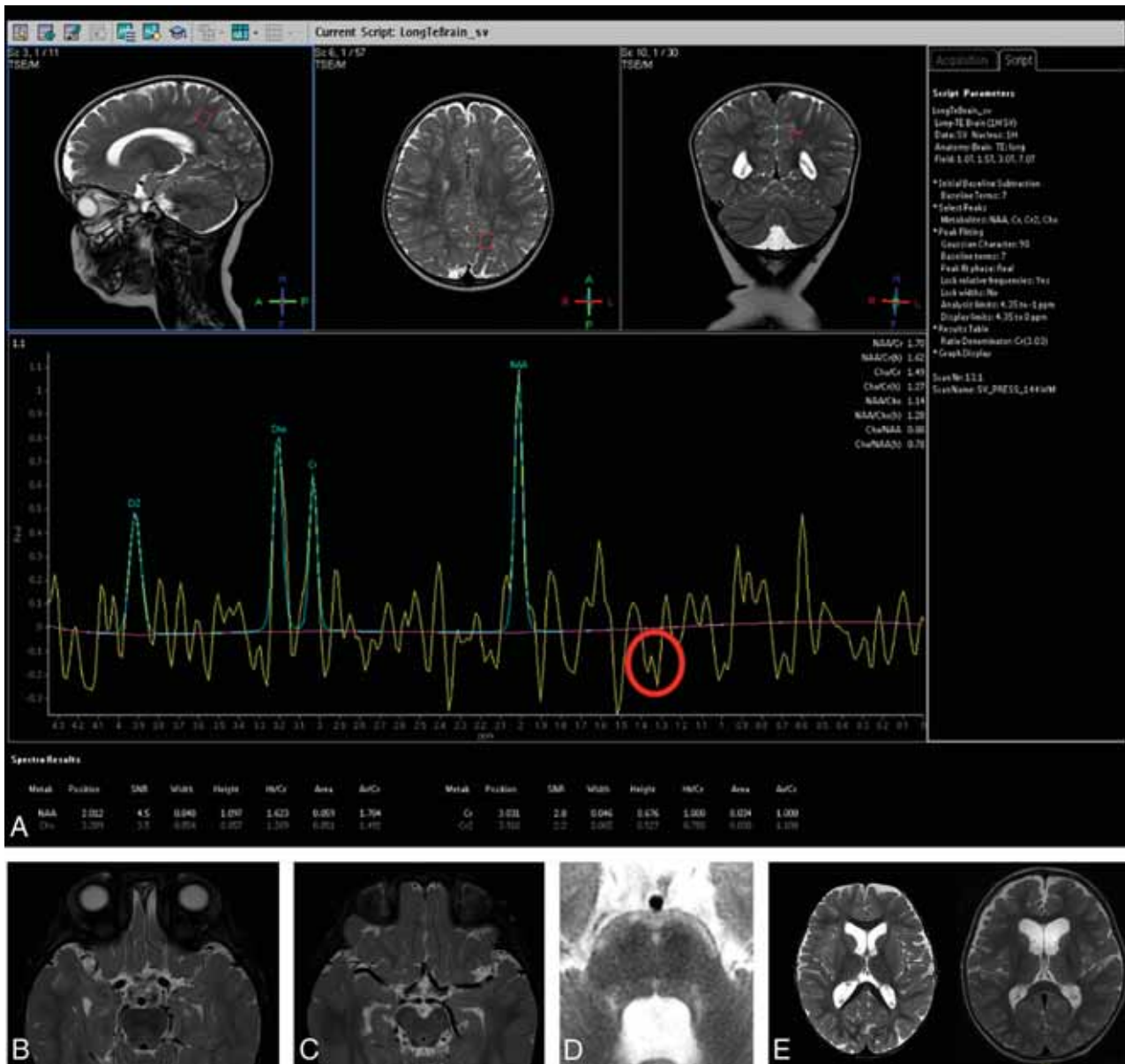
FIG 2. Brain imaging findings. *A*, Reference T2-weighted sagittal, axial, and coronal MR images of the brain from patient 1 and MR spectroscopy. There is mild diffuse cerebral parenchymal volume loss with commensurate ex vacuo ventriculomegaly. Note placement of a sampling voxel for MR spectroscopy in the subcortical white matter of the mesial left parietal lobe. MR spectroscopy shows an abnormal inverted doublet peak between 1.3 and 1.4 parts per million, corresponding to lactate (*red circle*). *B*, T2-weighted axial image of the brain shows ectasia of the basilar artery and bilateral intradural internal carotid arteries. *C*, T2-weighted axial image of the brain shows ectasia of the MCAs and posterior cerebral arteries bilaterally. *D*, Symmetric T2-weighted signal hyperintensity in patient 4 is demonstrated in the anterior edge of the pons, pontine raphe, and middle cerebellar peduncles. *E*, Axial T2-weighted images at level of foramen of Monro in patients 1 and 4 show mild cerebral parenchymal volume loss with ex vacuo dilation of the cerebral ventricles and cortical sulci.

arterial anomalies" were found in the bibliography of this report.[11,12] Neither MR imaging nor catheter-directed angiography was performed in any of the cases from these reports. Consequently, our literature review was unable to confirm any cases of nonshunting spinal cord arterial ectasia.

DISCUSSION

This report describes 4 cases of early-onset childhood myelopathy, each expressing a similar pattern of clinical and neuroimaging features and each associated with an unusual form of arterioectatic spinal angiopathy (AESA). All children initially presented with hypotonia and impaired ambulatory motor skills during the first 2 years of life. Most showed rapid progression to quadriparesis, and half died from disease-related complications within 6 years of onset. The clinical and neuroimaging features of AESA have striking overlap with those expressed in venous congestive myelopathy due to spinal cord AVM/AVF. Clinical recognition of the former and differentiation from the latter are critical to prevent misguided and potentially harmful vascular interventions. Our
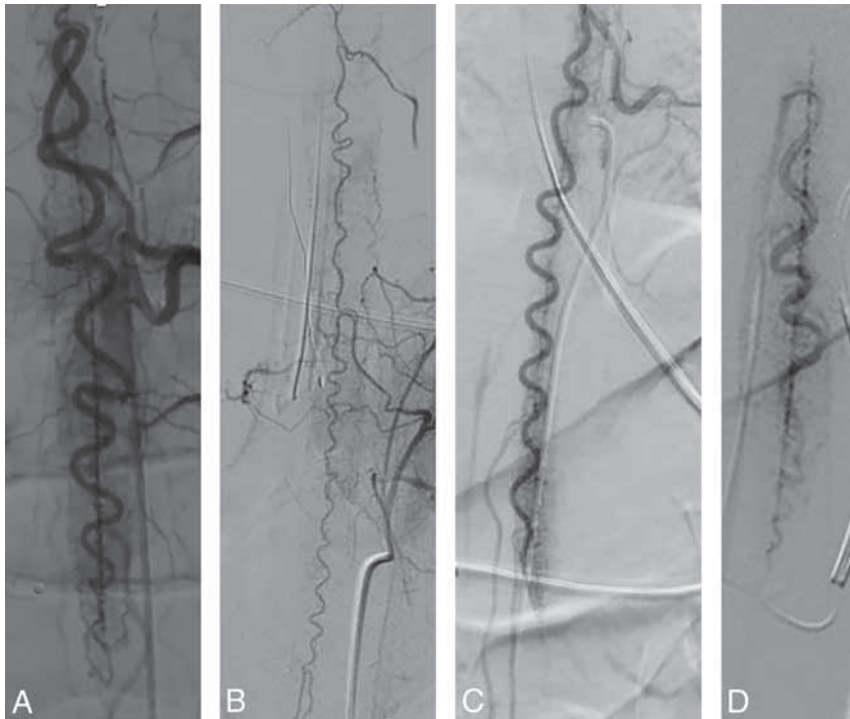
FIG 3. Catheter-directed angiography findings. *A,* Frontal projection of a left T11 posterior intercostal artery angiogram in the early arterial phase from patient 1 shows marked ectasia of the dominant lower thoracic RMA and descending ramus of the anterior spinal artery (ASA). The ascending ramus of the ASA is mildly enlarged. The left posterolateral spinal artery is mildly enlarged. There is a uniform, unusually intense parenchymal capillary blush and early appearance of parenchymal draining veins. Note striking ectasia of the central sulcal penetrators. *B,* Frontal projection of a left supreme intercostal artery angiogram in the early arterial phase from patient 4 shows moderate diffuse ectasia of the ASA and central sulcal penetrators. Two RMAs are shown to be moderately ectatic. Note patchy intensification of the parenchymal capillary blush. *C,* Frontal projection of left posterior intercostal artery angiogram in the early arterial phase from patient 3 shows marked ectasia of the dominant lower thoracic RMA and descending ramus of the ASA. There is striking ectasia of the central sulcal penetrators. There is a uniform, unusually intense parenchymal capillary blush most prominent in the region of the conus medullaris and early appearance of parenchymal draining veins. *D,* Frontal projection of the right posterior intercostal artery angiogram in the early arterial phase from patient 2 shows ectasia of the dominant lower thoracic RMA and descending ramus of the ASA. Note striking ectasia of central sulcal penetrators.
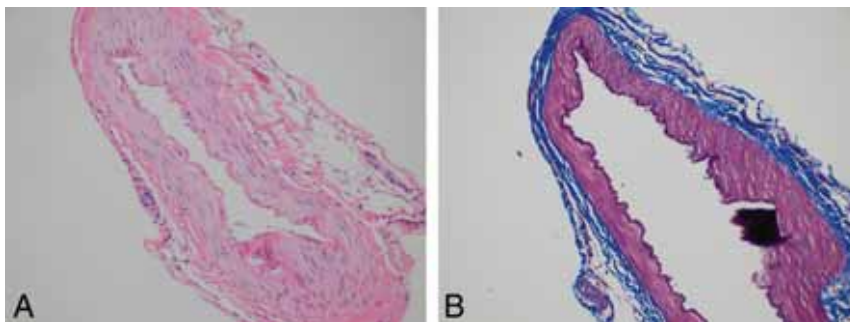
FIG 4. RMA histopathology. Patient 1. *A,* Hematoxylin and eosin–stained axial cross-section perpendicular to the long axis of the vessel at medium power (original magnification ×50) shows a normal trilaminar arterial wall architecture with no evidence of inflammation. *B,* Trichrome-stained axial cross-section perpendicular to long axis of the vessel at medium power (original magnification ×50) delineates normal elastic tissue architecture and integrity of the artery.

literature review confirms that AESA is a currently unrecognized form of spinal cord vascular pathology. Perhaps the most important factor contributing to the lack of prior recognition is the similarity that AESA bears to childhood spinal cord AVM/AVF. All of the cases presented in this series were initially misdiagnosed as AVM/AVF. It is likely that other cases were also misdiagnosed and perhaps even treated as AVM/AVF.

Every child in the current series showed ectasia and tortuosity of the spinal cord vasculature on MR imaging. Each case also demonstrated T2 signal hyperintensity in the central and anterior spinal cord, as well as cord tumefaction. This combination of MR imaging findings is common in children with intradural spinal AVF and adults with spinal dural AVF, though spinal dural AVF has not been convincingly reported in children.[13] Notably, gold standard catheter-directed DSA excluded AVF in all our patients. The overlapping neuroimaging features of AESA and spinal cord AVF of childhood may indicate that some aspects of pathogenesis are shared. The pattern of spinal cord signal abnormality and tumefaction demonstrated in our patients suggests vasogenic edema and cord swelling, as seen in children with an intradural spinal AVF. In both conditions, the spinal cord experiences an imbalance between arterial inflow and venous outflow, resulting in vascular congestion. In the former, spinal cord arterial inflow is augmented, and in the latter, spinal cord venous drainage is diminished. The entire spinal cord and ventral medulla are shown to be affected in our patients. Clinically severe (lethal) cases also showed variable cord enhancement, indicating cord–blood barrier disruption.

In contrast to children with intradural spinal AVF, patients with AESA demonstrate cord hyperemia causing early, dense parenchymal staining on DSA. AESA is further characterized by brisk, diffuse angiographic filling of spinal cord veins draining hyperemic spinal cord capillary beds. This pattern of circulation is a characteristic finding on which the diagnosis of AESA may be based. The angiographic features of spinal cord parenchymal venous drainage

in AESA contrasts with those seen in cases of an AV shunt with medullary venous hypertension (ie, spinal dural AVF) in which there is an absent or delayed angiographic appearance of the veins serving the affected spinal cord segments.[14] Marked arterial ectasia, out of proportion to venous ectasia, is another diagnostic hallmark of AESA. In our series, catheter-directed DSA shows ectasia and tortuosity of the anterior spinal artery and corresponding central sulcus perforators. Most cases show relatively mild enlargement of posterolateral spinal arteries, suggesting that ectasia is proportional to the size of the vascular territory within the cord. This finding loosely correlates the magnitude of angiopathic changes with blood-flow demand.

AESA as defined by the clinical and neuroimaging features reported here has not been previously described in the peer-reviewed, indexed medical literature. Two cases satisfying the diagnostic criteria for AESA set forth here were described in a book chapter on spinal cord AVM.[15] These patients underwent catheter-directed DSA for further evaluation of myelopathy, one at 2 years of age and the other at 5 years of age. In both cases, spinal DSA revealed ectasia of the anterior spinal artery and central sulcus perforators with corresponding cord hyperemia.

The etiology of AESA and its precise relationship to myelopathy are presently unknown. Analysis of blood, CSF, and RMA tissue from our patients showed no evidence of inflammation. Furthermore, glucocorticoid steroid therapy showed no beneficial effect in 1 patient. Early in our experience, the observation of spinal cord hyperemia and edema led us to hypothesize that neurologic impairment might be the consequence of abnormally increased arterial perfusion of the spinal cord, unbalanced by venous drainage. We thus speculated that controlled reduction of spinal cord hyperemia by surgical ligation of the dominant RMA might reduce cord edema and improve neurologic function. Unfortunately, this intervention was not beneficial, suggesting that cord hyperperfusion is not a primary driver of myelopathy.

Multiple findings suggest that AESA is a manifestation of metabolic myelopathy due to mitochondrial disease. Among these findings are elevated CSF lactate and a cerebral MR spectroscopy lactate peak in 1 case, systemic lactic acidosis and encephalopathy in a second case, and elevated CSF pyruvate in a third. Transaminasemia, premature cataracts, and microcytic anemia in our cohort further support a mitochondrial disease origin.[16,17] Notably, none of our patients demonstrated evidence of myopathy (cardiac or skeletal muscle). Numerous metabolic disorders including mitochondrial diseases presenting with myelopathy in early childhood manifest MR imaging features that resemble those reported here.[18,19] In our cohort, longitudinally extensive spinal cord lesions spanning >3 vertebral bodies were observed. This feature is characteristic of myelopathy in children with primary mitochondrial disease.[19] Moreover, in our series, MR imaging revealed T2 signal hyperintensity and tumefaction involving the central and anterior cord. This MR imaging pattern of myelopathy has also been reported in a subset of children with primary mitochondrial disease.[19] Additionally, cervical cord involvement with extension into the medulla is a common feature of childhood mitochondrial myelopathy seen in our cases.[19]

Pathogenic mutations that cause mitochondrial disease can occur in the nuclear genome or the mitochondrial genome.[20] Notably, 1 patient in this series was heterozygous for a dominant pathologic mutation of a transferrin receptor gene (TFRC). Transferrin receptors are believed to play a vital role in the regulation of normal mitochondrial function and fragmentation.[21] Additionally, mouse models show mitochondrial dysfunction in heterozygous transferrin receptor mutants.[22] Incidentally, abnormalities of transferrin receptor function may also explain associated anemia and childhood-onset cataracts.[23-26] Although 1 other patient in this series underwent extensive testing of nuclear and mitochondrial DNA without identification of a pathologic mutation, previous studies have shown that such testing yields a positive result in only 10%–20% of children with clinical mitochondrial disease.[27-29]

Arteriopathy as a primary or secondary manifestation of mitochondrial disease is now widely recognized.[30] Microvascular and macrovascular forms are well-described.[30] In patients with mitochondrial disorders, secondary arteriopathies are manifestations of the vascular effects of metabolic dysfunction in distinct organ systems such as the liver or pancreas. One model of secondary arteriopathy in AESA could be based on an abnormally increased metabolic demand in the diseased spinal cord imposing an increased blood-flow requirement that promotes adaptive or maladaptive expansive remodeling of spinal cord arteries. If the AESA phenotype requires the combined effects of 2 mutations, one controlling mitochondrial function and the other controlling arterial adaptation to blood flow demand, it would account for the extreme rarity of AESA. Notably, primary mitochondrial arteriopathy is often characterized by arterial ectasia and aneurysm formation.[30] Diagnostic markers of primary mitochondrial arteriopathy include abnormal expression of succinate-dehydrogenase or cyclooxygenase in vascular tissue or abnormal cristae formation in mitochondria from vascular smooth-muscle cells and pericytes.[30] The former relies on immunohistochemical staining of fresh-frozen tissue, and the latter relies on electron microscopy of glutaraldehyde-fixed tissue.

Immunohistochemical and electron microscopy studies of affected vascular tissue may improve our understanding of AESA pathogenesis in the future. Abnormal ectasia of the aorta and cerebral arteries has been reported as a primary feature of clinical mitochondrial disorders.[30] Mitochondrial arteriopathies involving retinal vessels, cochlear vessels, cervicocerebral vessels, brachial vessels, iliac vessels, skeletal muscle vessels, and cutaneous vessels have been reported.[31] Asymptomatic generalized cerebral arterial ectasia was present in 1 patient from the current series, suggesting that AESA may be part of an angiopathy spectrum that variably affects the entire CNS. Notably, 2 of our patients showed cerebral parenchymal volume loss, and a third experienced progressive encephalopathy, suggesting a diffuse CNS process.

Our review of the literature has not revealed prior cases of mitochondrial disease expressing AESA as a trait.[30-35] It is possible that the cases described in this report represent the extreme end of a spectrum in which milder forms are more prevalent but difficult to detect. Mild forms of AESA may not be detected on MR imaging, just as perimedullary vascular flow voids may be inapparent in patients with spinal dural AVFs.[36,37] CNS mitochondrial disorders are known to express a wide range of phenotypic heterogeneity.[38] Subclinical mitochondrial vasculopathies revealed by specialized,

nonclinical tests have been found in numerous studies.[24] It is also possible that mild forms of AESA are overshadowed or preempted by other complications of mitochondrial disease such as heart failure, respiratory failure, and encephalopathy.[39] Aortic root ectasia manifest on echocardiography was only recently recognized in children with mitochondrial cardiomyopathy, even though echocardiography was performed in this population for decades prior.[40] Patients with severe forms of AESA likely succumb to complications of AESA before other features of mitochondrial disease manifest. Recognition of AESA as a feature of mitochondrial disease would thus be prevented. Because severe forms of AESA bear a striking similarity to spinal cord AVM/AVF, it is likely that most cases are misdiagnosed because many centers lack the expertise needed to differentiate AESA from AVM/AVF. Moreover, absence of a pre-existing diagnostic framework that accommodates AESA thwarts recognition.

Endothelial dysfunction is believed to be an important feature of mitochondrial arteriopathies, and observational data suggest that intravenous L-arginine infusion may have therapeutic benefits, particularly in patients with mitochondrial encephalopathy experiencing strokelike episodes.[41,42] It is possible that L-arginine therapy may be helpful in children with AESA. One patient in this series failed to respond to carnitine supplementation. While carnitine supplementation is commonly administered to patients with mitochondrial disorders because of theoretic biochemical effects, therapeutic efficacy has not been shown outside a subset of patients with mitochondrial myopathy.[5,43] Mitochondrial augmentation and transplantation strategies are currently being investigated as a therapeutic approach to mitochondrial diseases.[20]

An alternative, though a less likely possibility, is that AESA is a transitional form of spinal cord vascular malformation whose developmental progression toward the AVM phenotype has been at least temporarily arrested at an early stage. In animal models, initiation of the brain AVM phenotype begins with angioectasia in precapillary and capillary regions of the developing cerebral circulation, exposing the cerebral microcirculation to an atypical arterial pattern of flow.[44] Transition to the brain AVM phenotype occurs when exposure to this anomalous flow signal triggers aberrant developmental programing. It is possible that AESA fails to progress toward the AVM phenotype because precapillary angioectasia is unaccompanied by the aberrant genetic programming needed for the transition. While clinical experience and animal models suggest that the window of developmental vulnerability for the phenotypic transition to AVM is limited to early childhood, longer-term follow-up is needed to determine whether AESA can transform to AVM, given the young age of patients in known cases.[44] Although we did not identify genetic markers of dysfunctional vascular biology in our AESA cohort, novel pathogenic mutations in regulatory regions of DNA or copy number mutations cannot be excluded.

Cerebral proliferative angiopathy (CPA), which has been reported as an atypical cerebral AVM phenotype, has some features that overlap with those of AESA.[45] The original description of CPA emphasized the presence of "capillary angioectasia" on catheter-directed DSA. The term denotes abnormal enlargement of capillaries. In the setting of catheter-directed DSA, capillary angioectasia is indirectly inferred by the presence of an unusually dense parenchymal capillary blush, accompanied by the brisk appearance of parenchymal draining veins. Thus, capillary angioectasia may be regarded as a feature of AESA. While direct evidence of vascular proliferation with cell-labeling methods was not shown in the original CPA case series, "angioproliferation" was presumed on the basis of transdural vascularization of AVMs and perinidal brain parenchyma. Lasjaunias et al[45] suggested that angioproliferative vascular changes in CPA were induced by cerebral ischemia engendered by AVM blood-flow steal. Similarly, in AESA, it is possible that angiopathy is the result of altered blood-flow demand attributable to metabolic derangement within the CNS parenchyma.

In contrast to CPA however, AESA is not associated with transdural vascularization or angioproliferative changes by extension. Moreover, published examples[45] of CPA feature a discrete focal intraparenchymal nidal type AV shunt zone demonstrable on MR imaging and catheter-directed DSA. This aspect of CPA sharply differentiates it from AESA, which conspicuously lacks a focal intraparenchymal nidal AV shunt zone where blood circulates directly from arteries to veins without passing through parenchymal capillaries. Moreover, in CPA, catheter-directed angiography shows the vasculature within the intraparenchymal nidal AV shunt zone to be disproportionately ectatic relative to the extraparenchymal feeding arteries, which are frequently small and stenotic. In contrast, diffuse arterioectasia[45] involving the extraparenchymal vasculature is the most striking feature associated with AESA.

CONCLUSIONS

AESA is a noninflammatory pathologic vascular manifestation of preschool children characterized by diffuse enlargement and tortuosity of spinal cord arteries, spinal cord hyperemia, and cord edema in the absence of AV shunting. AESA is associated with a highly lethal multisegmental myelopathy that mimics venous congestive myelopathy on MR imaging but which shows distinct pathognomonic findings on catheter-directed spinal DSA. While the clinicopathologic, genetic, and neuroimaging features of AESA overlap with those of mitochondrial disease, the pathogenesis remains uncertain.

Disclosure forms provided by the authors are available with the full text and PDF of this article at www.ajnr.org.

REFERENCES

1. Rodesch G, Hurth M, Alvarez H, et al. **Classification of spinal cord arteriovenous shunts: proposal for a reappraisal–the Bicêtre experience with 155 consecutive patients treated between 1981 and 1999.** *Neurosurgery* 2002;51:374–79; discussion 79–80 CrossRef Medline
2. Consoli A, Smajda S, Trenkler J, et al. **Intradural spinal cord arteriovenous shunts in the pediatric population: natural history, endovascular management, and follow-up.** *Childs Nerv Syst* 2019;35:945–55 CrossRef Medline
3. Cullen S, Alvarez H, Rodesch G, et al. **Spinal arteriovenous shunts presenting before 2 years of age: analysis of 13 cases.** *Childs Nerv Syst* 2006;22:1103–10 CrossRef Medline
4. Rodesch G, Hurth M, Alvarez H, et al. **Spinal cord intradural arteriovenous fistulae: anatomic, clinical, and therapeutic considerations in a series of 32 consecutive patients seen between 1981 and 2000 with emphasis on endovascular therapy.** *Neurosurgery* 2005;57:973–83; discussion 73–83 CrossRef Medline

5. Parikh S, Saneto R, Falk MJ, et al. **A modern approach to the treatment of mitochondrial disease.** *Curr Treat Options Neurol* 2009;11:414–30 CrossRef Medline

6. Spetzler RF, Detwiler PW, Riina HA, et al. **Modified classification of spinal cord vascular lesions.** *J Neurosurg* 2002;96:145–56 CrossRef Medline

7. Abruzzo TA, Kurosawa Y, Choutka O, et al. **Genetic determinants of cerebral arterial adaptation to flow-loading.** *Curr Neurovasc Res* 2018;15:175–85 CrossRef Medline

8. Merry GS, Appleton DB. **Spinal arterial malformation in a child with hereditary hemorrhagic telangiectasia: case report.** *J Neurosurg* 1976;44:613–16 CrossRef Medline

9. Niino M, Isu T, Tashiro K. **Nonhemorrhagic venous infarction of the spinal cord without spinal vascular malformation.** *J Neurol* 1999;246:852–54 CrossRef Medline

10. Viamonte M, Tuna I, Rees J. **Dilated cerebral arteriopathy in classical Pompe disease: a novel finding.** *Pediatr Neurol* 2020;108:117–20 CrossRef Medline

11. Brion S, Netsky MG, Zimmerman HM. **Vascular malformations of the spinal cord.** *AMA Arch Neurol Psychiatry* 1952;68:339–61 CrossRef Medline

12. Wyburn-Mason R. *The Vascular Abnormalities and Tumors of the Spinal Cord and Its Membranes.* Henry Kimpton; 1943

13. Pearl M, Gailloud P. **Spinal vascular malformations in children.** *J Stroke Cerebrovasc Dis* 2017;26:915 CrossRef Medline

14. Eckart Sorte D, Obrzut M, Wyse E, et al. **Normal venous phase documented during angiography in patients with spinal vascular malformations: incidence and clinical implications.** *AJNR Am J Neuroradiol* 2016;37:565–71 CrossRef Medline

15. Lasjaunias P, TerBrugge KG, Berenstein A. **Spinal cord arteriovenous malformations.** In: Lasjaunias P, TerBrugge KG, Berenstein A. *Surgical Neuroangiography.* 2nd ed. Springer Berlin; 1987:721–66

16. Rahman S. **Mitochondrial disease in children.** *J Intern Med* 2020;287:609–33 CrossRef Medline

17. Finsterer J, Zarrouk-Mahjoub S, Daruich A. **The eye on mitochondrial disorders.** *J Child Neurol* 2016;31:652–62 CrossRef Medline

18. Tabarki B, Hakami W, Alkhuraish N, et al. **Spinal cord involvement in pediatric-onset metabolic disorders with mendelian and mitochondrial inheritance.** *Front Pediatr* 2020;8:599861 CrossRef Medline

19. Alves CA, Goldstein A, Teixeira SR, et al. **Involvement of the spinal cord in primary mitochondrial disorders: a neuroimaging mimicker of inflammation and ischemia in children.** *AJNR Am J Neuroradiol Neuroradiol* 2021;42:389–96 CrossRef Medline

20. Lightowlers RN, Chrzanowska-Lightowlers ZM, Russell OM. **Mitochondrial transplantation-a possible therapeutic for mitochondrial dysfunction? Mitochondrial transfer is a potential cure for many diseases but proof of efficacy and safety is still lacking.** *EMBO Rep* 2020;21:e50964 CrossRef Medline

21. Senyilmaz D, Virtue S, Xu X, et al. **Regulation of mitochondrial morphology and function by stearoylation of TFR1.** *Nature* 2015;525:124–28 CrossRef Medline

22. Okuno K, Naito Y, Yasumura S, et al. **Haploinsufficiency of transferrin receptor 1 impairs angiogenesis with reduced mitochondrial complex I in mice with limb ischemia.** *Sci Rep* 2019;9:13658 CrossRef Medline

23. Conway AJ, Brown FC, Rank G, et al. **Characterization of Tfrc-mutant mice with microcytic phenotypes.** *Blood Adv* 2018;2:1914–22 CrossRef Medline

24. Wussuki-Lior O, Abu-Horowitz A, Netzer I, et al. **Hematologic biomarkers in childhood cataracts.** *Mol Vis* 2011 17:1011–15 Medline

25. Aljohani AH, Al-Mousa H, Arnaout R, et al. **Clinical and immunological characterization of combined immunodeficiency due to TFRC mutation in eight patients.** *J Clin Immunol* 2020;40:1103–10 CrossRef Medline

26. Jabara HH, Boyden SE, Chou J, et al. **A missense mutation in TFRC, encoding transferrin receptor 1, causes combined immunodeficiency.** *Nat Genet* 2016;48:74–78 CrossRef Medline

27. Chinnery PF. Primary mitochondrial disorders overview. In: Adam MP, Mirzaa GM, Pagon R eds. *GeneReviews* June 8, 2000

28. Koenig MK. **Presentation and diagnosis of mitochondrial disorders in children.** *Pediatr Neurol* 2008;38:305–13 CrossRef Medline

29. Zeviani M, Di Donato S. **Mitochondrial disorders.** *Brain* 2004;127:2153–72 Medline

30. Finsterer J, Zarrouk-Mahjoub S. **Mitochondrial vasculopathy.** *World J Cardiol* 2016;8:333–39 CrossRef Medline

31. Finsterer J, Mahjoub SZ. **Primary mitochondrial arteriopathy.** *Nutr Metab Cardiovasc Dis* 2012;22:393–99 CrossRef Medline

32. Finsterer J. **Dilative arteriopathy in metabolic myopathies, particularly Pompe's disease.** *Acta Neurol Belg* 2012;112:15–18 CrossRef Medline

33. Finsterer J, Bastovansky A. **Dilative arteriopathy and leucencephalopathy as manifestations of a neurometabolic disease.** *Open Neurol J* 2015;9:28–31 CrossRef Medline

34. Naidu S, Bibat G, Lin D, et al. **Progressive cavitating leukoencephalopathy: a novel childhood disease.** *Ann Neurol* 2005;58:929–38 CrossRef Medline

35. Thajeb P, Dai D, Chiang MF, et al. **Genotype-phenotype correlation of maternally inherited disorders due to mutations in mitochondrial DNA.** *Taiwan J Obstet Gynecol* 2006;45:201–07 CrossRef Medline

36. Barreras P, Heck D, Greenberg B, et al. **Analysis of 30 spinal angiograms falsely reported as normal in 18 patients with subsequently documented spinal vascular malformations.** *AJNR Am J Neuroradiol* 2017;38:1814–19 CrossRef Medline

37. Gilbertson JR, Miller GM, Goldman MS, et al. **Spinal dural arteriovenous fistulas: MR and myelographic findings.** *AJNR Am J Neuroradiol* 1995;16:2049–57 Medline

38. Stellingwerff MD, Figuccia S, Bellacchio E, et al. **LBSL: case series and DARS2 variant analysis in early severe forms with unexpected presentations.** *Neurol Genet* 2021;7:e559 CrossRef Medline

39. Eom S, Lee HN, Lee S, et al. **Cause of death in children with mitochondrial diseases.** *Pediatr Neurol* 2017;66:82–88 CrossRef Medline

40. Brunetti-Pierri N, Pignatelli R, Fouladi N, et al. **Dilation of the aortic root in mitochondrial disease patients.** *Mol Genet Metab* 2011;103:167–70 CrossRef Medline

41. Ganetzky RD, Falk MJ. **8-year retrospective analysis of intravenous arginine therapy for acute metabolic strokes in pediatric mitochondrial disease.** *Mol Genet Metab* 2018;123:301–08 CrossRef Medline

42. Koenig MK, Emrick L, Karaa A, et al. **Recommendations for the management of strokelike episodes in patients with mitochondrial encephalomyopathy, lactic acidosis, and strokelike episodes.** *JAMA Neurol* 2016;73:591–94 CrossRef Medline

43. Gimenes AC, Bravo DM, Napolis LM, et al. **Effect of L-carnitine on exercise performance in patients with mitochondrial myopathy.** *Braz J Med Biol Res* 2015;48:354–62 CrossRef Medline

44. Murphy PA, Kim TN, Huang L, et al. **Constitutively active Notch4 receptor elicits brain arteriovenous malformations through enlargement of capillary-like vessels.** *Proc Natl Acad Sci U S A* 2014;111:18007–12 CrossRef Medline

45. Lasjaunias PL, Landrieu P, Rodesch G, et al. **Cerebral proliferative angiopathy: clinical and angiographic description of an entity different from cerebral AVMs.** *Stroke* 2008;39:878–85 CrossRef Medline

Spontaneous Spinal CSF Leaks Stratified by Age, Body Mass Index, and Spinal Level

M.D. Mamlouk, P.Y. Shen, P. Jun, and M.F. Sedrak

ABSTRACT

BACKGROUND AND PURPOSE: There are 3 main types of spinal CSF leaks, and the imaging appearances are well-reported. Specific patient demographics and spinal locations of the various types of spinal leaks are less frequently described. The purpose of this article was to stratify the various types of spontaneous CSF leaks on the basis of age, body mass index, and spinal level.

MATERIALS AND METHODS: Retrospective review was performed for all patients with spontaneous spinal CSF leaks identified on CT myelography. Age, body mass index, and spinal CSF leak type and level were recorded.

RESULTS: Sixty-five patients (37 women and 28 men) had spinal CSF leaks. Type 1 CSF leaks (dural tears) were observed in 25 patients (mean age, 44.5 years; mean body mass index, 24.3) and were most common in the upper thoracic spine (72%), particularly at the T1–T2 level (36%). Type 2 CSF leaks (ruptured meningeal diverticula) were observed in 4 patients (mean age, 45.5 years; mean body mass index, 27.5) and were all seen in the lower thoracic spine. Type 3 CSF leaks (CSF-venous fistulas) were observed in 36 patients (mean age, 58.8 years; mean body mass index, 27.0) and were most common on the right side (72%) and in the lower thoracic spine (56%).

CONCLUSIONS: Type 1 CSF leaks occurred in younger patients with a normal body mass index, while patients with type 3 CSF leaks were relatively older and had an elevated body mass index. Type 1 leaks mostly occurred in the upper thoracic spine, and types 2 and 3 leaks mostly occurred in the lower thoracic spine.

ABBREVIATIONS: BMI = body mass index; CTM = CT myelography; CVF = CSF-venous fistula; SIH = spontaneous intracranial hypotension; W = Shapiro-Wilk test statistic

S pontaneous intracranial hypotension (SIH) is typically secondary to a spinal CSF leak, and there are 3 main types: dural tears (type 1), ruptured meningeal diverticula (type 2), and CSF-venous fistulas (type 3).[1] In the past several years, our awareness and detection of these spinal CSF leaks have increased secondary to novel techniques such as dynamic prone myelography for dural tears and decubitus myelography for ruptured meningeal diverticula and CSF-venous fistulas (CVFs).[2-4]

Despite these advancements, there are many unanswered questions, including why spontaneous CSF leaks occur and in

what demographics. It is known that spinal CSF leaks are more common in adults than in children and in females versus males.[5,6] In 2016, Schievink et al[1] reported the average patient age at presentation for the various types of CSF leaks; however, our detection of CVFs has grown exponentially since that date. Body mass index (BMI) is another feature that has not been well-described in patients with spontaneous CSF leaks. It has been established that obesity is a risk factor for cranial CSF leaks;[7] however, there is minimal discussion about how BMI relates to spinal CSF leaks. To our knowledge, only 2 prior reports exist in a small number of patients, including a publication by Rosebrock et al,[8] which reported ventral dural CSF leaks in patients with low BMI values, while Schievink et al[9] reported BMI as it relates to CVF in the setting of morbid and super obesity. Last, a holistic evaluation of the spinal leak location of the various types of spinal leaks has been described in only small series.[10] The purpose of this article was to stratify the various types of spontaneous CSF leaks on the basis of age, BMI, and spinal leak level and to determine if there are key differences in these characteristics; this knowledge can help guide physicians in determining which type of CSF leak and location is most likely to aid in the diagnostic work-up.

Patient demographics of spinal CSF leaks

Demographics	All Patients	Type 1	Type 2	Type 3	P Value[a]
No. of leaks	65	25 (39%)	4 (6%)	36 (55%)	
Age at symptoms onset (yr)					<.00001
Mean (SD)	52.4 (13.1)	44.5 (10.3)	45.5 (8.1)	58.8 (11.9)	
95% CI	49.3–55.6	40.4–48.5	37.6–53.4	54.9–62.6	
Range	28–91	28–68	34–53	39–91	
Sex (No.)					.81
Female	37	14	4	19	
Male	28	11	0	17	
BMI					.015
Mean (SD)	26.0 (4.5)	24.3 (3.1)	27.5 (7.9)	27.0 (4.7)	
95% CI	24.9–27.1	23.1–25.5	19.7–35.3	25.4–28.5	
Range	16–39	18–31	21–39	16–39	
Leak location (No.)					<.0002
Cervical	2	2	0	0	
Upper thoracic (T1–T6)	31	18	0	13	
Lower thoracic (T7–T12)	29	5	4	20	
Lumbar	3	0	0	3	
Bern SIH score					.44
Mean (SD)	5.7 (2.4)	5.4 (2.0)	5.8 (3.3)	5.9 (2.6)	
Range	0–9	0–8	1–8	0–9	

[a] P values were compared between type 1 and 3 groups.

MATERIALS AND METHODS

Institutional review board (Kaiser Permanente Medical Center) approval was obtained, which waived the requirement for informed consent. The study population consisted of all patients with spontaneous spinal CSF leaks from August 2018 to March 2022 from a single institution. Inclusion criteria consisted of the following: 1) SIH diagnosis according to the International Classification of Headache Disorders, 3rd edition;[11] 2) pretreatment Bern SIH scores on contrast-enhanced brain MRIs;[12] and 3) spinal CSF leak detection using dynamic prone CT myelography (CTM) for ventral dural tears and decubitus CTM for ruptured meningeal diverticula and CVFs. The spinal CSF leak level was obtained in each patient, and the levels were further subdivided into cervical spine, upper thoracic spine (T1–T6 levels), lower thoracic spine (T7–T12 levels), and lumbar spine. In the setting of dural tears, the presence or absence of a calcified disc was specified. In the setting of ruptured meningeal diverticula and CVFs, the laterality was documented. Independent reviews of the myelograms were performed by 2 neuroradiologists with 8 and 11 years of experience with myelograms.

The sex, age, and BMI at the time of CSF leak diagnosis were recorded. To identify any differences in age, BMI, and spinal leak level among the 3 types of CSF leaks, we performed homoscedastic t tests (Excel; Microsoft), and P values < .05 were considered statistically significant. This same statistical analysis was also performed on the Bern SIH scores, though it was not a main analysis of our study. Before t test calculations, the Shapiro-Wilk test (https://www.statskingdom.com/shapiro-wilk-test-calculator.html) was calculated for each data set to determine the normal Gaussian distribution, with a test statistic (W) between 0.938 and 1 regarded as a normal distribution for our data set.

Last, a brief discussion on the type of CSF leak treatment will be mentioned and whether there was improvement of clinical symptoms. A detailed analysis of the treatment outcomes is beyond the scope of this article.

RESULTS

There were 65 total patients (37 women, 28 men) with spontaneous CSF leaks (Table). The mean Bern SIH scores in the patient cohorts with types 1, 2, and 3 CSF leaks were 5.4, 5.8, and 5.9, respectively. Type 1 CSF leaks (dural tears) were observed in 25 patients (mean age, 44.5 years; mean BMI, 24.3). Type 2 CSF leaks (ruptured meningeal diverticula) were observed in 4 patients (mean age, 45.5 years; mean BMI, 27.5). Type 3 CSF leaks (CVFs) were observed in 36 patients (mean age, 58.8 years; mean BMI, 27.0). Given the small sample and insufficient power of the type 2 leaks, this cohort was excluded from all statistical analysis. Type 1 and 3 leaks demonstrated normal Gaussian distributions for patient age (W = 0.952 type 1 and W = 0.957 type 3) and BMI (W = 0.985 type 1 and W = 0.977 type 3). Patient age and BMI were statistically significant between types 1 and 3 (P < .00001 and P = .015, respectively).

The BMIs were also compared with age- and sex-matched national BMI averages, and the range of type 1 CSF leak BMIs was 3.6–7 and 5.3–7.5, less than national average BMIs for males and females, respectively. The range of type 3 CSF leak BMIs was 0.6–4.1 and 0.1–5.6, less than the national average BMIs for males and females, respectively.[13] The Bern SIH scores were not statistically significant (P = .44).

For type 1 CSF leaks, the leak level was most commonly in the upper thoracic spine (18/25, 72%), and 9/25 (36%) were at the T1–T2 level. Twenty of 25 patients (80%) with type 1 leaks had an associated calcified disc. Type 2 CSF leaks occurred at the left T9–T10, right T10–T11, left T11–T12, and right T12–L1 levels. Type 3 CSF leaks were more commonly on the right side (26/36, 72%) and usually lower thoracic (T7–T12) in location (20/36, 56%). The spinal leak level was statistically significant between types 1 and 3 (P < .0002). Representative images of each spinal leak type are seen in the Figures 1–3.

Of the 25 patients with type 1 CSF leaks, all were treated with CT-guided blood and/or fibrin glue patches, and 6 patients had
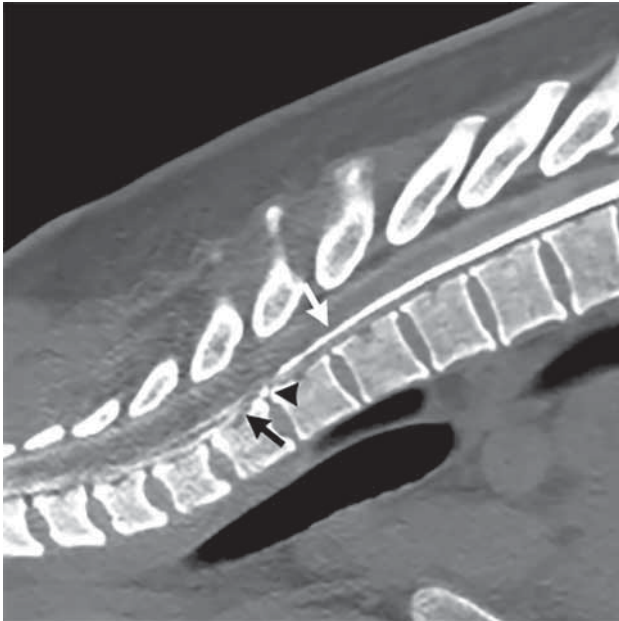
FIG 1. Type 1 CSF leak (dural tear): dynamic CT prone myelogram in the sagittal plane shows normal myelographic contrast in the subarachnoid space (*white arrow*) until there is a transition point at the T1–T2 level where there is a calcified disc (*black arrowhead*) that results in a split of contrast between the subarachnoid and ventral extradural spaces (*black arrow*).
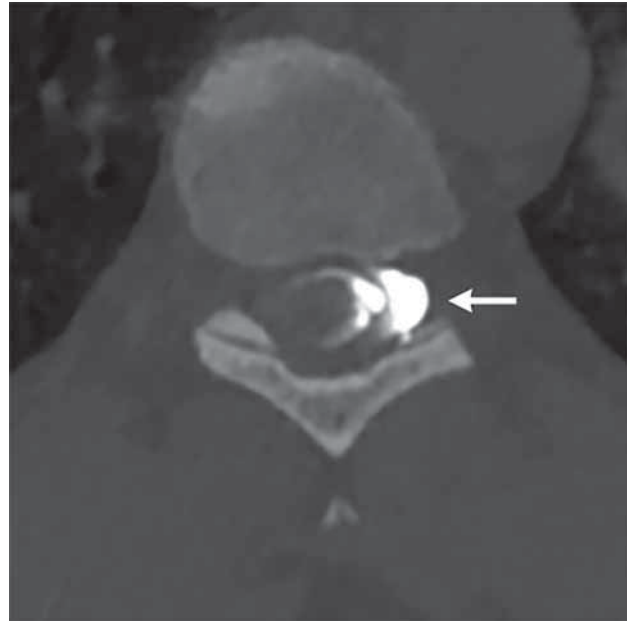

FIG 2. Type 2 CSF leak (ruptured meningeal diverticulum): left decubitus CT myelogram in the axial plane shows contrast leaking from the left T9–T10 meningeal diverticulum into the neural foramen (*arrow*).

surgical repair of the dural leak. All 4 patients with type 2 CSF leaks were treated with CT-guided fibrin glue patches. Of the 36 patients with type 3 CSF leaks, the initial 2 were treated with surgical ligation of the CVF and the remaining 34 were treated with CT-guided fibrin glue occlusion using the technique described in another publication.[14] All 65 patients had clinical improvement in symptoms.

DISCUSSION

Our study shows that age, BMI, and spinal leak level vary by spinal CSF leak type. Patients with type 1 CSF leaks (dural tears) are typically younger (mean age, 44.5 years) and have a normal BMI (mean, 24.3), while patients with type 3 CSF leaks (CVFs) are relatively older (mean age, 58.8 years) and have an elevated BMI (mean, 27.0). This easily obtained patient information could help provide guidance in the spinal CSF leak imaging pathway. Furthermore, type 1 CSF leaks were most common in the upper thoracic spine, and types 2 and 3 were most common in the lower thoracic spine.

Patients with type 1 CSF leaks had lower average BMIs than those patients with type 2 or 3 CSF leaks and also had lower BMIs than national averages. The type 1 patient characteristics match those in a smaller study that previously reported patient BMIs to be lower than the national average.[8] Furthermore, a majority of type 1 CSF leaks in our study were usually secondary to calcified discs or microspurs (80%) that resulted in dural tears. The thoracic spine was the most likely location in our study (92%), and this is supported with another study.[15] In our study, the upper thoracic spine at the T1–T2 level was the most common site (36%), and this high frequency of upper thoracic dural

leaks was also reported in at least 1 other study.[16] While thoracic disc-related leaks were observed more frequently in the upper thoracic spine, thoracic disc herniations, in general, are reported to more commonly occur in the lower thoracic spine, given that it has more mobility than the upper thoracic spine. Thoracic discs also have a high predisposition for calcification and dural tears.[17,18] We speculate that 1 possible reason that CSF leaks occur is due to the fixed biomechanics of the thoracic spine and the apposition of the dura to posterior vertebral bodies, given the normal kyphotic curvature.[19] In our study, patients with type 1 CSF leaks had normal BMIs, and some patients had BMIs as low as 18. We postulate that a lower BMI may be accompanied by less spinal epidural fat, thus acting as less of a protective barrier to the calcified discs, thereby resulting in a dural tear. Another publication has also proposed the same possibility,[8] but further studies are needed to verify this theory.

On the other hand, type 3 spinal CSF leaks generally occurred in overweight patients. It has been suggested that elevated spinal pressure or pre-existing idiopathic intracranial hypertension may be a potential etiology in some patients with CVFs, akin to the phenomenon that occurs with skull base leaks. This elevated pressure has also been postulated in the setting of de novo CVFs that occur after successful CVF treatment, whereby the elevated pressure is driving the creation of a new fistula.[20] Arachnoid granulations are closely related to paraspinal veins, and rupture of these granulations has been suggested as a possible inciting event of CVFs.[21] Overweight patients have a higher susceptibility to elevated CSF pressures, possibly accounting for this arachnoid granulation rupture, and this could explain why patients with CVFs are more common in this population. While BMIs in this cohort were in the overweight category, they were slightly less compared with national averages, and we suspect that our patient population
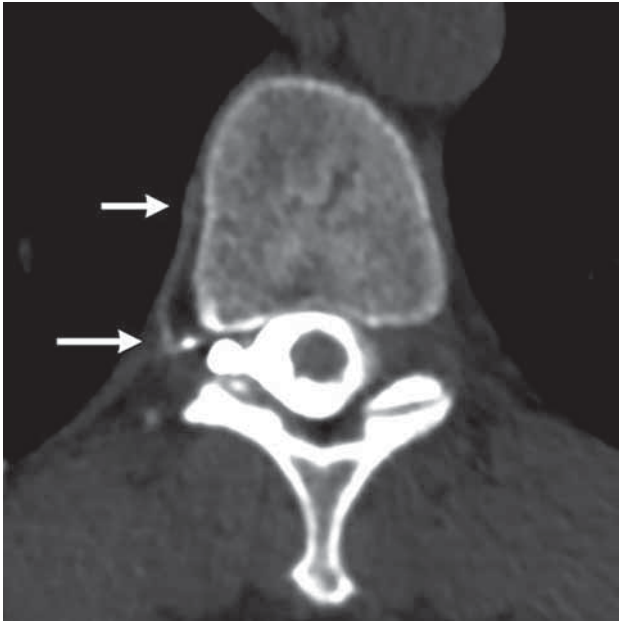
FIG 3. Type 3 CSF leak (CVF): right decubitus CT myelogram in the axial plane shows a paraspinal vein (*arrows*) that was contiguous with the right T10–T11 meningeal diverticulum.

in Northern California has lower BMIs than in the rest of the country, but this information was not readily available for accurate comparison. Last, type 3 spinal leaks were most common on the right side and the lower thoracic spine. This laterality and spinal location correspond to information in another study,[22] but a separate study has reported more CVFs on the left side.[21]

Type 2 spinal CSF leaks were the least common in our patient population. This finding contrasts with an older study that stated that type 2 leaks were the most common type of CSF leak.[1] In that study, it is possible that many of these type 2 leaks may have been CVFs arising from meningeal diverticula, which may not have been well-detected because decubitus myelographic techniques for CVFs were not discovered at that time.[23] In fact, CVFs were the most commonly detected CSF leak in our study, and with greater recognition of this entity, perhaps it will be the most common type of spinal leak. On the basis of the small number of patients in our study who had type 2 CSF leaks, it is difficult to make specific conclusions on age and BMI; however, the spinal levels in all 4 patients were the lower thoracic spine. This finding mirrors the most common location of CVFs, and we suspect that these 2 types of spinal leaks may have some similarities in pathogenesis.

The imaging pathway for CSF leak detection in patients with SIH varies per institution. In our spinal CSF leak program, after obtaining contrast-enhanced brain MR imaging, we perform a noncontrast total spine MR imaging with T2 fat-suppressed sequences to identify the presence or absence of an extradural collection. If there is a ventral extradural collection, we perform an ultrafast or dynamic prone CTM to identify the presumed dural tear. If the extradural collection is more eccentric on the MR imaging and there is concern for a ruptured meningeal diverticulum, we perform dynamic decubitus CTM to identify the ruptured meningeal diverticulum. If there is no extradural collection

on the spine MR imaging, we perform decubitus CTM to identify the CVF.

While an imaging pathway such as this one usually identifies the specific CSF leak type and cause, determining the pretest probability of the spinal leak type based on age and BMI could potentially provide guidance in this imaging work-up. For example, type 1 spinal leaks were more common in the upper thoracic spine; therefore, an adequate Trendelenburg angle is needed when performing the dynamic myelography to ensure that the contrast flows to the upper thoracic spine. This knowledge can help minimize unnecessary scans in the lower thoracic spine. In fact, on the basis of this knowledge of type 1 leaks, we have changed our dynamic prone CTM technique. We used to inject a small volume of preservative-free iohexol contrast (Omnipaque 300; GE Healthcare) in the lumbar spine (1–2 mL) and then scan the total spine from caudal to cranial, cranial to caudal, and caudal to cranial. However, we observed that the contrast did not always traverse the upper thoracic spine, and there was often no leak in the lower spine; therefore, the patient had unnecessary radiation. Currently, we inject 3 mL of contrast with 1 acquisition of the total spine. If there is no spinal leak identified in the lower spine, we inject 2–3 mL more and then scan a more cranial part of the spine with some overlap of the normal area in 1 acquisition. We repeat this process until we identify the CSF leak, administering a maximum of 10 mL. This technique has resulted in less radiation to patients than our initial technique. Thus, understanding the pretest probability of the spinal CFS leak type and location can help with the diagnostic work-up.

The recognition of mean age and BMI in patients with spinal CSF leaks may also help when the diagnosis of SIH is equivocal. Because there is no absolute imaging test or clinical symptom to exclude the diagnosis of SIH, some patients may undergo many imaging examinations, myelograms, and treatments, even if the diagnosis of SIH and spinal CSF leak is not definitive. These demographic features of age and BMI may represent additional data points to help with decision-making in this difficult-yet-not uncommon scenario.

Our study has limitations, including its retrospective nature. Second, we did not obtain opening pressures consistently in our patients, which could help provide additional information. Nevertheless, it is known that opening pressures are normal in most patients with CSF leaks,[24] and this datum point may not have added noteworthy information. Last, most of our patients were from 1 geographic state, which could result in differences in body habitus. Nonetheless, our hospital is a major tertiary referral center for our multihospital network consisting of >20 hospitals over a very large area; therefore, the population did have some geographic diversity.

CONCLUSIONS

Age and BMI may help predict the type of spinal leak in patients with SIH. In our study, we found that patients with dural tears (type 1) were typically younger and had normal BMIs, while patients with CVFs (type 3) were relatively older and had an elevated BMI. Type 1 leaks were more common in the upper thoracic spine, while type 2 and 3 leaks were more common in the lower thoracic spine. Further studies are needed to validate these

results, but this information may help guide the imaging work-up in spinal CSF leak detection.

REFERENCES

1. Schievink WI, Maya MM, Jean-Pierre S, et al. **A classification system of spontaneous spinal CSF leaks.** *Neurology* 2016;87:673–79 CrossRef Medline
2. Dobrocky T, Mosimann PJ, Zibold F, et al. **Cryptogenic cerebrospinal fluid leaks in spontaneous intracranial hypotension: role of dynamic CT myelography.** *Radiology* 2018;289:766–72 CrossRef Medline
3. Mamlouk MD, Ochi RP, Jun P, et al. **Decubitus CT myelography for CSF-venous fistulas: a procedural approach.** *AJNR Am J Neuroradiol* 2021;42:32–36 CrossRef Medline
4. Kim DK, Brinjikji W, Morris PP, et al. **Lateral decubitus digital subtraction myelography: tips, tricks, and pitfalls.** *AJNR Am J Neuroradiol* 2020;41:21–28 CrossRef Medline
5. Schievink WI. **Spontaneous intracranial hypotension.** *N Engl J Med* 2021;385:2173–78 CrossRef Medline
6. Carlton Jones L, Butteriss D, Scoffings D. **Spontaneous intracranial hypotension: the role of radiology in diagnosis and management.** *Clin Radiol* 2022;77:e181–94 CrossRef Medline
7. Schwartz N, Brown KD, Sasaki-Adams D, et al. **Multifocal skull base defects with associated spontaneous cerebrospinal fluid leaks.** *Otol Neurotol* 2021;42:e624–28 CrossRef Medline
8. Rosebrock RE, Diehn FE, Luetmer PH, et al. **Penetrating osseous spicules causing high-flow ventral CSF leaks in the setting of relatively low BMI: a preliminary study.** *Clin Neuroradiol* 2018;28:539–43 CrossRef Medline
9. Schievink WI, Maya M, Prasad RS, et al. **Spinal CSF-venous fistulas in morbidly and super obese patients with spontaneous intracranial hypotension.** *AJNR Am J Neuroradiol* 2021;42:397–401 CrossRef Medline
10. Farb RI, Nicholson PJ, Peng PW, et al. **Spontaneous intracranial hypotension: a systematic imaging approach for CSF leak localization and management based on MRI and digital subtraction myelography.** *AJNR Am J Neuroradiol* 2019;40:745–53 CrossRef Medline
11. **Headache Classification Committee of the International Headache Society (IHS) The International Classification of Headache Disorders, 3rd edition.** *Cephalalgia* 2018;38:1–211 CrossRef Medline
12. Dobrocky T, Grunder L, Breiding PS, et al. **Assessing spinal cerebrospinal fluid leaks in spontaneous intracranial hypotension with a scoring system based on brain magnetic resonance imaging findings.** *JAMA Neurol* 2019;76:580–87 CrossRef Medline
13. Fryar CD, Carroll MD, Gu Q, et al. **Anthropometric reference data for children and adults: United States, 2015-2018.** *Vital Health Stat* 2021;3:1–44 Medline
14. Mamlouk MD, Shen PY, Sedrak MF, et al. **CT-guided fibrin glue occlusion of cerebrospinal fluid-venous fistulas.** *Radiology* 2021;299:409–18 CrossRef Medline
15. Beck J, Ulrich CT, Fung C, et al. **Diskogenic microspurs as a major cause of intractable spontaneous intracranial hypotension.** *Neurology* 2016;87:1220–26 CrossRef Medline
16. Luetzen N, Dovi-Akue P, Fung C, et al. **Spontaneous intracranial hypotension: diagnostic and therapeutic workup.** *Neuroradiology* 2021;63:1765–72 CrossRef Medline
17. McInerney J, Ball PA. **The pathophysiology of thoracic disc disease.** *Neurosurg Focus* 2000;9:e1 CrossRef Medline
18. Gille O, Soderlund C, Razafimahandri HJ, et al. **Analysis of hard thoracic herniated discs: review of 18 cases operated by thoracoscopy.** *Eur Spine J* 2006;15:537–42 CrossRef Medline
19. Kranz PG, Luetmer PH, Diehn FE, et al. **Myelographic techniques for the detection of spinal CSF leaks in spontaneous intracranial hypotension.** *AJR Am J Roentgenol* 2016;206:8–19 CrossRef Medline
20. Malinzak MD, Kranz PG, Gray L, et al. **Postsurgical recurrence of CSF-venous fistulas in spontaneous intracranial hypotension.** *Neurol Clin Pract* 2021;11:e356–58 CrossRef Medline
21. Kranz PG, Amrhein TJ, Gray L. **CSF venous fistulas in spontaneous intracranial hypotension: imaging characteristics on dynamic and CT myelography.** *AJR Am J Roentgenol* 2017;209:1360–66 CrossRef Medline
22. Brinjikji W, Garza I, Whealy M, et al. **Clinical and imaging outcomes of cerebrospinal fluid-venous fistula embolization.** *J Neurointerv Surg* 2022 Jan 24. [Epub ahead of print] CrossRef Medline
23. Schievink WI, Maya MM, Moser FG, et al. **Lateral decubitus digital subtraction myelography to identify spinal CSF-venous fistulas in spontaneous intracranial hypotension.** *J Neurosurg Spine* 2019 Sept 13. [Epub ahead of print] CrossRef Medline
24. Kranz PG, Tanpitukpongse TP, Choudhury KR, et al. **How common is normal cerebrospinal fluid pressure in spontaneous intracranial hypotension?** *Cephalalgia* 2016;36:1209–17 CrossRef Medline

Surgical Ligation of Spinal CSF-Venous Fistulas after Transvenous Embolization in Patients with Spontaneous Intracranial Hypotension

W.I. Schievink, R.B. Tache, and M.M. Maya

ABSTRACT

SUMMARY: A spinal CSF-venous fistula is an increasingly recognized type of CSF leak that causes spontaneous intracranial hypotension. The detection of these fistulas requires specialized imaging such as digital subtraction myelography or dynamic CT myelography, and several treatment options are available. A novel treatment for these CSF-venous fistulas consisting of transvenous embolization with the liquid embolic agent Onyx has been described recently, but some patients require further treatment if embolization fails. The purpose of this study was to evaluate the safety and effectiveness of surgery following transvenous embolization. In a series of 6 consecutive patients who underwent surgical ligation of the fistula after endovascular embolization, there were no surgical complications. Postoperatively, complete resolution of symptoms was reported by 5 of the 6 patients, and brain MR imaging findings of spontaneous intracranial hypotension resolved in all patients. This study suggests that surgical ligation of spontaneous spinal CSF-venous fistulas after endovascular embolization is effective and safe.

ABBREVIATIONS: DSM = digital subtraction myelography; SIH = spontaneous intracranial hypotension; SIHDAS = SIH Disability Assessment Score

Spontaneous intracranial hypotension (SIH) is a condition characterized by low CSF volume in the craniospinal compartment.[1] The classic symptom is an orthostatic headache, but numerous other clinical manifestations have been reported.[1] With very rare exceptions,[2] the cause of SIH is a CSF leak at the level of the spine, and several types of spontaneous spinal CSF leaks have been identified.[3] The most recently recognized type of CSF leak is the CSF-venous fistula, which is a type of CSF leak not associated with the presence of extradural CSF and not visible on routine spine MR imaging or CT myelography.[3,4] Digital subtraction myelography (DSM) or dynamic CT myelography performed with the patient in the lateral decubitus position is the preferred method to identify these fistulas.[5-8] Since the first description of spontaneous spinal CSF-venous fistulas in 2014, many centers around the world have reported success with the identification and treatment of these fistulas.[4-8] In addition to epidural blood patching, several specific treatment options are available for these fistulas: percutaneous fibrin sealant injection,[9] transvenous embolization,[10] and microsurgical ligation of the fistula.[7,11] Excellent results with resolution of symptoms and abnormal findings on brain MR imaging have been reported for all 3 of

these treatment modalities. Transvenous embolization was first described by Brinjikji et al,[10] in 2021, and is the most recently developed treatment option, with excellent results reported in up to 80% of patients.[12] Surgical ligation of the CSF-venous fistula is an option if embolization fails. The purpose of this study was to evaluate the safety and effectiveness of an operation following transvenous embolization.

MATERIALS AND METHODS

This study was approved by the Cedars-Sinai Medical Center institutional review board.

Using a registry that has been prospectively maintained since January 2001 at our quaternary referral center for SIH, we identified all patients with SIH who underwent surgical ligation of a CSF-venous fistula following transvenous embolization with Onyx (Covidien). The diagnosis of SIH was based on the criteria of the International Classification of Headache Disorders, third edition,[13] with minor modifications. These criteria require objective evidence of SIH, consisting of brain MR imaging showing stigmata of SIH (eg, pachymeningeal gadolinium enhancement or brain sagging), spinal imaging showing a CSF leak (ie, the presence of extradural CSF or a CSF-venous fistula), or low CSF opening pressure (ie, <6.0 cm of CSF). The modification consists of also including patients who do not have headaches but whose symptoms are best explained by SIH.

All patients underwent brain MR imaging and MR myelography (heavily T2-weighted MR imaging). Brain MR imaging was

scored for the following findings typical of SIH: subdural fluid collections, enhancement of pachymeninges, engorgement of venous structures, pituitary enlargement, and sagging of the brain.[14] Specifics of the MR myelography technique are reported elsewhere.[15] For DSM, the technique as described by Hoxworth et al[16] was used with some minor modifications. Briefly, DSM is performed with the patient under general endotracheal anesthesia with deep paralysis and suspended respiration for maximal detail and temporal resolution. Patients are positioned in the lateral decubitus position in a biplane angiography suite, with tilt table capability. Pillows or foam padding are placed to optimize the cervicothoracic alignment. A fluoroscopically-guided lumbar puncture is performed with a 22-ga needle. An opening pressure is obtained at this time using standard manometry. Then, an accurate needle position is confirmed with an injection of 0.5 mL of iohexol (Omnipaque; GE Healthcare).

Patients are then further positioned on the basis of the area of interest by tilting the table to achieve contrast flow to the cervicothoracic spine. Great care is taken to maximize contrast opacification of the lateral dural sac by adjusting the degree of tilting to a patient-specific spinal curvature and anatomy. Finally, contrast is injected manually, 1 mL per second, with suspended respiration for 40–120 seconds while acquiring biplane subtraction images at 1–2 frames per second. All imaging studies (ie, brain MR imaging, MR myelography, and DSM) were analyzed by a board-certified neuroradiologist and a board-certified neurosurgeon. Any discrepancies were adjudicated by a second board-certified neuroradiologist.

For transvenous embolization, the technique as described by Brinjikji et al[10,12] was used. Briefly, the right common femoral vein was punctured to access the inferior vena cava. A 6F Benchmark guide catheter (Penumbra) was then advanced to the azygous vein with a coaxial technique using an inner 5F Select Berenstein catheter (Boston Scientific) and Terumo guidewire. A double-lumen (Eclipse 2L; MedLine Group) or single-lumen (Scepter XC; MicroVention) balloon microcatheter with a Synchro2 (Stryker) or

Hybrid (Balt) microwire was used to access the paraspinal vein at the level of the fistula determined by DSM. The balloon microcatheter was positioned close to the neuroforaminal venous network, and Onyx-18 was injected slowly with the balloon inflated to prevent reflux into the azygous vein.

The surgical technique consisted of a hemilaminotomy and foraminotomy, exposing the lateral common thecal sac and exiting the nerve root sleeve. A titanium Yasargil aneurysm clip (B Braun) was then placed over the fistulous connection, or the fistula was coagulated with bipolar electrocautery if the fistula could be visualized, or a titanium aneurysm clip was placed over the nerve root sleeve without dividing the underlying nerve root. The operation did not require any modification from that used for CSF-venous fistulas not previously treated with endovascular embolization.

All patients (or their family/caregivers) completed a modified Migraine Disability Assessment score questionnaire to assess the severity of the symptoms before and after the last treatment.[17] The modification consists of substituting "symptoms of SIH" for "headaches." We refer to this modified questionnaire as the SIH Disability Assessment Score (SIHDAS) questionnaire. A score of 0–5 (grade I) is considered to equate to little or no disability, 6–10 (grade II) is mild disability, 11–20 (grade III) is moderate disability, and >20 (grade IV) is severe disability.

RESULTS

The mean age of the 4 women and 2 men was 64 years (range, 44–79 years). An orthostatic headache was the principal symptom in 5 patients, and 1 patient presented with coma. Disability as measured by the SIHDAS score varied from mild to severe (SIHDAS score grade II in 2 patients, grade III in 2 patients, and grade IV in 2 patients). The initial brain MR imaging findings were normal in 1 patient and showed the typical changes of SIH in 5 patients. The MR imaging findings consisted of pachymeningeal enhancement only in 1 patient; pachymeningeal enhancement and pituitary enlargement in 1 patient; pachymeningeal enhancement, venous dilation, and pituitary enlargement in 1 patient; subdural hematomas, pachymeningeal enhancement, pituitary enlargement, and brain sagging in 1 patient; and pachymeningeal enhancement, venous dilation, pituitary enlargement, and brain sagging in 1 patient. All patients had undergone bilateral lateral decubitus DSMs. Opening pressures ranged from 4 to 15 cm of CSF (<6 cm of CSF in 2 patients). Four patients had a single CSF-venous fistula, and 2 patients had bilateral CSF-venous fistulas for a total of 8 CSF-venous fistulas: Three fistulas were right-sided, and 5 fistulas were left-sided (Fig 1). All CSF-venous fistulas were located in the thoracic spine. Epidural blood patching was the initial treatment in all patients, with excellent-but-temporary relief of
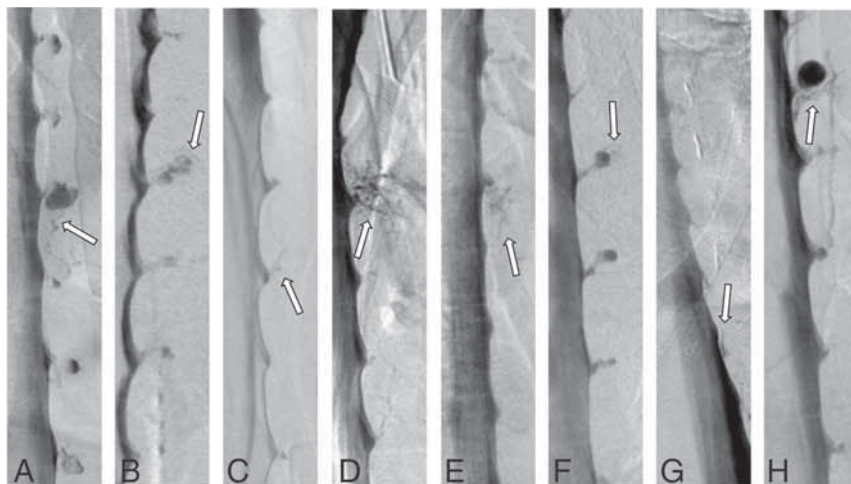

FIG 1. Lateral decubitus DSMs showing 8 spontaneous spinal CSF-venous fistulas (arrows) in 6 patients. A, A right T8 fistula. B, A left T1 fistula. C, A left T8 fistula. D, A right T5 fistula. E, A left T7 fistula. F, A left T6 fistula. G, A left T11 fistula. H, A right T3 fistula. A and B and C and D, Bilateral fistulas in 2 patients. Multiple CSF-venous fistulas are found in about one-tenth of patients.[18]
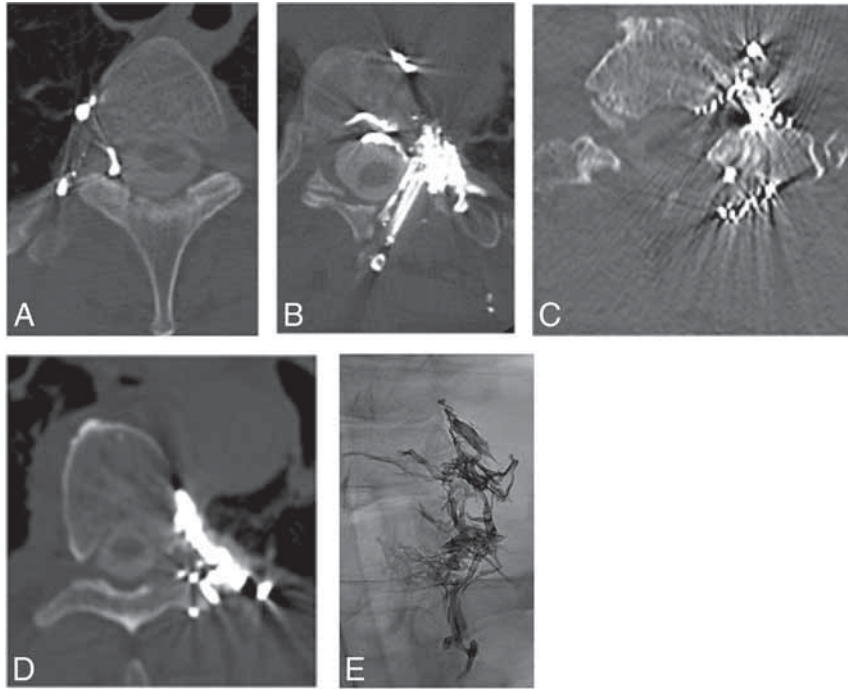
FIG 2. Post-transvenous embolization CT scans (*A–D*) and an anterior-posterior radiograph (*E*) showing Onyx within the neural foramen in 4 patients (*A–C* and *E*) and just outside the neural foramen in 1 patient (*D*). The CT scan in *B* shows the results after surgical clip ligation following transvenous embolization.
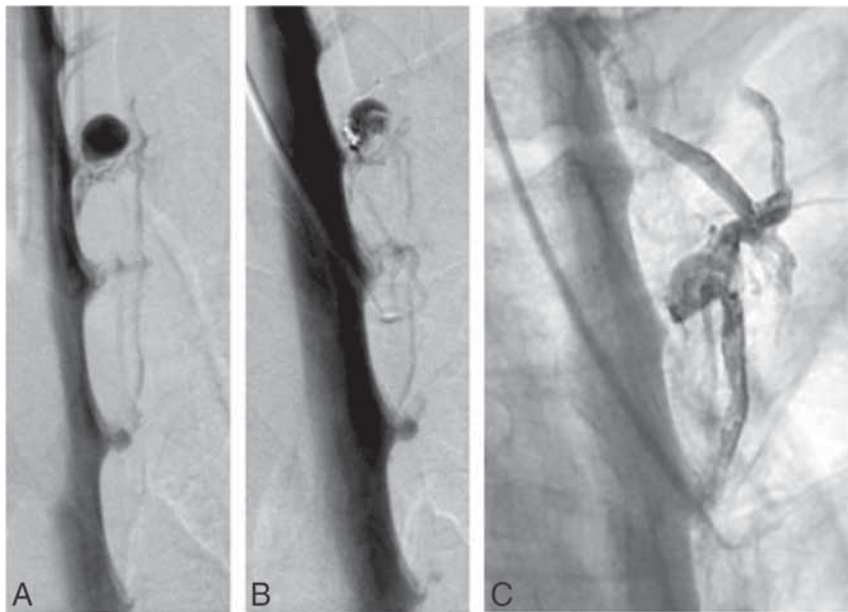

FIG 3. *A* and *B,* Pre-transvenous embolization lateral decubitus DSM and post-transvenous embolization lateral decubitus DSM showing a residual/recurrent CSF-venous fistula. Anterior-posterior post-transvenous embolization radiograph (*C*) shows the distribution of intravascular Onyx.

embolization as a treatment technique. The operation following endovascular treatment was performed between July 2021 and February 2022.

Transvenous embolization was performed at our institution in 5 patients and at another institution in 1 patient. In 1 patient, the targeted paraspinal vein thrombosed during the embolization procedure, and Onyx could not be delivered. Onyx was successfully delivered in the other 5 patients, including within the veins of the neural foramen in 4 patients (Fig 2). There were no procedural complications, and all patients reported initial improvement of symptoms, including the patient with paraspinal vein thrombosis. After recurrence of symptoms, DSM was repeated in 3 of the 6 patients before surgical ligation of the recurrent/residual CSF-venous fistula (Fig 3). There was no evidence of recruitment of fistulous vascular connections from adjacent spinal levels.

An operation was performed between 1 and 6 months after the transvenous embolization (mean, 5 months). At the operation, variable amounts of Onyx could be visualized surrounding the nerve root sleeve in all 4 patients who had Onyx delivered within the neural foramen (Fig 4). The Onyx-filled vasculature was compressible and was easily resected from around the nerve root sleeve. These maneuvers allowed unobstructed visualization and clip placement over the nerve root for noneloquent thoracic nerve roots (3 patients) and direct visualization and subsequent clip placement and bipolar coagulation of the fistulous site itself for a CSF-venous fistula of the first thoracic nerve root in 1 patient. Uneventful clip ligation of the nerve root was also recorded for the 2 patients who did not have Onyx delivered within the neural foramen. There were no surgical complications and resolution of symptoms was reported by 5 of the 6 patients (grade I on the SIHDAS scale), while 1 patient had residual symptoms of SIH (grade III on the SIHDAS scale). Clinical follow-up ranged from 1 to 6 months (mean, 4 months). Before the surgical procedure, brain MR imaging findings had normalized in 3 of the 6 patients. Postoperatively, resolution of brain MR imaging findings of SIH was noted for the remaining 3 patients as well.
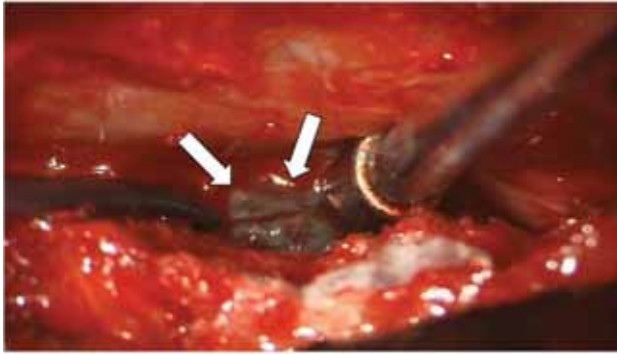
symptoms in 4 patients, and no symptom improvement in 2 patients. Six of the 8 CSF-venous fistulas in 6 patients were treated with transvenous embolization. The other 2 CSF-venous fistulas were treated with only surgical ligation before the development of

FIG 4. Intraoperative photograph showing Onyx (*arrows*) within the epidural veins.

DISCUSSION

Patients and their health care providers are fortunate that the armamentarium for treating spontaneous spinal CSF-venous fistula is expanding. In the absence of any data from robust randomized trials, it is likely that all 3 specific treatment options will remain viable, at least in the foreseeable future. In this study, we found that an operation after transvenous embolization is effective and safe. Complete symptom resolution was obtained in all except 1 patient, and there were no surgical complications.

The best results of transvenous embolization are obtained when Onyx is placed within the veins of the neural foramen. Onyx is an intravascular embolic agent that is permanent and could hinder surgical dissection around the nerve root sleeve. We found that at the operation, the Onyx was compressible and easily resectable, allowing undisturbed surgical dissection and clip ligation of the fistula. Another concern of embolization is that with subtotal occlusion of the fistula, recruitment of new fistulous connections could occur at adjacent spinal levels, but we did not observe that in any of the presently reported patients who underwent repeat DSM following unsuccessful embolization before surgical clip ligation.

Our study has several limitations. It represents a highly selected group of patients referred to a quaternary referral center for SIH, and the generalizability of our findings is unknown. The number of patients was relatively small, and follow-up ranged from only 1 to 6 months. However, transvenous embolization of spontaneous spinal CSF-venous fistulas is a recently developed technique that was first reported in 2021[10] and was first used in our institution in February 2021.

CONCLUSIONS

In this series of patients with SIH who underwent surgical ligation of a spinal CSF-venous fistula following transvenous embolization, surgery was effective and safe.

Disclosure forms provided by the authors are available with the full text and PDF of this article at www.ajnr.org.

REFERENCES

1. Schievink WI. **Spontaneous intracranial hypotension.** *N Engl J Med* 2021;385:2173–78 CrossRef Medline
2. Schievink WI, Michael LM, II, Maya M, et al. **Spontaneous intracranial hypotension due to skull-base CSF leak.** *Ann Neurol* 2021;90:514–16 CrossRef Medline
3. Schievink WI, Maya MM, Jean-Pierre S, et al. **A classification system of spontaneous spinal CSF leaks.** *Neurology* 2016;87:673–79 CrossRef Medline
4. Schievink WI, Moser FG, Maya MM. **CSF-venous fistula in spontaneous intracranial hypotension.** *Neurology* 2014;83:472–73 CrossRef Medline
5. Farb RI, Nicholson PJ, Peng PW, et al. **Spontaneous intracranial hypotension: a systemic imaging approach for CSF leak localization and management based on MRI and digital subtraction myelography.** *AJNR Am J Neuroradiol* 2019;40:745–53 CrossRef Medline
6. Kranz PG, Gray L, Amrhein TJ. **Decubitus CT myelography for detecting subtle CSF leaks in spontaneous intracranial hypotension.** *AJNR Am J Neuroradiol* 2019;40:754–76 CrossRef Medline
7. Schievink WI, Maya MM, Moser FG, et al. **Lateral decubitus digital subtraction myelography to identify spinal CSF-venous fistulas in spontaneous intracranial hypotension.** *J Neurosurg Spine* 2019;31:902–05 CrossRef Medline
8. Carlton JL, Goadsby PJ. **Same-day bilateral decubitus CT myelography for detecting CSF-venous fistulas in spontaneous intracranial hypotension.** *AJNR Am J Neuroradiol* 2022:43:645–48 CrossRef Medline
9. Mamlouk MD, Shen PY, Sedrak MF, et al. **CT-guided fibrin glue occlusion of cerebrospinal fluid-venous fistulas.** *Radiology* 2021;299:409–18 CrossRef Medline
10. Brinjikji W, Savastano LE, Atkinson JL, et al. **A novel endovascular therapy for CSF hypotension secondary to CSF-venous fistulas.** *AJNR Am J Neuroradiol* 2021;42:882–87 CrossRef Medline
11. Wang TY, Karikari IO, Amrhein TJ, et al. **Clinical outcomes following surgical ligation of cerebrospinal fluid-venous fistula in patients with spontaneous intracranial hypotension: a prospective case series.** *Oper Neurosurg (Hagerstown)* 2020;18:239–45 CrossRef Medline
12. Brinjikji W, Garza I, Whealy M, et al. **Clinical and imaging outcomes of cerebrospinal fluid-venous fistula embolization.** *J Neurointerv Surg* 2022 Jan 24. [Epub ahead of print] CrossRef Medline
13. **Headache Classification Committee of the International Headache Society (IHS) The International Classification of Headache Disorders, 3rd edition.** *Cephalalgia* 2018 38:1–211 CrossRef Medline
14. Schievink WI. **Spontaneous spinal cerebrospinal fluid leaks and intracranial hypotension.** *JAMA* 2006;295:2286–96 CrossRef Medline
15. Tay ASS, Maya M, Moser FG, et al. **Computed tomography vs heavily T2-weighted magnetic resonance myelography for the initial evaluation of patients with spontaneous intracranial hypotension.** *JAMA Neurol* 2021;78:1275–76 CrossRef Medline
16. Hoxworth JM, Patel AC, Bosch EP, et al. **Localization of rapid CSF leak with digital subtraction myelography.** *AJNR Am J Neuroradiol* 2009;30:516–19 CrossRef Medline
17. Stewart WF, Lipton RB, Kolodner K, et al. **Reliability of the migraine disability assessment score in a population-based sample of headache sufferers.** *Cephalalgia* 1999;19:107–14 CrossRef Medline
18. Schievink WI, Maya MM, Moser FG, et al. **Multiple spinal CSF leaks in spontaneous intracranial hypotension: do they exist?** *Neurol Clin Pract* 2021;11:e691–97 CrossRef Medline
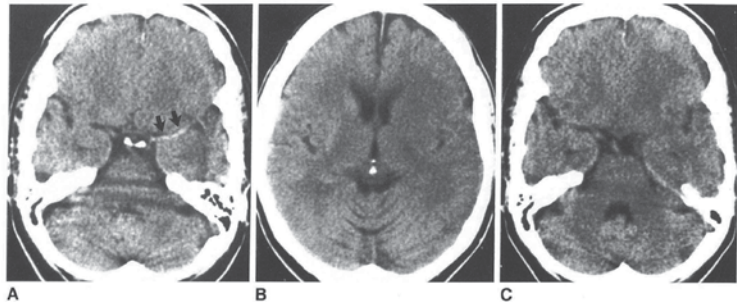
Celebrating 35 Years of the AJNR
July 1987 edition

An Early CT Sign of Ischemic Infarction: Increased Density in a Cerebral Artery

Barry D. Pressman[1]
E. James Tourje[1]
Joseph R. Thompson[2]

The diagnosis of ischemic cerebral infarction by CT usually is not poss__ hr after the event. A sign that allows earlier diagnosis is increased densit__ vessel secondary to a thrombus or embolus. We report 19 cases of incr__ in a middle cerebral artery or one of its major branches visible on the init__ patients subsequently clinically proven to have suffered a cerebrovascul__ three cases angiography confirmed the presence of embolus or thromb__ the CT scans. In several cases subsequent CT scans showed the densit__ thereby confirming its nature as thrombus or embolus. Recognition of t__ allow earlier diagnosis of ischemic infarction, which may be important i__ appropriate therapeutic regimen.

The early diagnosis of ischemic infarction by CT depends on the r__ often subtle changes of reduced attenuation and slight mass effect __ of cerebral infarction that may be present shortly after the ictus is incr__ in a major cerebral artery. Gacs et al. [3] reported this finding in a __ study, and they considered it most likely secondary to intraluminal cl__ We have found this sign to be useful in the early recognition of no__ cerebral infarction. It has been seen in a number of patients in the fir__ the ictus, and frequently it is the only CT finding or is an important __ finding in association with other subtle changes of infarction.

Carotid Cavernous Fistulae: Indications for Urgent Treatment

Van V. Halbach[1]
Grant B. Hieshima[1]
Randall T. Higashida[1]
Murray Reicher[2]

Angiographic and clinical data from 155 patients with carotid cavernou__ retrospectively reviewed to determine angiographic features associated__ risk of morbidity and mortality. These features included presence of a ps__ large varix of the cavernous sinus, venous drainage to cortical veins, an__ venous outflow pathways distant from the fistula. Clinical signs and __ characterized a hazardous carotid cavernous fistula included increas__ pressure, rapidly progressive proptosis, diminished visual acuity, he__ transient ischemic attacks. Cortical venous drainage from the carotid c__ is secondary to occlusion or absence of the normal venous outflow p__ associated with signs and symptoms of increased intracranial pressure a__ risk of intraparenchymal hemorrhage. Angiographic demonstration of a c__ varix, with extension of the sinus into the subarachnoid space, is ass__ increased risk of fatal subarachnoid hemorrhage. Identification of thes__ tures provides a basis for making decisions about treatment.
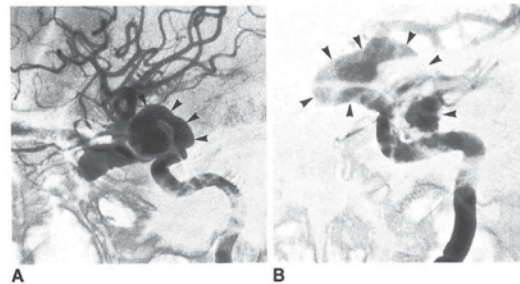
Carotid cavernous fistulae (CCFs) are spontaneous or acquire__ between the carotid artery and the cavernous sinus, and can be clas__ or indirect. Direct connections between the internal carotid artery a__ sinus may occur as a consequence of trauma, ruptured intracav__ aneurysms, collagen deficiency syndromes, arterial dissection, fibromuscular dys__ plasia, and direct surgical trauma [1–10]. Indirect fistulae are usually supplied from__ dural branches of the external carotid artery but can be supplied from dural __ branches of the internal carotid artery. Although the cause is often unknown, __ factors associated with the development of indirect fistulae include pregnancy, __ sinusitis, trauma, surgical procedures, and cavernous sinus thrombosis. Symptoms__ caused by CCFs are related to their size, duration, location, adequacy and route__ of venous drainage, and presence of arterial and venous collaterals [11].

Surgical and angiographic techniques that have been described for the closure __ of CCFs include carotid occlusion; trapping procedures; direct surgical exposure__ and closure; and embolization with muscle, glue, thrombus, wires, and, more__ recently, detachable balloons [12–19].

Unfortunately, the natural history of CCFs is incompletely understood. Sponta-__ neous closure, which is more common in indirect than direct CCFs, as well as__ closure following diagnostic angiography, has been documented by Seeger et al.__ [20]. Carotid compression therapy has been successful in closure of 17% of direct__ and 30% of indirect CCFs [21]. While aggressive forms of therapy may be__ successful in closure of CCFs, no technique is without risk. Ideally, the decision to__ institute a potentially hazardous treatment should be based on full understanding__ of the disease's natural history.

To identify those patients whose poor natural history mandated the need for__ emergent or aggressive therapy, we evaluated the angiographic and clinical data__ from 155 patients with CCFs. The delineation of high-risk features enables rational__ choices to be made regarding the timing and method of treatment.